ISSN 2542-1565

Vol. 18 2025 No. 02

GEOGRAPHY ENVIRONMENT SUSTAINABILITY

«The journal GEOGRAPHY, ENVIRONMENT, SUSTAINABILITY was founded in 2008 by Russian Geographical Society, the Lomonosov Moscow State University Geography Department, and the Russian Academy of Sciences Institute of Geography. Since that time the journal publishes **4 issues per year**, containing original research papers and reviews. The journal issues are open source and distributed through subscriptions, library exchanges of leading universities, and via the website through the world»

FOUNDERS OF THE JOURNAL: Russian Geographical Society, Faculty of Geography, Lomonosov Moscow State University and Institute of Geography of the Russian Academy of Sciences

The journal is published with financial support of the Russian Geographical Society.

The journal is registered in Federal service on supervision of observance of the legislation in sphere of mass communications and protection of a cultural heritage. The certificate of registration: ПИ № ФС77-67752, 2016, December 21.

PUBLISHER
Russian Geographical Society
Moscow, 109012 Russia
Novaya ploshchad, 10, korp. 2
Phone 8-800-700-18-45
E-mail: press@rgo.ru
www.rgo.ru/en

EDITORIAL OFFICE
Lomonosov Moscow State University
Moscow 119991 Russia
Leninskie Gory, 1,
Faculty of Geography, 1806a
Phone 7-495-9391552
Fax 7-495-9391552
E-mail: ges-journal@geogr.msu.ru
www.ges.rgo.ru

DESIGN
Layout designer: Tereshkin Anton
Moscow, 115088,
26 Simonovsky Val str., bldg. One
Phone: +7 (903) 108-04-44
E-mail: smile.tai@gmail.com

DOI prefix: 10.24057

Format A4 (210x297mm)

"GEOGRAPHY, ENVIRONMENT, SUSTAINABILITY" is the only original English-language journal in the field of geography and environmental sciences published in Russia. It is supposed to be an outlet from the Russian-speaking countries to Europe and an inlet from Europe to the Russian-speaking countries regarding environmental and Earth sciences, geography and sustainability. The main sections of the journal are the theory of geography and ecology, the theory of sustainable development, use of natural resources, natural resources assessment, global and regional changes of environment and climate, social-economical geography, ecological regional planning, sustainable regional development, applied aspects of geography and ecology, geoinformatics and ecological cartography, ecological problems of oil and gas sector, nature conservations, health and environment, and education for sustainable development.

Date of publication: March 31st, 2025.

EDITORIAL BOARD

EDITORIAL OFFICE

CONTENTS

RESEARCH PAPER

TRANSPORTATION AND URBAN FUNCTIONS' PLANNING IN THE CITY OF BÉJAÏA, ALGERIA: IMPROVING ENVIRONMENT AND LIFE QUALITY WITH A VIEW TO LAND VALORIZATION

Amira K. Bakour[1*], Ratiba Baouali[1], Nedjima Mouhoubi[2], Sofiane Bounouni[2]

[1]LREAU Laboratory (Laboratoire de Recherche et Etudes en Aménagement et Urbanisme), Department of Geography and Territorial Planning, Faculty of Earth Sciences, Geography and Territorial Planning (FSTGAT), University of Sciences and Technology Houari Boumediene (USTHB), BP 32 Bab Ezzouar, Algiers, 16111, Algeria

[2]Department of Architecture, Faculty of Technology, Abderrahmane Mira University, Targa Ouzemmour Road, Béjaïa, 06000, Algeria

***Corresponding author:** abakour@usthb.dz

Received: February 13th 2024 / Accepted: April 7th 2025 / Published: June 30th 2025

https://doi.org/10.24057/2071-9388-2025-3257

ABSTRACT. Several Algerian cities are increasingly experiencing notable traffic congestion due to the unequal distribution of urban functions. This research specifically analyses and assesses the urban functions planning's impacts on transportation in Béjaïa city, as well as the consequences of the traffic generated on the environment and citizens' life quality. For such objectives, the study analyzed the distribution of trip-generating activities, the adequacy of their planning with the urban transport network, and the inhabitants' perceptions regarding the environment and life quality. To this end, the study employed a mixed-methods approach for data collection and analysis. This methodology includes qualitative field observations and quantitative data collected through questionnaire surveys. The results indicated a significant correlation between the urban functions' planning and the generated traffic flows. The zoning observed in Béjaïa generates a disconnection between origin and destination, leading to longer distances traveled and a deteriorated environment. Indeed, around 80% of the respondents expressed dissatisfaction with the location of Béjaïa's urban functions and life quality. Thus, it is recommended to revise zoning regulations, reevaluate industrial zones, improve the mobility plan sustainably, and promote community participation in the urban planning process. These research findings serve as a reference for researchers and decision-makers to enhance future urban planning in Béjaïa and other cities around the world.

KEYWORDS: environment and life quality, land valorization, transportation, urban functions' planning, Béjaïa city

CITATION: Bakour A. K., Baouali R., Mouhoubi N., Bounouni S. (2025). Transportation And Urban Functions' Planning In The City Of Béjaïa, Algeria: Improving Environment And Life Quality With A View To Land Valorization. Geography, Environment, Sustainability, 2 (18), 6-19

https://doi.org/10.24057/2071-9388-2025-3257

ACKNOWLEDGEMENTS: The authors would like to thank all the residents and users of Béjaïa city who responded to the questionnaire surveys and all the department employees who helped us in the data collection.

Conflict of interests: The authors reported no potential conflict of interests.

INTRODUCTION

The significant majority of developing regions around the world, including Algeria, are continuously affected by accelerated urbanization, leading to the deterioration of urban life (Aggoune 2024; Meddour 2022). Thus, the city of Béjaïa, situated in northern Algeria, is an evolving urban space facing several challenges related to transportation and urban planning. In many cities, the latter is determined by land-use zoning (Chin et al. 2024). It organizes the disposition of inhabitants, activities, works, and means of communication in accordance with regulations and programs aimed at the well-being of the citizens (Haghani et al. 2023; Merlin and Choay 2010).

Urban functions assign specificities to the city and provide land reserves. As indicated by Zhou (2022), residents' urban life is mainly defined by residential, employment, entertainment, and leisure functions. Additionally, urban structures include industrial, traffic, and commercial functions (Hu et al. 2020; Zhou et al. 2020). Business and service functions also contribute to the vibrancy of city centers (Niu and Silva 2021) by initiating economically dynamic policies, such as family businesses and startups (Andabayeva et al. 2024). The function therefore emanates from the numerous activities that characterize it. These activities adapt to urban life requirements given the spatial distribution of the facilities (Chin et al. 2024). The intermediate objective of studying this distribution is to achieve a deeper understanding of the intra-urban supply

of services and activities as it has evolved throughout time (Erraougui 2023). In Portland, Oregon, there is a focus on encouraging mixed-use projects through zoning and land use regulations with the aim of promoting healthier cities, as they facilitate walking and riding bikes (Raea et al. 2020). The presence of these urban functions on the territory of a city, including Béjaïa, influences, to a large extent, its image and the life quality of its users.

The enhancement of quality of life is increasingly crucial for a global urban population that is expanding as a result of accelerated urbanization processes (Mouratidis 2021). Nowadays, the urban quality of life is measured through aspects beyond the limit of the variety of activities (administrative, educational, cultural, etc.). These include proximity to services and jobs, environmental quality, a sense of security, as well as access to public transport and smart mobility technologies. A case in point is Vienna, which is recognized as one of the most livable cities worldwide (Haas 2024)[1]. This city is favoring health and efficiency by embracing innovations and new technologies in mobility. In Algeria, Article 03 of Law 11-04 of February 17, 2011, laying down the rules governing the activity of real estate development, highlights the necessity for upgrading viability networks and enhancing outdoor common areas (Guerroudj 2017).

Transportation systems are also intrinsically linked to the urban functions, facilitating circulation and accessibility, according to Le Corbusier (Denèfle et al. 2006)[2]. This relationship has led to several research studies. They focus on exploring the effects of urban sprawl on displacement behavior by conducting a household survey in 2018 in Béjaïa (Bounouni et al. 2020). In addition, previous studies employed a mixed-methods approach to evaluate the relationship between urban transport policies and the self-reported needs of citizens in Port Louis, Mauritius (Thondoo et al. 2020). Their findings demonstrated that citizen-centered approaches allow the review of urban transport planning policies, thus promoting healthier and more equitable cities in developing countries. These outcomes may be of significant relevance to Algerian cities, with particular applicability in Béjaïa. The contributions also highlight the need to review urban systems and their mobility requirements (Baklanov et al. 2021). Such goals can be achieved by managing the existing infrastructure through traffic regulation (Khelf 2021). For example, Medellin, in Colombia, implemented an effective urban transport policy by means of a metro-cable system. This has encouraged the development of informal neighborhoods (Klouche 2019). Traffic flows are higher in mixed zones with significant commercial activities (Al Tal et al. 2022). Accordingly, the researchers were interested in examining the feasibility of reducing car travel by modifying land use rules. Consequently, the supply of transport conditions the configuration of rapidly urbanizing regions, as is the case in Béjaïa.

The field of urban transportation planning has notably evolved in response to accelerated urbanization. Recent literature emphasizes the fundamental role of smart transportation systems in improving mobility and city livability. The concept of Mobility-as-a-Service (MaaS) enables the users to access real-time information about available transport options and thereby reduces private car use (Signor et al. 2019). Moreover, the 15-minute city has emerged to manage the main daily activities of the citizens within a short distance, as is the case in Paris (UN-Habitat 2022). It therefore reduces traffic congestion and promotes social cohesion (University College of Estate Management 2024)[3]. Since they enhance access to essential services and reduce the negative effects of excessive motorization, implementing these approaches in Béjaïa could improve the environment and life quality.

The literature has considerably expanded on transportation systems and environmental quality. The expansion of urban fabrics has led to increased motorization, contributing primarily to air pollution and greenhouse gas emissions (Universitas Gadjah Mada 2020)[4]. Effective urban transport planning may assist in addressing these issues. The integration of sustainable transport policies consistently resulted in reduced air pollution and improved public health (Hoen et al. 2021). The green infrastructure (pedestrian pathways and parks) offers ecological advantages, as it encourages active transportation modes. Furthermore, researchers state that efficient public transportation planning can alleviate traffic congestion and consequently private car reliance (Litman 2024). Urban transport planners aim to design transport networks prioritizing pedestrians' and cyclists' accessibility. In Addis Ababa, Ethiopia, the Scaling Up Safe Street Designs has addressed road safety and environmental issues (UN-Habitat 2022). The project emphasizes the value of walking and cycling for all residents, including people with disabilities. These transport systems have the potential to preserve the environment and ensure economic growth in developing regions, such as Béjaïa.

The urban fabric in the city of Béjaïa is characterized by a large number of dysfunctions, resulting in the emergence of socio-spatial segregation (Attar and Saraoui 2022). The latter can influence social cohesion and urban development. This phenomenon of urban dysfunction and socio-spatial segregation is profoundly exacerbated by inadequate transport infrastructure. It is observed in numerous cities around the world, as a result of the separation of different social groups due to unequal access to housing quality, services, and employment (Najib 2017). The same author's study has found that this phenomenon of dysfunction manifests in Besançon, Mulhouse, and Strasbourg (France). Populations in neighborhoods are disadvantaged given the presence of social housing and poor urban amenities. In England and Wales, the creation of deeply socio-spatial structures is a result of the highest levels of income inequality (Nieuwenhuis et al. 2020). The urban design in Tehran influences segregation outcomes by interfacing with physical space and social dynamics (Shamskooshki 2021). The Afro-Ecuadorian population in Machala, Ecuador, is experiencing significant disparities, resulting in inadequate housing and urban infrastructure (Uzcátegui-Sánchez et al. 2023). Therefore, the socio-spatial dynamics of cities are profoundly linked to urban transportation. The provision of appropriate transport infrastructure in Béjaïa can foster social cohesion and improve its population's

[1]Haas C. U. (2024). Smart Cities: 6 Pioneers Leading the Way in Transforming Transportation. [online] Available at: https://www.linkedin.com/pulse/smart-cities-6-pioneers-leading-way-transforming-christian-u-haas-gbloe?trk=public_post [Accessed 19 Jan. 2025].
[2]Denèfle S., Bresson S., Dussuet A., and Roux N. (2006). Living, Le Corbusier: Social practices and architectural theory. [online] Open Edition books. (In French with English summary). Available at: https://books.openedition.org/pur/12487 [Accessed 10 Feb. 2024].
[3]University College of Estate Management (2024). A guide to 15-minutes-cities: why are they so controversial. [online] Available at: https://www.ucem.ac.uk/whats-happening/articles/15-minute-city/ [Accessed 07 Nov. 2024].
[4]Universitas Gadjah Mada (2020). Trends in Urbanization and Motorization Affects Reduction in Air Quality. [online] Available at: https://ugm.ac.id/en/news/20145-trends-in-urbanization-and-motorization-affects-reduction-in-air-quality/ [Accessed 07 Nov. 2024].

quality of life. These studies referenced above employed various methodologies to understand socio-spatial segregation. They particularly utilized the mixed-methods approach that combined quantitative surveys and qualitative interviews. Thus, they calculated segregation indices and levels, as well as explored residents lived experiences and perceptions (access to services, social interactions, etc.). Furthermore, researchers utilized geospatial mapping to visualize segregation patterns and analyze spatial distributions across urban environments. Dysfunctions in the cities can lead to several negative consequences, as demonstrated in the research works (Najib 2017; Nieuwenhuis et al. 2020; Shamskooshki 2021; Uzcátegui-Sánchez et al. 2023). Social isolation diminishes interaction between disparate social groups, fostering miscommunication and discriminatory attitudes. Cycles of poverty, which are frequently witnessed by segregated populations, restrict access to employment opportunities and quality education. However, the cities mentioned in these studies tried to address the negative consequences encountered. For this purpose, they implemented inclusive urban planning strategies. The creation of more integrated urban environments leads to enhancing the residents' life quality. This approach prioritizes social equity and fosters community engagement. Therefore, this strategy contributes to renewing sensitive areas and improving accessibility. To this end, segregated zones have been connected with different activities and services through enhanced transportation networks. In Béjaïa, the residents' experiences have been shaped by socio-economic factors that have effects on patterns of dysfunction and segregation. These are revealed by the historical context of the city. Accordingly, inclusive transport and urban functions' planning could considerably address these issues.

Sparsely structured systems are defined by inequitable distribution and segregation, whereas densely structured systems are distinguished by integration (Hillier 2016). Indeed, urban activities in Béjaïa are not located in the same neighborhoods. The various civilizational events influenced contemporary socio-spatial dynamics. Thus, they have shaped Béjaïa's urban development from its Phoenician traces, through French colonization, to the present era. The application of past planning practices, namely the Master Urban Plan established in the 1970s, often ignored cultural contexts and local needs. Such neglect has led to fragmented urban structures characterized by inequality. Understanding these historical influences is essential to addressing existing disparities through effective urban policies. It is necessary to connect each Béjaïa neighborhood with its functions by an efficient transport network, facilitating access to different services. In addition, displacements generated by urban activities significantly influence the environment and life quality.

In light of these considerations and recent studies, our research work involves developing a novel approach for our study area. The main objectives are to critically analyze and assess urban functions planning's impacts on transport systems in Béjaïa and the consequences of the traffic generated on the environment and life quality. Accordingly, the following questions arise: How can the location of infrastructures whose urban functions decline be assessed? What are the impacts of urban functions' planning on the transport sector in Béjaïa? What are the consequences of the mobility generated by urban activities on the quality of life of city users and the environment? To address these questions, we will first analyze the planning and distribution of the activities generating displacement in the city. Additionally, we will analyze the adequacy of their planning in relation to the urban transport network. In the second part, the results of the questionnaire dealing with the modes and flows of travel in Béjaïa will be interpreted and analyzed. These will allow us to better understand the citizens' experiences and perceptions regarding the environment and life quality.

The purpose of this study is to identify the problems to be solved and the provisions used by the land valorization operating modes. Thus, urban planners and decision-makers can solve the inherited problems related to the planning of urban functions and transportation in Béjaïa City.

MATERIALS AND METHODS

Study area: the city of Béjaïa

Covering an area of 3,223.50 km^2 (Directorate of Programming and Budget Monitoring 2020)[5], the Béjaïa Province is located in the northeast of Algeria, east of the capital. Approximately, the Babors and Bibans surround it to the east and extend to the southeast, thus dominating the plains of Médjana and Bordj-Bou-Arreridj. Additionally, the ridges of Djurdjura surround it to the west (Gaid 2008). Administratively, the Province of Jijel delimits the Province of Béjaïa to the east, the Provinces of Tizi Ouzou and Bouira to the west, and the Provinces of Sétif and Bordj-Bou-Arreridj to the south. Our study area, the city of Béjaïa, is located north of the Béjaïa Province and rises amphitheatrically on the Mediterranean coast. The commune of Toudja surrounds it to the west, the commune of Oued Ghir to the south, and the communes of Tala Hamza and Boukhelifa to the southeast (Fig. 1). It covers an area of 120.22 km^2 (BETUR 2012).

The urban fabric of Béjaïa is the result of several mutations that took place through two key moments of its evolution: the intramural city, from the Phoenician era (7th century BC) to the period of French colonization (1833–1871), and the extramural city, from the French colonial period (1871–1962) to the present day. After independence, a massive rural exodus to the cities was observed in the territory of Béjaïa city and its surroundings. This occurred to improve the living environment and expand training and teaching opportunities, which were almost non-existent for children and teenagers in their Kabyle villages (Younes 2022).

During the 1970s, Béjaïa experienced an industrial development that allowed some citizens of the region to settle in the city to work in the industry and trade sectors. Moreover, according to Chadli and Hadjiedj (2003), the spread of industrial activity is associated with the development of urban centers and large agglomerations. The past planning practices constituted a significant factor in population growth and, consequently, a rapidly urbanized city. The implementation of strategic and inclusive urban functions' planning could ensure effective and sustainable transportation planning, with the objective of improving the environment and the city users' quality of life.

This study utilized a methodological approach to achieve the envisaged objectives through two complementary strategies: qualitative and quantitative methods. These mixed methods enabled a comprehensive analysis of the impacts of urban functions' planning on transport systems and the subsequent effects on the environment and the

[5]Directorate of Programming and Budgetary Monitoring (2020). Annual indicators for the Province of Béjaïa. Province of Béjaïa, (In French with English summary).

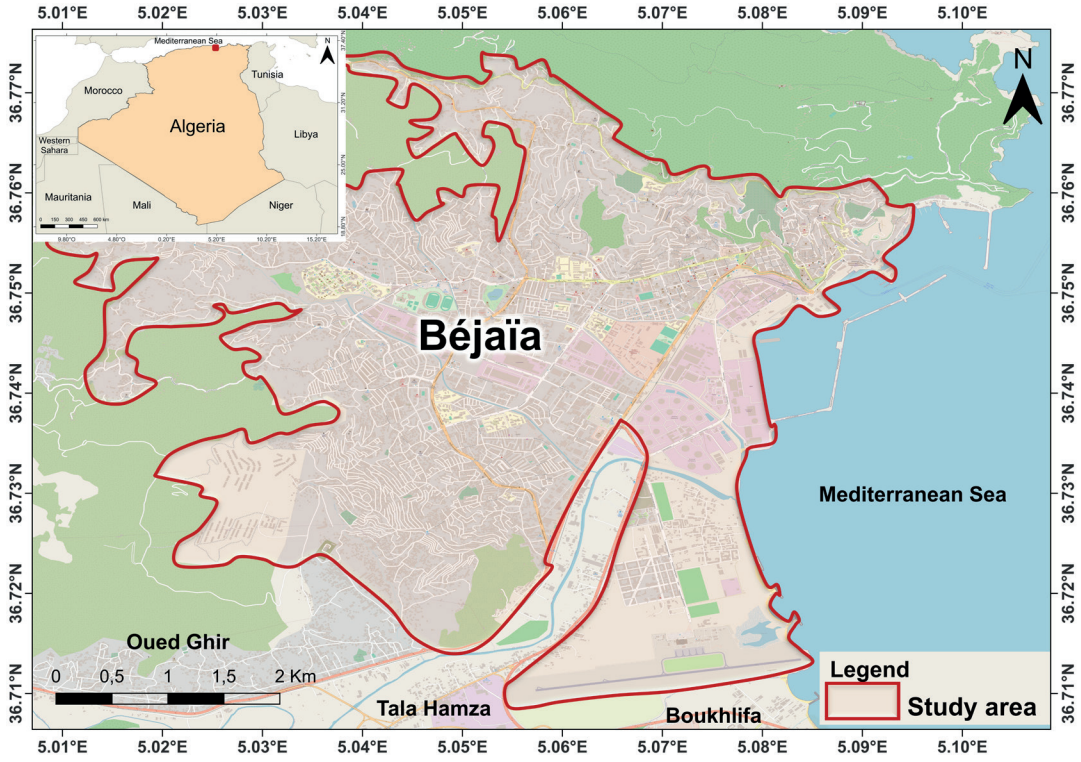

Fig. 1. Location map of the study area Béjaïa City

life quality of citizens in Béjaïa. The systematic approach presented below ensures the relevance of the results to inform future urban planning processes.

Data mapping was employed for a comprehensive understanding of the collected data. It permitted the mapping of the spatial distribution of urban functions and the transport network. To achieve this, an updated map of Béjaïa (the study area) was created using the QGIS software as a reference tool to analyze the surveys' results. To improve visual representation, the maps were processed in PowerPoint software (data and legends). This technique enabled a precise analysis aligned with the research objectives.

Analysis of the adequacy between the distribution of trip-generating activities and the urban transport network (qualitative study)

Data sources and collection methods

To assess the impacts of the urban function's planning on transportation and the consequences of the generated displacements on the environment and the citizens' quality of life, it was necessary to use a qualitative approach based on field observations. The latter is a technique used to collect, describe, and interpret spatial practices, as well as to analyze social uses and interactions in urban spaces (Morange et al. 2016). For a qualitative study (spatial analysis of trip-generating activities and the urban transport network), field observations were conducted in October 2021 in the city of Béjaïa across three key urban areas (the historic core, the University Hospital Center, and peripheral areas). These were selected on the basis of their importance in terms of trip generation and interactions with the transport network. This sampling rationale was employed to ensure that the observations were representative of the most relevant activity areas and transport nodes. Alongside an updated map of the city (created using QGIS software), a logbook was utilized to record our notes and reports regarding the different activities' distribution and their interactions with the urban transport network. The logbook provided a valuable tool for accurately organizing data, given the lack of updated sources related to the location of urban functions in our study area.

To understand and examine the history of Béjaïa and its urban planning problems, we used information from our chosen literature review, which includes reliable sources like Sidi Boumedine 2013, Lamrani 2018, and Traki and Boukrif 2019.

Along with the logbook and updated map's notes and reports, we analyzed data obtained from the different departments and directorates of the Béjaïa Province regarding statistical directories for the years 2016, 2018, and 2020, as follows: the statistical directorate for the Béjaïa Province for the year 2016, the estimation of population by gender and calculation of density at 31/12/2018, and the annual indicators for the Béjaïa Province for the year 2020, obtained from the Directorate of Programming and Budgetary Monitoring; the activity report for the year 2018, obtained from the Employment Directorate of the Béjaïa Province[6]. These data sources' collection constituted a fundamental basis for evaluating the evolution of employment and population over time.

Data analysis

Following data collection and with the aim to address this study's objectives, qualitative analysis was employed. The data from field observations was subjected to spatial analysis to identify irregularities and areas for improvement in terms of transport accessibility and the distribution of activities. To strengthen these analyses, focused on urban functions' planning and location's effects on transportation systems, several spatial analysis methods were incorporated. In the first step, we analyzed the historical context of urban planning failures, the location and distribution of displacement-generating activities throughout the city of Béjaïa, and the evolution of employment. Indeed, the activities generating trips and mobility are divided

[6]Employment Directorate of the Province of Béjaïa (2018). Activity report Year 2018. (In French with English summary).

into two parts: the activities' zones and the evolution of employment (Chabbi and Abid 2008). Next, we examined the adequacy of their planning with the urban transport network of our study area, emphasizing the distribution of nodes and the level of concentration of trips on the urban fabric (traffic congestion) compared to the distribution of urban functions.

The method of combining the analysis of urban functions' planning and the connectivity of transport networks enabled us to visualize the spatial interaction and coverage of different urban functions, examine traffic flows within urban infrastructures, and identify potential areas for further improvements that might be introduced to increase mobility. Analysis of zones around Béjaïa's main nodes identified areas experiencing a lack of access to essential facilities such as health services, schools, and shopping areas. As stated by Bakour (2023), the development and balanced functioning of territories in general and cities in particular are profoundly influenced by the traffic system, specifically the road network. An efficient and well-maintained road network contributes to reducing congestion, saving time and energy, and enhancing the quality of life.

Questionnaire survey: the perceptions of Béjaïa's citizens on the environment and life quality (quantitative study)

Data collection process

For the collection of quantitative data on the transportation modes and flows of displacements generated by the activities in Béjaïa, it was necessary to approach the inhabitants through a questionnaire. The results of this tool provided an evaluation of the citizens' perceptions regarding urban mobility, the environment, and life quality satisfaction.

The questionnaire structure consists of three parts. The first concerns the socio-demographic characteristics of the respondents. This part collected information on their gender, age, level of education, and employment status. The second part is reserved for trip patterns, where the displacement frequency is recorded, the origins and destinations for trips made during a typical day, and the mode of transport used (walking, public transport, and private car). The third part assesses the respondents' satisfaction regarding quality of life in terms of the location of urban functions, transportation services, and environmental conditions in the city of Béjaïa.

The constitution of the representative sample of 300 citizens was determined after analyzing its socio-economic characteristics, specifically the number of inhabitants and the active population of Béjaïa. These are documented in the statistical directories previously mentioned for 2018 (the estimation of population by gender, calculation of density, and the activity report) and 2020 (the annual indicators for the Béjaïa Province). The composition of the samples took into account the following criteria: gender (male and female), age (the age groups 05–19, 19–55, and over 55 were identified as the most frequent categories of the study users, according to the various statistical directories), and socio-professional category (student, worker, retired, and jobless).

The surveys were conducted during field observations (October 2021) in the different neighborhoods of the city's three key urban areas selected. The respondents were surveyed on weekdays (excluding Friday) from 09:00 a.m. to 04:00 p.m. to ensure adequate participation given the difficult circumstances of the COVID-19 pandemic (social distancing measures).

Data analysis

The analysis of the questionnaire results was conducted using statistical software that generated cross-tabulations and cross-graphs. The visual representations served to facilitate the interpretation. The quantitative analyses enabled us to effectively evaluate the consequences of the traffic generated by Béjaïa's urban functions on the environment and life quality. This analytical approach defined the citizens' perceptions of the life quality in terms of the distribution of the different urban functions, mobility (modes of transport used and flows of travel generated), and environmental quality in the city of Béjaïa.

To further enrich our interpretations, various statistical analyses were integrated. Statistical tests were applied to determine relationships between variables such as socio-demographic characteristics and modes of transport used, as well as perceptions of the environment and life quality. Additionally, the assessment of the influence of different factors on citizens' satisfaction with urban functions' planning and transportation services was established. Statistical modeling of these relationships permitted obtaining insights into the key variables that most affect quality of life perceptions.

Limitations

The limitations of field observations include their subjective nature. To avoid excessive interpretations of the results, we linked our observations with available data from statistical directories by creating an updated map of the city of Béjaïa and the results of our questionnaire survey to ensure the validation of our findings and to support them by referring to other studies.

Concerning the questionnaire survey, the limitations comprised the impact of social distancing measures caused by the COVID-19 pandemic on population participation. To address these issues, the survey was conducted on a diverse sample and utilized clear, unbiased questions to obtain accurate perceptions.

RESULTS

Analysis of the distribution of trip-generating activities and the adequacy of their planning with the urban transport network in Béjaïa City

The study of the distribution of trip-generating activities in Béjaïa reveals significant urban planning and mobility challenges. The concentration of activities in this city lacks justification. This geographically strategic site contains multiple assets of physics-spatial authorizations, while the plain of Béjaïa is a large-scale area perfectly valid to accommodate activities with high added value. In spite of this city's potential, historical urban planning decisions have led to persistent transportation problems.

A critical review of past urban planning strategies, in particular the Master Urban Plan of Béjaïa established in the 1970s, indicates that the actors of the city committed errors concerning the vision of urbanization during the study of this plan. This urban planning instrument, which was mainly used for the distribution of state programs on the territory of the city (Sidi Boumedine 2013), failed to take into account the urban environment, its physical and spatial characteristics, as well as the expectations of the residents. This was a situation that was repeated in other Provinces in Algeria. Indeed, the decision to install an industrial zone in the center of Béjaïa in 1977 (Traki and Boukrif 2019) has contributed to current mobility issues. Historical evidence

indicates that this zone was developed in the extension of several scattered businesses; for example, agribusinesses at the plains of the Soummam Valley region on the port area of Béjaïa and railway stations (Lamrani et al. 2018), dating from the time of French colonization, particularly between 1900 and 1962, including 118 industrial units in the commune of Béjaïa (Taleb-Ait Sidhoum 2011). This industrial zone's location results in a congested urban fabric characterized by inadequate transport planning.

Fig. 2 illustrates the map of the distribution of trip-generating activities in the commune of Béjaïa. Our field observations confirm that this commune has a large number of facilities offering a variety of activities, such as higher education institutions (University pole), industrial units in the center of the city, cultural centers, and administrative offices, which are mainly located on the Rue de la Liberté, one of the city's main axes, as well as health, educational, sporting, and residential activity occupying the periphery. These activities are unequally distributed. In spite of the functional mix found in the historic center, commonly known as the old city (health, educational, administrative, cultural, leisure, sports, residential, commercial, etc.), the city center is divided into functionally differentiated zones (the dominance of zoning) that have characterized the planning of Béjaïa's urban perimeter and segregated different urban functions.

In addition to this activities' distribution, the evolution of employment in Béjaïa is an important factor in generating displacements. According to the data from the Employment Directorate of the Béjaïa Province[7], the working population has increased from 372,920 in 2018 to 392,574 in 2020, compared with a total of 990,050 inhabitants at the end of the same year (Directorate of Programming and Budgetary Monitoring 2020). The 2018 statistics in Table 1 demonstrate that the building, public works, and industry sectors accounted for the highest rate of 67.39% of job offers.

The diagram drawn on the map (Fig. 3) highlights the urban transport network of Béjaïa relative to the employment centers. Our field observations indicate the continued concentration of displacements in the urban center. This is explained by the distribution of the most urban functions along the city's structuring axes, namely Rue de la Liberté, Boulevard Krim BELKACEM, and Aurès Road, which occupy the center of the city. These remain as major axes for commuting between residential areas and employment sites.

Our observations and analyses reveal realities on the nodes' magnitude scale in terms of distance and area in relation to their distribution in the urban fabric of Béjaïa. We noticed the strategic location of the major nodes at the main entrances and intersections of the primary roads within the transport network. To illustrate, the node resulting from the intersection of Rue de la Liberté and the Aurès road, as well as the node resulting from the junction of the boulevard de l'A.L.N. (National Liberation Army) and the boulevard Krim BELKACEM, serve as primary nodes facilitating access to different urban functions. However, due to the high volumes of traffic observed during peak hours, these nodes experience considerable congestion and environmental risks.

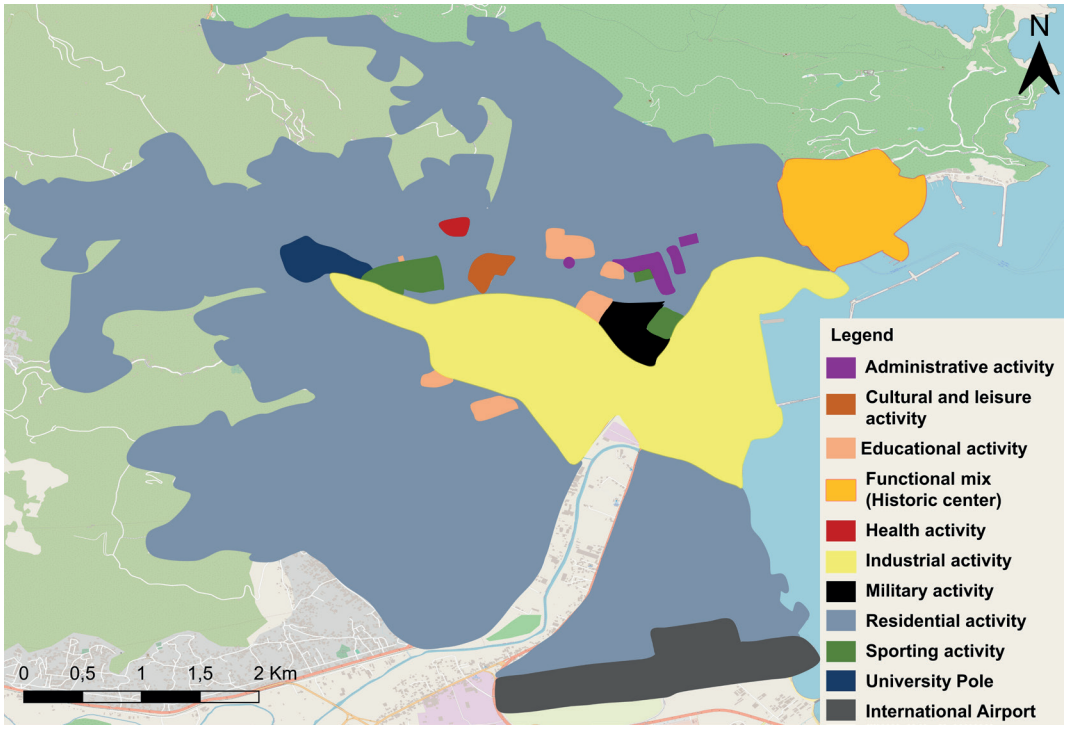

Fig. 2. Distribution of trip-generating activities in Béjaïa

Table 1. Job offers by sectors in 2018 in Béjaïa[7]

Designation	Job offers in 2018 (%)
Agriculture	1.30
Building and Public Works	**34.96**
Industry	**32.43**
Services	31.31
Total	100

[7]Employment Directorate of the Province of Béjaïa (2018). Activity report Year 2018. (In French with English summary).

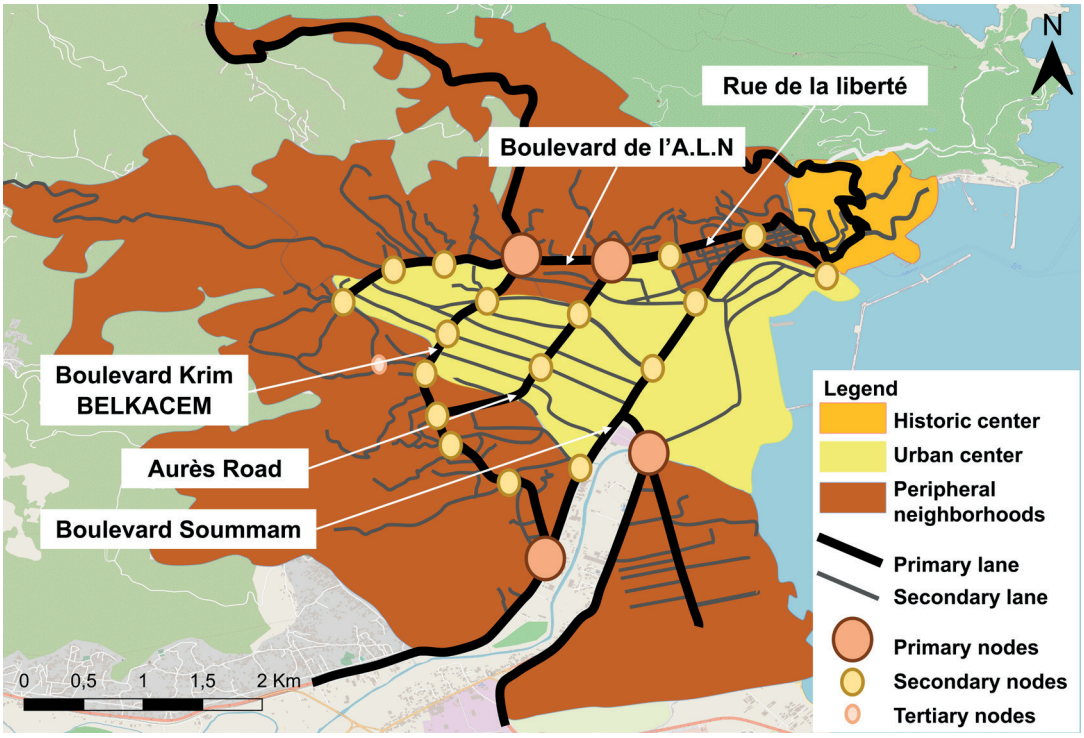

Fig. 3. Urban transport network of Béjaïa

The inadequacy of the Master Urban Plan, cited previously, to foresee an environment of central activities, particularly those of commerce and services, more appropriate to the functioning of the urban core has exacerbated these urban planning and transportation issues in Béjaïa. The design of this plan, based on a scenario of growth from the old center towards the west, has hindered the city from being endowed with a centrality of orientations east-west, to the extent of its load capacity at a sufficient scale, suitable for vertical and horizontal urban growth. This model of urbanization for this type of large area is valid for developing according to a bipolar system of multipolar peripheral character. This would enable Béjaïa to achieve the status of a city of multiple resources supporting activities of the tertiary sector, including those that are part of it, which come under finance, tourism, services provided on a large scale, higher education and scientific research, cultural institutions, travel agencies, shipping agencies, etc. What we have mentioned are branches of economic activity that could be divided into types of activities. The branches of tertiary activities are classified after the economic activity sectors, whose desired location is central. These mistakes have not allowed the local authorities to create a business center, which should radiate in all directions at regional, national, and international levels. Indeed, this multipolar system is the most suitable one for open cities occupying highly strategic sites, as is the case for the city of Béjaïa.

The peripheral residential areas are equipped with a series of proximity activities (education, health, commerce, etc.) but also two important new urban housing zones (ZHUN), namely, ZHUN of Ihaddaden and ZHUN of Sidi Ahmed. This formula was inaugurated at the end of the 1970s as an emergency solution under a new housing policy in Algeria (Dahmani and Moudjari 2013) to alleviate the pressing demand for housing by citizens. In addition, the concentration of housing around the city is due to the need for housing driven by strong population growth. From 1987 to 2013, the population of Béjaïa city increased by 56%, in addition to flows from peripheral communes at its main entrances through national roads 9, 12, and 24 (Merzoug 2016). Moreover, the resident population of our study area was estimated at 188,250 at the end of 2016 (Directorate of Programming and Budget Monitoring 2016)[8] and 190,766 at the end of 2018 (Directorate of Programming and Budget Monitoring 2018)[9].

The quality of life in Béjaïa is relatively deteriorated by an insufficient and incoherent urban transport network with overflowing traffic flows and, consequently, degradation of the environment. Users and residents of the city do not have enough pedestrian traffic spaces, particularly during peak hours, but also suffer from urban congestion constraints in the city and even on the outskirts. The consequences are undoubtedly the risk of road accidents and pollution. Moreover, what has attracted our attention is the vulnerability of the roads of the extensions (the surroundings of the city), which are winding and narrow in trees and converge towards the main axes of the city center, causing traffic and congestion problems at the nodes but also a significant flow that is difficult to evacuate.

Questionnaire survey analysis: Béjaïa citizens' perceptions of the environment and life quality relative to the displacements' modes and flows

Respondents' socio-demographic characteristics

The questionnaire survey provided valuable insights into the citizens' perceptions concerning the environment and life quality in relation to displacement modes and flows. As previously stated, its first part concerns the socio-demographic characteristics of the respondents. The representative sample of the surveyed population consisted of 64% women and 36% men. Fig. 4 illustrates the socio-professional categories of respondents. The largest

[8]Directorate of Programming and Budgetary Monitoring (2016). Statistical directorate for the Province of Béjaïa 2016. Province of Béjaïa, (In French with English summary).

[9]Directorate of Programming and Budgetary Monitoring (2018). Estimation of population by gender and calculation of density at 31/12/2018. Province of Béjaïa, (In French with English summary).

portion (72.67%) of respondents were aged between 19 and 55 years, of whom 46% were female and 26.67% were male. This age group is predominantly employed in different sectors of activity such as administration, health, and education, comprising 54% of the total respondents. The age group of 5–18 years, characterized mainly by an educated population, represents 22.67% of the total. Respondents over 55 were the least dominant, with 4.66% of the total. Retirement accounted for the majority of respondents in this category.

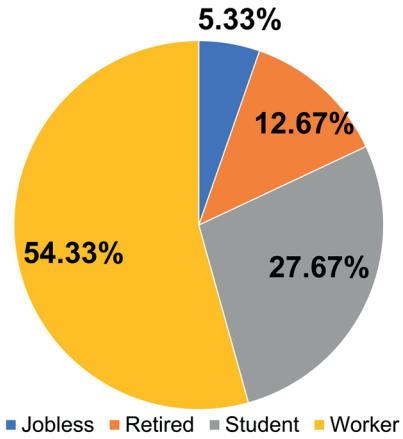

Fig. 4. Socio-professional categories of respondents

The majority of the population surveyed resided on the outskirts of Béjaïa, accounting for 70.67%. This reflects the concentration of the residential neighborhoods in this area in comparison to the lower rate of 20.67% in the city's urban center and 8.66% of the population surveyed in the historic center.

Modes of displacement used by the respondents in the city of Béjaïa

Analysis of displacement modes indicates the dominance of motorized transport use during the displacements of the respondents. Fig. 5 demonstrates that respondents mainly use private cars, particularly for commuting to work (60.13% of private car users aged between 19 and over 55 years), then for other purposes such as shopping and services (21.52%), and finally for studies (18.35%). These results are justified by the concentration of trip-generating activities in the center of Béjaïa. This situation increases the population's tendency towards incessant and excessive use of motorized means of transport, particularly private cars, to satisfy its growing mobility needs. Moreover, this aligns with the findings of the household survey among 600 households on urban sprawl and travel growth cited previously (Bounouni et al. 2020), indicating an increase in car trips from 44% in 2018 to 52.67% in 2021. This justifies the population's avoidance of using public transport, given the health situation in the country and the whole world.

The second motorized mode used by the respondents concerns public transport. Moreover, 46.56% of respondents (aged between 19 and over 55 years) chose this mode of transportation for work-related reasons, 33.59% for studies, and 19.58% of the remaining cases for other purposes (Table 2).

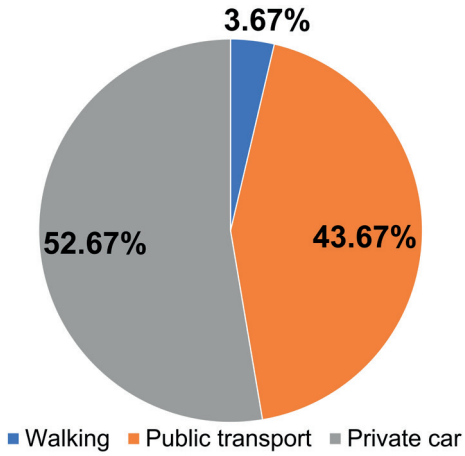

Fig. 5. Modes of displacement used by respondents

According to the results of the questionnaire, walking is primarily practiced by the educated population (aged between 05 and over 19 years). For educational reasons, 45.45% of respondents use this mode, and 36.36% of them use it in the context of work (aged between 19 and 55 years). Finally, 18.18% of the population surveyed practices walking for shopping. This strongly implies a reliance on motorized transport due to insufficient pedestrian infrastructure.

Table 2. Correlation between purposes and modes of displacement used by respondents

Modes of displacement	Purpose	Percentage (%)
Private Car	Work	60.13
	Studies	18.35
	Shopping	18.99
	Other purposes (services, leisure, etc.)	2.53
Public Transport	Work	46.56
	Studies	33.59
	Shopping	12.98
	Other purposes (services, leisure, etc.)	6.87
Walking	Work	36.36
	Studies	45.45
	Shopping	18.18

Displacement flows generated by activities

Based on the field survey results, namely the analysis of the distribution of various activities related to the urban functions in Béjaïa and the questionnaire, we have developed a map (Fig. 6) illustrating origins and destinations of displacement flows among city users.

Fig. 7 depicts that the proportion of trips that converge to the city's urban center represents 78.67% (across all age groups), due to its attractiveness reflected in the concentration of industry (the industrial zone and port are a significant source of employment), administration, and the various public infrastructures. Furthermore, according to Merzoug (2016), this attractive urban center in Béjaïa welcomes tens of thousands of people from neighboring communes as well as the resident population. However, the peripheral neighborhoods of the city accounted for 19% of total flows, mainly due to limited access to essential services such as health facilities (the University Hospital Centre of Béjaïa) or the Targa Ouzemmour university pole, which concerns a certain socio-professional category, namely teachers and students (aged between 18 and 55 years). Moreover, these peripheral neighborhoods are predominantly residential, as they contain the two ZHUNs (New Urban Housing Zones), mentioned previously, which receive only activities of proximity and basic necessity. Conversely, the flows towards the historic center of Béjaïa are reduced, thus representing 2.33%, according to the questionnaire survey. This decrease can be explained by the limited presence of cultural, recreational, and employment-generating infrastructures, in spite of the functional mix highlighted in our analysis.

The displacement flows towards the historic center, the urban center, and the peripheral areas of Béjaïa city, generated by the several urban functions related to diverse facilities, are reduced compared to the previous studies conducted in the same city. As is the case with the findings of Bounouni et al. (2020), the study mentioned above indicated that the flows towards the outskirts of the city represent 79.20%, the urban center 20.80%, and the historic center 3.16%. This finding can be justified by the challenging circumstances of the COVID-19 pandemic, including social distancing measures.

Users' satisfaction with environment and life quality

Our survey revealed that 79.33% of the users questioned expressed dissatisfaction with the location of Béjaïa's various urban functions and mobility (Fig. 8). Additionally, qualitative results indicated that perceived accessibility

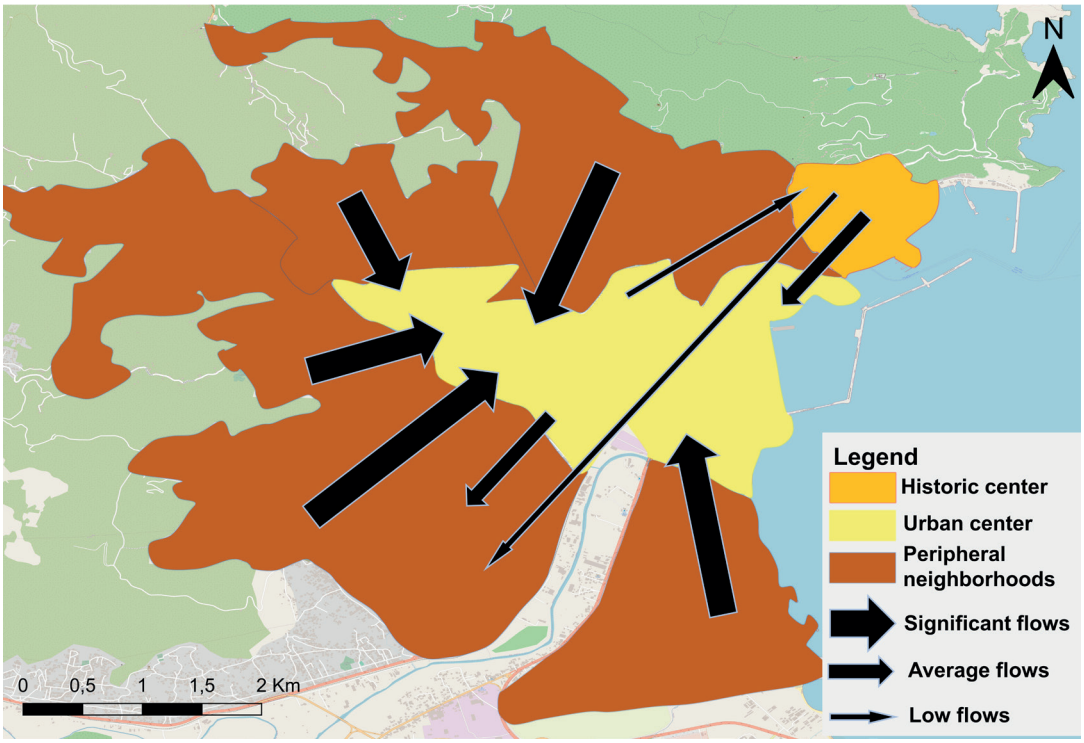

Fig. 6. Displacement flows generated by activities in Béjaïa

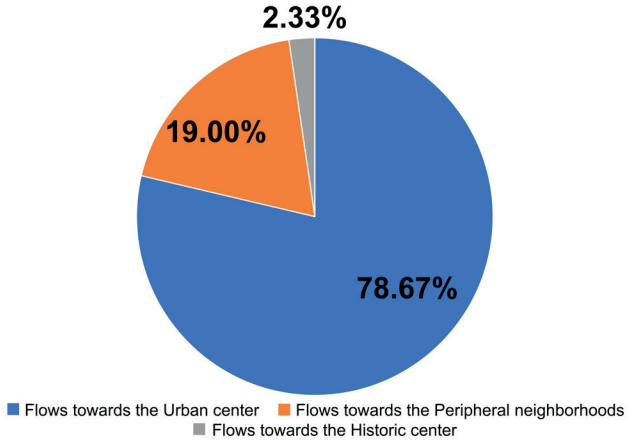

Fig. 7. Rates of displacement flows generated by activities in Béjaïa

significantly predicts satisfaction levels. This is mainly influenced by the numerous constraints cited previously and highlighted by the respondents: exacerbated zoning, lack of activities in the peripheral, limited accessibility to essential services, inadequate urban transport network, considerable distances traveled, and high transportation expenses. Consequently, 80.67% of the respondents expressed their deep dissatisfaction with the environment and life quality because of the presence of several forms of pollution, repetitive congestion, excessive use of motorized transport modes, and insufficient infrastructure for pedestrians.

These surveys' findings highlight that the Béjaïa citizens face significant challenges in terms of urban and transportation planning; thus, improving accessibility could improve residents' quality of life.

DISCUSSION

In this study, the analysis and assessment of urban functions' planning and their adequacy with the urban transport network in the city of Béjaïa provide a novel contribution to the field of urban planning. The integration of users' perceptions regarding the environment and life quality reveals several critical insights that address existing gaps in the literature reviewed. Compared to the previous studies, our research work develops an innovative approach that emphasizes the interconnection between urban planning and transportation. This result is achieved by evaluating the impacts of the distribution of the trip-generating activities that emanate from the diverse urban functions on the transport systems. This approach provides practical implications and an understanding of urban dynamics in our study area. Indeed, it enables planners' decisions to be aligned with the real experiences and needs of the city's users. The results of our study serve as a basis for the initiation of appropriate measures that optimize both functional efficiency and residents' satisfaction in terms of environment and life quality.

The findings demonstrate a significant correlation between the distribution of activities within Béjaïa's urban fabric, the traffic generated, and its subsequent effects on the environment and the citizens' quality of life. The analyses and surveys identified substantial challenges that contribute to urban planning and mobility issues on a broader scale. The significant differences in social and spatial conditions we found in our study area match well with earlier research, which showed that disadvantaged neighborhoods often have fewer urban activities nearby (Najib 2017; Nieuwenhuis et al. 2020; Shamskooshki 2021; Uzcátegui-Sánchez et al. 2023). The historical context of the Master Urban Plan reveals major deficiencies and failures in responding to the needs of the residents and the city's spatial characteristics. The current land-use rules, the exacerbation of the zoning observed, and the flows analyzed result in a disconnection between the city's urban facilities and urban mobility needs. This can lead to solutions to the issue concerning the revision of urban systems and their needs for mobility mentioned by Baklanov et al. (2021). The dominant residential function in peripheral areas disconnects the places of origin (home) from the destination (work). This disconnection generates longer distances traveled and encourages private car dependence. Consequently, this disconnection leads to an increase in traffic congestion and repetitive slowdowns, posing significant obstacles to mobility throughout the city. These planning inadequacies give rise to a considerable distance-time ratio in Béjaïa and contribute to urban sprawl, a phenomenon affecting many cities globally. These findings support the study of Bakour and Baouni (2015), who reported that this phenomenon is undoubtedly more pronounced in developing countries, given the lack of social, legislative, technical, financial, and political measures. The same patterns that Béjaïa is currently facing in relation to the challenges of accelerated urbanization have also been observed in other Mediterranean cities. To illustrate, the study of Tebbane Bouktit et al. (2024) indicated that Oued-Ghir and Tala-Hamza are encountering difficulties in optimizing their mobility needs to align with their spatial expansion. Indeed, developed countries have a duty to implement measures to prevent it. Béjaïa reliance on private cars underscores the urgent need to improve public transport systems and pedestrian infrastructure.

The analysis of traffic flows and simulation of the impacts on the perimeter of the city illustrate a correlation between the level of attractiveness of an area and the number of trips generated, reinforcing findings from the broader literature on urban sprawl, which also confirm that this situation

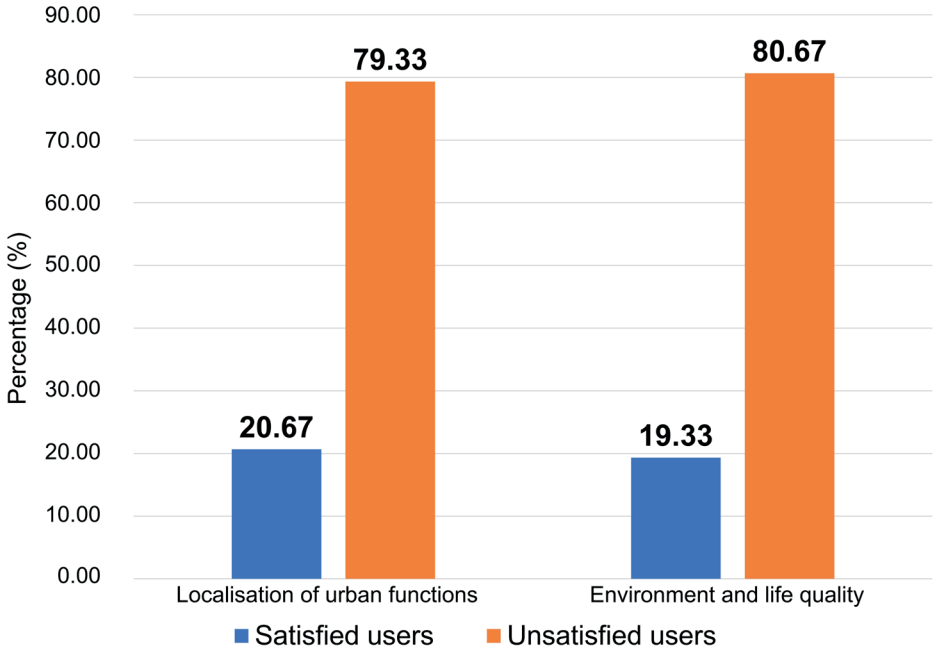

Fig. 8. Users' satisfaction with localization of urban functions, environment, and life quality in Béjaïa

leads to high traffic volumes (Bounouni et al. 2020). Thus, the observed concentration of employment opportunities and essential services' facilities generates significant flows of people in the city's urban center from the peripheral residential areas, the old city, and the communes bordering Béjaïa. This observation is corroborated by the study, which has stated that in addition to the local residents, Béjaïa's urban center attracts a large number of people from the surrounding communes (Merzoug, 2016). This conclusion highlights the need for decision-makers to implement effective transportation and urban planning to alleviate traffic congestion and accordingly ensure accessibility for citizens.

Our research findings also unexpectedly revealed that industrial zones can, to a large extent, stifle mobility and compromise the quality of life of the city's users. Although industrial activities are part of the non-agricultural economic sector, their locations often contradict the fundamental principles of urban planning, especially when situated in city centers. Moreover, the location of the industrial zone occupying most of the city of Béjaïa poses a significant threat to air quality and residents' health (fires, toxic fumes, explosions, etc.). These insights correlate with the consumption of land by transport that has a major impact on quality of life: air pollution, with harmful long-term health consequences (Du et al. 2021), causes a considerable number of cases of illness among people living near road traffic (ADEME 2022)[10]. This contradiction demonstrates a gap in the existing literature concerning the balance between economic development and urban life quality. Consequently, these core areas should be subjected to a re-evaluation of the industrial activity location, in addition to sufficient debate in terms of risks and correlational anomalies, to reduce industry negative effects on urban livability in Béjaïa and other similar regions.

The findings related to the assessment of the consequences of the displacements generated by urban functions on the environment and life quality emphasize the necessity for the promotion of sustainable transportation solutions. Our results align with global concerns about the issues related to greenhouse gas (GHG) emissions and land consumption (Padeiro 2010). The French Ministry of Ecological Transition (2023)[11] reported in their study on the climate in France, Europe, and the world that transport is the second largest emitter of carbon dioxide (CO^2) in the world, accounting for 21% of emissions, underlining the need to address this issue in the context of urban planning. According to the Ecological Transition Agency (ADEME 2022)[10], road infrastructure in urban spaces is the main source of noise emissions and a multitude of air pollutants, such as fine particles and nitrogen oxide emissions. Urban functions that generate significant flows in the center of Béjaïa may also contribute to the problem. Additionally, the respondents expressed their profound dissatisfaction with transportation conditions and life quality, namely traffic congestion and environmental degradation. The survey results showed that we need to tackle these issues and the health problems caused by pollution by using global strategies focused on sustainable development, like promoting public transport (Legendre 2003).

The implications of these results provide valuable perspectives for urban planners and decision-makers in Béjaïa and similar regions, extending beyond just academic contributions. In this context, our findings emphasize the need for a more equitable urban planning strategy that harmoniously combines residential and commercial activities, thus reducing the pressure on the urban center, alleviating travel distances, and promoting sustainable mobility solutions in our study area. This proposed perspective is consistent with the efficient urban planning interventions executed in various cities to enhance transportation networks and, consequently, accessibility between segregated zones and diverse activities and services (Najib 2017; Nieuwenhuis et al. 2020; Shamskooshki 2021; Uzcátegui-Sánchez et al. 2023). Introducing similar principles in Béjaïa could improve the environment and life quality, as it fosters connectivity between segregated zones.

In order to improve citizens' quality of life, the findings underscore the need for comprehensive strategies that integrate land use planning with sustainable transportation infrastructure development. By addressing historical failures in planning strategies and prioritizing inclusive mobility solutions, the city of Béjaïa has the potential to become a more resilient and accessible city.

Limitations

Our study provides valuable insights into urban and transportation dynamics in Béjaïa, but it is essential to acknowledge its limitations. First, the absence of updated sources related to the location and the definition of urban functions in the city of Béjaïa, such as inventories or statistical directories, in addition to the lack of data regarding the real composition and number of people in the city, does not allow us to capture all demographic nuances within the study area. The statistical directories provided only an estimation of the population. Also, the 2020 and 2021 statistics for Béjaïa were unavailable (there were only annual indicators of the Province, which covers the city of Béjaïa and other municipalities for the year 2020). Furthermore, our study mainly concerns examining the current conditions without detailed analysis to evaluate changes over time or the impact of specific interventions, for example, to define specific effects of industrial activities on transportation systems and life quality. However, the establishment of an updated map of urban functions and transport networks and the constitution of a representative sample allowed us to obtain accurate and comprehensive findings according to our research objectives.

CONCLUSIONS

The study provides a detailed analysis of the various urban functions' location, the urban transport network, as well as the environment and quality of life in the city of Béjaïa. Critical insights into the interactions between urban planning and transportation dynamics have been identified through a mixed-methods approach that combines qualitative observations and quantitative surveys.

The findings reveal that the distribution of trip-generating activities within Béjaïa's urban fabric is strongly correlated with the resulting traffic flows. The monocentric urbanization model is no longer relevant for medium-sized cities, as is the case for our study area. The research also indicates that the city of Béjaïa continues to experience multiple pressures related to the inability of its urban fabric to adapt to its functional dynamics. This imbalance

[10]ADEME (2022). Expertise: Impacts of transport on the environment. [online] (In French with English summary). Available at: https://www.ademe.fr/expertises/mobilite-transports/elements-contexte/impacts-transports-lenvironnement [Accessed 21 Mar. 2022].
[11]French Ministry of Ecological Transition (2023). Key climate statistics for France, Europe, and the world. Paris: Statistical data and studies departments, p. 92 (In French with English summary).

is clearly reflected in the zoning observed, caused by the historical planning failures. Additionally, the city's urban center serves as a focal point for various activities, attracting considerable displacement from peripheral residential areas and communes. This concentration underscores the attractiveness of the urban center, leading to negative impacts on the environment and quality of life for residents, such as increased distance from the center, frequent traffic congestion, and environmental degradation. Furthermore, the study demonstrates that socio-spatial disparities are emerging between the urban center and the peripheral neighborhoods, in which limited access to essential services is exacerbating the dependence on motorized transport. This contributes to longer travel distances, increased congestion, and a diminished quality of life for residents. Moreover, our research indicates that the industrial zone located in or near residential areas imposes significant risks for air quality and public health, in contradiction with the fundamental principles of urban planning. This can also be justified by the profound dissatisfaction of Béjaïa's citizens regarding life quality in terms of mobility and the environment.

These findings provide substantial alignment with the study's stated objectives. By analyzing and evaluating the impact of the location and planning of the various urban functions in Béjaïa on the urban transport network, as well as the consequences of the displacements generated on the environment and life quality, critical areas for intervention in the framework of this city's urban planning have been identified. The research offers valuable and practical insights for researchers and decision-makers to enhance future urban planning strategies with a view to land valorization in Béjaïa and other Algerian and similar cities around the world.

Based on the findings of our study, we propose several practical and critical recommendations related to land valorization's operating modes to address the issues uncovered. The impact of the location of urban functions on mobility is increasingly important, alongside improving urban planning vision, transportation systems, and life quality in Béjaïa and other similar regions around the world:

- Adopting integrated urban planning by changing the conditions of land use. The approach is based on the principle of revising zoning regulations to promote a mix of functions. Thus, it reduces car travel, enhances accessibility, and increases density to offer more proximity.

- Promoting sustainable transportation solutions by encouraging soft modes of transport with a small footprint, such as implementing pedestrian and cycling infrastructure, in order to alleviate traffic congestion and reduce greenhouse gas emissions.

- Revaluating strategically the industrial zones by assessing their location to minimize their negative impacts on public health and urban livability while ensuring economic development by integrating higher tertiary activities.

- Encouraging community engagement by fostering active participation from citizens in the urban planning process to ensure that decisions related to various developments closely meet their needs.

A comprehensive and global revision of Béjaïa's mobility plan through appropriate planning of the numerous activities could have significant practical implications for improving and optimizing transport strategies, promoting sustainability, and reducing constraints related to mobility. The key expectations of this vision are equally strategic, namely, the effective spatial integration of urban activities through urban fabrics, the establishment of social equity by promoting mixed-use developments, the prioritization of energy efficiency through the rational use of natural resources, and the promotion of a healthy environment that protects the well-being of the city's residents. Therefore, transportation is one of the priority sectors for land valorization, being responsible for the safety and health of the city's residents and users. Implementing the proposed practical recommendations in Béjaïa or other similar cities around the world may lead to enhanced urban planning focusing on accessibility and improved transportation systems prioritizing sustainability. These changes should thus promote a healthier environment and have a positive effect on Béjaïa and other cities' users' life quality, aiming to increase land value.

Based on our study's results and recommendations, further research should define the specific effects of industrial activities on transportation dynamics, as well as environmental and life quality. Moreover, it would be advantageous to explore the effectiveness of sustainable transportation strategies in alleviating emissions and, thus, improving urban air quality. Conducting comparative studies and analyses with other cities that experiencing accelerated urbanization and facing similar challenges could identify more practical solutions for improving transportation and urban planning issues. Future investigations addressing these areas could notably contribute to developing more accessible and resilient cities that emphasize the importance of the environment and quality of life, and thus the land valorization. By prioritizing these impactful research works, significant progress towards sustainable urban futures that will benefit all relevant stakeholders (decision-makers, urban planners, citizens, etc.) can be achieved.

REFERENCES

Aggoune K. (2024). A dynamic urban landscape in Algeria: actors, mechanisms and governance challenges. Al Bashaer Economic Journal, X(02), 650-662.

Al Tal R., Theodory R., and Bazlamit S.M. (2022). Assessing The Intersected Relationship Between Land Use And Transportation Planning. Geography, Environment, Sustainability, 4(15), 80-89, DOI: 10.24057/2071-9388-2022-008.

Andabayeva G., Movchun V., Dubovik M., Kurpebayeva G., and Cai X. (2024). Labor market dynamics in developing countries: analysis of employment transformation at the macro-level. Journal of Innovation and Entrepreneurship, 13(65), https://doi.org/10.1186/s13731-024-00417-0

Attar A. and Saraoui S. (2022). Evaluation of the main properties of the urban system by the correlation between the method of space syntax and the empirical approach of Kevin Lynch. The case of Béjaïa City in Algeria. International Journal of Innovative Studies in Sociology and Humanities, 7(6), 141-157, DOI: https://doi.org/10.20431/2456-4931.0706014.

Baklanov A., Chubarova N. E., Kolosov V. A., Malkhazova S. M., and Porfiriev B. N. (2021). Introduction To Geography Of Covid-19 Pandemic: Environmental Issues, Public Health And Socio-Economic Consequences. Geography, Environment, Sustainability, 14 (4), 105-108, DOI: 10.24057/2071-9388-2021-044.

Bakour M. and Baouni T. (2015). Urban sprawl and the dynamics of the Algiers metropolitan area: Should administrative structures be promoted? Cahiers de géographie du Québec, 59(168), 377 - 406 (In French with English summary). https://doi.org/10.7202/1037255ar

Bakour M. (2023). Implementing a decision-making system for better sustainability of mobility infrastructures. The case of the road network. Journal de la Ville, de l'Urbanisme et du Développement Durable, 2, 6-13 (In French with English summary).

BETUR (Transport Studies Office Subsidiary of the Algiers Metro Company). (2012). Study of the traffic plan for the city of Béjaïa: Site reconnaissance. Transport Directorate of the Province of Béjaïa, (In French with English summary).

Bounouni S., Baouni T., and Belli-Riz P. (2020). Growth of car travel in the face of urban sprawl case of the city of Béjaïa. Les Cahiers du Cread, 36 (4), 111 - 140 (In French with English summary).

Chabbi M. and Abid H. (2008). Urban mobility in greater Tunis: trends and prospects. Marseille: Plan Bleu, (In French with English summary).

Chadli M. and Hadjiedj A. (2003). The contribution of small towns to the urban growth in Algeria. Cybergeo: European Journal of Geography, [online] 251, p. 12 (In French with English summary) https://doi.org/10.4000/cybergeo.3851

Chin W. C. B., Fu Y., Lim K. H., Schroepfer T., and Cheah L. (2024). Identifying urban functional zoning by analysing the spatial distribution of amenities. Environment and Planning B: Urban Analytics and City Science, 51(6), 1274-1289, DOI: 10.1177/23998083231217376.

Dahmani K. and Moudjari M. (2013). Social housing practises: setbacks and successes. Algiers: Office des Publications Universitaires, (In French with English summary).

Du W., Chen D., Petäjä T., and Kulmala M. (2021). Air pollution: a more serious health problem than COVID-19 in 2020. Boreal Environment Research, 26, 105–116.

Erraougui K. (2023). Urban functions and attractiveness of the territory: the case of the city of Sidi Allal El Bahraoui Province of Khémisset, Morocco. Revue Territoire Environnement et Développement, 2(2), 67-74 (In French with English summary), https://doi.org/10.34874/IMIST.PRSM/ted-v2i2.39382

Gaid M. (2008). History of Béjaïa and its region, from antiquity to 1954. Algiers: Editions MIMOUNI, (In French with English summary).

Guerroudj T. (Sous la direction) (2017). Thematic compendium of planning laws and rules. Algiers: Les Alternatives Urbaines, (In French with English summary).

Haghani M., Sabri S., De Gruyter C., Ardeshiri A., Shahhoseini Z., Sanchez T W., and Acuto M. (2023). The landscape and evolution of urban planning science. Cities, 136 (2023), 104261, 1-24. https://doi.org/10.1016/j.cities.2023.104261

Hillier B. (2016). What are cities for? And how does this relate to their spatial form? The Journal of Space Syntax, 6(2), 199-212.

Hoen A., Hilster D., Király J., de Vries J., and de Bruyn S. (2021). Air pollution and transport policies at city level. Module 2: policy perspectives. Report for CE Delft, p. 67.

Hu F., Liu W., Lu J., Song C., Meng Y., Wang J., and Xing H. (2020). Urban function as a new perspective for adaptive street quality assessment. Sustainability, 12(4), 1296, doi:10.3390/su12041296.

Khelf M. (2021). Contribution to the study of congestion and road traffic regulation for the evaluation of traffic in urban areas (Doctoral thesis, Constantine 1 - Frères Mentouri University (Constantine)). (In French with English summary).

Klouche D. (2019). The four "P"s: The imperative necessity of renaissance through urbanism. Vies de Villes: Architecture, urbanisme & société, 27, p. 134 (In French with English summary).

Lamrani L., Bellache Y., and Ferguene A. (2018). Territorial construction and local dynamics: the case of the Soummam valley in Algeria. Les Cahiers du Cread, 34(1), 5 - 41. (In French with English summary).

Legendre M. (2003). Environment and health. Santé publique, 15(3), 291 – 302 (In French with English summary), doi.org/10.3917/spub.033.0291

Litman T. A. (2024). Evaluating Public Transit Benefits and Costs: Best Practices Guidebook. Victoria Transport Policy Institute, p. 141. Available at: https://vtpi.org/tranben.pdf [Accessed 07 Nov. 2024].

Meddour O. (2022). Sustainable Urban Development and the Challenge of Urban Risks in Algeria. International Journal of Innovative Studies in Sociology and Humanities, 7(10), 64-74. DOI: https://doi.org/10.20431/2456-4931.071007

Merlin P. and Choay F. (Sous la direction) (2010). Dictionary of urbanism and planning. Paris: Presses Universitaires de France (PUF), (In French with English summary).

Merzoug S. (2016). Urban centres in Algeria: how to reconcile attractivity and mobility through the management of urban transport? Case of the city of Béjaïa. Recherche - Transports – Sécurité, 32, 1 - 17 (In French with English summary). Available at: https://hal.science/hal-01670585/document [Accessed 22 Jan. 2022].

Morange M. and Schmoll C. (2016). Qualitative tools in geography: methods and applications. Dunod Editeur, Armand Colin: Collection Cursus, (In French with English summary).

Mouratidis K. (2021). Urban planning and quality of life: A review of pathways linking the built environment to subjective well-being. Cities, 115, 103229, https://doi.org/10.1016/j.cities.2021.103229

Najib K. (2017). Socio-spatial inequalities in the cities and their recent evolutions: comparison between Besançon, Mulhouse, and Strasbourg. Cybergeo: European Journal of Geography. Espace, Société, Territoire, [online] document 808 (In French with English summary). https://doi.org/10.4000/cybergeo.27975

Nieuwenhuis J., Tammaru T., van Ham M., and Manley D. (2020). Does segregation reduce socio-spatial mobility? Evidence from four European countries with different inequality and segregation contexts. Urban Studies, 57(1), 176-197, DOI: 10.1177/0042098018807628

Niu H. and Silva E. A. (2021). Delineating urban functional use from points of interest data with neural network embedding: A case study in Greater London. Computers, Environment, and Urban Systems, 88, 101651, https://doi.org/10.1016/j.compenvurbsys.2021.101651

Padeiro M. (2010). Location of economic activities and sustainable development: a review of the current state of research. Report for PUCA: Laboratory City Mobility Transport, p. 57 (In French with English summary). Available at: https://www.researchgate.net/publication/260451467_Localisation_des_activites_economiques_et_developpement_durable_une_revue_de_l'etat_actuel_des_travaux [Accessed 29 Jul. 2024].

Raea S.M., Alsulami A. N. M., Aljuaid T. H., Alruqaie R. I. M., Albather M. H., Alamri B. J., Alharbi M. A. M., Albalawi M. F., Alhawiti M. E., Alsanad I. S., Aljohani M. A., Alhejaili M. A. M., Alarfi M. D. M., and Alyamani A. M. A. (2020). Designing healthy cities: Linking infrastructure to quality of life. International Journal of Health Sciences, 4(S1), 509-529. https://doi..org/10.53730/ijhs.v4nS1.15432

Shamskooshki H. (2021). The perception of socio-spatial segregation: The Interaction of Physical and Social Urban Space. Study case of Tehran Neighborhoods (Doctoral thesis, Fakultät Architektur und Urbanistik der Bauhaus-Universität Weimar). Available at: https://www.db-thueringen.de/servlets/MCRFileNodeServlet/dbt_derivate_00063622/Shamskooshki.pdf [Accessed 18 Sep. 2024].

Sidi Boumedine R. (Sous la direction) (2013). Urban planning in Algeria. Failure of instruments or instruments of failure? Algiers: Les Alternatives Urbaines, (In French with English summary).

Signor L., Karjalainen P., Kamargianni M., Matyas M., Polydoropoulou A., Pagoni I., Tsirimpa A., Stefanelli T., Galli G., Malgieri P., Bousse Y., Mizaras V., Aifadopoulou G., Hoadley S., De Roeck M., Kishchenko K., and Geier T. (2019). Mobility as a Service (MaaS) and Sustainable Urban Mobility Planning. ERTICO – ITS Europe (editor), p. 42. Available at: https://urban-mobility-observatory.transport.ec.europa.eu/document/download/6b706858-11c6-41c2-b9f7-466e2bec0499_en?filename=maas_and_sustainable_urban_mobility_planning.pdf [Accessed 07 Nov. 2024].

Taleb – Ait Sidhoum H. (2011). Economic openness and entrepreneurial dynamics: An essay on modelling the territorial determinants of company creation in the Province of Béjaïa (Doctoral thesis, Mouloud MAMMERI University (Tizi Ouzou)), (In French with English summary). Available at: https://dspace.ummto.dz/items/ada43e73-d0b0-4b60-8b73-9ba12b6160c8 [Accessed 26 Jan. 2022].

Tebbane Bouktit K., Alkama D., and Bensehla S. (2024). Analyzing urban sprawl and urbanisation dynamics: a case study of Béjaïa, Oued-Ghir, and Tala-Hamza. Bulletin of the Serbian Geographical Society, 104(1), 95-112, https://doi.org/10.2298/GSGD2401095T.

Thandoo M., Marquet O., Marquez S., and Nieuwenhuijsen M. J. (2020). Small cities, big needs: Urban transport planning in cities of developing countries. Journal of Transport and Health, 19, 100944, https://doi.org/10.1016/j.jth.2020.100944

Traki D. and Boukrif M. (2019). The articulation of local economy and territorial and local development: the case of industrial zones in the Province of Béjaïa. Arsad Journal For Economic and Management Studies, 1, 345 – 374 (In French with English summary).

UN-Habitat. (2022). Chapter 6: Urban Planning for the Future of Cities. World Cities Report, 179-210. Available at: https://unhabitat.org/sites/default/files/2022/07/chapter_6_wcr_2022.pdf [Accessed 08 Jan. 2025].

Uzcátegui-Sánchez C., Zerpa-de Hurtado S., and Santamaría-Mendoza A. (2023). Socio-spatial segregation in Machala- Ecuador. An analysis of inequalities and possible challenges. Revista Metropolitana de Ciencias Aplicadas, 6(3), 179-190. Available at: https://www.redalyc.org/articulo.oa?id=721778125021 [Accessed 18 Sep. 2024].

Younes K. (2022). Béjaïa, Past – Present. Algiers: Editions DALIMEN, (In French with English summary).

Zhou G., Li C., and Zhang J. (2020). Identification of urban functions enhancement and weakening based on urban land use conversion: A case study of Changchun, China. PloS ONE, 15(6), https://doi.org/ 10.1371/journal.pone.0234522

Zhou N. (2022). Research on urban spatial structure based on the dual constraints of geographic environment and POI big data. Journal of King Saud University – Science, 34(3), 101887, https://doi.org/10.1016/j.jksus.2022.101887

RESEARCH PAPER

UTILIZATION OF REMOTE SENSING DATA IN DETERMINING THE THRESHOLD VALUE OF URBAN ECOLOGICAL QUALITY INDEX IN BANDUNG CITY, WEST JAVA, INDONESIA

Auzaie Ihza Mahendra[1*], Prima Widayani[1], Sigit Heru Murti[1]
[1]Department of Geographical Information Science, Universitas Gadjah Mada, Yogyakarta 55281, Indonesia
***Corresponding author:** auzaieihzamahendra@mail.ugm.ac.id
Received: May 24th 2024 / Accepted: March 24th 2025 / Published: June 30th 2025
https://doi.org/10.24057/2071-9388-2025-3413

ABSTRACT. Bandung City has the highest land conversion rate in Indonesia and was named a city with a moderate environmental quality index status in 2022. This status has been exacerbated by the diminishing green spaces in the city due to rapid urbanization. Conducting ecological assessments has become increasingly important, one approach being the utilization of remote sensing data. Remote sensing data, specifically Landsat 8 OLI/TIRS, processed to derive the RSEI (Remote Sensing Ecological Index) based on the PCA value of PC1, requires further development. Several limitations of the RSEI in assessing ecological quality, such as the subjectivity of remote sensing data, the use of equal interval methods for index classification, and the inability to validate the results, are the focus of development in this study. Based on these weaknesses, the RSEIT offers advancements in integrating actual data to support RSEI, determining index thresholds, and enabling model validation. The findings of this study demonstrate that: (1) ecological issues such as floods, waste accumulation, and landslides are the most prevalent problems in the study area; (2) compared to RSEI, which relies solely on remote sensing data, RSEIT is a model that can be validated with actual data. During the dry and rainy seasons, it achieves threshold values of 0.474 and 0.566, respectively, demonstrating a model performance accuracy exceeding 70%. The average validation results show an overall accuracy of 83.34%, a sensitivity of 78.55%, and a specificity of 87.50% across both seasons; and (3) urban centers, characterized by extensive surface hardening, minimal vegetation, and numerous ecological issues, predominantly fall under the poor RSEIT category, especially during the dry season. In contrast, suburban areas with higher proportions of green space and fewer ecological problems are largely classified under the good RSEIT category, particularly during the rainy season. This study can be further enhanced by refining the threshold aspects and strengthening actual data collection through the involvement of various stakeholders with expertise in ecology.

KEYWORDS: remote sensing, Landsat 8 OLI/TIRS, Bandung City, RSEIT, threshold, seasonal differences

CITATION: Mahendra A. I., Widayani P., Murti S. H. (2025). Utilization of Remote Sensing Data in Determining the Threshold Value of Urban Ecological Quality Index in Bandung City, West Java, Indonesia. Geography, Environment, Sustainability, 2 (18), 20-31
https://doi.org/10.24057/2071-9388-2025-3413

ACKNOWLEDGEMENTS: This research is supported and funded by "Program Rekognisi Tugas Akhir Universitas Gadjah Mada Year 2024".

Conflict of interests: The authors reported no potential conflict of interests.

INTRODUCTION

Urbanization, which has resulted in the degradation of green spaces and a decline in ecological quality, has created a sense of urgency for urban ecological monitoring. In general, the concept of urban ecology refers to the dynamics and reciprocal activities that occur between biotic and abiotic in urban ecosystems. Urbanization is one of the contexts that greatly affects urban dynamics, and Bandung City is no exception. An increase in population that is not matched by the availability of facilities will have its own consequences for the ecological environment and will ultimately be destructive (Ary et al. 2018). When compared to other cities in Indonesia, research by Widiawaty et al. (2019) indicates that Bandung City has the highest rate of land-use conversion in the country. Meanwhile, the ecological footprint of the regional area in Bandung City is 0.04 or <1, which signifies that the natural carrying capacity of Bandung City has been exceeded or is in deficit relative to the needs of its population (Muchtar et al. 2024). This condition has led to challenges such as air quality issues, waste management, water quality concerns, and the insufficient extent of green open spaces that do not meet national standards.

In terms of ecological spatial aspects specifically in green open space study, Budiman et al. (2014) research on changes in green open space in Bandung City in 1991, 2000, and 2013 showed a change in pattern, where in 1991 green open space tended to cluster in the periphery, while in 2000 and 2013 it became randomly spread due to the

development of built-up land that increasingly intervened in the periphery of Bandung City. Meanwhile, research by Kustiwan and Ladimananda (2012) reported a decrease from 14.41% in 2004 to 10.56% in 2020. These changes were attributed to the increasing demand for residential land, public facilities, and industrial centers. Rapid population growth, coupled with industrial expansion, rising population density, and increased motor vehicle use, significantly impacts environmental quality (Lestiani et al. 2013). The spatial aspect plays a crucial role in ecological assessment, which can be conducted, among other methods, through remote sensing.

In ecological assessment, Indonesia generally employs environmental quality evaluation methods that are locally regulated under the Environmental Quality Index (IKLH - Indeks Kualitas Lingkungan Hidup). The IKLH integrates assessments of air, water, soil, and seawater quality indices (Ministry of Environment and Forestry of the Republic of Indonesia 2022). The methodology includes field monitoring and laboratory analysis of observation samples. According to the 2022 IKLH report, Bandung City achieved an environmental quality index score of 55.70, categorized as moderate. However, as noted by Suprayogi et al. (2013), the implementation of the IKLH has yet to incorporate spatial analysis for each variable used. Meanwhile, according to the 2022 Regional Environmental Management Performance Information Document (IKPLHD- Dokumen Informasi Kinerja Pengelolaan Lingkungan Hidup Daerah) of Bandung City, which is regulated by the local government, there are five priority environmental issues that are the primary focus of the regional administration. These include land conversion and usage, degradation of water and air quality, disaster risk management, and improving efficiency in waste management (Environmental Office Bandung City 2022)

Remote sensing is one field that can offer solutions to assess environmental quality. Satellite imagery, which has the ability to record the earth's surface in wide coverage at various scales can be an option for labor and cost efficiency. Remote sensing products in the form of satellite images themselves have the ability to extract ecological variables such as vegetation, water, air, and soil (Caio et al. 2015; Kwok 2018; Reza and Abdullah 2011). In the assessment of ecological quality, Xu (2013) introduced the Remote Sensing Ecological Index (RSEI), which integrates four environmental indicators greenness index, moisture index, dryness index, and land surface temperature using satellite image data to monitor ecological conditions. These indicators are analyzed through principal component analysis (PCA) on the first principal component (PC1) and classified into five classes using the equal interval method. However, Wang et al. (2023) argued that the RSEI remains probabilistic and cannot be universally implemented due to the varying characteristics of Earth's surface regions.

Several studies in Indonesia have applied RSEI-based approaches to assess ecological quality, such as those conducted by Dai et al. (2023) along the Jakarta-Bandung High-Speed Railway corridor, Indrawati et al. (2020) in Semarang City, and Giofandi et al. (2024) in Pekanbaru City. These studies highlight the limitations noted by Wang et al. (2023), including the absence of field validation and continued reliance on probabilistic methods. This condition underscores the need to integrate actual input data that reflects field conditions into RSEI outputs, enabling the establishment of threshold values and direct field validation of the results.

The determination of thresholds using field data can enhance the objectivity of outcomes, as actual data collected from the field can aid in identifying real-world conditions that satellite imagery may fail to detect. Furthermore, determining thresholds based on actual data also improves the effectiveness of results, particularly those derived from validation processes (Palapa and Maramis 2014). In line with this statement, research by (Henrys and Jarvis 2019) highlights that remote sensing data, when supported by primary field data, can provide better objectivity. One analysis method used in determining threshold values is the receiver operating characteristic (ROC), where the ROC curve evaluates binary data within "good" and "poor" categories, formulated based on sensitivity and specificity values, which can be used to determine the cut-off threshold (Obuchowski et al. 2005).

Bandung City is currently experiencing a decline in its ecological dynamics, as indicated by the IKPLHD document, which highlights the need for the city to address five priority ecological issues. Meanwhile, the environmental quality index in Bandung City in 2022 reached 55.70, categorized as moderate. The reduction in green zones within the city exacerbates this situation. This condition presents an opportunity in this study to enhance the capability of the RSEI in modeling ecological conditions by integrating existing ecological data with remote sensing data (RSEI) to develop a threshold-based ecological modeling framework (RSEIT). RSEIT has been developed by integrating actual data with remote sensing data (RSEI), determining ecological index thresholds, and validating the accuracy of RSEIT. In 2023, Bandung City implemented this model during both the dry and rainy seasons.

MATERIALS AND METHODS

Study Area

This research was conducted in Bandung City, West Java Province. Bandung City is astronomically at 6°50'10"S - 6°54'50"S and 107°35'52"E - 107°41'54"E, with an area of 167.31 km2. Bandung City borders West Bandung Regency and Bandung Regency on the north side, Cimahi City on the west side, and Bandung Regency on the east and south sides. Bandung City has a geographical position with unique characteristics because it is located in a basin surrounded by hills and mountains. This results in the average temperature of Bandung City being 23.6 °C, which is classified as low for the average temperature in Indonesia (Lestiani et al. 2013).

Bandung City climatologically has two seasons a year and has a tropical climate. The division of the seasons is divided into two ranges: April to September, which is the dry season, and October to March, which is the rainy season. Bandung City has unique physical characteristics because it is surrounded by mountains and is located in a basin area. Morphologically, Bandung City is dominated by flat to sloping morphology and sloping to steep on the north side with elevations ranging from 645 to 1820 meters above sea level. This makes areas that are at low elevations with flat to gentle slopes find many built-up land objects, such as settlements, public facilities, and industrial areas, as well as green land, especially rice fields, while in areas that tend to be high with steep slopes, more green land is found, such as forests and plantations. Figure 1 illustrates the research location, featuring object samples and a false-color composite of Landsat 8 imagery in Bandung City. The composite constructed using near-infrared, red, and green bands, highlights vegetation, built-up areas, and inundated objects (wet rice fields). Each square depicted on the map represents observed objects in the field, where ecological conditions are significantly influenced by these surface features.

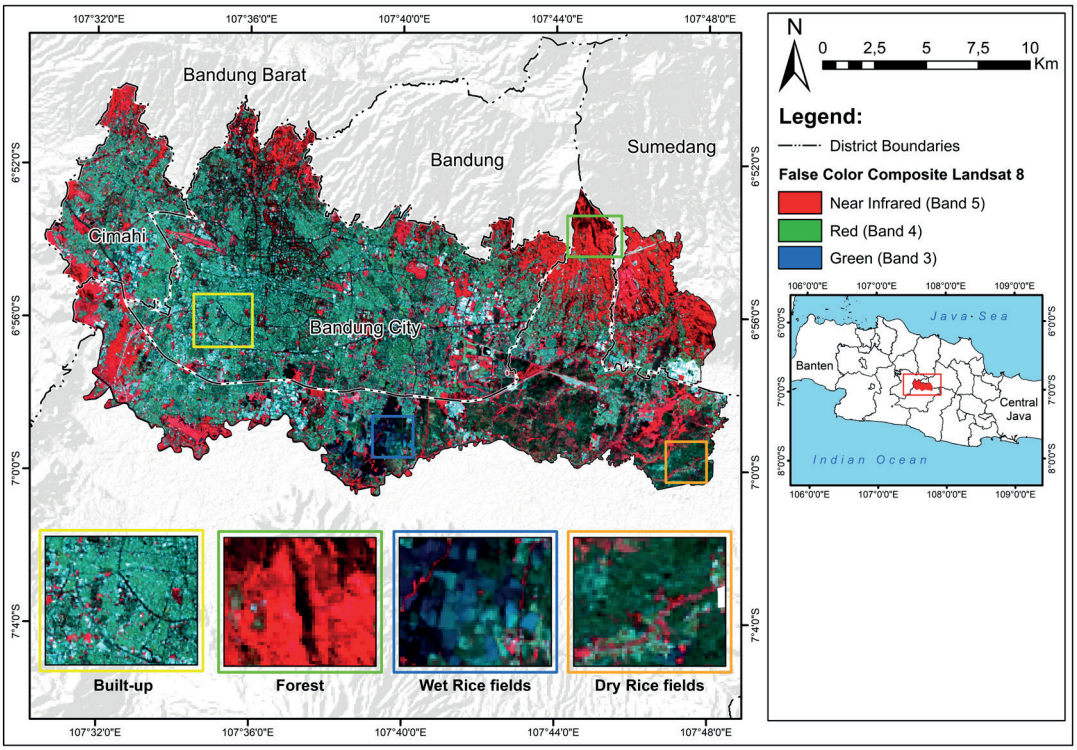

Fig. 1. Study area at Bandung City, West Jawa, Indonesia

Data Source

The data used in this study include remote sensing data in the form of Landsat 8 OLI/TIRS images to build RSEI data, 30 field interview data, and 20 data belonging to the Indonesian National Disaster Management Agency (https://bnpb.go.id/) on ecological issues and disaster event data around the research area, hereinafter referred to as actual data. The Landsat 8 OLI/TIRS image recorded in 2023 used in this study was sourced from the United States Geological Survey (https://www.usgs.gov/). To obtain more comprehensive results, the data was divided into two recording times, namely during the dry season and during the rainy season. The dry season recording was acquired on September 6, 2023, and the wet season was acquired on May 24, 2023, both in path/row 122/065. When choosing the recording time, apart from considering the season, researchers also considered the percentage of cloud cover, where the cloud cover contained in both recording times was below 20%.

Remote Sensing Ecological Index (RSEI)

RSEI was first introduced in 2013 and first applied to the study of ecological change in Tzhangingchow, Fujian Province (Xu 2013). Xu (2013) introduced a remote sensing ecological index (RSEI) that integrates four environmental indicators through satellite image data in the form of greenness index, moisture index, dryness index, and surface temperature to monitor ecological quality (Eq. 1-4). The purpose of RSEI is to test the ability of remote sensing imagery to monitor ecological quality quickly and objectively, which can be visualized. The capabilities of the RSEI-based index itself can be further developed, especially in urban ecological areas (Firozjaei et al. 2021; Wang et al. 2020).

Table 1. RSEI indicator formula

Indicators	Formula	No.
Greenness (NDVI)	$NDVI = (B5 - B4) / (B5 + B4)$	(1)
Moisture (Wetness Index)	$Wet = (0.1511 \times B2) + (0.1972 \times B3) + (0.3283 \times B4) + (0.3407 + B5) - (0.7117 \times B6) - (0.4559 \times B7)$	(2)
Dryness (NDBSI)	$NDBSI = \frac{IBI + SI}{2}$ $IBI = \frac{(B5 + B4) - (B5 - B2)}{(B5 + B4) + (B5 - B2)}$ $SI = \frac{2B6/(B6+B5) - [B5/(B5+B4) + B3/(B3+B6)]}{2B6/(B6+B5) + [B5/(B5+B4) + B3/(B3+B6)]}$	(3)
Surface Temperature (LST)	$L\lambda = ML \times Qcal + AL - Oi$	(4)

Source: (Niu and Li 2020; Seddon et al. 2016; Xu and Zhang 2013; Yue et al. 2019a)

NDVI is a method that can be used to view vegetation cover at various scales by utilizing near and red infrared channels (Seddon et al. 2016; Xu and Zhang 2013). Many studies have found that NDVI is sensitive to low vegetation cover, including urban areas with high building density (Li et al. 2017; H. Wang et al. 2015). NDVI in the RSEI study itself can be used to represent greenness indicators using the near infrared and red bands.

The wetness indicator in RSEI can be represented by the wetness index (WET), where WET is obtained through tassel cap transformation (TCT) to indicate the level of moisture in vegetation and soil objects (Niu and Li 2020). NDBSI in the appearance of field objects symbolizes the influence of urbanization flows and human activity factors that create drought, represented by the level of land development and soil openness. These factors will cause a drought due to the conversion of green land, which causes the deterioration of environmental quality (Yue et al. 2019b). NDBSI is composed of two indices, namely soil index (SI) and Index-based Built-up Index (IBI). LST in Landsat 8 OLI/TIRS imagery is obtained through the thermal channel in band 10, which can be used to represent surface temperature indicators. To obtain LST data, the first step is to convert the digital number (DN) into radians at the top of the atmosphere (ToA).

The four RSEI indicators need to go through a normalization process to avoid non-uniform value ranges; for example, the NDVI value, which is in the range of -1 - 1 is different from the LST value, which has units of °C, so a normalization process is needed to change the value range on each indicator to 0 - 1 with the following equation (Eq. 5-6):

$$NI = (I - Imin) / (Imax - Imin) \quad (5)$$

$$NI = (Imax - I) / (Imax - Imin) \quad (6)$$

where NI is the normalized value, I is the calculated indicator value, Imin is the minimum value of the indicator and Imax is the maximum value of the indicator (Xu, 2013). In the normalization formula number 5 is used for NDVI and WET indicators, while formula number 6 is used for NDBSI and LST indicators to avoid negative correlation, especially for NDVI indicators.

After the four indicators are normalized, the data is ready to be analyzed through PCA. PCA is an analysis that has the ability to identify important variables, where PCA excels in eliminating the impact of the collinearity of the four indicators that make up RSEI (Seddon et al. 2016). PCA analysis in RSEI is used to integrate four indicators that have been normalized and weighted based on the contribution of each index to the value in PC1 (Zhu et al. 2020).

Actual Data Acquisition

The actual data used to find the RSEI threshold value and modeling validation totaled 50 data points, divided into 30 interview data points and 20 disaster event data points throughout 2023. Both interview data and disaster event data serve to provide information on ecological issues, both natural and human-induced. The actual data primarily functions to assess the performance of the RSEI model through ROC AUC analysis and model validation while also determining the threshold value. These data are further categorized into two subsets: training data and validation data, with a distribution of 70% and 30%, respectively. The 50 actual data points will be used for analysis to determine the threshold value and validation, ultimately enabling the determination of the RSEIT interval, particularly the boundary between the good and poor RSEIT classes.

This study used interviews to assess how residents of Bandung City view their local ecological conditions. A total of 30 respondents were selected with specific criteria, such as (1) being more than 17 years old; (2) having a length of stay in the research location of at least 10 years; and (3) having a minimum education of high school. In relation to the area, the respondents were determined randomly but still considered the geographical conditions of the surveyed area so that the output results were more optimal and reflected the actual conditions.

The disaster event data sourced from the Indonesian National Disaster Management Agency (https://bnpb.go.id/) is publicly available. The website provides information regarding the locations of disaster occurrences in the year 2023. Based on this data, 20 regions were selected, but these regions were not included in the interview process.

Determination of Thresholds and Validation Assessment

Receiver Operating Characteristic (ROC) is an analysis often used to measure the performance of a model (Mas et al. 2013). ROC works by utilizing actual and predicted data pairs in the form of contingency tables and area under the curve or (AUC). The contingency table is composed of four categories of paired table results, namely true positive (TP), true negative (TN), false positive (FP), and false negative (FN) (Fig. 2). Meanwhile, AUC is the area under the curve, AUC is used to assess the accuracy performance of actual data which has a value range of 0-1. If the AUC value is <0.5, it means that the tested model has low accuracy and indicates that the model is poor (Fawcett 2006; Zou et al. 2007).

		Prediction	
		Positive (0)	Negative (1)
Actual	Positive (0)	True Positive (TP)	False Positive (FP)
	Negative (1)	False Negative (FN)	True Negative (TN)

Fig. 2. ROC contingency

In this study, the results of RSEI modeling will be analyzed using ROC curves that utilize 70% of training data to generate an AUC value, which is then validated by utilizing 30% of actual data. Training and validation data appear in binary form, where the data is categorized as good (no ecological problems) with code "0" and categorized as poor (there are ecological problems) with code "1". The binary data will be analyzed together with the RSEI modeling that has been made to get the threshold value. In connection with the validation of the ROC curve, an analysis of overall accuracy, sensitivity, and specificity is used (Eq. 7-9):

$$Sensitivity\,(TPR) = \frac{TP}{TP + FN} \quad (7)$$

$$1 - Specificity\,(FPR) = \frac{FP}{FP + FN} \quad (8)$$

$$OverallAccuracy = \frac{TP + TN}{TP + TN + FP + FN} \quad (9)$$

Sensitivity indicates the ability of the RSEIT model to detect true positive cases (TP), in which case the RSEIT class is good; specificity indicates the ability of the model to detect true negative cases (TF), in which case the RSEIT class is poor; and overall accuracy indicates the ability of the model to detect all cases.

RESULTS

Components of RSEI

RSEI indicators collected in 2023 using Landsat 8 OLI/TIRS imagery in both seasons can be categorized into two components, which are positively correlated (NDVI and WET) and negatively correlated (NDBSI and LST). In the NDBSI and LST indicators in the normalization process, the values are reversed. This approach aims to avoid the negative correlation of the NDVI and WET indicators so that the 1-RSEI$_0$ calculation process is not carried out. The normalization results seen in (Fig. 3) show that the highest NDVI and WET are in the periphery of the research area. This is because the area has green land cover, both in the form of stands and non-stands. In the NDBSI and LST indicators, due to the reversal in the normalization process, areas that have high values tend to be green land, like the NDVI and WET indicators, where high values should be in the built-up land zone.

The mean values formed in the two seasons shown in (Fig. 4) each have different means in NDVI, WET, and LST, but the same mean value occurs in the NDBSI indicator. The NDVI, WET, and LST indicators differ by 0.02, 0.04, and 0.03, respectively, while the NDBSI has no difference in value. From the overall mean value of RSEI indicators, indicators other than NDVI have a correlation that is not aligned with the influence of the season. The higher NDVI indicator in the dry season may be due to the influence of the rainy season causing inundation in the green zone area in the southeast of the study area, so the ability of NDVI in the rainy season cannot detect plants in the area.

The PCA results shown in (Table 2) show that PC1 in both seasons has a value above 80%, which indicates PC1 has higher information compared to PC2, PC3, and PC4, where PC1 in the dry season has a higher percentage than the rainy season. In line with this, research by Niu and Li (2020) showed that the higher characteristics of PC1 compared to other PCs can be used as a basis for the formation of the RSEI index. The NDVI indicator appears less

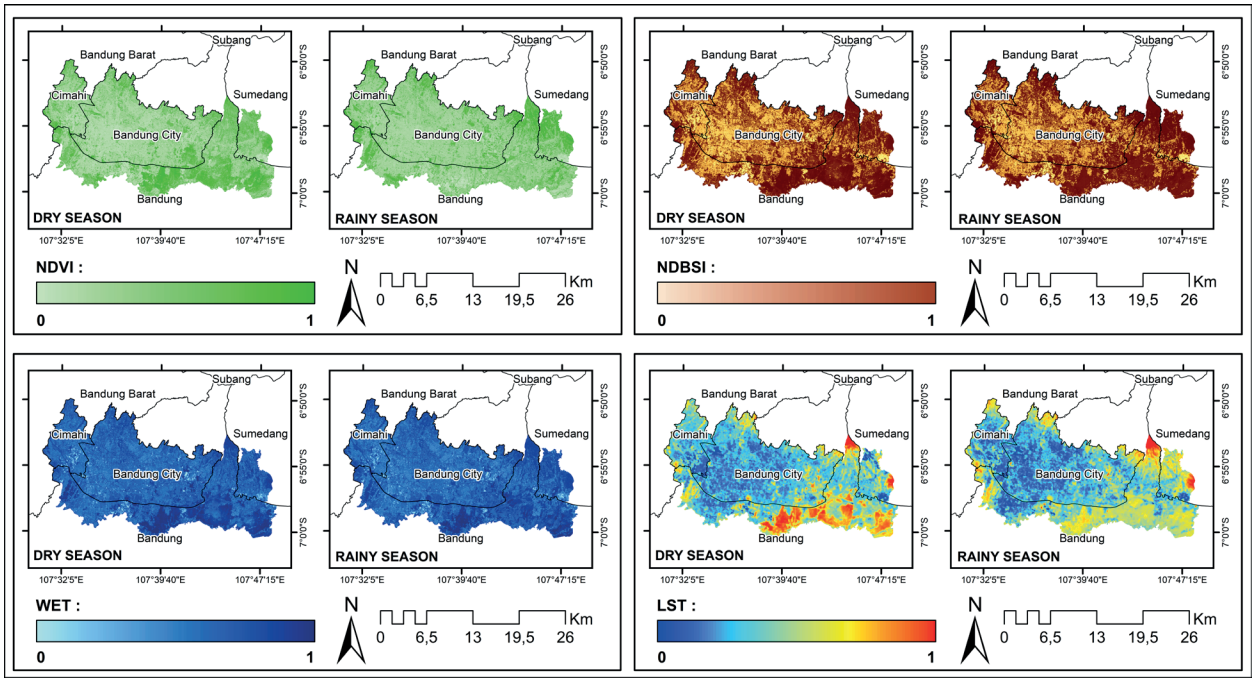

Fig. 3. RSEI indicator map (NDVI, WET, NDBSI, and LST)

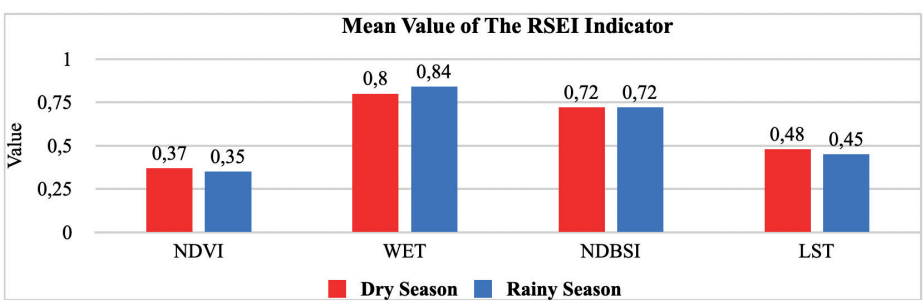

Fig. 4. RSEI indicator mean value diagram

aligned with seasonal conditions. The use of the NIR band in the NDVI algorithm tends to produce higher NDVI during the dry season because the wavelengths in the band are absorbed by water objects. This is because many rice fields and wetlands on the southeast side of Bandung City are waterlogged during the rainy season and overgrown with vegetation during the dry season.

Actual Data Acquisition Results

Bandung City has 5 types of ecological problems throughout 2023 that are considered to interfere with community activities, where problems in the form of flooding are dominant in the region with a percentage of 40%, followed by waste problems by 10%, landslides by 8%, and heat island effect and earthquakes each by 2%. Of the total 5 problems, there is a total of 62% of data indicating that the ecology has a poor status. Meanwhile, 38% of the data states that the ecological conditions in the region are classified as safe because they have never experienced ecological disturbances, especially disasters. Fig. 5 below illustrates the spatial distribution of the actual data collection.

The spatial distribution of ecological issues in Bandung City, particularly flooding, is widespread across the central area, as well as the southern and southeastern parts. Flooding often occurs due to rainwater runoff from elevated areas and the overflow of rivers passing through the study area, such as the Citarum River, especially during the rainy season. The flooding problem in the urban center and the southern parts of Bandung City is primarily caused by extensive surface sealing, which reduces the land's ability to absorb water. In contrast, flooding in the southeastern area, which is predominantly

Table 2. PCA analysis result

PC	Percent of Eigenvalues (%)	
	Dry Season	Rainy Season
PC1	81,61%	80,55%
PC2	13,33%	11,20%
PC3	4,35%	7,50%
PC4	0,70%	0,73%

Source: Primary data Processing

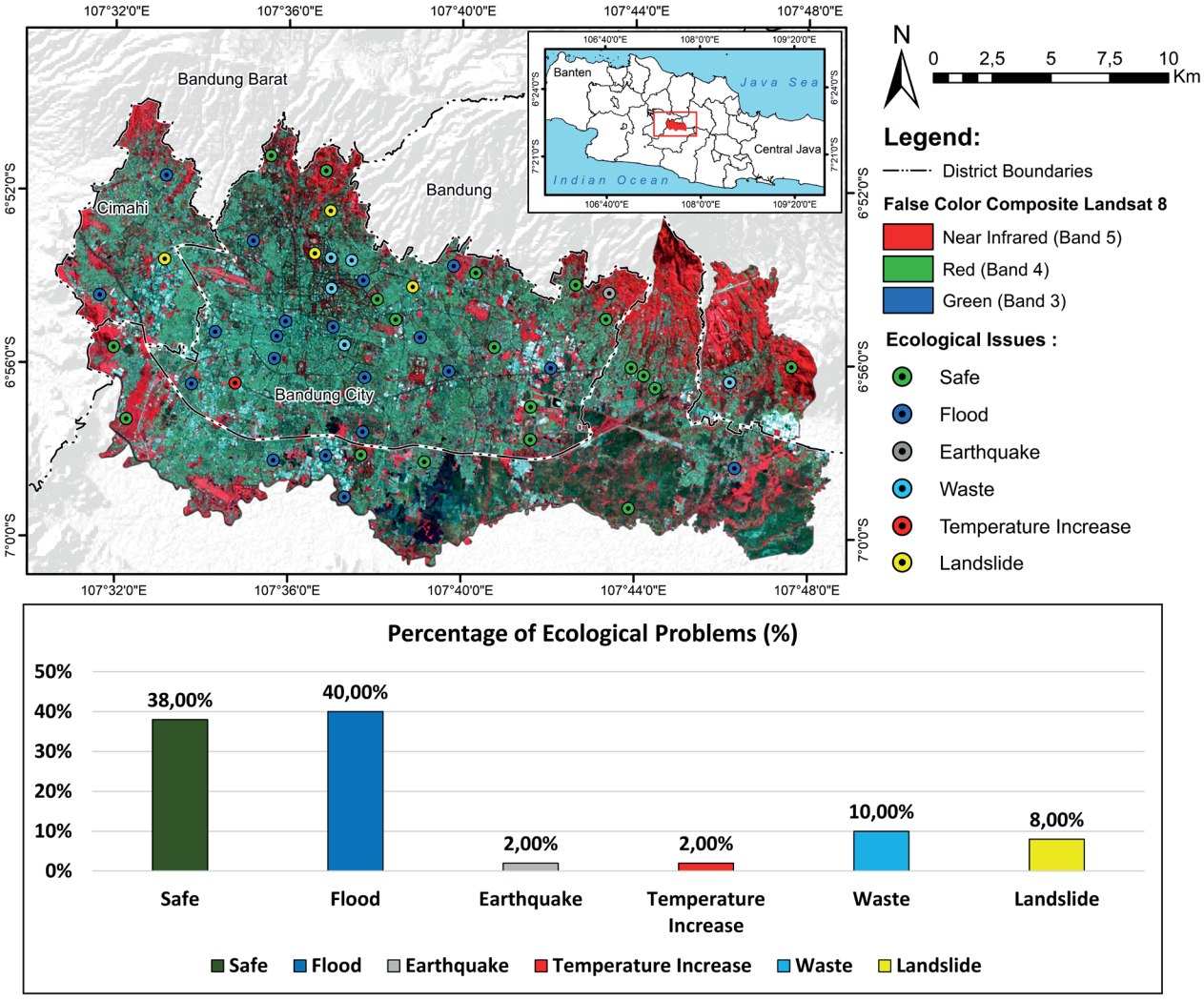

Fig. 5. Respondent distribution map and ecological problem statistics

agricultural land with flat topography, is mainly caused by waterlogging due to soil saturation and low porosity, preventing the land from absorbing and draining water efficiently. Waste management issues in Bandung City have intensified following the closure of the Sarimukti landfill due to a fire, making it difficult for residents to manage domestic waste, leading to the accumulation of trash in residential areas. This situation results in visible waste piles along roadsides and in front of homes. Landslide issues occur in the higher-elevation areas with sloping terrain. Unstable soil conditions, exacerbated by land-use changes from vegetation to residential areas, compromise soil stability. The loss of plant roots, which serve to bind the soil, and the creation of built-up land increase the surface load, further destabilizing the area. The heat island effect persists in the urban center of Bandung City, caused by the high building density in the area without adequate green spaces. Additionally, the scarcity of green zones and tree planting programs contributes to air pollution, along with the prevalence of roads and motor vehicle emissions. Although earthquakes are rare, the Lembang Fault in the northern region poses a potential threat to the safety of residents.

Determination of Threshold Value

The threshold value was determined by utilizing mean RSEI data in PC1 on built-up land and actual data. The built-up land data was used to obtain the mean value of the RSEI index in 2023 for each neighborhood. The data used as field samples is presented in binary form, where the data is categorized as good (no ecological problems) with code "0" and categorized as poor (ecological problems exist) with code "1". Both data will be analyzed together through ROC-AUC curve analysis to determine the threshold value.

The use of field data to determine threshold values yields objective results in the development of the RSEI model into RSEIT. Actual field data helps identify real-world conditions that cannot be captured by satellite imagery. Furthermore, determining the threshold based on real conditions produces results that accurately represent the actual field situation through the validation process conducted (Palapa and Maramis 2014). In line with this statement, the study by (Henrys and Jarvis 2019) indicates that remote sensing data supported by primary field data provides better objectivity. One of the analyses used to determine threshold values is the receiver operating characteristic (ROC) curve, which can test binary data in good and poor categories, formulated based on sensitivity and specificity values, and can be used to generate the cut-off threshold value (Obuchowski et al. 2005). In this context, RSEIT is not only a model but also has the capability to be validated both in terms of model performance and based on actual field conditions.

The AUC value, which shows the performance of the model as shown in (Fig. 6), shows that in the dry season and rainy season, both obtained AUC values of 0.732 and 0.734, respectively. According to research by Carter et al. (2016), predicting a model with an ROC that obtains an AUC value of > 0.7 can be considered logical, especially if only a small sample is used. Through this statement, it can be interpreted that the resulting model has the ability to separate RSEI into good and poor classes. Furthermore, to determine the consistency of the performance of the ROC AUC model, it is necessary to conduct a validation test.

The threshold value formed from the analysis obtained a value of 0.4737 in the dry season and 0.5662 in the rainy season. The cutoff value or threshold value is the determinant of good and poor class boundaries in RSEIT modeling which is used as a reference in the moderate class. Determining the threshold value in this study will certainly produce a different spatial distribution, where Xu (2013) set the value of the moderate class at 0.4 with the equal interval method.

ROC curve validation, as shown in (Table 3), uses three assessments in the form of an overall accuracy value, a

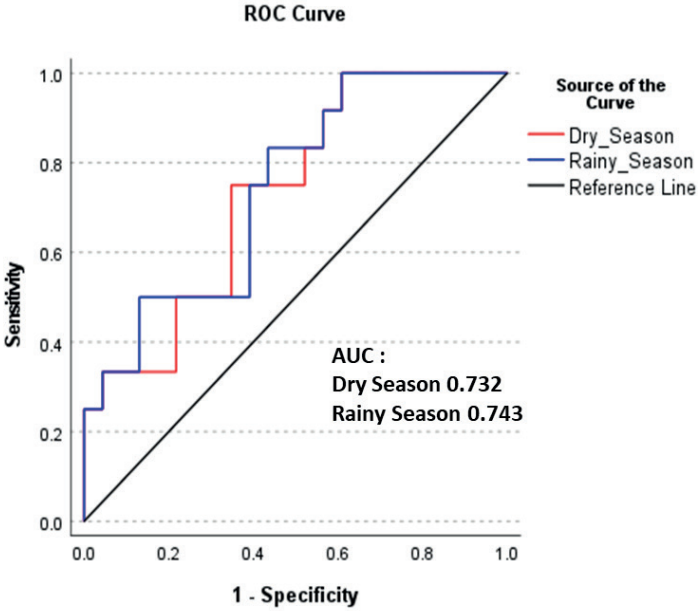

Fig. 6. ROC curve analysis results

Table 3. Results of threshold analysis and validation test

Season	Threshold	Overall Accuracy	Sensitivity	Specificity
Dry Season	0.474	80.00%	71.40%	87.50%
Wet Season	0.566	86.67%	85.70%	87.50%

Source: Primary data processing

sensitivity value, and a specificity value obtained through 30% of the validation data. The overall accuracy value formed in both seasons is greater than 80%. This value can be interpreted as indicating that the resulting model can predict good and poor classes with an accuracy above 80% in the field. The sensitivity value is a value that shows the ability of the model to detect true cases (TP). In this case, the RSEIT class is good, with an ability level of 71.40% in the dry season and 85.70% in the rainy season. Meanwhile, the specificity value used to measure the model's ability to detect true negative cases (TN), in this case the RSEI class is poor, which in both seasons shows an ability of 87.50%.

Threshold Value Based Ecological Index Classification (RSEIT)

The RSEIT classification uses 5 classifications to measure ecological quality in Bandung City, namely very poor, poor, moderate, good, and very good classes. The difference in threshold values between the rainy season and the dry season greatly affects the spatial distribution of RSEIT in each class. Further, (Table 4) shows the RSEI class interval.

In general, the RSEIT intervals formed in both seasons show a higher difference than the interval determined by Xu (2013) of 0.4 in the moderate class. The difference between the RSEI classification applied by Xu (2013) and the RSEIT classification is 0.074 in the dry season and 0.166 in the rainy season. In the very poor, poor, good, and very good classes, the equal interval method is still utilized. In both the dry and wet seasons, the very poor and poor classes used intervals of 0.237 and 0.283, respectively, while the good and very good classes used intervals of 0.176 and 0.145, respectively. The equal interval classification is still used in these classes because RSEIT only looks for thresholds in the moderate class. The interval scale set in the RSEIT classification in the moderate class has a higher value compared to RSEI, which will cause differences in spatial distribution and area in each class.

The spatial distribution of RSEIT in both seasons shown in (Fig. 7) shows a different distribution pattern in both seasons, where in the dry season the distribution in all classes is more varied than in the rainy season. The poor and very poor classes have almost the same distribution in both seasons, where the distribution tends to be centered

Table 4. Class interval RSEIT

Classification	Dry Season Interval	Rainy Season Interval
Very Poor	> 0.236	< 0.282
Poor	0.237 - 0.473	0.283 - 0.565
Moderate	0.474 - 0.648	0.566 - 0.710
Good	0.649 - 0.825	0.711 - 0.855
Very Good	0. 825 <	0.855 <

Source: Primary data processing

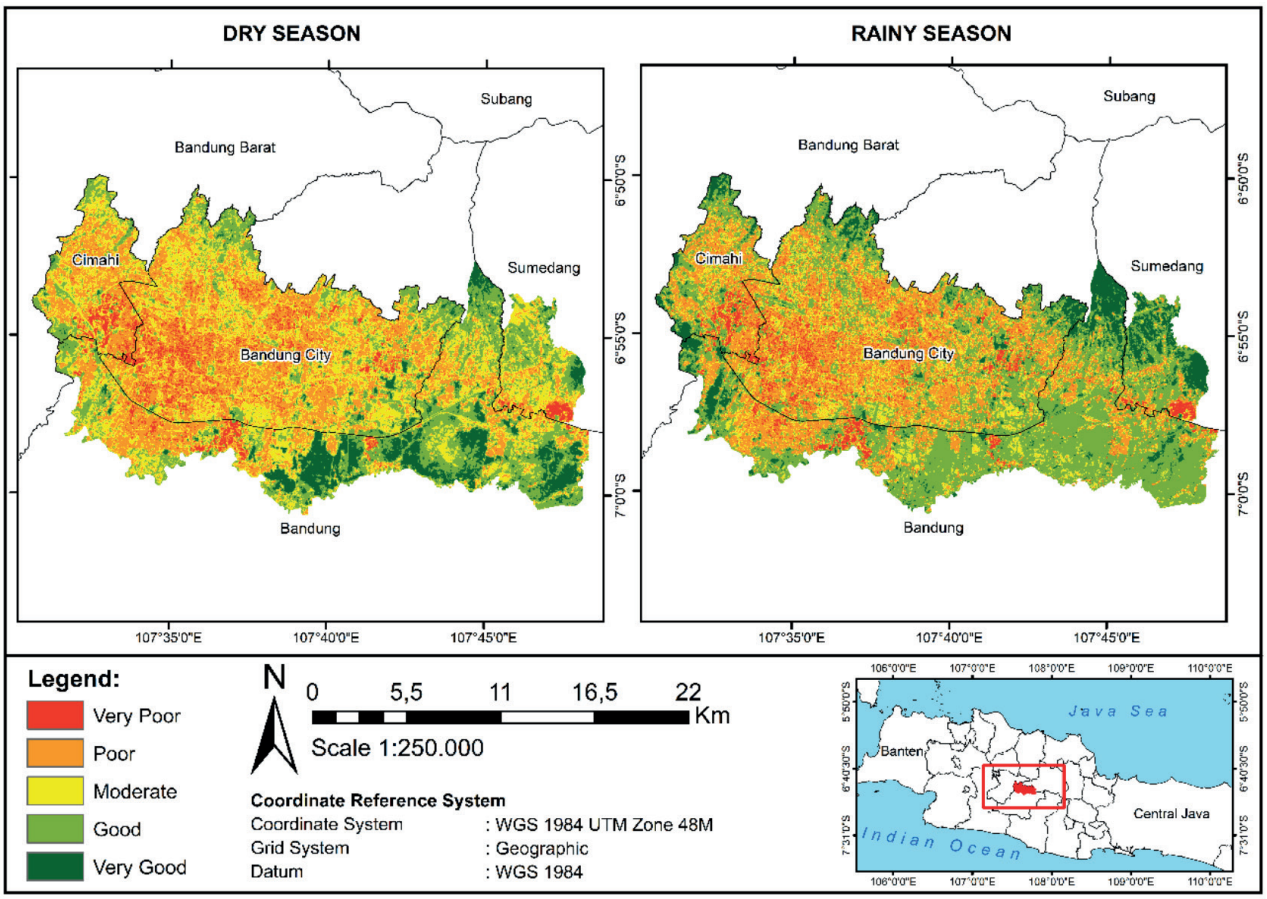

Fig. 7. RSEIT spatial distribution map

in the central area of Bandung City, where there is a lot of built-up land such as settlements, public facilities, and industrial areas. The moderate class in both seasons shows the clearest difference between all classes; in the dry season, the moderate class tends to be evenly distributed in the research area, while in the rainy season, the moderate class tends to be very small. In the good and very good classes, in general, the distribution is on the outskirts of Bandung City, which is found in many green land objects such as forests, plantations, and rice fields. But specifically, it can be seen that the distribution of good and very good classes is more concentrated during the rainy season, even in urban areas of Bandung City.

The percentage of RSEIT area displayed in (Fig. 8) shows that the seasonal factor responded to the spectral value of image data and, when integrated with 50 actual data points, shows logical results in each RSEIT class area. In line with this statement, research by Indrawati et al. (2020) stated that seasonal factors greatly affect the ecological index formed. RSEIT statistics show that the very poor and poor classes will be wider during the dry season with a difference in area of 0.05% and 3.13%, respectively, while the good and very good classes will tend to be wider during the rainy season with a difference in area of 41.72% and 1.14%, respectively. On the other hand, the moderate class is widely higher during the dry season than during the rainy season with a difference of 15.32%.

The formation of spatial distribution patterns and the extent of the RSEIT area can be viewed from the aspect of the season that affects the NDVI and WET indicators, as well as the aspect of the threshold value. In terms of seasonal influence, NDVI and WET indicators associated with vegetated green zones will be higher during the rainy season. This is in line with statements in previous studies, where ecological quality is strongly influenced by the presence of vegetation; the higher the vegetation cover, the better the ecological condition of the area (Cheng and He 2019; Su et al. 2022). In the aspect of threshold values that reflect actual conditions in the field, it proves that the concentration of ecological problems in urban areas makes poor and very poor index classes tend to be formed in urban areas, while good and very good classes tend to be formed in urban peripheries.

DISCUSSION

Remote sensing is currently one of the most important elements in assessing ecological quality. The ability of remote sensing data to provide spatial and temporal resolution is a distinct advantage for examining large areas, such as the area used in this study. RSEI is one method that can currently be used to analyze urban ecological quality. Xu (2013) introduced RSEI, which uses basic data in the form of remote sensing data that integrates four environmental indicators using PCA. PCA on PC1 is the basis for forming five RSEI classes with an equal interval model. Niu and Li (2020) shows that the higher characteristics of PC1 compared to other PCs can be used as the basis for the formation of the RSEI index. A total of 5 classes broken down based on equal interval calcification does not pay attention to actual conditions in the field. In line with this, Wang et al. (2023) research states that RSEI still has weaknesses, such as the fact that the fact that the resulting output is still probabilistic and cannot be applied in general. Furthermore, in several similar studies, RSEI was not validated, meaning that actual field conditions were not taken into account. Compared to RSEI, RSEIT has the ability to determine threshold values through ROC AUC analysis, and its results can be tested through overall accuracy, sensitivity, and specificity calculations.

Research on ecological indices based on the Remote Sensing Ecological Index (RSEI) is generally similar across different regions, with minimal variation in methods and results, as assessments rely solely on indicators derived from remote sensing data. Several studies on RSEI in Indonesia and Asia, such as those by Dai et al. (2023) on the Jakarta-Bandung High-Speed Railway in Indonesia, Indrawati et al. (2020) in Semarang City, dan Giofandi et al. (2024) in Pekanbaru City, as well as studies in Asia by Diep et al. (2024) in Chan Tho City, Vietnam dan Zhang et al. (2024) in Wuhan City, China, generally conclude that ecological quality assessments remain limited to the RSEI approach without further development using additional data or methods. Specifically, these studies indicate that areas with high RSEI quality are often located in regions with high elevations, steep slopes, abundant vegetation, low temperatures, and low humidity. Conversely, areas with poor ecological quality are typically found in regions dominated by urbanized, built-up land, characterized by flat topography, sparse vegetation, low humidity, and high temperatures. This condition highlights that RSEI-based ecological assessments focus solely on four physical environmental variables derived from remote sensing sensors, with the eigenvalue relationships (particularly on PC1) serving as a benchmark to determine the extent to which each RSEI variable contributes to the overall ecological quality.

In fact, for the ecological assessment of Bandung City in 2023 across both seasons, areas with high (good) ecological index values do not always align with being free from ecological issues based on actual data. For example, the northern region of Bandung City (Figure 5), which is still lush, heavily vegetated, and sparsely populated, faces ecological challenges such as earthquake and landslide threats due to its steep terrain and proximity to the Lembang Fault. To address this, the RSEIT model enhances the capabilities of the RSEI algorithm by incorporating actual data, determining threshold values through ROC curve analysis in conjunction with RSEI data, and conducting model validation tests to evaluate the extent

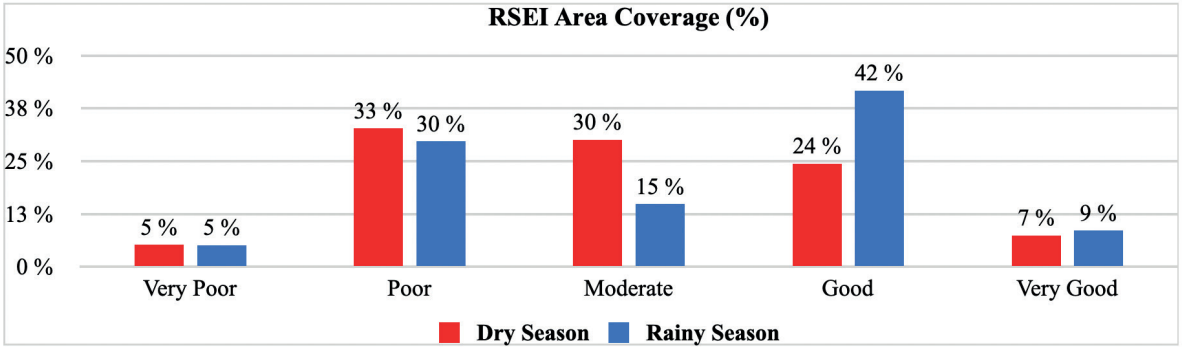

Fig. 8. RSEIT area coverage diagram

to which the RSEIT model represents factual conditions. This approach offers an alternative for producing ecological quality assessments (RSEIT) that better reflect actual field conditions, particularly in areas with high index values that still face ecological challenges and vice versa.

Research areas that have ecological problems can be a measure of good or poor ecological quality. Through 50 actual data points for 2023 used as input to determine the threshold value, it was found that 62% of the study areas have ecological problems, with a ratio of 4 out of 5 problems directly connected to natural problems such as natural disasters. The distribution of areas with ecological problems also adjusts the physical characteristics of the area, such as flooding, waste, and the heat island effect, which tend to be clustered in urban areas that have low elevation in built-up land zones, while landslides and earthquakes tend to be scattered in upland areas with land cover dominated by green zones. These findings are field facts that can be utilized to test the extent to which remote sensing data can detect ecological conditions according to actual conditions through threshold analysis.

The ROC analysis value shown in the (Fig. 6) obtained an AUC value of > 0.7; this value can still be considered for use, especially if the sample used has a relatively small amount. The performance of the RSEIT model, which produces a threshold value of 0.4737 in the dry season and 0.5662 in the rainy season, needs to be tested for its application to 30% of the of the validation data. The threshold value used in the RSEIT index classification shows a higher value during the rainy season with a difference of 0.092; this is strongly influenced by the spectral response in the rainy season, where NDVI and WET indicators have an important role. During the rainy season, the level of wetness and greenness increases, especially in the training area. This is in accordance with the statement of Xu and Deng (2022), where ecological conditions are largely determined by the greenery element of vegetation. The results of the validation assessment on RSEIT data in both seasons showed an average value of overall accuracy, sensitivity, and specificity of 83.34%, 78.55%, and 87.50%, respectively. These results show that RSEIT has a capability of over 70% in its implementation in the field.

The spatial distribution of RSEIT in both seasons (Fig. 7) exhibits a distinct pattern, with a more varied distribution across all classes during the dry season compared to the rainy season. The poor and very poor classes have almost the same distribution in both seasons, where the distribution tends to be centered in the central area of Bandung City, where there is a lot of built-up land such as settlements, public facilities, and industrial areas.

The impervious surface in urban centers, without being balanced by green spaces such as city parks and vegetation planting, results in high values of NDBSI and LST, both of which are negatively correlated with RSEIT. Furthermore, based on actual data, this condition is exacerbated by the ecological issues commonly found in urban areas. The moderate class in both seasons shows the clearest difference between all classes, where in the dry season the distribution of the moderate class tends to be evenly distributed in the research area, while in the rainy season the distribution of the moderate class tends to be very small. In the good and very good classes, in general, the distribution is on the outskirts of Bandung City, which is found in many green land objects such as forests, plantations, and rice fields. The peripheral areas, which are often characterized by green zones, result in high values for the WET and NDVI variables, both of which show a positive correlation with RSEIT. Meanwhile, ecological issues are generally less prevalent in these peripheral areas. But specifically, the distribution of good and very good classes is formed during the rainy season, even in urban areas of Bandung City. Based on previous research, the spatial distribution of RSEIT is strongly influenced by land cover and land use, and the reflection of spectral values recorded on the sensor will adjust the recorded object (Yuan et al. 2021). In line with the spatial distribution formed, the RSEIT statistics of poor and very poor classes will be wider during the dry season, while the good and very good classes will tend to be wider during the rainy season. On the other hand, in the moderate RSEIT class, it tends to be higher during the dry season than during the rainy season. In line with this statement, according to research by Indrawati et al. (2020) in Semarang City, the ecological conditions formed are strongly influenced by the current seasonal conditions.

CONCLUSIONS

This research aims to determine the threshold value of the urban ecological quality index (RSEIT) in Bandung City in 2023. This research produced three findings that can be summarized: (1) Ecological problems are most prevalent in urban areas of Bandung City, where community activities are concentrated. Actual data shows that 63% of the study area experienced ecological problems mainly caused by nature. There are at least 3 main problems that occur, namely flooding, garbage, and landslides; (2) The RSEIT model obtained threshold values of 0.474 and 0.566 during the dry and rainy seasons, respectively. According to the ROC analysis, the RSEIT modeling demonstrated performance exceeding 0.7, classifying it as suitable for further validation testing. Additionally, the validation results for both seasons showed average values for overall accuracy, sensitivity, and specificity of 83.34%, 78.55%, and 87.50%, respectively, all exceeding 70%. These results directly indicate that the RSEIT model is capable of being validated based on actual field conditions, and (3) furthermore, urban centers with high surface imperviousness, limited vegetation, and prevalent ecological issues are predominantly classified under the poor category by RSEIT, especially during the dry season. In contrast, suburban areas, which maintain a higher proportion of green spaces and face fewer ecological problems, are more frequently classified under the good category, particularly during the rainy season.

Nevertheless, this study is still limited to a single threshold value for distinguishing between good and poor ecological quality (moderate class). The entire RSEIT classification system (very poor, poor, moderate, good, very good) should also employ threshold values supported by a set of qualified actual data. Although actual data sourced from disaster occurrence records and interviews can serve as references for factual condition information, it would be preferable for the data collection process to also involve other parties, such as academics and local policymakers, to enrich the data pool and provide more detailed information. Such involvement would enhance the RSEIT output in terms of model performance and validation, bringing it closer to reality.

REFERENCES

Ary M. F. A. A., Rondonuwu D. M., & Warouw, F. (2018). Kampung Susun Di Manado. Social Design. Jurnal Arsitektur DASENG, 7(2).

Budiman, A., Sulistyantara, B., & Zain, A. F. (2014). Deteksi Perubahan Ruang Terbuka Hijau Pada 5 Kota Besar Di Pulau Jawa (Studi Kasus : DKI Jakarta, Kota Bandung, Kota Semarang, Kota Jogjakarta, Dan Kota Surabaya). Jurnal Lanskap Indonesia, 6(1).

Caio C. de Araujo Barbosa, Atkinson, P. M., & Dearing, J. A. (2015). Remote sensing of ecosystem services: A systematic review. In Ecological Indicators (Vol. 52). https://doi.org/10.1016/j.ecolind.2015.01.007

Carter, J. V., Pan, J., Rai, S. N., & Galandiuk, S. (2016). ROC-ing along: Evaluation and interpretation of receiver operating characteristic curves. Surgery (United States), 159(6). https://doi.org/10.1016/j.surg.2015.12.029

Cheng, Z., & He, Q. (2019). Remote Sensing Evaluation of the Ecological Environment of Su-Xi-Chang 466 City Group based on Remote Sensing Ecological Index (RSEI). Remote Sensing Technology and Application, 34(3), 531–539.

Dai, X., Chen, J., & Xue, C. (2023). Spatiotemporal Patterns and Driving Factors of the Ecological Environmental Quality along the Jakarta–Bandung High-Speed Railway in Indonesia. Sustainability, 15(16), 12426. https://doi.org/10.3390/su151612426

Diep, N. T. H., Nguyen, N. T., Hieu, D. C., Huong, N. T. T., & Trang, D. H. (2024). Environmental Quality Monitoring Using Remote Sensing Ecological Index (RSEI) in Can Tho City, Vietnam. IOP Conference Series: Earth and Environmental Science, 1345(1). https://doi.org/10.1088/1755-1315/1345/1/012018

Environmental Office Bandung City. (2022). Performance Information Document Environmental Management Bandung City in 2022.

Fawcett, T. (2006). An introduction to ROC analysis. Pattern Recognition Letters, 27(8). https://doi.org/10.1016/j.patrec.2005.10.010

Firozjaei, M. K., Fathololoumi, S., Kiavarz, M., Biswas, A., Homaee, M., & Alavipanah, S. K. (2021). Land Surface Ecological Status Composition Index (LSESCI): A novel remote sensing-based technique for modeling land surface ecological status. Ecological Indicators, 123. https://doi.org/10.1016/j.ecolind.2021.107375

Giofandi, E. A., Syahzaqi, I., Sekarjati, D., Putriana, A. M., Putti, H. M. D. M., & Sekarrini, C. E. (2024). Assessment Of Remote Sensing Approach For Urban Ecological Quality Evaluation In Pekanbaru City, Riau Province Indonesia. GEOGRAPHY, ENVIRONMENT, SUSTAINABILITY, 17(1), 28–35. https://doi.org/10.24057/2071-9388-2023-2640

Henrys, P. A., & Jarvis, S. G. (2019). Integration of ground survey and remote sensing derived data: Producing robust indicators of habitat extent and condition. Ecology and Evolution, 9(14). https://doi.org/10.1002/ece3.5376

Indrawati, L., Sigit Heru Murti, B. S., & Rachmawati, R. (2020). Integrated ecological index (IEI) for urban ecological status based on remote sensing data: A study at Semarang - Indonesia. IOP Conference Series: Earth and Environmental Science, 500(1). https://doi.org/10.1088/1755-1315/500/1/012074

Indrawati, L., Sigit Heru Murti, B. S., Rachmawati, R., & Aji, D. S. (2020). Effect of Urban Expansion Intensity on Urban Ecological Status Utilizing Remote Sensing and GIS: A Study of Semarang-Indonesia. IOP Conference Series: Earth and Environmental Science, 451(1), 012018. https://doi.org/10.1088/1755-1315/451/1/012018

Kustiwan, I., & Ladimananda, A. (2012). Pemodelan Dinamika Perkembangan Perkotaan dan Daya Dukung Lahan di Kawasan Cekungan Bandung. Tataloka, 14(2).

Kwok, R. (2018). Ecology's remote-sensing revolution. In Nature (Vol. 556, Issue 7699). https://doi.org/10.1038/d41586-018-03924-9

Lestiani, D. D., Santoso, M., Kurniawati, S., & Markwitz, A. (2013). CHARACTERISTIC OF AIRBORNE PARTICULATE MATTER SAMPLES COLLECTED FROM TWO SEMI INDUSTRIAL SITES IN BANDUNG, INDONESIA. Indonesian Journal of Chemistry, 13(3), 271–277. https://doi.org/10.22146/ijc.21287

Li, Y., Cao, Z., Long, H., Liu, Y., & Li, W. (2017). Dynamic analysis of ecological environment combined with land cover and NDVI changes and implications for sustainable urban–rural development: The case of Mu Us Sandy Land, China. Journal of Cleaner Production, 142, 697–715. https://doi.org/10.1016/j.jclepro.2016.09.011

Mas, J. F., Filho, B. S., Pontius, R. G., Gutiérrez, M. F., & Rodrigues, H. (2013). A suite of tools for ROC analysis of spatial models. ISPRS International Journal of Geo-Information, 2(3). https://doi.org/10.3390/ijgi2030869

Ministry of Environment and Forestry of the Republic of Indonesia. (2022). Indeks Kualitas Lingkungan Hidup.

Muchtar, H. S., Wijaya, I. N. S., & Setyono, D. A. (2024). Pembangunan Berkelanjutan Perkotaan Dalam Aspek Ekologi Kota Bandung. Planning for Urban Region and Environment Journal (PURE), 13(3), 193–204.

Niu, X., & Li, Y. (2020). REMOTE SENSING EVALUATION OF ECOLOGICAL ENVIRONMENT OF ANQING CITY BASED ON REMOTE SENSING ECOLOGICAL INDEX. The International Archives of the Photogrammetry, Remote Sensing and Spatial Information Sciences, XLIII-B3-2020, 733–737. https://doi.org/10.5194/isprs-archives-XLIII-B3-2020-733-2020

Obuchowski, N. A., Blackmore, C. C., Karlik, S., & Reinhold, C. (2005). Fundamentals of clinical research for radiologists. American Journal of Roentgenology, 184(2). https://doi.org/10.2214/ajr.184.2.01840364

Palapa, T. M., & Maramis, A. A. (2014). Pemantauan Melalui Observasi Lapang, Pencitraan Satelit, dan SIG Tambang Talawaan-Tatelu. Prosiding Seminar Nasional Sains Dan Pendidikan Sains IX 2014, 594–601.

Reza, M. I. H., & Abdullah, S. A. (2011). Regional Index of Ecological Integrity: A need for sustainable management of natural resources. In Ecological Indicators (Vol. 11, Issue 2). https://doi.org/10.1016/j.ecolind.2010.08.010

Seddon, A. W. R., Macias-Fauria, M., Long, P. R., Benz, D., & Willis, K. J. (2016). Sensitivity of global terrestrial ecosystems to climate variability. Nature, 531(7593), 229–232. https://doi.org/10.1038/nature16986

Su, S., Zhaoning, G., Wenjing, Z., Yuan, Z., & Yifei, W. (2022). Change of vegetation coverage 560 and assessment of ecological environment quality in Beiyun River Basin. Acta Scientiae Circumstantiae, 42(1), 19–27.

Suprayogi, S., Tivianton, A., Nurchayati, W., & Mukarromah, D. (2013). Relevansi Spasial Indeks Kualitas Lingkungan Hidup dengan Pengetahuan Siswa akan Kesiapsiagaan Perubahan Lingkungan dan Iklim (Studi Kasus: SMU, SMP, SD sekitar Kota Yogyakarta, D.I. Yogyakarta). Prosiding Seminar Nasional Geografi UMS.

Wang, H., Liu, D., Lin, H., Montenegro, A., & Zhu, X. (2015). NDVI and vegetation phenology dynamics under the influence of sunshine duration on the Tibetan plateau. International Journal of Climatology, 35(5). https://doi.org/10.1002/joc.4013

Wang, J., Ma, J. L., Xie, F. F., & Xu, X. J. (2020). [Improvement of remote sensing ecological index in arid regions: Taking Ulan Buh Desert as an example]. Ying Yong Sheng Tai Xue Bao = The Journal of Applied Ecology, 31(11), 3795–3804. https://doi.org/10.13287/J.1001-9332.202011.011

Wang, Z., Chen, T., Zhu, D., Jia, K., & Plaza, A. (2023). RSEIFE: A new remote sensing ecological index for simulating the land surface eco-environment. Journal of Environmental Management, 326, 116851. https://doi.org/10.1016/J.JENVMAN.2022.116851

Widiawaty, M. A., Dede, Moh., & Ismail, A. (2019). ANALISIS TIPOLOGI URBAN SPRAWL DI KOTA BANDUNG MENGGUNAKAN SISTEM INFORMASI GEOGRAFIS. Seminar Nasional Geomatika, 3. https://doi.org/10.24895/sng.2018.3-0.1007

Xu, H. (2013). A remote sensing urban ecological index and its application. Acta Ecol, 7853–7862.

Xu, H., & Deng, W. H. (2022). Rationality analysis of MRSEI and its difference with RSEI. Remote Sensing Technology, 37, 1–7.

Xu, H., & Zhang, T. (2013). Assessment of consistency in forest-dominated vegetation observations between ASTER and Landsat ETM+ images in subtropical coastal areas of southeastern China. Agricultural and Forest Meteorology, 168. https://doi.org/10.1016/j.agrformet.2012.08.012

Yuan, B., Fu, L., Zou, Y., Zhang, S., Chen, X., Li, F., Deng, Z., & Xie, Y. (2021). Spatiotemporal change detection of ecological quality and the associated affecting factors in Dongting Lake Basin, based on RSEI. Journal of Cleaner Production, 302, 126995. https://doi.org/10.1016/j.jclepro.2021.126995

Yue, H., Liu, Y., Li, Y., & Lu, Y. (2019a). Eco-Environmental Quality Assessment in China's 35 Major Cities Based On Remote Sensing Ecological Index. IEEE Access, 7, 51295–51311. https://doi.org/10.1109/ACCESS.2019.2911627

Yue, H., Liu, Y., Li, Y., & Lu, Y. (2019b). Eco-environmental quality assessment in china's 35 major cities based on remote sensing ecological index. IEEE Access, 7. https://doi.org/10.1109/ACCESS.2019.2911627

Zhang, W., Zhang, W., Ji, J., & Chen, C. (2024). Urban Ecological Quality Assessment Based on Google Earth Engine and Driving Factors Analysis: A Case Study of Wuhan City, China. Sustainability (Switzerland) , 16(9). https://doi.org/10.3390/su16093598

Zhu, H., Wang, J. L., Cheng, F., Deng, H., Zhang, E. W., & Li, Y. X. (2020). [Monitoring and evaluation of eco-environmental quality of lake basin regions in Central Yunnan Province, China]. Ying Yong Sheng Tai Xue Bao = The Journal of Applied Ecology, 31(4), 1289–1297. https://doi.org/10.13287/J.1001-9332.202004.011

Zou, K. H., O'Malley, A. J., & Mauri, L. (2007). Receiver-operating characteristic analysis for evaluating diagnostic tests and predictive models. Circulation, 115(5). https://doi.org/10.1161/CIRCULATIONAHA.105.594929

RESEARCH PAPER

EVALUATING SINKHOLE HAZARD SUSCEPTIBILITY USING LOGISTIC REGRESSION MODEL IN KHLONG I PAN SUB-WATERSHED, SURAT THANI AND KRABI PROVINCE, THAILAND

Katawut Waiyasusri[1*], Parichat Wetchayont[2], Keerati Sripramai[2]

[1]Suan Sunandha Rajabhat University, Faculty of Humanities and Social Sciences, Geography and Geo-informatics Program, 1 U-Thong Nok Road, Dusit, Bangkok, 10300, Thailand

[2]Navamindradhiraj University, Faculty of Science and Health Technology, Disaster Management Program, 3 Khao Road, Wachira Phayaban, Dusit District, Bangkok, 10300, Thailand

***Corresponding author:** katawut.wa@ssru.ac.th

Received: May 5th 2024 / Accepted: April 24rd 2025 / Published: June 30th 2025

https://doi.org/10.24057/2071-9388-2025-3431

ABSTRACT. Sinkholes have frequently occurred over the past 20 years in the Khlong I Pan sub-watershed (KIPs) in Surat Thani and Krabi Province, Thailand. It was found that the earth collapsed more than 34 times. The objective of this research is to evaluate the sinkhole susceptibility using Logistic Regression (LR) analysis at the sub-watershed scale. This methodology used 14 variables affecting sinkhole occurrence to analyze the area, and create a sinkhole susceptibility map using LR. The results found that the variables that affect sinkhole formation include Well Density (WD), geology, Land Use (LU), Total Hardness (TH), Total Dissolved Solids (TDS), slope, Chlorine (Cl), distance to stream, elevation, Topographic Wetness Index (TWI), distance to village, soil, distance to active fault, and distance to well, respectively. All such variables are expressed by the exp β value coefficient. When prepared as a Karst sinkholes (KS) susceptibility map, it was found that a very high sinkhole susceptibility level covers an area of up to 399.86 km^2 (19.16% of the total area). They appear mainly in the eastern region of the KIPs, especially at the confluence of the Khlong I Pan stream and the Khlong Trom stream. The other area is the central mountain range and the western mountain range, where geological structures with a casque topography are found. The results of this research suggest using the KS Susceptibility Map as a guideline for planning and monitoring potential future sinkholes.

KEYWORDS: karst, sinkhole, susceptibility, Khlong I Pan sub-watershed, Surat Thani Province, Krabi Province, logistic regression

CITATION: Waiyasusri K., Wetchayont P., Sripramai K. (2025). Evaluating sinkhole hazard susceptibility using Logistic Regression Model In Khlong I Pan Sub-Watershed, Surat Thani and Krabi Province, Thailand. Geography, Environment, Sustainability, 2 (18), 32-47

https://doi.org/10.24057/2071-9388-2025-3431

ACKNOWLEDGEMENTS: Gratefully acknowledge for Suan Sunandha Rajabhat University Research Grant.

Conflict of interests: The authors reported no potential conflict of interests..

INTRODUCTION

A sinkhole is a type of natural disasters that often occurs in limestone or karst topography (Cvijić 1925; Trofimova 2018; De Waele and Gutierrez 2022). Most of these topographical features are composed of carbonate bedrock such as limestone ($CaCO_3$) and dolomite ($CaMg(CO_3)_2$) (Zeng and Zhou 2019). When carbonate rocks contact with acidic rainfall and groundwater, the carbonate rocks are dissolved to form tall limestone pinnacles and subsurface caves, called karst topography, with large caverns containing stalactites and stalagmites and groundwater streams (La Rosa et al. 2018; De Castro et al. 2024). Accordingly, sinkholes generally form when the surface layer above the holes or caves is collapsed by the groundwater level dropping, landslides and subsidence of the upper surface, underground excavation, groundwater extraction, or earthquakes. Sinkholes cause substantial damage to life and property.

Researchers in the United States created karst topographic maps by collecting geological data and documenting the occurrence of valleys with historical evidence of sinkholes. However, a lack of data, including geological data, soil series, hydrogeology, and data on urban expansion in each region, has left the situation unclear (Veni 2002). Continuous improvements have been made to try to predict sinkhole formation, and it has been concluded that hydrogeological conditions are the main variable that makes sinkholes more likely to collapse (Nam et al. 2020; Wood et al. 2023). There are many reports of sinkholes around the world, such as in Tangshan, China (Hu et al. 2001), the Ebro Valley, Zaragoza, Spain (Galve et al. 2009a), Sango, Tennessee, USA (Siska et al. 2016) and major urban areas of Brazil (Galvão et al. 2015; de Queiroz Salles et al. 2018). All of these areas have subsidence phenomena due to their unique geological and geomorphological characterization (Stefanov et al. 2023). Geo-information

technology is widely used in research studies to find sinkhole susceptibility because it is possible to define algorithms and conditions to evaluate and predict areas at risk of sinkhole formation. The researchers used spatial analysis to determine sinkhole susceptibility by using variables that affect sinkhole formation in multivariate analysis (Wu et al. 2018; Jia et al. 2019). There are many approached models of multivariate analysis, including spatial overlay analysis, probabilistic modeling, conditional probability, analytic hierarchy process (AHP), LR modeling, and machine learning. Research by Zhou et al. (2016) analyzed sinkholes that occur in Jili Village in Guangxi, China, using an LR model. The results show that the highest susceptibility area for sinkholes is in the foothills and Datou Hill. This information was beneficial for developing a mitigation plan for the communities living near the sinkhole area. Kim et al. (2018) applied an LR model to assess sinkhole susceptibility in urban areas caused by underground wastewater drainage. The model addresses key variables such as slope and pipe material that are sensitive to sinkholes in the area. Jia et al. (2019) used machine learning and a cloud model to analyze areas sensitive to sinkhole formation using topography and geology characteristics variables. This technique shows the sensitivity of the geological structure. Hu et al. (2021) used analytical hierarchy process and LR models to test the accuracy of the techniques to assess the susceptibility to sinkholes in the Wuhan city area of China. The results show that LR models have better performance than analytical hierarchy process models. In conditions of climate change, rainfall amounts change, causing rainfall patterns to become more variable. Xu et al. (2023) emphasized the significance of rainfall variables in causing soil erosion on karst terrain in Southwestern China, suggesting future terrain subsidence and erosion trends. Amin et al. (2023) utilized machine learning to analyze subsidence in Central Iran, identifying geological structure and underground pores as crucial factors in predicting sinkhole-prone areas. Maleki et al. (2023) investigated sinkhole susceptibility in Iran's Bistoon-Parav karst region, considering 10 variables including precipitation, lithology, and vegetation. Their findings highlighted lithology as the most influential factor, accounting for 31.52% of sinkhole occurrences. Ramírez-Serrato et al. (2024) tried to find sinkholes in Mexico City by using linear regression models to import data on 13 variables that affect the occurrence of sinkholes, including population density, WD, distance to faults, fractures, roads, streams, elevation, slope, clay thickness, lithology, subsidence rate, geotechnical zones, and soil texture. The findings demonstrate the efficacy of regression models in predicting susceptibility to sinkhole occurrences. Utilizing advancements in geoinformatics technology enables the comprehensive analysis of diverse databases, facilitating the effective assessment of areas prone to sinkhole formation. Such analyses can generate risk maps, offering guidelines for managing vulnerable areas and implementing preventative measures to mitigate potential loss of life and property resulting from these disasters.

In Thailand, sinkholes are prevalent in karst landscapes, particularly in limestone formations dating back to the Permian period, around 286-245 million years ago. Notable rock groups susceptible to sinkholes include the Rachaburi, Saraburi, and Ngao groups. The Rachaburi group, originating from the Middle to Upper Permian period, spans the lower western and southern regions of Thailand (Sone et al. 2012). The Saraburi group extends across the lower Chao Phraya plains and western edge of the Korat plateau, formed during the Upper Carboniferous to Lower Permian period (Udchachon et al. 2022). Sinkholes are primarily found in the northern region of Thailand, where the Ngao group, formed during the Upper Permian period, is prevalent (Pondthai et al. 2023).

Human activities such as groundwater extraction, saltwater pumping, traffic vibrations, and construction exacerbate sinkhole formation, particularly in areas with limestone, dolomite, and marble bedrock prone to dissolution. The Department of Mineral Resources documented sinkhole occurrences from 1995 to 2005, with 66 areas experiencing large sinkholes, notably 25 following the 2004 earthquakes and tsunamis along the Andaman Sea coast in southern Thailand (Frost-Killian 2008; Szczuciński 2020). Urbanization and increased groundwater usage in southern cities contribute to heightened sinkhole risks due to land surface changes and associated land use alterations.

Today, climate change is a major challenge that greatly affects human life, the environment, and economic development. In particular, changes in seasonal rainfall patterns can make sinkholes more severe. This is particularly true for sinkholes that arise from fluctuations in the average annual rainfall and groundwater storage levels.To achieve preventive measures to reduce the loss of life and property caused by such disasters, and consistent with the principles of the United Nations Sustainable Development Goals (SDGs), Goal 13 addresses taking urgent action to combat climate change and its impacts. Arora and Mishra (2023) suggest that current climate change is the primary cause of increased frequency and severity of natural disasters, resulting in widespread damage to people and the economic system. However, the impact of climate change on sinkhole hazard has been barely explored. This issue is due to the lack of continuous recording of hydrological, hydrogeological, and meteorological data. The processes need to be studied and recorded for future research to more effectively assess sinkhole hazard areas. In Thailand, there is a policy for disaster risk reduction, which is the Disaster Prevention and Mitigation Act 2007 (Fakhruddin and Chivakidakarn 2014). Additionally, the Sendai Framework for Disaster Risk Reduction (2015-2030) also utilized in Thailand for creating the substantial reduction of disaster risk in local areas with national strategies (Kelman 2015).

Sinkholes are increasingly common in Krabi and Surat Thani Provinces, particularly in Plai Phraya and Khao Phanom Districts, as well as Phanom, Phrasaeng, and Chai Buri Districts. The upcoming Land Bridge project, part of the Southern Economic Corridor, poses additional risks due to planned infrastructure development. Despite this, the area has not conducted any sinkhole susceptibility studies. This research aims to assess sinkhole susceptibility in the Krabi and Surat Thani Provinces' KIPs using GIS-based LR analysis, considering geological, geomorphological, and socio-economic factors. The findings will assist in managing vulnerable areas, offering insights for planning and monitoring potential hazards in regions lacking sinkhole risk maps at the local level.

MATERIALS AND METHODS

Study area

The KIPs lies within the Ta Pi watershed, a significant river basin in southern Thailand, spanning latitudes 8°10' N to 8°50' N and longitudes 98°40' E to 99°20' E, covering approximately 2,087.039 km^2. Situated between Krabi and Surat Thani provinces, it includes Plai Phraya, Khao Phanom, and Ao Luek Districts in Krabi, and Khian Sa, Phrasaeng,

and Chai Buri Districts in Surat Thani. The area's topography ranges from 7 to 1,346 meters above mean sea level, with the southern part being mountainous, including Khao Phanom peak within Khao Phanom Bencha National Park. The western side features scattered limestone mountains with karst topography.

The drainage pattern exhibits two key characteristics: the western upstream area displays a dendritic pattern with streams like Klong Ya and Khlong Bang Liao flowing into Khlong I Pan southwest to east. In the south, rivers like Khlong Sai Khao and Khlong Chang Tai flow south to north, forming a dendritic pattern upstream and a parallel pattern in the central basin, merging into Khlong Trom, which joins Khlong I Pan in the north.

Geologically, sedimentary rock predominates, including Quaternary alluvium along riverbanks, colluvium farther away, and old river terraces (Dheeradilok 1995; Leknettip et al. 2023). Tertiary sediments, notably the Krabi group, appear in the northeast, featuring shale, slate, calcareous shale, sandstone, siltstone, and minerals like limestone and lignite (Benammi et al. 2001). Limestone rocks are scattered throughout the upstream area, covering approximately 30-40% of the study area, from the Carboniferous-Permian-Triassic periods.

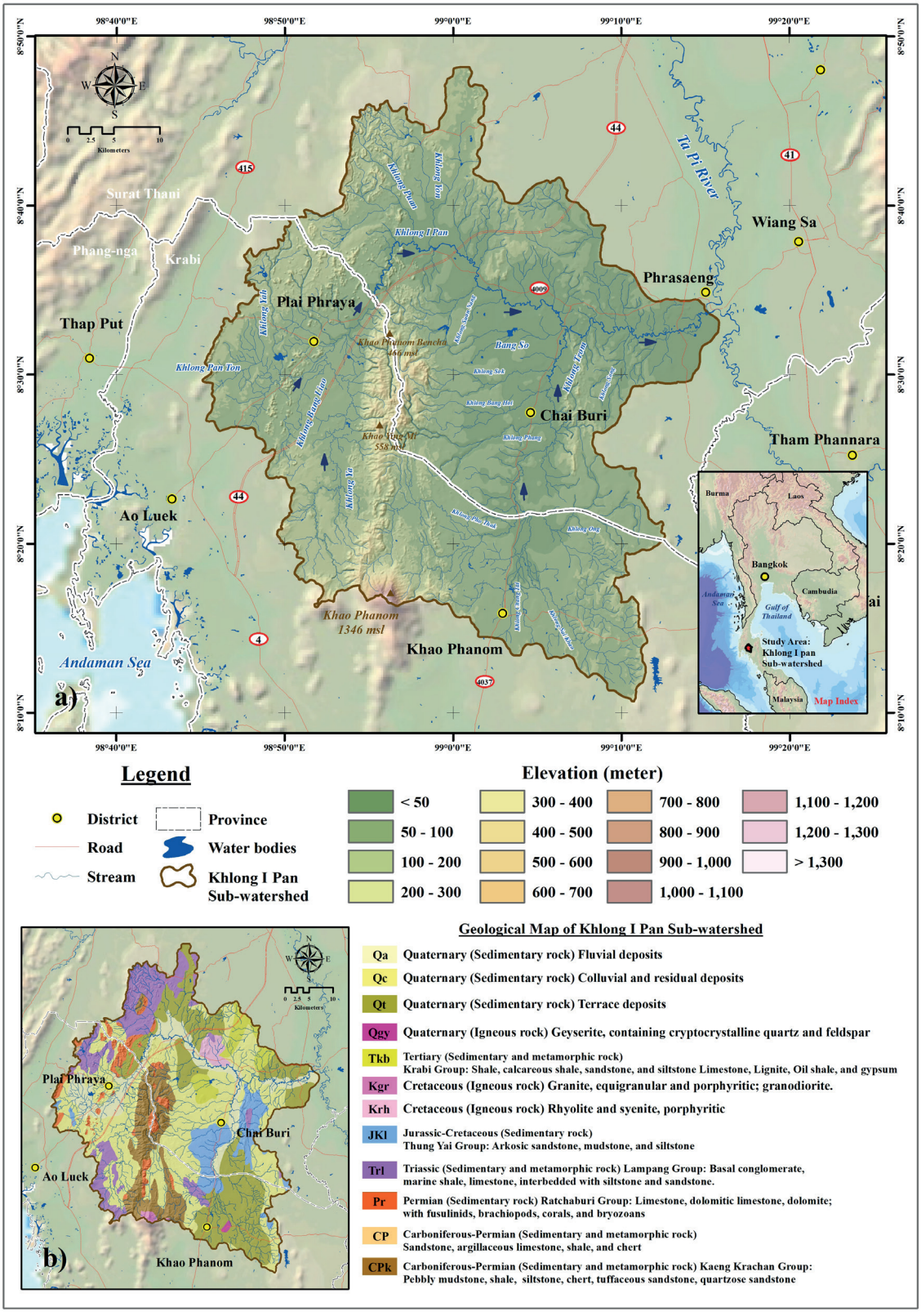

Fig. 1. Location map (a) and geological map (b) for the study area

Data Preparation

This research utilized secondary data from various sources to evaluate sinkhole susceptibility in the KIPs area. The data comprised sinkhole occurrences between 2002-2022 and spatial data analyzing factors influencing their formation. Physical factors such as elevation, slope, soil type, geology, distance to streams, active faults, terrain wetness index, Total Hardness (TH), Total Dissolved Solids (TDS), and Chlorine (Cl) were collected, alongside socio-economic factors including land use, well density, and distances to wells and villages. These spatial datasets are crucial variables for assessing sinkhole risk areas, organized in a raster database format with a grid cell size of 30×30 m.

Method

The research process consists of the following steps: (1) sinkhole area analysis, (2) spatial database analysis of driving factors, and (3) statistical approach. The details of each step are briefly explained below (Fig. 2).

Sinkholes area analysis

To identify sinkhole occurrences in the research area from past to present, secondary data spanning 2002 to 2022 were sourced from the Department of Mineral Resources. Additionally, primary data obtained from interpreting sinkhole areas in 1:50,000 scale topographic maps from the Royal Thai Survey Department were utilized. Upon acquiring data from both sources, a conversion from analog to digital format was performed using ArcMap 10.4 software. Subsequently, the data underwent LR statistical analysis in the next stage of the process.

Spatial database analysis of driving factors

The selection of factors affecting sinkhole formation is important for susceptibility analysis (Wei et al. 2021; Hu et al. 2021). This research has selected the factors that directly affect and are related to the occurrence of sinkholes in this study area. The first important spatial data is elevation (digital elevation model-DEM) obtained from the Royal Thai Survey Department (RTSD) in shapefile format, including elevation point, contour line, and water source and water route information. Such data will be analyzed by spatial analysis using the Topo to Raster technique in ArcGIS 10.4 software. The result is DEM data with a 30×30 m grid cell size (Fig. 3a). This data can be analyzed for other variables such as slope (Fig. 3b) and TWI (Fig. 3g). TWI is an index indicating water accumulation and flow tendency to lower basin areas due to the Earth's gravity (Chen and Yu 2011). High TWI values indicate prone areas, which may be the swamp areas, low slopes, or basins. This variable will be applied to search for areas where sinkholes occur in the study area. TWI analysis can be calculated from Eq. 1 (Hamid et al. 2020):

$$TWI = In\left(\frac{A_s}{\tan\beta}\right) \quad (1)$$

where, A_s indicates the definite catchment area and denotes the slope gradient.

Other physical factors that were applied in this research include soil (Fig. 3c), geology (Fig. 3d), distance to active fault (Fig. 3e), and distance to stream (Fig. 3f). The variables soil and geology are nominal data that are converted to raster data format. Data on variables distance to active fault and distance to stream were analyzed using the Euclidean distance technique in spatial analysis tools.

Furthermore, socio-economic factors are related to sinkhole formation, including LU (Fig. 4a), WD (Fig. 4b),

Table 1. Spatial data layers used in this research

Driving Factor	Variable (Theme)	Year	Source
	Sinkholes area	2002-2022	Derived from Department of Mineral Resources Royal Thai Survey Department (RTSD)
Physical factor	Elevation (digital elevation model-DEM)	2020	Derived from Royal Thai Survey Department (RTSD)
	Slope	2020	Derived from the DEM
	Soil	2017	Derived from Land Development Department (LDD)
	Geology	2017	Derived from Department of Mineral Resources
	Distance to active fault	2017	Derived from Department of Mineral Resources
	Distance to stream	2021	Derived from Department of Water Resource, Thailand
	TWI	2021	Derived from the DEM
	Total Hardness (TH)	2021	Derived from Department of Groundwater Resources
	Total Dissolved Solids (TDS)	2021	Derived from Department of Groundwater Resources
	Chlorine (Cl)	2021	Derived from Department of Groundwater Resources
Socio-economic factor	Land use	2021	Derived from Land Development Department (LDD)
	Well Density	2021	Derived from Department of Groundwater Resources
	Distance to well	2021	Derived from Department of Groundwater Resources
	Distance to village	2021	Derived from Royal Thai Survey Department (RTSD)

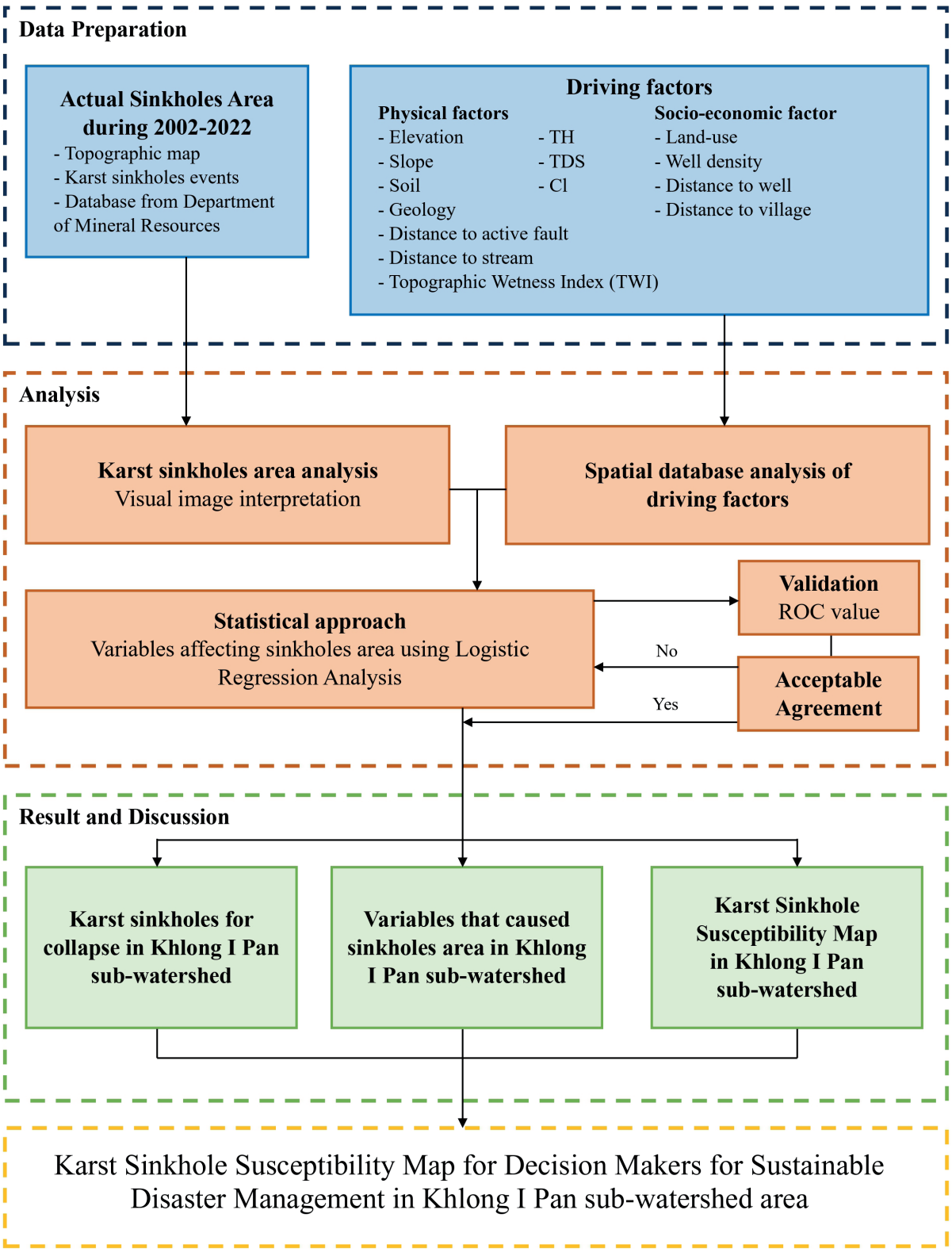

Fig. 2. Flow chart of methodology

distance to well (Fig. 4c), and distance to village (Fig. 4d). The LU data is nominal data received from the Land Development Department (LDD). The data was converted to raster data format. Data on variables distance to village and distance to well were analyzed using the Euclidean distance technique in spatial analysis tools. The WD variable can be analyzed using a mathematical function in ArcMap 10.2 with the Kernel Density (Eq. 2). The results will indicate the density of the artesian well. This variable is one of the variables that will be used for LR statistical analysis next. The Kernel Density (Nistor and Nicula 2021) calculated from the following equation (Eq. 2):

$$\int_h (x) = \frac{1}{n}\sum_{i=1}^{n}\left(\frac{n}{k}\right)K_h\left(x - x_1\right) \quad (2)$$

where f is density f; K is the kernel — a non-negative function; h > 0 is a smoothing parameter called the bandwidth; x_1, x_2, ..., x_n is a univariate independent and identically distributed sample.

The chemical property variables were Total Hardness (TH) (Fig. 4e), Total Dissolved Solids (TDS) (Fig. 4f), and Chlorine (Cl) (Fig. 4g). The data of all three variables were derived from the Department of Groundwater Resources. In this research, the data of all three variables were subjected to

spatial interpolation using the Inverse Distance Weighting (IDW) method in ArcMap 10.2.

Statistical approach

From the sequence of steps to find sinkhole area analysis and spatial database analysis of driving factors, it is necessary to search for variables that affect the formation of sinkholes in order to know the context of the collapse that occurred in the KIPs. There were 14 variables used in the analysis, including elevation, slope, soil, geology, distance to stream, distance to active fault, TWI, Total Hardness (TH), Total Dissolved Solids (TDS), Chlorine (Cl), LU, WD, distance to well, and distance to village. Such variables will be analyzed using LR analysis.

LR is a technique for discovering the empirical relationships between a binary dependent and several independent categorical and continuous variables (Ozdemir 2016; Kim et al. 2020; Cao et al. 2020). LR analysis is calculated using the following Eq. 3:

$$Log\left(\frac{P_i}{1-P_i}\right)=\beta_0+\beta_1 x_{1,i}+\beta_2 x_{2,1}+\ldots\beta_n x_{n,1} \quad (3)$$

where P is the flood-prone area, x_i are independent variables, and β is the coefficient value. The LR method was used to provide the variables that were used to analyze which variables influenced subsidence by considering the initial and dependent variables of every grid cell in the study area. The results from the LR analysis can be used to produce sinkhole susceptibility maps, which are classified into 5 classes: very high, high, moderate, low, and very low.

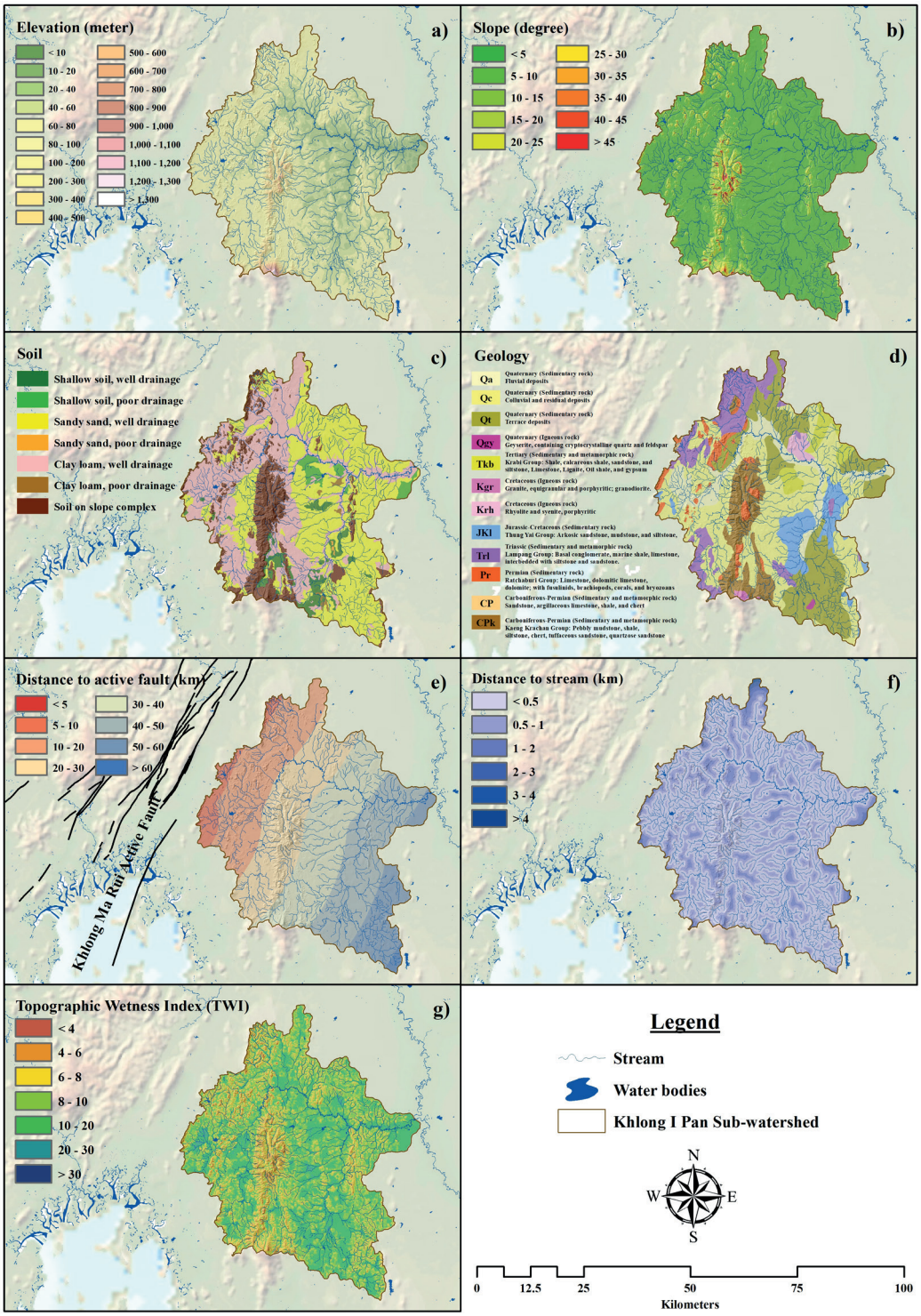

Fig. 3. Spatial database analysis of physical factors: Elevation (a), Slope (b), Soil (c), Geology (d), Distance to active fault (e), Distance to stream (f), and TWI(g)

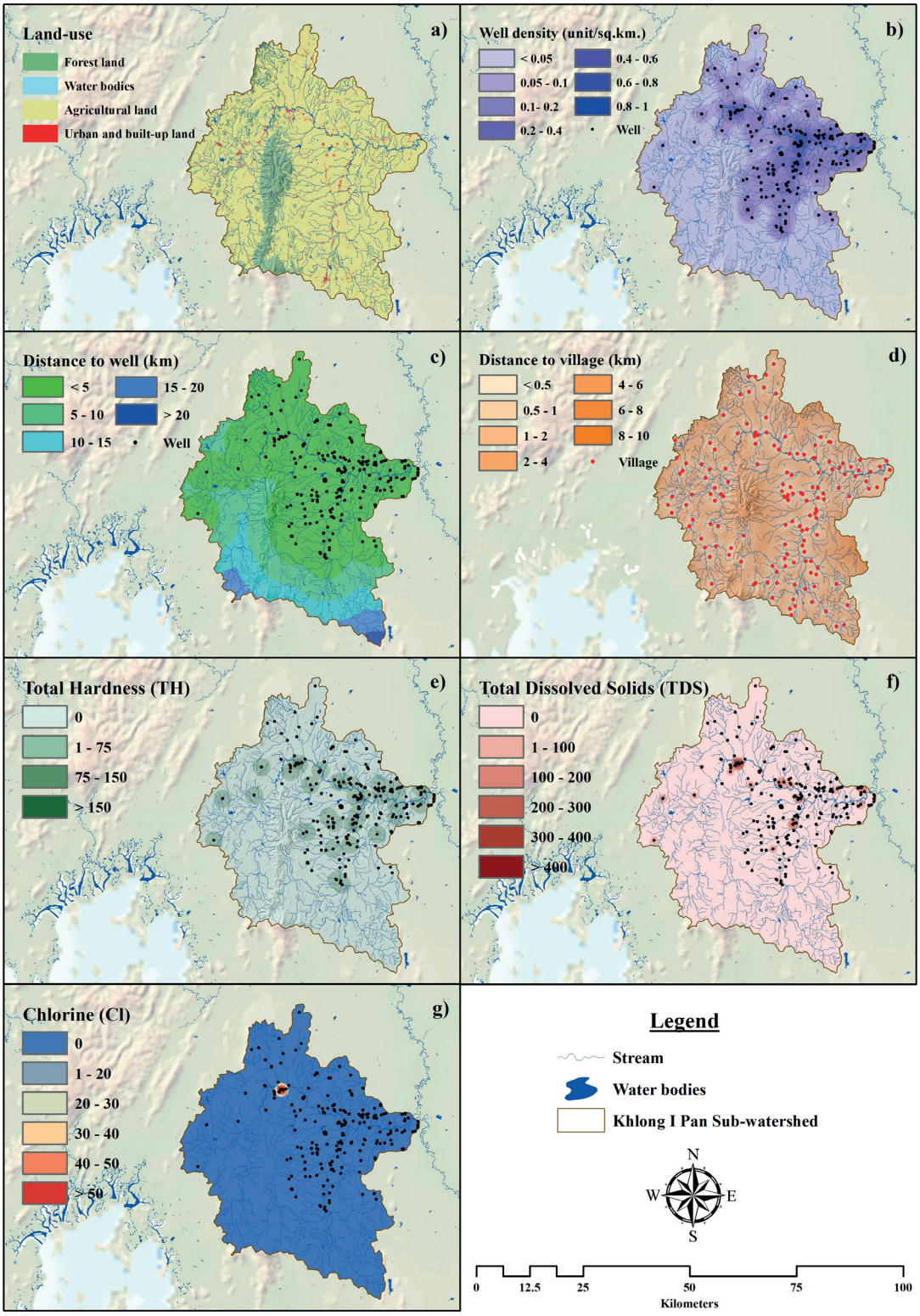

Fig. 4. Spatial database analysis of socio-economic factors: LU (a), WD (b), Distance to well (c), Distance to village (d), TH (e), TDS (f), and Cl (g)

RESULTS

Sinkholes in KIPs area

The KIPs boast a unique karst geography characterized by sedimentary rocks interspersed with limestone formations, particularly evident in the northern, central, and western regions, where a north-south-oriented limestone mountain range prevails. Over the past two decades (2002-2022), 34 sinkholes collapsed in the area, covering a total of 3.52 km^2. Most sinkholes are concentrated in the northern and central-southern regions of the KIPs, with a notable cluster in Khao Phanom District, totaling 9 sinkholes. The largest sinkhole, spanning 2.049 km^2, appeared near Bankhoasamyot School in Khian Sa District, Surat Thani province, characterized by undulating plain topography and rubber plantations. This sinkhole formed on September 26, 2016, during heavy rain brought by a monsoon trough, resulting in a chasm nearly 100 meters deep. Another significant sinkhole, covering 0.47 km^2, occurred in the east of the Phanom Bencha mountain range in Khlong Noi Sub-district, Chai Buri District, Surat Thani, within a forested area. In Khao Phanom District, Krabi Province, the largest concentration of sinkholes (12) was found, primarily in community and agricultural areas, including rubber and palm oil plantations. Details are outlined in Table 2.

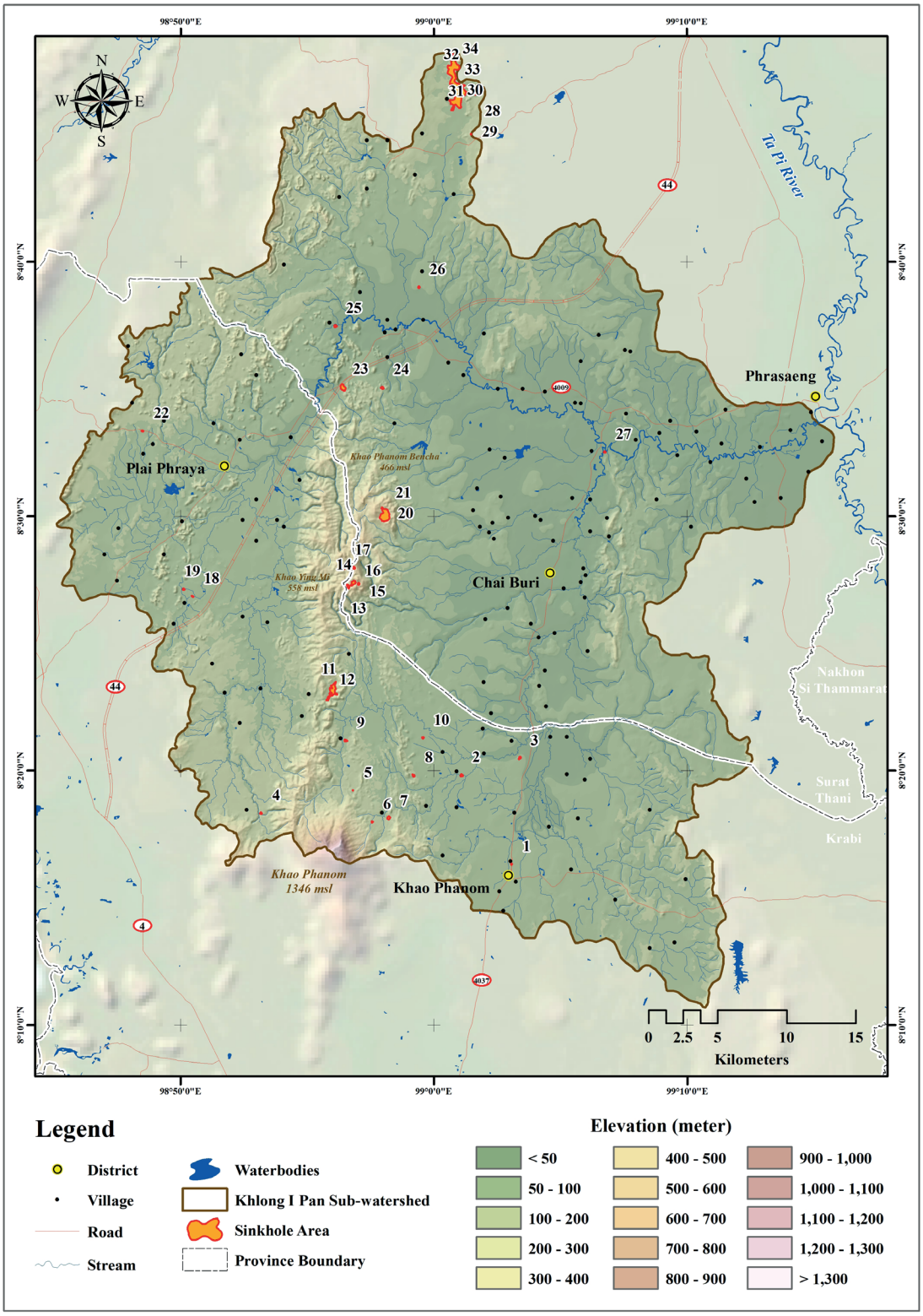

Fig. 5. Sinkhole disasters map in KIPs area

Table 2. Sinkhole disasters in KIPs during 2002-2022

No.	Location			Province	District	Sub-district	Area (km^2)
	Latitude	Longitude	Sinkhole Event				
1	8° 16' 19.60"	99° 3' 3.92"	Khao Phanom Temple	Krabi	Khao Phanom	Khao Phanom	0.004
2	8° 19' 49.06"	99° 1' 5.73"	Yuan Sao Village	Surat Thani	Khiri Rat Nikhom	Tha Khanon	0.020
3	8° 20' 30.25"	99° 3' 23.47"	Yuan Sao Village	Surat Thani	Khiri Rat Nikhom	Tha Khanon	0.022
4	8° 18' 19.69"	98° 53' 10.16"	Ban Chong Mai Dam Mosque	Krabi	Ao Luek	Khlong Hin	0.013
5	8° 17' 59.07"	98° 57' 33.67"	Ban Thumkob Village	Krabi	Khao Phanom	Na Khao	0.008
6	8° 19' 13.60"	98° 56' 47.91"	Ton Han Village	Krabi	Khao Phanom	Na Khao	0.001
7	8° 18' 8.61"	98° 58' 13.01"	Ton Han Village	Krabi	Khao Phanom	Na Khao	0.032
8	8° 19' 48.44°	98° 59' 11.89"	Ton Phong Village	Krabi	Khao Phanom	Na Khao	0.017
9	8° 21' 10.81"	98° 56' 31.13"	Khao Phanom Bencha Rangland	Krabi	Khao Phanom	Na Khao	0.022
10	8° 21' 17.78"	98° 59' 34.02"	Ban Khao Din School	Krabi	Khao Phanom	Na Khao	0.012
11-12	8° 23' 8.19"	98° 55' 59.52"	Khao Mae Mu	Krabi	Khao Phanom	Na Khao	0.303
13	8° 27' 14.74"	98° 56' 36.77"	Khuan Sai Village	Surat Thani	Chai buri	Chai buri	0.037
14	8° 27' 22.59"	98° 56' 48.83"	Khuan Sai Village	Surat Thani	Chai buri	Chai buri	0.071
15	8° 27' 20.31"	98° 57' 1.72"	Khuan Sai Village	Surat Thani	Chai buri	Chai buri	0.016
16	8° 27' 58.18"	98° 56' 50.65"	Khuan Sai Village	Surat Thani	Chai buri	Chai buri	0.016
17	8° 27' 57.96"	98° 56' 26.11"	Khuan Khlong Ya	Krabi	Plai Phraya	Plai Phraya	0.032
18	8° 26' 51.01"	98° 50' 28.32"	Wat Bang Liao School	Krabi	Plai Phraya	Plai Phraya	0.010
19	8° 27' 7.55"	98° 50' 7.02"	Bang Liao Village	Krabi	Plai Phraya	Khiriwong	0.012
20-21	8° 30' 2.30"	98° 58' 3.79"	Khao Phanom Bencha Rangland	Krabi	Khao Phanom	Na Khao	0.470
22	8° 33' 20.95"	98° 48' 29.24"	Khao Khen Village	Krabi	Plai Phraya	Khao Khen	0.010
23	8° 35' 3.55"	98° 56' 24.34"	Bang Sawan	Surat Thani	Phrasaeng	Bang Sawan	0.117
24	8° 35' 2.81"	98° 57' 57.75"	Bon Khuan Village	Surat Thani	Phrasaeng	Sai Sopha	0.028
25	8° 37' 28.56"	98° 56' 6.42"	Ban Mak Village	Surat Thani	Phrasaeng	Bang Sawan	0.023
26	8° 39' 0.41"	98° 59' 24.16"	Si Nakhon Village	Surat Thani	Phrasaeng	Bang Sawan	0.013
27	8° 32' 31.67"	99° 6' 45.11"	Kuan Sian Village	Surat Thani	Phrasaeng	Sai Khueng	0.010
28	8° 46' 46.48"	99° 1' 33.10"	Khao Sam Yot	Surat Thani	Khian Sa	Ban Sadet	0.151
29	8° 45' 1.25"	99° 1' 27.94"	Mongkhon Phithak Thammaram Temple	Surat Thani	Khian Sa	Ban Sadet	0.003
30-34	8° 46' 59.80"	99° 0' 52.30"	Khao Sam Yot Village	Surat Thani	Khian Sa	Ban Sadet	2.049

Affecting Variables in sinkhole formation in KIPs

The analysis focused on 14 variables crucial for investigating sinkhole formation in the KIPs, employing the LR statistical process. Table 3 illustrates the variables affecting sinkhole formation, with their impact expressed through β values. A positive β value signifies increased sinkhole susceptibility with higher variable values, while a negative value suggests the opposite. The relative operating characteristic (ROC) demonstrates the regression equation's ability to predict sinkhole risk areas based on probability. The ROC value obtained for sinkhole area probability was 0.947 (Fig. 6), indicating high effectiveness, as values closer to 1.00 signify comprehensive analysis of sinkhole risk areas using all 14 variables.

All variables were significant at the $p < 0.01$ entry and $p > 0.02$ removal levels. ROC relative operating

The study identified 8 variables with negative β values influencing sinkhole occurrence: geology, distance to well, distance to active fault, soil, terrain wetness index (TWI), distance to village, elevation, and distance to stream. Conversely, 3 variables exhibited positive β values: well density (WD), land use (LU), and slope. The Exp β values indicate the variables' impact on sinkhole formation, with higher values indicating greater influence. WD emerged as the most influential variable, followed by geology, LU, TH, TDS, slope, CI, distance to stream, elevation, TWI, distance to village, soil, distance to active fault, and distance to well, respectively, with Exp β values of 2.385, 1.880, 1.195, 1.119, 1.048, 1.007, 1.000, 0.998, 0.991, 0.957, 0.950, 0.687, 0.333, and 0.159 (Table 3).

Well density (WD) displayed the highest Exp β value, indicating its significant influence on sinkhole formation, particularly in areas with high artesian well density levels, ranging from 0.4-1.0 unit/km^2 in the eastern and central study areas. These regions, situated downstream in the KIPs, boast numerous artesian wells due to the natural groundwater flow from high to low areas. This phenomenon is prominent in densely populated districts like Chai Buri, Phrasaeng, and Khian Sa.

Table 3. LR analysis of the sinkholes area and affecting variable in KIPs area

Variable	KS area	
	Coefficient β value	Coefficient *Exp* β value
Elevation (digital elevation model-DEM)	-0.009	0.991
Slope	0.007	1.007
Soil	-0.376	0.687
Geology	-5.219	1.880
Distance to active fault	-0.665	0.333
Distance to stream	-0.002	0.998
TWI	-0.065	0.957
TH	0.121	1.119
TDS	0.050	1.048
CI	0.001	1.000
LU	1.633	1.195
Well Density	10.750	2.385
Distance to well	-1.761	0.159
Distance to village	-0.045	0.950
Constant	7.077	
The relative operating characteristic (ROC)	0.947	

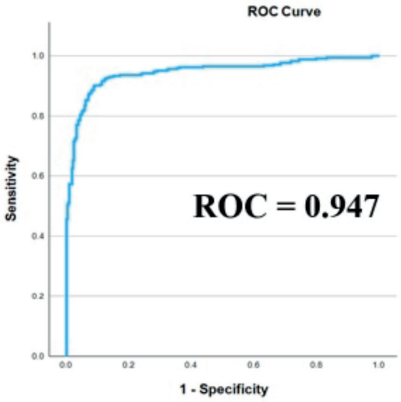

Fig. 6. The relative operating characteristic (ROC) value: sinkhole area

Geological variables are one of the important variables affecting sinkhole hazard and show strong negative β values. Since the geological variables are on a nominal scale, it is necessary to convert them to an ordinal scale and start from sedimentary rocks to igneous and metamorphic rocks. The study area is mostly covered by sedimentary rocks, including sedimentary rocks of the Carboniferous, Permian, Triassic, Tertiary, and Quaternary periods, with sedimentary rocks covering most of the area, and igneous rocks, including igneous rocks of the Cretaceous and Quaternary periods. From the LR analysis, the results of the geological variables show that the ancient sedimentary rocks affect the formation of sinkholes, especially the rocks in the limestone group that are in the Carboniferous and Permian periods.

Geological variables exhibit a notable Exp β value, albeit to a lesser extent, and a negative β value. The study revealed that grid cells with lower values in the study area predominantly consist of sedimentary rocks dating back to the Carboniferous, Permian, Triassic, and Tertiary periods. These rocks commonly contain limestone, dolomite limestone, dolomite, and gypsum formations, which are particularly prevalent in Permian-era formations (Pr). The study area features the Ratchaburi group (Pr), characterized by these rock types. Additionally, Carboniferous-Permian (CP) rocks include the Kaeng Krachan group (CPk), supporting the Pr series rocks. Some CP and CPk rock layers contain argillaceous limestone interspersed with other sedimentary rocks like siltstone and tuffaceous sandstone. Triassic-period sedimentary rocks include the Lampang group (Trl), featuring gray-black limestone. Tertiary sedimentary rocks, found in the Krabi group (Tkb), also comprise limestone, dolomite limestone, dolomite, and gypsum. Limestone predominantly covers the geological features in the study area, resulting in karst topography spanning from CPk, CP, and Pr formations continuously to the southern Phanom Bencha mountain range. The Trl and Pr sections cover the western mountain range with a northeast-southwest orientation, featuring scattered tower karst formations like Khao Lom Fang. The Tkb rock group encompasses low hills on the eastern side of the study area.

The LU variable ranks third in Exp β value after geology. It exhibits a positive β value, with higher values indicating urban, built-up, and agricultural areas. In the KIPs, agricultural land predominates, covering 1,805 km^2, accounting for 86.51% of the area. Much of this agricultural land is dedicated to oil palm and rubber plantations, covering 898.37 km^2 and 834.97 km^2, respectively. These agricultural practices involve land stripping and leveling, with some areas featuring drainage trenches. Such activities can render the soil surface fragile, and prone to subsidence, particularly in areas with underground burrows or karst terrain. Urban areas and buildings have a comparatively lesser impact on land subsidence, given the limited presence of buildings and infrastructure, affecting only specific areas.

After LU variables, the subsequent influential variables affecting sinkhole occurrence include slope, distance to stream, elevation, terrain wetness index (TWI), distance to village, soil, distance to active fault, and distance to well, respectively. Slope variable: Areas with moderate to high slopes, approximately 10-40 degrees, are prone to land collapse. Distance to stream variable: Proximity to waterways increases susceptibility to sinkhole formation. Elevation variable: Sinkholes are likely to occur at elevations ranging from approximately 10-100 meters above mean sea level. TWI variable: Low TWI values signify low terrain moisture levels, contributing to sinkhole formation. Distance from village variable: Areas not far from villages are particularly sensitive to collapse. Soil variable: Shallow soil-covered areas are at risk of subsidence. Distance from well variable: Proximity to artesian wells increases susceptibility to collapse.

Additionally, the distance to the active fault variable indicates the presence of the Khlong Ma Rui Active Fault in the northwest of the KIPs. Oriented northeast-southwest, this fault poses earthquake and tsunami risks, with potential tremors affecting karst topographic areas, which are also prone to sinkhole disasters.

The TH, TDS, and Cl variables showed positive β values. The results showed that higher concentrations of the chemical status of groundwater would result in an increased sinkhole probability.

Sinkhole susceptibility map in KIPs

According to the sinkhole susceptibility analysis in KIPs using the LR method by using the β value to create a database, it has been prepared as a map for disaster management at the sub-watershed level to represent the sinkhole susceptibility map (Fig. 7). The results of this study were to analyze spatial data in GIS as shown in Eq. 4.

$$\begin{aligned} Y = {} & 7.077 + (\text{“}WD\text{”} \times 10.750) + (\text{“}Geology\text{”} \times \\ & -5.219) + (\text{“}LU\text{”} \times 1.633) + (\text{“}Slope\text{”} \times \\ & 0.007) + (\text{“}Distance\ to\ stream\text{”} \times \\ & -0.002) + (\text{“}Elevation\text{”} \times -0.009) + \\ & (\text{“}TWI\text{”} \times -0.065) + (\text{“}TH\text{”} \times 0.121) + \\ & (\text{“}TDS\text{”} \times 0.050) + (\text{“}Cl\text{”} \times 0.001) + \\ & (\text{“}Distance\ to\ village\text{”} \times -0.045) + \\ & (\text{“}Soil\text{”} \times -0.376) + (\text{“}Distance\ to \\ & active\ fault\text{”} \times -0.665) + (\text{“}Distance \\ & to\ well\text{”} \times -1.761) \end{aligned} \quad (4)$$

The results of the β value of various variables make the findings a highlight of this research. That can express the level of risk as appropriate spatial data according to related variables and affecting the occurrence of sinkholes in the KIPs area in particular. Results of the study of KS susceptibility show that sinkhole susceptibility areas in the watershed can be classified into five levels: very high risk areas, high risk areas, moderate risk areas, low risk areas, and areas at very low risk of sinkhole, respectively (Table 4).

In the KIPs area, regions with a very high sinkhole susceptibility level cover approximately 399.86 km^2, constituting 19.16% of the total area. These high-risk zones are predominantly situated in the eastern part of KIPs, particularly near the convergence of Khlong I Pan and Khlong Trom streams. Additionally, mountainous areas, such as the central and western ranges, exhibit elevated sinkhole risk due to their karst geological formations. Surrounding the very high susceptibility zones, both high- and moderate-risk areas span over 421.73 km^2 (20.21%) and 422.18 km^2 (20.23%), respectively. Conversely, low- and very low-risk zones are primarily located in the southern region, notably in the upstream areas of KIPs along streams like Khlong Ya, Khlong Pho Thak, Khlong Chang Tai, and Khlong Sai Khao. These areas cover 430.41 km^2 (20.62%) and 412.85 km^2 (19.78%), respectively, with minimal sinkhole risk attributed to fewer artesian wells and the prevalence of modern sedimentary rocks, distant from active fault lines.

Table 4. KS susceptibility area in KIPs area (km²)

Sinkholes susceptibility level	Area	
	km²	%
Very high	399.86	19.16
High	421.73	20.21
Medium	422.18	20.23
Low	430.41	20.62
Very Low	412.85	19.78
Total	2087.03	100.00

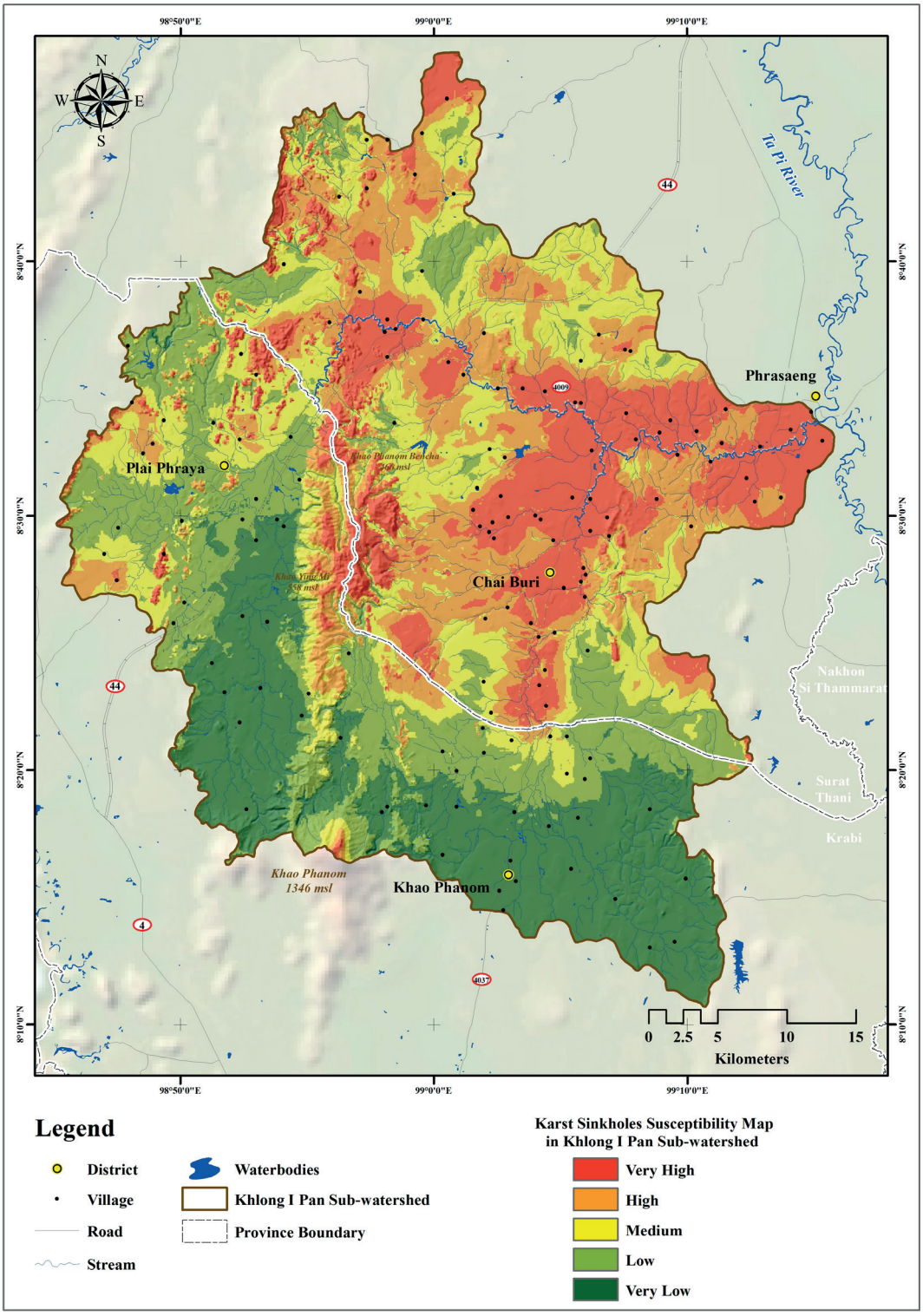

Fig. 7. Sinkholes susceptibility map in KIPs

DISCUSSION

Sinkholes, influenced by complex factors, pose prediction challenges. Mitigation is aided by gathering diverse variables and using consistent analysis. Sinkhole susceptibility maps provide crucial spatial data for community readiness. This study selected 14 factors, integrated them into a GIS database for statistical analysis, and produced a map for effective local risk management.

Over the past two decades (2002-2022), sinkhole areas were studied using secondary data from sinkhole events, the Department of Mineral Resources of Thailand, and visual image interpretation. The study identified 34 sinkholes covering 3.52 km^2, concentrated along the Phanom Bencha mountain range. That area is an important upstream area of the Khlong I Pan tributary stream. Notably, a large subduction basin was discovered near Bankhoasamyot School in Surat Thani province. The area has an undulating plain topography.

As a result of this research, it can be seen that the technique for finding sinkhole areas using visual image interpretation is still a suitable method for finding actual sinkholes efficiently. Consistent with the research of Orhan et al. (2020) that used the principle of finding sinkhole areas with visual analysis of the aerial photographs of the district and on-site fieldwork. As a result, accurate sinkhole data was obtained and used to create a sinkhole susceptibility map using remote sensing and GIS processes in the Konya sub-watershed area, Türkiye. Even in regions with a tropical climate, such as the Metropolitan Region of Belo Horizonte, Minas Gerais, Brazil, sinkhole landforms can be searched using this technique by analyzing hydrograph control, topography, cross-section elevation profiles, and high-resolution satellite imagery (de Castro Tayer and Rodrigues 2021). As for the geologically sensitive region, the Zagros Mountains, Kermanshah Province, Iran, the area is the largest active fault in the Zagros overthrust. Techniques for finding sinkholes and subsidence areas using visual image interpretation of World Imagery and Google Earth can accurately display the actual sinkhole (Maleki et al. 2023). There are some weaknesses that must be noted with this analysis technique, especially human-assisted image processing which requires the individual's experience (Dou et al. 2015). Certain regions may require reliance on visual analysis of remote sensing imagery and on-site research, despite the drawbacks of subjectivity, time intensiveness, limited reproducibility, and inadequacy for examining extensive territories. (Chen et al. 2018). Future research processes may require technology that can process data quickly and with high efficiency, using machine learning to create models that can discover and detect actual KS for collapse areas. Artificial intelligence should be trained to learn from the processing of visual image interpretation from experienced people frequently to obtain data on the collapse of the terrain caused by sinkholes.

Sinkhole occurrence factors in the KIPs area were analyzed using LR statistical methods. The study results found that socio-economic factors are sensitive to landscape collapse. In particular, prominent variables such as WD and LU show strong Exp β values at levels of 2.385 and 1.195, respectively. As for the physical factor variables that are sensitive to the collapse of the terrain, it was found that the geology and slope variables showed strong Exp β values at the levels of 1.880 and 1.007, respectively. It can be seen that the study area has a high level of artesian WD ranging from 0.4-1.0 unit/km^2 that is distributed in the eastern area continuing into the central part of the study area. Most of these areas have LU conditions where the area has been opened for agriculture to grow crops such as rubber, palm oil, and rice fields, further accelerating the collapse of the land more easily. It can be seen from the KS susceptibility map that the area is classified as the area with the highest risk of collapse. It covers most of the eastern area, continuing into the central part of the study area. This is different from the findings of Cahalan and Milewski (2018) which indicated high aquifer fluctuations and shallow overburden thickness. This is caused by activities on the topographic surface that are the primary variable affecting the subsidence of the land. In addition, the original geological landform with karst topography covers the central and western mountain ranges in the study area. It creates greater susceptibility to the collapse of the terrain in areas with very steep slopes. There are different variables that affect the occurrence of sinkholes in each area. These findings can be seen from the research of Wood et al. (2023) that sought to find sinkhole vulnerability in karst and pseudokarst regions of the contiguous United States, both present and anticipated. They identified important variables such as the thickness of the soil layer, soil type, and humidity that are the main variables that affect collapse until a sinkhole occurs, which is different from the results of this research.

The geochemical variables used in the study area were TH, TDS, and Cl. It was found that if the concentration level of these variables is high, it easily affects the formation of sinkholes. This is different from the results of the study by Ozdemir (2016) who stated that if the concentration level of Calcium (Ca) and Magnesium (Mg) increases, the probability of sinkholes decreases. However, the results of this study have shown that the TH variable is an important variable that affects the formation of sinkholes. The concentration levels of Ca and Mg were found in these variables. This conclusion is consistent with the study approach of Amin et al. (2023) who stated that Ca and Mg are likely to be dissolving carbonate rocks from limestone and dolomite. In the study area, the amount of this element was found to be quite high. It is possible that high levels of TH found in groundwater indicate that the underground caves have been severely eroded, resulting in high levels of Ca and Mg in the groundwater. The variables TDS and Cl were found to have little influence on sinkhole formation.

However, LR analysis has the capability to manage both continuous and categorical variables concurrently, which is not required in standard distributions. Additionally, the LR analysis technique can accurately identify regions prone to various geological hazards like KS (Zhou et al. 2016; Ozdemir 2016; Subedi et al. 2019; Kim et al. 2019). In summary, the overall picture from the discussion of the results reveals the differences in variables that affect the occurrence of sinkholes that occur in different contexts in each area. However, with the variables used in the LR analysis process, the results of the β value coefficient of the variables used in the study will vary according to the physical characteristics of the area. Therefore, if studying KS susceptibility in other areas, one should be aware of the factors that will be studied first in areas at risk of sinkhole formation.

KS susceptibility mapping is vital for disaster planning, yet the 2005 sinkhole risk map from the Department of Mineral Resources of Thailand lacks transparency and updates, making it ineffective for local disaster management. This study aimed to improve data resolution, revealing that nearly half of the study area has high susceptibility to sinkholes. Contrary to the outdated map's three risk levels, this research identified five levels, reflecting nuanced susceptibility. Discrepancies between actual sinkhole occurrences and the department's map highlight its inaccuracy. Local-level mapping provides crucial risk insight for communities and authorities, particularly in high-risk areas, aiding disaster preparedness and mitigating potential losses.

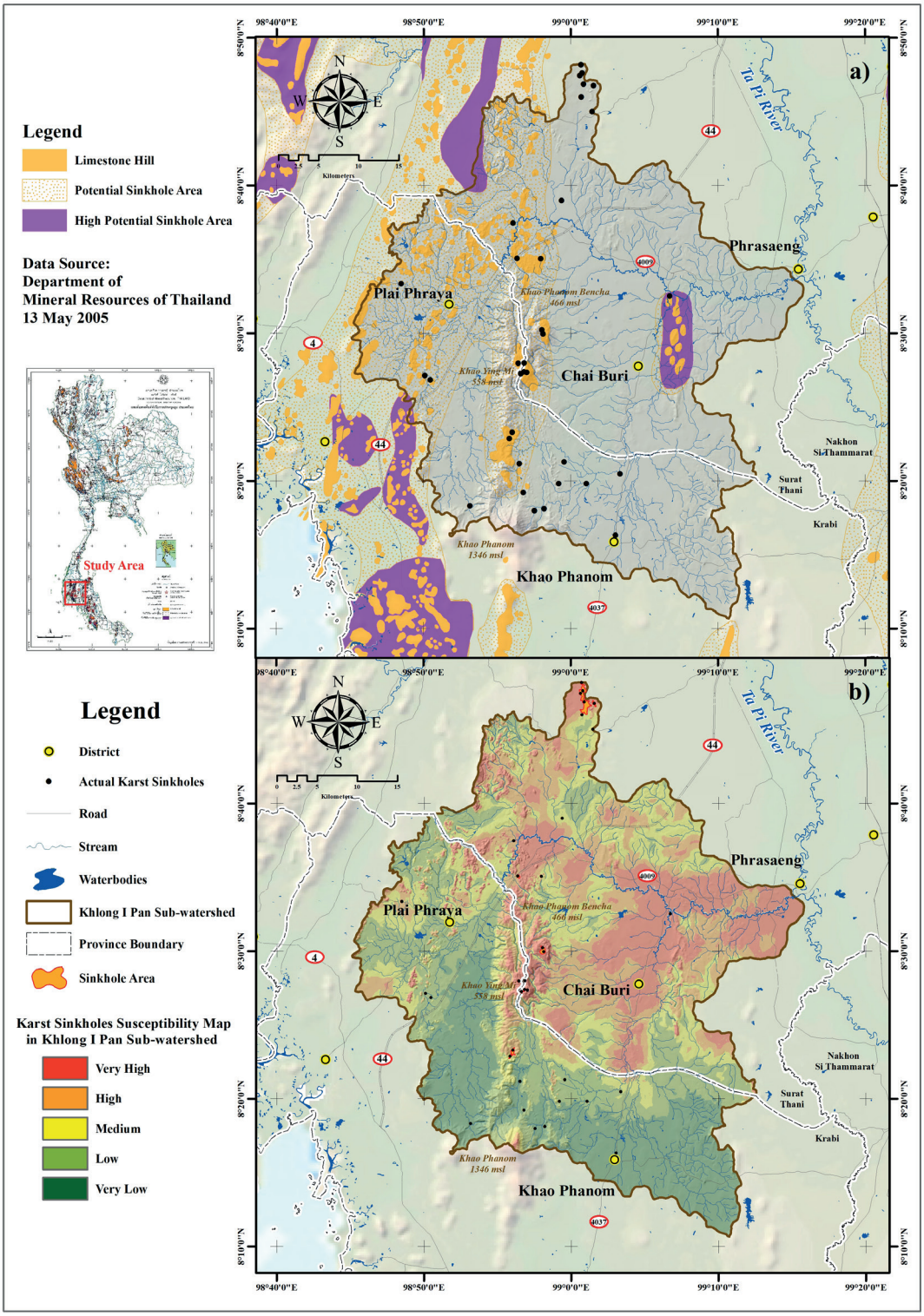

Fig. 8. Comparison between the old set of well risk maps of the Department of Mineral Resources of Thailand (a) and the current set of KS susceptibility mapping (b) obtained from this research

CONCLUSIONS

Sinkholes are unpredictable phenomena, often occurring in karst landscapes. This study aims to mitigate their impact by analyzing various factors contributing to sinkhole formation in the local area. Statistical methods, including LR analysis combined with GIS, were employed to create susceptibility maps for sinkholes. The research identified several key variables affecting sinkhole formation, such as well density, geology, land use, slope, distance to streams, elevation, terrain wetness index, proximity to villages, soil type, distance to active faults, and distance to wells. These variables were quantified using coefficient values and incorporated into the susceptibility mapping process. The findings revealed that over half of the study area exhibited a very high or high susceptibility to sinkholes. This research provides empirical evidence supporting the effectiveness of detailed, community-level sinkhole risk assessment, potentially replacing existing sinkhole risk maps maintained by the Department of Mineral Resources in Thailand. Future studies should expedite the exploration of sinkhole susceptibility across Thailand, considering the unique variables influencing sinkhole formation in different regions. Government agencies involved in disaster management should prioritize comprehensive research efforts to prepare for and mitigate sinkhole risks nationwide, ensuring the safety and sustainability of local communities in the future.

REFERENCES

Amin P., Ghalibaf M.A. Mermut, A.R. Delavarkhalafi, A. and Latifi,M.A. (2023). Prediction of sinkhole hazard using artificial intelligence model with soil characteristics and GPR data in arid alluvial land in Central Iran. Environmental Earth Sciences, 82(15), 372, DOI: 10.1007/s12665-023-11055-2.

Arora N. K. and Mishra I. (2023). Sustainable development goal 13: recent progress and challenges to climate action. Environmental Sustainability, 6(3), 297-301, DOI: 10.1007/s42398-023-00287-4.

Benammi M., Chaimanee Y., Jaeger J. J., Suteethorn V. and Ducrocq S. (2001). Eocene Krabi basin (southern Thailand): paleontology and magnetostratigraphy. Geological Society of America Bulletin, 113(2), 265-273, DOI: 10.1130/0016-7606(2001)113<0265:EKBSTP>2.0.CO;2.

Cahalan M. D. and Milewski A. M. (2018). Sinkhole formation mechanisms and geostatistical-based prediction analysis in a mantled karst terrain. Catena, 165, 333-344, DOI: 10.1016/j.catena.2018.02.010.

Cao Y., Jia H., Xiong J., Cheng W., Li K., Pang Q. and Yong Z. (2020). Flash Flood Susceptibility Assessment Based on Geodetector, Certainty Factor, and LR Analyses in Fujian Province, China. ISPRS International Journal of Geo-Information, 9(12), 748, DOI: 10.3390/ijgi9120748.

Chen C. and Yu F. (2011). Morphometric analysis of debris flows and their source areas using GIS. Geomorphology, 129(3-4), 387–397, DOI: 10.1016/j.geomorph.2011.03.002.

Chen H., Oguchi T. and Wu P. (2018). Morphometric analysis of sinkholes using a semi-automatic approach in Zhijin County, China. Arabian Journal of Geosciences, 11, 412, DOI: 10.1007/s12517-018-3764-3.

Cvijić J. (1925). Karst i čovek (Karst and man). Glasnik Geografskog društva / Bulletin of the Geographical Society, 11, 1 –11.

de Castro Tayer, T. and Rodrigues P.C.H. (2021). Assessment of a semi-automatic spatial analysis method to identify and map sinkholes in the Carste Lagoa Santa environmental protection unit, Brazil. Environmental Earth Sciences, 80, 83, DOI: 10.1007/s12665-020-09354-z.

Dou J., Li X., Yunus A. P., Paudel U., Chang K. T., Zhu Z. and Pourghasemi H. R. (2015). Automatic detection of sinkhole collapses at finer resolutions using a multi-component remote sensing approach. Natural Hazards, 78, 1021-1044, DOI: 10.1007/s11069-015-1756-0.

Dou J., Li X., Yunus A. P., Paudel U., Chang K. T., Zhu Z. and Pourghasemi H. R. (2015). Automatic detection of sinkhole collapses at finer resolutions using a multi-component remote sensing approach. Natural Hazards, 78, 1021-1044, DOI: 10.1007/s11069-015-1756-0.

De Castro D.L., Bezerra F.H. and Oliveira Jr J.G. (2024). Integrated geophysical approach for detection and size-geometry characterization of a multiscale karst system in carbonate units, semiarid Brazil. Open Geosciences, 16(1), 20220606, DOI: 10.1515/geo-2022-0606.

de Queiroz Salles L., Galvão P., Leal L.R.B., de Araujo Pereira R.G.F., da Purificação C.G.C. and Laureano F.V. (2018). Evaluation of susceptibility for terrain collapse and subsidence in karst areas, municipality of Iraquara, Chapada Diamantina (BA), Brazil. Environmental earth sciences, 77, 593, DOI: 10.1007/s12665-018-7769-8.

De Waele J. and Gutierrez F. (2022). Karst Hydrogeology, Geomorphology and Caves. Chichester: John Wiley & Son, DOI: 10.1002/9781119605379.

Dheeradilok P. (1995). Quaternary coastal morphology and deposition in Thailand. Quaternary International, 26, 49-54, DOI: 10.1016/1040-6182(94)00045-7.

Fakhruddin S. H. M. and Chivakidakarn, Y. (2014). A case study for early warning and disaster management in Thailand. International journal of disaster risk reduction, 9, 159-180, DOI: 10.1016/j.ijdrr.2014.04.008.

Frost-Killian S. (2008). Geohazards the risks beneath our feet. Quest, 4(2), 28-31.

Galvão P., Halihan T. and Hirata R. (2015). Evaluating karst geotechnical risk in the urbanized area of Sete Lagoas, Minas Gerais, Brazil. Hydrogeology Journal, 23(7), 1499, DOI: 10.1007/s10040-015-1266-x.

Galve J.P., Gutiérrez F., Remondo J., Bonachea J., Lucha P. and Cendrero A. (2009). Evaluating and comparing methods of sinkhole susceptibility mapping in the Ebro Valley evaporite karst (NE Spain). Geomorphology, 111, 160–172, DOI: 10.1016/j.geomorph.2009.04.017.

Hamid H.T.A., Wenlong W. and Qiaomin L. (2020). Environmental sensitivity of flash flood hazard using geospatial techniques. Global Journal of Environmental Science and Management, 6(1), 31-46, DOI: 10.22034/GJESM.2020.01.03.

Hu J., Motagh M., Wang J., Qin F., Zhang J., Wu W. and Han Y. (2021). Karst collapse risk zonation and evaluation in Wuhan, China based on analytic hierarchy process, LR, and InSAR angular distortion approaches. Remote Sensing, 13(24), 5063, DOI: 10.3390/rs13245063.

Hu R.L., Yeung M.R., Lee C.F., Wang S.J. and Xiang J.X. (2001). Regional risk assessment of karst collapse in Tangshan, China. Environmental Geology, 40, 1377–1389, DOI: 10.1007/s002540100319.

Jia X.L., Dai Q.M. and Yang H.Z. (2019). Susceptibility zoning of karst geological hazards using machine learning and cloud model. Cluster Computing, 22(Suppl 4), 8051-8058, DOI: 10.1007/s10586-017-1590-0.

Kim K., Kim J., Kwak T.Y. and Chung C.K. (2018). LR model for sinkhole susceptibility due to damaged sewer pipes. Natural Hazards, 93, 765-785, DOI: 10.1007/s11069-018-3323-y.

Kim H.I., Han K.Y. and Lee J.Y. (2020). Prediction of Urban Flood Extent by LSTM Model and LR. KSCE Journal of Civil and Environmental Engineering Research, 40(3), 273–283, DOI: 10.12652/Ksce.2020.40.3.0273.

Kim Y. J., Nam B. H. and Youn H. (2019). Sinkhole detection and characterization using LiDAR-derived DEM with LR. Remote Sensing, 11(13), 1592, DOI: 10.3390/rs11131592.

Kelman I. (2015). Climate change and the Sendai framework for disaster risk reduction. International Journal of Disaster Risk Science, 6, 117-127, DOI: 10.1007/s13753-015-0046-5.

La Rosa A., Pagli C., Molli G., Francesco C., De Luca C., Amerino P. and D'Amato Avanzi G. A. (2018). Growth of a sinkhole in a seismic zone of the northern Apennines (Italy). Natural Hazards and Earth System Sciences, 18(9), 2355–2366, DOI: 10.5194/nhess-18-2355-2018.

Leknettip S., Chawchai S., Choowong M., Mueller D., Fülling A. and Preusser F. (2023). Sand ridges from the coastal zone of southern Thailand reflect late quaternary sea-level history and environmental conditions in Sundaland. Quaternary Science Reviews, 316, 108264, DOI: 10.1016/j.quascirev.2023.108264.

Maleki M., Salman M., Sahebi-Vayghan S. and Szabo S. (2023). GIS-based sinkhole susceptibility mapping using the best worst method. Spatial Information Research, 31(5), 537-545, DOI: 10.1007/s41324-023-00520-6.

Nam B., Kim Y. and Youn H. (2020). Identification and quantitative analysis of sinkhole contributing factors in Florida's karst. Engineering Geology, 271, 105610, DOI: 10.1016/j.enggeo.2020.105610.

Nistor, M. and Nicula A. (2021). Application of GIS Technology for Tourism Flow Modelling in the United Kingdom. Geographia Technica, 16(1), 1-12, DOI: 10.21163/GT_2021.161.01.

Orhan O., Yakar M. and Ekercin S. (2020). An application on sinkhole susceptibility mapping by integrating remote sensing and geographic information systems. Arabian Journal of Geosciences, 13, 886, DOI: 10.1007/s12517-020-05841-6.

Ozdemir A. (2016). Sinkhole susceptibility mapping using LR in Karapınar (Konya, Turkey). Bulletin of Engineering Geology and the Environment, 75, 681–707, DOI: 10.1007/s10064-015-0778-x.

Pondthai P., Arjwech R., Mathon K. and Taweelarp S. (2023). Investigation of Subsurface and Geological Structures Contributing to Collapse Sinkholes in Covered Karst Terrain, Northeast Thailand. Environment & Natural Resources Journal, 21(6), 513-523, DOI: 10.32526/ennrj/21/20230131.

Ramírez-Serrato N.L., García-Cruzado S.A., Herrera G.S., Yépez-Rincón F.D. and Villarreal S. (2024). Assessing the relationship between contributing factors and sinkhole occurrence in Mexico City, Geomatics, Natural Hazards and Risk, 15(1), 2296377, DOI: 10.1080/19475705.2023.2296377.

Siska P.P., Goovaerts P. and Hung I.-K. (2016). Evaluating susceptibility of karst dolines (sinkholes) for collapse in Sango, Tennessee, USA. Progress in Physical Geography: Earth and Environment, 40(4), 579-597, DOI: 10.1177/0309133316638816.

Sone M., Metcalfe I. and Chaodumrong P. (2012). The Chanthaburi terrane of southeastern Thailand: Stratigraphic confirmation as a disrupted segment of the Sukhothai Arc. Journal of Asian Earth Sciences, 61, 16-32, DOI: 10.1016/j.jseaes.2012.08.021.

Stefanov P., Prodanova H., Stefanova D., Stoycheva V. and Petkova G. (2023). Monitoring of water cycle in karst geosystems and its integration into ecosystem assessment framework. Journal of the Bulgarian Geographical Society, 48, 15-26, DOI: 10.3897/jbgs.e101301.

Subedi P., Subedi K., Thapa B. and Subedi P. (2019). Sinkhole susceptibility mapping in Marion County, Florida: Evaluation and comparison between analytical hierarchy process and LR based approaches. Scientific Reports, 9, 7140, DOI: 10.1038/s41598-019-43705-6.

Szczuciński W. (2020). Postdepositional changes to tsunami deposits and their preservation potential. In: Engel, M., Pilarczyk, J., May, S.M., Brill, D., and Garrett E., ed., Geological records of tsunamis and other extreme waves. Amsterdam: Elsevier, 443–469, DOI: 10.1016/B978-0-12-815686-5.00021-3.

Trofimova E. (2018) Unesco World Karst Natural Heritage Sites: Geographical And Geological review. Geography, Environment, Sustainability, 11(2), 63-72, DOI: 10.24057/2071-9388-2018-11-2-63-72.

Udchachon M., Thassanapak H., Burrett C. and Feng Q. (2022). The boundary between the Inthanon Zone (Palaeotropics) and the Gondwana-derived Sibumasu Terrane, northwest Thailand—evidence from Permo-Triassic limestones and cherts. Palaeobiodiversity and Palaeoenvironments, 102, 383–418, DOI: 10.1007/s12549-021-00508-w.

Veni G. (2002). Revising the karst map of the United States. Journal of Cave and Karst Studies, 64(1), 45–50.

Wei A., Li D., Zhou Y., Deng Q. and Yan L. (2021). A novel combination approach for karst collapse susceptibility assessment using the analytic hierarchy process, catastrophe, and entropy model. Natural Hazards, 105, 405-430, DOI: 10.1007/s11069-020-04317-w.

Wood N.J., Doctor D.H., Alder J. and Jones J. (2023). Current and future sinkhole susceptibility in karst and pseudokarst areas of the conterminous United States. Frontiers in Earth Science, 11, 1207689, DOI: 10.3389/feart.2023.1207689.

Wu Y., Jiang X., Guan Z., Luo W. and Wang Y. (2018). AHP-based evaluation of the karst collapse susceptibility in Tailai Basin, Shandong Province, China. Environmental earth sciences, 77, 436, DOI: 10.1007/s12665-018-7609-x.

Xu X., Yan Y., Dai Q., Yi X., Hu Z. and Cen L. (2023). Spatial and temporal dynamics of rainfall erosivity in the karst region of southwest China: Interannual and seasonal changes. Catena, 221, 106763, DOI: 10.1016/j.catena.2022.106763.

Zeng Y. and Zhou W. (2019). Sinkhole remedial alternative analysis on karst lands. Carbonates and Evaporates, 34(1), 159-217, DOI: 10.1007/s13146-018-0467-5.

Zhou G., Yan H., Chen K. and Zhang R. (2016). Spatial analysis for susceptibility of second-time KS: A case study of Jili Village in Guangxi, China. Computers & geosciences, 89, 144-160, DOI: 10.1016/j.cageo.2016.02.001.

RESEARCH PAPER

SCALING THE LANDSCAPE: REVEALING LAND USE AND COVER CHANGE PATTERNS IN THE COLOMBIAN ANDES

Luisa Díez-Echavarría[1,2,*], Clara Villegas-Palaciob, Santiago Arango-Aramburo[2]
[1]Instituto Tecnológico Metropolitano. Carrera 31 #54-10 Medellín, Colombia. ZIP code:050012.
[2]Decision Science Group, Universidad Nacional de Colombia, Medellín campus. Avenida 80 #65 - 223 Medellín, Colombia. ZIP code: 050036.
***Corresponding author:** luisadiez@itm.edu.co, lfdieze@unal.edu.co
Received: December 26th 2024 / Accepted: May 14th 2025 / Published: June 30th 2025
https://doi.org/10.24057/2071-9388-2025-3804

ABSTRACT. Formulating hypotheses about the drivers of land use and cover change (LULCC) involves identifying patterns within the dynamics of the territory. Conventional basin-level analyses often mask localized patterns driven by social issues such as governance and community dynamics. This study examines the variations in LULCC patterns over 35 years (1985–2019) by employing hierarchical intensity analysis of change across different spatial extents of the Grande and Chico River basins in the Colombian Andes. To better capture the influence of governance dynamics, the basin was delineated into two subzones with distinct governance characteristics: Zone A, where community-led conservation efforts and protected areas coexist, and Zone B, characterized by limited community participation and less active governance. Results reveal that the intensity of change accelerated significantly after 2010. During this period, forest and paramo ecosystems in the entire basin showed stationary losses, while pasture and non-vegetated areas exhibited systematic gains. Notably, Zone A demonstrated systematic pasture expansion. In contrast, pasture change in Zone B remained statistically dormant. Transition analysis indicated that cropland was the primary source of pasture gains. Qualitative insights from 3 semi-structured interviews corroborated that governance structures, local institutions, and the growing economic appeal of dairy farming are key drivers of LULCC, particularly in Zone A. These findings emphasize the need to integrate multi-scale quantitative assessments with local governance contexts to inform more effective land-use planning and conservation policy.

KEYWORDS: land use and land cover change, hierarchical analysis of intensity of change, scale, extent

CITATION: Díez-Echavarría L., Villegas-Palaciob C., Arango-Aramburo S. (2025). Scaling The Landscape: Revealing Land Use And Cover Change Patterns In The Colombian Andes. Geography, Environment, Sustainability, 2 (18), 48-62
https://doi.org/10.24057/2071-9388-2025-3804

ACKNOWLEDGEMENTS: Luisa Díez-Echavarría: conceptualization, methodology, implementation, framing, writing; Luisa Díez-Echavarría, Clara Villegas-Palacio, and Santiago Arango-Aramburo: conceptualization, editing, and revisions.

Conflict of interests: The authors reported no potential conflict of interests.

INTRODUCTION

Studying the land use and cover change (LULCC) processes is important to understand their positive and negative effects on the provision of ecosystem services (Lambin et al. 2003). Such studies start from hypotheses about their causes, where the proximate ones are the direct actions for change, which are often the result of human decisions or mediating agents; and the underlying drivers are the contextual processes that affect those decisions (E. Lambin & Geist, 2008; van Vliet et al., 2016; Verburg et al., 2011). The presence of decision-making agents as moderators between underlying drivers and proximate causes improves the understanding of the role of governance elements such as actors, institutions, and policies (van Vliet et al., 2016). Therefore, it is important to recognize that in many cases, LULCC is a major sustainability problem (Jianchu et al., 2005; Kramer et al., 2017) and as a product of decisions or behaviors of agents embedded in institutional, social, and economic structures that constrain or promote their behavior (Binder et al., 2016; Feola & Binder, 2010; Rindfuss et al., 2004).

Hypothesizing the causes of LULCC involves identifying patterns in the dynamics of the territory. Considering that patterns are not always homogeneous in the common units of analysis (e.g., basins or functional zones), it is important to identify the spatial and temporal differences that may exist to determine an appropriate rate of change (Ruiz Rivera & Galicia, 2016). The scale of observation of phenomena is composed of the dimensions of *resolution and extent*. Carefully choosing these dimensions can favor the detection of patterns (De Koning et al., 1998; Gibson et al., 2000; Kok & Veldkamp, 2001; Sietz et al., 2017; Vincent, 2007). The finest scales (higher resolution or lesser extent) can more readily evidence some LULCC patterns than the broadest ones (Jantz & Goetz, 2007). The studies by (Turner et al., 1989) and (Wu, 2004) assess the effect of the scale on its two dimensions. In fact, most investigations focus on the resolution dimension (Kok & Veldkamp, 2001); however, in this case, we are interested in the extent dimension.

The research questions of this study are: Do different spatial extents of the Grande and Chico rivers basin in the Colombian Andes reveal different patterns of LULCC change, and can these patterns be associated with an underlying

driver? To answer this question, we identified and compared LULCC patterns between 1985 and 2019 in the entire basin and in parts of it, which are defined according to governance-related characteristics. Although there are multiple underlying drivers that affect the LULCC processes, governance receives particular interest in this study because it regulates and influences agents' behavior (Berbés-Blázquez et al., 2016; E. F. Lambin et al., 2003; Nunan, 2018; Verburg et al., 2015).

We performed the hierarchical analysis of the intensity of change proposed by Aldwaik & Pontius (2012, 2013) and Robert Gilmore Pontius (2022). Unlike methodologies such as change matrices, this analysis allows us to thoroughly examine the spatial and temporal configurations of LULCC and conclude whether the change is due to systematic processes that need to be studied or to random processes. Although several studies have adopted this methodology (see Farfán Gutiérrez et al. (2016); Ellis et al. (2020); and Feng et al. (2020)), none have contrasted the analyses across different extents of the territories.

The present study offers information about whether the effects of policies and other governance elements on LULCC should be analyzed across the entire basin or in smaller areas within it, given the differences in the dynamics of change across different areas. The paper is structured as follows: Section 2 describes the study zone and the hierarchical analysis of intensity of change; Section 3 presents the results by level of analysis; and Sections 4 and 5 contain the discussion and conclusions of the study.

METHODOLOGY

Study zone and data

This study was conducted in the basin of the Grande and Chico Rivers in the northern region of Antioquia, Colombia. The basin has an area of about 127,986 ha, and its economic structure is based on dairy farming and other agricultural activities, so most of the land is used for these purposes (Corantioquia & Universidad Nacional de Colombia, 2015). It is considered a strategic basin because of the production of dairy products for the whole country (Berrio-Giraldo et al., 2021) and the presence of the Santa Inés paramo and the Río Grande II reservoir. This reservoir supplies water not only to the population settled in the basin but also to the population of Valle de Aburrá (the second most populated center in the country) and meets the national energy demand (Corantioquia, 2020).

We used six land use and cover maps (Fig. 1) from 1985, 1995, 2000, 2010, 2015, and 2019. The categories analyzed were *forest (F), paramo (P), water (W), pasture (PS), crop (C), non-vegetated (NV)*, and unclassified (UC), as described in Table 1. Each map has 1,432,143 pixels, where each pixel has a resolution of 30 m × 30 m and represents one of the seven classes. The maps were provided by Professor Johan Oszwald from the University of Rennes (personal communication, 2020) and were constructed using a supervised classification system with a maximum likelihood algorithm (overall accuracy of 89.67% and a Kappa coefficient of 0.85). It used Landsat images from the TM-5, ETM+7, and OLI-8 sensors available in Google Earth Engine. The images correspond to dates between January 1, 1985, and July 1, 2019.

In recent years, there has been a tendency in the basin to establish environmental management and protection policies in strategic areas, as shown in the left panel of Fig. 2. For example, the environmental authority Corantioquia declared in 2010 and updated in 2020 the Integrated Management District (DMI, as per its acronym in Spanish), which covers the paramo area (Corantioquia, 2010; PNUD & Corantioquia, 2020) and a total extent of 21,603.06 ha. Also, in 2015, the same authority created the Local System of Protected Areas (SILAP as per its acronym in Spanish) in one of its municipalities (Corantioquia & Alcadía de Santa Rosa de Osos, 2015), with a total area of 13,880.42 ha. Both policies delimit preservation, restoration and sustainable use zones.

To assess the effect of different extents (with the same resolution), the analysis of intensity of change of the *entire basin* was also broken down into *Zone A* and *Zone B*, as shown in the right panel of Fig. 2. Although there are several criteria to divide and select the study zones like subbasins or functional zones, in this work we considered governance criteria: villages where the effect of governance is expected to be greater (or lower) due to the area under protection policies and the community attitudes to conservation issues. *Zone A* (see land use and cover map in Fig. A.1 of the annexes) has an approximate area of 24,892 ha (276,583 pixels), and environmental management and protection policies have been implemented in 73.5% of the territory. In addition, the Santa Inés paramo is located in this zone, characterized by having a more active and participatory community in terms of conservation (Marsiglia Rivera, 2017). By contrast, *Zone B* (see land use and cover map in Fig. A.2 of the annexes) has an approximate area of 104,000 ha (1,155,560 pixels), and environmental policies have been implemented in

Table 1. Categories description (Berrio-Giraldo et al., 2024; Corantioquia & Universidad Nacional de Colombia, 2015; Machado et al., 2019)

Category	Description
Forest (F)	Oak forest and stubble. According to the Life Zones Areas, most of the area has very humid low montane forest (bmh-MB) and, to a lesser extent, very humid montane forest (bmh-M).
Paramo (P)	Santa Inés is a paramo where the main water sources that supply several municipalities originate. It is home to important plant formations (195 plant species) with immense genetic and biological value.
Water (W)	Water associated with the Río Grande II reservoir.
Pasture (PS)	Pasture is the basis of the economic structure dedicated to dairy production and dairy agroindustry. Overgrazing is observed in most of the basin.
Crop (C)	Commercial crops such as tree tomatoes and potatoes (commercial scale), and to a lesser extent subsistence agriculture. Potato crops are used to "improve the land" for cattle ranching due to the removal of topsoil to obtain organic matter and the use of high concentrations of fertilizers to adapt the soil.
Non-vegetated	Non-vegetated cover includes infrastructure, housing and mining.
Unclassified (UC)	Unclassified category due to the presence of clouds.

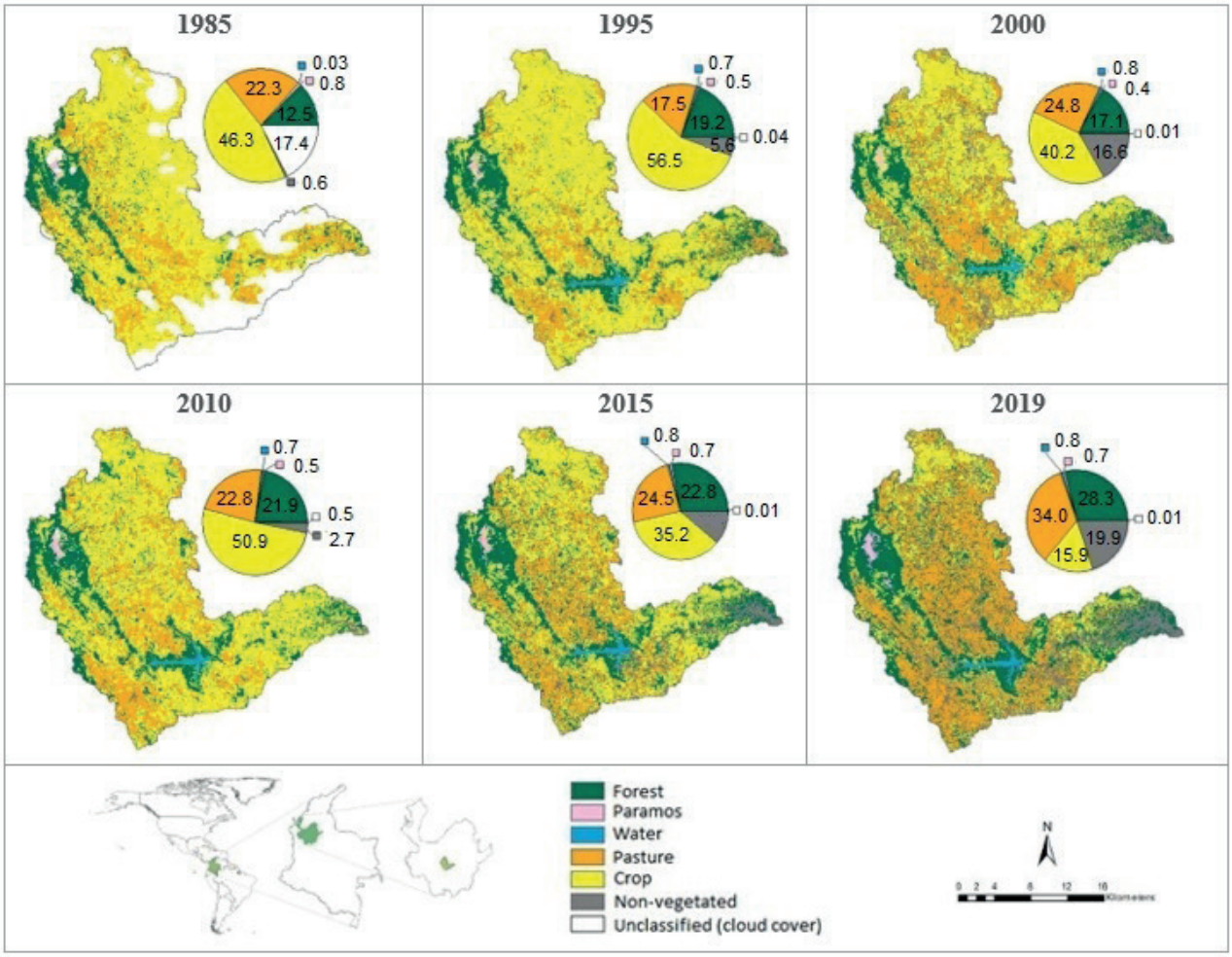

Fig. 1. Land cover maps of the Grande and Chico rivers basin (Antioquia) for six dates

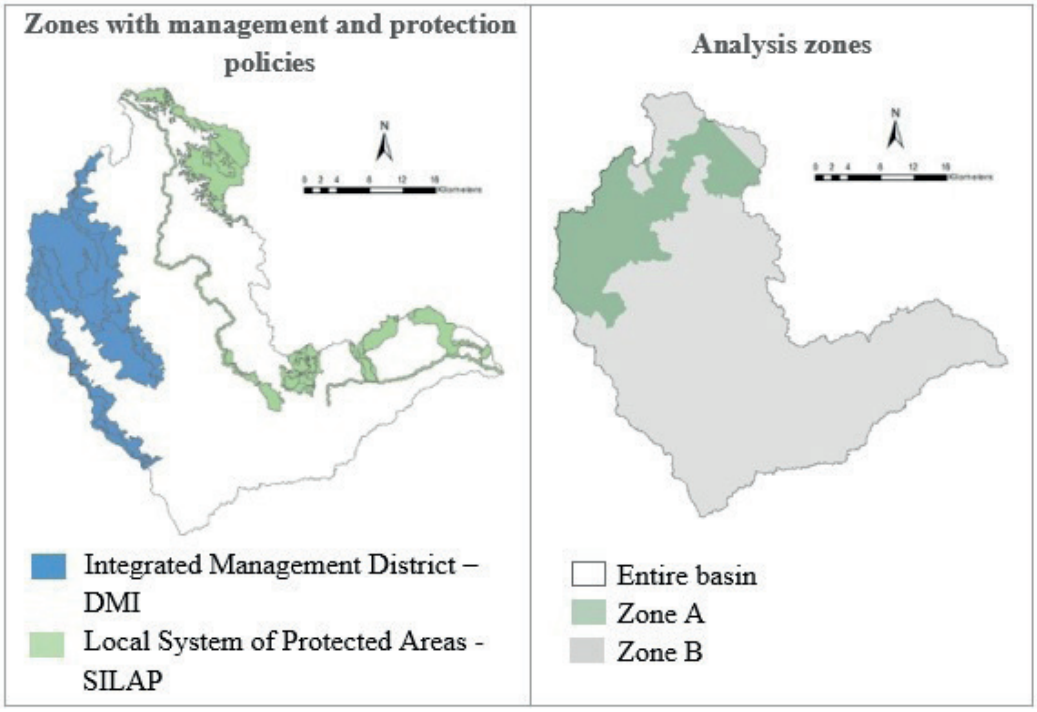

Fig. 2. Zones with management and protection policies in the basin (left) and analysis zones (right)

only 27.5% of the territory. This zone is characterized by having a less active and participatory community in terms of conservation (Berrio-Giraldo et al., 2021).

Given the differences in governance characteristics in both zones, *zone A* is expected to have more area and transitions to the pasture (*PS*) category compared to *zone B*, which is expected to have more area and transitions to *forest (F)*.

Hierarchical analysis of intensity of change

The hierarchical analysis of intensity of change is a methodology proposed by Aldwaik & Pontius (2012, 2013) and Robert Gilmore Pontius (2022). It consists of identifying *stationary patterns*, that is, similar changes across time intervals (Aldwaik & Pontius, 2012), as well as *systematic transitions*, understood as patterns of consequent losses and gains in the use and cover categories (Aldwaik & Pontius, 2013). Thus, it is possible to determine whether the change patterns are the result of systematically intensive processes or are due to random or uniform causes (Pontius et al., 2004). This methodology combines three levels of analysis that gradually increase in detail: interval, category, and transition, which are described in this section. Table 2 shows the notation used in the equations that describe the methodology.

The methodology requires land use and cover maps at different time points, which are employed to create the change matrices. A matrix can be constructed from the changes identified between a pair of maps from different dates, which constitute an interval. The matrices are calculated as shown in Table 3, where the diagonal is the area that remained unchanged for the analyzed time interval. The rest of the cells refer to the area of change, the *Total* Y_{t+1} row shows the area of each category at the second moment (final time point of the interval), and the *Total* Y_t column shows the area of each category at the first moment (initial time point of the interval).

Once we have changed matrices *T-1*, we proceed to analyze change at three levels. At the *interval level*, the most general, we identify how the intensity and size of change vary across the time intervals studied, in terms of Boolean categories: change versus persistence. We compare the annual change for each interval $[Y_t Y_{t+1}]$, denoted as S_t (Eq. 1), with a uniform rate U (Eq. 2) or Uniform Intensity (UI) that would exist if the annual changes were uniformly distributed over the entire time period Y_T-Y_1 (34 years for this study). If $S_t > U$, there is a rapid change; if $S_t < U$, the change is slow.

$$S_t = \frac{area\ of\ change\ for\ interval\left[Y_t, Y_{t+1}\right]}{duration\ of\ interval\left[Y_t, Y_{t+1}\right] * area\ of\ study\ zone} * 100 = \frac{\sum_{j=1}^{J}\left[\left(\sum_{i=1}^{J} C_{tij}\right) - C_{tij}\right]}{\left(Y_{t+1} - Y_t\right)\sum_{j=1}^{J}\left[\left(\sum_{i=1}^{J} C_{tij}\right)\right]} * 100 \quad (1)$$

$$U = \frac{area\ of\ change\ for\ all\ intervals}{duration\ of\ all\ intervals\ * area\ of\ study\ zone} 100 = \frac{\sum_{t=1}^{T-1}\left\{\sum_{j=1}^{J}\left[\left(\sum_{i=1}^{J} C_{tij}\right) - C_{tij}\right]\right\}}{\left(Y_T - Y_t\right) * \sum_{t=1}^{T-1}\left[\left(Y_{t+1} - Y_i\right)\left(\sum_{j=1}^{J}\sum_{i=1}^{J} C_{tij}\right)\right]} 100 \quad (2)$$

Table 2. Notation used in the equations (Aldwaik & Pontius, 2013)

J	Number of categories
i	Index for the category at the initial time point of the interval
j	Index for the category at the final time point of the interval
m	Index for the losing category in the transition of interest
n	Index for the gaining category in the transition of interest
T	Number of time points or maps, equivalent to six in this case
t	Index for the initial time point of interval $[Y_t Y_{t+1}]$, where t ranges from 1 to T-1
Y_t	Year at time point t
C_{tij}	Number of pixels that transition from category i to category j for interval $[Y_t Y_{t+1}]$
S_t	Annual change for interval $[Y_t Y_{t+1}]$
U	Uniform annual change over the time extent $[Y_1 Y_6]$
G_{tj}	Annual intensity of gain of category j for interval $[Y_t Y_{t+1}]$ related to the size of category j at time point t+1
L_{ti}	Annual intensity of loss of category i for interval $[Y_t Y_{t+1}]$ related to the size of category i at time point t
R_{tin}	Annual intensity of transition from category i to category n for interval $[Y_t Y_{t+1}]$ related to the size of category i at time point t, where $i \neq n$
W_{tn}	Uniform annual intensity of transition from all categories other than n to category n for interval $[Y_t Y_{t+1}]$ related to the size of categories other than n at time point t
Q_{tmj}	Annual intensity of transition from category j to category m for interval $[Y_t Y_{t+1}]$ related to the size of category j at time point t+1, where $j \neq m$
V_{tm}	Uniform annual intensity of transition from all categories other than m to category j for interval $[Y_t Y_{t+1}]$ related to the size of all the categories other than m at time point t+1

Table 3. Change matrix (Aldwaik & Pontius, 2013)

Time point	Time point t+1				
	Category *1*	Category *j*	Category *J*	Total Y_i	Loss *i*
Category *1*	C_{t11}	C_{t1j}	C_{t1J}	$\sum_{i=1}^{J} C_{t1j}$	$\sum_{i=1}^{J} C_{t1j} - C_{t11}$
Category *i*	C_{ti1}	C_{tij}	C_{tiJ}	$\sum_{i=1}^{J} C_{tij}$	$\sum_{i=1}^{J} C_{tij} - C_{tij}$
Category *J*	C_{tJ1}	C_{tJj}	C_{tJJ}	$\sum_{i=1}^{J} C_{tJj}$	$\sum_{i=1}^{J} C_{tJj} - C_{tJJ}$
Total Y_{t+1}	$\sum_{i=1}^{J} C_{tiJ}$	$\sum_{i=1}^{J} C_{tij}$	$\sum_{i=1}^{J} C_{ti1}$	$\sum_{i=1}^{J}\left(\sum_{i=1}^{J} C_{tJj} - C_{tJJ}\right)$	$\sum_{j=1}^{J}\sum_{i=1}^{J} C_{tij}$
Gain of *j*	$\sum_{j=1}^{J} C_{ti1} - C_{t11}$	$\sum_{j=1}^{J} C_{tij} - C_{tjj}$	$\sum_{j=1}^{J} C_{tiJ} - C_{tJJ}$	$\sum_{j=1}^{J}\left(\sum_{i=1}^{J} C_{tiJ} - C_{tjj}\right)$	

At the *category level*, we study how the intensity and size of the net gains and losses of each category vary across time intervals. At this level, the analysis is integrated with the previous level by comparing the metrics of losses L_{ti} (Eq. 3) and gains G_{tj} (Eq. 4) with the UI of losses and gains of all categories S_t (Eq. 1). In other words, the observed intensities are compared with an annual UI of change that would exist if the change within each interval were uniformly distributed across the spatial extent. If L_{ti}, $G_{tj} > S_t$, the category is active; if L_{ti}, $G_{tj} < S_t$ the category is dormant.

$$G_{tj} = \frac{\text{area of net gain of category } j \text{ for interval } [Y_t, Y_{t+1}]}{\text{duration of interval } [Y_t, Y_{t+1}] * \text{area of category } j \text{ at } Y_{t+1}}$$

$$100 = \frac{\left(\sum_{i=1}^{J} C_{tij}\right) - C_{tij}}{\left(Y_T - Y_t\right) * \sum_{i=1}^{J} C_{tij}} 100 \quad (3)$$

$$L_{ti} = \frac{\text{area of net loss of category } i \text{ for interval } [Y_t, Y_{t+1}]}{\text{duration of interval } [Y_t, Y_{t+1}] * \text{area of category } i \text{ at } Y_{t+1}}$$

$$100 = \frac{\left(\sum_{j=1}^{J} C_{tij}\right) - C_{tii}}{\left(Y_{t+1} - Y_t\right) * \sum_{j=1}^{J} C_{tij}} 100 \quad (4)$$

At the *transition level*, the most detailed, we identify how the intensity and size of the transitions of a category vary across the other categories available for that transition. As for the gain scheme of category *n*, R_{tin} (Eq. 5) accounts for the observed intensity of the annual transition from category *i* to category *n* for interval $[Y_t Y_{t+1}]$ in relation to the size of category *i* at time point *t*. That is, if a pixel is category *n* at time point *t*, category *n* cannot gain that same pixel at time point *t*+1. W_{tn} (Eq. 6) presents the hypothetical intensity of uniform gain of category *n* over the entire study zone. In the comparison, if $R_{tin} > W_{tn}$, then the gains of *n* target category *i* (category *i* is transitioning towards *n*); but, if $R_{tin} < W_{tn}$, then *j* cannot be changed by *n*.

$$R_{tin} = \frac{\text{area of transition from } i \text{ to } n \text{ for interval } [Y_t, Y_{t+1}]}{\text{duration of interval } [Y_t, Y_{t+1}] * \text{area of category } i \text{ at } Y_{t+1}}$$

$$100 = \frac{\left(\sum_{j=1}^{J} C_{tij}\right) - C_{tii}}{\left(Y_{t+1} - Y_t\right) * \sum_{j=1}^{J} C_{tij}} 100 \quad (5)$$

$$W_{tn} = \frac{\text{area of net gain of } n \text{ for interval } [Y_t, Y_{t+1}]}{\text{duration of interval } [Y_t, Y_{t+1}] * \text{area that is not category } n \text{ at } Y_{t+1}}$$

$$100 = \frac{\left(\sum_{i=1}^{J} C_{tin}\right) - C_{tin}}{\left(Y_{t+1} - Y_t\right) * \sum_{j=1}^{J}\left[\left(\sum_{i=1}^{J} C_{tij}\right) - C_{tnj}\right]} 100 \quad (6)$$

In the loss scheme of category *m*, Q_{tmj} (Eq. 7) accounts for the observed intensity of the annual transition from category *m* to category *j* for interval $[Y_t Y_{t+1}]$ in relation to the size of category *j* at time point *t*+1. For its part, V_{tm} (Eq. 8) presents the hypothetical intensity of uniform loss of category *m* over the entire study zone. Following the same logic as in the case of gains, if $Q_{tmj} > V_{tm}$, then losses *m* of target category *j* (category *j* is transitioning towards *m*); but, if $Q_{tmj} < V_{tm}$, then *m* cannot be changed by *j*.

$$Q_{tmj} = \frac{\text{area of transition from } m \text{ to } j \text{ for interval } [Y_t, Y_{t+1}]}{\text{duration of interval } [Y_t, Y_{t+1}] * \text{area of category } j \text{ at } Y_{t+1}}$$

$$100 = \frac{C_{tmj}}{\left(Y_{t+1} - Y_t\right) * \sum_{j=1}^{J} C_{tij}} 100 \quad (7)$$

$$V_{tm} = \frac{\text{area of net gain o } m \text{ for interval } [Y_t, Y_{t+1}]}{\text{duration of interval } [Y_t, Y_{t+1}] * \text{area that is not category } m \text{ at } Y_{t+1}}$$

$$100 = \frac{\left(\sum_{j=1}^{J} C_{tmj}\right) - C_{tmm}}{\left(Y_{t+1} - Y_t\right) * \sum_{i=1}^{J}\left[\left(\sum_{j=1}^{J} C_{tij}\right) - C_{tim}\right]} 100 \quad (8)$$

At this level of analysis, we try to determine whether the transitions are *systematic*. A transition from category *m* to *n* is systematic in an interval when, simultaneously, the gains of *n* target *m* and the losses of *m* target *n*; that is, when $R_{tmn} > W_{tn}$ and $Q_{tmn} > V_{tm}$.

Therefore, at each of the three levels, the observed intensities (percentages of the map obtained with Eqs. 1–8) are compared with a UI of change that would exist if the change were uniformly distributed over time and space. When the change patterns persist across intervals, there is stationary change (Farfán Gutiérrez et al., 2016).

The results of the hierarchical analysis of intensity of change are validated by the opinions of three actors selected through convenience sampling. For selecting the actors, we considered the following criteria: (1) At least

one of them must inhabit and work in the municipality corresponding to the study area; (2) the actor must be related and know the study area for more than 10 years; and (3) the actor must have different experiences and interests (e.g., conservation role or productive role).. In sum, the selected actors were i) an officer of the Municipal Agricultural and Livestock Technical Assistance Unit, ii) an ex-officer of DMI and actual NGO member, and iii) an officer of the environmental authority. Opinions were collected through semi-structured interviews comprising 20 questions, conducted in May and June 2022. The first two actors were interviewed in person, while the last one was interviewed virtually.

RESULTS

This section analyzes the results of the changes in five time intervals, both in the *entire basin* and in *zones A* and *B*, resulting in fifteen change matrices. The matrices take the form shown in Table 4, which corresponds to the *entire basin* during the first interval (1985–1995), where there were changes in 57,952 ha (45% of the total area).

Despite the importance of the information presented in the matrices, it is necessary to classify the types of change found: *net change* is the difference between the total area of each category within the two-time points, *total change* is the sum of the gain area, and the loss area of each category, and *exchange* is the difference between total change and net change, that is, the area of each category can be the same within the two-time points, but with different locations (Manandhar et al., 2010; Pontius et al., 2004). Table 5 details these values, with the crop (C) category reporting the largest area of change.

First level: time interval

At this level, we seek to identify in what time intervals the annual rate of overall change is relatively slow or fast. To this end, we compare the observed intensities (Eq. 1) with an annual UI of change, which would exist if the change within each interval were uniformly distributed across all times (Eq. 2).

Fig. 3 shows the annual intensity on the left and the observed change on the right for the *entire basin* and *zones A* and *B*. We observe that in no time interval and in no analysis zone were there uniform changes because the observed annual rates of change were above or below the reference line (5.46, 4.06, and 5.80, respectively). In addition, no stationary patterns were found because the speed of change across intervals was variable. The annual intensity of change was fast in the second, fourth, and fifth time intervals, which suggests that, since 2010, there has been an acceleration in the change processes for all zones. Note that high values of observed change do not necessarily

Table 4. Matrix of changes in the land use and covers (ha) of the entire basin between 1985 and 1995. The land covers are forest (F), paramo (P), water (W), pasture (PS), crop (C), non-vegetated (NV), and unclassified (U). Diagonal entries show persistence, while off-diagonal entries show transition

Land use-cover 1985	Land use-cover 1995								
	F	P	W	PS	C	I	UC	Total 1985	Loss
F	13417.29	6.66	9.81	150.21	2387.97	183.87	0.99	16156.8	2739.51
P	29.88	364.77	2.25	45.72	510.57	104.58	16.74	1074.51	709.74
W	1.53	-	16.02	0.27	0.09	22.77	-	40.68	24.66
PS	2847.6	0.09	285.48	13001.58	10992.69	1607.22	0.09	28734.75	15733.17
C	5122.08	120.87	511.2	6307.02	43630.56	4012.47	5.4	59709.6	16079.04
NV	19.35	0.27	72.36	59.85	148.77	482.58	0.09	783.27	300.69
U	3243.33	143.46	-	3036.06	15179.4	762.93	28.08	22393.26	22365.18
Total 1995	24681.06	636.12	897.12	22600.71	72850.05	7176.42	51.39	70940.88	
Gain	11263.77	271.35	881.1	9599.13	29219.49	6693.84	23.31		

Table 5. Percentage of total change (TC), net change (NC), and exchange (EXC) between each interval of the six time points for the *entire basin*

	1985-1995			1995-2000			2000-2010			2010-2015			2015-2019		
	TC	NC	EXC	TC	NC	EXC	TC	NC	EXC	TC	NC	EXC	TC	NC	EXC
F	10.86	6.61	4.25	7.38	2.06	5.32	10.23	4.82	5.41	11.85	5.86	5.99	11.69	0.96	10.74
P	0.76	0.34	0.42	0.42	0.09	0.33	0.30	0.11	0.19	0.37	0.16	0.22	0.37	0.05	0.32
W	0.70	0.66	0.04	0.10	0.08	0.02	0.08	0.06	0.02	0.14	0.04	0.09	0.13	0.02	0.11
PS	19.65	4.76	14.89	13.52	7.27	6.25	15.57	1.98	13.59	14.54	1.63	12.91	17.02	9.51	7.51
C	35.14	10.19	24.95	27.87	16.33	11.54	31.69	10.66	21.03	27.61	15.66	11.95	26.18	19.33	6.85
NV	5.43	4.96	0.47	16.40	11.02	5.38	16.65	13.88	2.77	11.02	8.43	2.59	19.21	8.79	10.42
U	17.37	17.33	0.04	0.17	0.10	0.07	0.60	0.33	0.27	0.48	0.46	0.01	0.01	0.00	0.01

imply high intensity because the latter depends on the duration of the time interval (Eq. 1). For example, in the case of the entire basin, a change of 45% of the area in 10 years (Interval 1) is different from a change of 33% of the area in 5 years (Interval 2).

As for the differences among zones, although they have similar behaviors (the same intervals are above the UI line), they differ in their magnitudes. We observe lower activity in *Zone A* than in *Zone B* in terms of intensity of change (left panel) when comparing the UI values (4.06 and 5.80) and realizing that the values of each interval are closer to the UI in the first case, as well as in terms of observed change (right panel) when comparing the percentages. Moreover, the activity in *Zone A* is lower than that in the entire basin, while the activity in *Zone B* is higher.

Second level: changes in categories

At the second level of analysis, we determine whether the pattern of a category is stable across time intervals in terms of intensity of gains (Eq. 4) and losses (Eq. 3). Fig. 4 presents the intensities of each analysis zone in the five intervals. In all cases, we observe that the intensity of the changes is not uniformly distributed across categories because the bars do not end exactly at the UI line of each interval. Moreover, both the behaviors and magnitudes differ across zones.

In general, the category that has remained active (above the UI line) for all intervals and zones is *non-vegetated (NV)*, always in terms of gains. In other words, it is a stationary change in gains. The *water (W)* and *forest (F)* categories have remained dormant both in terms of losses and gains, except in the first interval (1985–1995). In the case of the *water (W)* category, its activity rate (9.82 in the entire basin and *Zone B*) is explained by the creation of the Río Grande II reservoir in 1991. As for the *forest (F)* category, the rate of gains (4.56 in the entire basin and 5.78 in *Zone B*) displays values close to the UI. Therefore, we can say that, since 1995, these two categories have had stationary inactivity in terms of losses and gains.

When comparing the zones, the UI values of *Zone A* are always lower than those of the *entire basin*, while the UI values of *Zone B* are always higher. This variation may be explained by the proportion of the categories, in the sense that *Zone A* has the highest proportion of *forest (F)* of the three zones (Fig. A.1), and this category is one of the least active in the basin. We should also consider that the *forest (F)* activity in *Zone A* is always lower than in *Zone B*, both in terms of losses and gains.

Each table shows the annual percentage of change for each category, including the UI value. If the bars are above the value, the category is active; if they are below, the category is dormant.

We also wanted to find out which categories are active in the time intervals of fast change (2, 4, and 5). In the *entire basin*, we found that, in these three intervals, the *crop (C)* category was active in terms of losses and the *pasture (PS)* category was active in terms of gains. This demonstrates the prevalence of livestock farming as economic activity in the zone (Corantioquia & Universidad Nacional de Colombia, 2015). Furthermore, since the acceleration in the intensity of change in 2010, the *pasture (PS)* category was active in terms of gains in *Zone A* (with intensities of 6.88 and 9.91 in intervals 4 and 5, respectively), while dormant in *Zone B* (with intensities of 6.57 and 9.74 in intervals 4 and 5, respectively), despite having similar values.

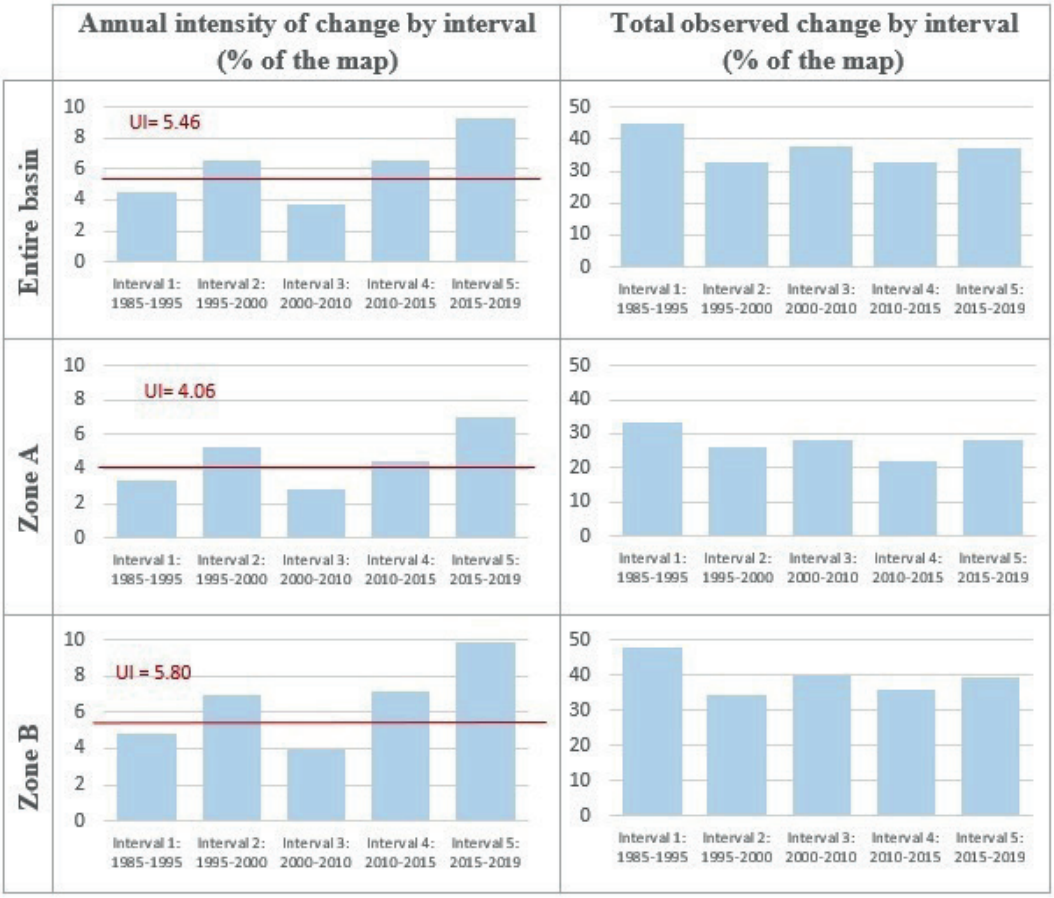

Fig. 3. Analysis of change at the interval level, broken down by zones. On the left, we find the annual intensity of change for each time interval (the red line represents the intensity value if the changes were uniform). If the intensity of change is above the red line, the period has a fast change; if it is below the red line, the period has a slow change. On the right, we find the observed change for each interval

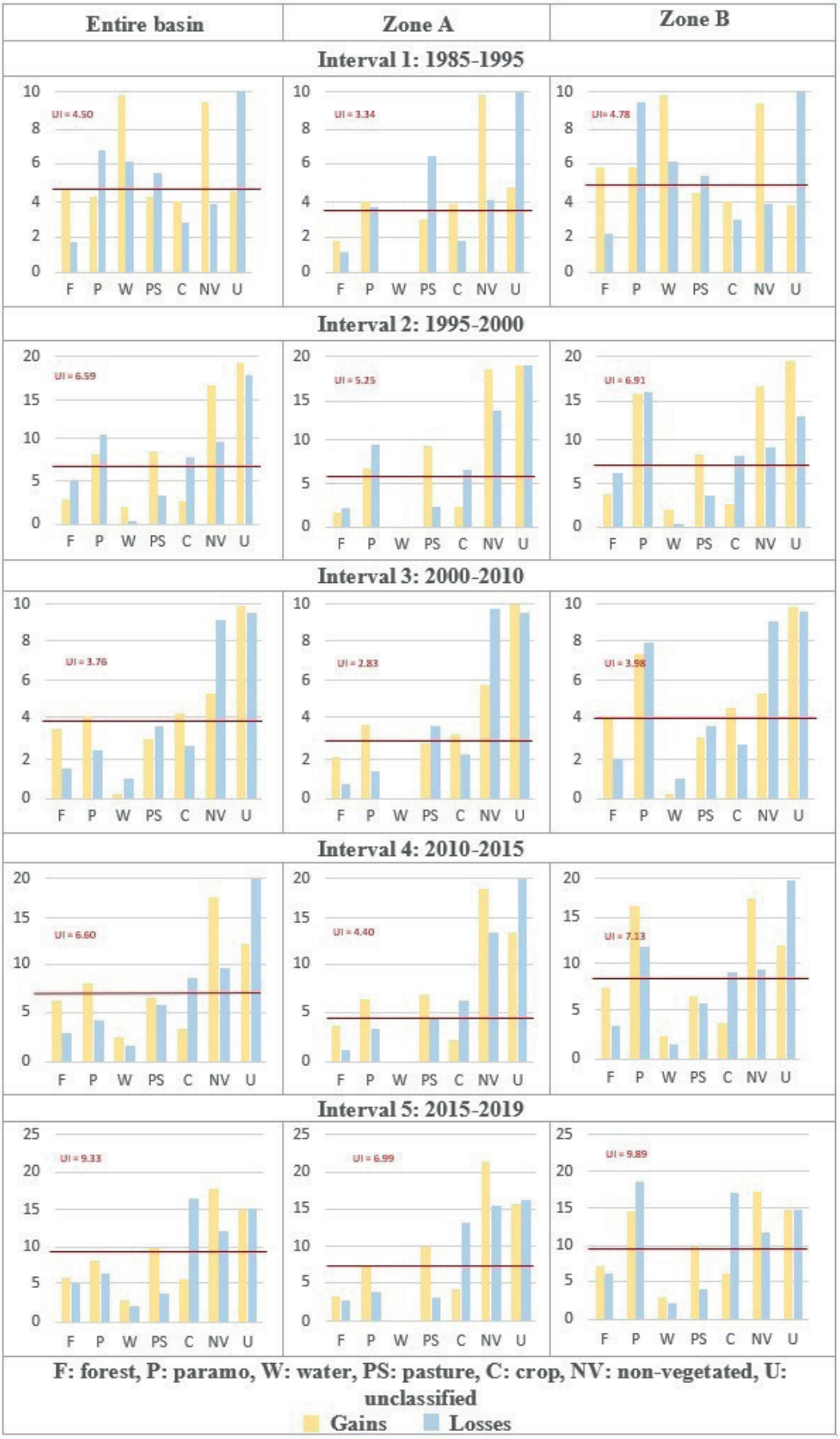

Fig. 4. Analysis of the intensity of change in the categories in the five intervals, broken down by zones

Third level: transitions

Having previously identified the categories that have specific patterns of loss and gain, at the third level of analysis we determine which transitions are particularly intense in a given time interval. In other words, we identify the categories that are targeted (Eq. 5) or *avoided* (Eq. 7), by comparing the observed intensity of each transition with a UI that would exist if the transition were uniformly distributed across the categories available for that change (Eqs. 6 and 8).

For this level of analysis, we present the relevant transition patterns found in the previous levels: i) the stationary change in terms of *non-vegetated (NV)* gains across all intervals and zones, ii) the *pasture (PS)* gain in the fast change intervals in the entire basin and *Zone A*, and iii) the *crop (C)* loss in the fast change intervals across all zones.

Fig. 5 presents the intensity of change from all categories to *non-vegetated (NV)* across all zones. As constant patterns in all intervals and zones, we found that the *crop (C)* category is always susceptible to being replaced by *non-vegetated (NV)* because its intensity of transition is above the UI. Also, we avoid the *forest (F)* category during this transition, as its intensity of transition falls below the UI.

Fig. 6 presents the intensity of transition from all categories to *pasture (PS)* in the two zones that showed active behavior at the category level (*entire basin* and *Zone A*) for the three fast change intervals. We observed that, in the two zones, the *crop (C)* and *non-vegetated (NV)* categories are always targeted to be changed to *pasture (PS)* because their intensity of transition is above the UI. Furthermore, this transition does not involve the other categories.

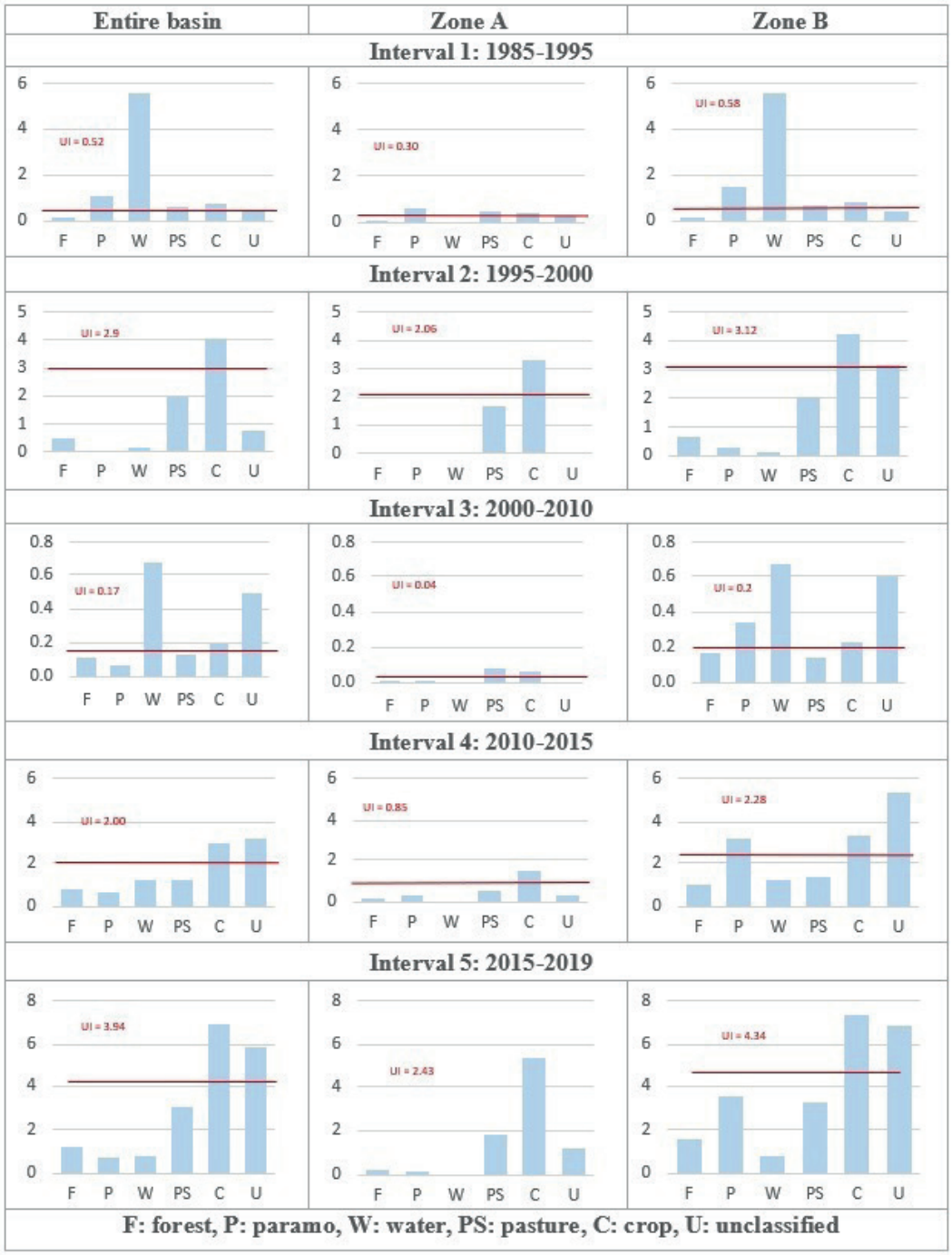

Fig. 5. Analysis of the intensity of the change from all categories to non-vegetated (NV) across all zones and intervals. Percentage of change from each category to non-vegetated (NV), including the UI value. If the bars are above the value, the category is targeted to be changed to non-vegetated (NV); if they are below, the category is avoided from being changed to non-vegetated (NV)

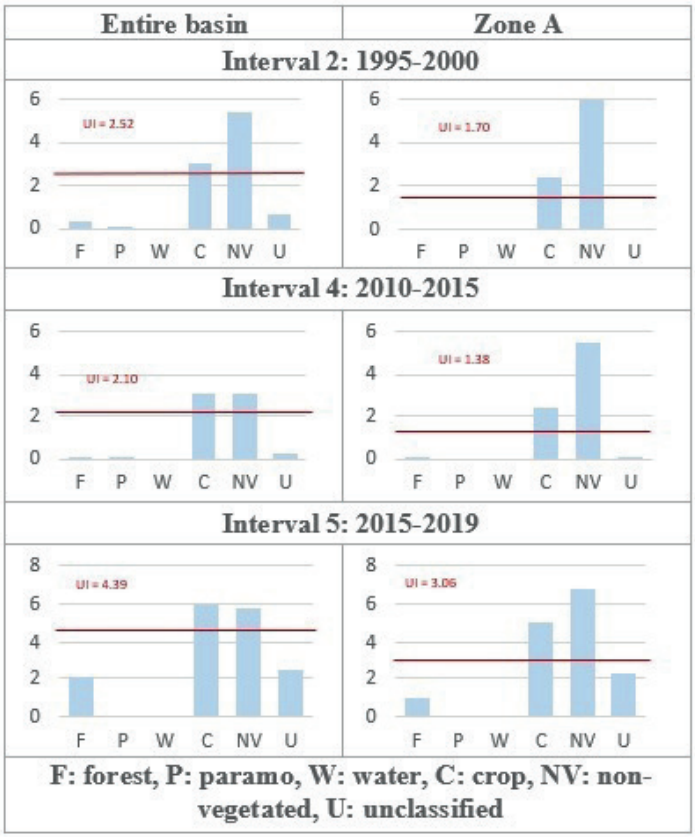

Fig. 6. Analysis of intensity of change from all categories to *pasture (PS)* for the fast intervals in the *entire basin* and *Zone A*. Percentage of change from each category to *pasture (PS)*, including the UI value. If the bars are above the value, it is considered as a target category to be changed to *pasture (PS)*; if they are below, the category is avoided to be changed to *pasture (PS)*

Fig. 7 shows the intensity of transition from *crop (C)* to the other categories for the rapid change intervals and in all zones. Among the stationary transition patterns, we observe that, for the three fast change intervals, there is a transition from *crop (C)* to *non-vegetated (NV)* in all three zones, to *pasture (PS)* in *Zone A*, and to *paramo (P)* in *Zone B* because their intensity of transition is above the UI. In addition, *forest (F)* is the avoided category in this transition across all zones. These results align with the observations in Fig. 5 and Fig. 6, where the target category for the transitions is *crop (C)*.

Analysis of change patterns

Based on the evidence from the three levels, we found an acceleration in the change processes since 2010 for all zones. *Non-vegetated (NV)* gains for all time intervals and *crop (C)* losses since 2010 were also identified as stationary patterns.

Zone A exhibits a lower intensity of change, mainly because it has a greater proportion of *forest (F)* than *Zone B* (Fig. A.1 of the annexes) and the *entire basin*; moreover, this category is the least active. We highlight the *non-vegetated (NV) – pasture (PS) and crop (C) – pasture (PS)* transitions. In fact, the *pasture (PS)* category has had active gains since the acceleration in changes in 2010. Based on these results and the tendencies revealed by (Berrio-Giraldo et al., 2021, 2024), (Corantioquia & Universidad Nacional de Colombia, 2015) and (España, 2020), we hypothesize that the changes in *Zone A* are the result of livestock farming becoming increasingly attractive to landowners, especially over the last decade.

According to the interviews, actor 1 supports this hypothesis for four reasons: (i) "unlike agriculture, dairy farming provides a daily cash flow, which is very important to farmers"; (ii) "the rest of the basin has a rooted dairy culture, which makes the business more feasible"; (iii) "dairy companies have a strong presence in the daily life of farmers; for example, the cooperative Colanta gives them loans, sells to them on credit, trains them, pick their milk… Everything!"; and (iv) "the boom and appreciation of land value: a farm in pasture is worth more than in oak. It has a better price and is more marketable". Similarly, actor 2 states: (i) "livestock farming is cash flow"; (ii) "here *[Zone A]* people already have a livestock farming tradition"; (iii) "there is always someone who buys the milk. Many companies guarantee work," and (iv) "dairy farming has more prestige than agriculture". For their part, actor 3 says that "the companies located in this zone launch important and constant marketing campaigns to captivate dairy farmers." Among other different reasons, actor 1 says that "in this zone *[Zone A]*, due to the types of soil and elevation, conditions are not optimal to produce commercial crops and their marketing is not as good there as it is in the other zone *[Zone B]*." In addition, actor 3 points out that "farmers have acquired a high level of knowledge in the management of pastures."

In contrast, *Zone B* presents a higher intensity of change, mainly because it has a greater proportion of *pasture (PS), crop (C),* and *non-vegetated (NV)* than *Zone A* (Fig. A.2 of the annexes) and the entire basin. We recognize that the factors making livestock farming appealing in *Zone A* may also apply to *Zone B*, given the substantial annual gains in *pasture (PS)*. However, according to the methodology of the hierarchical analysis of the intensity of change, such a change in *Zone B* would be driven by random processes due to the area of the category. To develop hypotheses regarding the causes of change in *Zone B*, we recommend applying the methodology in other extents.

Finally, thanks to the implementation of management and protection policies, along with community

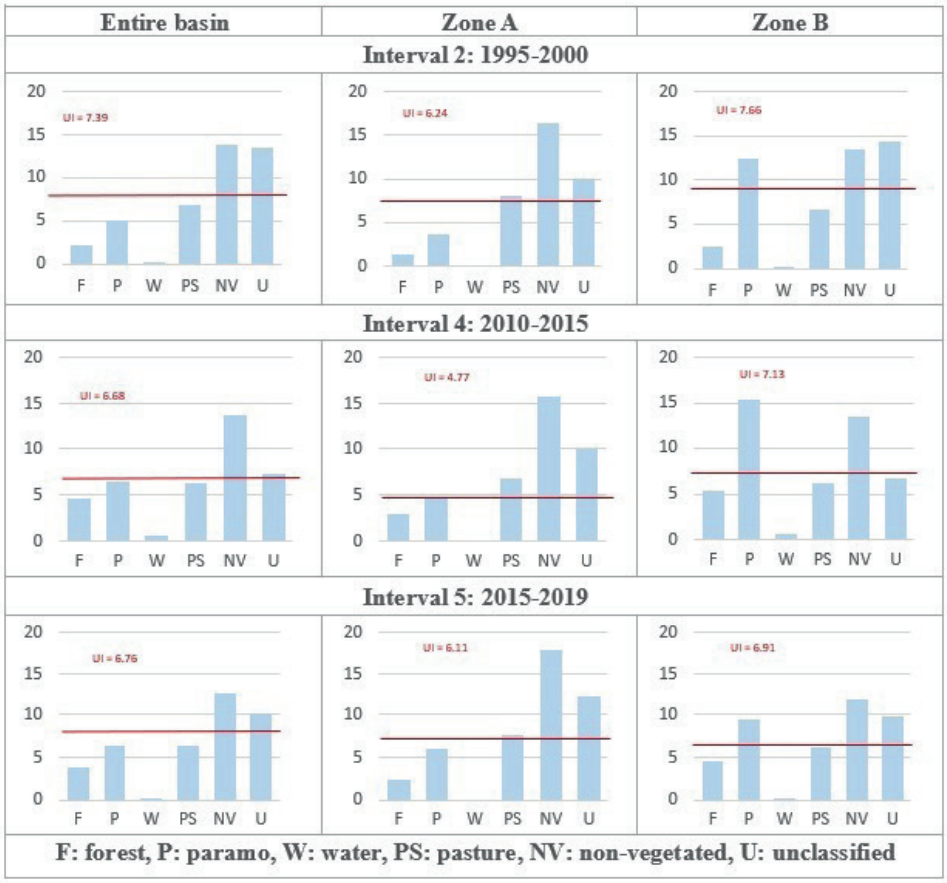

Fig. 7. Analysis of intensity of change from crop (C) to all other categories for the fast change intervals and in all zones. The *percentage* of change to each category from crop (C), including the UI value. If the bars are above the value, it is considered a *target category to be changed from crop (C); if they are below, the category is avoided from being changed from crop (C)*

participation in conservation initiatives in *Zone A*, we would expect a lower intensity of *pasture (PS)* gains than in *Zone B*. It is worth mentioning that this scenario is not an indicator of policy performance because *pasture (PS)* gains do not imply systematic losses in categories such as *forest (F)* and *paramo (P)*. However, provided the evidence of a counter-intuitive change process, we recommend conducting studies in this zone to understand the role of governance and its effect on ecosystem services in the long term.

DISCUSSION

LULCC studies typically use biogeographic criteria, such as basins, sub-basins, or functional zones, to delimit the areas of interest. However, the diverse and heterogeneous causes of LULCC across different regions suggest that alternative delimitations should also be considered. This study proposes using governance conditions as a criterion for delimiting study areas, aiming to reveal previously unknown facts about the drivers and patterns of LULCC.

We found that varying the spatial extent of the study can uncover different types of underlying drivers for the observed changes. By analyzing LULCC across diverse areas, it is possible to isolate multiple causes and gain a deeper understanding of the change patterns. Reducing the spatial extent, in particular, can reveal finer details in LULCC patterns, as supported by the findings of Turner et al. (1989) and Wu (2004).

Once the zone has been selected, other challenges appear. Aldwaik & Pontius, (2012) present the need to understand how large dormant categories can influence the analysis. The comparison between the three zones contributes to this need by showing that larger proportions of dormant categories, such as f*orest (F)* in *Zone A*, lower the UI and highlight other active changes.

Regarding the study zone, Berrio-Giraldo et al. (2021, 2024) and España (2020) observed that the villages in *Zone A* have slower LULCC modulated by environmental protection policies, and higher institutional efficiency, as well as by the intrinsic motivation of the community (Marsiglia Rivera, 2017), but they also recognize that *pasture (PS)* has become increasingly important for livestock activities in the entire basin. The dynamics of transitions to *pasture (PS)* that are revealed in this zone are not only local in the basin but also national (Rodríguez Eraso et al., 2013) and regional (see (Guarderas et al., 2022; Wassenaar et al., 2007; Zimmerer & Vaca, 2016)).

Environmental management and protection policies are often designed without community involvement and later communicated, which can lead to conflict (Velásquez Cartagena, 2020). A clear example of this is the transformation of low stubble lands (*forest (F)* in this work) for the expansion of extensive cattle farming (dairy and dual-purpose), a practice driven by the economic interests of local communities, cooperatives, and dairy companies operating in the basin (PNUD & Corantioquia, 2020). Due to noncompliance with existing policies, the DMI was updated in 2020 to address this issue. The revised document emphasizes key strategies such as monitoring restoration on public lands, strengthening control and surveillance, reinforcing the role of forest rangers, and supporting the transition to sustainable agricultural practices. While all these measures are important, the last two play a crucial role in reducing land use conflicts by fostering institutional legitimacy and trust, thereby increasing compliance with regulations (Bodin et al., 2006; Ostrom, 1990) Specifically, forest rangers not only ensure control and surveillance but also act as intermediaries between the community and environmental authorities, helping to align interests.

Additionally, sustained and adequate support for sustainable practices must be tailored to the community's needs to ensure long-term success.

While our research's results are consistent with previous studies in the basin, the country, and the region, the implications and policy recommendations differ due to the more in-depth contextual analysis enabled by the methodology. Specifically, the inactivity or increases of *forest (F)* in the villages of *Zone A* that are observed at the aggregate level (entire basin) could provide positive signals, but the health of ecosystem functions and services cannot be guaranteed until the effect of increased *pasture (PS)* at the disaggregated level (smaller zones) is understood.

To address this complexity, we argue that hierarchical analysis of the intensity of change and other methodologies like nested clustering (see (Sietz et al., 2017)) can be used together to identify LULCC patterns more effectively across scales. Hierarchical analysis serves as an initial step to quantify and visualize the magnitude and distribution of changes across different spatial extents (e.g., basin, sub-basin, villages), providing a broad overview of significant areas of change. Nested clustering can then be applied within these critical zones to group areas based on similarities in LULCC processes or drivers, such as governance conditions or socioeconomic dynamics. This two-step approach ensures that both aggregate trends and localized drivers are captured, linking macro-level patterns with micro-level complexities. By integrating these methodologies, it becomes possible to identify priority areas for intervention while accounting for both overarching trends and finer-scale nuances, essential for informing governance strategies and sustainable land management in heterogeneous regions.

CONCLUSIONS

Many studies analyzing land use and land cover change (LULCC) rely on generic spatial units, such as entire basins. In our study, we have investigated whether different spatial extents within the Grande and Chico Rivers basin in the Colombian Andes reveal distinct LULCC patterns and whether these patterns can be linked to underlying drivers. Our findings highlight the importance of disaggregating analyses and using spatial units defined by specific criteria, such as governance, to identify the scale at which key LULCC processes are most accurately characterized.

More precisely, we found that LULCC patterns vary between the entire basin and its subzones, especially after 2010, a period marked by a significant acceleration in land transformations across all scales. Although the basin as a whole experienced an overall intensification of change, only Zone A – characterized by stronger local governance and community-based conservation efforts- exhibited systematic and sustained gains in pastureland. The evidence suggests that localized socio-economic dynamics, particularly those related to dairy production, are central drivers of LULCC in the region.

Transition-level analysis confirmed that cropland was the primary source of pasture expansion, both in the entire basin and in Zone A. For example, the intensity of crop-pasture transitions during the 2015–2019 interval reached 5.11, notably exceeding the expected uniform intensity of 3.06. These quantitative trends were reinforced by qualitative data from semi-structured interviews, which revealed that dairy farming has become an increasingly attractive livelihood option in Zone A. Interviewees emphasized several motivating factors, including daily cash income, cooperative support, cultural tradition, social prestige, and the increasing value of pastureland.

Overall, this research highlights the importance of integrating scale-sensitive LULCC metrics with contextual analysis of governance and local dynamics. By doing so, it is possible to detect shaded patterns that broader-scale analyses might overlook. These insights are crucial for informing conservation and land-use planning efforts that are responsive to the socio-ecological complexity.

REFERENCES

Aldwaik, S. Z., & Pontius, R. G. (2012). Intensity analysis to unify measurements of size and stationarity of land changes by interval, category, and transition. Landscape and Urban Planning, 106(1), 103–114. https://doi.org/10.1016/j.landurbplan.2012.02.010

Aldwaik, S. Z., & Pontius, R. G. (2013). Map errors that could account for deviations from a uniform intensity of land change. International Journal of Geographical Information Science, 27(9), 1717–1739. https://doi.org/10.1080/13658816.2013.787618

Berbés-Blázquez, M., González, J. A., & Pascual, U. (2016). Towards an ecosystem services approach that addresses social power relations. Current Opinion in Environmental Sustainability, 19, 134–143. https://doi.org/10.1016/j.cosust.2016.02.003

Berrio-Giraldo, L., Villegas-Palacio, C., & Arango-Aramburo, S. (2021). Understating complex interactions in socio-ecological systems using system dynamics: A case in the tropical Andes. Journal of Environmental Management, 291, 112675. https://doi.org/10.1016/j.jenvman.2021.112675

Berrio-Giraldo, L., Villegas-Palacio, C., Arango-Aramburo, S., & Berrouet, L. (2024). Trajectories of socio-ecological systems: A case study in the tropical Andes. Ambio. https://doi.org/10.1007/s13280-024-02002-x

Binder, C. R., García-Santos, G., Andreoli, R., Diaz, J., Feola, G., Wittensoeldner, M., & Yang, J. (2016). Simulating Human and Environmental Exposure from Hand-Held Knapsack Pesticide Application: Be-WetSpa-Pest, an Integrative, Spatially Explicit Modeling Approach. Journal of Agricultural and Food Chemistry, 64(20), 3999–4008. https://doi.org/10.1021/acs.jafc.5b05304

Bodin, Ö., Crona, B., & Ernstson, H. (2006). Social networks in natural resource management: What is there to learn from a structural perspective? Ecology and Society, 11(2). https://doi.org/10.5751/ES-01808-1102r02

Corantioquia. (2010). Acuerdo 358. 36.

Corantioquia. (2020). Plan de acción 2020-2023. + sostenibilidad + vida.

Corantioquia, & Alcadía de Santa Rosa de Osos. (2015). Consolidación de iniciativas de conservación en el municipio de Santa Rosa de Osos - Antioquia.

Corantioquia, & Universidad Nacional de Colombia. (2015). Plan de Ordenación y Manejo de la Cuenca de los Ríos Grande y Chico.

De Koning, G. H. J., Veldkamp, A., & Fresco, L. O. (1998). Land use in Ecuador: a statistical analysis at different aggregation levels. Agriculture, Ecosystems and Environment, 70(2–3), 231–247. https://doi.org/10.1016/S0167-8809(98)00151-0

Ellis, E. A., Navarro Martínez, A., García Ortega, M., Hernández Gómez, I. U., & Chacón Castillo, D. (2020). Forest cover dynamics in the Selva Maya of Central and Southern Quintana Roo, Mexico: deforestation or degradation? Journal of Land Use Science, 15(1), 25–51. https://doi.org/10.1080/1747423X.2020.1732489

España, L. (2020). Trayectorias de cobertura vegetal y usos del suelo en la Cuenca de los Ríos Grande-Chico ¿Un problema de la política pública y gobernanza? Universidad Nacional de Colombia.

Farfán Gutiérrez, M., Rodríguez-Tapia, G., & Mas, J. F. (2016). Análisis jerárquico de la intensidad de cambio de cobertura/uso de suelo y deforestación (2000-2008) en la Reserva de la Biosfera Sierra de Manantlán, México. Investigaciones Geograficas, 2016(90), 89–104. https://doi.org/10.14350/rig.48600

Feng, Y., Lei, Z., Tong, X., Gao, C., Chen, S., Wang, J., & Wang, S. (2020). Spatially-explicit modeling and intensity analysis of China's land use change 2000–2050. Journal of Environmental Management, 263(February). https://doi.org/10.1016/j.jenvman.2020.110407

Feola, G., & Binder, C. R. (2010). Towards an improved understanding of farmers' behaviour: The integrative agent-centred (IAC) framework. Ecological Economics, 69(12), 2323–2333. https://doi.org/10.1016/j.ecolecon.2010.07.023

Gibson, C. C., Ostrom, E., & Ahn, T. K. (2000). The concept of scale and the human dimensions of global change: a survey. Ecological Economics, 32, 217–239.

Guarderas, P., Smith, F., & Dufrene, M. (2022). Land use and land cover change in a tropical mountain landscape of northern Ecuador: Altitudinal patterns and driving forces. PLOS ONE, 17(7), e0260191. https://doi.org/10.1371/journal.pone.0260191

Jantz, C. A., & Goetz, S. J. (2007). Analysis of scale dependencies in an urban land-use-change model. International Journal of Geographical Information Science, 19(2), 217–241. https://doi.org/10.1080/13658810410001713425

Jianchu, X., Fox, J., Vogler, J., Peifang, Z., Yongshou, F., Jie, Q., & Leisz, S. (2005). Land use and land cover changes and farmer vulnerability in Xishuangbanna prefecture in southwestern China. Envoronmental Management, 36(3), 404–413. https://doi.org/10.1007/s00267-003-0289-6

Kok, K., & Veldkamp, A. (2001). Evaluating impact of spatial scales on land use pattern analysis in Central America. Agriculture, Ecosystems and Environment, 85(1–3), 205–221. https://doi.org/10.1016/S0167-8809(01)00185-2

Kramer, D. B., Hartter, J., Boag, A. E., Jain, M., Stevens, K., Nicholas, K. A., McConnell, W. J., & Liu, J. (2017). Top 40 questions in coupled human and natural systems (CHANS) research. Ecology and Society, 22(2). https://doi.org/10.5751/ES-09429-220244

Lambin, E. F., Geist, H. J., & Lepers, E. (2003). Dynamics of land-use and land-cover change in tropical regions. Annual Review of Environment and Resources, 28(January 2003), 205–241. https://doi.org/10.1146/annurev.energy.28.050302.105459

Lambin, E., & Geist, H. (2008). Land-Use and Land-Cover: Local Processes and Global Impact. In Global Change – The IGBP Series. Spr. https://doi.org/10.1017/CBO9781107415324.004

Machado, J., Villegas-Palacio, C., Loaiza, J. C., & Castañeda, D. A. (2019). Soil natural capital vulnerability to environmental change. A regional scale approach for tropical soils in the Colombian Andes. Ecological Indicators, 96(65), 116–126. https://doi.org/10.1016/j.ecolind.2018.08.060

Manandhar, R., Odeh, I. O. A., & Pontius, R. G. (2010). Analysis of twenty years of categorical land transitions in the Lower Hunter of New South Wales, Australia. Agriculture, Ecosystems and Environment, 135(4), 336–346. https://doi.org/10.1016/j.agee.2009.10.016

Marsiglia Rivera, S. (2017). Capacidad adaptativa de los sistemas sociales ante la pérdida o deterioro de los servicios ecosistémicos. Universidad Nacional de Colombia.

Nunan, F. (2018). Navigating multi-level natural resource governance: an analytical guide. Natural Resources Forum, 42(3), 159–171. https://doi.org/10.1111/1477-8947.12149

Ostrom, E. (1990). Governing the Commons: The Evolution of Institutions for Collective Action. Cambridge Univ. Press.

PNUD, & Corantioquia. (2020). Actualización del plan de manejo del Distrito de Manejo Integrado Sistema de Páramos y Bosques Altoandinos del noroccidente medio antioqueño (DMI SPBANMA).

Pontius, R. G. (2022). Metrics That Make a Difference.

Pontius, R. G., Shusas, E., & McEachern, M. (2004). Detecting important categorical land changes while accounting for persistence. Agriculture, Ecosystems and Environment, 101(2–3), 251–268. https://doi.org/10.1016/j.agee.2003.09.008

Rindfuss, R. R., Walsh, S. J., Ii, B. L. T., Fox, J., & Mishra, V. (2004). Developing a science of land change: Challenges and methodological issues. PNAS, 101(39), 13976–13981. https://doi.org/10.1073/pnas.0401545101

Rodríguez Eraso, N., Armenteras-Pascual, D., & Alumbreros, J. R. (2013). Land use and land cover change in the Colombian Andes: dynamics and future scenarios. Journal of Land Use Science, 8(2), 154–174. https://doi.org/10.1080/1747423X.2011.650228

Ruiz Rivera, N., & Galicia, L. (2016). La escala geográfica como concepto integrador en la comprensión de problemas socio-ambientales. Investigaciones Geográficas, 89(89), 137–153. https://doi.org/10.14350/rig.47515

Sietz, D., Ordoñez, J. C., Kok, M. T. J., Janssen, P., Hilderink, H. B. M., Tittonell, P., & Van Dijk, H. (2017). Nested archetypes of vulnerability in African drylands: where lies potential for sustainable agricultural intensification? Environmental Research Letters, 12(9), 095006. https://doi.org/10.1088/1748-9326/aa768b

Turner, M. G., O'Neill, R. V., Gardner, R. H., & Milne, B. T. (1989). Effects of changing spatial scale on the analysis of landscape pattern. Landscape Ecology, 3(3–4), 153–162. https://doi.org/10.1007/BF00131534

van Vliet, J., Magliocca, N. R., Büchner, B., Cook, E., Rey Benayas, J. M., Ellis, E. C., Heinimann, A., Keys, E., Lee, T. M., Liu, J., Mertz, O., Meyfroidt, P., Moritz, M., Poeplau, C., Robinson, B. E., Seppelt, R., Seto, K. C., & Verburg, P. H. (2016). Meta-studies in land use science: Current coverage and prospects. Ambio, 45(1), 15–28. https://doi.org/10.1007/s13280-015-0699-8

Velásquez Cartagena, R. (2020). Diseño de estrategias de conservación: aproximación crítica a la implementación del sistema local de áreas protegidas del municipio de Santa Rosa de Osos, Antioquia, a partir de la identificación de vacíos de conservación [Universidad de Antioquia]. https://bibliotecadigital.udea.edu.co/bitstream/10495/18554/5/VelasquezRobinson_2020_ConservacionVacioImplementacion.pdf

Verburg, P. H., Crossman, N., Ellis, E. C., Heinimann, A., Hostert, P., Mertz, O., Nagendra, H., Sikor, T., Erb, K. H., Golubiewski, N., Grau, R., Grove, M., Konaté, S., Meyfroidt, P., Parker, D. C., Chowdhury, R. R., Shibata, H., Thomson, A., & Zhen, L. (2015). Land system science and sustainable development of the earth system: A global land project perspective. Anthropocene, 12, 29–41. https://doi.org/10.1016/j.ancene.2015.09.004

Verburg, P. H., Ellis, E. C., & Letourneau, A. (2011). A global assessment of market accessibility and market influence for global environmental change studies. Environmental Research Letters, 6(3), 034019. https://doi.org/10.1088/1748-9326/6/3/034019

Vincent, K. (2007). Uncertainty in adaptive capacity and the importance of scale. Global Environmental Change, 17(1), 12–24. https://doi.org/10.1016/j.gloenvcha.2006.11.009

Wassenaar, T., Gerber, P., Verburg, P. H., Rosales, M., Ibrahim, M., & Steinfeld, H. (2007). Projecting land use changes in the Neotropics: The geography of pasture expansion into forest. Global Environmental Change, 17(1), 86–104. https://doi.org/10.1016/j.gloenvcha.2006.03.007

Wu, J. (2004). Effects of changing scale on landscape pattern analysis: Scaling relations. Landscape Ecology, 19(2), 125–138. https://doi.org/10.1023/B:LAND.0000021711.40074.ae

Zimmerer, K. S., & Vaca, H. L. R. (2016). Fine-grain spatial patterning and dynamics of land use and agrobiodiversity amid global changes in the Bolivian Andes. Regional Environmental Change, 16(8), 2199–2214. https://doi.org/10.1007/s10113-015-0897-8

Appendices

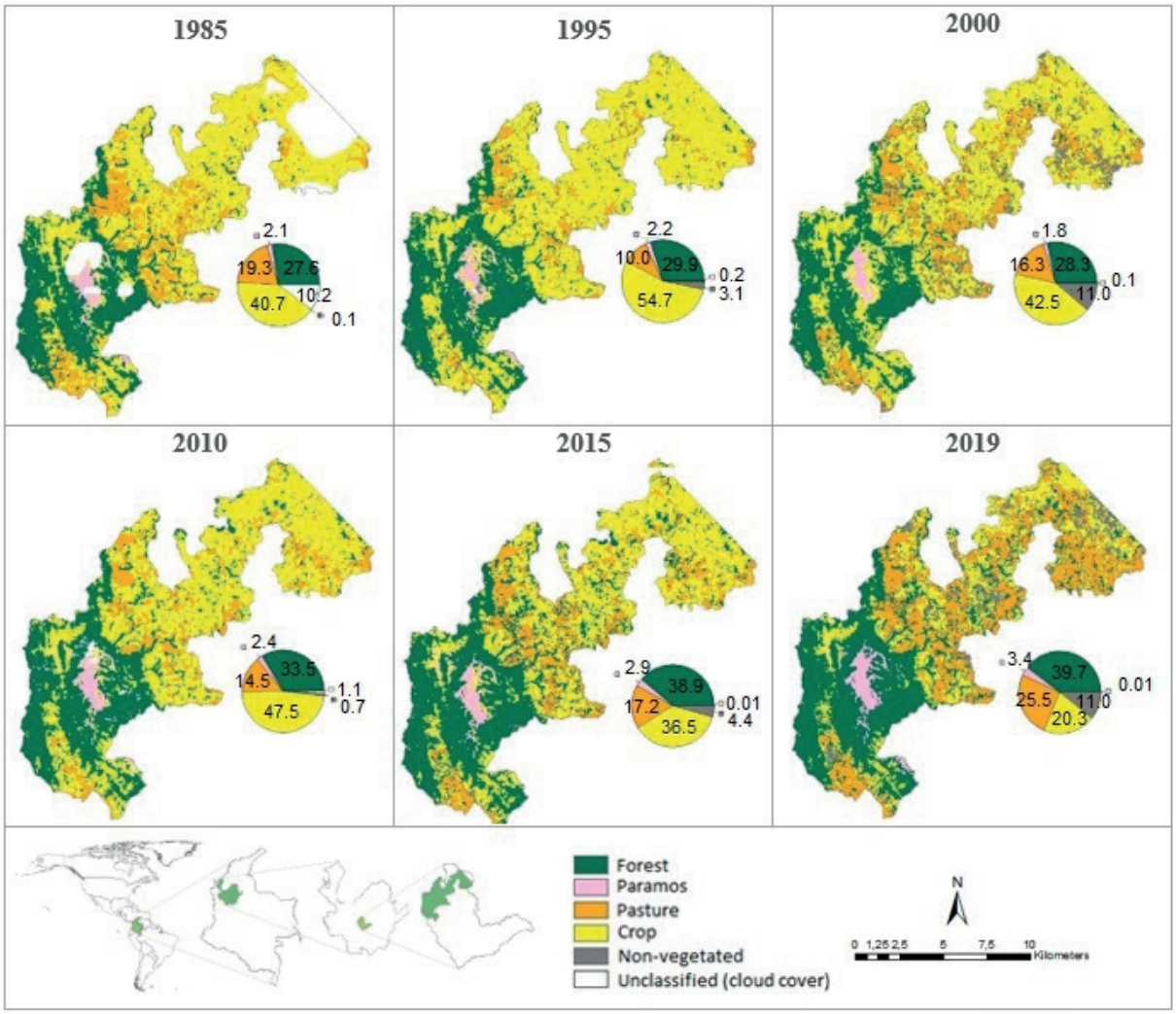

Fig. A.1. Land cover maps of *Zone A* in the Grande River basin (Antioquia) for six dates

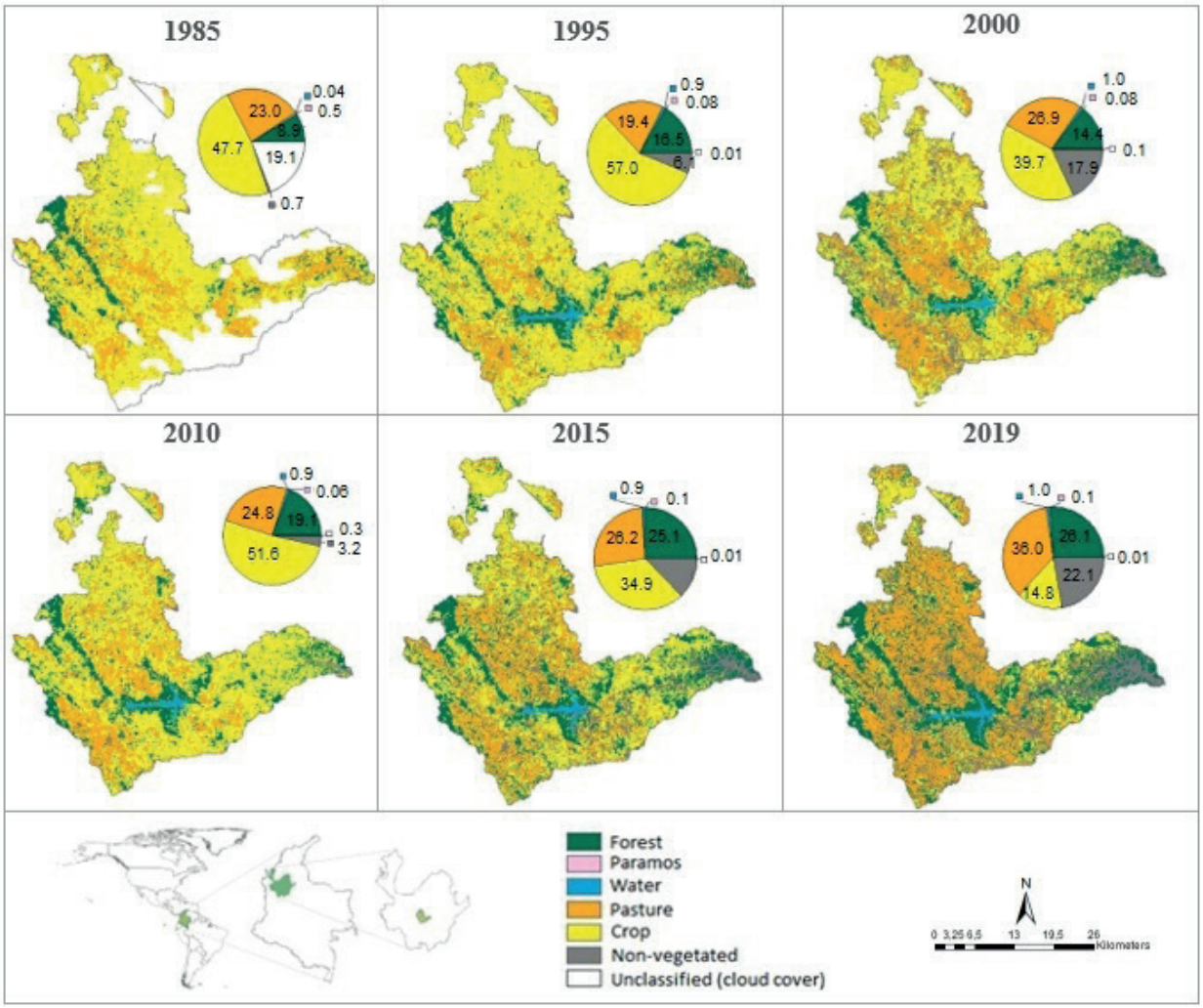

Fig. A.2. Land cover maps of *Zone B* in the Grande River basin (Antioquia) for six dates

RESEARCH PAPER

VARIATION IN CONE AND SEED PRODUCTIONS OF TAURUS CEDAR (*CEDRUS LIBANI* A. RICH.) POPULATIONS

Nebi Bilir[1], Tatyana P. Novikova[2], Arthur I. Novikov[3*]

[1]Isparta University of Applied Sciences, Faculty of Forestry, Isparta, 32260, Türkiye

[2]Voronezh State University of Forestry and Technologies named after G.F. Morozov, Faculty of Computer Science and Technology, 8, Timiryazeva str., Voronezh, 394087, Russian Federation

[3]Agrophysical Research Institute, 14, Grazhdansky av., Saint-Peterburg, 195220, Russian Federation

***Corresponding author:** arthur.novikov@agrophys.ru

Received: August 19th 2024 / Accepted: February 16th 2025 / Published: June 30th 2025

https://doi.org/10.24057/2071-9388-2025-3561

ABSTRACT. Reproductive characteristics are important tools for sustainable forestry and to transmit present gene diversity to future generations by forestry practices. Knowledge and estimation of fertility variation and its linkage parameters, such as population size and gene diversity in seed crops calculated by reproductive traits, are used widely because of their many advantages. Forestry practices use estimates of these parameters for various purposes, including natural regeneration, establishment, and management of seed sources.. In this study, cone and seed production and their effect on fertility variation were examined in two natural populations (P1 & P2) of Taurus cedar (*Cedrus libani* A. Rich.) sampled from the southern part of Türkiye. Numbers of mature cones, which were two years old and filled with seeds, were counted from fifty trees selected phenotypically from each population in 2023. The averages of cone and seed number were 90 and 33, and 5321 and 3115 per tree in the populations P1 and P2, respectively. Among individuals within a population, and between populations, there were large differences in cone and seed production. The percentages of filled seeds were 94% in P1 and 83% in P2. There were significant differences ($p<0.05$) between populations in terms of the production and percentage of filled seeds, according to results of analysis of variance. Estimated fertility variations ($\Psi<2$) were in good accordance with the target ($\Psi<3$). The effective number of parents ranged from 30.1 (60% of number of individuals) to 41.4 (83%). Besides, data sets can be used to fill the FLR-Library.

KEYWORDS: gene diversity, population size, reproductive, sibling coefficient, stand, FLR-Library

CITATION: Bilir N., Novikova T. P., Novikov A. I. (2025). Variation IN Cone and Seed ProductionS of Taurus Cedar *(CEDrus Libani* A. Rich.) populatıons . Geography, Environment, Sustainability, 2 (18), 63-69

https://doi.org/10.24057/2071-9388-2025-3561

ACKNOWLEDGEMENTS: The synthesis of samples and genetic research was carried out by N.B. The development, conceptualization, and validation of the FLR-model were carried out by T.P.N. and A.I.N. within the framework of the grant from the Russian Science Foundation (RSF), grant number 23-26-00102, https://rscf.ru/project/23-26-00102/.

Conflict of interests: The authors reported no potential conflict of interests.

INTRODUCTION

C. libani is widely distributed in the Taurus Mountains of southern Türkiye, along with some local populations in the Black Sea region of Türkiye, and there are remaining populations in Lebanon and Syria (Boydak 2003). The species occurs mainly between 800 and 2100 m asl. Taurus cedar also has natural distribution as small populations, groups, or individuals both at 500-600 m and 2400 m as lower and higher altitudes (Boydak 2003; Odabaşı 1990). To improve legibility, replace with: Taurus cedar, which is a remarkable evergreen conifer, can live for up to 1000 years or more, growing into a monumental tree with a 3 m stem diameter and 50 m height (Boydak 2003).. Monoecious Taurus cedar has 3-5 cm male and 1-1.5 cm female strobili with mature cones that are 8-10 cm in length and 4-6 cm in diameter (Boydak 2003; Odabaşı 1990) (Fig. 1).

Depending on its elevation, pollination occurs in September or early October. Between April and June of the following year, cone lets develop into mature cones in about 25-26 months after flowering (Evcimen 1963; Bilir, Kang 2021). *C. libani* is classified as one of the important species ecologically and commercially for Turkish forestry. It is also a target species of the "National Tree Breeding and Seed Production Programme" (Koski, Antola 1993) because of its valuable wood and non-wood products, social-cultural importance for rural area, and adaptation ability to various and changeable ecological conditions such as climate. Taurus cedar is widely used in plantation, afforestation, and other forestry practices such as forest restoration as a natural or exotic species due to these characteristics (Bilir, Kang 2021). Fertility data is one of the important guides to establishing successful plantations in different environmental conditions and to giving future direction to breeding programs and other forestry practices. Fertility is also one of the major tools used for various purposes in theoretical and applied forestry (Griffin 1982; Xie, Knowles 1992; Bila 2000; Kang et al. 2003; Kang, Bilir 2021).

Fig. 1. Male strobili and cones of Taurus cedar

However, differences in fertility and related factors have been measured using reproductive features like strobili, cones, flowers, and seeds in different plant species. (Xie, Knowles 1992; Roeder et al. 1989; Savolainen et al. 1993). Although many studies have looked at fertility differences mainly through individual strobili production, there has been very little research on cone and seed production in different plant species like *C. libani* (i.e., Bilir, Kang 2014; Yazıcı, Bilir 2017; Bilir, Özel 2017; Bilir, Kang 2021; Yazıcı et al. 2023). Additionally, variation in cone and seed production and their fertility in *C. libani* has not yet been comparatively investigated.

The importance of both the quantity and quality of seed supply is being understood. Seed procurement and its quality using frontier techniques (Bernardes et al. 2022; Novikova et al. 2022; Novikova et al. 2023; Novikov et al. 2021a; Novikov et al. 2021b; Novikov et al. 2019a, 2019b) is an important stage of the program and practices. It is also known that the quality of genetically improved seed crops, along with other morphological (i.e., grading) and physiological characteristics, is very important for successful forestry practices (Yazıcı et al. 2023) like planting.

The aims of this study are to estimate variations of cone and seed productions, to calculate the fertility variation and linkage parameters (i.e., population size, gene diversity) in two natural populations of *C. libani* based on cone and seed productions, and to discuss possible forestry practices of the species.

MATERIALS AND METHODS

Data collection

Two natural populations of Taurus cedar were sampled in the southern part of Türkiye (Fig. 2, Table 1). Data on the numbers of mature cones, two-years (N_C) and filled seeds (N_S) were collected from fifty trees selected phenotypically and 100 m apart in 2023. Four cones were harvested from each direction of sampled trees for seed extraction. Extracted seeds were floated to separate empty and filled seeds on water for 12-16 hours. Thereafter, the number of empty and filled seeds was counted (Fig. 3), and the percentage of filled seeds (N_S%) was calculated.

Data analysis

The ANOVA-test of the SPSS statistical package (SPSS 2011) was used for analyzing the productivity indicators of cones and seeds in the Taurus cedar populations. If we define the letter l for the number of each surveyed tree, and the letter k for the population number, then the indicator variant is expressed by the symbol $Y_{kl(C)}$ or $Y_{kl(S)}$ for the productivity of cones (*C*) or productivity of seeds (*S*), respectively. A variant of the productivity indicator Y_{kl} includes the terms $\mu+R_l+e_{kl}$, denoting for each specific Taurus cedar population *k* the average value of μ, the random effect of R_l in the *k*-th population (in this study *k*=2, the populations were designated as P1 and P2), and the error e_{kl} of determination of the model. Guided by the methodology for calculating the fertility of cones (Ψ_C) and seed fertility (Ψ_S), presented by Kang and Lindgren (1999), and Bilir (2011), the fertility of the *l*-th tree was determined as the proportion of individual cones or individual seeds in the *k* population. In this case (Ψ_C) is the sum of one and the square of the coefficient of variation CV_{CF} of the fertility values of cones, and (Ψ_S) is the sum of one and the square of the coefficient of variation CV_S of the fertility values of seeds of each *l*-th (l = 1...N) tree. Further, as shown in Kang, Lindgren (1998), Park et al. (2017), Genetic Diversity (GD) was calculated as the difference between one (1) and half (1/2) of the N_p index characterized by Kang et al. (2003) a quotient of dividing the census number *N* by the corresponding fertility Ψ.

Table 1. Geographic details of studied Taurus cedar populations

Populations	Age (year)	Latitude (N)	Longitude (E)	Average Altitude (m)	Aspect
P1	60	38º49'	30º45"	1500	North
P2	120	37º40'	30º51'	1580	Northwest

(a) (b)

Fig. 2. Sampled P1 (a) and P2 (b) Taurus cedar populations

(a) (b)

Fig. 3. Mature cones (a) and filled seeds (b) of the species used in this study

RESULTS AND DISCUSSION

Cone and seed production

The averages of cone and seed numbers in P1 and P2 populations were 90 and 33, and 5321 and 3115 per tree, respectively. Averages of cone production were 46 ranging from 19 to 76 for years of pooled aspects (Yazıcı, Bilir 2017), and 20 and 22 in two populations of Taurus cedar (Bilir, Kang 2014). The percentages of filled seeds were 94% and 83% in the populations. Among individual trees within a population and between populations, the numbers of cones, seeds, and filled seeds showed large differences (Table 2). For instance, there were more than twenty times the differences among individuals in both populations for the number of filled seeds (Table 2). Populations had significant differences (p<0.05) for cone and seed production and percentage of filled seeds as shown by results of analysis of variance. The results showed the importance of the selection of individual trees and populations for higher reproductivity. The most productive 10 trees (20% of total trees) produced 40% and 35% of total cone production in P1 and P2, respectively, while the percentages were 48% and 41% for the number of filled seeds in P1 and P2, respectively. Many biotic (i.e., population) and abiotic (i.e., altitude, crown closure) factors could explain these differences (i.e., Bila, Lindgren 1998; Bilir et al. 2005; Yazıcı, Bilir 2017 and 2023; Çatal et al. 2018; Çerçioğlu, Bilir 2018; Kang, Bilir 2021; Yazıcı et al. 2023; Bilir, Yazıcı 2024). Parental-balance curves in the populations were shown by means of cumulative gamete

contribution in Fig. 4. In both populations, individual seed productions were much closer to equal contribution than cone production (see Fig. 4). However, forestry practices could balance both characteristics.

Large differences in reproductivity were reported among trees within populations and among populations in Taurus cedar (i.e., Evcimen 1963; Odabaşı 1990; Bilir, Kang 2014; Çatal et al. 2018; Bilir, Kang 2021; Yazıcı, Bilir 2023), and in various plant species (e.g., Shea 1987; Kang et al. 2003; Bilir et al. 2005; Kang, Bilir 2021). Estimated coefficient of variations (*CV*) of the productions (Table 2) could be acceptable for natural populations *CV* ≤ 40% (Kang, Bilir 2021).

The average mature cone number was reported as 21 in the species (Bilir, Kang 2014), while the average cone number was 47 (Yazıcı, Bilir 2017), while the result of the study had higher cone production (Table 2). The results indicated the importance of populations and years in cone production. Good seed years occur once every two to three years, depending on altitude, in natural populations of the species (Boydak 2003). However, the present study had one-year data. Differences in biotic and abiotic characteristics of populations may have an impact on reproductive traits in the natural forest. Also, similar differences were found among individuals in populations regarding cone production and the number of filled seeds in natural populations of Taurus cedar (Evcimen 1963).

Fertility variation

Estimations of the cone and seed fertility and linkage parameters were given in Table 3. As seen from Table 3, seed fertility (Ψ_S) was higher than cone fertility (Ψ_C) in both populations.

Table 2. Basic statistical values for cone and seed production in the populations

Statistics	P1			P2		
	N_C	N_S	N_S%	N_C	N_S	N_S%
Mean	90.2	5320.5	93.5	32.9	3114.9	83.3
Range	20-250	750-18144	78.3-99.7	20-90	418-9685	39.5-97.2
CV%	60.1	82.3	5.2	46.1	64.2	16.9

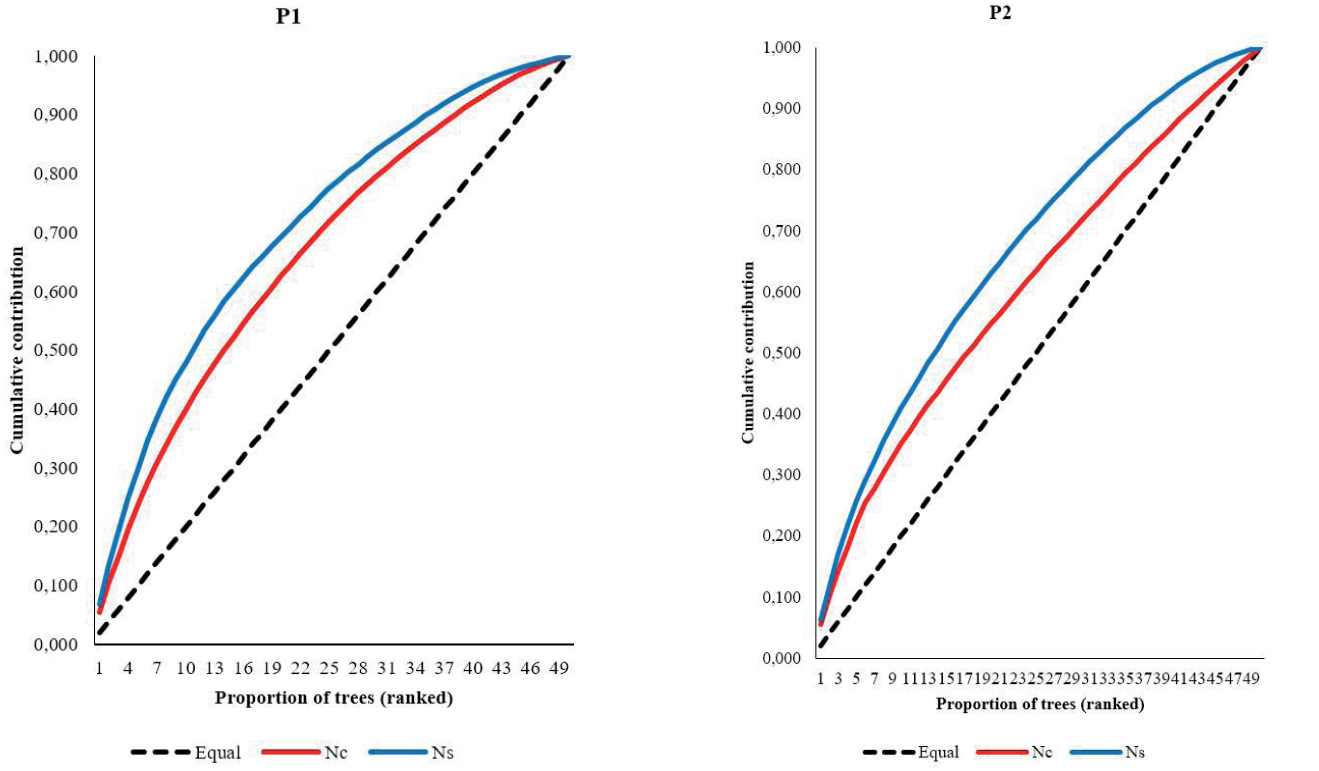

(a) (b)

Fig. 4. Parental-balance curves in the P1 (a) and P2 (b) populations

Table 3. Cone and seed fertility (Ψ_C & Ψ_S), effective number of parents ($N_{p(c)}$ & $N_{p(s)}$) and gene diversity (GD) in the populations

	P1		P2	
	N_C	N_S	N_C	N_S
Ψ_C & Ψ_S	1.35	1.66	1.21	1.41
$N_{p(c)}$ & $N_{p(s)}$	36.97 (0.74)*	30.06 (0.6)	41.40 (0.83)	35.41 (0.71)
GD	0.987	0.983	0.988	0.986

* relative effective number of parents in the parenthesis.

Cone and seed fertility variations (Ψ_C & Ψ_S) estimated of the proportion of individual production in the population were acceptable for the ideal population suggested for natural stands (Ψ<3) (Kang 2001; Kang, Bilir 2021). Seed fertility (Ψ_S) was lower than that of cone (Ψ_C) in both populations (Table 3). Fertility variations varied according to populations, years, and reproductive traits in Taurus cedar (Bilir, Kang 2014 and 2021; Yazıcı, Bilir 2023; Yazıcı et al. 2023).

The effective number of parents (N_p) which a mirror of the fertility variation, ranged from 30.1 (for Ns in P1, for 60% of census number) to 41.4 (for N_c in P2 for 83%) (Table 3). The results of the present study indicated that about 83% of individuals for N_C in the P2 behavior are under the ideal population. The size, equivalent to the target populations, was 12% (N_c) larger than N_s in P2. The difference in gene diversity was 0.004 between N_c and N_s (0.987 and 0.983) in P1 (see Table 3). The results indicated the importance of reproductive traits used in the estimations. Gene diversity was higher in P2 than P1 in both traits (see Table 3). However, it could be increased by forestry practices to harvest seed crops that have higher gene diversity for sustainable and adaptable forestry to different environmental conditions such as climate change.

Various reproductive traits, such as cone, strobili, fruit, and seed production, have been used to estimate fertility variation and linkage parameters in many plant species (Shea 1987; Roeder et al. 1989; Savolainen et al. 1993; Kang 2001; Bilir 2011; Kang, Bilir 2021). However, cone and seed were the last stage of reproductivity after pollination. Furthermore, collecting data on cone and seed production offers numerous advantages over strobilus counts. These advantages include ease of use, lower costs, and greater accuracy due to the longer lifespan and larger size of cones, as highlighted by various studies (Bilir, Kang 2014; Bilir, Kang 2021). The reproductive data for the study belonged to only two populations and one year. Therefore, more data is needed from different populations and years, including good and poor seed years, for estimating fertility variation and linkage parameters in the species.

The following steps are necessary for the practical application of the data from this study. In the tenth block (Novikova 2022a) (Fig. A.1(b)) of the third group of the FLR-algorithm, the which has six basic groups (Novikova 2022b) (Fig. A.1(a)) on the technological operations of the forest restoration process, it is necessary to additionally include data from this study (Fig. A.1(c)), along with data from a previous study (Yazıcı et al. 2023).

CONCLUSIONS

Results of the present study belong to one year and a limited area and number of populations of Taurus cedar. Future studies should be carried out to give large conclusions depending on geographic variation in the natural distribution of Taurus cedar. However, results of the study could be used in the local area of the species for different purposes, such as balancing variation in seed crop for higher gene diversity by various forestry practices. Local foresters should observe fertility variation to transmit gene diversity to future generations in an environmentally friendly way.

REFERENCES

Bernardes R.C., De Medeiros A., da Silva L., Cantoni L., Martins G.F., Mastrangelo T., Novikov A.I. and Mastrangelo C.B. (2022). Deep-learning approach for fusarium head blight detection in Wheat seeds using low-cost imaging technology. Agriculture, 12, 1801. https://doi.org/10.3390/agriculture12111801.

Bila A.D. (2000). Fertility variation and its effects on gene diversity in forest tree populations [Ph.D. Thesis] Umeå, Sweden, Swedish University of Agricultural Science, Acta Universitatis Agriculturae Sueciae, Silvestria.

Bila A.D. and Lindgren D. (1998). Fertility variation in Milletia stuhlmannii, Brachystegia spiciformis, Brachystegya bohemii and Leucaena leucocephala and its effects on relatedness in seeds. For. Genet. 5, 119–129.

Bilir N. (1997). Nursery stage of provanence on Taurus cedar (Cedrus libani A. Rich) in Eastern Black Sea region [MSc. Thesis] Trabzon, Türkiye, Black Sea Technical University.

Bilir N., Kang K.-S. and Lindgren D. (2005). Fertility variation in six populations of Brutian pine (Pinus brutia Ten.) over altitudinal ranges. Euphytica, 141, 163-168. https://doi.org/10.1007/s10681-005-6803-6.

Bilir N., Prescher F., Lindgren D. and Kroon J. (2008) Variation in cone and seed characters in clonal seed orchards of Pinus sylvestris. New Forests, 36, 187-199. https://doi.org/10.1007/s11056-008-9092-9.

Bilir N. (2011). Fertility variation in wild rose (Rosa canina) over habitat classes. Int. J. Agric. Biol., 13, 110–114.

Bilir N. and Kang K.-S. (2014). Estimation of fertility variation by strobili and cone productions in Taurus cedar (Cedrus libani A. Rich.) populations. In: Proceedings of the Proceedings of the IUFRO Forest Tree Breeding Conference; Prague, Czech Republic, 25-29 August, 2014.

Bilir N. and Özel H.B. (2017). Fertility variation in a natural stand of Taurus cedar (Cedrus libani A. Rich.). In: Proceedings of the International Forestry and Environment Symposium (IFES); Trabzon, Türkiye, 7-10 November, 2017.

Bilir N. and Kang K.-S. (2021). Fertility variation, seed collection and gene diversity in natural stands of Taurus cedar (Cedrus libani). Eur. J. For. Res., 140, 199–208. https://doi.org/10.1007/s10342-020-01324-1.

Bilir N. and Yazıcı N. (2024). Effects of climatic factors on strobilus production of Taurus cedar (Cedrus libani A. Rich.) populations. Theoretical and Applied Climatology, 155, 2151–2159. https://doi.org/10.1007/s00704-023-04754-0

Boydak M. (2003). Regeneration of Lebanon cedar (Cedrus libani A. Rich.) on karstic lands in Türkiye. For. Ecol. Manage, 178, 231-243. https://doi.org/10.1016/S0378-1127(02)00539-X.

Çatal, Y., Bilir N. and Özel H.B. (2018). Effect of growth characteristics on cone and seed production in Taurus cedar (Cedrus libani A. Rich.). Fresenius Environmental Bulletin, 27, 3832-3836.

Çerçioğlu M. and Bilir N. (2018). Altitudinal fertility variation in natural populations of Anatolian black pine [Pinus nigra Arnold. Subsp. pallasiana (Lamb.) Holmboe]. Human Journals, 4(8), 136-142.

Eler U. (1990). Seed yield in Calabrian cluster pine (Pinus brutia Ten.) by age. In Forest Research Institute, Technical Bulletin; Forest Research Institute: Antalya. Türkiye, 53–78. https://doi.org/10.3390/f14061130.

Evcimen B.S (1963). Commercial importance and management of Turkish Taurus cedar. Ankara, Türkiye, General Directorate of Forestry Press.

Griffin A.R. (1982). Clonal variation in radiata pine seed orchards. I. Some flowering, cone, and seed production traits. Australian Forest Research, 12, 4, 295-302.

Kamalakannan R., Varghese M., Park J.-M., Kwon S-H., Song J.-H. and Kang K.-S. (2015). Fertility variation and its impact on effective population size in seed stands of Tamarindus indica and Azadirachta indica. Silvae Genet., 64, 91-99. https://doi.org/10.1515/sg-2015-0008.

Kang K.-S. and Lindgren D. (1998). Fertility variation and its effect on the relatedness of seeds in Pinus densiflora, Pinus thunbergii and Pinus koraiensis clonal seed orchards. Silvae Genet., 47, 196–201.

Kang K.-S. and Lindgren D. (1999). Fertility variation among clones of Korean pine (Pinus koraiensis S. et Z.) and its implications on seed orchard management. For Genet 6:191–200.

Kang K.-S. (2001). Genetic gain and gene diversity of seed orchard crops [PhD Thesis], Umeå, Sweden: Swedish University of Agricultural Science.

Kang K.-S., Bila A.D., Harju A.M. and Lindgren D. (2003). Estimation of fertility variation in forest tree populations. Forestry, 76, 329-344. https://doi.org/10.1093/forestry/76.3.329.

Kang K.-S. and Bilir N. (2021). Seed orchards (Establishment, Management and Genetics. Ankara, Türkiye, OGEM-VAK Press, 189.

Koski V. and Antola J. (1993). National tree breeding and seed production programme for Türkiye 1994-2003. [online] Available at: https://ortohum.ogm.gov.tr [accessed on May 12, 2024].

Novikov A.I., Sokolov S.V., Drapalyuk M.V., Zelikov V.A. and Ivetić V. (2019a). Performance of Scots pine seedlings from seeds graded by colour. Forests, 10, 1064. https://doi.org/10.3390/f10121064.

Novikov A., Ivetić V., Novikova T., Petrishchev E. (2019b). Scots pine seedlings growth dynamics data reveals properties for the future proof of seed coat color grading conjecture. Data, 4(3), 106. https://doi.org/10.3390/data4030106.

Novikov A.I., Zolnikov V.K. and Novikova T.P. (2021a) Grading of Scots pine seeds by the seed coat color: how to optimize the engineering parameters of the mobile optoelectronic device. Inventions, 6, 7. https://doi.org/10.3390/inventions6010007.

Novikov A.I., Lisitsyn V.I., Tigabu M., Tylek P. and Chuchupal S. (2021b) Detection of Scots pine single seed in optoelectronic system of mobile grader: mathematical modeling. Forests, 12, 240. https://doi.org/10.3390/f12020240.

Novikova T.P., Mastrangelo C.B., Tylek P., Evdokimova S.A. and Novikov A.I. (2022). How can the engineering parameters of the NIR grader affect the efficiency of seed grading? Agriculture, 12, 2125. https://doi.org/10.3390/agriculture12122125.

Novikova T.P. (2022a). Study of a set of technological operations for the preparation of coniferous seed material for reforestation. Forestry Engineering Journal, 11, 150-160. https://doi.org/10.34220/issn.2222-7962/2021.4/13.

Novikova T.P. (2022b). The choice of a set of operations for forest landscape restoration technology. Inventions, 7, 1. https://doi.org/10.3390/inventions7010001.

Novikova T.P., Tylek P., Mastrangelo C.B., Drapalyuk M.V., Kharin S.V. and Novikov A.I. (2023). The root collar diameter growth reveals a strong relationship with the height growth of juvenile scoots pine trees from seeds differentiated by spectrometric feature. Forests, 14, 1164. https://doi.org/10.3390/f14061164.

Odabaşı T. (1990). Research on cone and seed characteristics of Cedrus libani. [online] Available at: https://www.ogm.gov.tr [accessed on Jun 12, 2024].

Park J.M., Kwon S.H., Lee H.J., Na S.J., El-Kassaby Y.A. and Kang K.-S. (2017). Integrating fecundity variation and genetic relatedness in estimating the gene diversity of seed crops: Pinus koraiensis seed Orchard as an example. Can. J. For. Res., 47, 366-370. https://doi.org/10.1139/cjfr-2016-0223.

Roeder K., Devlin B., Lindsay B.G. (1989). Application of maximum likelihood methods to population genetic data for the estimation of individual fertilities. Biometrics, 45, 363-379. https://doi.org/10.2307/2531483.

Savolainen O., Karkkainen K., Harju A., Nikkanen T. and Rusanen M. (1993). Fertility variation in Pinus sylvestris: a test of sexual allocation theory. Am. J. Bot., 80, 1016-1020. https://doi.org/10.2307/2445748.

Shea K.L. (1987). Effects of population structure and cone production on out crossing rates in Engelmann spruce and Subalpine fir. Evolution, 41, 124-136. https://doi.org/10.2307/2445748.

SPSS (2011). IBM SPSS Statistics for Windows, Version 20.0., NY: IBM Corp.

Yazıcı N. and Bilir N. (2017). Aspectual fertility variation and its effect on gene diversity of seeds in natural stands of Taurus cedar (Cedrus libani A. Rich.). Int. J. Genomics, 2960624, 1-5. https://doi.org/10.1155/2017/2960624.

Yazıcı N. and Bilir N. (2023). Impact of crown closure on cone production and effective number of parents in natural stands of Taurus cedar (Cedrus libani A. Rich.). Forests, 14, 1130. https://doi.org/10.3390/f14061130.

Yazıcı N., Novikova T.P., Novikov A.I., Bilir N. (2023). Gene diversity in seed crop of Taurus cedar (Cedrus libani A. Rich.) over an altitudinal range. Geography, Environment, Sustainability, 16, 4, 63-71. https://doi.org/10.24057/2071-9388-2023-2922.

Xie C.Y. and Knowles P. (1992). Male fertility variation in an open-pollinated plantation of Norway spruce (Picea abies). Canadian Journal of Forest Research, 22, 1463-1468. https://doi.org/10.1139/x92-196.

APPENDIX A

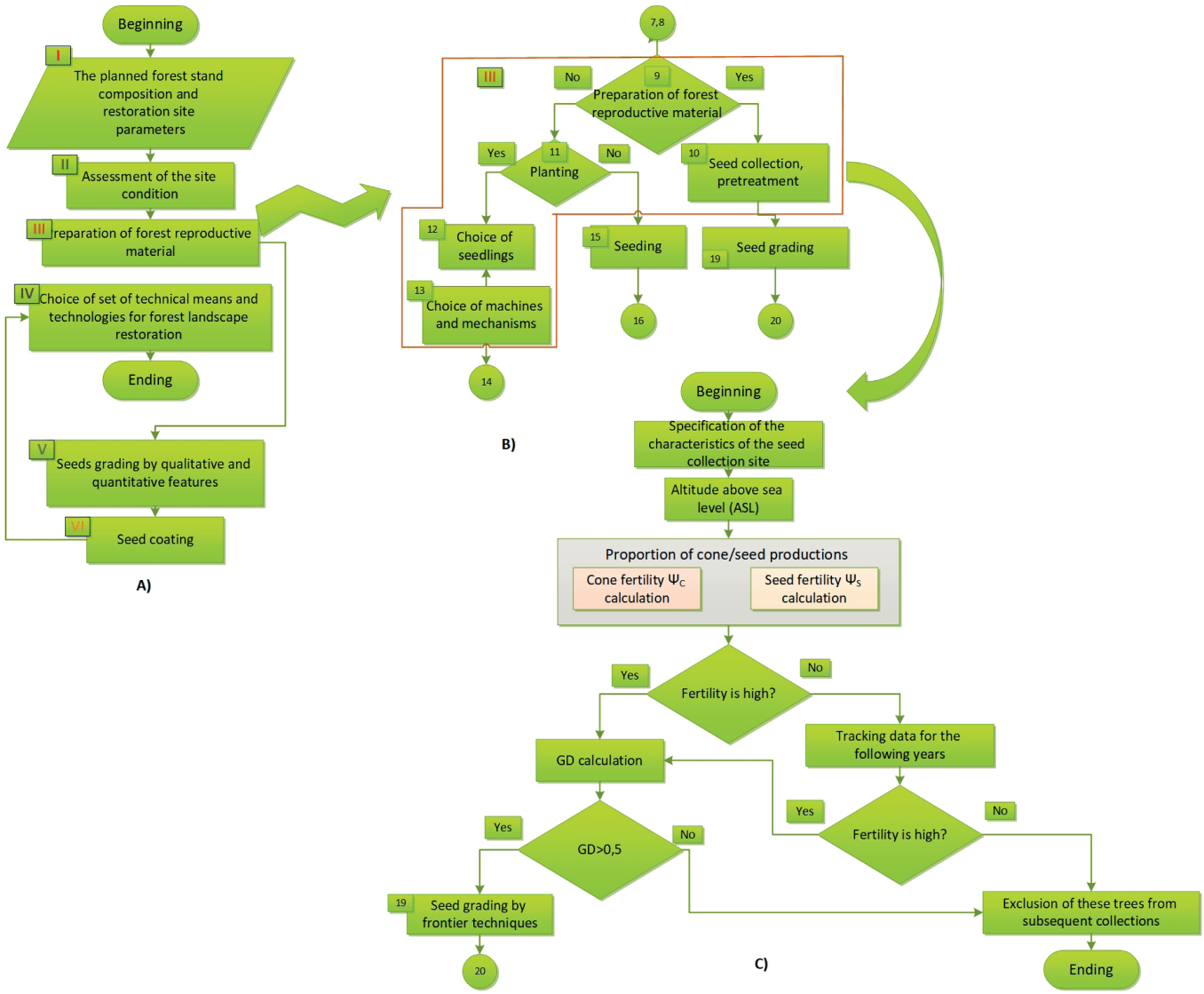

Fig. A.1. FLR-algorithm of the forest restoration technology (A), decomposing of the «Preparation of forest reproductive material» module (B), modification of block III of module 10 (Yazıcı et al. 2023) by evaluation algorithm operators of Taurus cedar cone and seed fertility (C) used in this study. Figures A) and B) are adapted and modified from the paper by co-author T.N. (Novikova 2022a), figure (C) is the T.N.'s own composition

RESEARCH PAPER

OPTIMIZING URBAN PLANNING THROUGH SPATIAL NETWORK ANALYSIS: A CASE STUDY OF DANANG CITY

Thinh Duy Do[1*], Thoi Duy Do[1]
[1]Ho Chi Minh City University of Technology and Education, 1 Vo Van Ngan Street, Ho Chi Minh City, Vietnam
***Corresponding author:** thinhdd@hcmute.edu.vn
Received: September 7th 2024 / Accepted: March 26th 2025 / Published: June 30th 2025
https://doi.org/10.24057/2071-9388-2025-3594

ABSTRACT. Urban planning is a complex process that addresses present conditions while shaping future development. However, it often relies on subjective assessments by planners and managers. This study explores the spatial network of Da Nang City through Multiple Centrality Assessment (MCA) and Space Syntax Analysis to provide an objective basis for urban planning. Key indicators, including Connectivity (Space Syntax), are calculated to assess movement, accessibility, flow, and social interaction within the urban network. Additionally, Closeness, Betweenness, Straightness, and Angular Centrality (MCA) are measured, highlighting the significance of streets and intersections in shaping urban dynamics. The findings are evaluated against Da Nang's urban planning framework to assess its effectiveness and propose solutions for optimizing the master plan. The study identifies strengths and areas for improvement in the city's layout, resulting in a proposed urban structure organized around five functional cores to enhance connectivity, efficiency, and sustainable growth. This research offers data-driven insights to assist urban planners in refining Da Nang's spatial framework, contributing to the city's long-term resilience and sustainable development.

KEYWORDS: Space Syntax, Multiple Centrality Assessment, urban configuration, spatial network, sustainable urban development

CITATION: Thinh Duy Do, Thoi Duy Do (2025). Optimizing Urban Planning Through Spatial Network Analysis: A Case Study of Danang City. Geography, Environment, Sustainability, 2 (18), 70-81
https://doi.org/10.24057/2071-9388-2025-3594

ACKNOWLEDGEMENTS: The authors would like to thank M.Arch Tran Duc Quang from Da Nang University of Technology - Da Nang University for providing valuable research materials. We also express our gratitude to Ho Chi Minh City University of Technology and Education for providing partial financial support.

Conflict of interests: The authors reported no potential conflict of interests.

INTRODUCTION

The urban spatial network is fundamental to the functioning of a city, influencing the flow of human activity, social interactions, and economic processes. The configuration of the street network plays a vital role in determining how effectively these elements operate. A well-organized street system improves connectivity and accessibility, facilitating smoother movement and shaping land use patterns (Hillier et al. 1993). Recognized as a cornerstone of urban mobility, the structure of urban networks has been studied extensively. Hillier (1996) pioneered Space Syntax, a methodology for examining spatial configurations, which has since been instrumental in revealing how street layouts affect movement dynamics (Seamon, 2015).

A key analytical tool in understanding urban networks is betweenness centrality, which quantifies how frequently a street segment falls along the shortest route between other points. This concept, rooted in graph theory, has become an essential metric for estimating the potential movement of pedestrians and vehicles within urban areas (Turner, 2007). By identifying likely paths of movement, betweenness centrality provides insights into how specific streets might shape land use and economic activity.

Research into the relationship between urban spatial structures and land use has increasingly focused on betweenness centrality. Porta et al. (2006) demonstrated that streets with higher centrality scores are more likely to support dense land use activities, such as commercial and retail functions (Porta et al., 2006b). High-centrality streets naturally attract greater foot traffic, making them ideal locations for businesses that depend on visibility and accessibility.

The interaction between land use and urban form is shaped by numerous factors, including social, economic, and environmental considerations. However, the spatial arrangement of the urban network plays a decisive role in directing land use patterns. Streets with high centrality often accommodate retail and public services, while quieter residential zones are typically located along streets with lower centrality (Marshall and Banister, 2007). Jiang and Claramunt (2004) identified a strong connection between street centrality and the diversity of land use, with high-centrality areas supporting mixed uses that foster urban vibrancy and economic growth, whereas low-centrality zones are often characterized by single-use developments, such as residential or industrial areas (Jiang and Claramunt, 2004).

Incorporating betweenness centrality into urban planning has proven effective in designing more integrated and efficient urban environments. Sevtsuk and Mekonnen (2012) highlighted the value of centrality indices in guiding

the placement of infrastructure, transportation routes, and new developments (Sevtsuk and Mekonnen, 2012). Similarly, Shi et al. (2024) underscored the role of spatial analytics in optimizing the siting of commercial projects in fast-growing urban areas, with betweenness centrality serving as a critical factor in planning decisions (Shi et al., 2024).

Urban planning in Vietnam has traditionally been driven by population size, which serves as the primary metric for determining land use and transportation networks. Consequently, the spatial configuration of urban areas often reflects the current state of cities and their projected growth, relying heavily on the judgment and experience of planners. The absence of comprehensive legal frameworks for spatial planning and land use regulation frequently results in adjustments and reconfigurations during project implementation to address unforeseen challenges.

Da Nang, Vietnam's third-largest city, received approval in 2019 from the Prime Minister to undertake a comprehensive urban planning overhaul through 2030, with a longer-term vision extending to 2045 (Prime, 2019). This ambitious initiative encompasses multiple aspects of urban development, focusing on land use, infrastructure, and spatial reorganization. The plan emphasizes restructuring Da Nang's urban framework to promote integrated growth. Key priorities include refining spatial development models, reorganizing urban zones, and aligning economic and social infrastructure. Additionally, the project seeks to integrate road, rail, and waterway networks while promoting non-motorized transport and expanding public transit systems to enhance connectivity and reduce congestion. Another critical aspect involves developing mixed-use zones that combine residential, commercial, and cultural facilities, fostering vibrant and multifunctional urban spaces (Danang People's, 2020)

This study employs Multiple Centrality Assessment (MCA) and the Space Syntax methodology to address gaps in Da Nang's ongoing urban planning efforts. By interpreting the urban network as a spatial configuration, the study examines key indicators, including Connectivity (Space Syntax), along with Closeness, Betweenness, Straightness, and Angular Centrality (MCA) (Porta et al., 2006a). These metrics are analyzed in relation to the city's development plans to assess their alignment and identify areas requiring revision. The study offers valuable insights into Da Nang's spatial network, equipping planners and policymakers with a data-driven foundation for enhancing urban resilience, refining spatial strategies, and promoting long-term sustainable growth.

Literature Review

Research exploring the relationship between street space configuration, betweenness centrality, and land use consistently reveals strong correlations. Rui and Ban (2014) demonstrated that various centrality measures in Stockholm are closely linked to distinct land-use types, illustrating how street characteristics reflect broader urban development patterns (Rui and Ban, 2014). Hillier et al. (1993) introduced the concept of configurational paradigms, proposing that the design of urban grids significantly influences pedestrian movement, with retail areas thriving due to the natural flow of foot traffic (Hillier et al., 1993). Porta et al. (2009) reinforced these findings through a study in Bologna, showing that areas with greater street centrality have denser concentrations of retail and service activities, particularly those associated with global betweenness (Porta et al., 2009). Extending this framework to American cities, Berhie and Haq (2017) highlighted that retail clusters often align with configurational hotspots, shaping residential location choices and commuting patterns (Berhie and Haq, 2017).

Further expanding on these insights, Das (2024) integrated the Gravity Index, Straightness, Betweenness, and Closeness Centrality to analyze the interplay between land use and street network configuration (Das and Ram, 2024). Collectively, these studies underscore the critical role of street configuration and centrality in shaping urban landuse and movement. However, much of this research has been conducted in Western cities, where landuse and urban structures are formalized and clearly delineated. In contrast, the informal and dynamic nature of landuse in Vietnam necessitates further investigation to understand how these relationships manifest in less rigid urban contexts.

Similarly, studies in Asian cities, such as Liu's (2016) research on Wuhan, reveal strong links between street centrality and land-use intensity. Liu's work demonstrates that these relationships vary across land-use types and within subcategories of the same landuse. However, the focus was primarily on landuse intensity rather than the distribution of land uses across the street network (Liu et al., 2016). Li (2019) expanded on the topic by examining the spatial distribution and intensity of landuse, identifying a consistent hierarchy in which different landuse types respond to location centrality, with commercial areas showing the highest sensitivity, followed by residential and industrial zones. This relationship was found to adhere to a power law, reflecting spatial variability in land-use intensity. Despite its broader scope, Li's study primarily examined urban structures at a macro scale and did not account for informal land-use conversions by residents, which often reshape urban networks (Li et al., 2019).

Additional studies by Song (2023), Yin (2022), and Wang (2018) delve into the dynamic relationship between urban transportation (street centrality) and land-use intensity (Song et al., 2023, Yin et al., 2022, Wang et al., 2018). These studies highlight the interactive feedback loop between urban form and mobility. Meanwhile, Kang (2015) investigates the influence of urban spatial network indices on user behavior, focusing on pedestrian movement and human interaction within urban environments (Kang, 2015).

The growing interest in the relationship between street configuration, accessibility, and social interaction reflects an increasing awareness among urban planners, geographers, and architects of the importance of spatial networks in shaping cities. Understanding these connections is essential for designing urban environments that are not only efficient and accessible but also socially vibrant and sustainable.

METHODOLOGY

Data preparation process

Da Nang, located in central Vietnam, serves as the administrative and commercial hub of the region (Fig. 1). As of 2019, the city had a population of 1,134,310 people (Danang People's, 2020) , making it the largest city in Central Vietnam and the fourth largest in the country. This study utilizes street network data extracted from Open Street Map (OSM) using the Python programming language and the Osmnx package developed by Jeff Boeing (Boeing, 2017). This data serves as the foundation for Connectivity analysis in DepthmapX. Furthermore, the Closeness, Betweenness, Straightness, and Angular Centrality indexes were analyzed using the Momepy package created by Martin Fleischman (Fleischmann, 2019). Data regarding urban spatial development orientation, land use, and transportation networks were compiled from the

approved master plan of 2013 and the General Planning adjustment for Da Nang in 2030, with a vision extending to 2045 (Danang, 2018).

Axial Map

Urban public space is predominantly linear in nature. The built environment's street grid can be visualized as a network of interlinked axes, with each axis representing the longest sight line within a particular urban space (Fig. 2). These axes form the foundation for calculating the spatial relationships between different urban areas. By simplifying the urban landscape into a spatial model composed of these axes, we can analyze the topological, geometric, and metric connections between various urban spaces. This approach allows for a more structured understanding of how different areas within a city are interconnected.

When creating an axial map, it is essential to draw it on a separate layer and adhere to some fundamental guidelines. The primary rule is to represent all streets, roads, paths, and similar elements as a set of the longest and fewest axial lines. These lines should be drawn to ensure that, at every change in direction, individual axial lines (also referred to as 'axes') overlap accurately. Although this may result in unsightly stubs at junctions and bends in curved streets, it is more important to avoid disconnecting streets that should be connected in the map. Another key principle in space syntax is the need to 'unlink' axial lines that visually cross each other but do not actually connect in reality. Urban spaces often contain overlapping axial lines that, despite appearing connected in a plan view, are not physically connected. Examples of such situations include overpasses, underpasses, tunnels, and stairways. Connecting these overlapping lines on the axial map would result in a

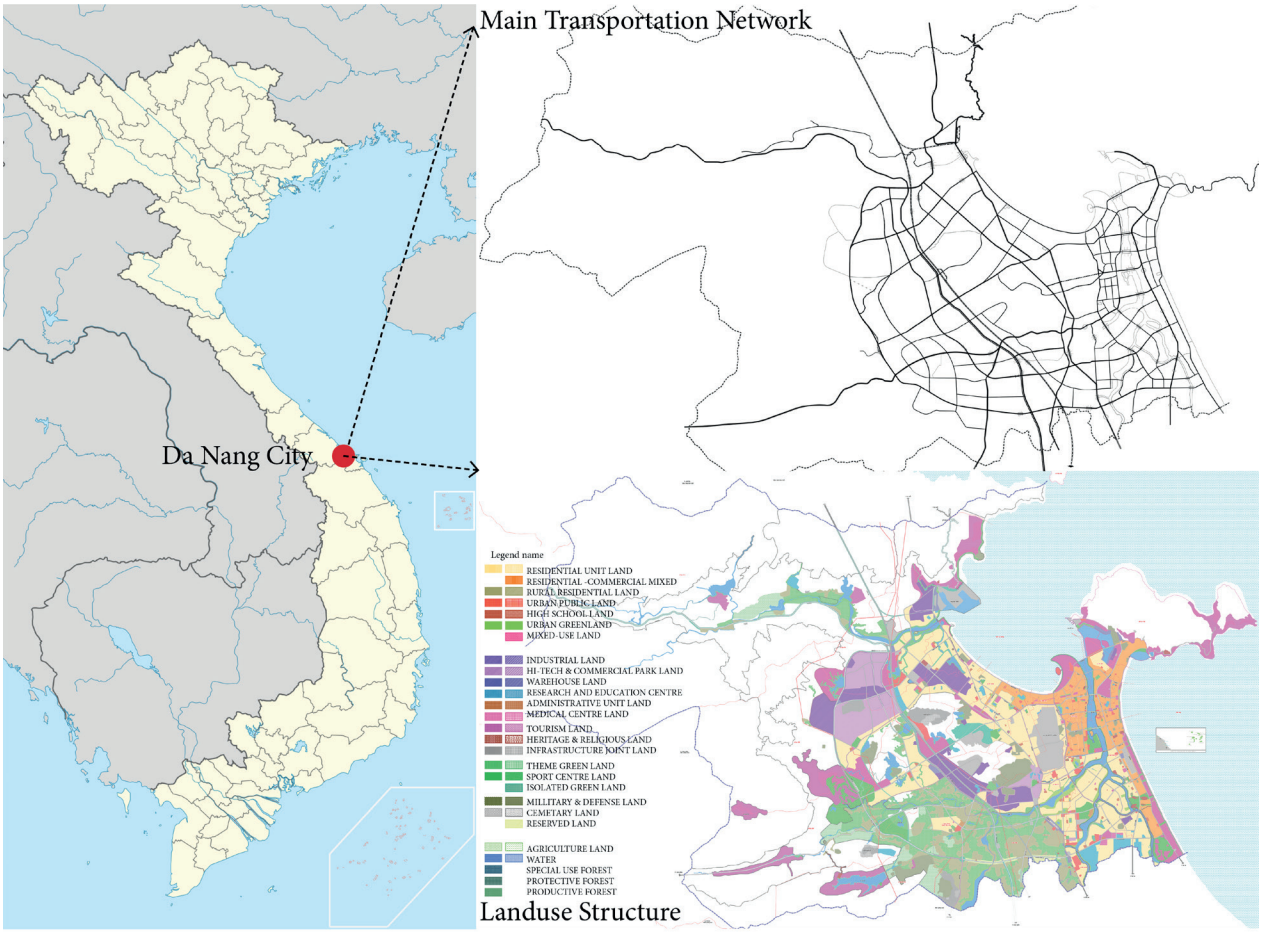

Fig. 1. Danang city location and research boundary

Fig. 2. An axial representation of an urban area in Danang

distorted and inaccurate analysis. Therefore, it's crucial to use space syntax software to unlink these lines to reflect the actual spatial relationships accurately (van Nes et al., 2021).

Space syntax theory and technique

Space syntax theory offers a framework for examining how spatial configuration impacts human behavior. It suggests that the organization of spaces, especially within urban settings, plays a crucial role in shaping movement patterns, social interactions, and other spatial dynamics (Batty, 2004). At the core of this theory is the analysis of street networks and the measurement of spatial characteristics, such as integration and connectivity (Al Sayed et al., 2014). By representing spatial layouts with axial lines and segments, space syntax allows for the measurement of how accessible and interconnected different spaces are (Matějček and Přibyl, 2020). These measurements have been demonstrated to correlate with pedestrian movement, social interactions, crime distribution, and economic activity (He et al., 2021). Space syntax, with its quantitative approach and predictive abilities, provides valuable insights for urban planning, architecture, and other fields focused on understanding and shaping the built environment. However, it is crucial to recognize the theory's limitations, such as its simplification of complex human behavior and the need for careful interpretation of results within particular contexts (Caniggia and Maffei, 2001).

The space syntax algorithm is a set of computational methods designed to analyze and quantify spatial configurations within buildings, urban environments, and other spatial systems. By using these algorithms, we can explore how spaces are connected, accessible, and integrated, as well as how these spatial characteristics influence human behavior and movement patterns. Essentially, the algorithm transforms physical spaces into networks of connections and calculates metrics that describe their spatial relationships (Van Nes, 2014).

An important index in Space Syntax utilized in this research is Connectivity, which measures the direct accessibility of a space (or node). It represents the number of immediate connections a space has with other spaces. Essentially, Connectivity indicates how many other spaces or axial lines directly connect to a particular space, making it a fundamental metric for understanding local accessibility within the spatial system. For a given space or axial line *i*, the Connectivity *k(i)* is calculated as (Eq. 1):

$$k(i) = \sum_{j \in N(i)} 1 \tag{1}$$

where *k(i)* - Connectivity of space *i, N(i)* - the set of spaces that are directly connected to space *i*

DepthmapX is an open-source software developed by Alasdair Turner at University College London, based on the Space Syntax research framework. It is extensively used in architecture, urban design, and spatial planning to analyze spatial networks. The software allows users to perform various analyses, including Visibility Graph Analysis (VGA), axial line analysis, and segment analysis, to gain insights into spatial connectivity and movement patterns (Turner, 2001). DepthmapX's graph-based analyses enable the measurement of spatial connectivity, integration, and choice, which are essential in urban planning and architectural design. These metrics assist planners and designers in assessing and optimizing the layout of cities, transportation systems, and buildings, thereby improving accessibility and functionality (Hillier & Hanson, 1988). The software also aids in wayfinding by analyzing how people navigate complex environments, such as airports and hospitals, offering valuable insights for enhancing spatial design. Additionally, DepthmapX produces visual outputs like heatmaps and spatial graphs, which help interpret and communicate spatial data effectively during the design process (Turner, 2007). In summary, DepthmapX is a vital tool for analyzing and optimizing the interaction between spatial configurations and human movement.

Multiple Centrality Assessment (MCA)

Multiple Centrality Assessment (MCA) is a spatial network analysis method rooted in graph theory that evaluates the structural importance of nodes and links within urban networks. By analyzing how streets and intersections contribute to overall connectivity and movement, MCA offers critical insights into urban accessibility, transportation efficiency, and land use patterns (Crucitti et al., 2006). This approach aids urban planners in understanding how spatial configurations shape pedestrian and vehicular flow, informing decisions on infrastructure and development. MCA incorporates key centrality measures that highlight various dimensions of network connectivity.

(1) Closeness centrality reflects how accessible a node is by measuring its average distance to all other nodes, often indicating well-integrated areas that facilitate movement and interaction (Freeman, 2002) (Eq. 2):

$$C_C(v) = \frac{1}{\sum_{u \in V} d(v,u)} \tag{2}$$

where $C_C(v)$ represents the closeness centrality of node *v*, $d(v,u)$ is the shortest path distance between node *v* and node *u*, and V denotes the set of all nodes in the network. A higher $C_C(v)$ value indicates greater accessibility and proximity to other nodes.

(2) Betweenness centrality identifies nodes that frequently appear on the shortest paths between others, underscoring their role as vital connectors or potential bottlenecks in the network (Newman, 2005). These nodes often correspond to commercial hubs or critical intersections (Eq. 3):

$$C_B(v) = \sum_{s \neq v \neq t} \frac{\sigma_{st}(v)}{\sigma_{st}} \tag{3}$$

where $C_B(v)$ denotes the betweenness centrality of node *v*, σ_{st} is the total number of shortest paths from node *s* to node *t*, and $\sigma_{st}(v)$ is the number of these paths that pass through node *v*. Nodes with high $C_B(v)$ are critical for facilitating movement within the network and act as bottlenecks or hubs for traffic flow.

(3) Straightness centrality measures the directness of routes between nodes, with higher values indicating more efficient paths that minimize detours (Crucitti et al., 2006). Complementing this, angular centrality assesses the degree of deviation in paths, emphasizing routes with fewer turns, which are typically more navigable and frequently used (Turner, 2007) (Eq. 4):

$$C_S(v) = \frac{1}{n-1} \sum_{u \in V, u \neq v} \frac{d_E(v,u)}{d(v,u)} \tag{4}$$

where $C_S(v)$ is the straightness centrality of node *v*, $d_E(v,u)$ represents the Euclidean distance between nodes *u*, $d(v,u)$ and is the shortest path distance, and *n* is the total number of nodes in the network. A $C_S(v)$ value closer to 1 indicates that the paths are highly efficient and direct.

(4) Angular centrality evaluates the angular deviation along paths, prioritizing routes with minimal turning costs to ensure smoother and more efficient navigation. This metric highlights navigational smoothness, making it particularly relevant in urban studies where wayfinding and the directness of routes play a critical role in influencing movement patterns (Eq. 5).

$$C_A(v) = \frac{1}{\sum_{u \in V} \theta(v,u)} \quad (5)$$

where $C_A(v)$ is the angular closeness centrality of node v, and $\theta(v,u)$ is the total angular deviation along the shortest path between nodes v and u. Nodes with high angular centrality values facilitate more efficient navigation by minimizing angular changes.

By integrating these metrics, MCA enables urban planners to identify high-connectivity areas, improve transportation networks, and optimize land use planning. This comprehensive analysis enhances the design of urban spaces, fostering resilience, accessibility, and sustainable development (Sevtsuk and Mekonnen, 2012).

RESULTS

Closeness Centrality Analysis

Closeness Centrality is a fundamental metric in network analysis used to evaluate the relative "proximity" of a node to all other nodes within a network. It measures the average shortest distance from a given node to all other nodes, providing insight into its potential to quickly access or interact with other parts of the network. In simpler terms, it identifies areas with strong accessibility and efficient connections. Closeness 400 and Global Closeness are two robust analytical tools frequently employed in infrastructure planning, each serving distinct purposes at varying scales of urban planning.

Fig. 3a shows how local closeness centrality (R = 400 m) is spread out, focusing on connection levels within a 400-meter area. Red and orange areas indicate places with good local access, usually found in city centers, transit stations, or crowded areas with effective internal networks. Conversely, blue and green areas reflect lower connectivity levels, often associated with suburban or peripheral regions where infrastructure is less developed. This analysis reveals significant spatial disparities in urban accessibility, underscoring the need for targeted infrastructure investments. Such insights are critical for guiding strategic interventions aimed at enhancing mobility, reducing fragmentation, and promoting equitable access to services across the city.

A comparison of the analysis results with existing and future land-use plans highlights four key areas for consideration (Fig. 4): Area 1: Although designated for mixed-use purposes, including residential, commercial, and tourism activities, this area exhibits relatively low local accessibility within the spatial structure; Area 2: Planned as a new residential area and envisioned as the southern urban center of the city, this region also demonstrates low connectivity in the analysis; Areas 3 and 4: While positioned near the newly planned satellite urban centers, these areas similarly show limited local accessibility, indicating the need for enhanced connectivity.

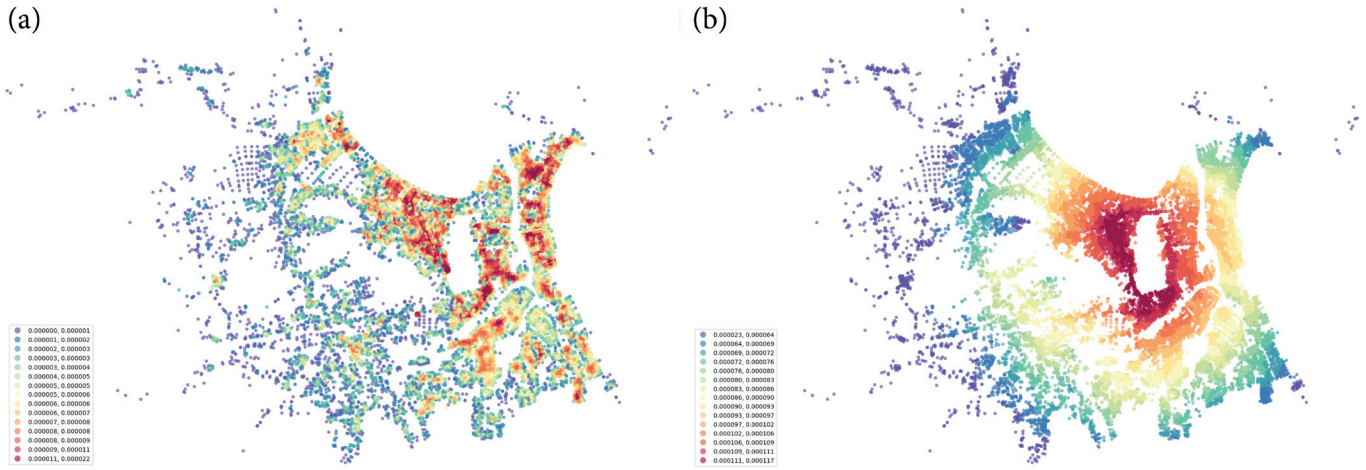

Fig. 3. Closeness Centrality Analysis of Da Nang: (a) R400; (b) Rn

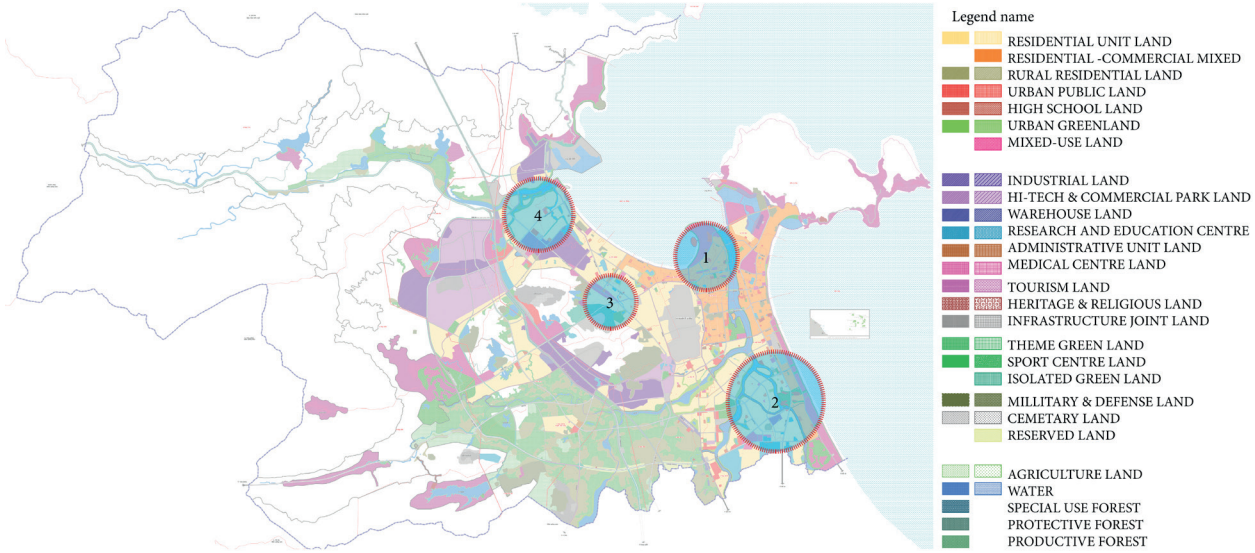

Fig. 4. The planned areas do not meet expectations due to the low local connectivity of the regions

The analysis of global closeness centrality (Fig. 3b) reveals a concentration of high-connectivity zones (red areas) within the city center, indicating a monocentric urban structure. This pattern is predominantly characterized by the dominance of areas surrounding the airport, encompassing districts such as Hai Chau, Thanh Khe, and parts of Lien Chieu and Cam Le. These districts exhibit superior connectivity and accessibility, making them the focal points of urban activity.

In contrast, peripheral districts such as Son Tra and Ngu Hanh Son display low global centrality values, suggesting potential challenges in accessing essential services and economic opportunities. Such evidence highlights the pressing need for infrastructure development in these areas to improve connectivity, reduce spatial inequalities, and foster balanced urban development. Strategic investments in transportation networks could significantly enhance mobility, strengthen the urban fabric, and promote equitable growth across all regions of the city.

Betweenness Centrality Analysis

The edge-based betweenness centrality of an urban road network highlights the importance of various roads in facilitating movement and connectivity across the city. Betweenness centrality measures how often a particular edge (road segment) lies on the shortest path between pairs of nodes, indicating the criticality of that edge in terms of traffic flow and connectivity.

Red and dark orange lines indicate roads with high betweenness centrality, representing key traffic conduits like highways and major transit corridors. Yellow to light purple lines show moderate to low centrality, typically local streets or minor connectors. Purple and blue lines reflect very low centrality, representing cul-de-sacs, dead ends, or peripheral paths. The concentration of high-betweenness edges in the city center and along major corridors highlights the structural importance of these routes (Fig. 5). These areas are essential for maintaining traffic efficiency and reducing congestion. Peripheral roads with low betweenness suggest limited integration with the core network, indicating potential areas for future infrastructure development to enhance connectivity. Roads with the highest betweenness values may face greater risk of congestion or disruption if blocked, underscoring the need for network redundancy and alternative routes to distribute traffic more evenly.

When compared with the planned transportation network, most major roads in Da Nang's master plan align with roads that exhibit high betweenness centrality. However, there are still certain roads with high betweenness centrality (highlighted in black in Fig. 6) that have been overlooked in the planned primary transportation network. Additionally, the circled areas in Fig. 6 warrant reconsideration during the planning of the internal road network. These areas remain disconnected from the primary planned network, highlighting the need for better integration to enhance connectivity across the entire urban system.

Straightness centrality of spatial network

Reflects efficient paths with minimal detours, the straightness centrality of an urban road network, indicating how directly connected each road segment is to others in the network. Straightness centrality measures the efficiency of travel along a network, comparing the shortest path (geodesic distance) to the actual path along the network. High straightness values signify minimal detours, reflecting well-aligned, direct routes (Fig. 7a).

The color gradient from red to blue represents roads with varying levels of straightness centrality, where red indicates high straightness and blue represents low straightness. Areas with high straightness centrality play a crucial role in facilitating efficient movement and reducing travel expenses. In contrast, peripheral regions with low straightness suggest fragmented or less direct infrastructure, potentially increasing travel times and limiting accessibility.

Overall, the urban structure of central Da Nang is relatively coherent and well-oriented, providing convenience for both residents and tourists. However, certain areas highlighted in Fig. 7b require attention to

Fig. 5. Betweenness Centrality Analysis of Da Nang City

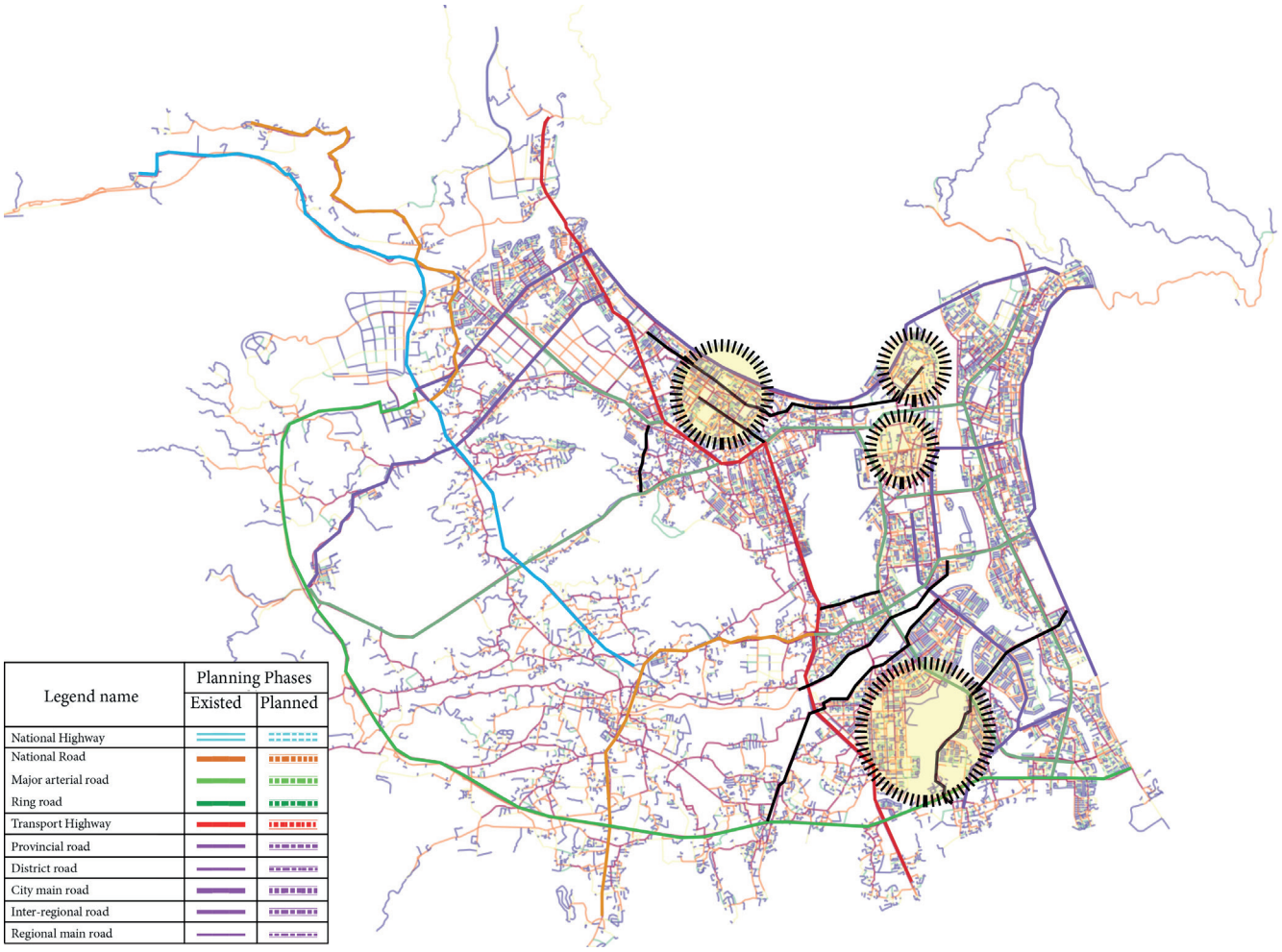

Fig. 6. Overlay analysis of the planned transportation network and Betweenness Centrality

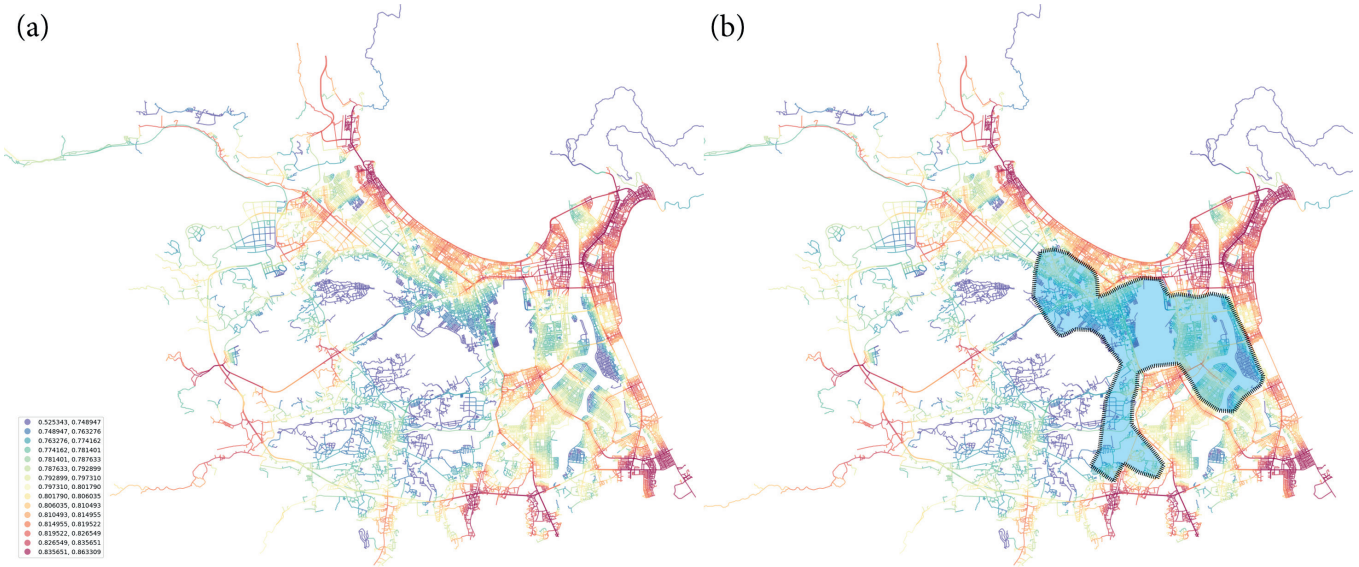

Fig. 7. Navigability analysis of Da Nang's spatial network

improve navigability. Enhancing these regions could involve restructuring the transportation network or implementing urban design solutions to improve coherence and orientation, ultimately fostering greater accessibility and ease of movement.

Exploring angular closeness centrality

Fig. 8a visualizes the angular closeness centrality (R = 400 m) of an urban road network, derived from a dual graph representation. This analysis captures the efficiency of movement across the network, emphasizing angular deviations or turns along paths instead of just physical distance. It reflects how easily nodes (road intersections) can access other nodes within a 400-meter radius, highlighting the importance of minimizing angular changes for smoother navigation.

The color gradient, ranging from red to blue, represents high to low angular closeness centrality. The dense clustering of red and orange in central and coastal areas indicates well-connected urban cores with efficient, direct routes that enhance mobility within these zones. In contrast, peripheral areas with blue and green segments signify lower accessibility and navigational efficiency, pointing to zones that could benefit from improved road alignment or infrastructure investments to reduce angular deviations.

At a global level, the dense red and orange network in the city center and along major corridors suggests robust connectivity across the entire urban area (Fig. 8b). These roads facilitate city-wide movement and play a crucial role in linking various districts and urban hubs, ensuring seamless travel across the city. Peripheral zones with blue and purple roads highlight areas with weaker connections to the overall network, presenting opportunities for targeted infrastructure development to improve accessibility. Roads with high angular closeness are critical for reducing travel time, alleviating congestion, and enhancing network resilience by providing direct routes that minimize detours.

At the local level (R = 400 m), the analysis reveals that the current urban core network has strong potential for supporting pedestrian and cycling activities, particularly in the new urban areas in the southern region. However, older urban districts like Lien Chieu, Hai Chau, and Thanh Khe remain less favorable for these activities due to the high frequency of angular turns in the network (Fig. 8a).

At the global level, the city-wide network demonstrates significant potential for cycling and motorbike activities (Fig. 8b). This connectivity provides a strong foundation for designing cycling routes that interlink the entire city, contributing to Da Nang's ambition of developing as a sustainable tourism-oriented city.

Spatial Network Connectivity

The spatial structure analysis, conducted using the axial map analysis method, is illustrated in Fig. 9. The color gradient, ranging from red to blue, represents connectivity values from high to low. Segments with high Total Connectivity indices often signify intersections where several main roads converge, making these areas ideal hubs for commercial or public activities. Conversely, segments with low Total Connectivity indices typically indicate quieter residential streets with limited accessibility and lower traffic flow, making them suitable for tranquil living environments.

The analysis reveals that the southwestern part of the city exhibits the highest total connectivity index for its transportation networks. In contrast, the central urban area, while having lower overall connectivity, demonstrates a more even distribution (Fig. 9).

Overlaying the connectivity analysis with the land use plan reveals that most areas designated for mixed residential and commercial use, as well as residential areas, align with regions of high connectivity indices, particularly within the urban core and in new urban zones to the south and northwest. Notably, an emerging area with high connectivity indices is planned as a green space and a technical infrastructure hub (marked with a red circle in Fig. 10).

However, despite planning for mixed residential, commercial, and tourism development, the analysis also identifies areas that fail to meet the desired connectivity levels. These zones, outlined with blue dashed lines in Fig. 10, were intended to provide high connectivity and accessibility to attract human activity but are hindered by the current street network structure. In contrast, the area outlined with red dashed lines demonstrates strong potential for attracting human activity, even though it is currently designated as an industrial zone (as shown in Fig. 10).

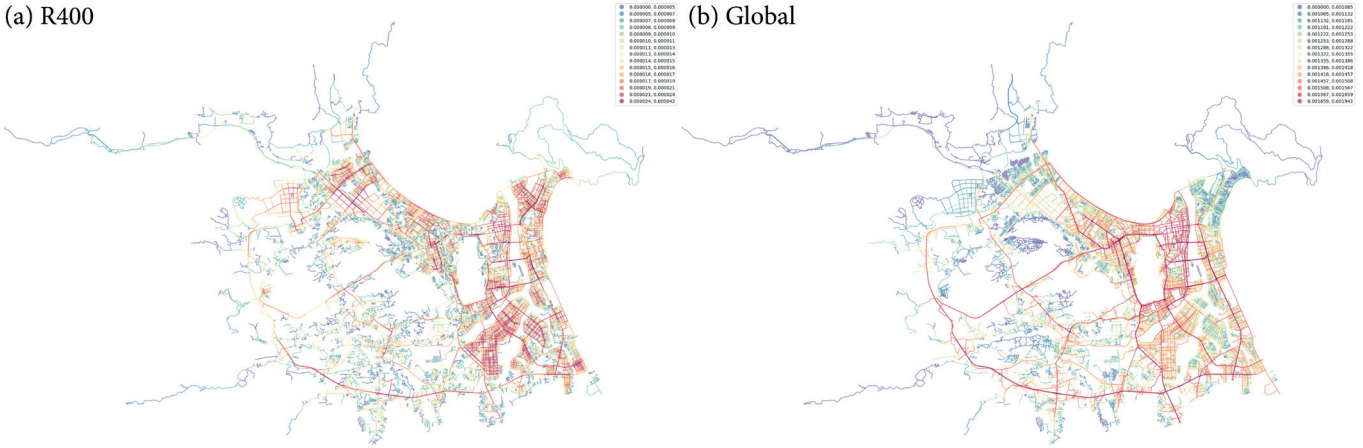

Fig. 8. Angular closeness centrality supporting pedestrian and cycling activities

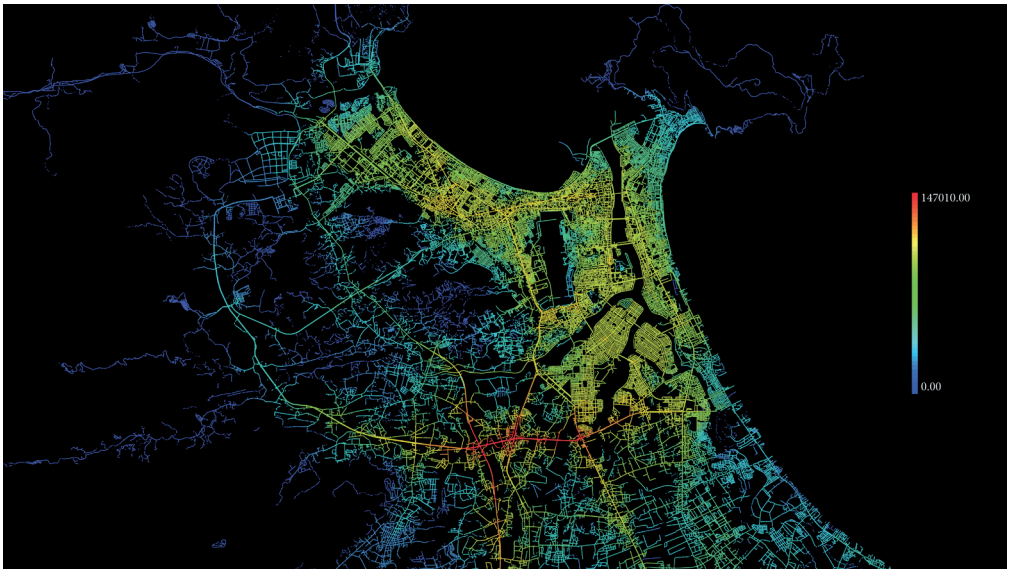

Fig. 9. Total Connectivity (R100)

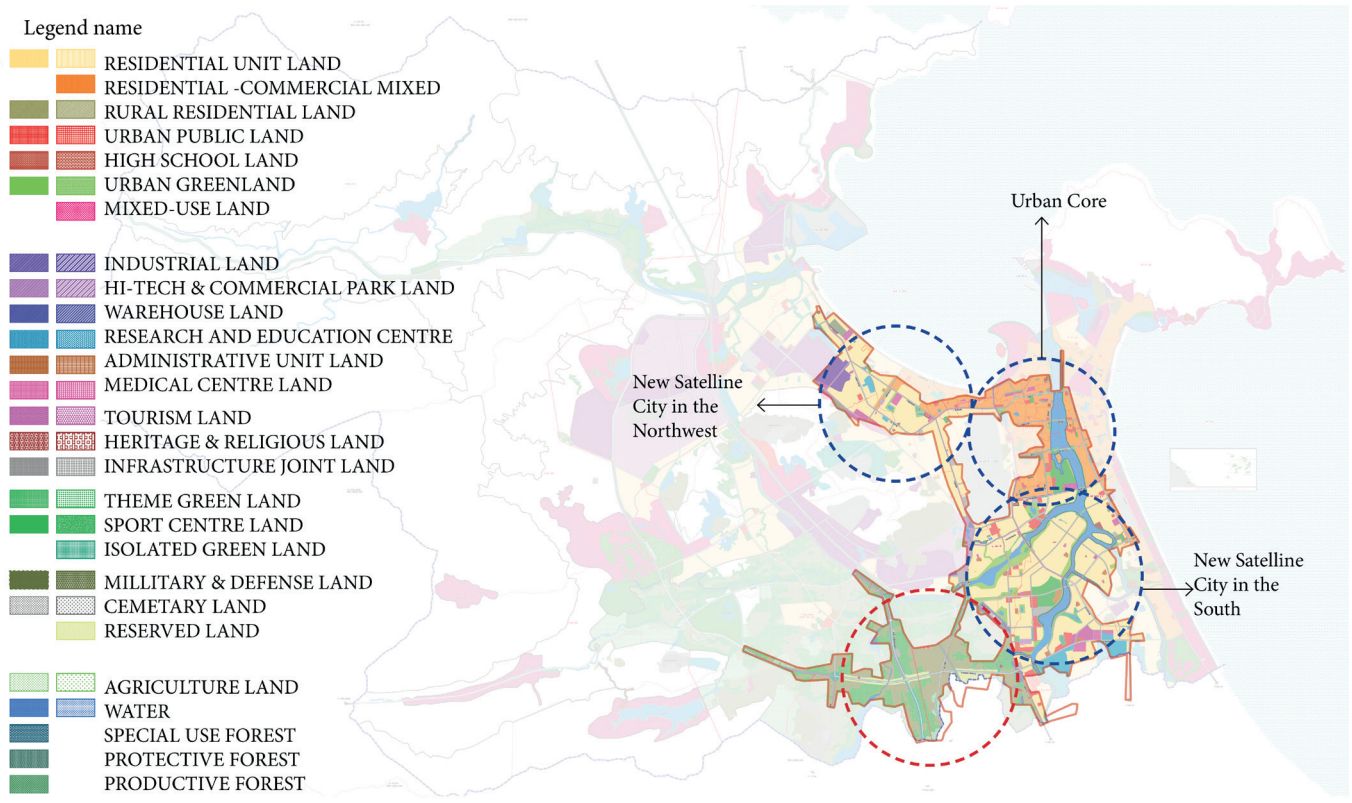

Fig. 10. Comparison of land use and high-connectivity areas in urban configuration using the overlay method

DISCUSSIONS

The Effectiveness of the Adjustment to the General Planning of Da Nang for 2030, with a Vision to 2045

The Adjusted Master Plan of Da Nang City to 2030, with a Vision to 2045 emphasizes the development of a multi-polar urban structure integrated with an efficient transportation network, an approach deemed appropriate (Danang People's, 2020). This aligns with the findings of this research, which focus on enhancing direct and efficient connections across the entire urban network.

The concept of multi-polar urban development envisions creating multiple urban centers or "poles" to decentralize economic activities, alleviate congestion in the urban core, and promote spatially balanced growth. Furthermore, the adjusted master plan proposes a hierarchy of urban zones and small urban models (Danang People's, 2020). This strategy is designed to create self-sufficient hubs equipped with essential services, amenities, and economic opportunities while maintaining strong connectivity to other centers. Such an interconnected structure ensures a more equitable distribution of resources and reduces dependency on the city core, contributing to greater urban resilience.

From a network analysis perspective, this approach closely aligns with the principles of global angular closeness centrality and global closeness centrality, emphasizing the importance of direct and efficient connections across the urban system (Hillier, 2007, Porta et al., 2006a). By prioritizing well-integrated routes between urban poles, the plan seeks to minimize travel times, optimize accessibility, and ensure seamless mobility for residents (Marshall, 2004). This synergy between urban planning strategies and spatial network theory supports not only functional efficiency but also the city's capacity to adapt to future growth and demographic shifts. Integrating these principles into planning frameworks underscores the transformative potential of data-driven, systemic approaches to sustainable urban development (Gehl, 2013).

Based on the existing urban structure, the research findings indicate that much of the city's primary transportation network is reasonably well-designed. However, there is a need to refine detailed urban network planning to enhance connectivity within the city's main transportation system at a broader level.

As observed in the overall urban design framework, most urban axes and focal points are concentrated in areas close to the water, such as along both sides of the Han River and the Danang Bay shoreline (Danang People's, 2020, Danang, 2018). The study also highlights the need for urban planning and design solutions to improve coherence and navigability in older urban areas. Since these older areas were developed organically, the efficiency of their paths, which heavily influences navigation and direct movement, remains limited, making it challenging to achieve coherence.

The study further identifies a strong potential for developing cycling and pedestrian-friendly routes within Danang's spatial network. However, the current master plan does not adequately address the construction of dedicated infrastructure for cyclists and pedestrians (Danang People's, 2020). As a tourism-oriented city, equipping such non-motorized transport infrastructure is essential. This research provides a vital scientific basis for integrating these types of infrastructure into the urban structure.

The planned urban network largely corresponds with roads exhibiting high choice indices, reflecting an overall efficient transportation planning strategy. However, the network remains incomplete, as certain road segments fail to support seamless movement, leading to gaps in connectivity at the local level. Despite these shortcomings, the network provides a strong foundation for essential urban functions such as public transport hubs, commercial centers, and key public services, as these areas are likely to experience significant use and integrate effectively with the local system.

To improve and complete the city's primary transportation network, modifications to the local traffic network are essential, especially in surrounding areas,

to strengthen connectivity at the neighborhood level (Turner, 2007). The research also highlights that revising land use patterns can help attract activity flows within this framework. For instance, although Nguyen Huu Tho Street near Danang Airport shows a low choice index in the overall street network, data from the Danang Department of Transportation (Danang People's Committee, 2020) reveals significant traffic flow along this road due to the diverse land use types surrounding it. This observation aligns with other studies that underscore the strong link between land use planning and street-level activity (Do & Do, 2024), as well as the influence of road infrastructure on urban settlements and the socioeconomic characteristics of residents(Won et al., 2015).

Implications for Danang's General Planning

For general urban planning, it is crucial to reorganize the functions of various urban core areas to enhance their service capacity, guided by analyses of the urban network structure. As illustrated in Fig. 11, the city's spatial structure is divided into six distinct zones.

The central urban area stems from the historic core, while two new satellite urban zones have been established to the south and west of this core. These satellite areas are designed to support and reduce the burden on the historic urban core, aligning with the objectives of Da Nang's updated master plan (Danang People's Committee, 2020). This study proposes the establishment of three new supportive urban areas in Danang, strategically located in the northwest, west, and southwest. These areas are envisioned as hub cities that facilitate connections between the city and external regions (see Fig. 11). Serving as critical nodes for urban activities, these hubs play a pivotal role in distributing various activities between internal and external areas. The overall spatial structure is designed to create a hierarchical relationship within the urban network. Arrows illustrate the interactions between urban sub-regions, clarifying the distinct roles of each area within the broader network. Furthermore, this reorganization supports the preservation and enhancement of urban ecological values, ensuring a balance between development and environmental sustainability (Do et al., 2018).

To complement the promotion of mixed land use, it is essential to review and adjust land use structures to align with the functions of the proposed urban framework. Strategic allocation of land types is crucial: residential, commercial, public service areas, green spaces, and other uses should be concentrated in the core urban area and the new satellite urban zones. In suburban regions, facilities such as industrial zones, production areas, road and waterway infrastructure, and large commercial trading hubs should be prioritized. Additionally, static transportation infrastructure should be integrated with open spaces and green areas to enhance connectivity and foster seamless interaction between local regions.

CONCLUSION

The structure of an urban spatial network plays a crucial role in shaping a city's development patterns. As a result, many cities worldwide adopt the transit-oriented development (TOD) model in their urban planning strategies. However, Asian cities, including those in Vietnam, have not effectively leveraged public transportation to guide urban development.. Instead, urban growth typically follows a straightforward pattern of expansion along transportation routes, where construction takes place wherever roads exist.

Fortunately, theories such as space syntax and graph theory provide tools to quantify the geometric properties of spatial structures, enabling the identification of issues related to movement within the urban network. These theories also emphasize the connection between urban configuration and key factors like social interactions, human mobility, and accessibility, offering valuable insights for improving urban development practices.

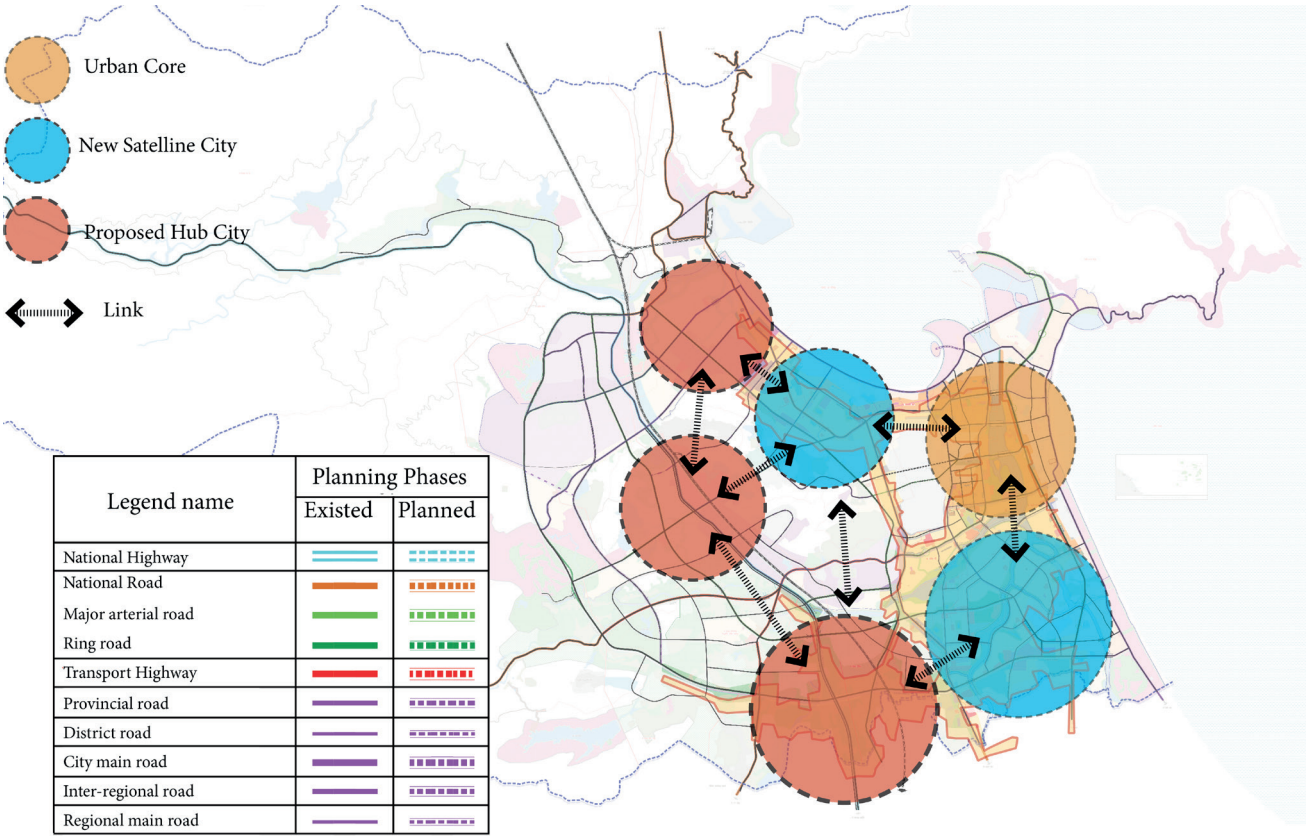

Fig. 11. Proposed urban structure of Danang

Da Nang's general urban plan has undergone several adjustments, yet no scientific basis has been used to evaluate its effectiveness in relation to the city's actual development. This study applies space syntax theory and graph theory to assess the adjustment project of the General Planning of Da Nang for 2030, with a vision to 2045. The analysis examines various aspects, including urban spatial development, land use, and transportation networks. The findings provide urban and transportation planners with a reliable scientific foundation for refining future urban plans and improving Da Nang's overall planning.

This study identifies the strengths and weaknesses of the General Planning of Da Nang for 2030, with a vision to 2045. Balancing these variables is essential to achieving the desired outcomes.

The adjusted master plan adopts a multi-polar urban structure integrated with an efficient transportation network. This approach aligns with the study's findings, emphasizing direct and efficient connectivity to decentralize economic activities, reduce congestion in the urban core, and promote balanced growth. By incorporating the principles of global angular closeness and global closeness centrality, the plan enhances mobility, accessibility, and resilience to future changes.

While the primary transportation network is efficient, gaps in local connectivity persist. Targeted adjustments to the local traffic network and mixed land use patterns can optimize underperforming areas. Furthermore, integrating cycling and pedestrian infrastructure is vital to support Da Nang's tourism-oriented and sustainable development goals.

The study also advocates for the development of three new urban hubs in the northwest, west, and southwest to distribute activities and ease pressure on the historic urban core. Aligning land use structures with these hubs will ensure the effective integration of residential, commercial, industrial, and green spaces, fostering connectivity and ecological preservation.

By combining spatial network analysis with urban planning principles, this research provides actionable insights to refine Da Nang's master plan, supporting sustainable, resilient, and inclusive urban development.

However, this study primarily examines the city at a macro level. Incorporating both quantitative and qualitative research—particularly by comparing the spatial structure of traffic with land use planning at the master plan level—offers valuable opportunities for future planning ideas and strategic orientations. Future research should explore the relationship between three critical factors—urban configuration, urban movements, and land use patterns—at different scales. Such studies will help explain and understand the specific adjustments needed to improve urban mobility effectively.

REFERENCES

Al_Sayed K., Turner A., Hillier B., Iida S. and Penn A. (2014). Space syntax methodology. 4th ed. London: Bartlett School of Architecture, University College London (UCL).

Batty M. (2004). A new theory of space syntax. London: Centre for Advanced Spatial Analysis, University College London. (CASA Working Paper No. 75).

Berhie G. K. and Haq S. (2017). Land use and transport mode choices: Space syntax analysis of American cities. Enquiry: The ARCC Journal for Architectural Research, [online] 14(1), 1–22. https://doi.org/10.17831/enq:arcc.v14i1.429

Boeing G. (2017). OSMnx: New methods for acquiring, constructing, analyzing, and visualizing complex street networks. Computers, Environment and Urban Systems, [online] 65, 126–139. https://doi.org/10.1016/j.compenvurbsys.2017.05.004

Caniggia G. and Maffei G. L. (2001). Architectural composition and building typology: Interpreting basic building (Saggi e documenti, 176). Firenze: Alinea Editrice. ISBN 978-8881254262.

Crucitti P., Latora, V., and Porta, S. (2006). Centrality measures in spatial networks of urban streets. Physical Review E: Statistical, Nonlinear, and Soft Matter Physics, 73(3 Pt 2), 036125. https://doi.org/10.1103/PhysRevE.73.036125

Danang People's Committee. (2020). Điều chỉnh Quy hoạch chung thành phố Đà Nẵng đến năm 2030, tầm nhìn đến năm 2045. Đà Nẵng: Ủy ban nhân dân TP Đà Nẵng – Sakae Corporate Advisory & Surbana Jurong.

Da Nang Urban Planning Institute (UPIO). (2018). Master planning of Danang city (adjusted toward 2030 and vision to 2050). Đà Nẵng: Da Nang Urban Planning Institute.

Das J. and Ram S. (2024). Exploring the relationship of transport network and land use patterns: An approach through weighted centrality assessment. Urban, Planning and Transport Research, [online] 12(1), Article 2323946. https://doi.org/10.1080/21650020.2024.2323946

Fleischmann M. (2019). Momepy: Urban morphology measuring toolkit. Journal of Open Source Software, [online] 4(43), 1807. https://doi.org/10.21105/joss.01807

Freeman L. C. (2002). Centrality in social networks: Conceptual clarification. In: Social Network: Critical Concepts in Sociology, Vol. 1. London: Routledge, pp. 238–263

Gehl J. (2013). Cities for People. Washington, DC: Island Press.

He M., Xu H., Wang R., Chen J., Liu S. and Li T. (2021). Research on site selection of old campus bookstore based on the combination of space syntax and analytic hierarchy process: Take Huangjiahu Campus of Wuhan University of Science and Technology as an example. IOP Conference Series: Earth and Environmental Science, [online] 662, 012071. https://doi.org/10.1088/1755-1315/662/1/012071

Hillier B., Penn A., Hanson J., Grajewski T. and Xu J. (1993). Natural movement: Or, configuration and attraction in urban pedestrian movement. Environment and Planning B: Planning and Design, 20(1), 29–66. https://doi.org/10.1068/b200029

Hillier B. (2007). Space is the machine: A configurational theory of architecture. Cambridge: Cambridge University Press.

Jiang B. and Claramunt C. (2004). Topological analysis of urban street networks. Environment and Planning B: Planning and Design, 31(1), 151–162. https://doi.org/10.1068/b2901

Kang C.-D. (2015). The effects of spatial accessibility and centrality to land use on walking in Seoul, Korea. Cities, 46, 94–103. https://doi.org/10.1016/j.cities.2015.05.007

Li Q., Zhou S., and Wen P. (2019). The relationship between centrality and land use patterns: Empirical evidence from five Chinese metropolises. Computers, Environment and Urban Systems, 78, 101356. https://doi.org/10.1016/j.compenvurbsys.2019.101356

Liu Y., Wei X., Jiao L., and Wang H. (2016). Relationships between street centrality and land use intensity in Wuhan, China. Journal of Urban Planning and Development, 142(3), 05015001. https://doi.org/10.1061/(ASCE)UP.1943-5444.0000296

Marshall S. (2004). Streets and Patterns. London: Routledge.

Marshall S., and Banister D. (2007). Land Use and Transport: European Research Towards Integrated Policies. Bingley: Emerald Group Publishing Limited.

Matějček J. and Přibyl O. (2020). Space syntax: A multi-disciplinary tool to understand city dynamics. In: 2020 Smart City Symposium Prague (SCSP), 1st ed. New York: IEEE, 1–6. https://doi.org/10.1109/SCSP49902.2020.9119343

Newman M. E. J. (2005). A measure of betweenness centrality based on random walks. Social Networks, 27(1), 39–54. https://doi.org/10.1016/j.socnet.2004.11.009

Porta S., Crucitti P., and Latora V. (2006a). The network analysis of urban streets: A dual approach. Physica A: Statistical Mechanics and its Applications, 369(2), 853–866. https://doi.org/10.1016/j.physa.2005.12.063

Porta S., Crucitti P., and Latora V. (2006b). The network analysis of urban streets: A primal approach. Environment and Planning B: Planning and Design, 33(5), 705–725. https://doi.org/10.1068/b32045

Porta S., Strano E., Iacoviello V., Messora R., Latora V., Cardillo A., Wang F., and Scellato S. (2009). Street centrality and densities of retail and services in Bologna, Italy. Environment and Planning B: Planning and Design, 36(3), 450–465. https://doi.org/10.1068/b3319

Prime Minister of Vietnam. (2019). Decision No. 147/QĐ-TTg: Approval of the task of adjusting the general planning of Da Nang City to 2030, with a vision to 2045. Hanoi: Government Office.

Rui Y., and Ban Y. (2014). Exploring the relationship between street centrality and land use in Stockholm. International Journal of Geographical Information Science, 28(7), 1425–1438. https://doi.org/10.1080/13658816.2014.900300

Seamon D. (2015). The life of the place: A phenomenological commentary on Bill Hillier's theory of Space Syntax. Nordic Journal of Architectural Research, 27, 35–52.

Sevtsuk A., and Mekonnen M. (2012). Urban network analysis. Revue Internationale de Géomatique, N(287), 305. https://doi.org/10.3166/rig.287.305-322

Shi X., Liu D., and Gan J. (2024). A study on the relationship between road network centrality and the spatial distribution of commercial facilities—A case of Changchun, China. Sustainability, 16(5), 3920. https://doi.org/10.3390/su16053920

Song C., Liu Q., Song J., Yang D., Jiang Z., Ma W., Niu F., and Song J. (2023). The interactive relationship between street centrality and land use intensity—A case study of Jinan, China. International Journal of Environmental Research and Public Health, 20(9), 5127. https://doi.org/10.3390/ijerph20095127

Turner A. (2001). Depthmap: A program to perform visibility graph analysis. In: Proceedings of the 3rd International Symposium on Space Syntax, 1st ed. London: Space Syntax Laboratory, 12–31.

Turner A. (2007). From axial to road-centre lines: A new representation for space syntax and a new model of route choice for transport network analysis. Environment and Planning B: Planning and Design, 34(3), 539–555. https://doi.org/10.1068/b32045

Van Nes A. (2014). Space syntax in theory and practice. In: C. Steinitz, H. Arias and A. Rajabifard, eds., Geodesign by integrating design and geospatial sciences, 1st ed. Dordrecht: Springer, 237–257.

Van Nes A. and Yamu C. (2021). Analysing linear spatial relationships: The measures of connectivity, integration, and choice. In: A. Van Nes and C. Yamu, eds., Introduction to space syntax in urban studies, 1st ed. Cham: Springer, 35–86.

Wang S., Xu G. and Guo Q. (2018). Street centralities and land use intensities based on points of interest (POI) in Shenzhen, China. ISPRS International Journal of Geo-Information, 7(12), 425. https://doi.org/10.3390/ijgi7120425

Yin G., Liu T., Chen Y. and Hou Y. (2022). Disparity and spatial heterogeneity of the correlation between street centrality and land use intensity in Jinan, China. International Journal of Environmental Research and Public Health, 19(23), 15558. https://doi.org/10.3390/ijerph192315558

RESEARCH PAPER

SPATIO-TEMPORAL CHANGES OF PARTICULATE MATTER ($PM_{2.5}$) OVER BRAZIL AND ITS CORRELATION WITH METEOROLOGICAL VARIABLES

Khadija Shakrullah[1], Salman Tariq[2], Safdar A. Shirazi[3], Muhammad Nasar-u-Minallah[3*], Hafsa Shahzad[4], Ayesha Mariam[4]

[1]Department of Geography, Forman Christian College (A Chartered University) Lahore, 54000, Pakistan
[2]Department of Space Science, University of the Punjab, Lahore, 54550, Pakistan
[3]Institute of Geography, University of the Punjab, Lahore, 54590, Pakistan
[4]Remote Sensing GIS and Climatic Research lab (National Center of GIS and Space applications), Centre for Remote Sensing, University of the Punjab, Lahore, 54590, Pakistan
***Corresponding author:** nasarbhalli@gmail.com

Received: September 10th 2024 / Accepted: January 23rd 2025 / Published: June 30th 2025
https://doi.org/10.24057/2071-9388-2025-3600

ABSTRACT. Fine particulate matter ($PM_{2.5}$), classified as airborne, adversely affects human health and the environment. This study examined the concentration and variability of $PM_{2.5}$ and its correlation with meteorological variables in Brazil. The annual average highest concentration of $PM_{2.5}$ (kg-m^{-3}) 5.65×10^{-9} was found in the western part of the country. A low concentration of $PM_{2.5}$ (kg-m^{-3}), 0.21×10^{-9} was reported in North, East, and South Brazil. Mann-Kendall and Sen's slope statistics were applied to find the trend and magnitude in the time series. Mann-Kendall (MAK)-Tau shows a positive significant trend (1 to 0.41) detected in the south, midwest, and southeastern Brazil. The Mann-Kendall (MAK)-Tau trend test was applied. The Sen's Slope rate ranged from 6.98 to 4.54 in the midwest, south, and southeast regions of Brazil, respectively. In 24 years, an overall negative $PM_{2.5}$ trend of -3.17 and -5.18 is shown in the north and northeast, respectively. This study evaluated $PM_{2.5}$ correlation with prevailing meteorological variables using various statistical techniques computed in R-Studio. Cross-wavelet Transform (CWT) analysis was used to examine the time and magnitude of $PM_{2.5}$ with prevailing meteorological variables. The CWT analysis is statistically significant. The application of CWT analysis has revealed high leading and lagging in-phase and anti-phase correlations with prevailing meteorological variables, e.g., relative humidity, precipitation, temperature, and wind speed variables that have influenced the temporal concentration of $PM_{2.5}$.

KEYWORDS: Mann-Kendall test, wavelet transformation, $PM_{2.5}$, meteorological variables, Brazil

CITATION: Shakrullah K., Tariq S., Shirazi S. A., Nasar-u-Minallah M., Shahzad H., Mariam A. (2025). Spatio-Temporal Changes Of Particulate Matter ($Pm_{2.5}$) Over Brazil And Its Correlation With Meteorological Variables. Geography, Environment, Sustainability, 2 (18), 82-90
https://doi.org/10.24057/2071-9388-2025-3600

Conflict of interests: The authors reported no potential conflict of interests.

INTRODUCTION

$PM_{2.5}$ is classified as airborne fine particulate matter. Its diameter is 2.5 microns or less (≤ 2.5 µm). $PM_{2.5}$ is generated from combustion sources and is documented as an important contributor to air quality (Chen et al. 2020; Wu et al. 2023). $PM_{2.5}$ mass concentration standard value is diverse for each country. In 2006, the safety limits for particulate matter (PM) in the atmosphere were established by the World Health Organization (WHO). The value range for $PM_{2.5}$ was determined to be 10 µg/m^3(per annum) and 25 µg/m^3 (24-hour average). In 2021, WHO issued the updated values of $PM_{2.5}$ and PM_{10} concentration. The maximum annual value should be correspondingly 5 µg/m^3 and 15 µg/m^3, for $PM_{2.5}$ and PM_{10} (WHO 2021). $PM_{2.5}$ poses a significant adverse effect not only on climate, ecosystems, and visibility but also on human health (Faridi et al. 2019; Fatima et al. 2023; Wang et al. 2023).

Biomass burning and energy use are the main contributors to the emission and concentration of particulate matter in the atmosphere. Other anthropogenic activities, e.g., brick kilns, agricultural activities, industrial and vehicle emissions, and waste incineration, are key factors of atmospheric particulate matter (Guttikunda et al. 2019; Amnuaylojaroen et al. 2020; Amit et al. 2021; Nasar-u-Minallah et al., 2024a; Nasar-u-Minallah et al., 2024b; Nasar-u-Minallah et al., 2025). These variables largely affect changing air circulation conditions, particle proliferation, and distribution. Furthermore, the metrological parameters can be used as a gauge to improve the projected values of $PM_{2.5}$ concentration at ground level (Liu et al. 2009). Climatic variability also affects the concentration of $PM_{2.5}$. The meteorological parameters (e.g., humidity, precipitation, temperature, and wind speed) can affect the mass concentration of $PM_{2.5}$ its dispersion, dilution, and accumulation in the air on a large scale (Tai et al. 2010; Westervelt et al. 2016). $PM_{2.5}$ is correlated with

precipitation and wind speed. The high wind velocity will lead to turbulence and advection that increase the dispersion of pollutants. On the other hand, precipitation reduces the concentration of $PM_{2.5}$ through wet deposition and wet removal (Westervelt et al. 2016; Nguyen et al. 2017; Zhang et al. 2018). Several studies reported that meteorological factors are critical in the circulation and removal of particulate matter from the lower atmosphere (Sharma et al. 2017; Das et al. 2021; Singh et al. 2021; Nasar-u-Minallah 2024c). Saraswati et al. (2019) reported that the air pollutant's dispersion was primarily affected by the diurnal variation in boundary layer conditions and other meteorological factors. Precipitation, relative humidity, ambient temperature, wind velocity, and direction affect the concentration of particulate matter in ambient air and scatter them from areas of high to lower concentration (Begum et al. 2008; Saha et al. 2019; P. Sharma et al. 2022) A negative correlation is found between meteorological factors (such as dew point, wind gust, and ambient temperature) and $PM_{2.5}$ concentration at any given location (altitude and latitude) whereas, positively correlated with relative humidity (Das et al. 2021; Singh et al. 2021)

The carbon content in $PM_{2.5}$ scatters and absorbs the light and impacts atmospheric visibility (Shen et al. 2019). Approximately 50 percent variation in the concentration of $PM_{2.5}$ is reported due to diurnal variation in meteorological parameters (Tai et al. 2012). Wang & Ogawa (2015), they studied $PM_{2.5}$ and meteorological conditions in Nagasaki (Japan). The result indicated that $PM_{2.5}$ has a strong correlation with precipitation and a weak correlation with temperature. Several studies have carried out the correlation between $PM_{2.5}$ and meteorological parameters. In China (Wuhan) a study was led using Generalized Additive Models (GAM) on the correlation between $PM_{2.5}$ and meteorological parameters. The result indicated a 37% decrease in $PM_{2.5}$ concentration observed during precipitation (Zhang et al. 2018). Some studies have also reported seasonal variations of $PM_{2.5}$ with meteorological variables. For instance, Yang et al. (2017) stated that seasonal variation of $PM_{2.5}$ with temperature in different cities in China. In the winter, $PM_{2.5}$ has a strong correlation with temperature and a weak correlation in the autumn.

The disparity between $PM_{2.5}$ and temperature in different seasons was reported. Temperature showed a weak correlation with $PM_{2.5}$ in summer and autumn; however, there was a strong correlation in the spring and winter seasons (Chen et al. 2017). Conversely, an increase in temperature can cause variation in the formation of $PM_{2.5}$. The higher temperature increases the photochemical reaction involving $PM_{2.5}$. Additionally, a study conducted in Hong Kong from January – December 2013 reported a negative relationship between $PM_{2.5}$ and temperature (Zhao et al. 2019). Brazil is experiencing several socio-environmental challenges linked to air quality and climate variability. Brazil, being a continental country, is home to a diverse type of biomes. Apart from anthropogenic activities, diverse biomes are also a source of natural air pollution and spatio-temporal weather changes. Numerous studies have been carried out in Brazil focused on the concentration of primary pollutants, biomass burning (Squizzato et al. 2021; Castelhano et al. 2022) effect of particulate matter on health (Leão et al. 2023) $PM_{2.5}$ and PM_{10} concentrations (Braga et al. 2005) in major urban centers of Brazil. However, there is a dire need to conduct studies to evaluate the $PM_{2.5}$ concentration in Brazil (Pacheco et al., 2017). Finally, the literature on the correlation of particulate matter $PM_{2.5}$ with meteorological variables in Brazil is scarce, and to the best of our knowledge, no study has been carried out using cross-wavelet over the whole of Brazil.

This study aims to identify the gaps in previous studies and evaluate the variability of $PM_{2.5}$ and its correlation with meteorological parameters in Brazil over 24 years (2000-2024). For that purpose, the average maps of $PM_{2.5}$ and prevailing meteorological variables were prepared; in addition to that, we also used wavelet coherence to identify the relationship of $PM_{2.5}$ with other meteorological parameters. The Mann-Kendall test and Sen's slope methods were also used. The $PM_{2.5}$ concentration study is critical to getting a clear picture of the impact of anthropogenic activities on the environment. It is essential to develop effective planning and strategies to reduce air pollution. The effect of meteorological factors on $PM_{2.5}$ concentration is well-recognized and understood (Chen et al. 2020). There is a dire need for correct and precise daily $PM_{2.5}$ concentration assessment and projection to discourse environmental issues (Wang et al. 2022). Precise and accurate estimation of $PM_{2.5}$ could benefit the policymakers and enable them to initiate the measures that can help the public manage the means of transportation and travelling, thus decreasing the effect of $PM_{2.5}$ on their daily lives (Huang et al. 2021; Dong et al. 2022).

METHODS AND MATERIALS

Study Area

Brazil (geographic coordinates 10.00 S, 55.00 W) is the 5th largest country in the world and the largest in South America by geographical area (8,514,877 sq. km.) while 7th in terms of population size (217,663,781 souls). The climatic setup of the country is dominated by the equatorial and subtropical type of climate with high temperatures and erratic rainfall throughout the country, apart from the northeast of Brazil, which receives less rainfall and is virtually a semi-arid region (less than 700 mm of rain per annum).

Data sets

$PM_{2.5}$ ($kg\text{-}m^{-3}$) with spatial resolution 0.5°×0.625° was retrieved from the MERRA-2 reanalysis model. The surface radiative temperature (K) monthly product was taken at a spatial resolution of 1°×1° from the FLDAS model. Relative humidity (RH) (%) 700 hpa monthly product with a spatial resolution of 1°×1° was collected from Aqua Satellite through the AIRS instrument from 1-9-2002 to 01-01-2024. The wind speed ($m\ s^{-1}$) product was acquired at 0.5°×0.625° spatial resolution monthly through the MERRA-2 reanalysis model. Precipitation ($kg\ m^{-2}s^{-1}$) product with 0.5°× 0.625° spatial resolution and temporal resolution (monthly) was obtained from MERRA-2 reanalysis. The data sets were retrieved from NASA's Giovanni online web source[1]. Table 1 displays the data set used for this study.

ArcGIS 10.5 and R Studio were used to prepare the averaged maps of $PM_{2.5}$ and meteorological variables, such as humidity, precipitation, temperature, and wind speed, and calculate the Sen's slope and Mak Tau.

Mann-Kendal & Sen's Slope

The non-parametric Mann- Kendall (MK) test is adopted to evaluate the trend of $PM_{2.5}$. It is a robust method for analyzing the monotonic trend in time series, helping to

[1] https://giovanni.gsfc.nasa.gov/

Table 1. Satellite and model data used for the analysis

Data sets	Source	Spatial	Temporal	Duration
$PM_{2.5}$ (kg-m^{-3})	MERRA-2	0.05°×0.625°	Monthly	2000-2024
Relative Humidity (%)	AIRS	1°×1°.	Monthly	2002-2024
Wind Speed (m s^{-1})	MERRA-2	0.05°×0.625°	Monthly	2000-2024
Temperature (K)	FLDAS	1°×1°.	Monthly	2000-2024
Precipitation (kg m^{-2} s^{1})	MERRA-2	0.05°×0.625°	Monthly	2000-2024

identify increasing and decreasing trends in time series. It is calculated by following the equation (Eq. 1).

$$S = \sum_{l=1}^{n-1} \sum_{m=l+1}^{n} Sign\left(X_m - X_l\right) \quad (1)$$

From Eq. 1, S represents the MK-trend statistics, also known as Kendall's Tau (MAK-Tau). Whereas X_m and X_l are time series observations (Eq. 2).

$$Sign\left(X_m - X_l\right) = Sign\left(R_j - R_i\right) = \begin{cases} -1 for \left(X_m - X_l\right) < 0 \\ 0 for \left(X_m - X_l\right) = 0 \\ +1 for \left(X_m - X_l\right) > 0 \end{cases} \quad (2)$$

In the above equation (Eq. 2), R_j and R_i symbolize the rank of X_m and X_l time series values. The number of values tends to be normally distributed, and significance at 95% was determined using a p-value < 0.05. MAK-Tau is primarily used to test the correlation and strength between two variables. The values range from −1 to +1. Sen's slope is also a non-parametric test primarily used to identify the slope in time series data (Agarwal et al. 2021; Ray et al. 2021). Sen's slope is computed in Eq. 3.

$$Q_m = \frac{X_k + X_m}{K - m} for\ m = 1 \ldots N \quad (3)$$

From Eq. 3, Q_m represents the estimated slope for each pair of observations. The subscripts k and m are the time steps, where $K > m$. The Mann-Kendall's and Sen's slopes were calculated in R Studio.

Wavelet analysis

Several researchers have extensively used wavelet transformations for time series data. Firstly, wavelet analysis was used for seismic signal analysis (Chen et al. 2020). Nowadays, wavelet analysis has been extensively used in all fields (e.g., mathematics, science, engineering, and geophysics) (Zhang et al. 2017). Discrete wavelet (DWT) and continuous wavelet (CWT) are the two main types of wavelet transform analysis (Cholianawati et al. 2024a). Several studies used a cross-wavelet to analyze and find out the correlation between $PM_{2.5}$ and meteorological variables (Barik et al. 2020; Meng & Sun 2021; Fattah et al. 2023; Jang & Jung 2023; Cholianawati et al. 2024b). The Morlet wavelet function (ψ) and cross-wavelet power are used to understand the correlation between $PM_{2.5}$ and other meteorological variables (Eq. 4).

$$Wave\left(\tau, s\right) = \sum_t xt \frac{1}{\sqrt{s}} \psi^* \left(\frac{t - \tau}{s}\right) \quad (4)$$

In Eq. 4, xt denotes the time domain. Whereas $Wave(\tau,s)$ indicates time series in continuous wavelets, (xt, T =1,2,3…N) concerning wavelet ψ is defined. where s represents the wavelet scale, τ stands as the position of the wavelet window in time or the translated time index, and Ψ is the mother wavelet function with * representing/indicating its complex conjugate solution. The wavelet analysis of the time series of $PM_{2.5}$ and meteorological variables was computed in R-Studio using the wavelet comp package.

RESULTS AND DISCUSSION

Spatio-temporal distribution of $PM_{2.5}$ and meteorological variables

Fig. 1 shows the spatiotemporal correlation of $PM_{2.5}$ with meteorological variables from 2000-2024 in Brazil. Fig. 1a illustrates Brazil's spatiotemporal $PM_{2.5}$ (kg-m^{-3}) patterns from 2000-2024. The map indicates that the maximum $PM_{2.5}$ (kg-m^{-3}) concentration of 5.65×10^{-9} was found in the western part of the country. A low concentration of $PM_{2.5}$ (kg-m^{-3}), 0.21×10^{-9} was reported in eastern Brazil. The descriptive statistics of all study variables are provided in Table 2. The mega-cities of Brazil are home to millions of people residing there and vehicles as well, and they face numerous problems related to air pollution and particulate matter, which is one of them. Vehicles are considered the primary reason for pollutants' emission into the atmosphere in major urban centers of Brazil (de Fatima Andrade et al. 2012; Requia & Azevedo de Melo 2024). Numerous studies documented the other sources of particulate matter $PM_{2.5}$, e.g., biomass burning, aerosols from sea salt, and industrial waste and traffic congestion (Gioia et al. 2010; de Fatima Andrade et al. 2012; Souza et al. 2014). The central areas of Brazil receive a large number of gases and particulate matter emitted into the atmosphere due to the burning of biomass from July to October (dry season) (Butt et al. 2020).

Table 2. Descriptive statistics

	$PM_{2.5}$ (kg-m^{-3})	Humidity (%)	Wind Speed (m s^{-1})	Temperature (K)	Precipitation (kg m^{-2} s^{-1})
Mean	1.81×10^{-9}	46.71	3.55	298.41	4.96×10^{-5}
Median	5.82×10^{-11}	46.92	3.45	298.25	1.41×10^{-6}
Standard Deviation	1.61×10^{-9}	1.97	0.38	1.40	2.40×10^{-5}
Minimum	1.97×10^{-9}	41.34	2.83	295.54	1.24×10^{-5}
Maximum	5.78×10^{-9}	51.00	4.53	302.92	1.09×10^{-4}

$PM_{2.5}$ concentration induced by wildfire has been reported as high in the central-western part of Brazil, affecting the health of human beings (Butt et al. 2020; Ye et al. 2022; Jang & Jung 2023). A study found, that approximately 80% of $PM_{2.5}$ concentration in Brazil (Amazon region) was associated with deforestation (Urrutia-Pereira et al. 2021). It has been reported that wildfires from the north and west sides and transportation of wildfires from suburbs also influence the concentration of $PM_{2.5}$ in the country (Jang & Jung 2023). Fig.1b highlights the relative humidity in (%). The maximum relative humidity was observed in the north and midwest. The minimum RH was observed in the northeast, southeast, and south. Fig. 1c illustrates the spatio-temporal variability of precipitation over 24 years in the study area. The map depicts the highest precipitation, 9.88 (kg $m^{-2}s^{-1}\times10^{-5}$), in the east and north of Brazil. The precipitation of 1.37 (kg $m^{-2}s^{-1}\times10^{-5}$) is observed in the western and central parts of the country. Fig. 1d shows the temperature (K) in Brazil. The maximum temperature is 303K, found in the northeast and midwest of Brazil. In the north, the temperature range is approximately 296K-299K. The lowest temperature is found from southeast to south. The temperature range lies between 285K and 288K from southeast to south. Our findings are aligned with previous literature. Several studies have revealed that an increase in temperature and a substantial decrease in precipitation are observed in northeast Brazil (Marengo et al. 2017; Da Silva et al. 2019; Costa et al. 2020). Intensified extreme dry spells or events due to the El Niño Southern Oscillation were reported in northeast Brazil (Marengo et al. 2017)

Fig. 1e illustrates the wind speed (m s^{-1}) in the study area. The highest wind velocity, 5.62 (m s^{-1}) was found in the north and west of Brazil. The wind velocity between 4.56 (m s^{-1}) to 3.51 (m s^{-1}) is observed in the west of Brazil. The wind speed, ranging from 1.41 (m s^{-1}) to 0.35 (m s^{-1}) is seen from the east and central parts of the study area. Chen et al. (2017), reported that stronger wind speeds lead to faster parallel diffusion of pollutants, which eventually drops the $PM_{2.5}$ concentration. Wind speed conditions are considered the critical factor in the evaporation process of $PM_{2.5}$. The high wind velocity increased the dispersion of pollutants horizontally, eventually decreasing the $PM_{2.5}$ concentration (Chen et al. 2018). The acceleration of wind speed intensifies the $PM_{2.5}$ evaporation rate, leading to a significant decrease in the concentration of meteorological parameters such as temperature, wind velocity, temperature inversion, relative humidity, and atmospheric pressure, which significantly influence the dispersal and accretion of $PM_{2.5}$ (Ocak & Sezer Turalioglu 2008; Wang et al. 2023). Relevant studies have shown that the effect of $PM_{2.5}$ varies with different weather conditions. A study in China from 2015 to 2017 found that there was a weak link between particulate matter and both rain and humidity (Han et al. 2018).

Fig. 2a exhibits the variability in the spatial trends and magnitude of $PM_{2.5}$ using the Mann-Kendall trend test (Sen's slope) over Brazil during the study period 2000-2024. The trend rate ranges from 6.98 to 4.54 in the midwest, south, and southeast regions of Brazil, respectively. A negative trend of $PM_{2.5}$ ranging from -3.17 to -5.18 is observed in the north and northeast respectively. Fig. 2b spatial trend's magnitude (Mak-Tau) shows a positive trend (1 to 0.41) detected in the south, midwest, and southeastern Brazil, but this trend seems highly significant.

Cross Wavelet Analysis $PM_{2.5}$ and meteorological parameters

The Cross Wavelet Transform (CWT) is a tool used to study the relationship of time and magnitude in two-time series. Coherency explains a constant pattern and identifies the correlation between two variables. The wavelet uses the arrows to describe the pattern; the right arrows show an in-phase relationship. On the other hand, the left arrows depict the anti-phase, or inverse, correlation. In addition, the leading relationship is indicated by upward arrows. The downward arrow shows the lagging correlation between the two variables (Aguiar-Conraria et al. 2008).

In Fig. 3, the red color indicates the highest value, while the blue color indicates the lowest value. The coherency between $PM_{2.5}$ and relative humidity (Fig. 3a) mostly shows the leading and lagging situations. It illustrates a periodic cycle of 8 to 16 days, with cross wavelet power of ~1.2 to 1.5. The in-phase (direct) relationship is found between two variables. The value range indicates a strong positive relationship. The cross-wavelet transfer between $PM_{2.5}$ and precipitation is shown in Fig. 3b a positive covariance/ coherence in the dataset. A leading and lagging sequence phase is detected between two variables. The lagging variables, from 2000 to 2024, are dominated by an anti-phase relationship. Cross wavelet power of ~1.3 to 1.6 is found. The wavelet displays an 8- to 16-day periodic cycle.

There is a strong connection between $PM_{2.5}$ and temperature (Fig. 3c), which displays an anti-phase (inverse) relationship, along with leading and lagging states. A strong Cross wavelet power of ~1.3- 1.6 is seen in datasets. Substantial periodic cycles of 8–16 days are observed. The relationship between $PM_{2.5}$ and wind speed (Fig. 3d) exhibits in-phase (direct) situations in datasets, whereas leading and lagging phases. It displays a significant periodic cycle of 8–16 days, having cross wavelet power of ~1.5 to 1.8, and with several days are 150-200. Wavelet transformation helps in comprehending the aerosol nature in Brazil's regions. For instance, the long-term significant periodicities in the cross wavelet between precipitation and $PM_{2.5}$ indicate the presence of fine-mode aerosols in the atmosphere, which maintain the air pressure in the upper atmosphere. Similarly, the results of $PM_{2.5}$ with relative humidity indicate aerosol plumes exposed to sufficient atmospheric moisture, resulting in scattering and diffusion of PM particles. Moreover, $PM_{2.5}$ has an inverse relationship with temperature (Vaishali et al. 2023) as can be seen through the out-of-phase relationships seen from the wavelet figure. Overall, the links between $PM_{2.5}$ and all the meteorological variables help to understand these variables in Brazil. The dataset used in this study is a monthly dataset rather than a daily one, which is one reason why the periodic cycles mostly appear between 8-16. Moreover, the frequency shown in the period has prolific short-term periodicities between 2 and 4 periodic cycles, but high wavelet powers seem to be between 8-16 throughout the days. The periodic cycle shows the relationship of PM particles with meteorological variables in the upper atmosphere, which is highly significant in the medium-run range (8-16).

CONCLUSION

The harmful impact of $PM_{2.5}$ on visibility, climate change, and human health has recently attracted the attention of scientists worldwide. The findings of this study uncover the spatio-temporal variations of $PM_{2.5}$ concentration across Brazil. The highest concentration was observed in northern and western Brazil. The current study evaluates the correlation of $PM_{2.5}$ on meteorological variables using cross-wavelet analysis over Brazil. The averaged maps of $PM_{2.5}$ and meteorological parameters have been prepared. The cross-wavelet transformation was calculated in RStudio to determine the correlation of $PM_{2.5}$ with all meteorological

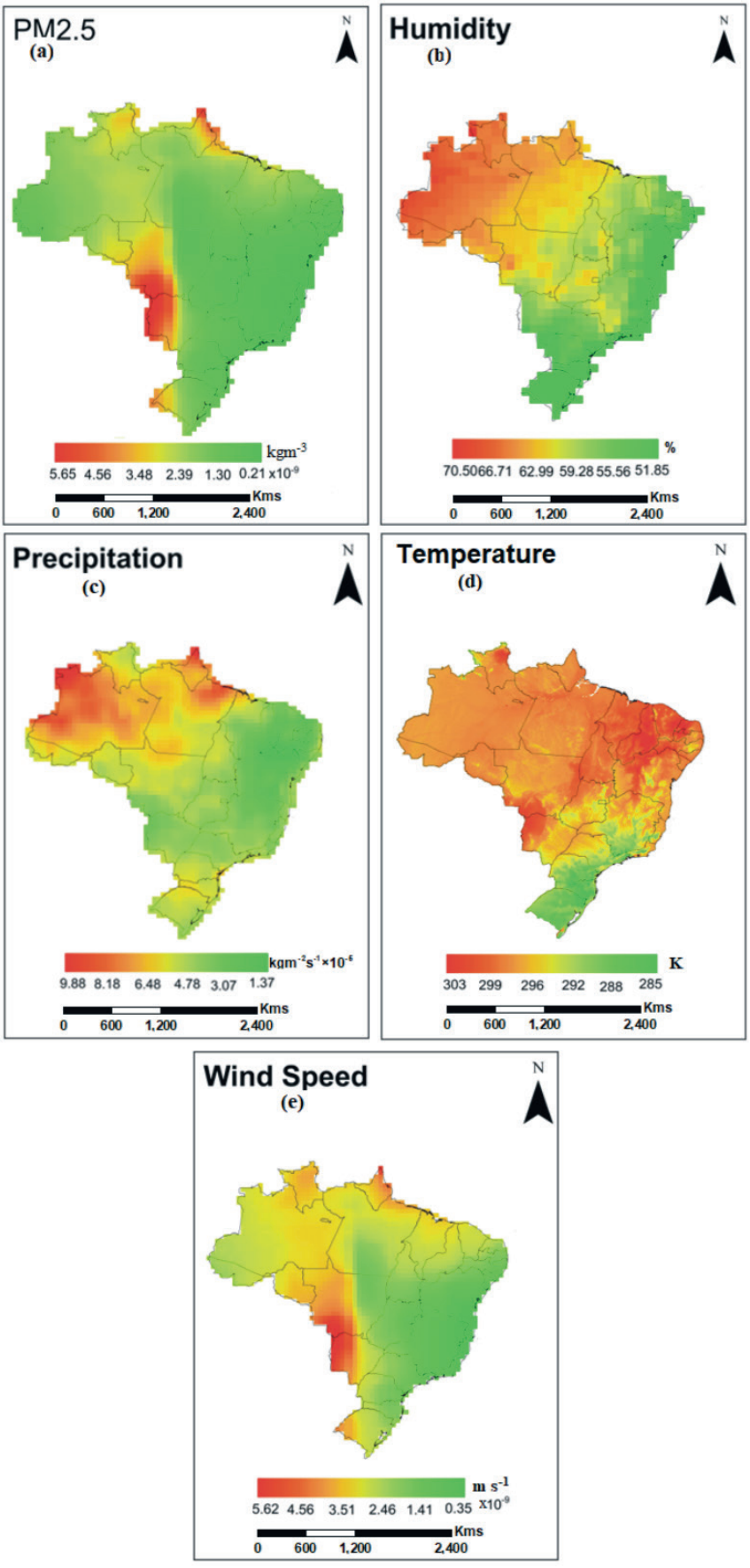

Fig. 1. Averaged maps of (a) $PM_{2.5}$, (b) humidity, (c) precipitation, (d) temperature, and (e) wind speed over the 2000-2024 period

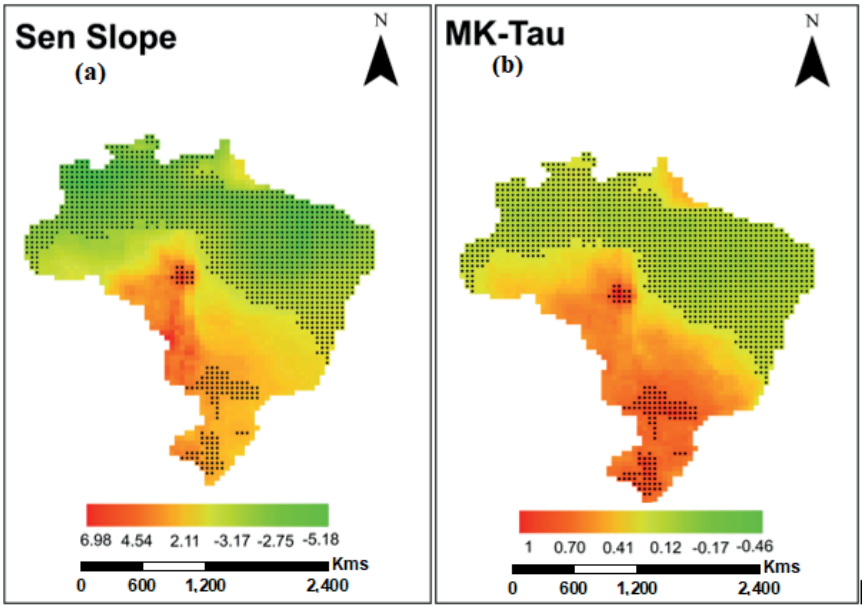

Fig. 2. (a) Sen's Slope and (b) Mann-Kendall (MAK)-Tau over the 2000-2024 period

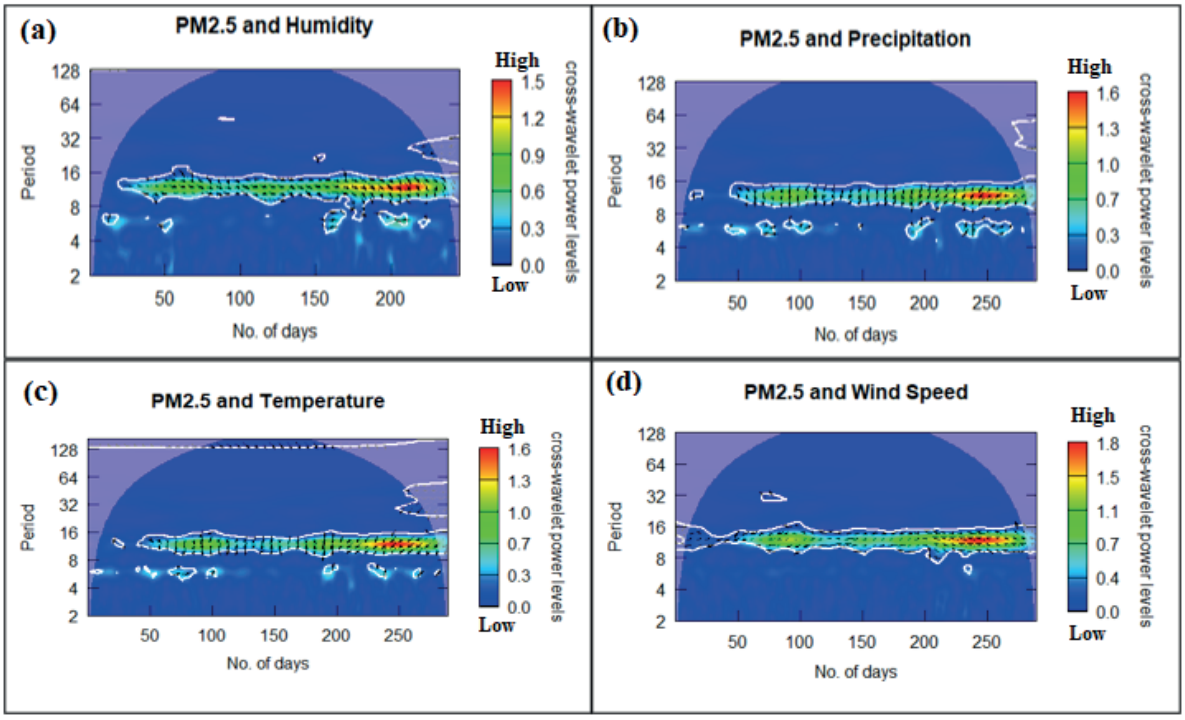

Fig. 3. $PM_{2.5}$ and meteorological variable cross wavelet spectra: (a) $PM_{2.5}$ and humidity, (b) $PM_{2.5}$ and precipitation, (c) $PM_{2.5}$ and temperature, and (d) $PM_{2.5}$ and wind speed

parameters, e.g. humidity, precipitation, temperature, and wind speed. All meteorological parameters exhibit/show remarkable periodicities of 8-16 days. $PM_{2.5}$ correlation was detected as an anti-phase (inverse) relationship with temperature and precipitation. In contrast, humidity and wind speed depicted the in-phase (synchronous/positive) relationship with $PM_{2.5}$. A leading and lagging phase is observed in all covariates. $PM_{2.5}$ results are slightly higher than the WHO standards in northern and western Brazil. There is a dire need to take measures to reduce the $PM_{2.5}$ concentration in the study area. The outcomes of this study would provide valuable insights for future research in Brazil. This study will help stakeholders create policies and strategies to reduce $PM_{2.5}$ in the atmosphere, which is more harmful to human health than any other particulate matter. This study has certain limitations due to the non-availability of the data set, and we used model data. The results and observations can be compared with ground data to validate the results to get a clear picture and help make robust decisions. Therefore, higher levels of $PM_{2.5}$ disagree with Sustainable Development Goal (SDG) 11.6.2. The main objective of SDG is to lessen the adverse effects of air pollutants on human health, including fine particulate pollution.

REFERENCES

Agarwal S., Suchithra A. S., & Singh S. P. (2021). Analysis and interpretation of rainfall trend using Mann-Kendall's and Sen's slope Method. Indian Journal of Ecology, 48(2), 453–457.

Aguiar-Conraria L., Azevedo N., & Soares M. J. (2008). Using wavelets to decompose the time-frequency effects of monetary policy. Physica A: Statistical Mechanics and Its Applications, 387(12), 2863–2878. https://doi.org/10.1016/j.physa.2008.01.063

Amit S., Barua L., & Kafy A. Al. (2021). A perception-based study to explore COVID-19 pandemic stress and its factors in Bangladesh. Diabetes and Metabolic Syndrome: Clinical Research and Reviews, 15(4), 102129. https://doi.org/10.1016/j.dsx.2021.05.002

Amnuaylojaroen T., Inkom J., Janta R., & Surapipith V. (2020). Long range transport of southeast Asian PM2.5 pollution to northern Thailand during high biomass burning episodes. Sustainability (Switzerland), 12(23), 1–14. https://doi.org/10.3390/su122310049

Barik G., Acharya P., Maiti A., Gayen B.K., Bar S., & Sarkar A. (2020). A synergy of linear model and wavelet analysis towards space-time characterization of aerosol optical depth (AOD) during pre-monsoon season (2007–2016) over the Indian sub-continent. Journal of Atmospheric and Solar-Terrestrial Physics, 211, 105478. https://doi.org/10.1016/j.jastp.2020.105478

Begum B.A., Biswas S. K., & Hopke P. K. (2008). Assessment of trends and present ambient concentrations of PM2.2 and PM10 in Dhaka, Bangladesh. Air Quality, Atmosphere and Health, 1(3), 125–133. https://doi.org/10.1007/s11869-008-0018-7

Braga C. F., Teixeira E. C., Meira L., Wiegand F., Yoneama M. L., & Dias J. F. (2005). Elemental composition of PM10 and PM2.5 in urban environment in South Brazil. Atmospheric Environment, 39(10), 1801–1815. https://doi.org/10.1016/j.atmosenv.2004.12.004

Butt E. W., Conibear L., Reddington C. L., Darbyshire E., Morgan W. T., Coe, H., Artaxo P., Brito J., Knote C., & Spracklen D. V. (2020). Large air quality and human health impacts due to Amazon forest and vegetation fires. Environmental Research Communications, 2(9). https://doi.org/10.1088/2515-7620/abb0db

Castelhano F. J., Pedroso A. C. N., Cobelo I., Borge R., Roig H. L., Adams M., Amini H., Koutrakis P., & Réquia W. J. (2022). The impact of long-term weather changes on air quality in Brazil. Atmospheric Environment, 283, 119182. https://doi.org/10.1016/j.atmosenv.2022.119182

Chen D., Xie X., Zhou Y., Lang J., Xu T., Yang N., Zhao Y., & Liu X. (2017). Performance evaluation of the WRF-chem model with different physical parameterization schemes during an extremely high PM2.5 pollution episode in Beijing. Aerosol and Air Quality Research, 17(1), 262–277. https://doi.org/10.4209/aaqr.2015.10.0610

Chen L., Zhu J., Liao H., Yang Y., & Yue X. (2020). Meteorological influences on PM 2.5 and O 3 trends and associated health burden since China's clean air actions. Science of the Total Environment, 744, 140837. https://doi.org/10.1016/j.scitotenv.2020.140837

Chen P., Zhang X.Y., Chen J., Wei N.Y., & Lin S.C. (2017). Tempo-spatial distribution of air pollution index in Nanning city. 115, 397–404. https://doi.org/10.2991/eesed-16.2017.54

Chen X., Yin L., Fan Y., Song L., Ji T., Liu Y., Tian J., & Zheng W. (2020). Temporal evolution characteristics of PM2.5 concentration based on continuous wavelet transform. Science of the Total Environment, 699, 134244. https://doi.org/10.1016/j.scitotenv.2019.134244

Cholianawati N., Sinatra T., Nugroho G. A., Permadi D. A., Indrawati A., Halimurrahman K. M., Romadhon M. S., Ma'ruf I. F., Yudhatama D., Madethen T. A. P., & Awaludin A. (2024a). Diurnal and Daily Variations of PM2.5 and its Multiple-Wavelet Coherence with Meteorological Variables in Indonesia. Aerosol and Air Quality Research, 24(3), 230158. https://doi.org/10.4209/AAQR.230158

Cholianawati N., Sinatra T., Nugroho G. A., Permadi D. A., Indrawati A., Halimurrahman K. M., Romadhon M. S., Ma'ruf I. F., Yudhatama D., Madethen T. A. P., & Awaludin A. (2024b). Diurnal and Daily Variations of PM2.5 and its Multiple-Wavelet Coherence with Meteorological Variables in Indonesia. Aerosol and Air Quality Research, 24(3), 1–18. https://doi.org/10.4209/aaqr.230158

Costa R. L., Macedo de Mello Baptista G., Gomes H. B., Daniel dos Santos Silva F., Lins da Rocha Júnior R., de Araújo Salvador M., & Herdies D. L. (2020). Analysis of climate extremes indices over northeast Brazil from 1961 to 2014. Weather and Climate Extremes, 28, 100254. https://doi.org/10.1016/j.wace.2020.100254

Da Silva P. E., Santos e Silva C. M., Spyrides M. H. C., & Andrade L. de M. B. (2019). Precipitation and air temperature extremes in the Amazon and northeast Brazil. International Journal of Climatology, 39(2), 579–595. https://doi.org/10.1002/joc.5829

Das M., Das A., Sarkar R., Mandal P., Saha S., & Ghosh S. (2021). Exploring short term spatio-temporal pattern of PM2.5 and PM10 and their relationship with meteorological parameters during COVID-19 in Delhi. Urban Climate, 39, 100944. https://doi.org/10.1016/j.uclim.2021.100944

De Fatima Andrade M., de Miranda R. M., Fornaro A., Kerr A., Oyama B., de Andre P. A., & Saldiva P. (2012). Vehicle emissions and PM 2.5 mass concentrations in six Brazilian cities. Air Quality, Atmosphere and Health, 5(1), 79–88. https://doi.org/10.1007/s11869-010-0104-5

Dong L., Hua P., Gui D., & Zhang J. (2022). Extraction of multi-scale features enhances the deep learning-based daily PM2.5 forecasting in cities. Chemosphere, 308(P2), 136252. https://doi.org/10.1016/j.chemosphere.2022.136252

Fatima M., Butt I., Nasar-u-Minallah M., Atta A., Cheng G. (2023). Assessment of Air Pollution and Its Association with Population Health: Geo-Statistical Evidence from Pakistan. Geography, Environment, Sustainability, 16(2), 93-101. https://doi.org/10.24057/2071-9388-2022-155.

Faridi S., Niazi S., Yousefian F., Azimi F., Pasalari H., Momeniha F., Mokammel A., Gholampour, A., Hassanvand M. S., & Naddafi K. (2019). Spatial homogeneity and heterogeneity of ambient air pollutants in Tehran. Science of the Total Environment, 697(1547). https://doi.org/10.1016/j.scitotenv.2019.134123

Fattah M. A., Morshed S. R., Kafy A. Al, Rahaman Z. A., & Rahman M. T. (2023). Wavelet coherence analysis of PM2.5 variability in response to meteorological changes in South Asian cities. Atmospheric Pollution Research, 14(5), 101737. https://doi.org/10.1016/j.apr.2023.101737

Gioia S. M. C. L., Babinski M., Weiss D. J., & Kerr A. A. F. S. (2010). Insights into the dynamics and sources of atmospheric lead and particulate matter in São Paulo, Brazil, from high temporal resolution sampling. Atmospheric Research, 98(2–4), 478–485. https://doi.org/10.1016/j.atmosres.2010.08.016

Guttikunda S. K., Nishadh K. A., Gota S., Singh P., Chanda A., Jawahar P., & Asundi J. (2019). Air quality, emissions, and source contributions analysis for the Greater Bengaluru region of India. Atmospheric Pollution Research, 10(3), 941–953. https://doi.org/10.1016/j.apr.2019.01.002

Han J., Wang J., Zhao Y., Wang Q., Zhang B., Li, H., & Zhai J. (2018). Spatio-temporal variation of potential evapotranspiration and climatic drivers in the Jing-Jin-Ji region, North China. Agricultural and Forest Meteorology, 256, 75–83. https://doi.org/10.1016/j.agrformet.2018.03.002

Huang G., Li, X., Zhang B., & Ren J. (2021). PM2.5 concentration forecasting at surface monitoring sites using GRU neural network based on empirical mode decomposition. Science of the Total Environment, 768, 144516. https://doi.org/10.1016/j.scitotenv.2020.144516

Jang Y. W., & Jung G. W. (2023). Temporal Characteristics and Sources of PM2.5 in Porto Velho of Amazon Region in Brazil from 2020 to 2022. Sustainability (Switzerland), 15(18). https://doi.org/10.3390/su151814012

Leão M. L. P., Zhang L., & da Silva Júnior F. M. R. (2023). Effect of particulate matter (PM2.5 and PM10) on health indicators: climate change scenarios in a Brazilian metropolis. Environmental Geochemistry and Health, 45(5), 2229–2240. https://doi.org/10.1007/s10653-022-01331-8

Liu Y., Paciorek C. J., & Koutrakis P. (2009). Estimating regional spatial and temporal variability of PM2.5 concentrations using satellite data, meteorology, and land use information. Environmental Health Perspectives, 117(6), 886–892. https://doi.org/10.1289/ehp.0800123

Marengo J. A., Torres R. R., & Alves L. M. (2017). Drought in Northeast Brazil—past, present, and future. Theoretical and Applied Climatology, 129(3–4), 1189–1200. https://doi.org/10.1007/s00704-016-1840-8

Meng Y., & Sun W. (2021). Relationship between the formation of pm2. 5 and meteorological factors in northern China: the periodic characteristics of wavelet analysis. Advances in Meteorology, 2021(1), 9723676. https://doi.org/10.1155/2021/9723676

Nasar-u-Minallah M., Zainab M., Jabbar M. (2024a). Exploring Mitigation Strategies for Smog Crisis in Lahore: A Review for Environmental Health, and Policy Implications. Environmental Monitoring and Assessment. 196, 1269. https://doi.org/10.1007/s10661-024-13336-0

Nasar-u-Minallah M., Jabbar M., and Parveen N. (2024b). Assessing and Anticipating Environmental Challenges in Lahore, Pakistan: Future Implications of Air Pollution on Sustainable Development and Environmental Governance. Environmental Monitoring and Assessment, 196, 865. https://doi.org/10.1007/s10661-024-12925-3

Nasar-u-Minallah M., Parveen N., Bushra and Jabbar M. (2024c). Assessing air quality dynamics in Punjab, Pakistan: Pre, during, and post COVID-19 lockdown and evaluating strategies for mitigating. GeoJournal, 89,125. https://doi.org/10.1007/s10708-024-11132-4

Nasar-u-Minallah, M., Jabeen, M., Parveen, N., Abdullah, M., Nuskiya, M.H.F. (2025). Exploring the seasonal variability and nexus between urban air pollution and urban heat islands in Lahore, Pakistan. Acta Geophys. (2025). https://doi.org/10.1007/s11600-025-01574-w.

Nguyen M. V., Park G. H., & Lee B. K. (2017). Correlation analysis of size-resolved airborne particulate matter with classified meteorological conditions. Meteorology and Atmospheric Physics, 129(1), 35–46. https://doi.org/10.1007/s00703-016-0456-y

Ocak S., & Sezer Turalioglu F. (2008). Effect of Meteorology on the Atmospheric Concentrations of Traffic-Related Pollutants in Erzurum, Turkey #. J. Int. Environmental Application & Science, 3(5), 325–335.

Pacheco M. T., Parmigiani M. M. M., de Fatima Andrade M., Morawska L., & Kumar P. (2017). A review of emissions and concentrations of particulate matter in the three major metropolitan areas of Brazil. Journal of Transport and Health, 4, 53–72. https://doi.org/10.1016/j.jth.2017.01.008

Ray S., Das S. S., Mishra P., & Al-Khatib A. M. G. (2021). Time Series SARIMA Modelling and Forecasting of Monthly Rainfall and Temperature in the South Asian Countries. Earth Systems and Environment, 5(3), 531–546. https://doi.org/10.1007/s41748-021-00205-w

Requia W. J., & Azevedo de Melo H. F. (2024). Effectiveness of public policies related to traffic emissions in improving air quality in Brazil: A causal inference study using Bayesian structural time-series models. Atmospheric Environment, 319, 120291. https://doi.org/10.1016/j.atmosenv.2023.120291

Saha D., Soni, K., Mohanan M. N., & Singh M. (2019). Long-term trend of ventilation coefficient over Delhi and its potential impacts on air quality. Remote Sensing Applications: Society and Environment, 15, 100234. https://doi.org/10.1016/j.rsase.2019.05.003

Saraswati G. M. P., Sharma,S. K., Mandal, T. K., & Kotnala R. K. (2019). Simultaneous Measurements of Ambient NH 3 and Its Relationship with Other Trace Gases, PM 2.5 and Meteorological Parameters over Delhi, India. Mapan - Journal of Metrology Society of India, 34(1), 55–69. https://doi.org/10.1007/s12647-018-0286-0

Sharma A., Mandal T. K., Sharma S. K., Shukla D. K., & Singh S. (2017). Relationships of surface ozone with its precursors, particulate matter and meteorology over Delhi. Journal of Atmospheric Chemistry, 74(4), 451–474. https://doi.org/10.1007/s10874-016-9351-7

Sharma P., Peshin S. K., Soni V. K., Singh S., Beig G., & Ghosh C. (2022). Seasonal dynamics of particulate matter pollution and its dispersion in the city of Delhi, India. Meteorology and Atmospheric Physics, 134(2), 1–18. https://doi.org/10.1007/s00703-021-00852-8

Shen Y., Zhang L., Fang X., Ji H., Li X., & Zhao Z. (2019). Science of the Total Environment Spatiotemporal patterns of recent PM 2 . 5 concentrations over typical urban agglomerations in China. Science of the Total Environment, 655, 13–26. https://doi.org/10.1016/j.scitotenv.2018.11.105

Singh B. P., Singh D., Kumar K., & Jain V. K. (2021). Study of seasonal variation of PM2.5 concentration associated with meteorological parameters at residential sites in Delhi, India. Journal of Atmospheric Chemistry, 78(3), 161–176. https://doi.org/10.1007/s10874-021-09419-8

Souza D. Z., Vasconcellos P. C., Lee H., Aurela M., Saarnio K., Teinilä K., & Hillamo R. (2014). Composition of PM2.5 and PM10 collected at Urban Sites in Brazil. Aerosol and Air Quality Research, 14(1), 168–176. https://doi.org/10.4209/aaqr.2013.03.0071

Squizzato R., Nogueira T., Martins L. D., Martins J. A., Astolfo R., Machado C. B., Andrade M. de F., & Freitas E. D. de. (2021). Beyond megacities: tracking air pollution from urban areas and biomass burning in Brazil. Npj Climate and Atmospheric Science, 4(1), 1–7. https://doi.org/10.1038/s41612-021-00173-y

Tai A. P. K., Mickley L. J., & Jacob D. J. (2010). Correlations between fine particulate matter (PM2.5) and meteorological variables in the United States: Implications for the sensitivity of PM2.5 to climate change. Atmospheric Environment, 44(32), 3976–3984. https://doi.org/10.1016/j.atmosenv.2010.06.060

Tai A. P. K., Mickley L. J., & Jacob D. J. (2012). Impact of 2000-2050 climate change on fine particulate matter (PM 2.5) air quality inferred from a multi-model analysis of meteorological modes. Atmospheric Chemistry and Physics, 12(23), 11329–11337. https://doi.org/10.5194/acp-12-11329-2012

Urrutia-Pereira M., Rizzo L. V., Chong-Neto H. J., & Solé D. (2021). Impact of exposure to smoke from biomass burning in the Amazon rain forest on human health. Jornal Brasileiro de Pneumologia, 47(5), 1–8. https://doi.org/10.36416/1806-3756/e20210219

Vaishali V., G., & Das R. M. (2023). Influence of Temperature and Relative Humidity on PM2.5 Concentration over Delhi. Mapan - Journal of Metrology Society of India, 38(3), 759–769. https://doi.org/10.1007/s12647-023-00656-8

Wang J., Han J., Li T., Wu T., & Fang C. (2023). Impact analysis of meteorological variables on PM2.5 pollution in the most polluted cities in China. Heliyon, 9(7), e17609. https://doi.org/10.1016/j.heliyon.2023.e17609

Wang J., & Ogawa S. (2015). Effects of meteorological conditions on PM2.5 concentrations in Nagasaki, Japan. International Journal of Environmental Research and Public Health, 12(8), 9089–9101. https://doi.org/10.3390/ijerph120809089

Wang J., Wang R., & Li Z. (2022). A combined forecasting system based on multi-objective optimization and feature extraction strategy for hourly PM2.5 concentration. Applied Soft Computing, 114, 108034. https://doi.org/10.1016/j.asoc.2021.108034

Westervelt D. M., Horowitz L. W., Naik V., Tai, A. P. K., Fiore A. M., & Mauzerall D. L. (2016). Quantifying PM2.5-meteorology sensitivities in a global climate model. Atmospheric Environment, 142, 43–56. https://doi.org/10.1016/j.atmosenv.2016.07.040

Wu S., Yan X., Yao J., & Zhao W. (2023). Quantifying the scale-dependent relationships of PM2. 5 and O3 on meteorological factors and their influencing factors in the Beijing-Tianjin-Hebei region and surrounding areas. Environmental Pollution, 337, 122517. https://doi.org/10.1016/j.envpol.2023.122517

Yang Q., Yuan Q., Li T., Shen H., & Zhang L. (2017). The relationships between PM2.5 and meteorological factors in China: Seasonal and regional variations. International Journal of Environmental Research and Public Health, 14(12). https://doi.org/10.3390/ijerph14121510

Ye T., Xu R., Yue X., Chen G., Yu P., Coêlho M. S. Z. S., Saldiva P. H. N., Abramson M. J., Guo Y., & Li S. (2022). Short-term exposure to wildfire-related PM2.5 increases mortality risks and burdens in Brazil. Nature Communications, 13(1), 1–9. https://doi.org/10.1038/s41467-022-35326-x

Zhang B., Jiao L., Xu G., Zhao S., Tang X., Zhou Y., & Gong C. (2018). Influences of wind and precipitation on different-sized particulate matter concentrations (PM2.5, PM10, PM2.5–10). Meteorology and Atmospheric Physics, 130(3), 383–392. https://doi.org/10.1007/s00703-017-0526-9

Zhang L., Cheng Y., Zhang Y., He Y., Gu Z., & Yu C. (2017). Impact of air humidity fluctuation on the rise of PM mass concentration based on the high-resolution monitoring data. Aerosol and Air Quality Research, 17(2), 543–552. https://doi.org/10.4209/aaqr.2016.07.0296

Zhao D., Xin J., Gong C., Quan J., Liu G., Zhao W., & Song T. (2019). The formation mechanism of air pollution episodes in Beijing city: Insights into the measured feedback between aerosol radiative forcing and the atmospheric boundary layer stability. Science of the Total Environment, 692, 371-381. https://doi.org/10.1016/j.scitotenv.2019.07.255

RESEARCH PAPER

MONITORING OF WATER SURFACE DYNAMICS OF THE SONG HINH HYDROPOWER RESERVIOR (VIETNAM) USING GOOGLE EARTH ENGINE

Quoc Khanh Nguyen[1], Mai Phuong Pham[1*], Trong Nhan Nguyen[2*]

[1]Joint Vietnam - Russia Tropical Science and Technology Research Center, Hanoi, 100000, Vietnam

[2]Faculty of Geodesy, Cartography and Geographic Information, University of Natural Resources and Environment, Ho Chi Minh, 70000, Vietnam

***Corresponding author:** ntnhan@hcmunre.edu.vn

Received: October 2nd 2024 / Accepted: April 4th 2025 / Published: June 30th 2025

https://doi.org/10.24057/2071-9388-2025-3636

ABSTRACT. Reservoirs are facing increasing hydrological pressure, making continuous and accurate monitoring of these resources essential for sustainable management. In this study, we utilized a method involving Google Earth Engine (GEE), a platform with strong data processing capabilities for big data, to analyze and interpret satellite images. The Otsu method was applied to automatically determine the threshold value for extracting the water surface of the Song Hinh reservoir using Landsat 5, 8, and 9 satellite imagery, and to assess changes in the reservoir's surface area. The research results indicated that the water surface area of the Song Hinh reservoir initially increased 4.4 times (1999-2000) and then remained relatively stable (2000-2024). However, during the 2000-2015 period, the water surface area experienced minor expansions and contractions, while during the 2015-2024 period, the surface area expanded insignificantly, with less contraction than in the previous period. Additionally, the analysis results of water surface area changes were used to support the development of Earth Engine Apps, also known as WebGIS, as a tool for monitoring surface water changes in the Song Hinh reservoir. In summary, the results obtained in this study are highly useful as a foundation for developing effective monitoring measures and sustainable resource management for the Song Hinh reservoir area.

KEYWORDS: Earth Engine Apps, GEE, Otsu method, water surface dynamic, The Song Hinh

CITATION: Nguyen Q. K., Pham M.P., Nguyen T. N. (2025). Monitoring Of Water Surface Dynamics Of The Song Hinh Hydropower Reservior (Vietnam) Using Google Earth Engine. Geography, Environment, Sustainability, 2 (18), 91-101
https://doi.org/10.24057/2071-9388-2025-3636

ACKNOWLEDGEMENTS: The study was supported by a project from the Joint Vietnam – Russia Tropical Science and Technology Research Center, Hanoi city, Vietnam (No. ST.Đ1.01/23).

Conflict of interests: The authors reported no potential conflict of interests.

INTRODUCTION

Natural and artificial reservoirs are essential sources of freshwater for humans and animals, agricultural irrigation, and industrial use. Reservoirs are under increasing hydrological pressure due to rising water demand, climate change, prolonged droughts, and water pollution. Therefore, continuous and accurate monitoring of these resources is necessary to ensure their sustainable management (Bocchino et al. 2023). Traditional ground-based instruments like gauging stations are still frequently used today to measure water levels. The data obtained from these tools are used to estimate the area and volume of reservoirs, as well as their changes over time, by using elevation curves (volume-area-elevation curves) derived from depth and topographic information specific to the reservoir (Tong et al. 2016, Hamoudzadeh et al. 2023). However, this on-site monitoring method has certain limitations, such as difficulties in installing and maintaining gauging stations in remote areas, equipment malfunctions, and the spatial discontinuity of elevation data (Duan and Bastiaanssen 2013; Fuentes et al. 2019). In contrast, the use of remote sensing (RS) technology can significantly reduce monitoring costs and provide regular data, facilitating continuous monitoring of reservoirs with consistent processes worldwide (Valadão et al. 2021).

For this issue, numerous studies have demonstrated that multi-spectral and multi-temporal RS is a highly feasible option, enabling continuous monitoring of reservoir changes (Jagadeesha and Palnitkar 1991; Busker et al. 2019; Yao et al. 2019; Binh Pham-Duc et al. 2023). Although many studies have applied RS in the analysis of long-term change detection (Alesheikh et al. 2007), several limitations arise related to the need for computation and processing of large amounts of satellite imagery, especially when using medium- and high-resolution images (Zhang et al. 2022). To address this issue, Google Earth Engine (GEE) can be used as a cloud computing platform along with advanced machine learning algorithms to analyze satellite images. GEE offers high-performance parallel computing capabilities, massive remote sensing data, geospatial data, and free access while providing a new approach for long-term time-series analysis and large-scale remote sensing analysis (Wang et al. 2021). Based on the development

tools for JavaScript or Python algorithms on the web, it not only enables rapid online visualization and RS data analysis but also supports the free development of Apps, also known as WebGIS (Kwong et al. 2022).

As mentioned above, RS can help enable the monitoring of water boundary changes. Many studies have employed different methods for water surface extraction, including the Normalized Difference Water Index (NDWI); however, this index has shown overall poor effectiveness [15] (Xing et al. 2022). In contrast, the Modified Normalized Difference Water Index (MNDWI) has demonstrated better adaptability and stability in distinguishing between water and land areas (Wang et al. 2017; Zhang and Liu 2022; Singh et al. 2015; Vasanthi and Joshitha, 2024), making it a preferred choice over NDWI. Additionally, Green/SWIR and Green/NIR ratios also allow for effective water surface extraction with a threshold value greater than 1 (Ng 2016). However, to clearly separate water and land objects in satellite images, an advanced technique is needed to automatically determine the threshold for water surfaces. For this issue, the Otsu is a useful method that helps optimally determine the threshold value in images (Otsu 1979).

The Otsu method is a widely used thresholding technique for gray-level images, with applications ranging from defect detection to OCR binarization and image pre-processing for historical document searching (Jianzhuang et al., 1991; Ng, 2006; Gupta et al., 2007). The method has been extended to 2D histograms for image segmentation, with techniques such as 2D histogram projection and wavelet transform proposed for threshold correction (Zhang et al., 2008). More research has looked into how the Otsu method compares to other clustering algorithms, like K-means, and found that their objective functions for multilevel thresholding are the same (Liu et al., 2009). Additionally, studies have focused on optimizing the Otsu method for multi-level thresholding using a two-stage optimization approach (Huang et al., 2009). A characteristic analysis of the Otsu threshold has also been conducted, highlighting its applications in various fields (Xu et al., 2011). Some changes have been suggested to the Otsu method to make automatic thresholding work better. These include the valley-emphasis method and a modified two-dimensional segmentation algorithm (Fan et al., 2012; Chen et al., 2012).

The Otsu's method, a popular image thresholding technique in computer vision and image processing, has several limitations that can affect its performance in certain scenarios. One major limitation is the difficulty in segmenting images with objects of complex and irregular geometry, especially those with many edges or inclusions (Ma et al. 2017). This limitations can lead to challenges in accurately detecting and separating different regions within the image. Additionally, the Otsu's method may not perform optimally when faced with images that have varying lighting conditions or noise levels. Despite its limitations, the Otsu's method remains a valuable tool for simple image thresholding tasks. It is known for its simplicity, efficiency, and parameter-free nature, making it a popular choice for many applications (Sha et al. 2016). The Otsu method continues to be a valuable tool in image processing and analysis, with ongoing research focusing on optimization, applications, and improvements to the original algorithm (Liu et al., 2014). OTSU can be applied to threshold vegetation indices such as NDVI (Normalized Difference Vegetation Index). For example, it can differentiate areas with high and low vegetation density (Xu et al., 2020). For soil indices, such as NDSI (Normalized Difference Soil Index) (Härer et al., 2018) or the Brightness Index (BI) (Deng and Zhang, 2021; Kakooei and Baleghi, 2020), OTSU can also be used to separate land regions. In cloud segmentation, OTSU can be employed to distinguish cloud regions in satellite images based on reflected light intensity, often using optical bands with high values in cloud areas. When processing satellite imagery for analyzing air pollution or dust, OTSU can help classify different pollution zones. The method's reliance on a simple histogram is a key limitation. Since OTSU only analyzes the image's histogram, it may not effectively separate indices lacking a clear bimodal distribution.

The Earth Engine Apps (EEapp) created on GEE is a powerful tool for analyzing and monitoring Earth's environment through satellite data. GEE provides a cloud platform that allows users to access, process, and analyze vast amounts of geospatial data efficiently. The EEapp enables researchers, scientists, and nonprofit organizations to track and monitor environmental changes such as climate change, deforestation, water fluctuations, and other natural phenomena. With a diverse data library, including petabytes of historical and current satellite data from sources like NASA, USGS, and ESA, users can easily perform complex analyses without needing to invest in high-tech infrastructure. The application provides powerful programming tools through JavaScript and Python APIs, allowing for the creation of custom maps and visual reports. GEE also supports collaboration and sharing of research results, helping the scientific community and policymakers make data-driven decisions based on accurate and up-to-date information. With its easy access and superior processing power, the EEapp is an indispensable tool for natural resource research and management.

Recent studies have demonstrated the effectiveness of using GEE in monitoring water surface changes. Wang et al. (2021) utilized Landsat 5, 7, and 8 images along with GEE to monitor water surface fluctuations at the Xiaolangdi reservoir, achieving an overall accuracy of 98.86% and a kappa coefficient of 0.96. Xing et al. (2022) used the GEE platform to track changes in the water surface in Shandong Province, China, from 1990 to 2020 using Landsat imagery. The results indicated that it could provide an important application for sustainable water resource management. Recently, GEE has also been applied in Vietnam to monitor water surface fluctuations in various water bodies (Vu Anh Minh et al. 2024; Binh Pham-Duc 2024). This method is considered a tool for effective water resource management in developing countries. It not only automatically detects, monitors, and evaluates water surface fluctuations over space and time for reservoirs but can also be extended to other surface water bodies and coastal lagoons (Condeca et al. 2022). However, in Vietnam, studies applying GEE to monitor water surface changes are still limited, particularly in multi-purpose reservoirs used for irrigation, aquaculture, flood regulation, and power generation. This situation highlights the need for research in these reservoirs.

The Song Hinh Hydropower Reservoir is a hydropower facility located on the Hinh River, a major river in Phu Yen Province, with the dam situated approximately 40 km southwest of Tuy Hoa city. The reservoir plays a crucial economic and environmental role for the local area and neighboring regions. The primary function of the Song Hinh Hydropower Plant is electricity generation with a designed capacity of 70 MW and an average annual output of 357 million kWh, which is integrated into the national grid to meet the economic needs of the population. After power generation, the water (averaging 36.99 m^3/s) provides supply for industrial activities, domestic use, and irrigation

for over 19,800 hectares of agricultural land downstream (Le Cong Tuan and Hoang Dinh Trung 2024). Monitoring water surface fluctuations of this important hydropower reservoir is significant for socio-economic development and environmental protection in the southern region of Phú Yên Province. In this study, Landsat 5, 8, and 9 images were collected for the Song Hinh Reservoir area from 1999 to 2024. We used the GEE method, a powerful cloud-based platform for processing large datasets, to analyze and interpret satellite images and applied the Otsu method to automatically determine threshold values for extracting the water surface of the Song Hinh Reservoir. The objectives of this study are (1) to extract the water surface using GEE and Otsu methods; (2) to identify spatial and temporal changes in the water surface area of the Song Hinh Reservoir using GIS software; and (3) to develop Earth Engine Apps as a basis for creating a WEBGIS system to support the management and monitoring of water resources in the reservoir as climate change and human activities increase. The results provide a scientific basis for environmental protection, water resource management, economic activities, and assist policymakers in developing effective strategies for resource management and environmental protection.

MATERIALS AND METHODS

Study area and data

Study area

The Song Hinh Hydropower Reservoir is the largest reservoir in the Hinh River basin of Phu Yen Province (Fig. 1), with a catchment area of 772 km^2. The reservoir has a normal water level of 209 meters, a dead storage level of 196 meters, a dam crest elevation of 215 meters, a total storage capacity of 357 million m^3, and a maximum flood discharge capacity of 6952 m^3/s (Hai et al. 2020). Construction of the reservoir began in 1993, power generation started in 1999, and it was inaugurated in 2001. Its primary functions are to provide water for irrigation, domestic use, and industrial purposes in the Son Giang and Son Thành areas; to supplement water for the Dong Cam irrigation system to ensure irrigation capacity for the summer-autumn crop; and to supply water to the Ban Thach River (Vi 2020). The Song Hinh Reservoir is located in the region with the highest rainfall in Phu Yen Province, with annual precipitation measured between 2200-2400 mm. Rainfall during the four-month rainy season (September-December) accounts for 69-72% of the annual total, and the average annual temperature is approximately 26°C.

Data sources

A GEE platform has been used to collect images, classify, and assess accuracy using machine learning and artificial intelligence algorithms (Tamiminia et al. 2020). This platform provides a powerful and flexible analytical environment for large datasets from Landsat. Accuracy improvement of the images is achieved through machine learning algorithms to ensure accurate results on changes to the Earth's surface. Notably, GEE is an open-source tool that offers computational resources and satellite data for free on a cloud computing platform, thereby reducing costs and benefiting users.

In this study, the images used are surface reflectance images from Landsat 5-TM, 8, and 9-OLI satellites with a spatial resolution of 30 meters, collected to create a comprehensive database for analyzing and extracting the water surface of the Song Hinh Reservoir from 1999

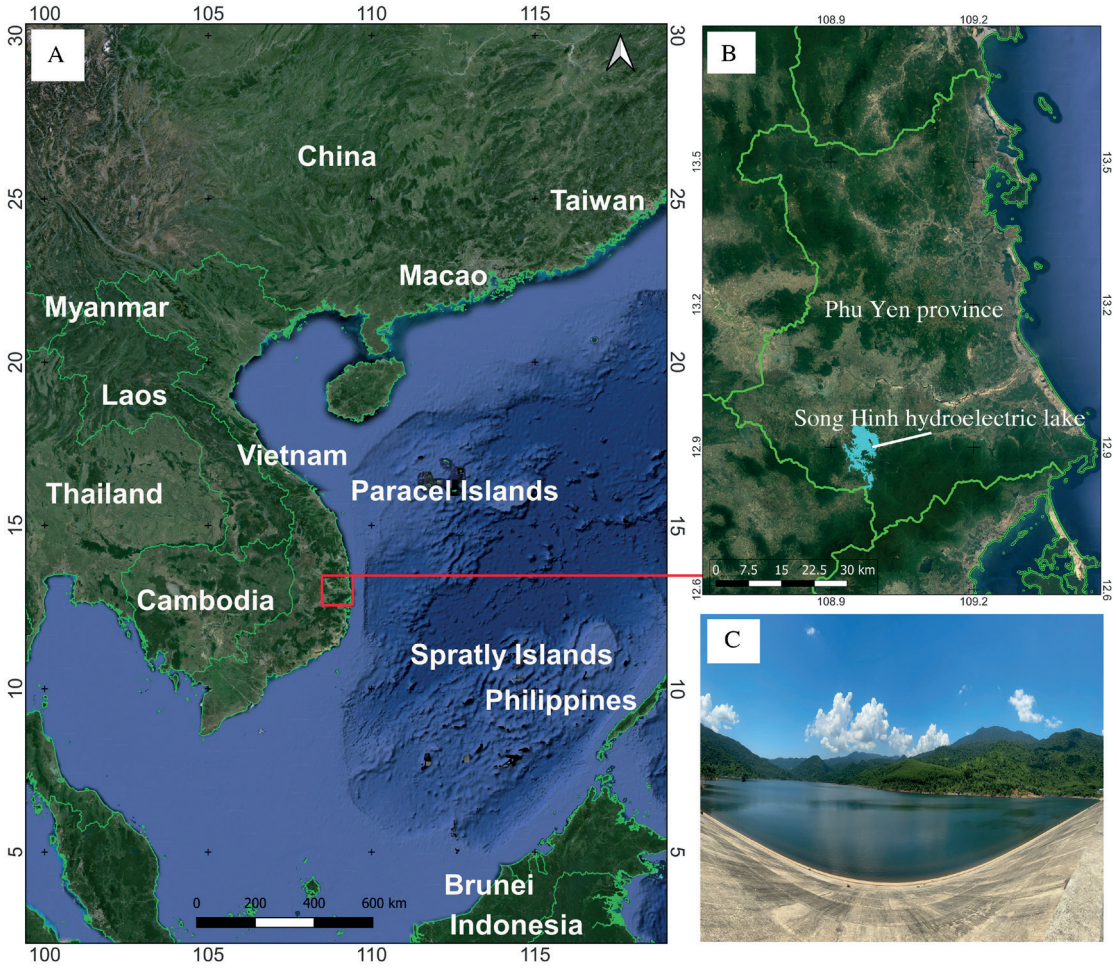

Fig. 1. Study area

to 2024. Table 1 provides detailed information about these image scenes. The collection of reflectance images allows for the removal of cloud-covered areas using the 'pixel qa' band. Image classification was performed for the years 1999, 2000, 2015, and 2024, using scripts and datasets specific to each period.

Image pre-processing

We processed the images by applying a cloud mask layer to each dataset, aiming to create composite images with an acceptable level of cloud cover. This cloud filtering process uses the 'pixel qa' band in the surface reflectance collections to remove clouds and cloud shadows, resulting in cloud-free RGB composites (Markert et al. 2018). For further analysis of the study area, we used the boundary of the Song Hinh Reservoir to crop the images, retaining only the portion within this area. This format ensures that the processed image data focuses on the Song Hinh Reservoir area and is not affected by external factors outside the study area.

METHODS

The Otsu's Method

The Otsu's Method is named after a Japanese researcher (Nobuyuki Otsu), who proposed the idea of assuming the gray levels of the target object and the background object in an image to construct a histogram with Gaussian distribution and equal variances (Otsu 1979). Thus, the Otsu's method is a technique for determining a threshold based on the gray level histogram with binomial distribution. However, this method is ineffective when the pixel variance between the object to be extracted and the background object in the image is too large or when the histogram is constructed as a unimodal distribution with a single peak (Ng 2016; Truong and Kim 2018). According to the Otsu's method, the threshold k^* is determined (Eq. 1) so that the two classes (C1 and C2) in the image have significant differences, meaning that the variance is maximized (Pritam and Prasenjit 2010).

$$k^* = argmax_{0 \le k \le L-1}\left\{\omega_1(k)\mu_1^2(k) + \omega_2(k)\mu_2^2(k)\right\} \quad (1)$$

where C1 is the class containing gray level values in the range [0,…, k]; C2 is the class containing gray level values in the range [k+1,…, L-1]; ω_1 and ω_2 are the probabilities of the two classes in the image, calculated according to Eq. 2:

$$\omega_1(k) = \sum_{i=1}^{k} P_i và \omega_2(k) \sum_{i=k+1}^{L-1} P_i \quad (2)$$

μ_1 and μ_2 are the mean values calculated using Eq. 3:

$$\mu_1(k) = \sum_{i=0}^{k} \frac{i \times p_i}{\omega_1(k)} và \mu_2(k) \sum_{i=k+1}^{L-1} \frac{i \times p_i}{\omega_2(k)} \quad (3)$$

After determining the threshold k^*, thresholding is performed to create a binary image. Pixels with gray levels greater than the threshold k^* are assigned a value of 1, while those with gray levels less than k^* are assigned a value of 0 (Eq. 4).

$$g(x,y) = \begin{cases} 1 f(x,y) > k^* \\ 0 f(x,y) < k^* \end{cases} \quad (4)$$

where $g(x,y)$ is the function representing the gray level value at point (x, y) on the output image; $f(x,y)$ is the function representing the gray level value at point (x, y) on the input image.

Using the JavaScript programming language to extract water surfaces and analyze spatial changes over time to determine the changes in the water surface of the Song Hinh Reservoir, and this is done on the GEE platform. Additionally, GEE supports designing WebGIS interfaces or Earth Engine Apps and developing interactive functionalities with the maps.

RESULTS

Water surface extraction for research stages

In this study, we used the near-infrared (NIR) band to construct a histogram by applying the Otsu's method on the NIR band of optical images from Landsat 5, 8, and 9, with a DN (Digital Number) threshold value to separate water surfaces, as water is fully absorbed in the infrared region. Water has a strong absorption characteristic in the NIR region, so water bodies in NIR images typically appear as areas with very low DN values. The Otsu's method works based on the image's histogram, which is a frequency distribution chart of DN values in the image. Otsu searches for the optimal segmentation threshold by optimizing the ratio between intra-class variance and inter-class variance, aiming to minimize the total variance within each class (Fig. 2, 3).

Using the Otsu's method to find the optimal DN threshold. This method automatically calculates the threshold so that the total variance within the classes is minimized. The threshold separates the image into two parts: one representing water (low DN values) and the other representing land and other objects (high DN values). Then, the DN threshold found by the Otsu's method is used to create a segmentation mask. DN values lower than the threshold are assigned as water, while DN values higher than the threshold are assigned as land or other objects. This method eliminates the need for manual threshold selection, saving time and reducing subjective errors. It aligns with the spectral characteristics of water in the NIR region, allowing for accurate water surface extraction. In water resource research and management, the use of the Otsu's method on the NIR band of Landsat images can help with the following: (1) monitoring water level changes: detecting and tracking changes in water bodies over time; (2) land cover classification: assisting in the classification

Table 1. Information on the satellite images used

Satellite images	ID Images	Time
Landsat 5	LANDSAT/LT05/C02/T1_L2/LT05_123051_19990319	1999-03-19
Landsat 5	LANDSAT/LT05/C02/T1_L2/LT05_123051_20000508	2000-05-08
Landsat 8	LANDSAT/LC08/C02/T1_L2/LC08_124051_20150407	2015-04-07
Landsat 9	LANDSAT/LC09/C02/T1_L2/LC09_123051_20240416	2024-04-16

and mapping of water and land areas; (3) natural resource management: supporting the management and protection of water resources. The Otsu method applied to the NIR band of Landsat images is a powerful, simple, and effective tool for separating water surfaces from other objects, thanks to water's strong absorption characteristics in the NIR region.

Spatiotemporal variations of the water surface in the Song Hinh Reservoir

Based on the results in Figs. 4 and 5, the water surface fluctuations across the study periods are evident. In the 1999-2000 period, the water surface of the Song Hinh Reservoir expanded significantly, with an area of approximately 39.28 hectares. There was no significant reduction in the water surface area during this period. The 2000-2015 period saw major stability, with an unchanged water surface area accounting for about 45.11 hectares. However, during this period, a small reduction in water surface area was observed (2.93 hectares), while the expanded area was 1.32 hectares. In the 2015-2024 period, the unchanged water surface continued to dominate, covering around 44.98 hectares. The reduction in water surface area was significantly smaller compared to previous periods, around 1.44 hectares, and the expanded water surface area was very minimal, only 0.14 hectares. Overall, the 1999-2000 period experienced the most substantial expansion of the water surface in the Song Hinh Reservoir, while in the 2000-2015 period, most of the water surface remained unchanged, with minor expansion and contraction. Data from the 2015-2024 period show the reservoir's water surface was relatively stable, with the shrinkage of the water surface trending lower than in previous periods, and expansion being very limited. These data reflect the spatiotemporal variations in the water surface over time, indicating environmental impacts and other factors affecting water resources.

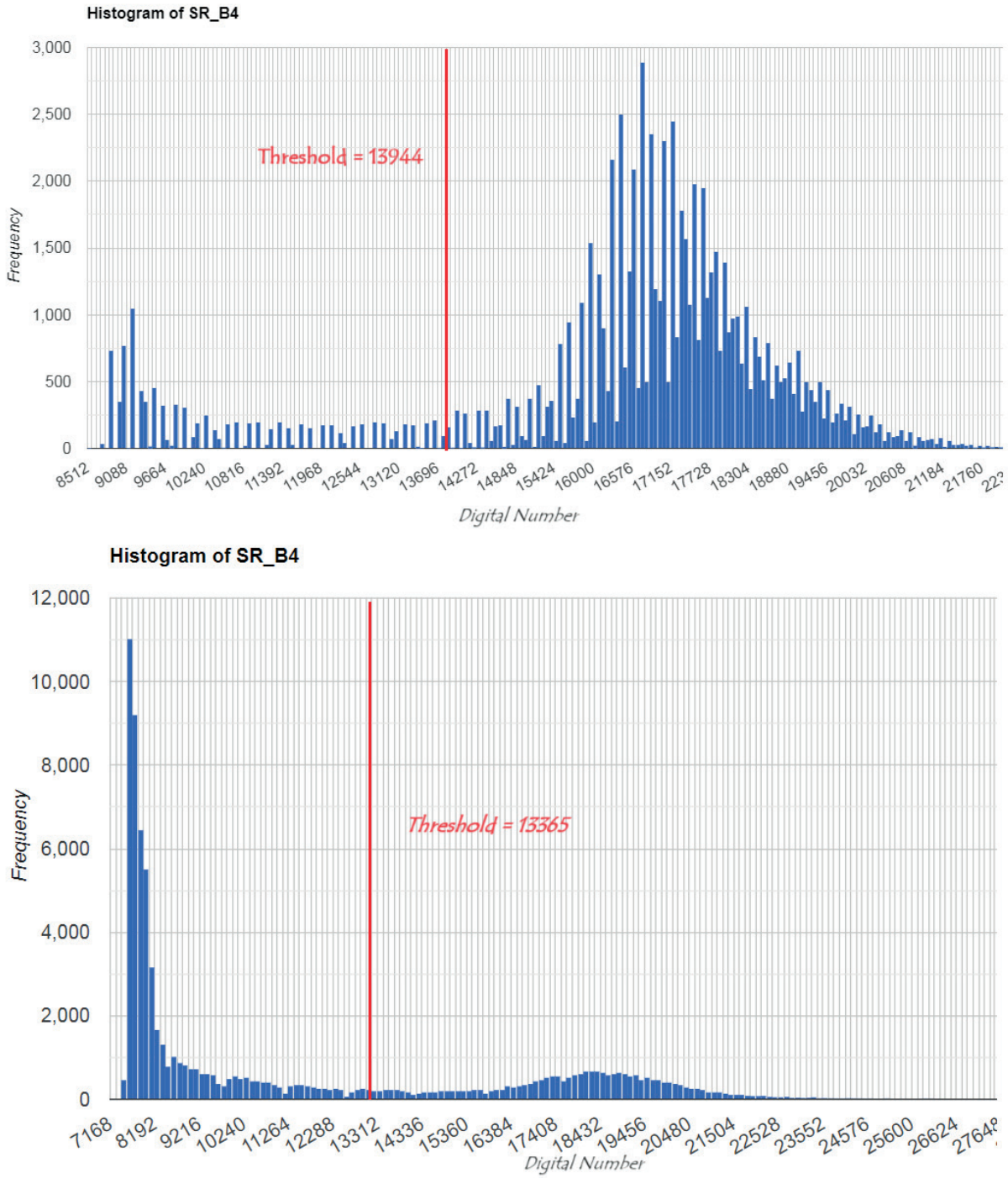

Fig. 2. DN threshold values for 1999 and 2000

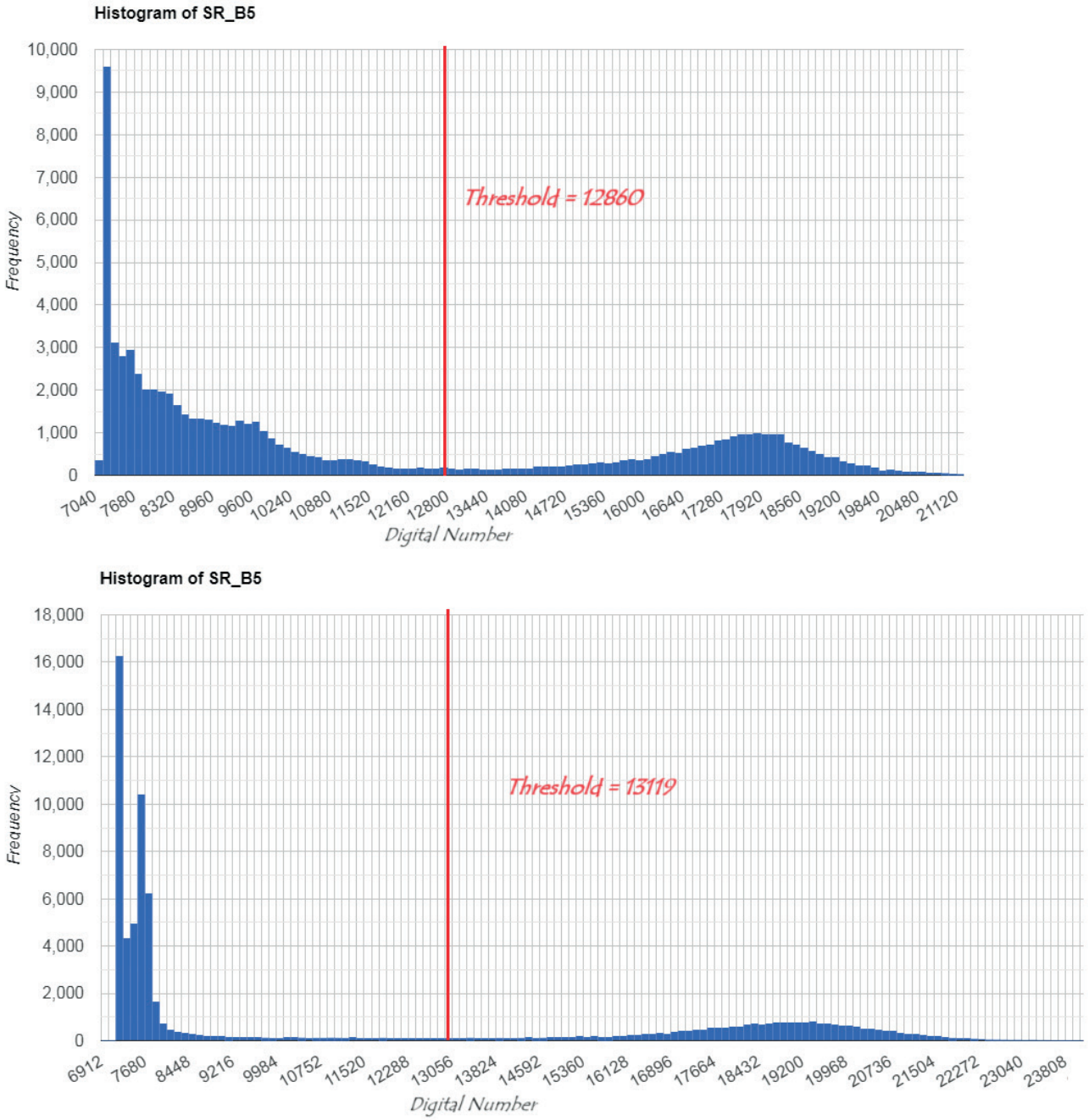

Fig. 3. DN threshold values for 2015 and 2024

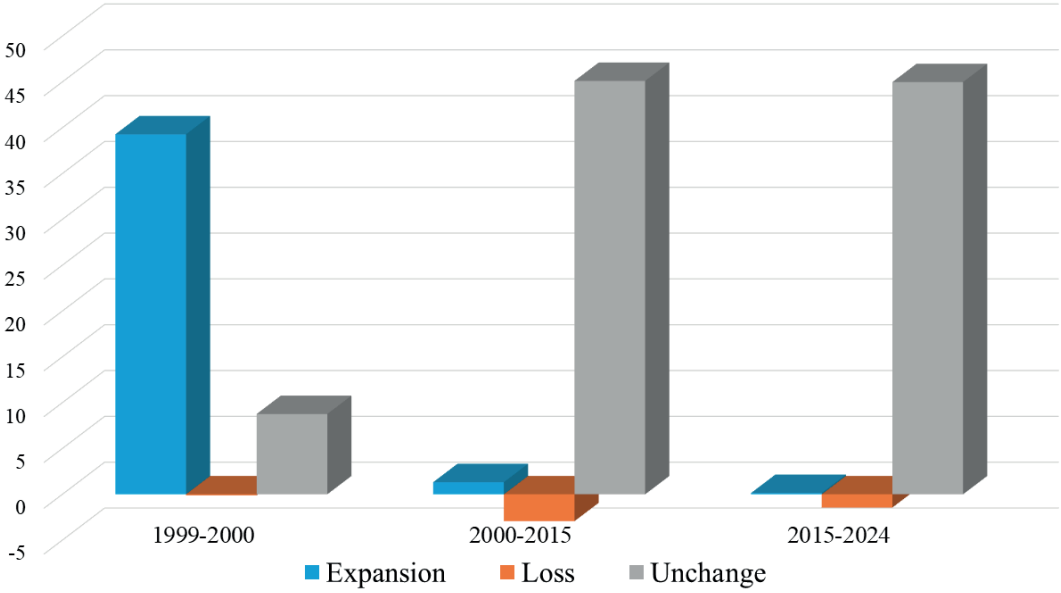

Fig. 4. Dynamic of water surface area (ha)

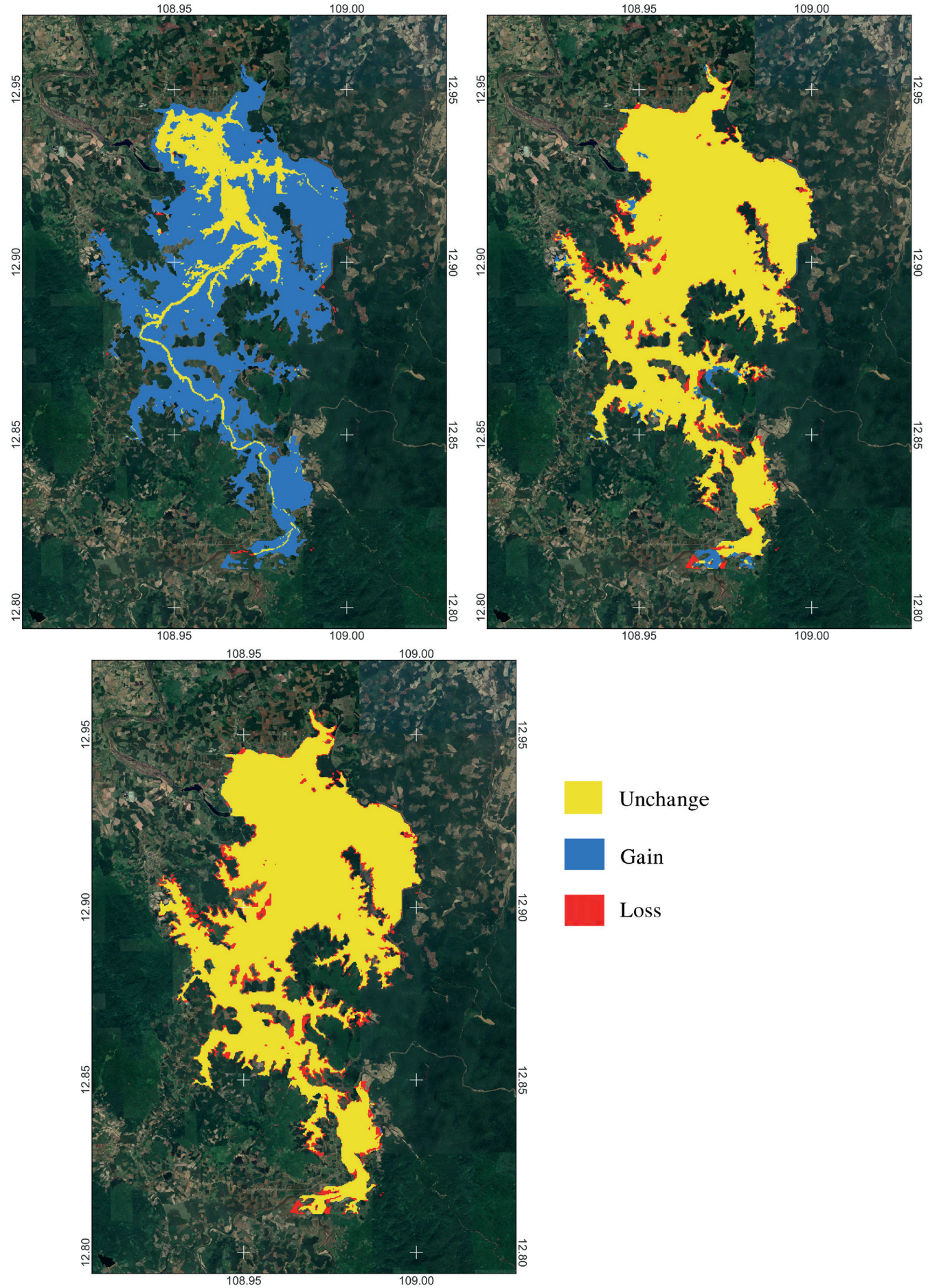

Fig. 5. Map of water surface area changes in the Song Hinh Reservoir: (a) 1999 - 2000; (b) 2000 - 2015; and (c) 2015 – 2024

Developing Earth Engine Apps

Through the analysis of water surface variations and utilizing the functions available on the GEE platform, we have developed an online Earth Engine App to allow users to monitor and analyze trends in water surface area over time (Fig. 6). This enables the assessment of the impacts of climate change, drought, or human activities on the reservoir. In addition to zooming in and out of the map to display different areas, users can interact with the app by creating time-series charts, which could potentially extend the application for water quality monitoring. Regular monitoring helps in the early detection of signs of depletion, pollution, or other relevant issues, enabling timely and effective water resource management (de Albuquerque Teixeira et al., 2024). GEE's capability to process and analyze satellite data in real-time and historically provides managers with a comprehensive and accurate overview of reservoir conditions. Data from GEE supports decisions for water resource management, such as water regulation and management for agriculture and industry. GEE can analyze water quality indicators such as chlorophyll levels and turbidity, allowing for early detection of pollution (Sherjah et al., 2023). For reservoirs near the coast, monitoring saltwater intrusion is crucial to protect freshwater ecosystems and drinking water sources. Researchers can use GEE data to conduct studies on hydrology, ecology, and climate change (VanDeWeghe et al., 2022). GEE data can also be used to develop predictive models for future water level changes in reservoirs (Lu and Sun, 2023). Using GEE in educational and outreach programs helps raise community awareness about the importance of protecting and managing water resources. Local communities can engage in monitoring and protecting the reservoir through user-friendly GEE applications (Boothroyd, 2021).

Limitations of the study

Selection of Satellite Images

Our study focuses on evaluating the changes in the water surface area of the Song Hinh Reservoir before and after the construction of the hydropower dam. This approach was guided by the unique characteristics of the region, where water surface fluctuations are primarily influenced by dam construction and reservoir operations rather than natural hydrological variations. To capture this transformation, we deliberately selected four satellite images representing distinct developmental stages of the reservoir. However, this selection presents certain limitations. By relying on a limited number of images, our analysis may not fully capture short-term variations in water extent due to seasonal or interannual hydrological dynamics. Furthermore, while we acknowledge the influence of precipitation patterns, inflow/outflow dynamics, and water level fluctuations, these factors were not explicitly incorporated into our analysis. Expanding the dataset to include a broader temporal range and integrating additional hydrological variables could provide a more comprehensive assessment of the reservoir's long-term dynamics.

Connection Between Water Level and Surface Boundary Estimation

While we recognize the importance of linking water level measurements with estimates of water surface area, our study primarily utilized Google Earth Engine (GEE) as a practical tool for detecting spatial changes in water boundaries. The efficiency of GEE in extracting and processing spatial data makes it a valuable resource for water resource monitoring. However, the absence of historical design data correlating water levels with surface areas for the Song Hinh Reservoir limited our ability to

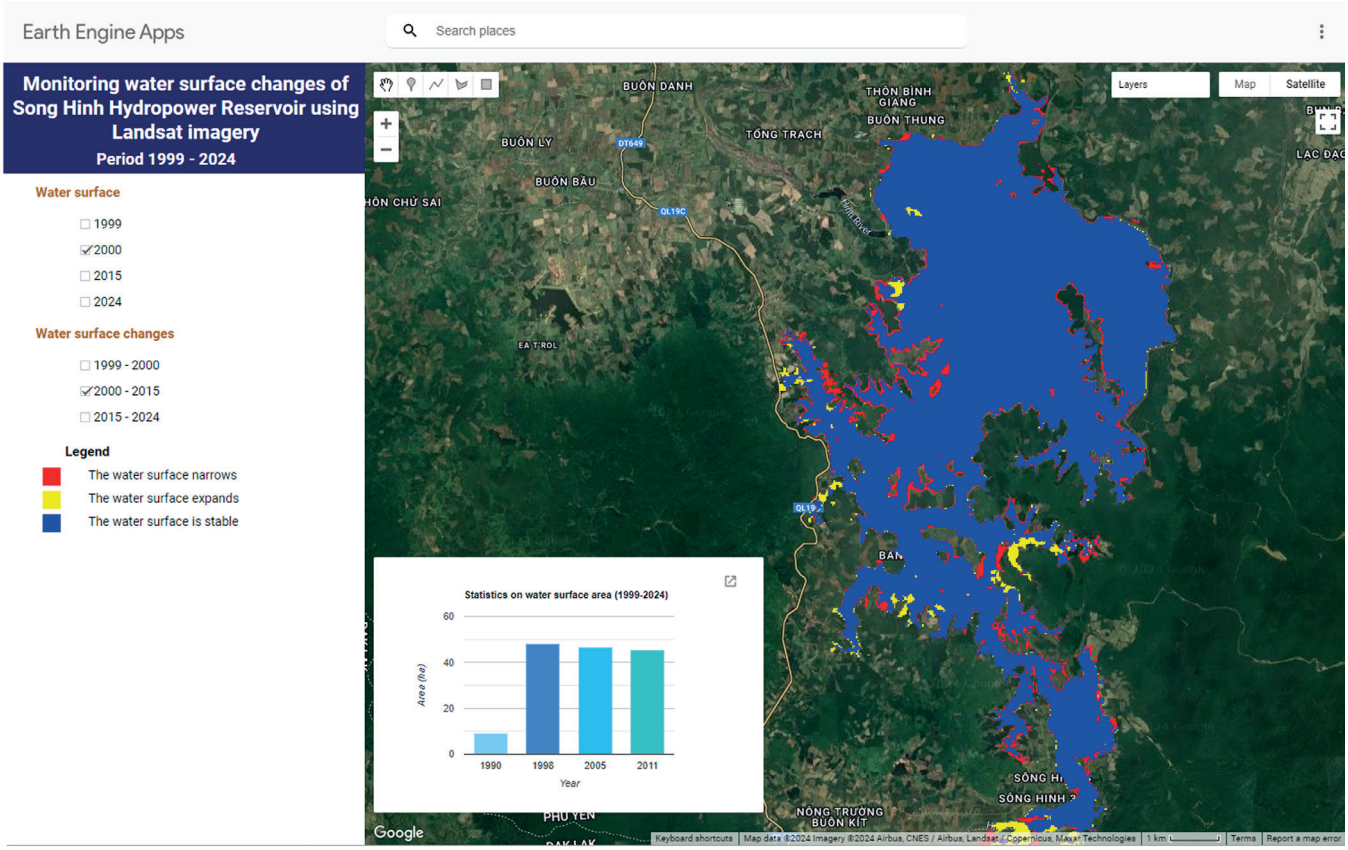

Fig. 6. Screenshot of the online application developed on GEE for monitoring water surface changes in the Song Hinh Reservoir from 1999 to 2024

conduct a direct quantitative analysis of this relationship. Although our methodology demonstrates the adaptability of GEE for spatial data analysis, future studies could benefit from incorporating water level records, hydrological modeling, or additional in situ measurements. Such an approach would enable a more precise assessment of reservoir storage capacity and operational changes over time.

Emphasis on the Potential of Google Earth Engine

One of the key contributions of our study is to highlight the applicability of GEE for analyzing water surface dynamics, especially in data-scarce regions. GEE's ability to integrate and process large datasets efficiently makes it a powerful tool for reservoir monitoring. However, our study primarily focused on spatial analysis without incorporating advanced hydrological simulations or validation against ground-based observations. Additionally, while GEE-generated outputs can be seamlessly integrated into WebGIS platforms, their accuracy depends on the quality of input satellite data and the classification algorithms used. Future research should explore the integration of GEE with machine learning approaches, multi-source satellite data fusion, and hydrodynamic modeling to enhance the accuracy and applicability of water resource assessments.

CONCLUSIONS

In this study, the Otsu method was used to extract water surface area in the NIR band of Landsat 5, 8, and 9 optical images with DN threshold values. The research results precisely clarified the historical periods when water surface area was affected, leading to an increase in water surface area during 1999-2000 and subsequent contraction (adjustment) in the following years. By the 2015-2024 period, the water surface area had stabilized with negligible increases and decreases. Major past water surface fluctuations were caused by hydroelectric dam construction activities, which expanded the water surface area to 39.28 hectares (approximately 4.4 times the area before 1999). The assessment results greatly contributed to the development of Earth Engine Apps for monitoring the Song Hinh Reservoir's water surface, aiding in the management, protection, and research of water resources while enhancing community awareness and participation in environmental protection. In summary, this study demonstrates that the GEE cloud computing platform can develop a web application with effective, comprehensive, and cost-efficient capabilities, providing rapid information to improve water resource monitoring.

REFERENCES

Alesheikh A.A., Ghorbanali A., and Nouri N. (2007). Coastline change detection using remote sensing. International Journal of Environmental Science and Technology, 4(1), 61–66, DOI: 10.1007/BF03325962.

Binh P.D. (2024). Comparison of multi-source satellite remote sensing observations for monitoring the variations of small lakes: a case study of Dai Lai Lake (Vietnam). Journal of Water and Climate Change, 15(1), 157, DOI: 10.2166/wcc.2023.505.

Bocchino F., Ravanelli R., Belloni V., Mazzucchelli P., and Crespi M. (2023). Water reservoirs monitoring through Google Earth Engine: Application to Sentinel and Landsat imagery. The International Archives of the Photogrammetry, Remote Sensing and Spatial Information Sciences, XLVIII-M-1-2023, 41–47, DOI: 10.5194/isprs-archives-XLVIII-M-1-2023-41-2023.

Boothroyd R.J., Williams R.D., Hoey T.B., Barrett B., and Prasojo O.A. (2021). Applications of Google Earth Engine in fluvial geomorphology for detecting river channel change. WIREs Water, 8(1), e21496, DOI: 10.1002/wat2.1496.

Busker T., De Roo A., Gelati E., Schwatke C., Adamovic M., Bisselink B., Pekel J., and Cottam A. (2019). A global lake and reservoir volume analysis using a surface water dataset and satellite altimetry. Hydrology and Earth System Sciences, 23(2), 669–690, DOI: 10.5194/hess-23-669-2019.

Chen Q., Zhao L., Lu J., Kuang G., Wang N., and Jiang Y. (2012). Modified two-dimensional Otsu image segmentation algorithm and fast realization. IET Image Processing, 6(4), 426–433, DOI: 10.1049/iet-ipr.2010.0078.

Condeça J., Nascimento J., and Barreiras N. (2022). Monitoring the storage volume of water reservoirs using Google Earth Engine. Water Resources Research, 58(3), e2021WR030026, DOI: 10.1029/2021WR030026.

de Albuquerque Teixeira A.M., Batista L.V., da Silva R.M., Freitas L.M.T., and Santo C.A.G. (2024). Dynamic monitoring of surface area and water volume of reservoirs using satellite imagery, computer vision and deep learning. Remote Sensing Applications: Society and Environment, 35, 101205, DOI: 10.1016/j.rsase.2024.101205.

Deng Z. and Zhang G. (2021). An improved forest fire monitoring algorithm with three-dimensional Otsu. IEEE Access, 9, 118367–118378, DOI: 10.1109/access.2021.3105382.

Duan Z. and Bastiaanssen W.G.M. (2013). Estimating water volume variations in lakes and reservoirs from four operational satellite altimetry databases and satellite imagery data. Remote Sensing of Environment, 134, 403–416, DOI: 10.1016/j.rse.2013.03.010.

Fan J.L. and Lei B. (2012). A modified valley-emphasis method for automatic thresholding. Pattern Recognition Letters, 33(6), 703–708, DOI: 10.1016/j.patrec.2011.12.009.

Fuentes I., Padarian J., van Ogtrop F., and Vervoort R.W. (2019). Comparison of surface water volume estimation methodologies that couple surface reflectance data and digital terrain models. Water, 11(4), 780, DOI: 10.3390/w11040780.

Gupta M.R., Jacobson N.P., and Garcia E.K. (2007). OCR binarization and image pre-processing for searching historical documents. Pattern Recognition, 40(2), 389–397, DOI: 10.1016/j.patcog.2006.04.043.

Hai D., Can D., and Tri D. (2020). Research and development of a tool to forecast water flow to Song Hinh Lake for flood forecasting in the lower reaches of the Ba River. Vietnam Journal of Hydrometeorology, 70–77, DOI: 10.36335/vnjhm.2020(710).

Hamoudzadeh A., Ravanelli R., and Crespi M. (2023). GEDI data within Google Earth Engine: preliminary analysis of a resource for inland surface water monitoring. The International Archives of the Photogrammetry, Remote Sensing and Spatial Information Sciences, XLVIII-M-1-2023, 131–136.

Härer S., Bernhardt M., Siebers M., and Schulz K. (2018). On the need for a time-and location-dependent estimation of the NDSI threshold value for reducing existing uncertainties in snow cover maps at different scales. The Cryosphere, 12(5), 1629–1642, DOI: 10.5194/tc-12-1629-2018.

Huang D.Y. and Wang C.H. (2009). Optimal multi-level thresholding using a two-stage Otsu optimization approach. Pattern Recognition Letters, 30(3), 275–284.

Jagadeesha C.J. and Palnitkar V.G. (1991). Satellite data aids in monitoring reservoir water and irrigated agriculture. Water International, 6(1), 27–37, DOI: 10.1080/02508069108686096.

Jianzhuang L., Wenqing L., and Yupeng T. (1991, June). Automatic thresholding of gray-level pictures using two-dimension Otsu method. International Conference on Circuits and Systems. IEEE, 325–327, DOI: 10.1109/ciccas.1991.184351.

Kakooei M. and Baleghi Y. (2020). Shadow detection in very high resolution RGB images using a special thresholding on a new spectral–spatial index. Journal of Applied Remote Sensing, 14(1), 016503–016503, DOI: 10.1117/1.jrs.14.016503.

Kwong I.H.Y., Wong F.K.K., and Fung T. (2022). Automatic mapping and monitoring of marine water quality parameters in Hong Kong using Sentinel-2 image time-series and Google Earth Engine cloud computing. Frontiers in Marine Science, 9, 871470, DOI: 10.3389/fmars.2022.871470.

Le C.T. and Hoang D.T. (2024). Phytoplankton species in Song Hinh Hydropower Reservoir, Phu Yen Province, Vietnam. African Journal of Biological Sciences, 6(9), 2246–2264, DOI: 10.33472/afjbs.6.9.2024.2246-2264.

Liu D. and Yu J. (2009). Otsu method and K-means. Ninth International Conference on Hybrid Intelligent Systems. IEEE, 1, 344–349, DOI: 10.1109/his.2009.74.

Liu T., Zhang X.N., Li Z., and Chen Z.Q. (2014). Research on the homogeneity of asphalt pavement quality using X-ray computed tomography (CT) and fractal theory. Construction and Building Materials, 68, 587–598, DOI: 10.1016/j.conbuildmat.2014.06.046.

Lua L. and Sun H. (2023). Dynamic monitoring of surface water areas of nine plateau lakes in Yunnan Province using long time-series Landsat imagery based on the Google Earth Engine platform. Geocarto International, 38(1), 2253196, DOI: 10.1080/10106049.2023.2253196.

Ma Y., Li Q., Zhou Y., He F., and Xi S. (2017). A surface defects inspection method based on multidirectional gray-level fluctuation. International Journal of Advanced Robotic Systems, 14(3), 1729881417703114, DOI: 10.1177/1729881417703114.

Ng H.F., Kheng C.W., and Lin J.M. (2016). A weighting scheme for improving Otsu method for threshold selection. Journal of Computers, 27(2), 12–21.

Otsu N. (1979). A threshold selection method from gray-level histograms. IEEE Transactions on Systems, Man, and Cybernetics, SMC-9(1), 62–66.

Pritam C. and Prasenjit A. (2010). Shoreline change and sea level rise along the coast of Bhitarkanika wildlife sanctuary, Orissa: An analytical approach of remote sensing and statistical techniques. International Journal of Geomatics and Geosciences, 1(3), 436–455.

Sha C., Hou J., and Cui H. (2016). A robust 2D Otsu's thresholding method in image segmentation. Journal of Visual Communication and Image Representation, 41, 339–351, DOI: 10.1016/j.jvcir.2016.10.013.

Shelestov A., Lavreniuk M., Kussul N., Novikov A., and Skakun S. (2017). Exploring Google Earth Engine platform for big data processing: Classification of multi-temporal satellite imagery for crop mapping. Frontiers in Earth Science, 5, 232994, DOI: 10.3389/feart.2017.00017.

Shen Y., Wang Y., Lv H., and Li H. (2015). Removal of thin clouds using cirrus and QA bands of Landsat-8. Photogrammetric Engineering & Remote Sensing, 81(9), 721–731, DOI: 10.14358/PERS.81.9.721.

Sherjah P.Y., Sajikumar N., and Nowshaja P.T. (2023). Quality monitoring of inland water bodies using Google Earth Engine. Journal of Hydroinformatics, 25(6), 432–450, DOI: 10.2166/hydro.2023.137.

Singh K.V., Setia R., Sahoo S., Prasad A., and Pateriya B. (2015). Evaluation of NDWI and MNDWI for assessment of waterlogging by integrating digital elevation model and groundwater level. Geocarto International, 30(6), 650–661, DOI: 10.1080/10106049.2014.965757.

Tamiminia H., Salehi B., Mahdianpari M., Quackenbush L., Adeli S., and Brisco B. (2020). Google Earth Engine for geo-big data applications: A meta-analysis and systematic review. ISPRS Journal of Photogrammetry and Remote Sensing, 164, 152–170, DOI: 10.1016/j.isprsjprs.2020.04.001.

Tong X., Pan H., Xie H., Xu X., Li F., Chen L., Luo X., Liu S., Chen P., and Jin Y. (2016). Estimating water volume variations in Lake Victoria over the past 22 years using multi-mission altimetry and remotely sensed images. Remote Sensing of Environment, 187, 400–413, DOI: 10.1016/j.rse.2016.10.012.

Truong M.T.N. and Kim S. (2018). Automatic image thresholding using Otsu's method and entropy weighting scheme for surface defect detection. Soft Computing, 22(2), 4197–4203, DOI: 10.1007/S00500-017-2709-1.

Valadão L.V., Cicerelli R.E., de Almeida T., Ma J.B.C., and Garnier J. (2021). Reservoir metrics estimated by remote sensors based on the Google Earth Engine platform. Remote Sensing Applications: Society and Environment, 24, 100652, DOI: 10.1016/j.rsase.2021.100652.

VanDeWeghe A., Lin V., Jayaram J., and Gronewold A.D. (2022). Changes in large lake water level dynamics in response to climate change. Frontiers in Water, 4, 805143, DOI: 10.3389/frwa.2022.805143.

Vasanthi A. and Joshitha K.L. (2024). Water Body Detection Utilizing NDWI, NDVI and NMDWI Indices in SEN-12 Spectral Imagery. First International Conference on Electronics, Communication and Signal Processing (ICECSP). IEEE, 1-5, DOI: 10.1109/icecsp61809.2024.10698263.

Vu Anh Minh, Dinh Nhat Quang, Nguyen Xuan Tinh, and Lars Ribbe. (2024). Spatio-temporal dynamics monitoring of surface water bodies in Nhat Le River Basin, Vietnam, by Google Earth Engine. Journal of Water and Climate Change, 15(3), 1262, DOI: 10.1080/10106049.2023.2253196.

Wang Q., Liu D., Yang H., Yin J., Bin Z., Zhu S., and Zhang Y. (2017). Comparative study on the water index of MNDWI and NDWI for water boundary extraction in eutrophic lakes. Advances in Geosciences, 7(6), 732–738, DOI: 10.12677/ag.2017.76074.

Wang R., Pan L., Niu W., Li R., Zhao X., Bian X., and Chen T. (2021). Monitoring the spatiotemporal dynamics of surface water body of the Xiaolangdi Reservoir using Landsat-5/7/8 imagery and Google Earth Engine. Open Geosciences, 13, 1290–1302, DOI: 10.1515/geo-2020-0305.

Xing W., Guo B., Sheng Y., Yang X., Ji M., and Xu Y. (2022). Tracing surface water change from 1990 to 2020 in China's Shandong Province using Landsat series images. Ecological Indicators, 140, 108993, DOI: 10.1016/j.ecolind.2022.108993.

Xu R., Zhao S., and Ke Y. (2020). A simple phenology-based vegetation index for mapping invasive spartina alterniflora using Google Earth engine. IEEE Journal of Selected Topics in Applied Earth Observations and Remote Sensing, 14, 190–201, DOI: 10.1109/jstars.2020.3038648.

Xu X., Xu S., Jin L., and Song E. (2011). Characteristic analysis of Otsu threshold and its applications. Pattern Recognition Letters, 32(7), 956–961, DOI: 10.1016/j.patrec.2011.01.021.

Yao F., Wang J., Wang C., and Crétaux J.F. (2019). Towards the continuous monitoring of the extreme events through satellite radar altimetry observations. Remote Sensing of Environment, 232, 111210, DOI: 10.1016/j.jhydrol.2021.126870.

Zhang J. and Hu J. (2008). Image segmentation based on 2D Otsu method with histogram analysis. International Conference on Computer Science and Software Engineering. IEEE, 6 , 105–108, DOI: 10.1109/CSSE.2008.206.

Zhang X. and Liu X. (2022). Comparative study on extraction of banded water and surface water in urban area based on MNDWI. 3rd International Conference on Geology, Mapping and Remote Sensing (ICGMRS), Zhoushan, China. IEEE 33–40, DOI: 10.1109/ICGMRS55602.2022.9849259.

Zhang Y., Du J., Guo L., Fang S., Zhang J., Sun B., Mao J., Sheng Z., and Li L. (2022). Long-term detection and spatiotemporal variation analysis of open-surface water bodies in the Yellow River Basin from 1986 to 2020. Science of The Total Environment, 845, 157152, DOI: 10.1016/j.scitotenv.2022.157152.

RESEARCH PAPER

MODELING FUTURE CARBON STOCK PREDICTIONS BASED ON LAND USE

Westi Utami[1,2*], Catur Sugiyanto[3], Noorhadi Rahardjo[4], Nurhadi[5]

[1]Doctoral Program of Environmental Science Universitas Gadjah Mada, Jl. Teknika Utara, Yogyakarta, 55284, Indonesia
[2]Department of Land Management Sekolah Tinggi Pertanahan Nasional, Jl. Tata Bumi No. 5, Yogyakarta, 55293, Indonesia
[3]Faculty of Economics and Bussiness Universitas Gadjah Mada, Jl. Sosio Humaniora, Yogyakarta, 55281, Indonesia
[4]Faculty Geography Universitas Gadjah Mada, Jl. Kaliurang, Yogyakarta, 55281, Indonesia
[5]Faculty of Social Science and Political Science, Universitas Gadjah Mada, Jl. Sosio Yusticia No.1, Yogyakarta, 55281, Indonesia

***Corresponding author:** westiutami@mail.ugm.ac.id

Received: October 18th 2024 / Accepted: April 25th 2025 / Published: June 30th 2025
https://doi.org/10.24057/2071-9388-2025-3684

ABSTRACT. The considerable influence of extensive land use change on the increasing levels of carbon emissions has significant implications for the occurrence of a multitude of disasters. The objective of this research is to develop a predictive model of future carbon stocks based on land use type. The data set includes land use maps from 2014, 2018, and 2022, obtained through visual interpretation of Pleiades data and associated driving variables, including socio-economic, locational, physical, land, and spatial planning factors. To predict land use in relation to future carbon stock values, the Multilayer Perceptron Neural Network Markov Chain (MLPNN-MC) algorithm was employed. Research related to this modeling is capable of producing an accuracy rate of 98%. The results of the prediction demonstrate that by 2034, there will be a reduction in the area of land used with high to low carbon stock, with a decrease of 153.2 ha, which equates to a reduction in carbon stock of 9,050 tonnes C/ha. To reduce carbon emissions, it is essential to implement policies that regulate land use change, optimize forest management, and conserve mangrove ecosystems. The monitoring and prediction of future carbon stocks plays a pivotal role in climate change mitigation, enabling more targeted and measurable actions to be taken.

KEYWORDS: carbon stock, climate change, land use, built-up expansion, machine learning, prediction modeling

CITATION: Utami W., Sugiyanto C., Rahardjo N., Nurhadi (2025). Modeling Future Carbon Stock Predictions Based On Land Use. Geography, Environment, Sustainability, 2 (18), 102-113
https://doi.org/10.24057/2071-9388-2025-3684

ACKNOWLEDGEMENTS: The author wishes to express gratitude to the fieldwork participants from the Faculty of Geography, Universitas Gadjah Mada. In addition, the author would like to thank the government, the Kulon Progo Regency Land Office, and the Geospatial Information Agency for providing secondary data.

Conflict of interests: The authors reported no potential conflict of interests.

INTRODUCTION

The occurrence of climate change disasters on a massive scale in various countries represents a significant threat to the sustainability of human life and the realization of sustainable development (Gao et al. 2024; Lin et al. 2024). The impact of global warming, exemplified by the occurrence of extreme temperatures from 2023 to 2024 in Southeast Asia and South Asia, has implications for the cessation and disruption of various community activities. The occurrence of temperatures reaching 44°C in India and up to 37°C in parts of Indonesia is a detrimental impact of global warming (Meteorological Climatological and Geophysical Agency/MCGA 2024). The World Meteorological Organization (WMO) and the MCGA have identified Asia, including Indonesia, as a region that is likely to experience a significant increase in the frequency and intensity of disasters associated with global warming (Dong et al. 2021). In addition to the effects of extreme temperatures, the consequences of climate change include the loss of land, the disappearance of small islands, an increase in the frequency of hydrometeorological disasters, the decline of biodiversity, an expansion of the range of diseases, the disruption of social, economic, cultural activities, and an intensification of ecosystem damage (Sutrisno et al. 2021; Abbass et al. 2022; Laino and Iglesias 2023; Kim et al. 2024).

A number of previous studies have demonstrated that massively occurring climate change disasters in various countries are significantly influenced by alterations in the value of terrestrial carbon (Liu et al., 2023; Zhang et al., 2024) and the combustion of energy and fuel derived from fossils (Hu et al., 2024; Zhang et al., 2024). The study conducted by Achmad et al. (2024); Nakakaawa et al. (2011) explained that forest ecosystems/vegetation in various countries have an important role in maintaining the global carbon (C) balance, which is estimated at 80% of aboveground C stocks and 20% of belowground C stocks. In this context, it is crucial to assess and monitor the availability of terrestrial carbon stock through land use data, as well as to assess and analyze the relationship between land use patterns and carbon stock (Liu et al., 2023; Wu et al., 2024). In addition,

further research is required on the modeling of future carbon stock predictions, as a basis for estimating the amount of carbon stock lost. A measured approach to the amount of carbon stocks in the future is an important part of formulating various targeted and appropriate mitigation policies to reduce the adverse effects of climate change disasters.

The high rate of land use change, particularly the reduction of vegetation cover, the decline of forest areas and mangroves, has significant implications for the increase in carbon emissions released into the atmosphere (Zhang et al., 2023; Chinembiri et al., 2023; Halim et al., 2023). The increasing demand for land for development and to fulfil socio-economic needs has implications for declining levels of carbon stock (Raqeeb et al., 2024). Furthermore, government initiatives to stimulate economic expansion through the expansion of mining, industrial, trade, and service areas, as well as accelerated infrastructure development, have also precipitated increased land use change, decreased vegetation cover, and resulted in reduced forest and mangrove areas in various countries (Cortés Arbués et al., 2024; Wu et al., 2024; Yusuf, 2021). Such alterations in land use have a direct impact on the carbon storage capacity of vegetation and plants, resulting in shifts in ecosystem functionality and alterations in soil carbon storage (Aneva et al., 2020; Segura et al., 2024).

Land use is not only related to economic conditions, but also plays an important role in social and environmental sustainability (Luo et al., 2024). Monitoring of land use change and land use prediction modeling are very important for determining global carbon stocks, providing land use restrictions and guidance for land use planning to maintain carbon stock balance (Dong, 2024; Huang et al., 2024; Zhang et al., 2024). However, based on previous literature review, studies on predicting future carbon stocks are still limited. So far, prediction analysis has been reviewed by Alam et al. (2021); Dey et al. (2021); Girma et al. (2022), who discuss predictions of built-up and non-built-up land use in relation to urban sprawl. While several studies analyzing carbon stock predictions based on land use, such as Dong (2024), were conducted without the use of driving force variables, the study by Wu et al. (2024) was limited to the use of economic and geographic variables, and the study by Shao et al. (2023) was limited to the use of physical and socio-economic factors. In addition to the limited use of drivers, several previous studies, namely Xu et al. (2024); Shao et al. (2023), still used medium resolution (Landsat) and low resolution (NOAA) satellite imagery as data sources. The use of limited driving forces, data sources from low-resolution satellite imagery, and the use of inappropriate algorithms may have implications for the inaccuracy of carbon stock prediction (Almubaidin et al., 2024; Bao et al., 2021; Jakariya et al., 2020; Ma et al., 2024; Meliho et al., 2023). The limitations and inaccuracies of predictive data are feared to lead to inaccurate policy-making in climate change mitigation. This research aims to address the existing gap in modeling future carbon stock predictions using more accurate and detailed data sources, comprehensive driving factors, and compatible algorithms through the implementation of the Multilayer Perceptron Neural Network Markov Chain (MLPNN-MC) algorithm. The MLPNN-MC algorithm represents the latest hybrid model/model development that is capable of generalizing each simulation and modeling multiple transitions simultaneously due to its three-layer structure comprising the input, output, and hidden layers (Mishra et al., 2014). The utilization of this algorithm has been demonstrated to yield highly accurate results, with accuracies ranging from 85% to 93%, as evidenced in several studies conducted Girma et al. (2022); Mishra and Rai (2016); Soni et al. (2022).

This carbon stock prediction modeling was conducted in a rural area affected by the national strategic project of constructing Yogyakarta International Airport (YIA). Initially, the area exhibited a high degree of dense vegetation cover, resulting in substantial carbon stock accumulation. However, substantial infrastructure development has led to significant alterations in land use and carbon storage. To date, there has been a paucity of research examining the relationship between infrastructure development, land use changes, carbon stock storage, and the modeling of future carbon stock predictions. The present study aims to address this research gap by employing advanced data analysis techniques, namely remote sensing satellite imagery and machine learning algorithms, to develop a more sophisticated and precise prediction model. The objective of this study is to formulate a prediction model for future land use in relation to carbon stocks in areas affected by the construction of YIA. To this end, the study will utilize more detailed data sources, more comprehensive driving variables, and the apply the MLPNN-MC algorithm to produce more accurate land use predictions to carbon stocks.

MATERIALS AND METHODS

Study Area

The research was conducted in the area affected by the construction of the YIA. The research methods employed included the modeling of predicted changes in carbon stock in 2026, 2030, and 2034. The construction of this infrastructure development project, which encompasses an area of approximately ±587 ha, has the potential to result in increased land use change. The research site encompasses 26 villages situated within Kulon Progo Regency, Yogyakarta, Indonesia. The study area encompasses Temon subdistrict (15 villages), Wates subdistrict (8 villages), and parts of Panjatan subdistrict (which includes 3 villages). The spatial distribution of the study area is illustrated in Fig. 1.

Data and data sources

The data presented in this study encompasses both dependent data, which pertains to multitemporal land use, and independent data, which encompasses driving forces. Multitemporal land use maps were obtained from Pleiades, a 0.5 m very high resolution satellite (Melis et al., 2021) in 2014, 2018 and 2022. The selection of images was based on the development process of the YIA, with 2014 being the initial state before the airport was built, 2018 being the land clearing/initial development stage, and 2022 being the post-development stage when the airport was operational. In addition to the consideration of the airport development process, the selection of satellite imagery with a 4-year/short period is capable of representing changing conditions with greater detail and of reflecting very dynamic driving forces. This will have a significant effect on the quality and accuracy of carbon stock prediction modelling. Image interpretation was carried out visually, as this method can provide a higher level of accuracy compared to maximum likelihood, random forest or other methods (Schepaschenko et al., 2019). The land use classification is divided into 2 (two), namely 1) high carbon stock reserve land consisting of mangroves, plantation, green belts, mixed gardens and dry land/rice fields; 2) low carbon stock land consisting of water bodies, infrastructure, rice fields, open land and built-up land. In order to determine the level of accuracy of land use, a sampling test was conducted where the number

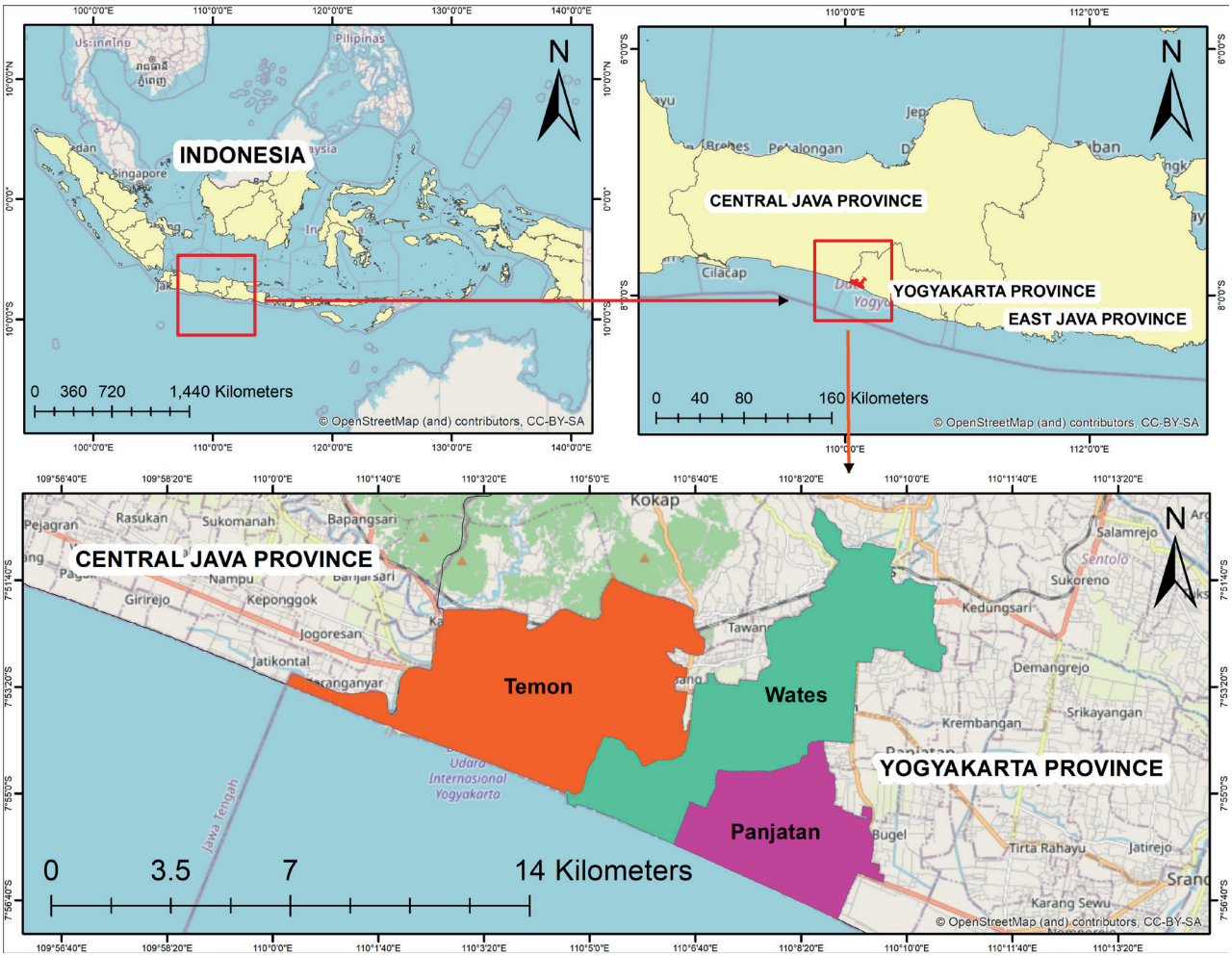

Fig. 1. Study area

of samples was determined using the Slovin formula with stratified random sampling. The number of land use samples in this study was 441 points, and from the results of the accuracy test in the field, there were 33 sample points that were less appropriate. Therefore, the accuracy test for land use can be formulated as follows (Eq. 1):

$$Accuracy\ value = \frac{Number\ of\ Correct\ Land\ Use\ Samples}{Total\ Land\ Use\ Samples} \times 100\% \quad (1)$$

Based on these calculations, the results of land use interpretation through Pleiades are able to produce a very high accuracy of 92%, so this data is eligible for further analysis. To determine the level of carbon stock by land use type, this study refers to the International Council for Local Environmental Initiative (ICLEI 2022) guidelines as described in Table 1. Based on Table 1, mangroves have the highest carbon sequestration capacity of 120, while the lowest are water bodies and infrastructure with a carbon sequestration value of 0.

This study formulates independent data in the form of driving forces, drawing from previous literature reviews and pre-field studies. These studies analyze the physical aspects, policies, land conditions, and socio-economic aspects of the community to derive more comprehensive driving forces. The driving forces used include socio-economic aspects, including population, type of work, original village income, and tax/levy sharing. Furthermore, the analysis encompasses physical aspects such as relative relief, flood vulnerability, landslides, drought, and tsunami vulnerability. Location-specific variables include city centers, airports, roads, industry, educational facilities, and health centers. This study also uses land and spatial planning aspects, including land value zones, land rights status, protected areas, and agricultural cultivation areas. Driving forces factors and data sources can be described in Table 2.

Methods

Driving Forces Analysis Through Spatial Regression

The driving forces variables utilized in this study encompass 21 variables, with the objective of ascertaining

Table 1. Land use reclassification based on Greenhouse Gas (GHG) Coefficient

Land Use	GHG	Class	Land Use	GHG	Class
Infrastructure, water body	0	Low	Dryland farming/fields	10	High
Rice fields	2		Green space/shrub	30	
Open fields	2.5		Plantation/Mixed garden	63	
			Mangrove	120	

Sources: International Council for Local Environmental Initiatives/ICLEI 2022

Table 2. Data and Data Sources of Driving Forces

Variables	Data Sources	Variables	Data Sources
Population, type of work, original village income, and tax/levy sharing	Secondary data from 26 villages/ sub-districts	Land value zones, land rights status,	Land Office data
Flood vulnerability, landslides, drought, and tsunami vulnerability	Data the Regional Disaster Management Agency in 2022	City centers, roads, airports, industry, educational facilities, and health centers	Pleiades imagery & Local Government
Relative Relief	National Digital Elevation Model	Protected areas, and agricultural cultivation areas	Detailed Spatial Planning Map

Sources: Data Analysis 2024

the driving forces that exert a substantial influence. These variables are subjected to spatial regression analysis, a method that has been selected on the basis of its capacity to accommodate spatial weight, thereby ensuring a more accurate representation of the prevailing conditions of dependent and independent data in the field (Caraka and Yasin 2017; Hasbi, et al. 2014). The determination of significant driving forces at the initial stage is of paramount importance to ensure the modeling results attain optimal accuracy. The Eq. 2 for determining spatial regression is outlined below.

$$Y = a + \beta_1 x_1 + \beta_2 x_2 + \ldots \beta_n x_n + \beta_{n+1} autocov \quad (2)$$

where x_i *(i= 1,2,3,…, n)* - driving forces, $\beta_{i\,(i=\,1,2,3,\ldots,\,n)}$ - regression coefficient, *n* - amount of data, *Y* - dependent variable, $x_{1,\ldots,n}$ - independent variable.

Scenario Carbon Stock Prediction

The modeling of carbon stock prediction is based on land use type and utilizes the MLPNN-MC algorithm. The MLPNN-MC algorithm was selected due to its capacity to analyze very complex data sets (Soni et al., 2022). A key element of this modeling is change analysis, which involves the identification of areas that undergo change and remain constant over a specified time period. In the subsequent stage, the driving forces factors are processed through the Land Change Modeler (LCM) multilayer perceptron to generate a potential transition map and to identify the relevant driving forces. In the subsequent stage, the Markov chain is utilized to predict future changes based on previous changes. The Markov chain process according to Memarian et al. (2012) can be explained in the Eq. 3.

$$F_x\left(X\left(t_{n+1}\right) \le \{X_{n+1} \middle| X\left(t_n\right)\} = X_n, X\left(t_{n-1}\right) = . \right.$$
$$x_{n-1}, \ldots, X\left(t_1\right) = x_1\Big) = \left(X\left(t_{n+1}\right) \le \right. \quad (3)$$
$$\left.\left(x_{n+1} \middle| Xt_n\right)\right) = x_n$$

where *X(t)* signifies with the marcov chain process at time *(t)*, t_n is the current time period, (t_{n-1}) defines the previous time periode, and (t_{n+1}) represent the future periode. The transition probability from one state *(i)* to another *(j)* by Memarian et al. (2012) can be explained the Eq. 4.

$$P_{i,j} = P_r\left(X[k+1] = \{j | X[k]\} = i\right) \quad (4)$$

where *X[k]* denotes the states *{x1,x2,x3,....}* between *i* and *j*. With these conditions, the probability matrix according to Memarian et al. (2012) is formulated as follows (Eq. 5):

$$\begin{bmatrix} P_{1,1} P_{1,2} \ldots P_{1,n} \\ P_{2,1} P_{2,2} \ldots P_{2,n} \\ \ldots \\ \ldots \\ P_{n,1} P_{n,2} \ldots P_{n,n} \end{bmatrix} \quad (5)$$

In this study, the independent variable of the carbon stock level is based on the type of land use over a 4-year period (2014, 2018, and 2022) with the consideration that the resulting change matrix is more detailed. The accuracy and validation tests in this study were carried out by creating a simulation of carbon stock predictions in 2022 based on the 2014 and 2018 maps and key drivers. The predicted carbon stock based on land use type in 2022 was then compared and analyzed with the carbon stock based on land use type in 2022. The Eq. 6 for determining the accuracy test is as follows:

$$Accuracy Test of Carbon Stock Prediction = \frac{Value\ of\ existing\ in\ 2022}{Value\ of\ Prediction\ in\ 2022} \times 100\,\% \quad (6)$$

This modeling prediction accuracy test is very important to ensure that the data, algorithms, and processes carried out meet accuracy standards. The prototype model that has passed the accuracy test is utilized as a foundation for the compilation of predictions concerning carbon stock levels in 2026, employing the 2018 and 2022 maps and driving forces factors. Furthermore, to produce predictions for 2030, data from 2022 and 2026 are utilized, and the same process is repeated to produce predictions for 2034, 2026 and 2030. Additionally, the study considers relevant driving forces. For a more detailed understanding of the research stages, refer to the research flow chart illustrated in Fig. 2.

RESULTS AND DISCUSSION

Multitemporal Land Use Map Database

Pleiades image interpretation results show that the most dominant land use type in 2018 and 2022 in the study area is in the form of: rice fields and built-up land, where both types of land use have very low carbon stock content (Singh et al., 2024). Conversely, land use in the form of mixed gardens and mangrove forests, which possess a high carbon stock capability, is only found in a very small area. The spatial distribution of land use data in 2018 can be explained in Fig. 3a, while in 2022 in Fig. 3b.

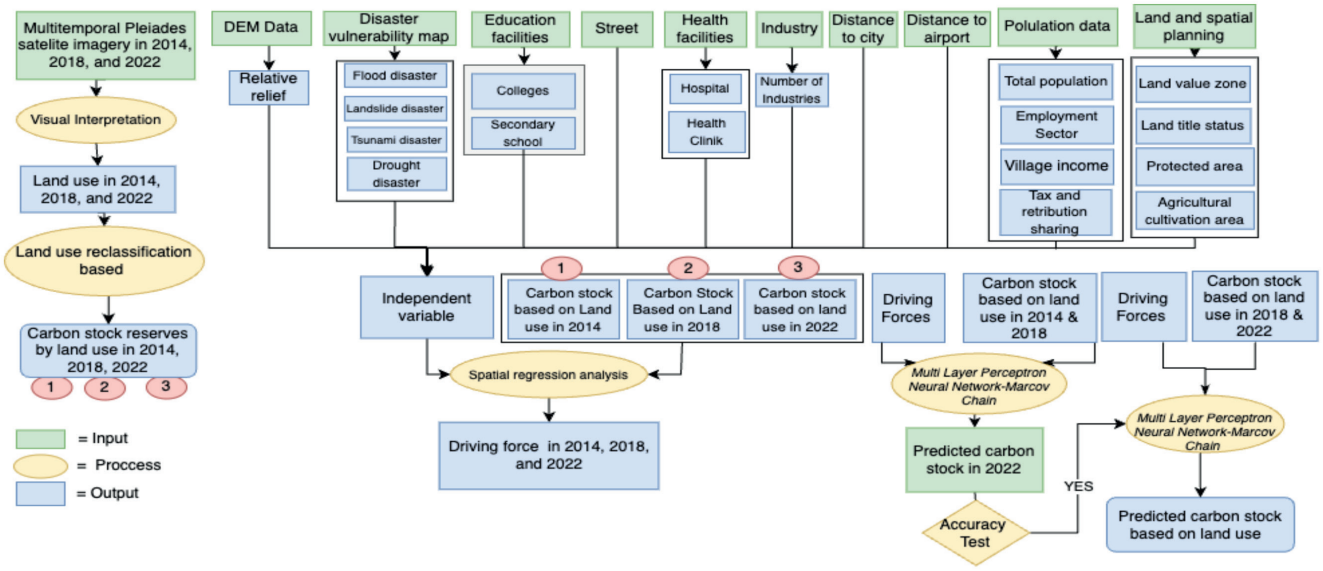

Fig. 2. Research flowchart

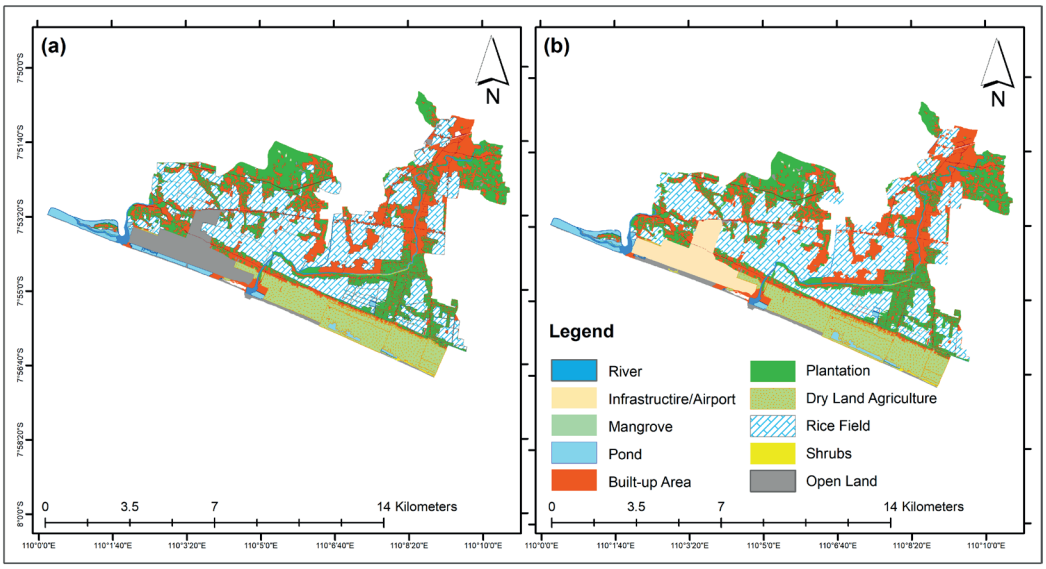

Fig. 3. (a) Land Use Map 2018; (b) Land Use Map 2022

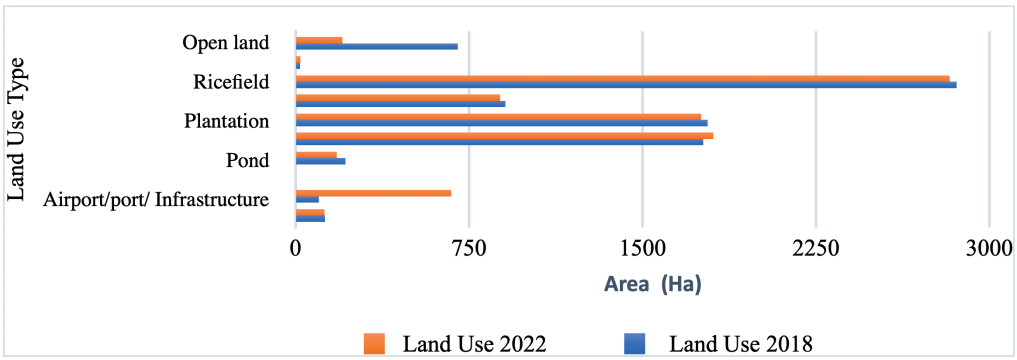

Fig. 4. Land Use Area in 2018 and 2022 (Source: data analysis 2024)

Based on Fig. 3, it shows that the development of YIA is one of the triggers for the increase in land use change. Airport development not only changes the land used for airports but also has implications for changing land for infrastructure development to support airports, land for settlements, and economic activities. Data on changes in land use areas from 2018 to 2022 can be explained in Fig. 4.

As illustrated in Fig. 4, there has been a notable decline in land use from areas with high carbon stock. This is evidenced by a reduction in plantations by 28 ha and dryland farming by 23 ha. During this period, there was also an increase in land use with low carbon stock value, namely 272 ha of infrastructure and 43 ha of built-up area. The decrease in land with high carbon stock and the increase in land use with low carbon stock will undoubtedly further contribute to the emission of carbon. This research reinforces the findings of Verma et al. (2020) that development tends to convert land from high carbon stock to low carbon stock land, a condition that certainly contributes to increasing carbon emissions.

Driving Forces Variables

The process of carbon stock alteration in response to land use in a given area is influenced by a multitude of

complex and dynamic variables. It is imperative to ascertain the most significant driving forces to ensure the accuracy of the resulting prediction model. To this end, spatial regression is employed to verify the impact of these driving factors on land use changes. The outcomes of the spatial regression accuracy test, which delineate the relationship between driving forces and carbon stock changes based on land use types, are delineated in Table 3.

The findings of the spatial regression analysis in Table 3 demonstrate that the driving forces factor employed exerts a profound influence on alterations in land utilization in relation to carbon values, as evidenced by the R-square value of 0.83 or 83%. Moreover, the analysis reveals that the most suitable model, as indicated by the highest R-square value and the lowest Akaike Information Criterion (AIC) value, is the spatial lag model. The distribution of significance values between variables is elucidated in Table 4.

The findings of the analysis demonstrate that the presence of driving factors with a probability value of less than 0.05 is indicated, including city centers, airports, roads, industries, and relative relief. These driving factors are associated with a decrease in carbon stocks. The resultant increase in land conversion is from mixed gardens/ plantations and dry land agriculture to built-up land and infrastructure. The closer an area is to these factors (airport, city centers, roads and industries), the higher the carbon stock decline. Conversely, the relative relief factor is one of the factors that can suppress the reduction of carbon stocks. Areas with high relative relief tend not to have massive land use change, which correlates with the high level of carbon stock in the area. And vice versa: the flatter the relative relief, the greater the tendency for the carbon stock to decrease. The findings of this study support previous research that the variables influencing land use change are complex and highly dynamic (Long and Yan, 2012; Mekonnen et al., 2022). This study also supports research by Rani et al. (2023); Xu et al. (2024) that the use of comprehensive variables that have a large influence on the rate of land use change is very important in developing land use forecasts. The limitations of the driving forces variables used and their lack of influence have implications for the inaccuracy of carbon stock predictions. The spatial distribution of driving force variables in this study is illustrated in Fig. 5.

Transition Potential Modelling

The training of the machine learning (MLP) network model was conducted using the Land Change Modeler, with the land use change triggers consisting of five variables and land use maps from 2014 and 2018. The results of the model sensitivity analysis are presented in Table 5. During the specified period, the model demonstrated a high level of accuracy with all variables, reaching an accuracy of 87.9%. The results of the sensitivity analysis, as elucidated in Table 5, demonstrate that the predominant driving forces are airports, while relative relief is the least significant.

Table 3. Spatial Regression Accuracy Test of Carbon Stock Reserve Variables in 2018

Model	R-square	AIC	Moran	Lagrange Lag	Lag error	Lag	Heteroke dasticity	Spatial Dependency
Classic	0.760553	311.175	0.00854	0.04880	0.29756	SARMA		
Spatial Error	0.827054	307.582				0.03642	0.02661	0.05802
Spatial Lag	0.834779	306.889					0.21018	0.01216

Source: Data Analysis, 2024

Table 4. Spatial Regression Analysis of Carbon Stock Reserve Variables in 2022

Variable	Coefficient	Std.Error	z-value	Probability
W_KRB.	0.622324	0.148483	4.19123	0.00003
CONSTANT	-542.544	148.27	-3.65915	0.00025
Protected	0.214102	1.4342	0.149283	0.88133
Agriculture	-0.737243	0.952464	-0.774038	0.43891
Road access	-0.00590488	0.00406924	-1.4511	0.14675
Flood	-0.294431	0.294713	-0.999045	0.31777
Land title	-9.38065	9.31859	-1.00666	0.31410
Relief	0.593635	0.273385	2.17143	0.02990
Land val_	2.32608e-05	6.50807e-05	0.357415	0.72078
City	36.9229	11.2262	3.28899	0.00101
Industry	104.1	71.4647	1.45667	0.05021
Airport.	31.4277	16.3897	1.91752	0.05017
Employment	5.29773	2.14639	2.46821	0.0135
Population	0.0193318	0.0168305	1.14861	0.25072

Source: Data Analysis, 2024

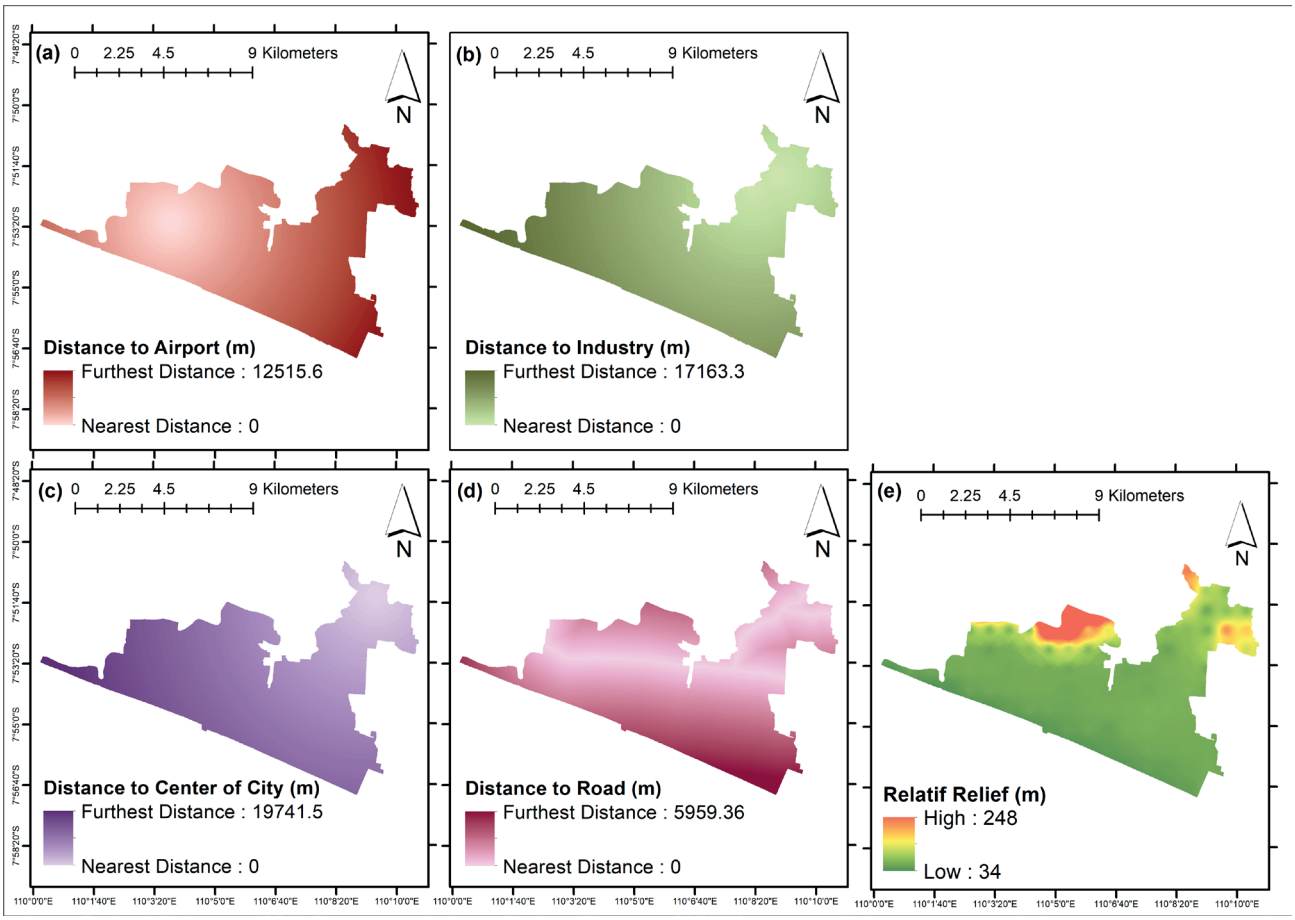

Fig. 5. Maps of drivers of carbon stock change based on land use: (a) distance to airport, (b) distance to industry, (c) distance to city center, (d) distance to road, (e) relative relief

Table 5. Transition sub model: Sensitivity of the model to forcing independent variables to be constant

a. Forcing a single independent variable to be constant			
Model	Accuracy (%)	Skill Measure	Influence Order
With all variables	87.94	0.7588	
Var 1 constant/city center	87.48	0.7496	4
Var 2 constant/airport	68.07	0.3613	1 (most influential)
Var 3 constant/industry	84.96	0.6992	2
Var 4 constant/road access	86.83	0.7366	3
Var 5 constant/relief	88.23	0.7646	5 (least influential)
b. Backwards stepwise constant forcing			
With all variables	87.94	0.7588	
Step 1: var.[5] constant	88.23	0.7646	
Step 2: var.[5,1] constant	88.02	0.7604	
Step 3: var.[5,1,4] constant	87.10	0.7420	
Step 4: var.[5,1,4,3] constant	76.48	0.5296	
c. Model skill breakdown by transition and persistence			
Class		Skill Measure	
Transition: High carbon to low carbon		0.7066	
Persistence: High Carbon		0.8109	

Source: data analysis through land change modeler

Prediction of carbon stock based on land use change and model validation

The validation of the carbon stock level change prediction model was conducted through a comparison of the results of the 2022 carbon stock level prediction with the classified carbon stock map, which underwent a rigorous testing process for accuracy in 2022. The 2022 carbon stock prediction map was derived from the 2014 and 2018 maps, along with the driving forces. The results of the analysis are illustrated in Fig. 6, which presents the findings on the suitability of patterns, spatial distribution, and visualization between the 2022 carbon stock prediction map (Fig. 6a) and the 2022 classified carbon stock map (Fig. 6b).

As demonstrated in Fig. 6, the predicted carbon stock map in 2022 exhibits a comparable pattern, shape, and area to the existing carbon stock map in 2022. The area with high carbon stock predicted was 2,752 ha, which is consistent with the existing carbon stock value of 2,689 ha. Subsequent to this, an accuracy test was conducted utilizing the confusion matrix, yielding an accuracy test result of 98%, signifying very high accuracy. The findings of this accuracy test demonstrate the viability of the algorithm, method, and variables employed in the development of carbon stock predictions in 2022 for application in the prediction of carbon stock based on land use types in 2026, 2030, and 2034. The land use prediction modeling approach utilizing a MLPNN-MC algorithm demonstrated an exceptional degree of accuracy, with an accuracy test reaching 98%. This condition is influenced by the supervised backpropagation, which is capable of more accurately generalizing the transition of land use change. Furthermore, this algorithm has the additional benefit of being able to perform supervised learning transitions in a more directed manner through the artificial neural network in MLPNN. This research corroborates the findings of previous studies on the advantages of MLPNN-MC in analyzing land use prediction modeling (Mirsanjari et al., 2021; Ren et al., 2019; Tariq et al., 2022). The high level of accuracy of land use prediction is also influenced by the data source for preparing detailed land use maps, as well as the use of complex driving forces variables. This research lends support to the assertion that the utilization of precise data sources is a fundamental element in the generation of accurate forecasts (James et al., 2020; Utami et al., 2024a). The Pleiades satellite images, which are capable of very high resolution, are able to produce highly detailed land use data, which in turn enables the generation of accurate predictions (Pu et al. 2018).

Modeling Carbon Stock Prediction Based on Land Use

The uncertainty of future land use represents a significant challenge for land management policy, with the potential for inappropriate policies to result in considerable environmental damage. The environmental damage caused by inappropriate land use is extensive and includes land degradation, water pollution, loss of biodiversity, damage to various ecosystems, and an increase in the frequency of natural disasters such as floods, landslides, droughts, and fires (Karamesouti et al., 2015; Peng et al., 2023). Furthermore, the uncertainty of land use in relation to the condition of carbon stock in the future also has implications for increasing carbon emissions, which have an impact on increasing climate change disasters (Mason et al., 2023; Hayes et al., 2023; Xu et al., 2024; Yan et al., 2024). The analysis of land use predictions in relation to carbon stock is a crucial aspect to consider, given the high level of disaster vulnerability in the study area, as evidenced by the prevalence of floods, landslides, droughts, abrasion, and tidal waves (Kulon Progo Regency, 2023).

A model was constructed to predict land use in relation to carbon stock value in 2026, based on land use maps from 2018 and 2022, as well as variables that trigger land use change. The results of the modeling exercise for the year 2026 are presented in Fig. 7a. The multitemporal land use data from the preceding period and the driving forces variables were then employed to construct a prediction map of land use in relation to carbon stocks for the years 2030 and 2034, as illustrated in Figs. 7b and 7c. In addition, the outcomes of the multitemporal land use prediction modeling can be presented in Fig. 7d.

The carbon stock prediction modeling as shown in Fig.7a, b, c provides an overview of the carbon stock condition in 2026, 2030, and 2034, which tends to decrease. The decline in carbon stocks is attributable to alterations in land use, with a transition from high carbon stock land in plantation areas and mixed gardens to low carbon stock (built-up land/settlement) in the northern part of the study area. In the southern part of the study area, the shift from dryland farming to ponds led to a reduction in carbon stocks. The findings of the predictive modeling calculation through MLPNN-MC demonstrate that in 2026, the land utilization exhibiting high carbon stock potential (i.e. plantations, dryland farming, green space) amounts to 2,637 ha, representing a decline from 2,689 ha in 2022. The analysis indicates that, by 2026, there will be a decrease in land from high to low carbon stock of 52 Ha, equivalent to

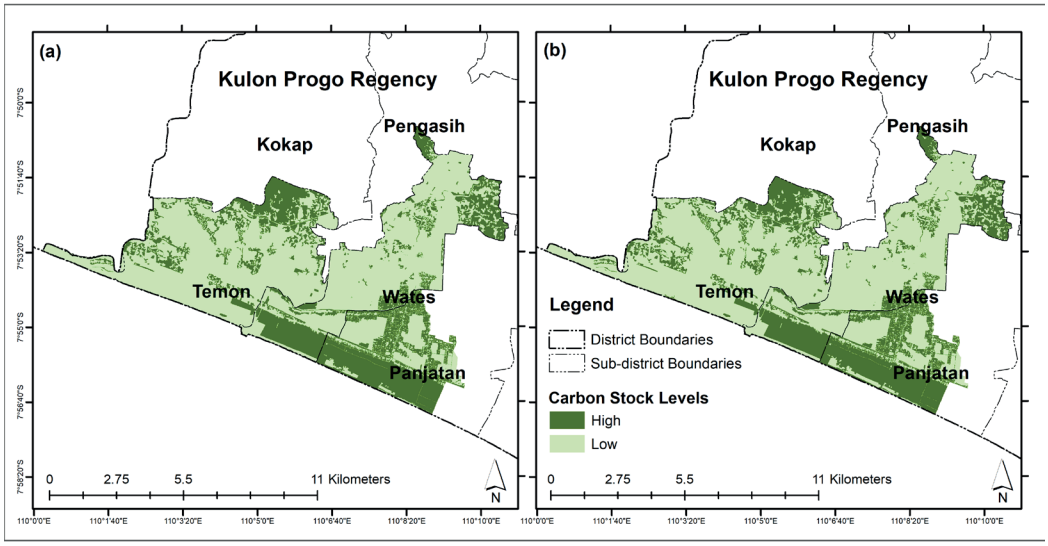

Fig. 6. Comparison of map : (a) Prediction map of carbon stock; (b) Maps of carbon stock level

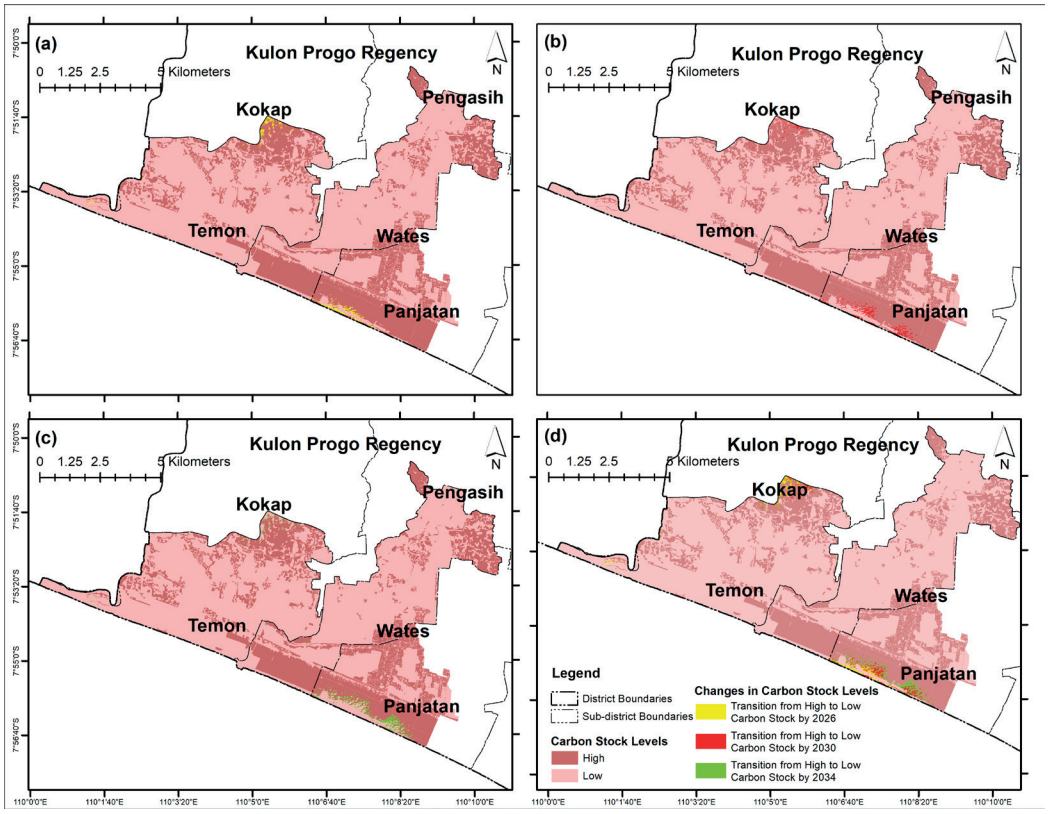

Fig. 7. Map of predicted carbon stock reserve levels by land use year (a) 2026; (b) 2030; (c) 2034; (d) multitemporal

3,050 tonnes C/ha. The reduction of carbon stocks has been demonstrated to result in an increase in carbon emissions, which in turn has been shown to lead to an escalation in climate change disasters. The increase in development and demand for land is undeniable, especially in developing countries, including Indonesia (Li et al., 2023; Liu et al., 2021). Data on the multitemporal decline in the area of high carbon stock land use in the study area are described in Fig. 8.

The findings of this study indicate that the decline in land area with high carbon stock within the study area between 2022 and 2034 is projected to amount to 153.4 Ha. The decline in carbon stock value from 2022 to 2034 is projected to amount to 9,665 tonnes C/ha, in accordance with the greenhouse gas coefficient established by ICLEI (2022). This transformation is primarily driven by the demand for land for airport development and the provision of land to support economic activities (trade and services). Following the development of the airport, a further decline in carbon stocks was observed in the study area. This accumulation of carbon stock decline, if mitigation measures are not implemented, will undoubtedly exacerbate the impact of global warming. The implementation of policies to protect forest areas, mangrove areas, and reforestation policies in green open space areas are crucial elements in maintaining the balance of carbon stocks (van Bijsterveldt et al., 2020; Dajam and Eid, 2024; Raqeeb et al., 2024; Alexandri et al., 2024).

The empirical evidence presented in this study indicates that by the year 2034, there will be a notable expansion in built-up land (settlements, trade and services) and a significant increase in the number of ponds in green belt areas, fields, dryland agriculture, plantations, and mixed gardens, with an estimated total area of 153 ha. In this case, efforts to control land use change in order to maintain the balance of carbon stock are required (Dachary-Bernard et al., 2018; Koroso, 2023; O'Driscoll et al., 2023). The empirical evidence presented in this study indicates that by the year 2034, there will be an increase in built-up land, specifically settlements, trade and service areas.

The research demonstrates that the factors influencing land use change are intricate and multifaceted. The utilization of a comprehensive range of variables, and multitemporal land use maps enables the investigation of dynamic land use patterns. The spatial modeling approach utilizing the MLPNN-MC algorithm enables a

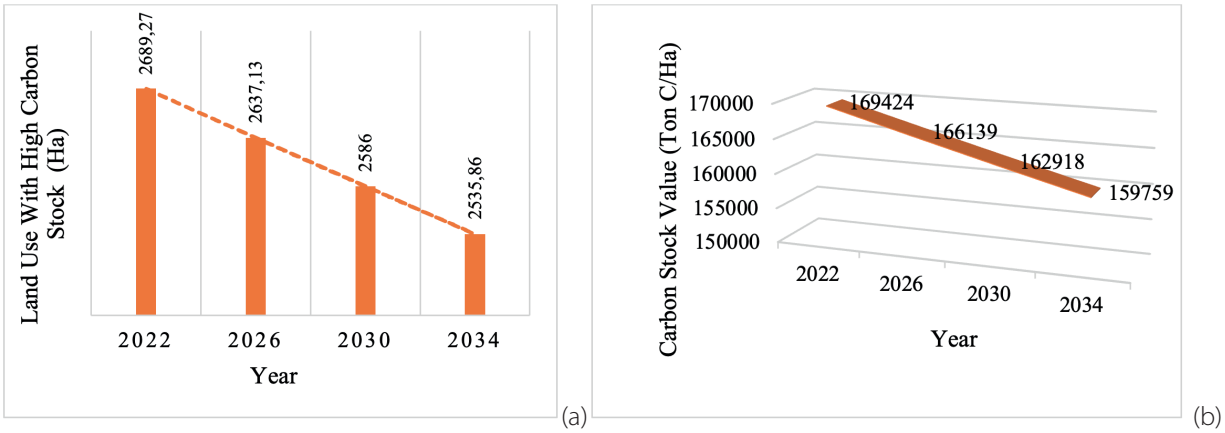

Fig. 8. (a) Area of land use with high carbon stock; (b) Carbon stock levels in 2022, 2026, 2030, and 2034

more comprehensive analysis of the transformation of land use change from one state to another, taking into account the influence of driving variables. The backpropagation technique employed in the MLPNN-MC algorithm enables the minimization of errors in spatial modeling of land use prediction, thereby facilitating the generation of accurate data with a success rate of 98%.

The findings of this study corroborate the previous studies, which indicate that land use has a significant influence on carbon stock changes (Wei et al., 2024; Achmad et al., 2024; Raqeeb et al., 2024). The role of land use in the form of mangroves and forests in absorbing carbon emissions is of great significance. In contrast, the construction of infrastructure, including roads, airports, and harbors, has been identified as a significant contributor to the increase in carbon emissions. The expansion of infrastructure is often accompanied by transportation activities, economic activities, and urbanization, which have implications for increasing energy demand and, consequently, high carbon emissions. Furthermore, these activities have an impact on current and future ecological conditions.

In light of these findings, it is imperative to implement measures to regulate land use in order to maintain equilibrium in carbon stock. This study reinforces the findings of previous research on the significance of land use planning policies based on carbon stock balance (Weindl et al., 2017). Such efforts may be made, for instance, through the optimization of mangrove ecosystems and forest areas through conservation, restoration, or reforestation (Dajam and Eid, 2024; Feller et al., 2017; Utami et al., 2024b). Furthermore, the allocation of land for green open spaces is imperative, given that reduced carbon stocks resulting in increased carbon emissions are a major driver of global warming. Land use predictions pertaining to prospective carbon stock levels furnish spatial data regarding the locations, patterns, and consequences of anticipated land transformations. The prediction carbon stocks represents a crucial aspect in the context of rising carbon emissions (Amadou et al., 2018; Araza et al., 2023). The database and findings presented in this study should serve as the foundation for stakeholders in the formulation of sustainable land management policies, the development of spatial utilization planning and control strategies, and the creation of planning, management, and control frameworks for human activities (social, cultural, and economic) with the aim of mitigating the impact of climate change disasters (Hamad et al., 2018; Ismaili et al., 2023; Xu et al., 2024). The integration of climate change mitigation with land use regulation and control represents a highly effective strategy for maintaining the balance of carbon stock (Xu et al., 2024). This study aims to address the limitations of previous research in carbon stock prediction modeling by enhancing the accuracy of predictions. However, the modeling is constrained to changes in land use types, without conducting a comprehensive assessment of vegetation types or vegetation density levels that may influence carbon values. The study employs a carbon stock scenario in 2034, utilizing driving factors such as social, economic, physical aspects and policies that are currently in effect. It is acknowledged that extreme changes in these factors are possible in the future, and that this has the potential to impact the predicted value of carbon stock. The development of predictive modeling research in the future is expected to further explore the carbon stock prediction modeling approach, with the aim of making it more comprehensive and accurate.

CONCLUSIONS

The impact of land use dynamics on the decline in terrestrial carbon stock levels is significant. Uncertainty in future land use and carbon stock levels can be overcome through modeling to predict land use based on carbon stock levels using the MLPNN-MC Algorithm. This study was able to produce a prediction accuracy rate of 98% for carbon stock levels, thus filling the gaps in previous modeling studies. The high level of accuracy can be attributed to the use of detailed sources for land use map data, comprehensive driving forces factors, and a compatible MLPNN-MC algorithm. The significant driving factors resulting from the spatial regression analysis and land change modeler include airports, city centers, industries, roads, and relative relief. The research findings predict that in 2034, there will be a decrease in land use area from high to low carbon stock of 153 ha, or a decrease in carbon stock levels of 9,665 tonnes C/ha. The modeling provides information on the spatial distribution of land use and carbon stock values that are subject to change. The carbon stock prediction database is an important component in the formulation of land use control policies and climate change mitigation efforts. Although this study was able to produce a high level of accuracy, further research is required to consider vegetation types and calculate all components of carbon stock values more comprehensively.

REFERENCES

Abbass K., Qasim M.Z., Song H., Murshed M., Mahmood H., & Younis I. (2022). A review of the global climate change impacts, adaptation, and sustainable mitigation measures. In Environmental Science and Pollution Research 29(28), 42539–42559, Springer Science and Business Media Deutschland GmbH. https://doi.org/10.1007/s11356-022-19718-6

Achmad A., Ramli I., Sugiarto S., Irzaidi I., & Izzaty A. (2024). Assessing and forecasting carbon stock variations in response to land use and land cover changes in Central Aceh, Indonesia. International Journal of Design and Nature and Ecodynamics, 19(2), 465–475. https://doi.org/10.18280/ijdne.190212

Alexandri E., Antón J.I., & Lewney R. (2024). The impact of climate change mitigation policies on European labour markets. Ecological Economics, 216, 1-14, https://doi.org/10.1016/j.ecolecon.2023.108022

Almubaidin M.A., Ismail N.S., Latif S.D., Ahmed A.N., Dullah H., El-Shafie A., & Sonne C. (2024). Machine learning predictions for carbon monoxide levels in urban environments. Results in Engineering, 22, 1-8, https://doi.org/10.1016/j.rineng.2024.102114

Amadou M.L., Villamor G.B., & Kyei-Baffour N. (2018). Simulating agricultural land-use adaptation decisions to climate change: An empirical agent-based modelling in northern Ghana. Agricultural Systems, 166, 196–209. https://doi.org/10.1016/j.agsy.2017.10.015

Aneva I., Zhelev P., Lukanov S., Peneva M., Vassilev K., & Zheljazkov V.D. (2020). Influence of the land use type on the wild plant diversity. Plants, 9(5), 602, https://doi.org/10.3390/plants9050602

Araza A., de Bruin S., Hein L., & Herold M. (2023). Spatial predictions and uncertainties of forest carbon fluxes for carbon accounting. Scientific Reports, 13(1), 1-15, https://doi.org/10.1038/s41598-023-38935-8

Bao Z., Zhang J., Wang G., Guan T., Jin J., Liu Y., Li M., & Ma T. (2021). The sensitivity of vegetation cover to climate change in multiple climatic zones using machine learning algorithms. Ecological Indicators, 124, 11-18, https://doi.org/10.1016/j.ecolind.2021.107443

Cortés Arbués I., Chatzivasileiadis T., Ivanova O., Storm S., Bosello F., & Filatova T. (2024). Distribution of economic damages due to climate-driven sea-level rise across European regions and sectors. Scientific Reports, 14(1), 1-15, https://doi.org/10.1038/s41598-023-48136-y

Dachary-Bernard J., Gaschet F., Hautdidier B., Lemarié-Boutry M., & Pouyanne G. (2018). Between environmental protection and urban development: How changes in land use planning affect coastal land markets in Aquitaine, France. In Sud-Ouest Europeen, 45, 71–88. Presses Universitaires du Mirail. https://doi.org/10.4000/soe.4034

Dajam A.S., & Eid E.M. (2024). Modelling the distribution pattern of soil organic carbon in protected and grazed areas of mangrove forests (Avicennia Marina). Sustainable Environment, 10(1), 1-14, https://doi.org/10.1080/27658511.2024.2369382

Dong L. (2024). Spatio-temporal evolution and prediction of carbon balance in the Yellow River Basin and zoning for low-carbon economic development. Scientific Reports, 14(1), 1-19, https://doi.org/10.1038/s41598-024-65113-1

Dong Z., Wang L., Sun Y., Hu T., Limsakul A., Singhruck P., & Pimonsree S. (2021). Heatwaves in Southeast Asia and Their Changes in a Warmer World. Earth's Future, 9(7), 1-13, https://doi.org/10.1029/2021EF001992

Feller I.C., Friess D.A., Krauss K.W., & Lewis R.R. (2017). The state of the world's mangroves in the 21st century under climate change. Hydrobiologia, 803(1), 1–12. https://doi.org/10.1007/s10750-017-3331-z

Gao X., Zhao M., Zhang M., Guo Z., Liu X., & Yuan Z. (2024). Carbon conduction effect and multi-scenario carbon emission responses of land use patterns transfer: a case study of the Baiyangdian basin in China. Frontiers in Environmental Science, 12. https://doi.org/10.3389/fenvs.2024.1374383

Halim M.A.R., Soeprobowati T.R., Hadiyanto H. (2023). Ecological assessment of the role of mangrove trees in carbon sequestration and biodiversity in Karimunjawa National Park Indonesia. Geography, Environment, Sustainability, 16(3), 1-13, https://doi.org/10.24057/2071-9388-2022-2565

Hamad R., Balzter H., & Kolo K. (2018). Predicting land use/land cover changes using a CA-Markov model under two different scenarios. Sustainability (Switzerland), 10(10), 1–23. https://doi.org/10.3390/su10103421

Hu Y., Sun Z.H., Zhang R.Q., & Li G. (2024). Spatial servive scope of carbon neutrality and its simulation prediction in the Loess Plateau of China. Applied Ecology and Environmental Research, 22(3), 2225–2240. https://doi.org/10.15666/aeer/2203_22252240

Huang X., Ibrahim M.M., Luo Y., Jiang L., Chen J., & Hou E. (2024). Land use change alters soil organic carbon: constrained global patterns and predictors. Earth's Future, 12(5), 1-16, https://doi.org/10.1029/2023EF004254

International Council for Local Environmental Initiatives – Local Governments for Sustainability. (2022). https://iclei.org/activity/forestryprotocol-12/

Ismaili A.H., Chemchaoui A., El Asri B., Ghazi S., Brhadda N., & Ziri R. (2023). Modeling predictive changes of carbon storage using invest model in the Beht Watershed (Morocco). Modeling Earth Systems and Environment, 9(4), 4313–4322. https://doi.org/10.1007/s40808-023-01697-3

Jakariya M., Alam M.S., Rahman M.A., Ahmed S., Elahi M.M.L., Khan A.M.S., Saad S., Tamim H.M., Ishtiak T., Sayem S.M., Ali M.S., & Akter D. (2020). Assessing climate-induced agricultural vulnerable coastal communities of Bangladesh using machine learning techniques. Science of the Total Environment, 742, 1-11, https://doi.org/10.1016/j.scitotenv.2020.140255

James D., Collin A., Mury A., & Costa S. (2020). Very high resolution land use and land cover mapping using Pleiades-1 stereo imagery and machine learning. International Archives of the Photogrammetry, Remote Sensing and Spatial Information Sciences - ISPRS Archives, 43(B2), 675–682. https://doi.org/10.5194/isprs-archives-XLIII-B2-2020-675-2020

Karamesouti M., Detsis V., Kounalaki A., Vasiliou P., Salvati L., & Kosmas C. (2015). Land-use and land degradation processes affecting soil resources: Evidence from a traditional Mediterranean Cropland (Greece). Catena, 132, 45–55. https://doi.org/10.1016/j.catena.2015.04.010

Kim G.Il, Oh J. H., Shin N.Y., An S.Il, Yeh S.W., Shin J., & Kug J.S. (2024). Deep ocean warming-induced El Niño changes. Nature Communications, 15(1), 1-8, https://doi.org/10.1038/s41467-024-50663-9

Koroso N.H. (2023). Urban land policy and urban land use efficiency: An analysis based on remote sensing and institutional credibility thesis. Land Use Policy, 132, 1-18, https://doi.org/10.1016/j.landusepol.2023.106827

Laino E., & Iglesias G. (2023). Scientometric review of climate-change extreme impacts on coastal cities. In Ocean and Coastal Management, 242, 1-13, Elsevier Ltd. https://doi.org/10.1016/j.ocecoaman.2023.106709

Li Q., Pu Y., & Gao W. (2023). Spatial correlation analysis and prediction of carbon stock of "Production-living-ecological spaces" in the three Northeastern Provinces, China. Heliyon, 9(8), 1-16, https://doi.org/10.1016/j.heliyon.2023.e18923

Lin Y., Chen L., Ma Y., & Yang T. (2024). Analysis and simulation of land use changes and their impact on carbon stocks in the Haihe River Basin by Combining LSTM with the InVEST Model. Sustainability (Switzerland), 16(6), 1-16, https://doi.org/10.3390/su16062310

Liu C., Liu Z., Xie B., Liang Y., Li, X., & Zhou K. (2021). Decoupling the effect of climate and land-use changes on carbon sequestration of vegetation in Mideast Hunan Province, China. Forests, 12(11), 1-14, https://doi.org/10.3390/f12111573

Liu J., Yan Q., & Zhang M. (2023). Ecosystem carbon storage considering combined environmental and land-use changes in the future and pathways to carbon neutrality in developed regions. Science of the Total Environment, 903, 1-16, https://doi.org/10.1016/j.scitotenv.2023.166204

Luo X., Luo Y., Le F., Zhang Y., Zhang H., & Zhai J. (2024). Spatiotemporal variation and prediction analysis of land use/land cover and ecosystem service changes in Gannan, China. Sustainability (Switzerland), 16(4), 1-22, https://doi.org/10.3390/su16041551

Ma X., Zou B., Deng J., Gao J., Longley I., Xiao S., Guo B., Wu Y., Xu T., Xu X., Yang X., Wang X., Tan Z., Wang Y., Morawska L., & Salmond J. (2024). A comprehensive review of the development of land use regression approaches for modeling spatiotemporal variations of ambient air pollution: A perspective from 2011 to 2023. In Environment International, 183. Elsevier Ltd. https://doi.org/10.1016/j.envint.2024.108430

Mason V.G., Burden A., Epstein G., Jupe L.L., Wood K.A., & Skov M.W. (2023). Blue carbon benefits from global saltmarsh restoration. Global Change Biology, 29(23), 6517–6545. https://doi.org/10.1111/gcb.16943

Meliho M., Boulmane M., Khattabi A., Dansou C.E., Orlando C.A., Mhammdi N., & Noumonvi K.D. (2023). Spatial prediction of soil organic carbon stock in the Moroccan High Atlas using machine learning. Remote Sensing, 15(10), 1-29, https://doi.org/10.3390/rs15102494

Melis M.T., Pisani L., De Waele J. (2021). On the use of tri-stereo pleiades images for the morphometric measurement of dolines in the Basaltic Plateau of Azrou (Middle Atlas, Morocco). Remote Sens (Basel), 13, 4087, 1-17, doi:10.3390/rs13204087

Mirsanjari M.M., Visockiene J.S., Mohammadyari F., & Zarandian A. (2021). Modelling of expansion changes of vilnius city area and impacts on landscape patterns using an artificial neural network. Ecological Chemistry and Engineering S, 28(3), 429–447. https://doi.org/10.2478/eces-2021-0029

Nakakaawa C.A., Vedeld P.O., Aune J.B. (2011). Spatial and temporal land use and carbon stock changes in Uganda: Implications for a future REDD strategy. Mitigation and Adaptation Strategies for Global Change, 16: 25-62 O'Driscoll C., Crowley F., Doran J., & McCarthy N. (2023). Land-use mixing in Irish cities: Implications for sustainable development. Land Use Policy, 128, 1-7, https://doi.org/10.1016/j.landusepol.2023.106615

Peng B., Yang J., Li Y., & Zhang S. (2023). Land use/land cover changes in Baicheng District, China during the Period 1954–2020 and their driving forces. Land, 12(10), 1-20, https://doi.org/10.3390/land12101845

Pu R., Landry S., & Yu Q. (2018). Assessing the potential of multi-seasonal high resolution Pléiades satellite imagery for mapping urban tree species. In International Journal of Applied Earth Observation and Geoinformation, 71, 144–158. https://doi.org/10.1016/j.jag.2018.05.005

Raqeeb A., Saleem A., Ansari L., Nazami S.M., Muhammad M.W., Malik M., Naqash M., & Khalid F. (2024). Assessment of land use cover changes, carbon sequestration and carbon stock in dry temperate forests of Chilas watershed, Gilgit-Baltistan. Brazilian Journal of Biology, 84, 1-16, https://doi.org/10.1590/1519-6984.253821

Ren Y., Lü Y., Comber A., Fu B., Harris P., & Wu L. (2019). Spatially explicit simulation of land use/land cover changes: Current coverage and future prospects. In Earth-Science Reviews, 190, 398–415. https://doi.org/10.1016/j.earscirev.2019.01.001

Segura C., Neal A.L., Castro-Sardiña L., Harris P., Rivero M.J., Cardenas L.M., & Irisarri J.G.N. (2024). Comparison of direct and indirect soil organic carbon prediction at farm field scale. Journal of Environmental Management, 365, 1-12, https://doi.org/10.1016/j.jenvman.2024.121573

Singh R.K., Biradar C.M., Behera M.D., Prakash A.J., Das P., Mohanta M.R., Krishna G., Dogra A., Dhyani S.K., & Rizvi J. (2024). Optimising carbon fixation through agroforestry: Estimation of aboveground biomass using multi-sensor data synergy and machine learning. Ecological Informatics, 79, 1-20, https://doi.org/10.1016/j.ecoinf.2023.102408

Soni S., Singh H., Qurashi J., Shuja M., Pandey M., & Arora A. (2022). Landuse/landcover monitoring and spatiotemporal modelling using multilayer perceptron and 'multilayer perceptron'-Markov Chain ensemble models: A case study of Dausa City, Rajasthan. IOP Conference Series: Earth and Environmental Science, 1032(1), 1-19, https://doi.org/10.1088/1755-1315/1032/1/012028

Sutrisno D., Darmawan M., & Helmi M. (2021). Climate change, land use cover change and its impact on Coastal Area. In 42nd Asian Conference on Remote Sensing, https://www.scopus.com/inward/record.uri?eid=2-s2.0-85127425731&partnerID=40&md5=c92c223b8265f2d34af27943937fd3d8

Tariq A., Yan J., & Mumtaz F. (2022). Land change modeler and CA-Markov chain analysis for land use land cover change using satellite data of Peshawar, Pakistan. In Physics and Chemistry of the Earth, 128. https://doi.org/10.1016/j.pce.2022.103286

Utami W., Sugiyanto C., & Rahardjo N. (2024a). Artificial intelligence in land use prediction modeling: a review. IAES International Journal of Artificial Intelligence (IJ-AI), 13(3), 2514. https://doi.org/10.11591/ijai.v13.i3.pp2514-2523

Utami W., Sugiyanto C., & Rahardjo N. (2024b). Mangrove area degradation and management strategies in Indonesia: A review. In Journal of Degraded and Mining Lands Management, 11, 3, 6037–6047. https://doi.org/10.15243/jdmlm.2024.113.6037 van Bijsterveldt C.E.J., van Wesenbeeck B.K., van der Wal D., Afiati N., Pribadi R., Brown B., & Bouma T.J. (2020). How to restore mangroves for greenbelt creation along eroding coasts with abandoned aquaculture ponds. Estuarine, Coastal and Shelf Science, 235, 106576. https://doi.org/10.1016/j.ecss.2019.106576

Verma D., Singh V., Bhattacharya P., & Kishwan J. (2020). Development, environmental impact and green growth: India. Ecology, Environment and Conservation, 26, S238–S244. https://www.scopus.com/inward/record.uri?eid=2-s2.0-85099239876&partnerID=40&md5=0b7cf0d2ed25d0fa0d9c2c6bce1764b6

Wei T., Yang B., Wang G., & Yang K. (2024). County land use carbon emission and scenario prediction in Mianyang Science and Technology City New District, Sichuan Province, China. Scientific Reports, 14(1), 1-17, https://doi.org/10.1038/s41598-024-60036-3

Weindl I., Popp A., Bodirsky B.L., Rolinski S., Lotze-Campen H., Biewald A., Humpenöder F., Dietrich J. P., & Stevanović M. (2017). Livestock and human use of land: Productivity trends and dietary choices as drivers of future land and carbon dynamics. Global and Planetary Change, 159, 1–10. https://doi.org/10.1016/j.gloplacha.2017.10.002

Wu W., Huang Z., Sun Z., Zhang J., Wang S., Fang M., Yang H., Lu H., Guo G., & Liu W. (2024). Simulation and attribution analysis of terrestrial ecosystem carbon storage of Hainan Island from 2015 to 2050. Science of the Total Environment, 917. https://doi.org/10.1016/j.scitotenv.2024.170348

Wu X., Shen C., Shi L., Wan Y., Ding J., & Wen Q. (2024). Spatio-temporal evolution characteristics and simulation prediction of carbon storage: A case study in Sanjiangyuan Area, China. Ecological Informatics, 80. https://doi.org/10.1016/j.ecoinf.2024.102485

Xu D., Yu C., Lin W., Yao J., & Zhou W. (2024). Spatiotemporal Evolution and Prediction of Land Use and Carbon Stock in Shanghai. Land, 13(3), 1-19, https://doi.org/10.3390/land13030267

Xu F., Chi G., & Wang H. (2024). Scenario Analysis of Carbon Emission Changes Resulting from a Rural Residential Land Decrement Strategy: A Case Study in China. Land, 13(1). https://doi.org/10.3390/land13010051

Yan X., Huang M., Tang Y., Guo Q., Wu X., & Zhang G. (2024). Study on the dynamic change of land use in Megacities and its impact on ecosystem services and modeling prediction. Sustainability (Switzerland), 16(13), 1-28, https://doi.org/10.3390/su16135364

Yusuf M. (2021). Mining and its effects on climate change. Aspects in Mining & Mineral Science, 7(3), 1-3, https://doi.org/10.31031/amms.2021.07.000662

Zhang D., Zhu Z. I., Chen S., Zhang C.I., Lu X., Zhang X., Zhang X., & Davidson M.R. (2024). Spatially resolved land and grid model of carbon neutrality in China, Sustainability Science Environmental Sciences, 121 (10), 1-12, https://doi.org/10.1073/pnas

Zhang J., Yang J., Liu P., Liu Y., Zheng Y., Shen X., Li B., Song H., & Liang Z. (2024). Effects of land use/cover change on terrestrial carbon stocks in the Yellow River Basin of China from 2000 to 2030. Remote Sensing, 16(10), 1-16, https://doi.org/10.3390/rs16101810

Zhang W., Yuan W., Xuan W., Lu Y., & Huang Z. (2024). Leveraging AI techniques for predicting spatial distribution and determinants of carbon emission in China's Yangtze River Delta. Scientific Reports, 14(1), 1-16, https://doi.org/10.1038/s41598-024-65068-3

Zhang X., Jia W., Sun Y., Wang F., & Miu Y. (2023). Simulation of spatial and temporal distribution of forest carbon stocks in long time series—based on remote sensing and deep learning. Forests, 14(3), 1-21, https://doi.org/10.3390/f14030483

RESEARCH PAPER

URBAN GREEN INFRASTRUCTURE OF RUSSIAN SOUTH: SPATIAL JUSTICE - ECOLOGICAL EFFICIENCY NEXUS

Olga A. Illarionova[1*], Oxana A. Klimanova[1], Elizaveta V. Grechman[1]
[1]Lomonosov Moscow State University, Leninskie Gory, GSP-1, Moscow, 119991, Russian Federation
***Corresponding author:** heatherpaw95@gmail.com
Received: October 28th 2024 / Accepted: March 26th 2025 / Published: June 30th 2025
https://doi.org/10.24057/2071-9388-2025-3691

ABSTRACT. The incorporation of nature-based solutions into urban planning and development policies has become a pressing issue in many large cities worldwide, aiming to improve the urban environment and the well-being of city-dwellers. However, the establishment and management of urban green infrastructure can be expensive and may lead to spatial injustice or be ecologically inefficient due to the planning decisions. This study focuses on the Spatial Justice-Ecological Efficiency Nexus of urban green infrastructure in large Caucasian cities of Russia, where urbanization rates are rapidly increasing. The hypothesis of this study is that green infrastructure in Russian cities predominantly has an ecological aspect, meaning that it provides a large volume of ecosystem services that are still unavailable to a significant portion of the urban population. To explore this topic, we aim to assess the balance between the social and ecological aspects of green infrastructure in six case study cities, including Makhachkala, Grozny, Nalchik, Maykop, Vladikavkaz, and Stavropol. The assessment framework includes 12 indicators, divided into two categories: spatial justice (6 indicators) and ecological efficiency (6 indicators). The spatial justice indicators assess the availability, accessibility, and distribution of green infrastructure, while the ecological efficiency indicators evaluate the performance of regulating and supporting ecosystem services. The results revealed that despite the common prevalence of ecological side in large Russian cities, the spatial justice side in the southern cities generally dominates over the ecological side, with most cities having an unbalanced nexus. Green infrastructure in the studied cities has a low ecological input, with a mean total score of around 300 points (out of 600), with most cities lacking protected areas and green areas beyond the edge effect. Meanwhile, the social side of the nexus is more developed, with an average score of 400. The study highlights the need for a more integrated approach to urban green infrastructure planning, considering both justice and ecological aspects to ensure a more just and sustainable urban environment. Overall, in this research we introduce a multidimensional approach to understanding the functions and qualities of green infrastructure that will allow for a more comprehensive assessment and planning of the rapidly growing southern cities. This study contributes to the understanding of the complex relationships between urban green infrastructure spatial justice and ecological efficiency, providing valuable insights for urban planners, policymakers, and stakeholders seeking to create more sustainable and equitable urban environment.

KEYWORDS: urban green infrastructure, social-ecological functions, green justice, ecological efficiency, spatial distribution, North Caucasian cities

CITATION: Illarionova O. A., Klimanova O. A., Grechman E. V. (2025). Urban Green Infrastructure Of Russian South: Spatial Justice - Ecological Efficiency Nexus . Geography, Environment, Sustainability, 2 (18) 114-125
https://doi.org/10.24057/2071-9388-2025-3691

ACKNOWLEDGEMENTS: The study was conducted as part of the state assignment of the Department of World Physical Geography and Geoecology, Faculty of Geography, Lomonosov Moscow State University. "Analysis of regional geo-ecological problems in the context of global environmental changes" (No. 121040100322-8).

Conflict of interests: The authors reported no potential conflict of interests.

INTRODUCTION

Today, many large cities around the world are striving to incorporate nature-based solutions into their planning and development policies in order to improve the urban environment and, as a result, the well-being of the urban population. Being the major source of ecosystem services and the core nature-based solutions in the city, green infrastructure aims to mitigate negative impacts of urban grey infrastructure, including different types of pollution, heat island effect, erosion, and psychological discomfort, and to provide a suitable place for daily recreation (Liu et al. 2021). Numerous studies (Shade et al. 2020; Evans et al. 2022) have also discussed the ability of urban green infrastructure to contribute significantly to the global mitigation of climate change and biodiversity loss, as well as positively influence food security by establishing interconnected blue-green networks throughout the cities with urban forests, green corridors, and urban agriculture. Several studies (Basnou et al. 2020; de Oliveira et al. 2022; Wang et al. 2022) on urban green infrastructure have proved to be efficient both on the local and global levels.

However, the establishment and management of urban green infrastructure has also proved to be expensive

in many cases and to perform so-called disservices. Considering the cost-related barriers, land- shortage, and land use regulations in urban areas, the development of green infrastructure often happens to be spontaneous or uneven (Shi 2020; Cousins 2021). As a result, some districts become much greener, safer, and more comfortable than others. Occasionally, it is the development of green infrastructure that aggravates the spatial injustice in cities. Several cases of "green gentrification" have been already described (Anguelovski et al. 2022; Rigolon et al. 2023), when lower-middle-income districts get an intense green development and attract the upper-middle-income population that gradually effects the district's land value and average prices, forcing the former population to move about.

An even more common controversy around urban green infrastructure is a conflict between its social and ecological aspects (Depietri 2022). The efficiency of primarily social functions to a significant extent depends on their spatial justice, meaning availability and accessibility to all city dwellers, including the even distribution of green elements in the city, as well as their management and functionality. In contrast, to perform the ecological functions (including mostly regulating and supporting ecosystem services) green infrastructure usually needs large, intact areas with limited access for the population. This assumption is not always accurate.Several studies (Fahrig 2020; Varentsov et al. 2023) have discovered that small green elements can be as efficient as large ones if they are interconnected and have good quality. Nevertheless, many features of green infrastructure required for their ecological efficiency (Yao et al. 2021) differ from those required for spatial justice (Yazar 2023). It is also worth mentioning that urban residents are beneficiaries of ecosystem services, performed by green infrastructure, in any case. However, the question arises as to which portion of the urban population benefits and to what extent. For example, the existing green area can be directly used as a place for recreation, and simultaneously it provides regulating services (air purification, climate regulation). However, if this green area has limited access (e.g., it is not public) or is not big enough, then a certain part of the population cannot use it as a recreational site.

This contradicting interaction gives birth to the Spatial justice - Ecological efficiency Nexus of urban green infrastructure. Generally, one side of the nexus prevails over the other in the city, resulting in the underdevelopment of either the social or ecological side and creating trade-offs at their interaction. However, the evidence demonstrates (Valente et al. 2020; Ferreira et al. 2021) that it is possible to support a balanced nexus with just and ecological features co-benefitting each other in the city.

The concept of the nexus has gained increasing prominence in urban ecological research as a framework for understanding the interconnectedness and interdependencies of critical resource systems within cities (Escobedo et al. 2019; Kumar et al. 2019). Traditional disciplinary approaches often fail to capture the complex interactions between different urban systems, leading to unintended consequences and inefficiencies. By adopting a nexus perspective on green infrastructure, researchers can analyze the synergistic effects and trade-offs associated with urban development and green area planning, identifying opportunities for integrated solutions that enhance sustainability and resilience (Amaral et al. 2021; Lampinen et al. 2023).

Regarding this research, our hypothesis is that green infrastructure in Russian cities predominantly has an ecological aspect, meaning that it provides a large volume of ecosystem services that are still unavailable to a significant portion of the urban population. This idea is based on our previous studies (Klimanova et al. 2018; Klimanova et al. 2020; Klimanova et al. 2021) and other works (Haase et al. 2019; Murtazova et al. 2023; Konstantinova et al. 2024) for large Russian cities that revealed an uneven distribution of vegetation yet large total green areas as well as planning and monitoring issues. However, we have not studied southern Russian cities in particular. Therefore, considering the natural and planning regional peculiarities, we expect differences in the range of ecosystem services provided by southern urban green infrastructure.

In the context of Russia, the early Soviet planning for large cities mostly considered the recommendations of 10 m^2 of managed green area per person, 3 ha as a minimum size of a district park and 15-minute walking accessibility from the residential zone. As a result, many Russian cities have been recently demonstrating high results on green infrastructure availability, accessibility and ecosystem services performance (Matasov et al. 2020; Klimanova et al. 2021; Varentsov et al. 2023; Skachkova 2024). However, the urban population in Russia has been increasing, especially at the expense of large cities. Urbanization rate of the Southern and North Caucasian Federal Districts has demonstrated exceptional growth due to the natural increase, by 20%[1] for all cities in the region on average since 2000. Besides, the Caucasian cities are becoming more popular with tourists, meaning that the quality of their urban environment is also an essential part for the general regions' touristic attractiveness (Litvinova 2020). New residential, business and leisure areas transform the old planning and create new infrastructure patterns inside the urban zone, affecting the green elements accessibility, availability and justice. This new touristic attractiveness of the Caucasian cities also raises the question of who this new green infrastructure is for: tourists or the local population.

In this study, we focus on the relation between justice and ecological aspects of urban green areas, unlike other studies on urban green infrastructure in Russia, including our previous assessments. The aim is not to evaluate ecological and justice aspects separately, but to assess their interaction and the consequences it poses on the efficiency and overall quality of green infrastructure.

The use of remote sensing and open-source data allows us to compare and evaluate numerous parameters simultaneously and not focus on a single aspect of green infrastructure, which is generally not enough to draw conclusions about its role in the well-being of the population and its contribution to improving the urban environment. In this paper, we hope to introduce a multidimensional approach to understanding the functions and qualities of green infrastructure. We believe that these concepts will allow for a more comprehensive assessment and planning of the various aspects of green areas.

Therefore, this study aims to assess the state of the Spatial justice - Ecological efficiency Nexus in the large Caucasian cities of Russia to define the type of interaction between the just and ecological aspects of these cities' green infrastructure and the emerging conflicts or co-benefits. To meet this aim, we set several specific objectives: 1) to introduce the concept of the Spatial justice - Ecological efficiency Nexus of urban green infrastructure; 2) to develop a method to assess this Nexus; 3) to determine the prevailing aspect of green infrastructure in the studied cities.

[1]Based on data for 2023 from The Federal State Statistics Service of Russia

MATERIALS AND METHODS

Study Area

The studied cities (Makhachkala, Grozny, Nalchik, Maykop, Vladikavkaz, Stavropol) belong to the North Caucasian and Southern Federal Districts of Russia. They are the administrative centers of the federal subjects with a population of over 100,000 inhabitants (Fig. 1).

The temperate climate in the Caucasian region changes from mild southern in Vladikavkaz, Nalchik, and Maykop to more continental in Stavropol and Grozny, and finally to semi-arid in Makhachkala. The natural conditions of the latter may be considered the least favorable for vegetation growth; however, it was concluded in several studies (Farrel et al. 2022) that the justice and intactness of green infrastructure is not always connected to the natural conditions but to the efficient management and planning. All of these cities have either a foothill location or a hilly terrain, which makes them particularly vulnerable to dangerous natural phenomena like floods, mudflows, and landslides.

Study design

The design of this study is based on the idea that the quality of green infrastructure is defined by numerous features that may affect each other positively or negatively or exist independently (Fig. 2). We call the interaction of two particular features in this study the Spatial justice - Ecological efficiency Nexus. Depending on the prevalence of one or another Nexus side, it may be balanced (both sides are similarly developed), or imbalanced (one aspect is significantly better developed, often at the expense of the other).

The quality of urban green infrastructure is usually defined by three main characteristics (Lindholst et al. 2016): 1) size, structure, configuration, location, and accessibility; 2) functionality and efficiency of ecosystem services performance; and 3) management, organization, and integrity. The assessment of the spatial justice of green infrastructure also depends much on these three groups of parameters, and usually it is the accessibility that is studied to the greatest extent, which is generally assessed by such parameters as the provision of a population with green elements, walking distance to them, and their distribution across the urban area (Maroko et al. 2009). The intactness, or ecological efficiency, of urban green infrastructure commonly depends on vegetation fragmentation, landscape position, connectivity, health, exposure to pollution, and species composition (Teixeira et al. 2021).

We developed a set of indicators to individually assess the ecological efficiency and spatial justice of urban green infrastructure in Russian Caucasian cities (Table 1). Spatial justice parameters consider the share, degree, or availability of 1) open public green elements; 2) green infrastructure per capita; 3) green infrastructure designed for daily recreation; 4) accessible green infrastructure in a 10-minute walk; 5) residential greenery; and 6) green infrastructure even distribution. All of these indicators are meant to describe the availability, accessibility, efficient use, and just distribution of green infrastructure in a city.

Ecological aspects include indicators that describe: 1) tree vegetation on steep slopes; 2) greenery of river zones; 3) urban tree cover; 4) protected areas; 5) green area without the edge effect; and 6) large or interconnected small green elements. These parameters define vegetation's ability to perform the most important supporting and regulating ecosystem services. For most indicators (except steep slope greenery and protected green areas) we considered only green infrastructure inside the built-up urban zone and those green elements, which are deeply incorporated into it.

Since urban area are not supposed to be 100% green or intact like natural ecosystems, optimum values (Table 1, column 3) were adjusted to the recommended values, according to scientific studies, urban planning guidelines, or expert estimations. To conduct an integrated assessment of the Nexus, all values were normalized from their primary optimum value to a 100-point scale (for example, for protected areas the primary optimum value is 30% of total urban green area, thus, if a city has 30% of its green infrastructure protected, it will score 100). Thus, for each indicator, 100 points is the maximum.

Fig. 1. Study area

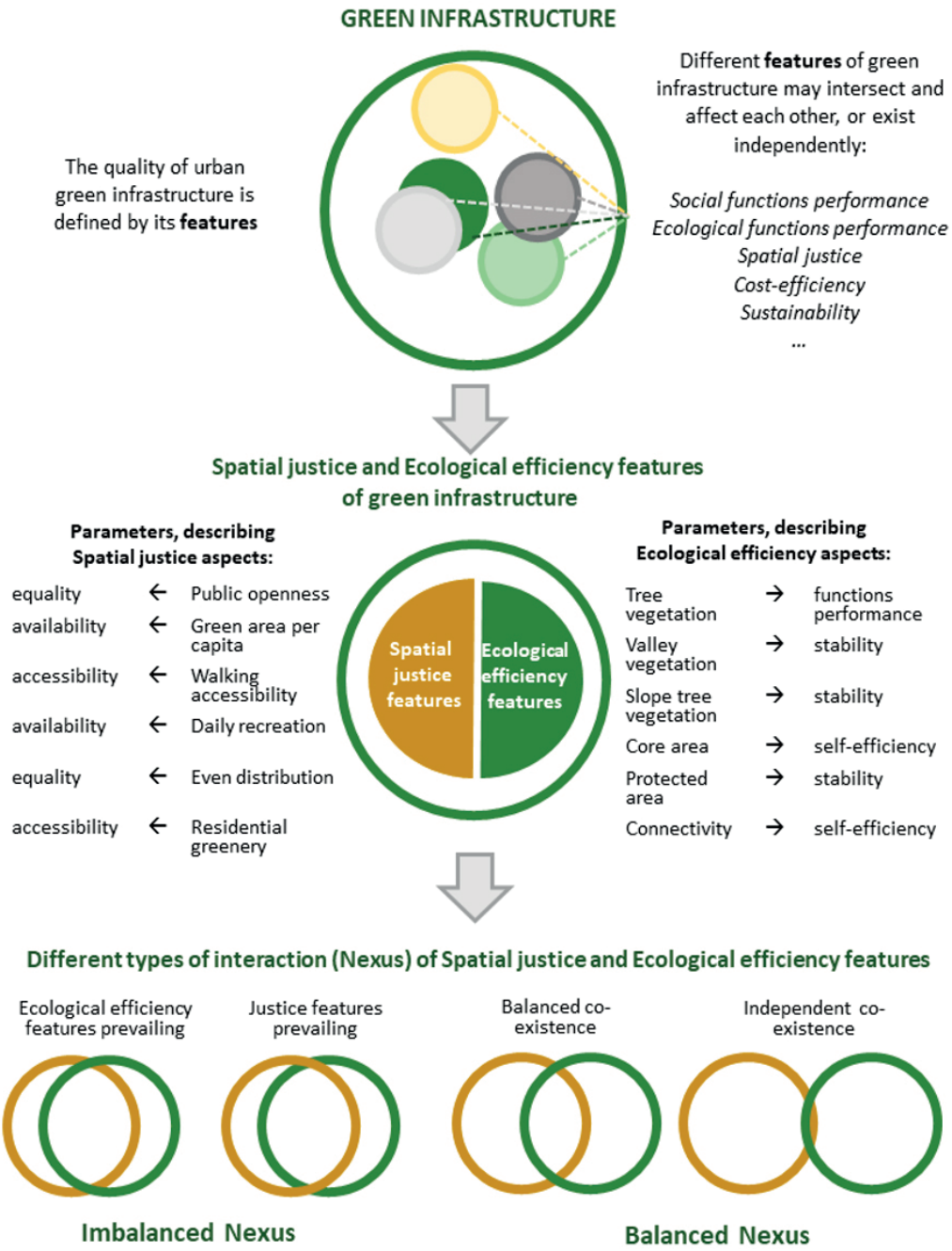

Fig. 2. The Spatial Justice – Ecological efficiency Nexus assessment design

Our assessment is based on various indirect indicators, such as the exposure to edge effects, the number of parks managed in accordance with general plans, and other factors from Table 1 that can be derived from publicly available data sources. These indicators provide information about the overall functionality and quality of green spaces. For example, if a park is managed for recreational use on a daily basis in accordance with its functional zoning as outlined in the general plan, we consider its management satisfactory. Similarly, we apply this logic to parks with protected status and parks that are not exposed to edge effects. These indirect indicators allow us to draw conclusions about the state of vegetation and ecological performance. However, direct assessment parameters like the age of trees, species diversity, vegetation state or visitors' activity, management arrangements, "non-green" infrastructure can give a more detailed result of the Nexus assessment.

Data

The base for the indicators' assessment is the urban landscape models for the study areas. We computed them by combining vegetation cover raster, derived from NDVI (basing on Sentinel-2 satellite images for summers months); valleys and watersheds raster, derived from Copernicus-30 digital elevation models; urban functional zoning and built-up types vector, derived from General Plans.

Methods

Most indicators were assessed by calculating green area for different territorial units (residential districts, steep slopes, river zones, protected areas), using the Tabulate Area instrument in ArcGIS software. Slope steepness was calculated by using the Slope instrument. We also considered slopes outside the urban core, as they pose a threat to the adjacent built-up zone. We also did not include small river valleys (with river length less than 10 km), because their influence in comparison to other indicators is less significant.

Table 1. Spatial justice and ecological efficiency parameters of green infrastructure Nexus and their meaning

Spatial justice indicators	Interpretation	Primary optimum value
Open public green area	Share (%) of publicly open urban green area from all urban green area	100% of all urban green infrastructure
Public green area per capita	Population provision (m^2/per.) with publicly open green area	9 m^2/per.
Green area, designed for daily recreation	Population provision (%) with urban green area, designed and maintained for daily recreation	Basing on the standard 4 ha / 1000 per. (Jenkins et al. 2005)
Accessible green area in 10-minute walk zone	Share (%) of parks larger than 1 ha within the 10-minute walk from residential areas	100% accessibility for residential area
Residential green area	Share (%) of green infrastructure in residential areas (excluding private sector)	50% of all residential area (Breuste 2023)
Even Distribution Index	Evenness of green elements distribution, based on Pierson's criterion	0
Ecological efficiency indicators	Interpretation	Primary optimum value
Steep slopes forestation	Share (%) of steep slopes (>12°), covered by tree vegetation	100% of steep slopes
River valleys greenery	Share (%) of urban river zones (200 m buffer from rivers longer than 50 km, 100 m – rivers longer than 10 km) covered by vegetation	50% of urban river zones
Urban tree vegetation	Share (%) of tree vegetation from all urban green infrastructure	50% of all urban vegetation (Borelli et al. 2023)
Urban protected areas	Share (%) of protected green area from all urban green infrastructure	30% of all urban vegetation
Green area outside the edge effect	Share (%) of green area without the edge effect (140 m)	50% of all urban vegetation
Green area connectivity	Share (%) of separate large (<10 ha) or interconnected small green elements from all urban green infrastructure	70% of all urban vegetation (Bolliger et al. 2020)

To assess the evenness of green infrastructure's distribution, we developed Even Distribution Index (EDI), based on Pierson's criterion (Eq. 1).

$$EDI = \left(N_{un} - N_{opt}\right) / N_{un} \quad (1)$$

where N_{un} – is a number of nominal square units (200×200 m, a common size for a built-up block) that divide the built-up area of the city; N_{opt} – is a number of nominal square units, which are optimally greened (by at least 50%).

The calculation of optimally and sub-optimally greened units (Fig. 3) was computed by using Attribute Table instruments. The square units were created by using the Grid Index Feature instrument.

The calculation of 10-minute walking accessibility was carried out with the construction of graphs on the road network. From OpenStreetMap vectors with "highway" key, we selected only those roads, which are suitable for pedestrians. For this, we chose linear features with tags "footway", "living street", "path", "pedestrian", "residential", "steps", "footway". All repeating parallel road lines were removed. Then we built a pedestrian roads graph. First, a set of linear features was converted into a single linear feature using the Dissolve tool, which was then converted into graph edges using the Features to Line tool. The graph nodes were built through the Network Dataset construction tool in ArcGIS Catalog using the calculated length of each edge. Next, we calculated the area of residential zones within a 10-minute walking distance

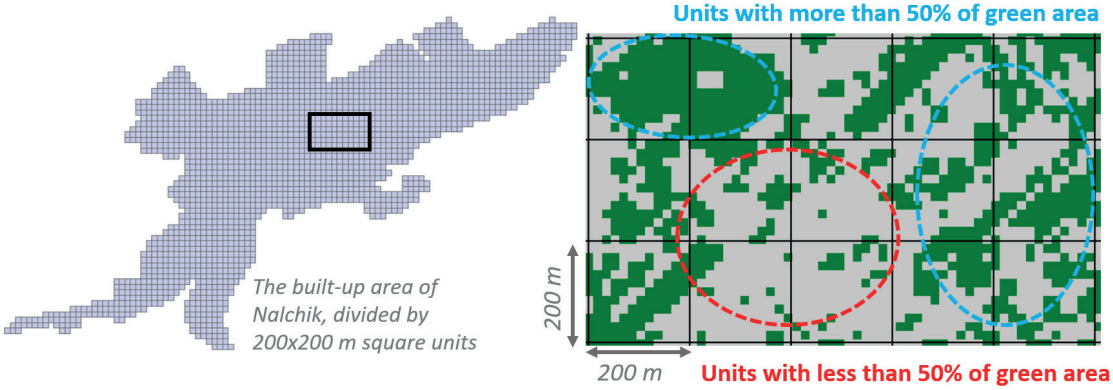

Fig. 3. The example of greened nominal square units' calculation in the built-up zone of Nalchik

(approximately 800 m). From the pre-digitized functional zoning scheme from the General Plans, the following zones were selected: residential private sector, residential mid-rise development, residential low-rise development, and residential multi-story development. We consider these zones as "residential areas".

We also used functional zoning to assess open public green areas and green areas designed for daily recreation. We regarded green infrastructure as open and public if it was located outside functional zones with limited access: residential private sector, engineering and utility-warehouse zones, industrial zones, zones of special public development (schools, hospitals), green areas for special purposes (military zones, airports), restricted areas, private gardens, and agricultural lands. As to the green infrastructure, designed for daily recreation, we selected green elements specifically mentioned as recreational areas in general plans (but only those, which were located close to business or residential zones) and other green elements with unlimited public access, located inside residential and central business areas with an area of more than 1 ha.

To conduct an integrated assessment of the Spatial justice - Ecological efficiency Nexus, we summed final normalized values separately for social and ecological parameters and compared the results to determine which nexus side dominates.

RESULTS

Ecological efficiency

The results show that generally green infrastructure in the studied cities has a low ecological input with a mean total score of about 300 points (max. 600). In general, Stavropol and Vladikavkaz have the most developed ecological side of the nexus, especially the first city, with almost all indicators scoring above 50 points and having a relatively high result for protected areas. In contrast, the latter city has varying ecological indicators with very low scores for areas beyond the edge effect and protected green areas. The current green infrastructure efficiently performs most of its ecological functions; however, the lack of protected and intact areas undermines its future stability and ability to do so, especially considering the growing population in the city and probable land sealing as a result. Grozny stands out among the studied cities due to its below-average ecological parameters. Especially concerning are a low forestation of steep slopes and a small share of tree vegetation inside the densely built-up zone that is important for a cooling effect during the hot summer. The two examples of a "leader city" and an "outsider city" (Fig. 4) of the ecological nexus side differ drastically from other studied cities with a score close to average (around 300). Most of them lack protected areas, green areas without edge effects and connected elements. Yet, their green infrastructure mostly consists of tree vegetation, and the steep slopes are significantly forested.

The least developed part of ecological aspect is the share of protected green areas, which is significantly less than 30% in most cities. The only exceptions are Stavropol and Makhachkala with relatively large protected areas of a regional significance (natural monuments and zakazniks[2]) within urban boundaries. A small share of green area, beyond the edge effect, is also closely connected to the lack of protected areas. Still, it is the protected areas indicator that effects the results most of all. The establishment of protected areas is a global challenge, since the goal of reaching 30% is not reached in most regions, especially in densely built-up areas. The phenomenon of large Russian cities is that by absolute estimates they are ones of the greenest cities in the world due to the relatively sparse development, Soviet planning and large areas of inconvenient for development land, like floodplains, ravines or steep slopes. Therefore, the problem of a low percentage of urban protected areas is not because of the lack of green areas in cities, but due to the opposite direction of policy instruments that aim to protect areas which are easy to protect, and to create urban green infrastructure that mostly meets social needs. Meanwhile, urban protected areas are a field that can become a compromising sphere in the Spatial justice – Ecological efficiency Nexus for its ability to evenly provide both social and ecological services for the city.

Due to the favorable natural conditions, the tree cover indicator is usually the best on this side of the nexus. Steep slopes are especially well forested in most case studies (by 70% on average), meaning that erosion control and landslide risk prevention functions are performed efficiently by urban green infrastructure. This is an important interconnection with the social sphere of the nexus because these functions directly influence the safety of the population living at the foothill.

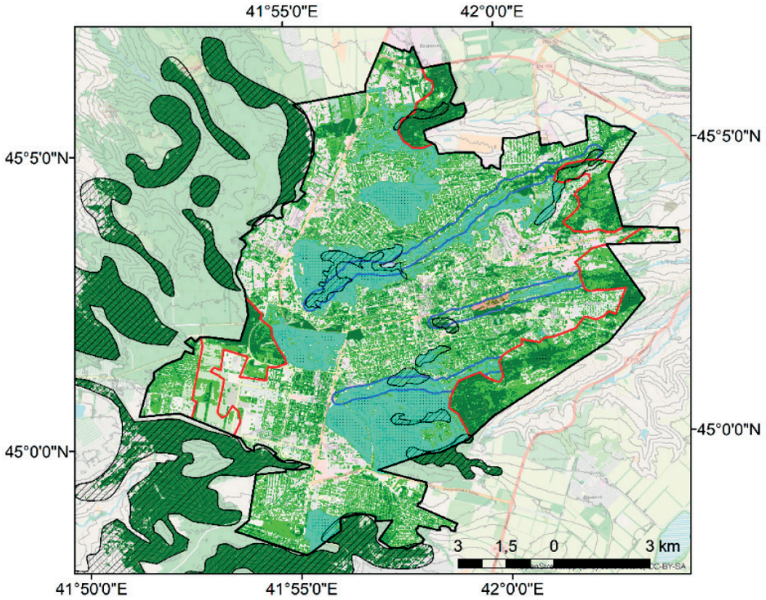

(a)

[2]State protected areas that are generally similar to IUCN protected areas categories III, IV and V.

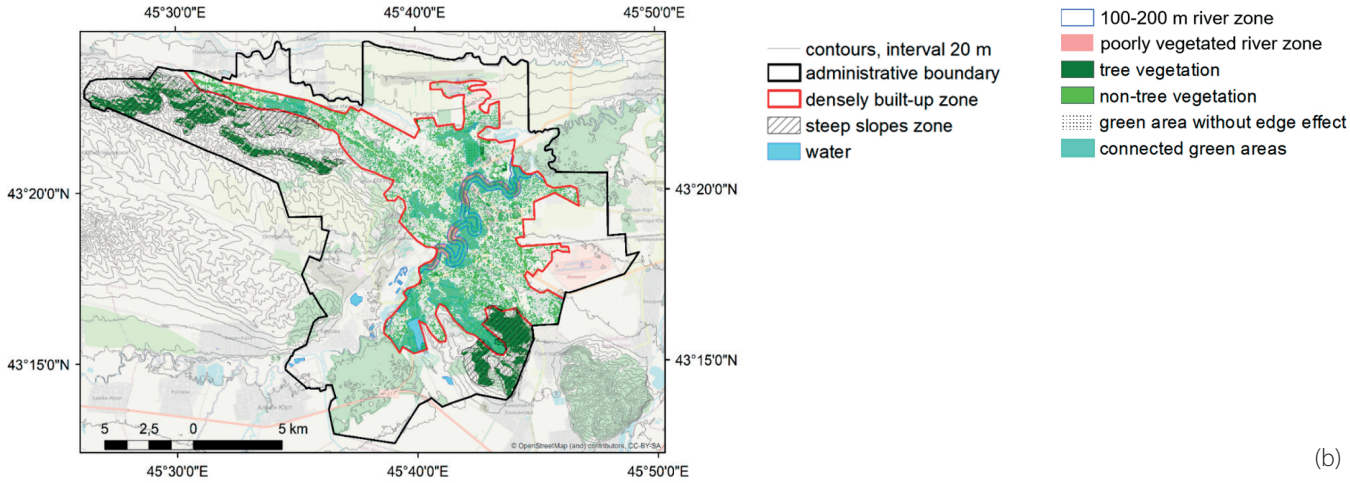

Fig. 4. Ecological efficiency parameters of the "outsider city" – Grozny

The greenery of river zones is also relatively successful in this regard (around 60% of river zones is vegetated), and the largest urban rivers generally have parks as their embankments. Compared to other Russian cities, our finding is an outstanding result, considering that many large cities have concrete main embankments with little vegetation or unmaintained parts. Yet, despite being green and well-maintained, river zones in the studied cities have few connections to urban green elements. Besides, the indicator for large and interconnected small elements is low (less than 40% of green area is interconnected or form large patches), with most vegetation concentrated in residential areas and a few disconnected, though large, parks. River zones are practically the largest green corridors in the studied cities, which paradoxically mostly perform a social role by providing public green areas rather than connecting other green elements. This is an important point of contact for social and ecological aspects of the nexus and a potential for ecological improvement, because by connecting nearby parks and unmanaged green patches to the green river zones with boulevards and corridors, the total interconnectivity of urban green infrastructure can increase significantly, thus making it more stable, resistant, and self-sufficient.

Spatial justice

Generally, the social side of the nexus is developed better, scoring on average 390, with one indicator (green area per capita) reaching the maximum value in every city. Even though we consider only the open public green infrastructure inside the built-up area for this parameter, it is still green enough to meet the WHO standard of 9 m^2/per. Moreover, the lowest absolute value in Makhachkala is still almost three times higher than this recommendation. This indicator demonstrates that overall, green elements are available for the North Caucasian cities. On the whole, the green infrastructure inside urban built-up areas is, on average, 60% open and accessible to the entire population. To increase clarity, use active voice: Private households and gardens, which constitute between 40% and 70% of all green areas with limited access, primarily restrict access. Industrial greenery does not occupy much area inside the built-up zone, and other types of green infrastructure with limited access are usually located outside the urban built-up zone. This result suggests that a rare provisioning function within urban green infrastructure in large Russian cities plays a significant role. Since private greenery is often used for agriculture, we may speculate that about 20% of urban green infrastructure inside the built-up zone is capable of performing a provisioning service, which is a crucial point for the social side of the nexus.

Other residential areas, excluding the private sector, are on average 30% green, with the worst results (about 20%) in cities with the old densely built-up districts (Maykop, Vladikavkaz). It means that a considerable share of the population receives a number of ecosystem services daily, and the environment of their living is being constantly regulated by vegetation. Yard vegetation (house-side trees, flower beds, yard lawns and bushes) forms places for daily recreation; however, it offers a limited variety of recreational services. Thus, other green elements, like parks and public areas, should be considered to assess the green infrastructure's potential for providing daily recreation. Besides, this indicator allows one to see how much green infrastructure is maintained and managed, which is important for its social efficiency. On the whole, the population is well provided with green elements for this kind of activity. The only outsider is Makhachkala, which has managed green elements for daily recreation within the urban built-up zone, meeting only 40% of the population's needs. The social justice of urban green infrastructure and its services are also assessed by their proximity to users. The assessment has revealed that 10-minute walking accessibility to urban parks with an area of at least 1 ha from residential areas (excluding private homes which are far from public green spaces) is among the least developed social parameters of the nexus. On average, only 50% of residential areas in the studied cities have public green spaces within walking distance. This result demonstrates that green infrastructure's availability is not a problem for most cities, but its accessibility is. Despite being well provided with open and functional green elements, their location is not evenly distributed for all districts and populations. This conclusion is also supported by low values of the Even Distribution Index, which demonstrates that the current vegetation distribution model does not even half coincide with a perfectly even model. For most cities, the EDI value is about 0.8. Unlike most northern cities in Russia, the greenest parts here are not concentrated on the outskirts or in the river valleys, but in the private sector and health resorts. There are also cases when EDI values for the same types of residential areas in one city drastically vary. It means that greening depends not only on the planning and configuration of development but also on the quality of greening in the specific area.

It is worth mentioning that high values of this social parameter shall not necessarily conflict with the ecological parameter of large and interconnected small elements, because even distribution does not necessarily mean solely

fragmented vegetation. The current green distribution model in most cities studied presents a mosaic of several poorly connected, well-green districts and those with little vegetation. The most even and optimal model can be found in Stavropol, where three large urban forests play the role of the main green massifs in the city, and evenly green built-up areas are distributed throughout the urban area.

In general, green infrastructure of all studied cities can be considered to be socially efficient, except for Makhachkala (Fig. 5), which has relatively low scores for all parameters (below 50). The best results are demonstrated by Stavropol and Nalchik, having the most available, accessible, and evenly distributed green elements. This assessment does not allow us to draw conclusions on other qualitative parameters of their green infrastructure (attractiveness, vegetation health condition, etc.). Yet, planning is one of the most challenging aspect of green infrastructure organization and its current disposition in these two cities is quite favorable for organizing the optimum green model. As for the other cities, the accessibility of green infrastructure can only be improved by establishing new, though small, public green spaces in sandlots, unmanaged areas with vegetation, or significantly sealed open spaces.

Nexus balance

The integrated assessment of Social-Ecological Nexus functioning of green infrastructure revealed that in all case studies, the social aspect of green infrastructure dominates over the ecological, and in three cities, this imbalance is quite drastic (Fig. 6). The relation between both nexus sides may be beneficial or contradictory. One of the most common conflicting aspects of Social-Ecological Nexus of urban green infrastructure is vegetation fragmentation. On the one hand, many studies confirm that large patches are better for the volume and variety of different ecosystem services.

On the other hand, the same green area, deconcentrated into smaller patches, provides services for more population and forms a more just urban environment. However, small elements happen to be more vulnerable, less resistant, and, as a result, more expensive to support and less efficient. The compromise for these two conflicting sides is green links for small patches, which is partly met in Stavropol, Vladikavkaz, and Nalchik. Other ecological parameters do not contradict that much with social parameters but rather complement them. The greenery of river zones or the establishment of protected areas benefits the social aspect, and the forestation of slopes improves the population's safety. The problem, however, is that high values of social parameters (other than green linkage) do not usually positively affect the ecological side of the nexus. In other words, high ecological efficiency can improve the social aspect, but high social development cannot dramatically increase the ecological efficiency of green infrastructure. Ecologically inefficient green infrastructure gradually affects the social side as many services become unavailable. It can be said that the bigger the gap between the ecological and social sides is, the more contradictory the relation between them gets.

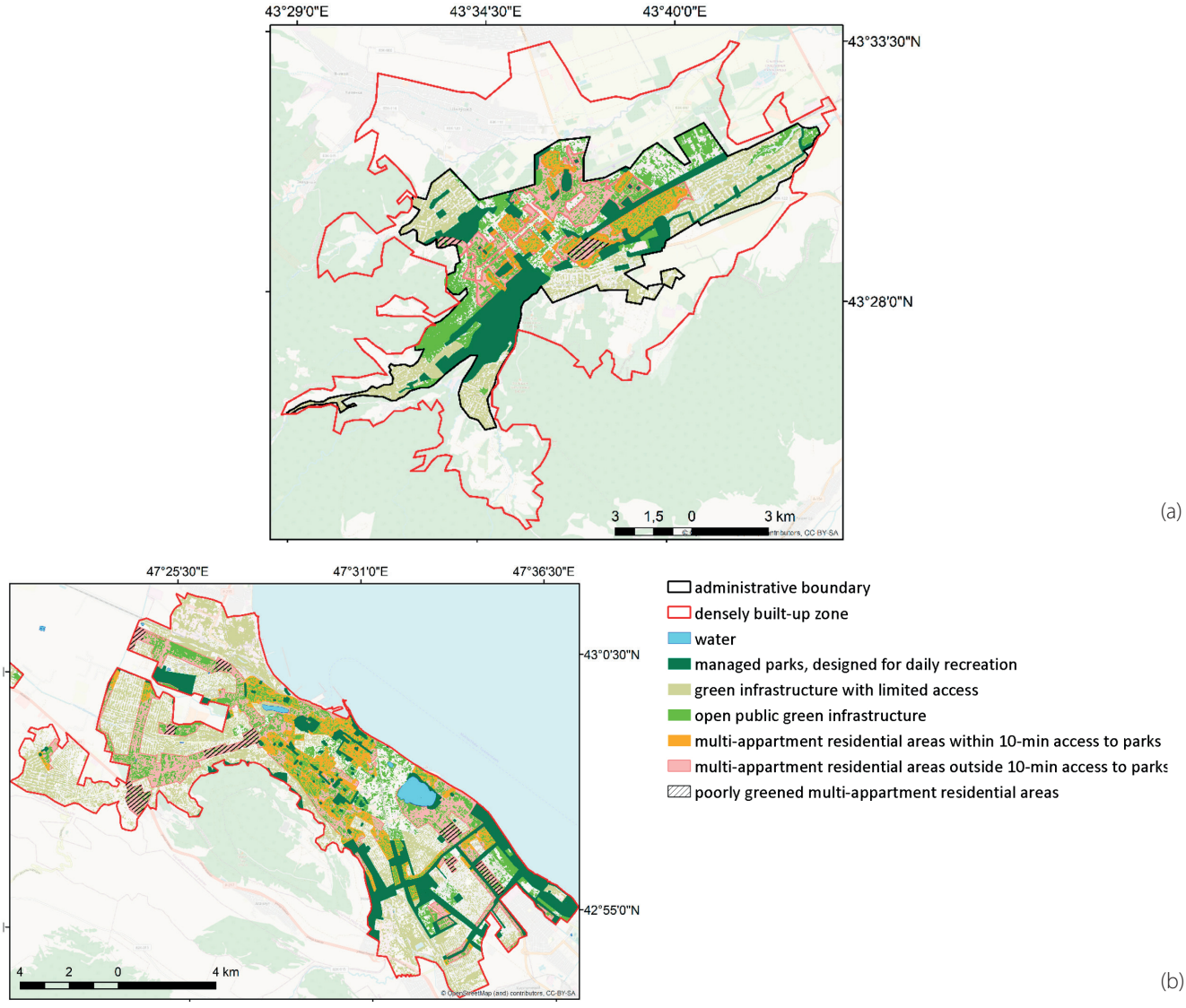

Fig. 5. Spatial justice parameters of the "outsider city" – Makhachkala

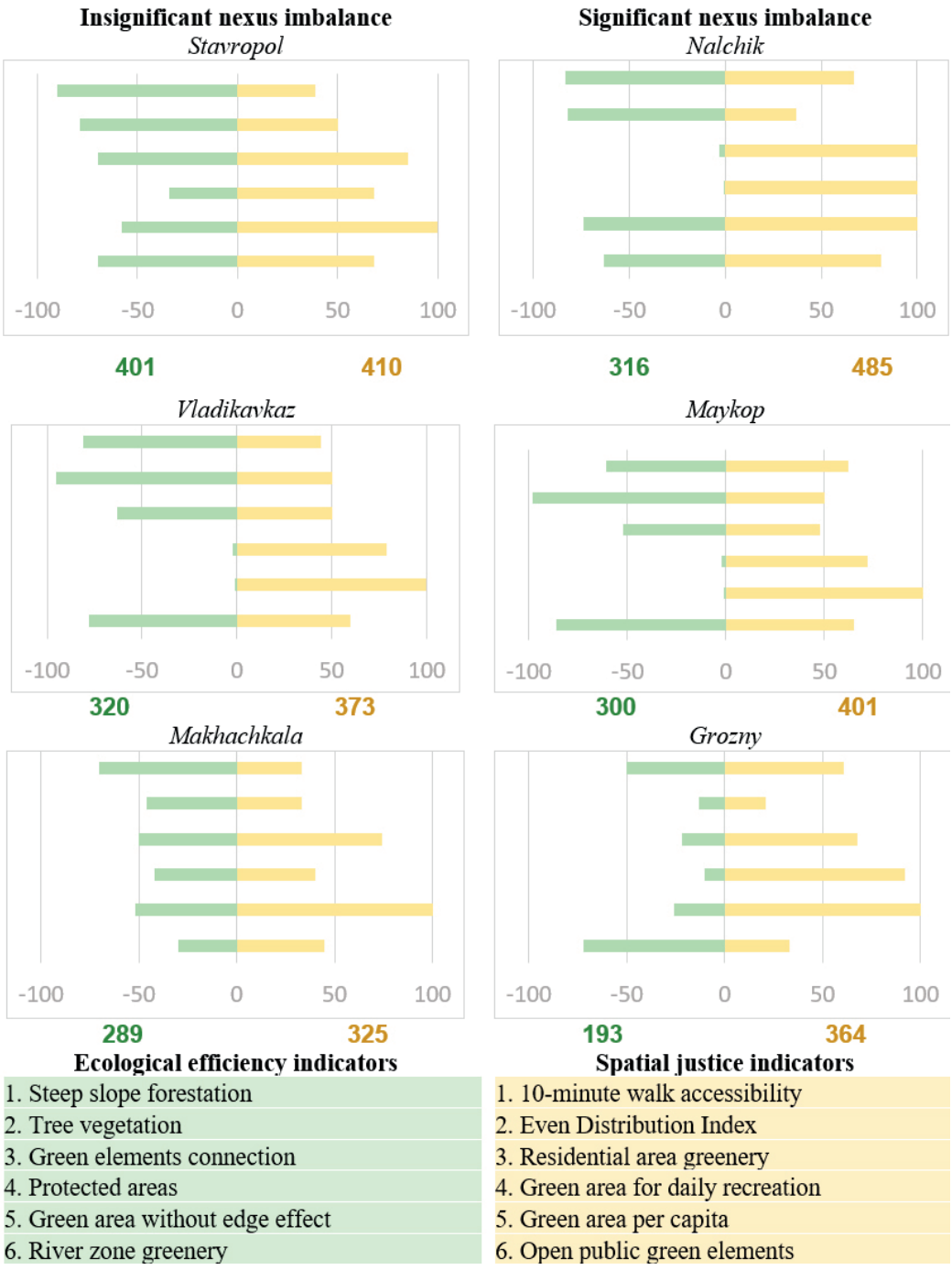

Fig. 6. Integrated assessment of the Spatial justice – Ecological efficiency Nexus in the studied cities (the numeration of diagram bars correlates with the numeration of indicators in the legend)

The most balanced nexus among the studied cities is found in Stavropol, with both sides scoring above 400 points and being equally developed. In Nalchik, Maykop, and Grozny, the social side of the nexus overwhelms the other one by more than 30%. This imbalance demonstrates that the urban population is currently more or less fairly provided with green areas, and all districts have a necessary amount of accessible, managed green infrastructure, but the green elements' integrity and ecological efficiency are vulnerable. The neglect of several ecological parameters, especially the lack of protected areas and green linkages, undermines the quality and availability of green spaces for future use by the population. Another case is Makhachkala, which has low results for both nexus sides. The opposite case is Grozny, with quite high scores for the social aspect but the lowest scores for ecological efficiency, meaning that its green infrastructure is vulnerable and its functioning is limited.

DISCUSSION

Unlike most large cities of the European part of Russia, the studied southern cities demonstrate less ecological efficiency. This pattern is partly explained by natural conditions because cities within the semi-arid zone have less natural vegetation, especially woody, and it is more challenging and expensive to link green elements. However, numerous studies (Meerow et al. 2021; Miroshnyk et al. 2022) emphasize that the efficiency and quality of urban green infrastructure largely depend on management and planning rather than natural conditions. This is because the urban environment, whether arid or humid, creates unfavorable conditions for most plants in any case.

Yet, when comparing our results on ecological efficiency with the population needs, the amount of the available green areas appears to be sufficient, like in most other Russian cities. Besides, due to the vast green yards and Soviet planning of district parks according to the old city plans, residential areas have enough vegetation to perform climate-regulating and

recreational functions for the city dwellers. These results are supported by other studies conducted for other Russian cities, including the southern ones (Danilina et al. 2021; Klimanova et al. 2021; Murtazova et al. 2023).

As a result, we can state that the green infrastructure of the studied cities shares many properties with other Russian cities, like the abundance of small district parks, green yards, and the concentration of tree vegetation on the steep slopes and in the river valleys. However, there are several crucial structural differences that make their green infrastructure distinctive regarding the Spatial Justice – Ecological Efficiency Nexus. For one, up to 50% of green area in many other Russian cities is concentrated in several large patches with an area of more than 50 ha (urban forest parks, suburban forests and agricultural lands). This structure is often responsible for better fragmentation and intactness results. Green infrastructure in the studied cities is mostly composed of small elements with an area of less than 10 ha, meaning that it is more fragmented and less connected. Besides, it is usually small river valleys that act as green corridors (Illarionova et al. 2024), and there are relatively few of them in the cities under study.

Another important aspect that affects the ecological efficiency of green areas is a lack of special protection status. This status does not necessarily mean that urban residents cannot visit green zones. Its purpose is to grant sustainable management, use and organization, and to efficiently combine different functions of green infrastructure. In fact, it can be a valid instrument to close the gap between conflicting sides of the Spatial justice – Ecological efficiency Nexus. However, our results show that most green infrastructure in the studied cities lacks this status. Despite being a promising tool for urban environment improvement, it seems unlikely that this particular parameter will be improved. According to the Resolution of the Government of Moscow dated December 27, 2024 N°. 3160-PP, urban protected natural areas were changed into urban protected green areas. The provisions of the Federal Law № 33 "On Specially Protected Natural Areas" that used to protect these areas are no longer in effect, and there is no longer a direct ban on activities that cause harm to ecosystems and their components. In the context of this research, there is a risk that other cities may follow this practice and also abolish the protected status of urban natural, thus further affecting the ecological efficiency of green infrastructure.

On the other hand, these cities are mostly low-rise and sparsely populated. Moreover, southern cities are increasingly gaining popularity as domestic tourist destinations, leading to the intensive development of recreational green elements for the city's guests.It is also a topic for further discussion and research, whether green infrastructure can be considered spatially just when developed and created primarily for tourists rather than the local population, and whether it can start green gentrification.

Limitations and future aspects

While our study provides valuable insights into the relation between ecological and justice aspects of green infrastructure, it is important to acknowledge certain limitations. To make the research more representative, it is necessary to assess pairs of green infrastructure spatial justice and ecological efficiency parameters that directly oppose each other (e.g., path density in forest parks and forest vegetation fragmentation, parks proximity to public transport and green zones intactness; variety of green elements for recreational activities and for regulating or supporting services).

Moreover, data on biodiversity and visitor activity, data on the state of vegetation, species, plants age, inner "non-green" infrastructure, park management and other components can provide a detailed picture of the actual impact of spatial distribution and ecological parameters on green infrastructure conditions. However, to consider these limitations, a lot of data sources are needed, which are difficult to gather for several large cities. It is also worth stressing that the number of case studies is not enough to define different types of Nexus Spatial justice – Ecological efficiency in Russian cities. In this study, we roughly divide cities with a balanced and unbalanced Nexus, yet there may be more types of Nexus sides interactions. Besides, more conclusions about the efficiency of green infrastructure and suggestions for its planning can be drawn based on the prevailing and underrepresented parameters of green elements if more cities are analyzed. Future research should address these limitations by employing new data sources to assess the most suitable two-by-two opposing parameters and by including more large cities in the study.

The concept of nexus in this domain of research should also be addressed cautiously, because the application of the nexus approach in an urban green infrastructure context requires further development of different methodologies for assessing the social, economic, and environmental impacts of nexus-based interventions. Future research should focus on refining these methodologies and exploring the role of urban governance, policy, social infrastructure, and vegetation state in facilitating the effective implementation of nexus-based strategies to support a sustainable urban environment.

CONCLUSIONS

Our assessment of the Spatial Justice – Ecological Efficiency Nexus of green infrastructure has revealed that most studied cities have an unbalanced nexus with a drastic prevalence of a social side. These high results for the social part are partly achieved because of the vast green area per relatively small population, meaning that North Caucasian cities have a lot of available green infrastructure. However, its accessibility is worse since the recommendations for the open public or recreational green areas in the walking vicinity to the residential districts are not met in most cities.

The analysis of ecological parameters has demonstrated that green elements in North Caucasian cities are mostly unstable due to the weak interconnection even along the large rivers and a lack of the protection status. The vast urban green areas mostly consist of tree vegetation (even in semi-arid Makhachkala) that can produce more supporting and regulating services for the urban environment than grasslands. However, most of these trees are under the edge effect, meaning that their state, intactness, and ecological functionality will be gradually decreasing.

The situation in the studied cities is not of the social aspects of green infrastructure prevailing at the expense of the ecological side. It is more like the current development affects more ecological functions, namely the sealing of river valleys, the unwillingness or inability to establish protected areas in the cities, and a lack of a unified planning system for the whole urban area that would consider the linkage of green elements at different spatial levels. The intensity of the current population growth and development in the urban area does not exceed the green infrastructure's potential to perform social functions yet. Besides, individual park projects and reconstructions generally positively affect the social aspect of green infrastructure. However, the neglect of the ecological side results in the cost increase and efficiency reduction of green elements that gradually lead to green injustice and shortage.

REFERENCES

Amaral M.H., Benites-Lazaro L.L., de Almeida Sinisgalli P.A., da Fonseca Alves H.P., & Giatti L.L. (2021). Environmental injustices on green and blue infrastructure: Urban nexus in a macrometropolitan territory. Journal of Cleaner Production, 289, 125829, DOI: 10.1016/j.jclepro.2021.125829.

Anguelovski I., Connolly J., Cole H., Garcia-Lamarca M., Triguero-Mas M., Baró F., Martin N., Conesa D., Shokry G., del Pulgar C., Ramos L., Matheney A., Gallez E., Oscilowicz E., Máñez J., Sarzo B., Beltrán M. and Minaya J. (2022). Green gentrification in European and North American cities. Nature communications, 13, 3816, DOI: 10.1038/s41467-022-31572-1.

Basnou C., Baró F., Langemeyer J., Castell C., Dalmases C. and Pino J. (2020). Advancing the green infrastructure approach in the Province of Barcelona: Integrating biodiversity, ecosystem functions and services into landscape planning. Urban Forestry & Urban Greening, 55, 126797, DOI: 10.1016/j.ufug.2020.126797.

Bolliger J., Silbernagel J. (2020). Contribution of connectivity assessments to green infrastructure. ISPRS International Journal of Geo-Information, 9, 4, 212, DOI: 10.3390/ijgi9040212.

Borelli S., Conigliaro M. and Di Cagno F. (2023). Urban forests: a global perspective. Rome: FAO, DOI: 10.4060/cc8216en.

Breuste J. (2023). The green city: general concept. In: J. Breuste, M. Artmann, C. Ioja, S. Qureshi, eds., Making Green Cities. Springer, Cham., 3-18, DOI: 10.1007/978-3-030-73089-5_1.

Cousins J. and Hill D. (2021). Green infrastructure, stormwater, and the financialization of municipal environmental governance. Journal of Environmental Policy & Planning, 23(5), 581-598, DOI: 10.1080/1523908X.2021.1893164.

Danilina N., Tsurenkova K., Berkovich V. (2021). Evaluating urban green public spaces: The case study of Krasnodar region cities, Russia. Sustainability, 13, 24, 14059, DOI: 10.1016/j.ufug.2018.02.011.

de Oliveira J., Bellezoni A., Shih W., Bayulken B. (2022). Innovations in Urban Green and Blue Infrastructure: Tackling local and global challenges in cities. Journal of Cleaner Production, 362, 132355, DOI: 10.1016/j.jclepro.2022.132355.

Depietri Y. (2022). Planning for urban green infrastructure: addressing tradeoffs and synergies. Current Opinion in Environmental Sustainability, 54, 101148, DOI: 10.1016/j.cosust.2021.12.001.

Evans D., Falagán N., Hardman C., Kourmpetli S., Liu L., Mead B. and Davies J. (2022). Ecosystem service delivery by urban agriculture and green infrastructure–a systematic review. Ecosystem Services, 54, 101405, DOI: 10.1016/j.ecoser.2022.101405.

Fahrig L. (2020). Why do several small patches hold more species than few large patches? Global Ecology and Biogeography, 29(4), 615-628, DOI: 10.1111/geb.13059.

Farrell C., Livesley S., Arndt S., Beaumont L., Burley H., Ellsworth D., Esperon-Rodriguez M., Fletcher T., Gallagher R., Ossola A., Power S., Marchin R., Rayner J., Rymer P., Staas L., Szota C., Williams N. and Leishman M. (2022). Can we integrate ecological approaches to improve plant selection for green infrastructure? Urban Forestry & Urban Greening, 76, 127732, DOI: 10.1016/j.ufug.2022.127732.

Ferreira J., Monteiro R. and Silva V. (2021). Planning a green infrastructure network from theory to practice: The case study of Setúbal, Portugal. Sustainability, 13(15), 8432, DOI: 10.3390/su13158432.

Escobedo F.J., Giannico V., Jim C.Y., Sanesi G., Lafortezza R. (2019). Urban forests, ecosystem services, green infrastructure and nature-based solutions: Nexus or evolving metaphors? Urban Forestry & Urban Greening, 37, 3-12, DOI: 10.1016/j.ufug.2018.02.011.

Jenkins J. and Pigram J. (2005). Outdoor recreation management. London: Routledge, DOI: 10.4324/9780203983584.

Illarionova O., Klimanova O. (2024). River zones as a tool for increasing the urban sustainability in large cities of Russia. E3S Web of Conferences, 555, 04003, DOI: 10.1051/e3sconf/202455504003.

Klimanova O., Kolbowsky E., Illarionova O. (2018). Impacts of urbanization on green infrastructure ecosystem services: The case study of post-soviet Moscow. Belgeo. Revue belge de géographie, 4, 30889, DOI: 10.4000/belgeo.30889.

Klimanova O., Illarionova O., Grunewald K., Bukvareva E. (2021). Green infrastructure, urbanization, and ecosystem services: The main challenges for Russia's largest cities. Land, 10, 12, 1292, DOI: 10.3390/land10121292.

Klimanova O. A., Bukvareva E. N., Kolbowsky E. Y., Illarionova O. A. (2023). Assessing ecosystem services in Russia: Case studies from four municipal districts. Land Use Policy, 131, 106738, DOI: 10.1016/j.landusepol.2023.106738.

Kumar P., Druckman A., Gallagher J., Gatersleben B., Allison S., Eisenman T.S., Morawska L. (2019). The nexus between air pollution, green infrastructure and human health. Environment international, 133, 105181, DOI: 10.1016/j.envint.2019.105181.

Lampinen J., García-Antúnez O., Lechner A.M., Olafsson A.S., Gulsrud N.M., Raymond C.M. (2023). Mapping public support for urban green infrastructure policies across the biodiversity-climate-society-nexus. Landscape and Urban Planning, 239, 104856, DOI: 10.1016/j.landurbplan.2023.104856.

Lindholst A., Konijnendijk C., Kjoller C., Sullivan S., Kristoffersson A., Fors H. and Nilsson K. (2016). Urban green space qualities reframed toward a public value management paradigm: The case of the Nordic Green Space Award. Urban forestry and urban greening, 17, 166-176, DOI: 10.1016/j.ufug.2016.04.007.

Litvinova T. (2020). North Caucasus image inside Russia in the context of tourism cluster development. Geojournal of Tourism and Geosites, 28(1), 275-288, DOI: 10.30892/gtg.28122-469.

Liu O. and Russo A. (2021). Assessing the contribution of urban green spaces in green infrastructure strategy planning for urban ecosystem conditions and services. Sustainable Cities and Society, 68, 102772, DOI: 10.1016/j.scs.2021.102772.

Maroko A., Maantay J., Sohler N., Grady K. and Arno P. (2009). The complexities of measuring access to parks and physical activity sites in New York City: A quantitative and qualitative approach. International Journal of Health Geographics, 8(34), DOI: 10.1186/1476-072X-8-34.

Matasov V., Yaroslavtsev A., Bukin S., Konstantinov P., Vasenev V., Grigoreva V., Romzaykina O., Dvornikov Y., Sayanov A. and Maximova O. (2021). Ecosystem services approach for landscaping project: the case of metropolia residential complex. In: V. Vasenev, ed., Advanced Technologies for Sustainable Development of Urban Green Infrastructure. SSC 2020. Springer, Cham., 319-330, DOI: 10.1007/978-3-030-75285-9_29.

Meerow S., Natarajan M., Krantz, D. (2021). Green infrastructure performance in arid and semi-arid urban environments. Urban Water Journal, 18, 4, 275-285, DOI: 10.1080/1573062X.2021.1877741.

Miroshnyk N.V., Likhanov A.F., Grabovska T.O., Teslenko I.K., Roubík H. (2022). Green infrastructure and relationship with urbanization–Importance and necessity of integrated governance. Land Use Policy, 114, 105941, DOI: 10.1016/j.landusepol.2021.105941.

Rigolon A. and Collins T. (2023). The green gentrification cycle. Urban Studies, 60(4), 770-785, DOI: 10.1177/00420980221114952.

Shade C., Kremer P., Rockwell J. and Henderson K. (2020). The effects of urban development and current green infrastructure policy on future climate change resilience. Ecology & Society, 25(4), DOI: 10.5751/ES-12076-250437.

Shi L. (2020). Beyond flood risk reduction: How can green infrastructure advance both social justice and regional impact? Socio-Ecological Practice Research, 2, 311-320, DOI: 10.1007/s42532-020-00065-0.

Skachkova M. E. (2024). Urban Green Infrastructure Assessment: Identification of Public Green Spaces Misuse. Geography, Environment, Sustainability, 17(4), 183-197, DOI: 10.24057/2071-9388-2024-3458.

Teixeira C., Fernandes C., Ahern J., Honrado J. and Farinha-Marques P. (2021). Urban ecological novelty assessment: Implications for urban green infrastructure planning and management. Science of The Total Environment, 773, 145121, DOI: 10.1016/j.scitotenv.2021.145121.

Valente D., Pasimeni M. and Petrosillo I. (2020). The role of green infrastructures in Italian cities by linking natural and social capital. Ecological Indicators, 108, 105694, DOI: 10.1016/j.ecolind.2019.105694.

Varentsov M., Vasenev V., Dvornikov Y., Samsonov T., Klimanova O. (2023). Does size matter? Modelling the cooling effect of green infrastructures in a megacity during a heat wave. Science of the Total Environment, 902, 165966, DOI: 10.1016/j.scitotenv.2023.165966.

Wang C., Ren Z., Dong Y., Zhang P., Guo Y., Wang W. and Bao G. (2022). Efficient cooling of cities at global scale using urban green space to mitigate urban heat island effects in different climatic regions. Urban Forestry & Urban Greening, 74, 127635, DOI: 10.1016/j.ufug.2022.127635.

Yao J., Xu P. and Huang Z. (2021). Impact of urbanization on ecological efficiency in China: An empirical analysis based on provincial panel data. Ecological Indicators, 129, 107827, DOI: 10.1016/j.ecolind.2021.107827.

Yazar M. and York A. (2023). Nature-based solutions through collective actions for spatial justice in urban green commons. Environmental Science & Policy, 145, 228-237, DOI: 10.1016/j.envsci.2023.04.016.

RESEARCH PAPER

WHICH CLIMATE MODEL EVALUATION METHODS CAN CONSISTENTLY SELECT SKILLFUL MODELS FROM THE CMIP6 ENSEMBLE?

Natalia V. Gnatiuk[1*], Iuliia V. Radchenko[1], Richard Davy[2], Jiechen Zhao[3,4], Leonid P. Bobylev[1]

[1]Nansen International Environmental and Remote Sensing Centre, 14-Liniya V.O. 7, St. Petersburg, 199034, Russia

[2]Nansen Environmental and Remote Sensing Center, Jahnebakken 3, Bergen, 5006, Norway

[3]Qingdao Innovation and Development Base of Harbin Engineering University, Sansha Road 1777, Qingdao, 266000, China

[4]First Institute of Oceanography, MNR & Decade Collaborative Center on Ocean-Climate Nexus and Coordination, Xianxialing Road 6, Qingdao, 266000, China

***Corresponding author:** gnatiuk.n@gmail.com

Received: October 29th 2024 / Accepted: May 15th 2025 / Published: June 30th 2025

https://doi.org/10.24057/2071-9388-2025-3694

ABSTRACT. When considering the possible use of climate model data, it is necessary to choose which model is most appropriate to use. There are many methods for evaluating and selecting climate models in the literature, but there is no established consensus on which method is the most robust for determining model skill. In this article, we tested seven widely used methods for evaluating climate models in the Arctic using CMIP6 surface air temperature data: a single statistical metric method (root mean square error, spatial trends), a single skill score method (Taylor skill score, probability density function), a combination of several statistical metric methods (Taylor diagram, interannual variability skill score, comprehensive rating metric, etc.), and a multiple statistical criteria method (percentile-based approach). To evaluate their consistency, each method was applied to two periods: 1951-1980 and 1981-2010. For each method, the models were ranked and classified into three quality groups (very good, satisfactory, unsatisfactory). The comparison of methods was performed by comparing the differences in the average values of the normalized statistical measures, the differences in the model ranks, and the definition of the model quality groups. For each method, an optimal set of models corresponding to the top 25% was selected. One of the main objectives of the study was to compare the ability of the methods to identify the best model for the selected ensemble, regardless of the time period (i.e., without sensitivity to natural variability). The results suggest a preference for methods using root mean square error and a percentile-based approach.

KEYWORDS: climate model, evaluation method, CMIP6, sub-ensemble, climate model selection

CITATION: Gnatiuk N. V., Radchenko I. V., Davy R., Zhao J., Bobylev L. P. (2025). Which Climate Model Evaluation Methods Can Consistently Select Skillful Models From The Cmip6 Ensemble? Geography, Environment, Sustainability, 2 (18), 126-149
https://doi.org/10.24057/2071-9388-2025-3694

ACKNOWLEDGEMENTS: The study was funded by the Russian Science Foundation (RSF) grant No. 23-77-01106, https://rscf.ru/en/project/23-77-01106/.

Conflict of interests: The authors reported no potential conflict of interests.

INTRODUCTION

At present, climate models are the most valuable tool in projecting future climate under different scenarios (Taylor et al. 2012; Stocker et al. 2014; Otero et al. 2018). Over the years, global climate models (GCMs) have been continuously developed by different modeling centers, incorporating diverse parameterizations. Consequently, future climate projections from these models can vary significantly, leading to substantial uncertainty in projected changes of climate variables (Knutti et al. 2010; Stocker et al. 2014). In addition to this considerable projection uncertainty, individual models often have significant biases. Therefore, a multi-model ensemble of GCM simulations is commonly employed in research, as it has been shown that ensemble means tend to cancel out individual model biases - i.e., the ensemble mean of a large group of models generally outperforms any single model in most cases (Gleckler et al. 2008; Knutti et al. 2010; Raju and Kumar 2020).

However, in the IPCC's Sixth Assessment Report (AR6), climate models were assigned weightings when assessing future projections for the first time. This was due to the "hot model" problem: a subset of CMIP6 models exhibited climate sensitivities outside the range estimated from multiple lines of evidence (Sherwood et al. 2020). This issue has prompted efforts within the community to establish robust model selection criteria (Hausfather et al. 2022). Research indicates that selecting skillful GCMs can reduce uncertainty in ensemble projections compared to using the full set of dozens of models (Herger et al. 2018; Gnatiuk et al. 2020). As a result, various model selection criteria and

evaluation methods have been introduced in the literature. A categorization mind map of these methods is provided in Appendix A.2.

One approach to reducing uncertainty is to select only those models that perform well in historical simulations when compared to observations. The primary assumption underpinning this approach is that model skill in historical simulations is a reliable predictor of model performance in future climate projections; that is, models that are skillful in historical simulations are also likely to be skillful in their response to forcing. Numerous studies have demonstrated that the response to forcing is sensitive to baseline climatology, which supports this assumption (Caballero and Huber 2013). However, if there is a substantial change in the relative importance of different processes shaping regional climate, then this assumption – that historical skill predicts future model performance – may not hold. Additionally, given the considerable internal variability within models, it is essential that the evaluation of model skill be conducted over a long period (several decades) to ensure a fair assessment of model performance (Jain et al. 2023). Furthermore, it is crucial that the criteria for model selection are not overly sensitive to the phase of natural variability within the climate system.

There is no consensus among researchers on best practice for climate model evaluation and selection (Knutti et al. 2010; Ahmadalipour et al. 2017; Herger et al. 2018; Calvin et al. 2023). This lack of agreement has resulted in a diverse range of approaches; for example, some studies employ only a single statistical metric for GCM evaluation (e.g., Walsh et al. 2008; Macadam et al. 2010; Sillmann et al. 2013; Agosta et al. 2015), while others utilize multiple statistical metrics (e.g., McMahon et al. 2015; Aghakhani Afshar et al. 2017; Ruan et al. 2019). For instance, the near-surface air temperature simulations from 17 GCMs were analyzed using just one statistical metric – root mean square error (RMSE) – and models were ranked from the lowest to the highest RMSE values (Reifen and Toumi 2009; Macadam et al. 2010). Herger et al. (2018) selected an optimal subset of 38 GCMs for surface air temperature and precipitation based on RMSE. RMSE was also employed for inter-model comparison and evaluation by Sillmann et al. (2013) and Zhou et al. (2014). Other statistical metrics have been used to assess GCM accuracy as well – for example, Kumar et al. (2013) evaluated 19 GCMs based on trends in temperature and precipitation across continental areas. Maxino et al. (2008) and Perkins et al. (2007) proposed a skill score that measures the common area between the probability density functions (PDFs) of modeled and observed data.

Many studies evaluating the accuracy of GCMs utilize the Taylor diagram, which combines three statistical criteria – standard deviation (STD), RMSE, and correlation coefficient (r) (Taylor 2001). This diagram is summarized into a single metric – the Taylor skill score (Taylor 2001; Inoue and Ueda 2011; Ogata et al. 2014; Sharmila et al. 2015; Kadel et al. 2018; Yang et al. 2020). It should be noted that even when employing the same evaluation methods, researchers often apply different thresholds for sub-ensemble selection, as there is frequently no clear criterion defining a model as "good" or "bad" within these evaluation frameworks. For example, the Taylor skill score has been utilized by Sharmila et al. (2015), Kadel et al. (2018), and Yang et al. (2020), but with varying thresholds.

Some studies evaluating GCMs have employed multiple statistical metrics. For example, McMahon et al. (2015) assessed 23 GCMs using RMSE, the Nash-Sutcliffe Efficiency coefficient (NSE), and the coefficient of determination (r^2) for temperature and precipitation patterns. Kumar et al. (2015) considered bias, trend analysis, and Taylor diagrams to evaluate simulations of extreme winds from 15 GCMs across 22 regions. Aghakhani Afshar et al. (2017) evaluated 14 GCMs for precipitation using four statistical criteria: r^2, NSE, percent of bias (PBIAS), and the ratio of root mean square error to the standard deviation of measured data (CPI). Furthermore, Aghakhani Afshar et al. (2017) categorized the statistical metrics into four groups – very good, good, satisfactory, and unsatisfactory – using a threshold criterion, ultimately selecting models with scores between 75% and 100%, which were ranked as the very good group. Jiang et al. (2015) evaluated 31 GCMs for total precipitation and three indices (the fraction of total rainfall from events exceeding the long-term 95th percentile, precipitation intensity, and maximum consecutive dry days) over China, employing a Taylor diagram and the Interannual Variability Skill Score (IVS; Chen et al. 2011). They further ranked the models using a Comprehensive Rating Metric. You et al. (2018) applied a similar analysis and model selection process as Jiang et al. (2015), but additionally analyzed trends and IVS for both the sub-ensemble and full ensemble across 16 temperature indices. This comprehensive rating metric has been utilized in many studies for model ranking, including those by Jiang et al. (2015), You et al. (2018), Rao et al. (2019), Ahmed et al. (2019, 2020), and Cai et al. (2021).

Other researchers have employed more complex methods involving multiple (up to seven) statistical criteria for evaluating the reliability of GCMs (e.g., Fu et al. 2013; Rupp et al. 2013; Ruan et al. 2019; Jia et al. 2019; Gnatiuk et al. 2020). These studies used different combinations of variables – such as air temperature, precipitation, wind speed, shortwave radiation, and nutrients – and a varying number of GCMs, ranging from 11 to 41. To compare the models, researchers ranked them based on their total scores and selected the relatively best GCMs: for example, 8 out of 41 models – around 20% (Rupp et al. 2013), the top 25% of models (Ruan et al. 2019; Gnatiuk et al. 2020), or the top 30% (Jia et al. 2019). All of these authors suggest the use of a method that incorporates multiple statistical criteria rather than relying on a single metric.

Furthermore, there is no universally accepted method for climate model evaluation and selection. A significant challenge is the trade-off associated with ensemble size: the stricter the filtering of non-skillful models, the smaller the ensemble becomes, which can increase the influence of individual model biases in the ensemble mean projections.

Any model selection criterion should also be robust – that is, it should consistently identify similar models as skillful across different time periods used for model evaluation. This task presents particular difficulties given the large natural variability and internal variability within models. Consequently, there has been a shift toward evaluating models based on processes rather than states (Eyring et al. 2019).

In summary, various methods are employed to evaluate and select appropriate GCMs for specific research questions (Herger et al. 2018; Raju and Kumar 2020; Calvin et al. 2023). Chai and Draxler (2014) recommend using several statistical metrics, including RMSE and mean absolute error (MAE). Raju and Kumar (2020) suggest considering the statistical metrics in a category-wise manner – for example, one metric for error, one for correlation, and one for skill score – and then computing the overall weight of the metrics, for instance, using a rating method. Fu et al. (2013), Ruan et al. (2019), Jia et al. (2019), and Gnatiuk et al. (2020) propose the application of multiple criteria for model evaluation.

Currently, there is no comprehensive comparison of these different methods for evaluating climate models; therefore, this study aims to fill this gap. We tested several widely used approaches, ranging from a single statistical metric to multiple metrics: (i) RMSE, (ii) spatial trends, (iii) TSS, (iv) PDF, (v) Taylor diagram, IVS, MR, (vi) Taylor diagram, MAE, trend, and (vii) a percentile-based method for evaluating CMIP6 surface air temperature (SAT) in the Arctic. To compare these methods with each other, we ranked GCMs according to their performance for each approach and selected the top 25%. Additionally, we conducted the analysis over two different periods – 1951-1980 and 1981-2010 – to assess the consistency of these methods.

MATERIALS AND METHODS

Study area and data

In this paper, we compare model evaluation methods based on surface air temperature in the Arctic (60-90° N). Simulations of historical surface air temperatures from 25 GCMs from the Coupled Model Intercomparison Project Phase 6 (CMIP6) were obtained from the Earth System Grid Federation portal[1]. Information about these models is provided in Table A.1. The list of model names is presented in Fig. 1. The model data were compared to observations from the Berkeley Earth database (Rohde et al. 2013; Rohde and Hausfather 2020). The Berkeley Earth database is a comprehensive global land-ocean temperature record that integrates monthly land temperature data from over 40,000 weather stations with sea surface temperature data from HadSST3 (Hadley Centre Sea Surface Temperature dataset, version 3). Using kriging-based spatial interpolation, it provides extensive spatial coverage for the period spanning from 1850 to the present. It offers average temperatures in 1° x 1° latitude-longitude grid cells for each month.

We selected seven of the most frequently used methods. Table A.3 summarizes the published works employing these methods. Each method is described in detail below:

i) Method of model comparison by ***root mean square error***

Root mean square error (*RMSE*) is a commonly used statistic to quantify differences between two fields of data (Eq. 1):

$$RMSE = \sqrt{\frac{\sum_{i=1}^{n}\left(Tm_i - To_i\right)^2}{n}} \quad (1)$$

where Tm_i is the temperature from the model and To_i is the temperature from observations at time step, *i*, with *n* representing the number of measurements in the time series. The smaller the RMSE, the better the agreement between the two data fields.

ii) Method of model comparison by ***trends***

Analysis of spatial trends using statistics such as the correlation coefficient *(r)*, standard deviation *(STD)*, and mean value ($\overline{T}$) is proposed by Kumar et al. (2013). The correlation coefficient r is calculated as (Yang et al. 2020) (Eq. 2):

$$r = \frac{\frac{1}{n}\sum_{i=1}^{n}\left(To_i - \overline{To}\right)\times\left(Tm_i - \overline{Tm}\right)}{STDo \times STDm} \quad (2)$$

where Tm_i is the temperature from a given model and To_i is the temperature from observations at time step *i*, $\overline{Tm}$ is the average temperature of the model, while $\overline{To}$ is the average temperature of the observations, *n* represents the number of observations in the time series, *STDm* is the standard deviation of the model temperatures, and *STDo* is the standard deviation of the observed temperatures.

STD is calculated as (Eq. 3):

$$STD = \sqrt{\frac{\sum_{i=1}^{n}\left(T_i - \overline{T}\right)}{n-1}} \quad (3)$$

where T_i is the temperature at time step *i*, $\overline{T}$ is the mean temperature, and *n* is the number of data points in the time series.

Trend (*Tr*) was calculated using the least squares method (Eq. 4):

$$Tr = \frac{\sum_{i=1}^{n}\left(T_i - \overline{T}\right)\times\left(Y_i - \overline{Y}\right)}{\sum_{i=1}^{n}\left(T_i - \overline{T}\right)^2} \quad (4)$$

where T_i is the temperature at time step *i*, $\overline{T}$ is the average temperature, Y_i is the time step of the time series, is the mean of the time series, *n* is the number of data points in the series.

Each model was ranked based on its ability to represent observations across three metrics: r, the difference between the mean values of models and observations, and the difference between the STD of models and observations.

iii) Method of model comparison by ***Taylor skill score***

The Taylor skill score (TSS) is calculated using r and STD statistical metrics (Taylor 2001) (Eq. 5):

$$TSS = \frac{4\times(1+r)^4}{\left(STDN + \frac{1}{STDN}\right)^2 \times (1+r)^4} \quad (5)$$

where *r* is the correlation coefficient and *STDN* is the ratio of the model's and observations' *STD*. The *TSS* is bounded between 0 and 1, with 1 indicating a perfect fit between the model and observations.

iv) Method of model comparison by S_{score}

The skill score based on PDFs (S_{score}) was proposed by Perkins et al. (2007) as a robust metric for evaluating and ranking climate models because it is less affected by observational errors than the mean value and standard deviation. The S_{score} measures the common area between the PDFs of observed and model data. The formula for S_{score} is expressed as (Eq. 6):

$$S_{score} = \sum_{1}^{n} minimum\left(Z_m, Z_o\right) \quad (6)$$

where *n* is the number of temperature bins, Z_m is the frequency of model data values within the corresponding bin, and Z_o is the frequency of observed data values within that bin. Therefore, the S_{score} ranges between 0 and 1, with a score of 1 indicating a perfect match between the observed and model distributions and a score of 0 indicating no overlap between them. When applying this skill score metric, we used bins that are 1°C wide.

v) Comprehensive rating metric based on Taylor diagram and interannual variability skill score

The Comprehensive Rating Metric (*MR*) was proposed by Jiang et al. (2015) (Eq. 7):

$$MR = 1 - \frac{1}{nm}\sum_{i=1}^{n} rank_i \quad (7)$$

where *n* is the total number of parameters, *m* is the number of models, and rank is the position of a given model based on its performance (with 1 being the best model). The metric ranges between 0 and 1, with higher *MR* values indicating better model skill. The *MR* was calculated for each of the metrics used in the Taylor diagram (*r, STDN, RMSE*), and an average *MR* value was derived for each metric.

Additionally, *MR* was calculated for the Interannual Variability Skill Score (*IVS*; Chen et al. 2011) (Eq. 8):

$$IVS = \left(\frac{STD_m}{STD_o} - \frac{STD_o}{STD_m} \right)^2 \quad (8)$$

where *STDm* is the standard deviation from the model and *STDo* is the standard deviation of the observations. Smaller *IVS* values indicate that the simulated variability more closely matches the observed variability.

vi) Method of model comparison by ***Taylor Diagram, bias and trend***

Kumar et al. (2015) proposed to evaluate models using Taylor diagram, bias, and trend statistics. Bias (B) is calculated as the mean of the differences between the model and observations (Eq. 9):

$$B = \frac{\sum_{i=1}^{n} T_{m_i} - T_{o_i}}{n} \quad (9)$$

where *n* is the number of observations in the time series.

vii) Percentile-based method

A percentile score-based model ranking method introduced by Gnatiuk et al. (2020) includes the analysis of the mean spatially averaged climatology of the annual cycle, interannual variability of parameters using r, RMSE, STD, the Climate Prediction Index (CPI – ratio of RMSE to the STD of the observations) (Agosta et al. 2015), as well as the spatial trends and biases (at each grid point) between the model data and reanalysis/observations to illustrate how temperature varies across the study area. The range of the statistical indices for each model was divided into four categories: 0-25% – very good, 25-50% – good, 50-75% – satisfactory, and 75-100% – unsatisfactory. Each category was assigned a score from 3 to 0, respectively. For correlation, the scoring was reversed. These scores were then summed for each model to obtain a total skill score. Based on this total skill score, the top 25% of GCMs were selected as an optimal ensemble.

Approach for comparing model evaluation methods

SAT in the Arctic was analyzed for two periods, 1951-1980 and 1981-2010, to evaluate the consistency of model evaluation methods. We assume that if the models selected by each individual method are consistent across these two periods, then the method can reliably identify skillful models regardless of potential inconsistencies arising from different phases of natural and internal variability. For each period, the statistical metrics were normalized to a scale from 0 to 1 (with 1 indicating perfect performance). The original statistical metrics prior to normalization are provided in the Appendices (Fig. A.10-A.13, Table A.14-A.17). Models were ranked based on their ability to simulate SAT; if multiple metrics were used, their mean value was employed for the final ranking. Following ranking, the top 25% (in this case, six models) were selected as the optimal model ensemble for each period (Aghakhani Afshar et al. 2017; Ruan et al. 2019; Gnatiuk et al. 2020). Additionally, three quality groups (QGs) of models were distinguished based on their rankings: the first 25% of the models were classified as very good (QG I), the last 25% as unsatisfactory (QG III), and the remaining 50% as satisfactory (QG II).

The consistency of the model evaluation methods was analyzed using mean absolute differences of normalized statistical metrics and mean absolute differences of ranks between two time periods of all models. The consistency of a method is considered better when the specified absolute differences are closer to zero. Furthermore, the study examined whether a model belonged to the same quality group in both periods. If this was the case, the model's ranking was defined as consistent. Finally, we summarized the percentage of models that were consistent according to each method. These values were then used to compare the evaluation methods.

RESULTS

Model evaluation according to each considered method

i) Method of model comparison by ***root mean square error*** (RMSE)

The results of the normalized values of RMSE along with the assigned model ranks and quality groups for two periods are presented in Fig. 1. Based on the ranking results, the following models were selected for the sub-ensemble (the best models are highlighted in green and belong to the first quality group, QG I):

- for the period 1951-1980: ACCESS-ESM1-5, AWI-CM-1-1-MR, CESM2-WACCM, GFDL-ESM4, MPI-ESM1-2-LR and NorESM2-LM;
- for the period 1981-2010: ACCESS-ESM1-5, CESM2-WACCM, EC-Earth3-Veg, FIO-ESM-2-0, MPI-ESM1-2-HR, and MPI-ESM1-2-LR.

In Fig. 1, the three far right columns display the evaluation of the method's consistency. The intermodel mean difference in normalized RMSE between 1981-2010 and 1951-1980 is 0.06; the mean difference in model ranks is 3.0; and the results of the consistency assessment based on the model classified into the same quality group in both periods are 60%. Additionally, during both periods, 3 models out of 25 were classified as QG I, 8 as QG II, and 4 as QG III.

It should be noted that in this case, RMSE normalization involved converting values so that 1 indicates perfect performance and 0 indicates poor performance, allowing for comparison across all methods using the mean of the statistic. For original RMSE values, see Fig. A.10.

A similar ranking of models and assignment of each model to a quality group was performed for the other six model evaluation methods. Figures analogous to Fig. 1 for these additional evaluation methods are presented in Figs. A.4-A.9. The results of the comparison of the model evaluation methods are summarized in Table 1.

Intercomparison of the model evaluation methods

The summarized results of the consistency assessment for all methods are presented in Table 1 and Fig. 2. The first column in Table 1 indicates the number of models that were included in the selected sub-ensemble across both periods. The value in parentheses represents the percentage of the possible six sub-ensemble models, corresponding to the top 25% of the full ensemble. For example, for method iii, no models were included in the selected sub-ensemble in either period. The highest consistency was observed for methods i and vii, where three and four models,

№	Model acronym	Period 1951-1980			Period 1981-2010			RMSE diff.	Model rank diff.	Consistency (QG)
		RMSE	Model rank	Quality group	RMSE	Model rank	Quality group			
1	ACCESS-CM2	0.62	20	III	0.54	24	III	0.08	4	yes
2	ACCESS-ESM1-5	0.96	3	I	0.98	4	I	0.03	1	yes
3	AWI-CM-1-1-MR	0.94	5	I	0.88	10	II	0.06	5	no
4	BCC-CSM2-MR	0.81	12	II	0.81	14	II	0.00	2	yes
5	CAMS-CSM1-0	0.62	19	II	0.56	23	III	0.06	4	no
6	CanESM5	0.90	10	II	0.97	7	II	0.07	3	yes
7	CESM2-WACCM	0.95	4	I	0.97	5	I	0.01	1	yes
8	CIESM	0.53	23	III	0.58	22	III	0.06	1	yes
9	EC-Earth3	0.55	22	III	0.78	16	II	0.24	6	no
10	EC-Earth3-Veg	0.75	16	II	0.99	3	I	0.24	13	no
11	FGOALS-f3-L	0.46	24	III	0.60	21	III	0.14	3	yes
12	FGOALS-g3	0.00	25	III	0.00	25	III	0.00	0	yes
13	FIO-ESM-2-0	0.90	8	II	1.00	1	I	0.10	7	no
14	GFDL-ESM4	0.98	2	I	0.94	8	II	0.04	6	no
15	INM-CM4-8	0.77	15	II	0.70	19	II	0.06	4	yes
16	INM-CM5-0	0.90	9	II	0.88	11	II	0.02	2	yes
17	IPSL-CM6A-LR	0.89	11	II	0.86	12	II	0.02	1	yes
18	KACE-1-0-G	0.61	21	III	0.71	18	II	0.10	3	no
19	MIROC6	0.80	13	II	0.82	13	II	0.02	0	yes
20	MPI-ESM1-2-HR	0.92	7	II	0.97	6	I	0.05	1	no
21	MPI-ESM1-2-LR	1.00	1	I	0.99	2	I	0.01	1	yes
22	MRI-ESM2-0	0.79	14	II	0.78	15	II	0.01	1	yes
23	NESM3	0.67	18	II	0.65	20	III	0.02	2	no
24	NorESM2-LM	0.94	6	I	0.92	9	II	0.01	3	no
25	NorESM2-MM	0.73	17	II	0.73	17	II	0.00	0	yes
							Mean	0.06	3.0	yes - 60%

- very good (I) - satisfactory (II) - unsatisfactory (II) - QUALITY GROUPS (QG)

I (3) II (8) III (4) / got into different groups (10) - number of models belong to each QG in two periods

Fig. 1. Results of normalized RMSE, model ranks, quality groups and consistency assessment for 25 models for the periods 1951-1980 and 1981-2010 for SAT over the Arctic

respectively, appeared in the selected sub-ensembles across both periods. The difference in mean normalized statistical metrics between the two periods (where 0 indicates perfect agreement) ranges from 0.06 (method i) to 0.36 (method iii). The most effective methods are (i) RMSE, (vi) Taylor diagram, bias and trend, and (vii) the percentile-based method. The difference in rank values between the two periods (where 0 indicates perfect agreement) varies from 3.0 (method i) to 8.9 (method ii). The best-performing methods are (i) RMSE, (vii) the percentile-based approach, and (iv) the S_{score} method. The last column in Table 1 and Fig. 2 (left) shows the percentage of models classified into the same quality group across both periods. The lowest consistency based on quality groups was observed for method iii at 40%, while the highest was for method vii at 72%. Thus, among the seven evaluated methods, the most effective model evaluation techniques are (vii) the percentile-based method and (i) RMSE.

Fig. 3 illustrates how many times each model was identified as the best model and included in the sub-ensemble (top 25%), as well as how many times it was defined as unsatisfactory (worst 25%) across 14 ranking cases (7 methods × 2 periods). The most frequently selected models for the sub-ensemble are ACCESS-ESM1-5, AWI-CM-1-1-MR, EC-Earth3-Veg, GFDL-ESM4, and MPI-ESM1-2-LR. Conversely, the GCMs most commonly identified as unsatisfactory are CAMS-CSM1-0, CIESM, FGOALS-g3, INM-CM4-8, and NESM3. Climate models such as AWI-CM-1-1-MR, BCC-CSM2-MR, INM-CM5-0, and MPI-ESM1-2-LR were never classified among the worst 25%. Similarly, models like CAMS-CSM1-0 and MIROC6 were never ranked in the top 25%.

Interannual variability of SAT over the Arctic for the periods 1951-1980 (left) and 1981-2010 (right), for observations, the full ensemble, and sub-ensembles using the seven model assessment methods, are presented in Figs. 4 and 5. In general, all sub-ensembles exhibit an interannual variability distribution pattern similar to that of the observations but with some errors (larger or smaller). The averaging of the full ensemble significantly smooths the interannual temperature amplitude. Overall, the SAT of the full ensemble and sub-ensembles based on methods iii and iv underestimate observations during the period 1951-1980; sub-ensembles based on methods i, ii, v, and vii better reproduce the SAT. During the period 1981-2010, models selected based on methods iii and ii underestimate SAT compared to observations; however, methods i, v, vi, and vii better reproduce the interannual variability of SAT.

Boxplots of the annual SAT over the Arctic for the periods 1951-1980 and 1981-2010 are shown in Fig. 5. The dashed line indicates the mean value of observations. In the first period, only the mean values for the sub-ensemble selected by method vii are close to the mean of observations. For other methods, deviations from the observational mean generally range from 0.5 to 1 degree Celsius. In the second period, the shape of the distribution

Table 1. Results of selected sub-ensembles using seven methods and an assessment of their consistency

Method	Same selected models	Mean Diff. in value	Mean Diff. in rank	Models belong to each QG in two period simultaneously	Consistency (QG)
i	3 (50%)	0.06	3.0	I (3) II (8) III (4) / got into different groups (10)	60%
ii	2 (33%)	0.18	8.9	I (2) II (10) III (1) / got into different groups (12)	52%
iii	0	0.36	8.3	I (0) II (7) III (3) / got into different groups (15)	40%
iv	2 (33%)	0.31	5.7	I (2) II (7) III (3) / got into different groups (13)	48%
v	1 (17%)	0.32	8.5	I (1) II (8) III (2) / got into different groups (14)	44%
vi	2 (33%)	0.12	6.7	I (2) II (7) III (3) / got into different groups (13)	52%
vii	4 (67%)	0.15	4.4	I (4) II (10) III (4) / got into different groups (7)	72%

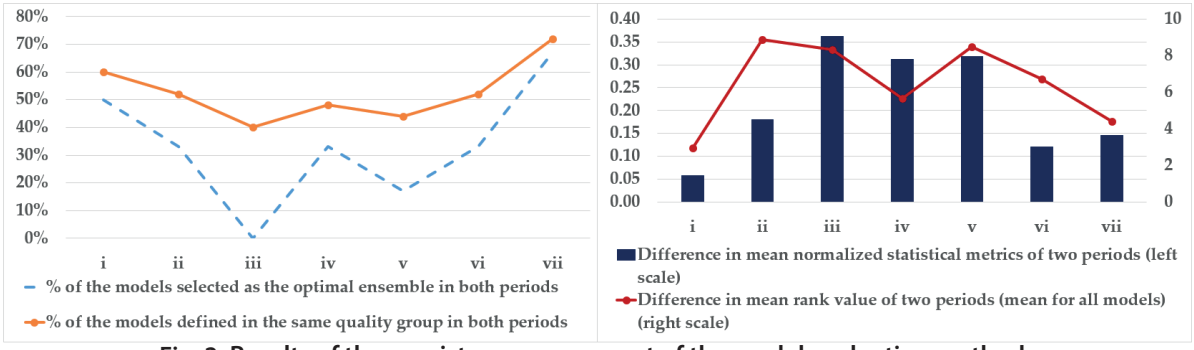

Fig. 2. Results of the consistency assessment of the model evaluation methods

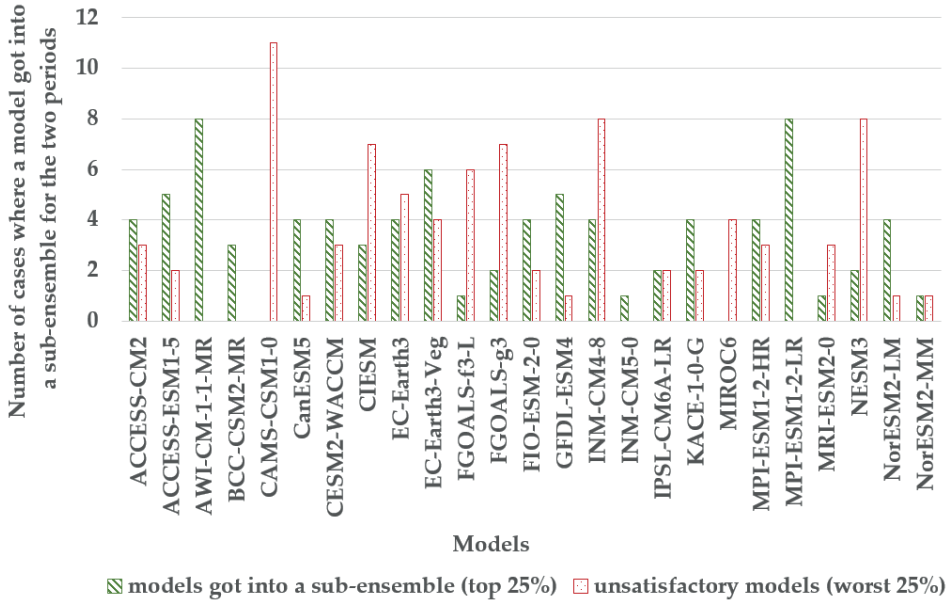

Fig. 3. Number of cases where a model entered a sub-ensemble (top 25% of models – in green) and where a model was defined as unsatisfactory (bottom 25% of models – in red) for two periods. The maximum number of cases is 14 (7 methods × 2 periods)

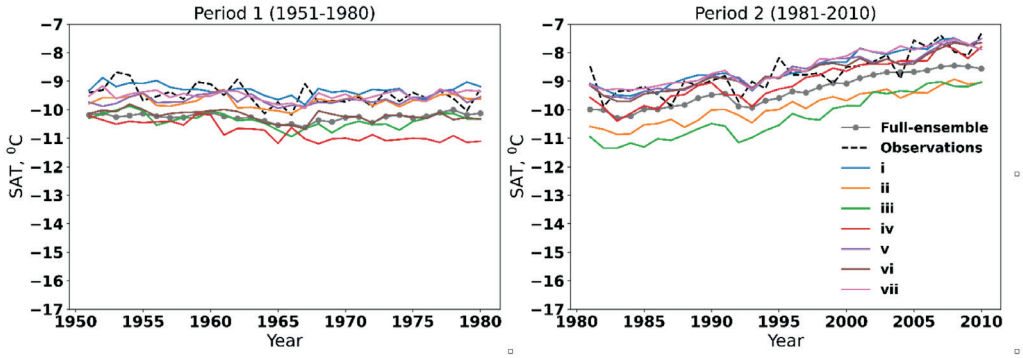

Fig. 4. Results of the annual SAT over the Arctic for observations, the full ensemble, and selected sub-ensembles using seven model assessment methods for 1951-1980 and 1981-2010

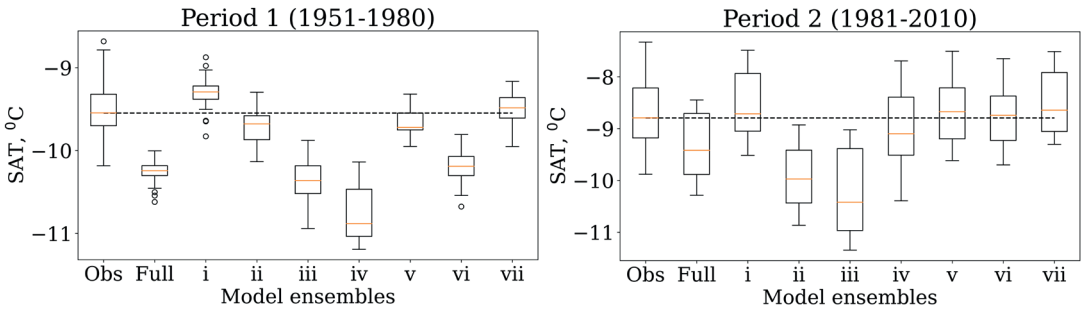

Fig. 5. Boxplots of the annual SAT over the Arctic for observations, the full ensemble, and selected sub-ensembles using the seven model assessment methods for 1951-1980 and 1981-2010

for all methods is closer to that of observations, except for methods ii and iii, which significantly underestimate them.

Regarding the annual cycle (Fig. 6), greater agreement is watched during the warm period and less during the cold period between the different sub-ensembles and observations. The exception is method iii, which underestimates SAT in all months. However, for some methods (e.g., iv and vii), the agreement is better in winter than in summer and autumn.

Fig. 7 shows the results of GCMs ranking by seven methods for the two periods. Such a comparison allows us to evaluate the consistency of the methods. We observe considerable disagreement in the results, with some methods ranking certain models as among the best, while others classify them as among the worst – for example, ACCESS-CM2, CIESM, EC-Earth3, EC-Earth3-Veg, and KACE-1-0-G. However, some models are consistently classified as either "good" or "bad" by most methods – for instance, AWI-CM-1-1-MR, CASM-CSM1-0, and MPI-ESM1-2-LR. From Fig. 7, we can clearly see the consistency of each method; for example, method (i) identifies the ACCESS-CM2 model as unsatisfactory in both periods – showing high consistency. Conversely, method (ii) classifies the same model as very good across both periods. However, when analyzing these two methods (i and ii) across all models, it becomes evident that the consistency of method (ii) is significantly lower and it more frequently assigns incorrect categories to models.

DISCUSSION AND CONCLUSIONS

Seven different model evaluation methods for the selection of a sub-ensemble were tested for CMIP6 SAT over the Arctic. All model evaluation methods were analyzed for two periods, 1951-1980 and 1981-2010, to assess their consistency. Specifically, differences in mean values, model rankings, and the matching of assigned quality groups were examined. The ability of a model evaluation method to identify the climate model as superior, regardless of the time (e.g., warming or cooling), confirms its robustness. For each evaluation method, a sub-ensemble comprising the top 25% of models was selected based on ranking, which was 6 out of 25 GCMs.

The intercomparison results indicate superior performance for the methods (i) root mean square error and (vii) the percentile-based approach. The models selected for the sub-ensemble under the (i) root mean square error method for both periods are ACCESS-ESM1-5, CESM2-WACCM, and MPI-ESM1-2-LR. Similarly, under the (vii) the percentile-based approach, the models selected for both periods are ACCESS-ESM1-5, AWI-CM-1-1-MR, GFDL-ESM4, and MPI-ESM1-2-LR. The most frequently included models - appearing more than 4 times out of 14 - under the tested evaluation methods across both periods (1951-1980 and 1981-2010) are ACCESS-ESM1-5, AWI-CM-1-1-MR, EC-Earth3-Veg, GFDL-ESM4, and MPI-ESM1-2-LR. The GCMs most commonly identified as unsatisfactory include CAMS-CSM1-0, CIESM, FGOALS-g3, INM-CM4-8, and NESM3.

Considering that the simulated distribution of interannual variability is comparable to observations, albeit with some systematic errors (Fig. 2), we recommend applying bias correction to the CMIP6 temperature data.

In general, comparing the results obtained here with those from other studies is challenging due to the use of different sets of model input data (e.g., 22, 25, 30, 35 models, etc.), various study regions, and differing meteorological parameters. Furthermore, most studies employ only one method of model evaluation and selection without comparing it to alternative approaches. Given the wide range of such methods, comparing their effectiveness for evaluation, ranking, and selecting climate models remains an important task.

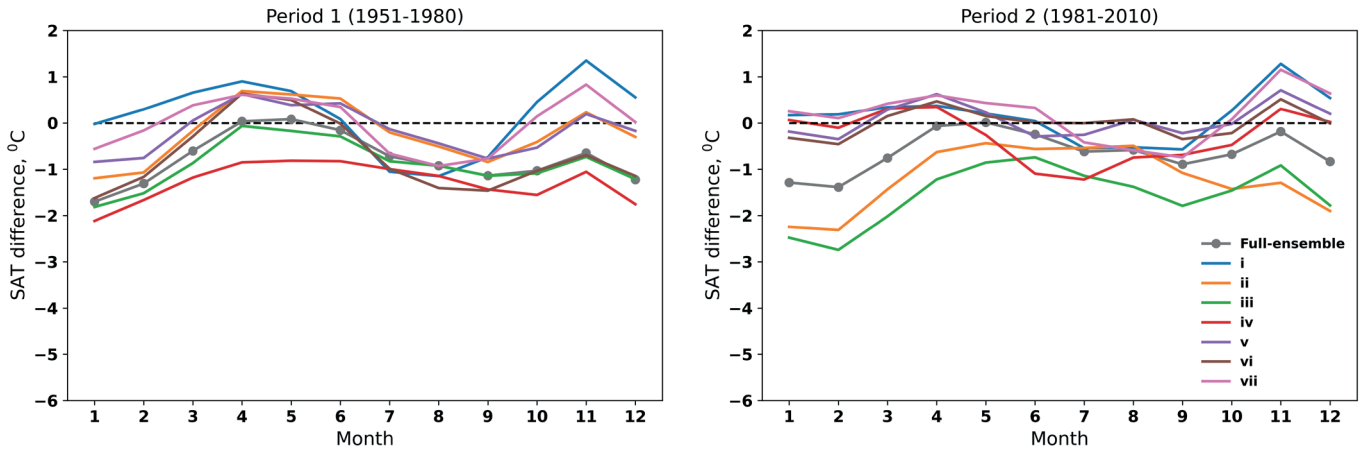

Fig. 6. Difference between the multi-year monthly SAT of observations, the full ensemble, and selected sub-ensembles using the seven methods for the periods 1951-1980 and 1981-2010 (closer to the dashed line indicates closer agreement with observations)

No	Models/methods	Period 1951-1980							Period 1981-2010						
		i	ii	iii	iv	v	vi	vii	i	ii	iii	iv	v	vi	vii
1	ACCESS-CM2	20	3	2	24	8	6	16	24	4	19	19	15	18	18
2	ACCESS-ESM1-5	3	24	22	19	9	18	4	4	11	5	13	17	13	4
3	AWI-CM-1-1-MR	5	13	16	11	1	3	3	10	9	2	10	1	3	5
4	BCC-CSM2-MR	12	9	11	8	15	5	11	14	16	4	6	12	10	11
5	CAMS-CSM1-0	19	20	24	22	17	23	21	23	18	25	22	25	25	23
6	CanESM5	10	5	12	20	12	8	12	7	3	18	8	4	1	8
7	CESM2-WACCM	4	19	20	7	18	14	6	5	10	8	5	23	16	24
8	CIESM	23	2	5	17	2	12	22	22	24	22	21	16	21	7
9	EC-Earth3	22	12	1	2	6	7	23	16	25	12	4	22	23	19
10	EC-Earth3-Veg	16	25	21	9	25	25	19	3	2	9	1	6	2	1
11	FGOALS-f3-L	24	10	13	21	19	20	24	21	1	13	15	9	14	20
12	FGOALS-g3	25	8	10	4	10	24	25	25	19	3	23	18	24	25
13	FIO-ESM-2-0	8	21	18	12	22	17	5	1	5	16	2	13	9	9
14	GFDL-ESM4	2	11	7	1	16	4	1	8	13	21	14	7	11	6
15	INM-CM4-8	15	1	4	25	4	2	20	19	22	24	20	24	22	21
16	INM-CM5-0	9	18	19	16	5	13	10	11	12	11	18	8	8	10
17	IPSL-CM6A-LR	11	15	17	23	14	16	7	12	14	7	24	2	4	16
18	KACE-1-0-G	21	22	9	14	11	10	17	18	6	1	7	5	5	14
19	MIROC6	13	17	25	10	13	21	15	13	7	23	25	19	19	15
20	MPI-ESM1-2-HR	7	6	23	13	3	19	8	6	21	20	17	10	12	3
21	MPI-ESM1-2-LR	1	4	3	18	7	1	2	2	15	10	16	11	6	2
22	MRI-ESM2-0	14	16	14	3	20	15	13	15	20	15	11	20	17	17
23	NESM3	18	23	8	6	24	22	18	20	23	6	9	21	20	22
24	NorESM2-LM	6	14	15	5	21	9	14	9	17	17	3	3	7	12
25	NorESM2-MM	17	7	6	15	23	11	9	17	8	14	12	14	15	13

- very good - satisfactory - unsatisfactory

Fig. 7. Ranking of the models based on the seven model evaluation methods for the periods 1951-1980 and 1981-2010

Among all the methods for estimating model skill examined in this article, we recommend using the following for temperature data: (i) root mean square error and (vii) a percentile-based method, as they produce the most consistent results. It should be noted that we did not assess the sensitivity of the choice of evaluation method to different variables; therefore, our findings should be applied with caution to other meteorological parameters. For example, methods based solely on RMSE may not be suitable for precipitation. When selecting climate models for other meteorological variables, more comprehensive approaches are likely to be more robust than those relying on a single statistical parameter.

REFERENCES

Aghakhani Afshar A., Hasanzadeh Y., Besalatpour A.A., and Pourreza-Bilondi M. (2017). Climate change forecasting in a mountainous data scarce watershed using CMIP5 models under representative concentration pathways. Theoretical and Applied Climatology, 129, 683-699, DOI: 10.1007/s00704-016-1908-5.

Agosta C., Fettweis X., and Datta R. (2015). Evaluation of the CMIP5 models in the aim of regional modelling of the Antarctic surface mass balance. Cryosphere, 9, 2311-2321, DOI: 10.5194/tc-9-2311-2015.

Ahmadalipour A., Rana A., Moradkhani H., Sharma A. (2017). Multi-criteria evaluation of CMIP5 GCMs for climate change impact analysis. Theoretical and Applied Climatology, 128, 71-87, DOI: 10.1007/s00704-015-1695-4.

Ahmed K., Sachindra D., Shahid S., et al. (2020). Multi-model ensemble predictions of precipitation and temperature using machine learning algorithms. Atmospheric Research, 236, 104806, DOI: 10.1016/j.atmosres.2019.104806.

Ahmed K., Sachindra D.A., Shahid S., et al. (2019). Selection of multi-model ensemble of general circulation models for the simulation of precipitation and maximum and minimum temperature based on spatial assessment metrics. Hydrology and Earth System Sciences, 23,4803-4824, DOI: 10.5194/hess-23-4803-2019.

Caballero R., Huber M. (2013). State-dependent climate sensitivity in past warm climates and its implications for future climate projections. Proceedings of the National Academy of Sciences, 110, 14162-14167, DOI: doi.org/10.1073/pnas.1303365110.

Cai Z., You Q., Wu F., et al. (2021). Arctic Warming Revealed by Multiple CMIP6 Models: Evaluation of Historical Simulations and Quantification of Future Projection Uncertainties. Journal of Climate, 34, 4871-4892, DOI: 10.1175/JCLI-D-20-0791.1.

Calvin K., Dasgupta D., Krinner G., et al. (2023). IPCC, 2023: Climate Change 2023: Synthesis Report. Contribution of Working Groups I, II and III to the Sixth Assessment Report of the Intergovernmental Panel on Climate Change [Core Writing Team, H. Lee and J. Romero (eds.)]. IPCC, Geneva, Switzerland.

Chai T. and Draxler R.R. (2014). Root mean square error (RMSE) or mean absolute error (MAE)? – Arguments against avoiding RMSE in the literature. Geoscientific Model Development, 7, 1247-1250, DOI: 10.5194/gmd-7-1247-2014.

Chen W., Jiang Z., and Li L. (2011). Probabilistic Projections of Climate Change over China under the SRES A1B Scenario Using 28 AOGCMs. Journal of Climate, 24, 4741-4756, DOI: 10.1175/2011JCLI4102.1.

Eyring V., Cox P.M., Flato G.M., et al. (2019). Taking climate model evaluation to the next level. Nature Climate Change, 9, 102-110, DOI: 10.1038/s41558-018-0355-y.

Fu G., Liu Z., Charles S.P., et al. (2013). A score-based method for assessing the performance of GCMs: A case study of southeastern Australia. Journal of Geophysical Research-Atmospheres, 118, 4154-4167, DOI: doi.org/10.1002/jgrd.50269.

Gleckler P.J., Taylor K.E., and Doutriaux C. (2008). Performance metrics for climate models. Journal of Geophysical Research-Atmospheres, 113, 1-20, DOI: 10.1029/2007JD008972.

Gnatiuk N., Radchenko I., Davy R., et al. (2020). Simulation of factors affecting Emiliania huxleyi blooms in Arctic and sub-Arctic seas by CMIP5 climate models: model validation and selection. Biogeosciences, 17, 1199-1212, DOI: 10.5194/bg-17-1199-2020.

Hausfather Z., Marvel K., Schmidt G.A., et al. (2022). Climate simulations: recognize the 'hot model' problem. Nature, 605, 26-29, DOI: 10.1038/d41586-022-01192-2.

Herger N., Abramowitz G., Knutti R., et al. (2018). Selecting a climate model subset to optimise key ensemble properties. Earth System Dynamics, 9, 135-151, DOI: 10.5194/esd-9-135-2018.

Inoue T., and Ueda H. (2011). Delay of the First Transition of Asian Summer Monsoon under Global Warming Condition. SOLA, 7, 81-84, DOI: 10.2151/sola.2011-021.

Jain S., Scaife A.A., Shepherd T.G., et al. (2023). Importance of internal variability for climate model assessment. npj Climate and Atmospheric Science, 6, 68, DOI: 10.1038/s41612-023-00389-0.

Jia K., Ruan Y., Yang Y., and You Z. (2019). Assessment of CMIP5 GCM Simulation Performance for Temperature Projection in the Tibetan Plateau. Earth and Space Science, 6, 2362-2378, DOI: 10.1029/2019EA000962.

Jiang Z., Li W., Xu J., and Li L. (2015). Extreme Precipitation Indices over China in CMIP5 Models. Part I: Model Evaluation. Journal of Climate, 28, 8603-8619, DOI: 10.1175/JCLI-D-15-0099.1.

Kadel I., Yamazaki T., Iwasaki T., and Abdillah M. (2018). Projection of future monsoon precipitation over the central Himalayas by CMIP5 models under warming scenarios. Climate Research, 75, 1-21, DOI: 10.3354/cr01497.

Knutti R., Furrer R., Tebaldi C., et al. (2010). Challenges in Combining Projections from Multiple Climate Models. Journal of Climate, 23, 2739-2758, DOI: 10.1175/2009JCLI3361.1.

Kumar D., Mishra V., and Ganguly A.R. (2015). Evaluating wind extremes in CMIP5 climate models. Climate Dynamics, 45, 441-453, DOI: 10.1007/s00382-014-2306-2.

Kumar S., Merwade V., Kinter J.L., and Niyogi D. (2013). Evaluation of Temperature and Precipitation Trends and Long-Term Persistence in CMIP5 Twentieth-Century Climate Simulations. Journal of Climate, 26, 4168-4185, DOI: 10.1175/JCLI-D-12-00259.1.

Macadam I., Pitman A.J., Whetton P.H., and Abramowitz G. (2010). Ranking climate models by performance using actual values and anomalies: Implications for climate change impact assessments. Geophysical Research Letters, 37, 16704, DOI: 10.1029/2010GL043877.

Maxino C.C., McAvaney B.J., Pitman A.J., and Perkins S.E. (2008). Ranking the AR4 climate models over the Murray-Darling Basin using simulated maximum temperature, minimum temperature and precipitation. International Journal of Climatology, 28, 1097-1112, DOI: 10.1002/joc.1612.

McMahon T.A., Peel M.C., and Karoly D.J. (2015). Assessment of precipitation and temperature data from CMIP3 global climate models for hydrologic simulation. Hydrology and Earth System Sciences, 19, 361-377, DOI: 10.5194/hess-19-361-2015.

Ogata T., Ueda H., Inoue T., et al. (2014). Projected Future Changes in the Asian Monsoon: A Comparison of CMIP3 and CMIP5 Model Results. Journal of the Meteorological Society of Japan, 92, 207-225, DOI: 10.2151/jmsj.2014-302.

Otero N., Sillmann J., and Butler T. (2018). Assessment of an extended version of the Jenkinson-Collison classification on CMIP5 models over Europe. Climate Dynamics, 50, 1559-1579, DOI: 10.1007/s00382-017-3705-y.

Perkins S.E., Pitman A.J., Holbrook N.J., and McAneney J. (2007). Evaluation of the AR4 Climate Models' Simulated Daily Maximum Temperature, Minimum Temperature, and Precipitation over Australia Using Probability Density Functions. Journal of Climate, 20, 4356-4376, DOI: 10.1175/JCLI4253.1.

Raju K.S., and Kumar D.N. (2020). Review of approaches for selection and ensembling of GCMs. Journal of Water and Climate Change, 11, 577-599, DOI: 10.2166/wcc.2020.128.

Rao X., Lu X., and Dong W. (2019). Evaluation and Projection of Extreme Precipitation over Northern China in CMIP5 Models. Atmosphere, 10, 691, DOI: 10.3390/atmos10110691.

Reifen C., and Toumi R. (2009). Climate projections: Past performance no guarantee of future skill? Geophysical Research Letters, 36, DOI: 10.1029/2009GL038082.

Rohde R., Muller R.A., Jacobsen R., et al. (2013). A New Estimate of the Average Earth Surface Land Temperature Spanning 1753 to 2011. Geoinformatics and Geostatistics: An Overview, 1:1, DOI: 10.4172/2327-4581.1000101.

Rohde R.A., and Hausfather Z. (2020). The Berkeley Earth Land/Ocean Temperature Record. Earth System Science Data, 12, 3469-3479, DOI: 10.5194/essd-12-3469-2020.

Ruan Y., Liu Z., Wang R., and Yao Z. (2019). Assessing the Performance of CMIP5 GCMs for Projection of Future Temperature Change over the Lower Mekong Basin. Atmosphere, 10, 93, DOI: 10.3390/atmos10020093.

Rupp D.E., Abatzoglou J.T., Hegewisch K.C., and Mote P.W. (2013). Evaluation of CMIP5 20 th century climate simulations for the Pacific Northwest USA. Journal of Geophysical Research-Atmospheres, 118, 884-894, DOI: 10.1002/jgrd.50843.

Sharmila S., Joseph S., Sahai A., et al. (2015). Future projection of Indian summer monsoon variability under climate change scenario: An assessment from CMIP5 climate models. Global and Planetary Change, 124, 62-78, DOI: 10.1016/j.gloplacha.2014.11.004.

Sherwood S.C., Webb M.J., Annan J.D., et al. (2020). An Assessment of Earth's Climate Sensitivity Using Multiple Lines of Evidence. Reviews of Geophysics, 58, e2019RG000678, DOI: 10.1029/2019RG000678.

Sillmann J., Kharin V.V., Zhang X., et al. (2013). Climate extremes indices in the CMIP5 multimodel ensemble: Part 1. Model evaluation in the present climate. Journal of Geophysical Research-Atmospheres, 118, 1716-1733, DOI: 10.1002/jgrd.50203.

Stocker T.F., Qin D., Plattner G.-K., et al. (2014). Climate Change 2013: The Physical Science Basis. Working Group I Contribution to the Fifth Assessment Report of the Intergovernmental Panel on Climate Change. Cambridge University Press, Cambridge, United Kingdom and New York, NY, USA.

Taylor K.E. (2001). Summarizing multiple aspects of model performance in a single diagram. Journal of Geophysical Research-Atmospheres, 106, 7183-7192, DOI: 10.1029/2000JD900719.

Taylor K.E., Stouffer R.J., and Meehl G.A. (2012). An Overview of CMIP5 and the Experiment Design. Bulletin of the American Meteorological Society, 93, 485-498, DOI: 10.1175/BAMS-D-11-00094.1.

Walsh J.E., Chapman W.L., Romanovsky V., et al. (2008). Global Climate Model Performance over Alaska and Greenland. Journal of Climate, 21, 6156-6174, DOI: 10.1175/2008JCLI2163.1.

Yang X., Yu X., Wang Y., et al. (2020). The Optimal Multimodel Ensemble of Bias-Corrected CMIP5 Climate Models over China. Journal of Hydrometeorology, 21, 845-863, DOI: 10.1175/JHM-D-19-0141.1.

You Q., Jiang Z., Wang D., et al. (2018). Simulation of temperature extremes in the Tibetan Plateau from CMIP5 models and comparison with gridded observations. Climate Dynamics, 51, 355-369, DOI: 10.1007/s00382-017-3928-y.

Zhou B., Wen Q.H., Xu Y., et al. (2014). Projected Changes in Temperature and Precipitation Extremes in China by the CMIP5 Multimodel Ensembles. Journal of Climate, 27, 6591-6611, DOI: 10.1175/JCLI-D-13-00761.1.

APPENDICES

Table A.1. CMIP6 models used for the evaluation of surface air temperature in the Arctic

ID	Model acronym	Modeling center (acronym, full name, city and country)	Resolution (° lon × ° lat)
1	ACCESS-CM2	ARCCSS (Australian Research Council Centre of Excellence for Climate System Science), CSIRO (Commonwealth Scientific and Industrial Research Organization, Aspendale, Victoria, Australia)	1.875×1.25
2	ACCESS-ESM1-5	Commonwealth Scientific and Industrial Research Organization, Aspendale, Victoria, Australia	1.875×1.25
3	AWI-CM-1-1-MR	Alfred Wegener Institute, Helmholtz Centre for Polar and Marine Research, Bremerhaven, Germany	0.938
4	BCC-CSM2-MR	Beijing Climate Center, Beijing, China	1.125
5	CAMS-CSM1-0	Chinese Academy of Meteorological Sciences, Beijing, China	1.125
6	CanESM5	Canadian Centre for Climate Modelling and Analysis, Environment and Climate Change Canada, Victoria, Canada	2.8125
7	CESM2-WACCM	National Center for Atmospheric Research, Climate and Global Dynamics Laboratory, Boulder, USA	1.25×0.94
8	CIESM	Department of Earth System Science, Tsinghua University, Beijing, China	1.25
9	EC-Earth3	European Union, Mailing address: EC-Earth consortium, Rossby Center, Swedish Meteorological and Hydrological Institute/SMHI, SE-601 76 Norrkoping, Sweden	0.703
10	EC-Earth3-Veg		
11	FGOALS-f3-L	Chinese Academy of Sciences, Beijing, China	1.25×1
12	FGOALS-g3		2
13	FIO-ESM-2-0	FIO (First Institute of Oceanography, Ministry of Natural Resources, Qingdao, China), QNLM (Qingdao National Laboratory for Marine Science and Technology, Qingdao, China)	1.25×0.94
14	GFDL-ESM4	National Oceanic and Atmospheric Administration, Geophysical Fluid Dynamics Laboratory, Princeton, USA	1.25
15	INM-CM4-8	Institute for Numerical Mathematics, Russian Academy of Science, Moscow, Russia	2×1.5
16	INM-CM5-0		
17	IPSL-CM6A-LR	Institut Pierre Simon Laplace, Paris, France	2×1.268
18	KACE-1-0-G	National Institute of Meteorological Sciences/Korea Meteorological Administration, Climate Research Division, Seogwipo-si, Jejudo, Republic of Korea	1.875×1.25
19	MIROC6	JAMSTEC (Japan Agency for Marine-Earth Science and Technology, Kanagawa, Japan), AORI (Atmosphere and Ocean Research Institute, The University of Tokyo, Chiba, Japan), NIES (National Institute for Environmental Studies, Ibaraki, Japan), and R-CCS (RIKEN Center for Computational Science, Hyogo, Japan)	1.406
20	MPI-ESM1-2-HR	Max Planck Institute for Meteorology, Hamburg Deutscher Wetterdienst, Offenbach am Main Deutsches Klimarechenzentrum, Hamburg, Germany	0.938
21	MPI-ESM1-2-LR	Max Planck Institute for Meteorology, Hamburg 20146, Germany; Alfred Wegener Institute, Helmholtz Centre for Polar and Marine Research, Bremerhaven, Germany	1.875
22	MRI-ESM2-0	Meteorological Research Institute, Tsukuba, Ibaraki Japan	1.125
23	NESM3	Nanjing University of Information Science and Technology, Nanjing, China	1.875
24	NorESM2-LM	NorESM Climate modeling Consortium consisting of CICERO (Center for International Climate and Environmental Research, Oslo), MET-Norway (Norwegian Meteorological Institute, Oslo), NERSC (Nansen Environmental and Remote Sensing Center, Bergen), NILU (Norwegian Institute for Air Research, Kjeller), UiB (University of Bergen, Bergen), UiO (University of Oslo, Oslo) and UNI (Uni Research, Bergen), Norway.	2.5×1.89
25	NorESM2-MM		1.25×0.94

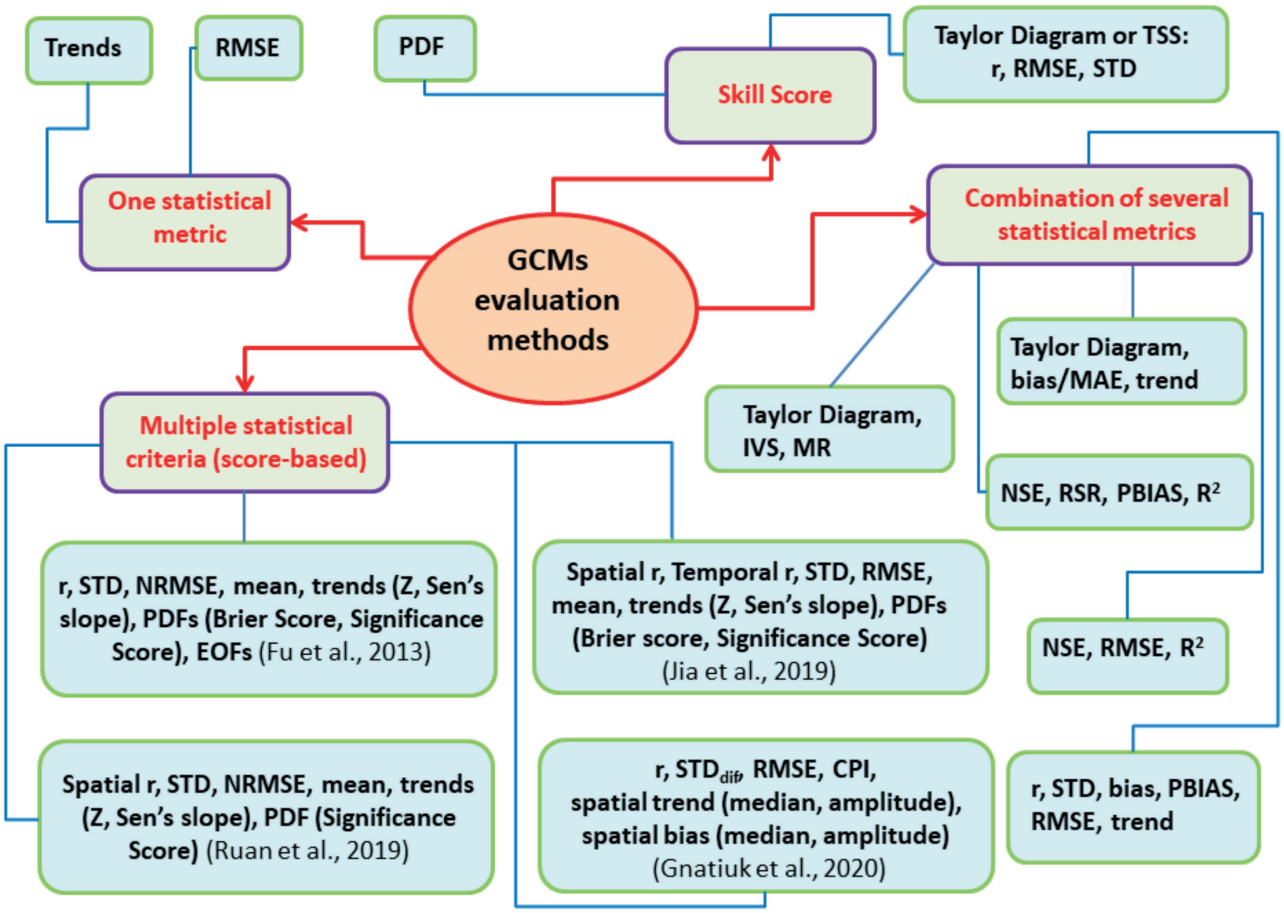

Fig. A.2. Mind map of methods for GCMs' evaluation found in the literature

Table A.3. Climate models selection methods in the literature (SLP – sea level pressure, H500 – geopotential height at 500 hPa, T500 – the temperature at 500 hPa, SST – sea surface temperature, SAT – surface air temperature, P – precipitation, SIC – sea-ice concentration, WS – wind speed, pCO_2 – dissolved CO_2 partial pressure, S – salinity, OCS – ocean surface current speed, SDSR – surface downwelling shortwave radiation)

#	Statistical metric	Reference	GCMs considered / selected	Variable considered	Ranking method
1	Root mean square error (RMSE)	1) (Walsh et al. 2008)	15/4	SLP, SAT, P	Based on the sum of ranks for all variables
		2) (Reifen and Toumi 2009)	17/ -	SAT	Ranking
		3) Macadam et al. 2010)	17/ -	SAT	Ranking
		4) (Sillmann et al. 2013)	18-31/-	Temp. and Precip. Indices (in total 27)	Ranking
		5) (Zhou et al. 2014)	24/total ensemble	Temp. and Precip. Indices (in total 20)	Ranking
		6) (Herger et al. 2018)	38/8 for SAT, 12 for P	SAT, P	Gurobi Optimization
2	Trends	1) (Kumar et al. 2013) (mean, spatial standard deviation, spatial correlation)	79 model runs from 19 GCMs/ -	SAT, P	
		2) (Saha et al. 2014) (temporal trends)	42/ -	Indian Summer Monsoon Rainfall	
3	Probability density function (PDF) – Skill score (SS)	1) (Perkins et al. 2007)	10/6; 13/10; 14/3	Maximum and minimum SAT, P	Ranked SS for each variable, select >0.8
		2) (Maxino et al. 2008)	9/3	Maximum and minimum SAT, P	Ranked averaged SS, select >0.8
		3) (Anandhi and Nanjundiah 2015)	19/5	P	Average rank of GCMs using SS
		4) (Sun et al. 2015)	14/ -	SAT (maximum, mean, minimum), P	SS
		5) (Bannister et al. 2017)	47/5	SAT (maximum, mean, minimum)	Ranking based on aggregated SS
		6) (Anandhi et al. 2019)	20/5	SAT (mean, max, min) P, WS	Ranking based on averaged SS
4	Taylor Diagram or Taylor Skill Score (TSS)	1) (Inoue and Ueda 2011) (Taylor's Skill Score)	19/total ensemble	300 hPa temp, 850 hPa zonal wind	
		2) (Ogata et al. 2014) (Taylor's Skill Score)	20 (cmip3)/20 24 (cmip5)/24	850 hPa zonal wind, P SST	
		3) (Sharmila et al. 2015)	20/4	Indian summer monsoon, precip.	threshold criteria (correlation ≥ 0.5 and normalized SD 0.8-1.2)
		4) (Kadel et al. 2018)	38/6	Summer Monsoon Season, precip.	threshold criteria (r≥ 0.6, std 0.5-1.5, rmse ≤ 1.0)
		5) (Ahmed et al. 2020)	36/18	SAT (maximum, minimum), P	based on TSS, Comprehensive Rating Metric (MR)
		6) (Yang et al. 2020)	25/9 for precip., 25/11 for temp.	SAT, P	based on threshold – 0.49
		7) (Wang et al. 2016)	28/7	SAT	based on TSS

5	Taylor Diagrams, Interannual Variability Skill Score, Comprehensive Rating Metric	1)(Jiang et al. 2015) 2)(Cai et al. 2021)	31/5 22/6	P, P intensity, Max consec. dry days SAT	Total complex rating metric Total complex rating metric
		3)(Rao et al. 2019)	32/5	total extreme P, max consecutive five days of P and wet days >10 mm	Total complex rating metric
		4)(You et al. 2018)	17/4	16 temperature extreme indices	Total complex rating metric
6	Combinations of several metrics	1)(Kumar et al. 2015): bias, trend analysis, and Taylor Diagrams	15/ -	Maxima WS	Four groups
		2)(Aghakhani Afshar et al. 2017): R2, NSE, PBIAS, RSR	14/4	P	Ranking based on the total sum of the ranks by NSE
		3)(McMahon et al. 2015): RMSE, NSE, R2	23/5	SAT, P	Ranking based on metrics
		4)(Ongoma et al. 2019): r, STD, bias, PBIAS, RMSE, trend	22/8	P	Ranking based on the overall score calculated using an individual score for each GCM, error and variable
7	Score-based methods using multiple statistical metrics	1) (Fu et al. 2013): r, STD, NRME, mean, trends (Z, Sen's slope), PDF (Brier Score, Significance Score), empirical orthogonal functions	25/ -	SAT, P, mean SLP	Ranking based on the overall score calculated using an individual score for each GCM and error
		2) (Jia et al. 2019): mean, temporal r, STD, r spatial, RMSE, PDF, trends (Z and Slope)	33/top-30% (10)	P	Ranking based on the overall score calculated using an individual score for each GCM and error
		3) (Ruan et al. 2019): mean, STD, RMSE, r spatial, PDF (Significance Score), trends (Z and Sen's slope)	34/top-25% (9)	SAT	Ranking based on the overall score for each variable and sea individually
		4) (Gnatiuk et al. 2020): r, RMSE, STD, CPI spatial trends, spatial bias	11-30/individual sub-set (top-25%) varies from 3 to 11	pCO_2, pH, NO_3, PO_4, SI, SST, S, OCS, 10m WS, SDSR	

№	Model acronym	Period 1951-1980						Period 1981-2010						Mean value diff.	Model rank diff.	Consistency (QG)
		r	Mean diff.	STD diff.	Mean value	Model rank	Quality group	r	Mean diff.	STD diff.	Mean value	Model rank	Quality group			
1	ACCESS-CM2	0.71	0.78	0.98	0.82	3	I	0.73	0.87	0.94	0.84	4	I	0.02	1	yes
2	ACCESS-ESM1-5	0.25	0.38	0.63	0.42	24	III	0.84	0.51	0.88	0.74	11	II	0.32	13	no
3	AWI-CM-1-1-MR	0.51	0.84	0.61	0.66	13	II	0.50	0.88	0.94	0.78	9	II	0.12	4	yes
4	BCC-CSM2-MR	0.73	0.84	0.58	0.72	9	II	0.24	0.83	0.95	0.67	16	II	0.05	7	yes
5	CAMS-CSM1-0	0.51	0.53	0.76	0.60	20	III	0.74	0.53	0.74	0.67	18	II	0.07	2	no
6	CanESM5	0.90	0.74	0.70	0.78	5	I	0.87	0.95	0.93	0.92	3	I	0.14	2	yes
7	CESM2-WACCM	0.00	0.85	0.98	0.61	19	II	0.64	0.76	0.86	0.75	10	II	0.14	9	yes
8	CIESM	0.68	0.93	0.94	0.85	2	I	0.15	0.41	0.80	0.45	24	III	0.39	22	no
9	EC-Earth3	0.31	0.84	0.94	0.70	12	II	0.60	0.00	0.00	0.20	25	III	0.50	13	no
10	EC-Earth3-Veg	0.22	0.00	0.44	0.22	25	III	1.00	0.91	0.89	0.93	2	I	0.71	23	no
11	FGOALS-f3-L	0.67	0.56	0.92	0.72	10	II	0.96	0.95	0.91	0.94	1	I	0.22	9	no
12	FGOALS-g3	0.69	0.92	0.62	0.74	8	II	0.41	0.71	0.88	0.67	19	II	0.08	11	yes
13	FIO-ESM-2-0	0.93	0.52	0.22	0.56	21	III	0.80	0.86	0.87	0.84	5	I	0.29	16	no
14	GFDL-ESM4	0.79	0.67	0.65	0.70	11	II	0.46	0.85	0.87	0.73	13	II	0.03	2	yes
15	INM-CM4-8	0.86	0.82	0.90	0.86	1	I	0.08	0.57	0.96	0.53	22	III	0.33	21	no
16	INM-CM5-0	0.21	0.73	0.90	0.61	18	II	0.61	0.90	0.71	0.74	12	II	0.12	6	yes
17	IPSL-CM6A-LR	0.60	0.59	0.73	0.64	15	II	0.32	0.96	0.89	0.72	14	II	0.08	1	yes
18	KACE-1-0-G	0.01	0.97	0.44	0.47	22	III	0.67	0.89	0.86	0.81	6	I	0.34	16	no
19	MIROC6	0.32	0.58	0.99	0.63	17	II	0.76	0.70	0.91	0.79	7	II	0.16	10	yes
20	MPI-ESM1-2-HR	0.81	0.46	0.98	0.75	6	I	0.00	0.73	0.89	0.54	21	III	0.21	15	no
21	MPI-ESM1-2-LR	0.43	0.97	0.99	0.80	4	I	0.38	0.89	0.79	0.69	15	II	0.11	11	no
22	MRI-ESM2-0	0.70	0.71	0.49	0.63	16	II	0.37	0.77	0.81	0.65	20	III	0.02	4	no
23	NESM3	1.00	0.31	0.00	0.44	23	III	0.36	0.25	0.81	0.47	23	III	0.04	0	yes
24	NorESM2-LM	0.05	0.91	0.99	0.65	14	II	0.23	0.93	0.86	0.67	17	II	0.02	3	yes
25	NorESM2-MM	0.54	0.89	0.82	0.75	7	II	0.74	0.72	0.88	0.78	8	II	0.03	1	yes
													Mean	0.18	8.9	yes-52%

- very good (I) - satisfactory (II) - unsatisfactory (III) - QUALITY GROUPS (QG)

I (2) II (10) III (1) / got into different groups (12) - number of models belong to each QG in two periods

Fig. A.4. Results of normalized spatial trends analysis, model rank and consistency assessment for 25 models over the Arctic for the period 1951-1980 and for the period 1981-2010 for method (ii) of model comparison by trends (see 2.2 Methods for model evaluation compared in the study)

№	Model acronym	Period 1951-1980			Period 1981-2010			TSS diff.	Model rank diff.	Consistency (QG)
		TSS	Model rank	Quality group	TSS	Model rank	Quality group			
1	ACCESS-CM2	0.99	2	I	0.49	19	II	0.50	17	no
2	ACCESS-ESM1-5	0.03	22	III	0.77	5	I	0.73	17	no
3	AWI-CM-1-1-MR	0.32	16	II	0.88	2	I	0.56	14	no
4	BCC-CSM2-MR	0.52	11	II	0.78	4	I	0.26	7	no
5	CAMS-CSM1-0	0.03	24	III	0.00	25	III	0.03	1	yes
6	CanESM5	0.51	12	II	0.52	18	II	0.01	6	yes
7	CESM2-WACCM	0.16	20	III	0.70	8	II	0.54	12	no
8	CIESM	0.92	5	I	0.29	22	III	0.63	17	no
9	EC-Earth3	1.00	1	I	0.58	12	II	0.42	11	no
10	EC-Earth3-Veg	0.05	21	III	0.66	9	II	0.60	12	no
11	FGOALS-f3-L	0.51	13	II	0.57	13	II	0.07	0	yes
12	FGOALS-g3	0.58	10	II	0.82	3	I	0.24	7	no
13	FIO-ESM-2-0	0.21	18	II	0.53	16	II	0.32	2	yes
14	GFDL-ESM4	0.65	7	II	0.33	21	III	0.33	14	no
15	INM-CM4-8	0.92	4	I	0.04	24	III	0.88	20	no
16	INM-CM5-0	0.19	19	II	0.59	11	II	0.40	8	yes
17	IPSL-CM6A-LR	0.26	17	II	0.71	7	II	0.46	10	yes
18	KACE-1-0-G	0.59	9	II	1.00	1	I	0.41	8	no
19	MIROC6	0.00	25	III	0.26	23	III	0.26	2	yes
20	MPI-ESM1-2-HR	0.03	23	III	0.46	20	III	0.43	3	yes
21	MPI-ESM1-2-LR	0.93	3	I	0.64	10	II	0.29	7	no
22	MRI-ESM2-0	0.40	14	II	0.53	15	II	0.13	1	yes
23	NESM3	0.65	8	II	0.72	6	I	0.07	2	no
24	NorESM2-LM	0.38	15	II	0.53	17	II	0.15	2	yes
25	NorESM2-MM	0.88	6	I	0.55	14	II	0.33	8	no
							Mean	0.36	8.3	yes-40%

- very good (I) - satisfactory (II) - unsatisfactory (III) - QUALITY GROUPS (QG)

I (0) II (7) III (3) / got into different groups (15) - number of models belong to each QG in two periods

Fig. A.5. Results of normalized TSS, model rank and consistency assessment for 25 models over the Arctic for the period 1951-1980 and for the period 1981-2010 for method (iii) of model comparison by Taylor skill score (see 2.2 Methods for model evaluation compared in the study)

№	Model acronym	Period 1951-1980			Period 1981-2010			S_{score} diff.	Model rank diff.	Consistency (QG)
		S_{score}	Model rank	Quality group	S_{score}	Model rank	Quality group			
1	ACCESS-CM2	0.07	24	III	0.42	19	II	0.35	5	no
2	ACCESS-ESM1-5	0.32	19	II	0.83	13	II	0.51	6	yes
3	AWI-CM-1-1-MR	0.66	11	II	0.87	10	II	0.21	1	yes
4	BCC-CSM2-MR	0.73	8	II	0.89	6	I	0.16	2	no
5	CAMS-CSM1-0	0.08	22	III	0.34	22	III	0.26	0	yes
6	CanESM5	0.32	20	III	0.88	8	II	0.56	12	no
7	CESM2-WACCM	0.77	7	II	0.91	5	I	0.15	2	no
8	CIESM	0.34	17	II	0.36	21	III	0.02	4	no
9	EC-Earth3	0.93	2	I	1.00	4	I	0.07	2	yes
10	EC-Earth3-Veg	0.72	9	II	1.00	1	I	0.28	8	no
11	FGOALS-f3-L	0.08	21	III	0.80	15	II	0.71	6	no
12	FGOALS-g3	0.85	4	I	0.32	23	III	0.52	19	no
13	FIO-ESM-2-0	0.65	12	II	1.00	2	I	0.35	10	no
14	GFDL-ESM4	1.00	1	I	0.83	14	II	0.17	13	no
15	INM-CM4-8	0.00	25	III	0.42	20	III	0.42	5	yes
16	INM-CM5-0	0.37	16	II	0.76	18	II	0.39	2	yes
17	IPSL-CM6A-LR	0.07	23	III	0.00	24	III	0.07	1	yes
18	KACE-1-0-G	0.41	14	II	0.88	7	II	0.47	7	yes
19	MIROC6	0.71	10	II	0.00	25	III	0.71	15	no
20	MPI-ESM1-2-HR	0.64	13	II	0.76	17	II	0.13	4	yes
21	MPI-ESM1-2-LR	0.33	18	II	0.77	16	II	0.44	2	yes
22	MRI-ESM2-0	0.91	3	I	0.87	11	II	0.04	8	no
23	NESM3	0.77	6	I	0.87	9	II	0.11	3	no
24	NorESM2-LM	0.77	5	I	1.00	3	I	0.23	2	yes
25	NorESM2-MM	0.39	15	II	0.85	12	II	0.46	3	yes
							Mean	0.31	5.7	yes-48%

- very good (I) - satisfactory (II) unsatisfactory (III) - **QUALITY GROUPS (QG)**

I (2) II (7) III (3) / got into different groups (13) - number of models belong to each QG in two periods

Fig. A.6. Results of normalized Sscore, model rank and consistency assessment for 25 models over the Arctic for the period 1951-1980 and for the period 1981-2010 for method (iv) of model comparison by Sscore (see 2.2 Methods for model evaluation compared in the study)

№	Model acronym	Period 1951-1980					Period 1981-2010					MR_{mean} diff.	Model rank diff.	Consistency (QG)
		MR_{IVS}	MR_{Taylor}	MR_{mean}	Model rank	Quality group	MR_{IVS}	MR_{Taylor}	MR_{mean}	Model rank	Quality group			
1	ACCESS-CM2	0.71	0.71	0.79	8	II	0.58	0.30	0.45	15	II	0.34	7	yes
2	ACCESS-ESM1-5	0.67	0.62	0.72	9	II	0.13	0.75	0.38	17	II	0.35	8	yes
3	AWI-CM-1-1-MR	0.92	0.87	1.00	1	I	1.00	1.00	1.00	1	I	0.00	0	yes
4	BCC-CSM2-MR	0.33	0.51	0.45	15	II	0.50	0.66	0.56	12	II	0.11	3	yes
5	CAMS-CSM1-0	0.50	0.16	0.41	17	II	0.04	0.00	0.00	25	III	0.41	8	no
6	CanESM5	0.46	0.56	0.55	12	II	0.88	0.68	0.79	4	I	0.23	8	no
7	CESM2-WACCM	0.25	0.44	0.36	18	II	0.25	0.17	0.20	23	III	0.17	5	no
8	CIESM	1.00	0.69	0.98	2	I	0.17	0.77	0.41	16	II	0.57	14	no
9	EC-Earth3	0.83	0.67	0.86	6	I	0.00	0.51	0.20	22	III	0.66	16	no
10	EC-Earth3-Veg	0.00	0.00	0.00	25	III	0.67	0.89	0.75	6	I	0.75	19	no
11	FGOALS-f3-L	0.38	0.22	0.35	19	II	0.79	0.55	0.68	9	II	0.33	10	yes
12	FGOALS-g3	0.75	0.40	0.69	10	II	0.33	0.40	0.34	18	II	0.34	8	yes
13	FIO-ESM-2-0	0.17	0.33	0.26	22	III	0.42	0.74	0.54	13	II	0.28	9	no
14	GFDL-ESM4	0.21	0.71	0.45	16	II	0.83	0.66	0.75	7	II	0.31	9	yes
15	INM-CM4-8	0.79	0.80	0.89	4	I	0.21	0.17	0.17	24	III	0.71	20	no
16	INM-CM5-0	0.88	0.64	0.88	5	I	0.71	0.74	0.71	8	II	0.16	3	no
17	IPSL-CM6A-LR	0.42	0.42	0.47	14	II	0.96	0.89	0.93	2	I	0.46	12	no
18	KACE-1-0-G	0.54	0.49	0.58	11	II	0.75	0.83	0.78	5	I	0.20	6	no
19	MIROC6	0.58	0.27	0.51	13	II	0.38	0.34	0.34	19	II	0.17	6	yes
20	MPI-ESM1-2-HR	0.96	0.62	0.92	3	I	0.63	0.64	0.62	10	II	0.30	7	no
21	MPI-ESM1-2-LR	0.63	1.00	0.86	7	II	0.46	0.85	0.61	11	II	0.24	4	yes
22	MRI-ESM2-0	0.29	0.33	0.34	20	III	0.29	0.42	0.33	20	III	0.01	0	yes
23	NESM3	0.04	0.42	0.21	24	III	0.08	0.43	0.21	21	III	0.00	3	yes
24	NorESM2-LM	0.13	0.44	0.28	21	III	0.92	0.77	0.85	3	I	0.58	18	no
25	NorESM2-MM	0.08	0.44	0.25	23	III	0.54	0.47	0.50	14	II	0.25	9	no
											Mean	0.32	8.5	yes-44%

- very good (II) - satisfactory (II) - unsatisfactory (III) - **QUALITY GROUPS (QG)**

I (1) II (8) III (2) / got into different groups (14) - number of models belong to each QG in two periods

Fig. A.7. Results of normalized MR for Taylor and IVS metrics for 25 models over the Arctic for the period 1951-1980 and for the period 1981-2010 for method (v) based on Taylor diagram and interannual variability skill score (see 2.2 Methods for model evaluation compared in the study)

№	Model acronym	Period 1951-1980								Period 1981-2010								Mean value diff.	Model rank diff.	Consistency (QG)
		RMSE	r	|dif_std|	|dif_T|	|B|	Mean value	Model rank	Quality group	RMSE	r	|dif_std|	|dif_T|	|B|	Mean value	Model rank	Quality group			
1	ACCESS-CM2	0.51	0.94	0.79	0.78	0.67	0.74	6	I	0.44	0.59	0.88	0.87	0.61	0.68	18	II	0.06	12	no
2	ACCESS-ESM1-5	0.79	0.11	0.76	0.38	0.96	0.60	18	II	0.79	0.93	0.55	0.51	0.96	0.75	13	II	0.15	5	yes
3	AWI-CM-1-1-MR	0.78	0.52	0.85	0.84	0.84	0.77	3	I	0.71	0.91	1.00	0.88	0.78	0.86	3	I	0.09	0	yes
4	BCC-CSM2-MR	0.67	0.73	0.58	0.84	0.88	0.74	5	I	0.65	0.86	0.81	0.83	0.87	0.80	10	II	0.06	5	no
5	CAMS-CSM1-0	0.52	0.09	0.69	0.53	0.73	0.51	23	III	0.45	0.06	0.54	0.53	0.68	0.45	25	III	0.06	2	yes
6	CanESM5	0.74	0.70	0.62	0.74	0.86	0.73	8	II	0.78	0.83	0.98	0.95	0.93	0.89	1	I	0.16	7	no
7	CESM2-WACCM	0.79	0.38	0.57	0.85	0.88	0.69	14	II	0.78	0.40	0.67	0.76	0.86	0.70	16	II	0.01	2	yes
8	CIESM	0.44	0.89	0.85	0.93	0.44	0.71	12	II	0.47	0.61	0.74	0.41	0.45	0.54	21	III	0.17	9	no
9	EC-Earth3	0.45	0.93	0.81	0.83	0.65	0.74	7	II	0.63	1.00	0.00	0.00	0.83	0.49	23	III	0.24	16	no
10	EC-Earth3-Veg	0.62	0.31	0.00	0.00	0.82	0.35	25	III	0.80	0.74	0.89	0.91	0.95	0.86	2	I	0.51	23	no
11	FGOALS-f3-L	0.38	0.71	0.61	0.56	0.59	0.57	20	III	0.49	0.66	0.94	0.95	0.69	0.75	14	II	0.18	6	no
12	FGOALS-g3	0.00	0.72	0.79	0.92	0.00	0.48	24	III	0.00	0.92	0.69	0.71	0.00	0.46	24	III	0.02	0	yes
13	FIO-ESM-2-0	0.75	0.46	0.52	0.52	0.93	0.63	17	II	0.81	0.66	0.78	0.86	0.91	0.80	9	II	0.17	8	yes
14	GFDL-ESM4	0.81	0.83	0.52	0.68	0.97	0.76	4	I	0.76	0.40	0.97	0.85	0.91	0.78	11	II	0.02	7	no
15	INM-CM4-8	0.64	0.90	0.81	0.82	0.71	0.78	2	I	0.57	0.00	0.75	0.57	0.67	0.51	22	III	0.27	20	no
16	INM-CM5-0	0.74	0.38	0.83	0.73	0.86	0.71	13	II	0.71	0.68	0.91	0.90	0.84	0.81	8	II	0.10	5	yes
17	IPSL-CM6A-LR	0.73	0.49	0.61	0.59	0.80	0.65	16	II	0.70	0.78	0.98	0.96	0.73	0.83	4	I	0.18	12	no
18	KACE-1-0-G	0.50	0.74	0.75	0.97	0.70	0.73	10	II	0.57	1.00	0.91	0.89	0.77	0.83	5	I	0.10	5	no
19	MIROC6	0.67	0.00	0.74	0.58	0.83	0.56	21	III	0.67	0.36	0.77	0.70	0.83	0.66	19	II	0.10	2	no
20	MPI-ESM1-2-HR	0.76	0.09	0.84	0.46	0.81	0.59	19	II	0.78	0.55	0.88	0.73	0.87	0.76	12	II	0.17	7	yes
21	MPI-ESM1-2-LR	0.83	0.91	0.74	0.97	0.92	0.87	1	I	0.80	0.75	0.81	0.89	0.86	0.82	6	I	0.05	5	yes
22	MRI-ESM2-0	0.66	0.63	0.58	0.72	0.74	0.67	15	II	0.63	0.67	0.68	0.77	0.72	0.70	17	II	0.03	2	yes
23	NESM3	0.55	1.00	0.02	0.32	0.76	0.53	22	III	0.52	0.98	0.31	0.25	0.74	0.56	20	III	0.03	2	yes
24	NorESM2-LM	0.77	0.64	0.50	0.92	0.83	0.73	9	II	0.75	0.62	0.98	0.93	0.79	0.81	7	II	0.08	2	yes
25	NorESM2-MM	0.61	1.00	0.38	0.90	0.76	0.73	11	II	0.59	0.65	0.87	0.72	0.75	0.72	15	II	0.01	4	yes
																	Mean	0.12	6.7	yes-52%

- very good (I) - satisfactory (II) - unsatisfactory (III) - QUALITY GROUPS (QG)

I (2) II (7) III (3) / got into different groups (13) - number of models belong to each QG in two period

Fig. A.8. Results of normalized Taylor Diagram statistics, bias and trend differences for 25 models over the Arctic for the period 1951-1980 and for the period 1981-2010 for method (vi) of model comparison by Taylor Diagram, bias and trend (see 2.2 Methods for model evaluation compared in the study)

№	Model acronym	Period 1951-1980			Period 1981-2010			Total score diff.	Model rank diff.	Consistency (QG)
		Total score	Model rank	Quality group	Total score	Model rank	Quality group			
1	ACCESS-CM2	0.58	16	II	0.41	18	II	0.17	2	yes
2	ACCESS-ESM1-5	0.89	4	I	0.86	4	I	0.03	0	yes
3	AWI-CM-1-1-MR	0.95	3	I	0.86	5	I	0.08	2	yes
4	BCC-CSM2-MR	0.68	11	II	0.73	11	II	0.04	0	yes
5	CAMS-CSM1-0	0.47	21	III	0.27	23	III	0.20	2	yes
6	CanESM5	0.68	12	II	0.82	8	II	0.13	4	yes
7	CESM2-WACCM	0.84	6	I	0.23	24	III	0.61	18	no
8	CIESM	0.47	22	III	0.86	7	II	0.39	15	no
9	EC-Earth3	0.47	23	III	0.41	19	II	0.06	4	no
10	EC-Earth3-Veg	0.53	19	II	1.00	1	I	0.47	18	no
11	FGOALS-f3-L	0.21	24	III	0.36	20	III	0.15	4	yes
12	FGOALS-g3	0.00	25	III	0.00	25	III	0.00	0	yes
13	FIO-ESM-2-0	0.89	5	I	0.82	9	II	0.08	4	no
14	GFDL-ESM4	1.00	1	I	0.86	6	I	0.14	5	yes
15	INM-CM4-8	0.53	20	III	0.36	21	III	0.16	1	yes
16	INM-CM5-0	0.74	10	II	0.77	10	II	0.04	0	yes
17	IPSL-CM6A-LR	0.79	7	II	0.64	16	II	0.15	9	yes
18	KACE-1-0-G	0.58	17	II	0.68	14	II	0.10	3	yes
19	MIROC6	0.63	15	II	0.68	15	II	0.05	0	yes
20	MPI-ESM1-2-HR	0.79	8	II	0.91	3	I	0.12	5	no
21	MPI-ESM1-2-LR	1.00	2	I	0.95	2	I	0.05	0	yes
22	MRI-ESM2-0	0.68	13	II	0.64	17	II	0.05	4	yes
23	NESM3	0.58	18	II	0.32	22	III	0.26	4	no
24	NorESM2-LM	0.68	14	II	0.73	12	II	0.04	2	yes
25	NorESM2-MM	0.79	9	II	0.73	13	II	0.06	4	yes
							Mean	0.15	4.4	yes-72%

- very good (I) - satisfactory (II) - unsatisfactory (II) - **QUALITY GROUPS (QG)**

I (4) II (10) III (4) / got into different groups (7) - number of models belong to each QG in two periods

Fig. A.9. Results of normalized values of total scores for 25 models over the Arctic for the period 1951-1980 and for the period 1981-2010 for method (vii) – Percentile-based method (see 2.2 Methods for model evaluation compared in the study)

№	Model acronym	Period 1951-1980			Period 1981-2010		
		Method i	Method iii	Method iv	Method i	Method iii	Method iv
		RMSE	TSS	S_{score}	RMSE	TSS	S_{score}
1	ACCESS-CM2	2.3	0.85	0.06	2.7	0.59	0.36
2	ACCESS-ESM1-5	0.7	0.07	0.26	0.6	0.81	0.60
3	AWI-CM-1-1-MR	0.8	0.31	0.53	1.1	0.90	0.63
4	BCC-CSM2-MR	1.4	0.47	0.58	1.4	0.82	0.64
5	CAMS-CSM1-0	2.2	0.07	0.07	2.6	0.20	0.32
6	CanESM5	1.0	0.45	0.26	0.7	0.61	0.63
7	CESM2-WACCM	0.7	0.17	0.61	0.7	0.76	0.65
8	CIESM	2.7	0.79	0.27	2.5	0.43	0.33
9	EC-Earth3	2.6	0.85	0.74	1.5	0.66	0.70
10	EC-Earth3-Veg	1.6	0.09	0.57	0.6	0.72	0.70
11	FGOALS-f3-L	3.0	0.45	0.08	2.4	0.66	0.58
12	FGOALS-g3	5.1	0.52	0.67	5.2	0.85	0.31
13	FIO-ESM-2-0	0.9	0.21	0.51	0.5	0.62	0.70
14	GFDL-ESM4	0.6	0.57	0.79	0.8	0.46	0.60
15	INM-CM4-8	1.6	0.79	0.01	1.9	0.23	0.36
16	INM-CM5-0	1.0	0.20	0.30	1.1	0.67	0.56
17	IPSL-CM6A-LR	1.0	0.25	0.07	1.2	0.76	0.12
18	KACE-1-0-G	2.3	0.52	0.33	1.9	0.99	0.63
19	MIROC6	1.4	0.05	0.56	1.4	0.41	0.12
20	MPI-ESM1-2-HR	0.9	0.07	0.51	0.7	0.56	0.56
21	MPI-ESM1-2-LR	0.5	0.80	0.27	0.6	0.71	0.57
22	MRI-ESM2-0	1.4	0.37	0.72	1.5	0.62	0.62
23	NESM3	2.0	0.57	0.61	2.2	0.77	0.63
24	NorESM2-LM	0.8	0.35	0.61	0.9	0.62	0.70
25	NorESM2-MM	1.7	0.76	0.31	1.8	0.64	0.62

- very good - satisfactory - unsatisfactory

Fig. A.10. Results of RMSE (method i), TSS (method iii) and S_{score} (method iv) for 25 models over the Arctic for the period 1951-1980 and for the period 1981-2010

№	Model acronym	Period 1951-1980			Period 1981-2010		
		r	Mean diff.	STD diff.	r	Mean diff.	STD diff.
1	ACCESS-CM2	0.20	0.014	0.001	0.36	0.009	0.002
2	ACCESS-ESM1-5	-0.20	0.044	0.011	0.47	0.037	0.005
3	AWI-CM-1-1-MR	0.03	0.010	0.011	0.16	0.008	0.002
4	BCC-CSM2-MR	0.22	0.010	0.012	-0.07	0.012	0.001
5	CAMS-CSM1-0	0.02	0.033	0.007	0.38	0.036	0.012
6	CanESM5	0.37	0.017	0.009	0.49	0.003	0.002
7	CESM2-WACCM	-0.42	0.010	0.000	0.29	0.017	0.006
8	CIESM	0.18	0.004	0.002	-0.16	0.045	0.008
9	EC-Earth3	-0.15	0.011	0.002	0.25	0.077	0.046
10	EC-Earth3-Veg	-0.23	0.071	0.016	0.61	0.006	0.004
11	FGOALS-f3-L	0.17	0.030	0.002	0.58	0.003	0.003
12	FGOALS-g3	0.18	0.005	0.011	0.08	0.021	0.005
13	FIO-ESM-2-0	0.40	0.033	0.023	0.43	0.009	0.005
14	GFDL-ESM4	0.28	0.023	0.010	0.13	0.010	0.005
15	INM-CM4-8	0.33	0.012	0.003	-0.22	0.033	0.001
16	INM-CM5-0	-0.24	0.019	0.003	0.26	0.007	0.013
17	IPSL-CM6A-LR	0.10	0.028	0.008	-0.01	0.001	0.004
18	KACE-1-0-G	-0.42	0.001	0.017	0.31	0.007	0.006
19	MIROC6	-0.14	0.029	0.000	0.39	0.022	0.003
20	MPI-ESM1-2-HR	0.29	0.038	0.000	-0.29	0.019	0.004
21	MPI-ESM1-2-LR	-0.04	0.001	0.000	0.05	0.007	0.009
22	MRI-ESM2-0	0.20	0.020	0.015	0.04	0.016	0.008
23	NESM3	0.46	0.049	0.030	0.03	0.058	0.008
24	NorESM2-LM	-0.38	0.005	0.000	-0.08	0.004	0.006
25	NorESM2-MM	0.06	0.007	0.005	0.37	0.021	0.005

- very good - satisfactory - unsatisfactory

Fig. A.11. Results of spatial trends statistics (r, Mean difference, STD difference) for 25 models over the Arctic for the period 1951-1980 and for the period 1981-2010 - method ii

№	Model acronym	Period 1951-1980			Period 1981-2010		
		MR_{IVS}	MR_{Taylor}	MR_{mean}	MR_{IVS}	MR_{Taylor}	MR_{mean}
1	ACCESS-CM2	0.68	0.60	0.64	0.56	0.28	0.42
2	ACCESS-ESM1-5	0.64	0.55	0.59	0.12	0.60	0.36
3	AWI-CM-1-1-MR	0.88	0.69	0.79	0.96	0.77	0.87
4	BCC-CSM2-MR	0.32	0.48	0.40	0.48	0.53	0.51
5	CAMS-CSM1-0	0.48	0.27	0.37	0.04	0.07	0.05
6	CanESM5	0.44	0.51	0.47	0.84	0.55	0.69
7	CESM2-WACCM	0.24	0.44	0.34	0.24	0.19	0.21
8	CIESM	0.96	0.59	0.77	0.16	0.61	0.39
9	EC-Earth3	0.80	0.57	0.69	0.00	0.43	0.21
10	EC-Earth3-Veg	0.00	0.17	0.09	0.64	0.69	0.67
11	FGOALS-f3-L	0.36	0.31	0.33	0.76	0.45	0.61
12	FGOALS-g3	0.72	0.41	0.57	0.32	0.35	0.33
13	FIO-ESM-2-0	0.16	0.37	0.27	0.40	0.59	0.49
14	GFDL-ESM4	0.20	0.60	0.40	0.80	0.53	0.67
15	INM-CM4-8	0.76	0.65	0.71	0.20	0.19	0.19
16	INM-CM5-0	0.84	0.56	0.70	0.68	0.59	0.63
17	IPSL-CM6A-LR	0.40	0.43	0.41	0.92	0.69	0.81
18	KACE-1-0-G	0.52	0.47	0.49	0.72	0.65	0.69
19	MIROC6	0.56	0.33	0.45	0.36	0.31	0.33
20	MPI-ESM1-2-HR	0.92	0.55	0.73	0.60	0.52	0.56
21	MPI-ESM1-2-LR	0.60	0.77	0.69	0.44	0.67	0.55
22	MRI-ESM2-0	0.28	0.37	0.33	0.28	0.36	0.32
23	NESM3	0.04	0.43	0.23	0.08	0.37	0.23
24	NorESM2-LM	0.12	0.44	0.28	0.88	0.61	0.75
25	NorESM2-MM	0.08	0.44	0.26	0.52	0.40	0.46

- very good - satisfactory - unsatisfactory

Fig. A.12. Results of MR for Taylor and IVS metrics for 25 models over the Arctic for the period 1951-1980 and for the period 1981-2010 - method v

№	Model acronym	Period 1951-1980					Period 1981-2010				
		RMSE	r	|dif_std|	|dif_T|	|B|	RMSE	r	|dif_std|	|dif_T|	|B|
1	ACCESS-CM2	2.26	0.33	0.06	0.01	2.13	2.66	0.59	0.08	0.01	2.51
2	ACCESS-ESM1-5	0.69	-0.28	0.08	0.04	0.18	0.63	0.77	0.29	0.04	0.12
3	AWI-CM-1-1-MR	0.76	0.02	0.04	0.01	0.94	1.09	0.76	0.00	0.01	1.39
4	BCC-CSM2-MR	1.36	0.17	0.16	0.01	0.67	1.43	0.73	0.12	0.01	0.77
5	CAMS-CSM1-0	2.24	-0.29	0.11	0.03	1.73	2.58	0.31	0.30	0.04	2.02
6	CanESM5	0.96	0.16	0.14	0.02	0.86	0.70	0.72	0.01	0.00	0.39
7	CESM2-WACCM	0.69	-0.08	0.17	0.01	0.72	0.69	0.49	0.21	0.02	0.80
8	CIESM	2.69	0.29	0.04	0.00	3.65	2.46	0.60	0.17	0.04	3.59
9	EC-Earth3	2.60	0.32	0.05	0.01	2.26	1.55	0.81	0.64	0.08	1.00
10	EC-Earth3-Veg	1.64	-0.13	0.44	0.07	1.08	0.60	0.67	0.07	0.01	0.24
11	FGOALS-f3-L	3.00	0.16	0.15	0.03	2.67	2.37	0.63	0.04	0.00	2.00
12	FGOALS-g3	5.14	0.17	0.07	0.01	6.62	5.16	0.76	0.20	0.02	6.68
13	FIO-ESM-2-0	0.94	-0.02	0.20	0.03	0.39	0.54	0.63	0.14	0.01	0.49
14	GFDL-ESM4	0.58	0.25	0.19	0.02	0.11	0.82	0.49	0.02	0.01	0.48
15	INM-CM4-8	1.56	0.30	0.05	0.01	1.82	1.91	0.28	0.16	0.03	2.14
16	INM-CM5-0	0.96	-0.08	0.04	0.02	0.81	1.09	0.64	0.06	0.01	0.96
17	IPSL-CM6A-LR	1.01	0.00	0.15	0.03	1.23	1.17	0.69	0.01	0.00	1.72
18	KACE-1-0-G	2.32	0.19	0.08	0.00	1.88	1.89	0.81	0.06	0.01	1.41
19	MIROC6	1.40	-0.36	0.09	0.03	1.05	1.36	0.47	0.15	0.02	1.03
20	MPI-ESM1-2-HR	0.86	-0.30	0.04	0.04	1.15	0.69	0.57	0.08	0.02	0.79
21	MPI-ESM1-2-LR	0.48	0.31	0.09	0.00	0.46	0.58	0.67	0.12	0.01	0.80
22	MRI-ESM2-0	1.45	0.11	0.17	0.02	1.63	1.54	0.63	0.21	0.02	1.79
23	NESM3	2.03	0.37	0.44	0.05	1.51	2.18	0.80	0.44	0.06	1.64
24	NorESM2-LM	0.78	0.11	0.20	0.00	1.03	0.89	0.60	0.01	0.00	1.32
25	NorESM2-MM	1.72	0.37	0.26	0.01	1.47	1.78	0.62	0.09	0.02	1.60

- very good - satisfactory - unsatisfactory

Fig. A.13. Results of Taylor Diagram statistics, bias and trend differences for 25 models over the Arctic for the period 1951-1980 and for the period 1981-2010 - method vi

Table A.14. Results of the CMIP6 model performance for SAT in the Arctic over the period 1951-1980 using the percentile-based method - method vii (RMSE - root-mean-square error, ^{0}C; r – correlation coefficient between models and reanalysis; CPI – climate prediction index; |dif_std| – modulus of standard deviation difference (model minus observations), ^{0}C; |Trm| - modulus of spatial trend mean difference (model minus observations), ^{0}C yr^{-1}; |Tra| - modulus of spatial trend amplitude difference (model minus observations), ^{0}C yr^{-1}; |Bm| - modulus of spatial bias mean difference (model minus observations), ^{0}C; |Ba| – modulus of spatial biases amplitude difference (model minus observations), ^{0}C)

ID	Model acronym	Seasonal variability (averaged over the territory)				Interannual variability (averaged over the territory)				Spatial variability			
		rmsd	r	CPI	|dif_std|	rmsd	r	CPI	|dif_std|	|Trm|	|Tra|	|Brm|	|Bra|
1	ACCESS-CM2	2.49	1.00	0.23	0.70	2.26	0.33	6.30	0.06	0.02	0.25	2.13	21.69
2	ACCESS-ESM1-5	0.99	1.00	0.09	0.20	0.69	-0.28	1.93	0.08	0.06	0.05	0.18	28.78
3	AWI-CM-1-1-MR	0.97	1.00	0.09	0.36	0.76	0.02	2.13	0.04	0.03	0.17	0.94	22.00
4	BCC-CSM2-MR	1.74	0.99	0.16	0.48	1.36	0.17	3.79	0.16	0.03	0.06	0.67	30.32
5	CAMS-CSM1-0	3.07	0.99	0.28	1.11	2.24	-0.29	6.24	0.11	0.05	0.06	1.73	25.97
6	CanESM5	1.30	1.00	0.12	0.35	0.96	0.16	2.68	0.14	0.03	0.16	0.86	28.05
7	CESM2-WACCM	1.17	1.00	0.11	0.92	0.69	-0.08	1.93	0.17	0.02	0.26	0.72	20.88
8	CIESM	2.98	0.99	0.27	0.27	2.69	0.29	7.49	0.04	0.01	0.28	3.65	19.95
9	EC-Earth3	2.72	1.00	0.25	0.13	2.60	0.32	7.24	0.05	0.02	0.23	2.26	26.14
10	EC-Earth3-Veg	1.58	1.00	0.14	0.28	1.64	-0.13	4.57	0.44	0.11	0.04	1.08	25.89
11	FGOALS-f3-L	3.32	1.00	0.30	1.45	3.00	0.16	8.36	0.15	0.05	0.26	2.67	25.17
12	FGOALS-g3	5.54	1.00	0.50	2.01	5.14	0.17	14.33	0.07	0.01	0.04	6.62	34.33
13	FIO-ESM-2-0	1.03	1.00	0.09	0.60	0.94	-0.02	2.62	0.20	0.05	0.11	0.39	21.31
14	GFDL-ESM4	0.77	1.00	0.07	0.18	0.58	0.25	1.63	0.19	0.02	0.10	0.11	21.85
15	INM-CM4-8	2.08	0.99	0.19	0.86	1.56	0.30	4.35	0.05	0.03	0.22	1.82	27.31
16	INM-CM5-0	1.35	1.00	0.12	0.37	0.96	-0.08	2.67	0.04	0.04	0.24	0.81	27.01
17	IPSL-CM6A-LR	1.13	1.00	0.10	0.54	1.01	0.00	2.82	0.15	0.04	0.21	1.23	23.00
18	KACE-1-0-G	2.64	1.00	0.24	1.07	2.32	0.19	6.47	0.08	0.01	0.08	1.88	23.25
19	MIROC6	1.42	1.00	0.13	0.23	1.40	-0.36	3.90	0.09	0.04	0.22	1.05	24.03
20	MPI-ESM1-2-HR	1.06	1.00	0.10	0.53	0.86	-0.30	2.41	0.04	0.05	0.23	1.15	20.04
21	MPI-ESM1-2-LR	0.67	1.00	0.06	0.36	0.48	0.31	1.35	0.09	0.01	0.20	0.46	23.88
22	MRI-ESM2-0	1.48	1.00	0.13	0.55	1.45	0.11	4.04	0.17	0.02	0.11	1.63	22.89
23	NESM3	2.36	1.00	0.21	0.95	2.03	0.37	5.67	0.44	0.07	0.01	1.51	25.80
24	NorESM2-LM	1.40	1.00	0.13	1.14	0.78	0.11	2.18	0.20	0.00	0.22	1.03	22.82
25	NorESM2-MM	1.72	1.00	0.16	0.00	1.72	0.37	4.80	0.26	0.00	0.11	1.47	21.40
	maximum	5.54	1.00	0.50	2.01	5.14	1.00	14.33	0.44	0.11	0.28	6.62	34.33
	75%	3.65	0.75	0.33	1.50	3.49	0.75	9.74	0.31	0.08	0.21	4.88	30.73
	50%	2.44	0.50	0.22	1.00	2.33	0.50	6.49	0.20	0.05	0.14	3.25	27.14
	25%	1.22	0.25	0.11	0.50	1.16	0.25	3.25	0.10	0.03	0.07	1.63	23.54
	minimum	0.67	0.00	0.06	0.00	0.48	0.00	1.35	0.04	0.00	0.01	0.11	19.95

Table A.15. Results of the CMIP6 model performance for SAT in the Arctic over the period 1981-2010 using the percentile-based method - method vii (RMSE - root-mean-square error, ^{0}C; r – correlation coefficient between models and reanalysis; CPI – climate prediction index; |dif_std| – modulus of standard deviation difference (model minus observations), ^{0}C; |Trm| - modulus of spatial trend mean difference (model minus observations), ^{0}C yr^{-1}; |Tra| - modulus of spatial trend amplitude difference (model minus observations), ^{0}C yr^{-1}; |Bm| - modulus of spatial bias mean difference (model minus observations), ^{0}C; |Ba| – modulus of spatial biases amplitude difference (model minus observations), ^{0}C)

ID	Model acronym	Seasonal variability (averaged over the territory)				Interannual variability (averaged over the territory)				Spatial variability			
		rmsd	r	CPI	|dif_std|	rmsd	r	CPI	|dif_std|	|Trm|	|Tra|	|Brm|	|Bra|
1	ACCESS-CM2	2.86	1.00	0.27	0.94	2.66	0.59	3.90	0.08	0.02	0.05	2.51	58.06
2	ACCESS-ESM1-5	0.94	1.00	0.09	0.28	0.63	0.77	0.93	0.29	0.04	0.09	0.12	55.90
3	AWI-CM-1-1-MR	1.36	1.00	0.13	0.56	1.09	0.76	1.60	0.00	0.00	0.06	1.39	60.97
4	BCC-CSM2-MR	1.74	1.00	0.16	0.50	1.43	0.73	2.10	0.12	0.00	0.02	0.77	60.91
5	CAMS-CSM1-0	3.31	1.00	0.31	1.23	2.58	0.31	3.79	0.30	0.05	0.00	2.02	59.10
6	CanESM5	0.73	1.00	0.07	0.24	0.70	0.72	1.03	0.01	0.01	0.02	0.39	67.82
7	CESM2-WACCM	1.18	1.00	0.11	0.83	0.69	0.49	1.00	0.21	0.01	0.02	0.80	61.63
8	CIESM	2.77	0.99	0.26	0.31	2.46	0.60	3.61	0.17	0.05	0.05	3.59	62.73
9	EC-Earth3	1.43	1.00	0.13	0.14	1.55	0.81	2.27	0.64	0.07	0.30	1.00	59.23
10	EC-Earth3-Veg	0.69	1.00	0.06	0.39	0.60	0.67	0.88	0.07	0.00	0.03	0.24	51.53
11	FGOALS-f3-L	2.65	1.00	0.25	1.20	2.37	0.63	3.48	0.04	0.00	0.05	2.00	71.32
12	FGOALS-g3	5.55	1.00	0.51	2.00	5.16	0.76	7.57	0.20	0.01	0.11	6.68	68.98
13	FIO-ESM-2-0	0.56	1.00	0.05	0.48	0.54	0.63	0.80	0.14	0.02	0.08	0.49	65.64
14	GFDL-ESM4	0.88	1.00	0.08	0.31	0.82	0.49	1.20	0.02	0.02	0.03	0.48	57.97
15	INM-CM4-8	2.27	1.00	0.21	0.97	1.91	0.28	2.80	0.16	0.04	0.06	2.14	70.04
16	INM-CM5-0	1.39	1.00	0.13	0.45	1.09	0.64	1.60	0.06	0.02	0.06	0.96	66.01
17	IPSL-CM6A-LR	1.35	1.00	0.13	0.49	1.17	0.69	1.72	0.01	0.01	0.04	1.72	65.80
18	KACE-1-0-G	2.15	1.00	0.20	0.96	1.89	0.81	2.77	0.06	0.01	0.01	1.41	62.17
19	MIROC6	1.41	1.00	0.13	0.22	1.36	0.47	2.00	0.15	0.03	0.04	1.03	57.84
20	MPI-ESM1-2-HR	0.82	1.00	0.08	0.36	0.69	0.57	1.01	0.08	0.03	0.03	0.79	60.29
21	MPI-ESM1-2-LR	0.77	1.00	0.07	0.51	0.58	0.67	0.85	0.12	0.01	0.04	0.80	55.22
22	MRI-ESM2-0	1.53	1.00	0.14	0.58	1.54	0.63	2.26	0.21	0.01	0.05	1.79	60.60
23	NESM3	2.57	0.99	0.24	1.00	2.18	0.80	3.19	0.44	0.06	0.09	1.64	62.79
24	NorESM2-LM	1.53	1.00	0.14	1.19	0.89	0.60	1.31	0.01	0.02	0.04	1.32	59.30
25	NorESM2-MM	1.77	1.00	0.16	0.13	1.78	0.62	2.61	0.09	0.03	0.03	1.60	60.45
	maximum	5.55	1.00	0.51	2.00	5.16	1.00	7.57	0.64	0.07	0.30	6.68	71.32
	75%	3.74	0.75	0.35	1.40	3.46	0.75	5.08	0.48	0.05	0.23	4.92	66.37
	50%	2.50	0.50	0.23	0.93	2.31	0.50	3.39	0.32	0.04	0.15	3.28	61.43
	25%	1.25	0.25	0.12	0.47	1.15	0.25	1.69	0.16	0.02	0.08	1.64	56.48
	minimum	0.56	0.00	0.05	0.13	0.54	0.00	0.80	0.00	0.00	0.00	0.12	51.53

№	Model acronym	Seasonal variablity				Interannual variability				Spatial variability				Total score	Rank
		rmsd	r	CPI	dif_std	rmsd	r	CPI	dif_std	|Trm|	|Tra|	|Bm|	|Ba|		
1	ACCESS-CM2	1	3	1	2	2	1	2	3	3	0	2	3	23	16
2	ACCESS-ESM1-5	3	3	3	3	3	0	3	3	1	3	3	1	29	4
3	AWI-CM-1-1-MR	3	3	3	3	3	0	3	3	2	1	3	3	30	3
4	BCC-CSM2-MR	2	3	2	3	2	0	2	2	2	3	3	1	25	11
5	CAMS-CSM1-0	1	3	1	1	2	0	2	2	2	3	2	2	21	21
6	CanESM5	2	3	2	3	3	0	3	2	2	1	3	1	25	12
7	CESM2-WACCM	3	3	3	2	3	0	3	2	3	0	3	3	28	6
8	CIESM	1	3	1	3	1	1	1	3	3	0	1	3	21	22
9	EC-Earth3	1	3	1	3	1	1	1	3	3	0	2	2	21	23
10	EC-Earth3-Veg	2	3	2	3	2	0	2	0	0	3	3	2	22	19
11	FGOALS-f3-L	1	3	1	1	1	0	1	2	2	0	2	2	16	24
12	FGOALS-g3	0	3	0	0	0	0	0	3	3	3	0	0	12	25
13	FIO-ESM-2-0	3	3	3	2	3	0	3	2	2	2	3	3	29	5
14	GFDL-ESM4	3	3	3	3	3	0	3	2	3	2	3	3	31	1
15	INM-CM4-8	2	3	2	2	2	1	2	3	2	0	2	1	22	20
16	INM-CM5-0	2	3	2	3	3	0	3	3	2	0	3	2	26	10
17	IPSL-CM6A-LR	3	3	3	2	3	0	3	2	2	0	3	3	27	7
18	KACE-1-0-G	1	3	1	1	2	0	2	3	3	2	2	3	23	17
19	MIROC6	2	3	2	3	2	0	2	3	2	0	3	2	24	15
20	MPI-ESM1-2-HR	3	3	3	2	3	0	3	3	1	0	3	3	27	8
21	MPI-ESM1-2-LR	3	3	3	3	3	1	3	3	3	1	3	2	31	2
22	MRI-ESM2-0	2	3	2	2	2	0	2	2	3	2	2	3	25	13
23	NESM3	2	3	2	2	2	1	2	0	1	3	3	2	23	18
24	NorESM2-LM	2	3	2	1	3	0	3	2	3	0	3	3	25	14
25	NorESM2-MM	2	3	2	3	2	1	2	1	3	2	3	3	27	9

Fig. A.16. Results of the percentile-based method with the final model score over the period 1951-1980 - method vii (Green color denotes a very good group, yellow – good, orange – satisfactory, and red – unsatisfactory group)

№	Model acronym	Seasonal variablity				Interannual variability				Spatial variability				Total score	Rank
		rmsd	r	CPI	dif_std	rmsd	r	CPI	dif_std	|Trm|	|Tra|	|Bm|	|Ba|		
1	ACCESS-CM2	1	3	1	1	1	2	1	3	2	3	2	2	22	18
2	ACCESS-ESM1-5	3	3	3	3	3	3	3	2	1	2	3	3	32	4
3	AWI-CM-1-1-MR	2	3	2	2	3	3	3	3	3	3	3	2	32	5
4	BCC-CSM2-MR	2	3	2	2	2	2	2	3	3	3	3	2	29	11
5	CAMS-CSM1-0	1	3	1	1	1	1	1	2	1	3	2	2	19	23
6	CanESM5	3	3	3	2	3	2	3	2	3	3	3	1	31	8
7	CESM2-WACCM	1	3	1	3	1	1	1	2	0	3	1	1	18	24
8	CIESM	3	3	3	3	3	2	3	3	3	3	3	0	32	6
9	EC-Earth3	2	3	2	3	2	3	2	0	0	0	3	2	22	19
10	EC-Earth3-Veg	3	3	3	3	3	2	3	3	3	3	3	3	35	1
11	FGOALS-f3-L	1	3	1	1	1	2	1	3	3	3	2	0	21	20
12	FGOALS-g3	0	3	0	0	0	3	0	2	3	2	0	0	13	25
13	FIO-ESM-2-0	3	3	3	2	3	2	3	3	3	2	3	1	31	9
14	GFDL-ESM4	3	3	3	3	3	1	3	3	2	3	3	2	32	7
15	INM-CM4-8	2	3	2	1	2	1	2	2	1	3	2	0	21	21
16	INM-CM5-0	2	3	2	3	3	2	3	3	2	3	3	1	30	10
17	IPSL-CM6A-LR	2	3	2	2	2	2	2	3	3	3	2	1	27	16
18	KACE-1-0-G	2	3	2	1	2	3	2	3	3	3	3	1	28	14
19	MIROC6	2	3	2	3	2	1	2	3	2	3	3	2	28	15
20	MPI-ESM1-2-HR	3	3	3	3	3	2	3	3	2	3	3	2	33	3
21	MPI-ESM1-2-LR	3	3	3	2	3	2	3	3	3	3	3	3	34	2
22	MRI-ESM2-0	2	3	2	2	2	2	2	2	3	3	2	2	27	17
23	NESM3	1	3	1	1	2	3	2	1	0	2	3	1	20	22
24	NorESM2-LM	2	3	2	1	3	2	3	3	2	3	3	2	29	12
25	NorESM2-MM	2	3	2	3	2	2	2	3	2	3	3	2	29	13

Fig. A.17. Results of the percentile-based method with the final model score over the period 1981-2010 - method vii (Green color denotes a very good group, yellow – good, orange – satisfactory, and red – unsatisfactory group)

A.18 REFERENCES TO TABLE A2

Aghakhani Afshar A., Hasanzadeh Y., Besalatpour A.A., and Pourreza-Bilondi M. (2017). Climate change forecasting in a mountainous data scarce watershed using CMIP5 models under representative concentration pathways. Theoretical and Applied Climatology, 129, 683-699, DOI:10.1007/s00704-016-1908-5.

Ahmed K., Sachindra D., Shahid S., et al. (2020). Multi-model ensemble predictions of precipitation and temperature using machine learning algorithms. Atmospheric Research, 236, 104806, DOI:10.1016/j.atmosres.2019.104806.

Anandhi A. and Nanjundiah R.S. (2015). Performance evaluation of AR4 Climate Models in simulating daily precipitation over the Indian region using skill scores. Theoretical and Applied Climatology, 119, 551-566, DOI:10.1007/s00704-013-1043-5.

Anandhi A., Pierson D.C., and Frei A. (2019). Evaluation of Climate Model Performance for Water Supply Studies: Case Study for New York City. Journal of Water Resources Planning and Management, 145, 06019006, DOI:10.1061/(ASCE)WR.1943-5452.0001054.

Bannister D., Herzog M., Graf H.-F., et al. (2017). An Assessment of Recent and Future Temperature Change over the Sichuan Basin, China, Using CMIP5 Climate Models. Journal of Climate, 30, 6701-6722, DOI:10.1175/JCLI-D-16-0536.1.

Cai Z., You Q., Wu F., et al. (2021). Arctic Warming Revealed by Multiple CMIP6 Models: Evaluation of Historical Simulations and Quantification of Future Projection Uncertainties. Journal of Climate, 34, 4871-4892. DOI:10.1175/JCLI-D-20-0791.1.

Fu G., Liu Z., Charles S.P., et al. (2013). A score-based method for assessing the performance of GCMs: A case study of southeastern Australia. Journal of Geophysical Research-Atmospheres, 118, 4154-4167, DOI:10.1002/jgrd.50269.

Gnatiuk N., Radchenko I., Davy R., et al. (2020). Simulation of factors affecting Emiliania huxleyi blooms in Arctic and sub-Arctic seas by CMIP5 climate models: model validation and selection. Biogeosciences, 17, 1199-1212, DOI:10.5194/bg-17-1199-2020.

Herger N., Abramowitz G., Knutti R., et al. (2018). Selecting a climate model subset to optimise key ensemble properties. Earth System Dynamics, 9, 135-151, DOI:10.5194/esd-9-135-2018.

Inoue T. and Ueda H. (2011). Delay of the First Transition of Asian Summer Monsoon under Global Warming Condition. SOLA, 7, 81-84, DOI:10.2151/sola.2011-021.

Jia K., Ruan Y., Yang Y., and You Z. (2019). Assessment of CMIP5 GCM Simulation Performance for Temperature Projection in the Tibetan Plateau. Earth and Space Science, 6, 2362-2378, DOI:10.1029/2019EA000962.

Jiang Z., Li W., Xu J., and Li L. (2015). Extreme Precipitation Indices over China in CMIP5 Models. Part I: Model Evaluation. Journal of Climate, 28, 8603-8619, DOI:10.1175/JCLI-D-15-0099.1.

Kadel I., Yamazaki T., Iwasaki T., and Abdillah M. (2018). Projection of future monsoon precipitation over the central Himalayas by CMIP5 models under warming scenarios. Climate Research, 75, 1-21, DOI:10.3354/cr01497.

Kumar D., Mishra V., and Ganguly A.R. (2015). Evaluating wind extremes in CMIP5 climate models. Climate Dynamics, 45, 441-453, DOI:10.1007/s00382-014-2306-2.

Kumar S., Merwade V., Kinter J.L., and Niyogi D. (2013). Evaluation of Temperature and Precipitation Trends and Long-Term Persistence in CMIP5 Twentieth-Century Climate Simulations. Journal of Climate, 26, 4168-4185, DOI:10.1175/JCLI-D-12-00259.1.

Macadam I., Pitman A.J., Whetton P.H., and Abramowitz G. (2010). Ranking climate models by performance using actual values and anomalies: Implications for climate change impact assessments. Geophysical Research Letters, 37, 16704, DOI:10.1029/2010GL043877.

Maxino C.C., McAvaney B.J., Pitman A.J., and Perkins S.E. (2008). Ranking the AR4 climate models over the Murray-Darling Basin using simulated maximum temperature, minimum temperature and precipitation. International Journal of Climatology, 28, 1097-1112, DOI:10.1002/joc.1612.

McMahon T.A., Peel M.C., and Karoly D.J. (2015). Assessment of precipitation and temperature data from CMIP3 global climate models for hydrologic simulation. Hydrology and Earth System Sciences, 19, 361-377, DOI:10.5194/hess-19-361-2015.

Ogata T., Ueda H., Inoue T., et al. (2014). Projected Future Changes in the Asian Monsoon: A Comparison of CMIP3 and CMIP5 Model Results. Journal of the Meteorological Society of Japan, 92, 207-225, DOI:10.2151/jmsj.2014-302.

Ongoma V., Chen H., Gao C. (2019). Evaluation of CMIP5 twentieth century rainfall simulation over the equatorial East Africa. Theoretical and Applied Climatology, 135, 893-910, DOI:10.1007/s00704-018-2392-x.

Perkins S.E., Pitman A.J., Holbrook N.J., and McAneney J. (2007). Evaluation of the AR4 Climate Models' Simulated Daily Maximum Temperature, Minimum Temperature, and Precipitation over Australia Using Probability Density Functions. Journal of Climate, 20, 4356-4376, DOI:10.1175/JCLI4253.1.

Rao X., Lu X., and Dong W. (2019). Evaluation and projection of extreme precipitation over northern China in CMIP5 models. Atmosphere, 10, 691, DOI:10.3390/atmos10110691.

Reifen C. and Toumi R. (2009). Climate projections: Past performance no guarantee of future skill? Geophysical Research Letters, 36, DOI:10.1029/2009GL038082.

Ruan Y., Liu Z., Wang R., and Yao Z. (2019). Assessing the Performance of CMIP5 GCMs for Projection of Future Temperature Change over the Lower Mekong Basin. Atmosphere, 10, 93, DOI:10.3390/atmos10020093.

Saha A., Ghosh S., Sahana A.S., and Rao E.P. (2014). Failure of CMIP5 climate models in simulating post-1950 decreasing trend of Indian monsoon. Geophysical Research Letters, 41, 7323-7330, DOI:10.1002/2014GL061573.

Sharmila S., Joseph S., Sahai A., et al. (2015). Future projection of Indian summer monsoon variability under climate change scenario: An assessment from CMIP5 climate models. Global and Planetary Change, 124, 62-78, DOI:10.1016/j.gloplacha.2014.11.004.

Sillmann J., Kharin V.V., Zwiers F.W., et al. (2013). Climate extremes indices in the CMIP5 multimodel ensemble: Part 2. Future climate projections. Journal of Geophysical Research-Atmospheres, 118, 2473-2493, DOI:10.1002/JGRD.50188.

Sun Q., Miao C., and Duan Q. (2015). Comparative analysis of CMIP3 and CMIP5 global climate models for simulating the daily mean, maximum, and minimum temperatures and daily precipitation over China. Journal of Geophysical Research-Atmospheres, 120, 4806-4824, DOI:10.1002/2014JD022994.

Walsh J.E., Chapman W.L., Romanovsky V., et al. (2008). Global Climate Model Performance over Alaska and Greenland. Journal of Climate, 21, 6156-6174, DOI:10.1175/2008JCLI2163.1.

Wang B., Liu D.L., Macadam I., et al. (2016). Multi-model ensemble projections of future extreme temperature change using a statistical downscaling method in south eastern Australia. Climatic Change, 138, 85-98, DOI:10.1007/s10584-016-1726-x.

Yang X., Yu X., Wang Y., et al. (2020). The Optimal Multimodel Ensemble of Bias-Corrected CMIP5 Climate Models over China. Journal of Hydrometeorology, 21, 845-863, DOI:10.1175/JHM-D-19-0141.1.

You Q., Jiang Z., Wang D., et al. (2018). Simulation of temperature extremes in the Tibetan Plateau from CMIP5 models and comparison with gridded observations. Climate Dynamics, 51, 355-369, DOI:10.1007/s00382-017-3928-y.

Zhou B., Wen Q.H., Xu Y., et al (2014). Projected Changes in Temperature and Precipitation Extremes in China by the CMIP5 Multimodel Ensembles. Journal of Climate, 27, 6591-6611, DOI:10.1175/JCLI-D-13-00761.1.

RESEARCH PAPER

GEOMORPHOLOGY AND SEDIMENTOLOGY OF EPHEMERAL STREAMS OF CALABRIA, SOUTHERN ITALY

Paolo Billi[1,2*] Antonio Biamonte[3]

[1]International Platform for Dryland Research and Education, Tottori University, 1390 Hamasaka, Tottori, 680-0001 Japan

[2]Dipartimento di Fisica e Scienze della Terra, Università di Ferrara, Via. G. Saragat, 1, Ferrara, 44122, Italy

[3]Politiche Ambientali, Energia e Cambiamenti Climatici, Regione Toscana, Via di Novoli, 26, Firenze, 50127, Italy

***Corresponding author:** bli@unife.it

Received: October 31th 2024 / Accepted: February 28th 2025 / Published: June 30th 2025

https://doi.org/10.24057/2071-9388-2025-3704

ABSTRACT. In southern Italy, especially in Calabria, rivers are dry for most of the time, but intense rainfalls may turn them into roaring monsters, causing devastating floods. These rivers, locally known as *"fiumaras"*, are poorly studied though they play an important role in landscape shaping and pose serious threats to the local infrastructures and urban settlements. Basic catchment and channel geomorphic data of several rivers were collected from the literature and in the field. A comparison is made with river catchments of similar size in more humid environments to demonstrate that local physiography, watershed geomorphology, and channel characteristics may exacerbate the risk of flooding. The sedimentology of the study rivers is investigated to verify if fiumaras have specific bedform associations or stratigraphic arrangements that can be used to interpret ancient sandstones and conglomerates as deposited in an active tectonic setting under the Mediterranean climate. Four representative rivers were selected for investigation on the alluvium architecture, and field campaigns were carried out to collect bed material samples and to identify the occurrence of coarse and fine-grained bedforms. The fiumaras have a braided morphology, but the longitudinal bars do not have a fine tail and result from dissection processes rather than large bedform deposition and downstream migration. The braid bar characteristics, the poor internal organization of the tabular beds, and the occurrence of the largest boulders on top of the bars indicate the prevalence of high deposition rates from hyperconcentrated flows.

KEYWORDS: ephemeral stream, fiumara, braided river, alluvium, hyperconcentrated flow, Calabria

CITATION: Billi P., Biamonte A. (2025). Geomorphology And Sedimentology Of Ephemeral Streams Of Calabria, Southern Italy. Geography, Environment, Sustainability, 2 (18), 150-163
https://doi.org/10.24057/2071-9388-2025-3704

ACKNOWLEDGEMENTS: The study did not receive any financial support.

Conflict of interests: The authors reported no potential conflict of interests.

INTRODUCTION

In Calabria, southern Italy, ephemeral or intermittent rivers are common (Sabato and Tropeano 2004). These rivers are dry for most of the time, and water flow is resumed only in response to high-intensity rainfalls. Their channels are short, coarse-grained, and steep, even in the most downstream reaches. In recent decades, several flash floods devastated infrastructures and urban settlements with negative repercussions on the economic development of the region. This kind of river system is known by the local name of *"fiumara"*, a word used all over Italy to indicate an ephemeral river with high and unpredictable discharge variability that changes from a dry bed into a roaring monster in minutes. In this paper, we decided to use the local name in its original form for clarity and cultural accuracy.

Fiumaras play an important role in shaping the landscape of the Calabria region. With their steep channels and very energetic flood flows, commonly associated with the mobilization of large quantities of coarse-grained bedload material, these ephemeral/intermittent rivers have strong impacts on several human activities, including agriculture, pastoralism, and the tourism industry, to name the most important. However, the hydrological, hydraulic, and geomorphological characteristics of these rivers have been the subject of only a handful of studies. Most previous research investigated the flash flood hazard associated with the fiumaras in Calabria using hydrological models (Ferrari et al. 1988; Versace et al. 1989 and 2017; Sabato and Tropeano 2004). Though fiumaras are ubiquitous in Calabria, flow data is scarce since only a few larger rivers are monitored in this region. Usually, the existing flow gauges are located in the mountain reaches and cover only a small portion of the catchment. Moreover, the available time series are short and discontinuous and do not allow for investigating the fiumaras' flood hydrographs, hydrology, and hydraulic characteristics. Other studies were focused on hydraulic issues such as the dominant discharge (Ferro and Porto 2012), the shear stress critical conditions for streambed particle entrainment (Porto and Gessler, 1990; Ferro and Porto 2011) or the sediment yield (Foti et al. 2022) using the empirical model of Gavrilovic (1972).

More of the same paucity of studies was encountered looking for investigations on the fluvial geomorphology and processes of the Calabrian fiumaras, with just a few exceptions of publications reporting about very basic geomorphic data (Billi and Biamonte, 1995; Versace et al. 2017). The fiumaras are a peculiar kind of ephemeral stream and, like their counterparts in more arid lands, lay down a thick alluvium of coarse-grained material whose sedimentological characteristics are poorly known. The understanding of the fiumaras depositional processes and features can contribute to recognizing old conglomerate and sandstone as deposited in arid and semi-arid environments and to assess their potential as reservoirs of hydrocarbon and ore deposits. While the sedimentology and bedforms of ephemeral, sand bed rivers are rather well documented (Williams 1971; Picard and High 1973; Shepherd 1987; Abdullatif 1989), much poorer information is available for gravel-bed, ephemeral streams (Dunkerley 1992; Hassan 2005; Laronne and Shlomi 2007; Billi 2008; Billi 2016). The fiumaras, though they may share some sedimentological characteristics with dryland rivers in other parts of the world, typically form under specific geotectonic and climate conditions. Their hydrology and morphological processes make them a peculiar kind of ephemeral stream within the Mediterranean area that, unfortunately, received very little attention from scientists (Sabato 1989), notwithstanding their relevance in landscape shaping.

Given the unavailability of flow data time series and aiming at reducing the gap of information on the geomorphology and sedimentology of the Calabrian fiumaras, this study was designed to pursue the following main goals:

1) to investigate the catchment morphology of selected fiumaras in Calabria to verify if their peculiar characteristics may contribute to exacerbating the hazard of devastating flash floods, often accompanied by high sediment supply and depositional rates in the coastal plain belt;

2) to investigate the main sedimentological characteristics of the Calabria fiumaras to verify, also through the comparison with ephemeral streams in different arid and semiarid environments, if their depositional structures, bedding arrangements, and bedforms are specific to this kind of river and if they can be used as diagnostic elements to interpret the depositional environment of ancient sandstone and conglomerate laid down by rivers like the fiumaras, found in an active tectonic setting and Mediterranean climate.

STUDY AREA

Calabria is a long and narrow, arch-shaped southwestern sub-peninsula of southern Italy (Fig. 1). It has a mountainous spine originated by thrust fault tectonics that emplaced the Calabrian orogen, consisting of basement rocks (granitoids, gneisses and shists), to become part of the southern Apennines. The Calabria arch is a fragment of the Alpine chain that, in the Miocene, was detached from the Sardinia-Corsica block and migrated to the present position (Cirrincione et al., 2015). Pleistocene terraced marine deposits at 1300 m asl witness a fast uplifting of the region through extensional tectonics. The highest mountain peaks range from 1100 to 2200 m asl. The result of such complex and intense geodynamics is a mountain range, taking up most of the region, interrupted by tectonic depressions and surrounded by narrow coastal plains; though, in some places, the mountain slopes may almost reach the sea. In such a physiography, most of the rivers are short and steep. Most rivers are ephemeral, with a wide range of discharge between the dry bed condition in the summer and high devastating flood flows in autumn or winter, except for a few (three or four) larger rivers that have a sustained base flow year-round.

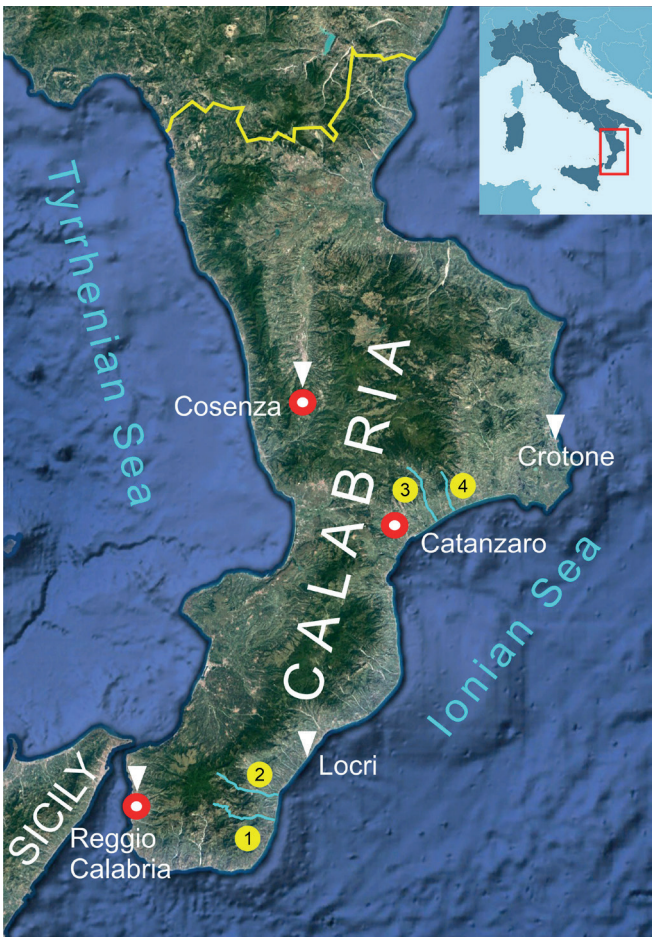

Fig. 1. Location map of the Calabria Region. The white triangles indicate the meteorological stations used in this study to characterize the climate of the region. The circled numbers indicate the four rivers investigated in the field: 1 = La Verde R.; 2= Bonamico R.; 3 = Simeri R.; 4 = Scilotraco R

The region is subjected to a typical Mediterranean climate (*Csa* according to the Koppen climate classification) characterized by high temperatures in the summer and the lowest monthly temperature less than 18°C but higher than -3°C (Fig. 2). Precipitation is mainly concentrated in the autumn and winter months, though some small differences are observed between the Tyrrhenian and the Ionian sides (Fig. 2). Annual precipitation and the number of rainy days range from 500 to over 2000 mm and from 60 to more than 120 days, respectively, on the eastern coast to the most elevated areas around the highest mountain peaks. The high mountain areas record the highest daily rainfall intensities of 175-200 mm (with peaks of 360–630 mm, Versace et al., 2017), whereas the southwestern coast records the lower values. Average rainfall intensities in three and one hour vary from 30-45 mm in the central northern portion to 65-75 mm in the southern mountain peaks and from 20 to 50 mm, respectively. Such high-intensity values are expected to be exceeded during extreme events (92 and 160 mm in three and one hours, respectively) and capable of generating high, devastating floods (6-20 $m^3s^{-1}km^{-2}$ – Versace et al, 2017), during which peak flow may be as much as three to four orders of magnitude higher than mean annual discharge (in semi-perennial rivers) (Fig. 2) These climate

data are based on ECMWF (European Centre for Medium-Range Weather Forecasts) data, collected between 1991 and 2021.

The monthly flow variation of a couple of fiumaras, taken as an example, is reported in Fig. 3. The flow gauges considered are in the headwaters of the respective catchments and take up only a very small portion of the watershed. The pattern of monthly mean discharge follows the typical Mediterranean distribution of monthly rainfall, with low flows in the summer and higher discharges in the autumn and winter months. In the Alli river, the recharge of the autumn rain is not enough to resume an appreciable discharge to sustain the freshwater biota, which is reached only after the December and January rains (see Fig. 3). The flow data used in Fig. 3 were obtained from the Annali Idrologici of the National Hydrological Service (Servizio Idrografico, 1916-1998) and cover the intervals 1925-1930, 1932-1942 and 1947-1979 for the Alli River and the interval 1964-1978 for the Trionto River. These data are not updated or uniform, but they can show the general river flow pattern typical of the Mediterranean environment.

DATA SOURCES AND METHODS

This study utilized two datasets. The first one, identified as Dataset 1, is based on the data of Biamonte (1993) and Billi and Biamonte (1995). The second dataset, Dataset 2, is based on data published by the University of Calabria and the Calabria Region Civil Protection (Versace et al., 2017). The data was split into two subsets because the data is not homogeneous for the rivers considered, their number, and the parameters measured (Table 1, 2). Dataset 1 was expanded by including the streambed gradient of the terminal reaches, that is, the downstream portion of the channels crossing the coastal plain from the exit of the mountainous portion of the catchment to the outlet into the Ionian or the Tyrrhenian seas. The streambed gradient of the terminal reaches was obtained from measurement by the ruler tool on Google Earth aerial images. More detailed information about this methodology can be found in Billi et al. (2018).

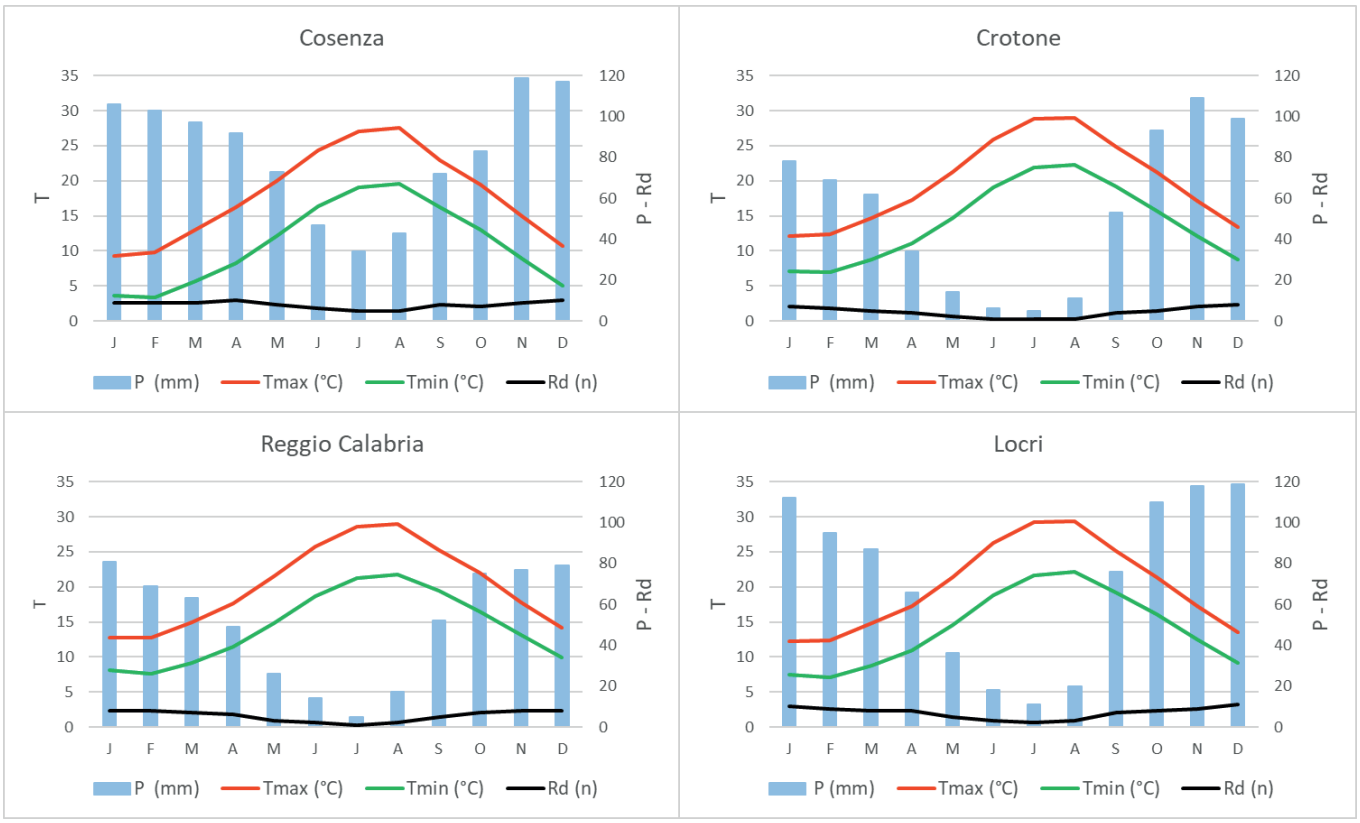

Fig. 2. Climatic diagrams of four meteorological stations covering the area where the majority of the fiumaras considered in this study are located. Rd stands for the number of rainy days

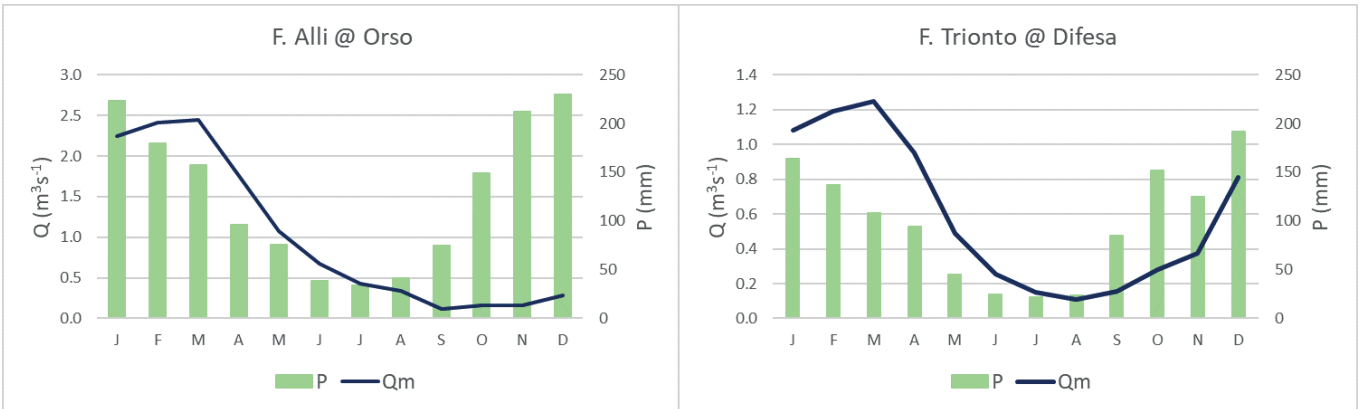

Fig. 3. Monthly variation of rainfall (P) and mean discharge (Qm) of the Alli and Trionto rivers. These rivers flow a few kilometers north and south of Catanzaro, respectively. The Alli River flow gauge at Orso undertakes a watershed area of 46 km², whereas the flow gauges of the Trionto River at Difesa undertakes a catchment area of only 31.7 km²

Dataset 1 includes 18 rivers, and the measured parameters were (Table 1): catchment area (*A*); river length (*L*); average slope of the catchment (*S*); river gradient (*J*); maximum elevation in the catchment (H_{max}); maximum width of the river bed (W_{max}); average valley bottom width (W_v); drainage density (*Dd*) (ratio of the total length of the drainage system to the catchment area); length of the terminal reach (*Ltr*); streambed gradient of the terminal reach (*Jtr*); catchment shape factor (*Sf*) (the catchment area divided by the catchment length squared (Horton, 1932) and relief ratio (*Rr)* (the highest minus the lowest elevation divided by the catchment length) (Schumm, 1956). Dataset 2 includes 37 rivers, but only data on catchment area, river length, catchment average slope gradient, river gradient, and elevation of the highest peak are reported. Tables 1 and 2 also report the mean, maximum, and minimum values and the variation coefficient (*CV*). All this data, except for the gradient of the terminal reaches of Dataset 1, were obtained from measurements on 1:10,000 topographical maps, integrated with observations from 1:33,000 aerial photographs. The shape factor was calculated as the ratio of the maximum basin length squared to the basin area (Horton, 1932). All the data were measured manually without the aid of any modern digital tool.

Field studies were conducted on four rivers with coarse sediments (Scilotraco, Simeri, Bonamico, and La Verde) to examine the alluvium stratigraphy , the occurrence of bedforms , and the grain size of the the riverbed. These rivers drain the eastern side of the Calabrian Apennine and flow into the Ionian Sea. Scilotraco and Simeri flow a few kilometers northeast of Catanzaro, whereas Bonamico and La Verde are located a few kilometers south of Locri (Fig. 1). In the Simeri and Scilotraco bed material samples were collected at 16 and 18 sites, respectively, for a total of 34 samples of surface material and 34 samples of subsurface sediment. The sampling sites are rather uniformly distributed along the main stem from the mouth into the Ionian Sea to about 7 and 8 km upstream in the Simeri and Scilotraco, respectively. The bed material samples were taken from the surface of a longitudinal bar located approximately in the middle of the streambed. Bed material samples were obtained from the Scilotraco and Simeri beds. The surface material was sampled by the transect line method (Leopold, 1970), including a minimum of 120 particles in each sample, whereas the volumetric method (Church et al., 1987) was used for the subsurface material. The size of each subsurface sample was such that the largest particle weight accounts for 10% of the total sample weight (Church et al., 1987). The volumetric samples were mechanically sieved by a mechanical shaker with sieves arranged on a ½ phi scale.

Table 1. Dataset 1

River	A, km^2	L, km	S, %	J, m/m	H_{max}, m asl	W_{max}, km	W_v, km	Dd, km/km^2	Ltr, km	Jtr, m/m	Sf	Rr
Abatemarco	64	21.5	41	0.0921	1980	0.21	2.60	5.82	10.15	0.0233	0.24	0.12
Alli	129	47.1	27	0.0340	1600	0.41	2.10	7.76	16.70	0.0090	0.10	0.04
Amendolea	150	41.2	36	0.0442	1821	0.95	2.75	7.17	19.45	0.0194	0.22	0.07
Arso	31	15.8	86	0.0506	800	0.20	3.60	6.81	7.40	0.0117	0.24	0.07
Avena	31	12.5	22	0.0760	950	0.42	0.68	6.04	10.20	0.0288	0.13	0.06
Favazzina	20	16.02	33	0.0971	1556	0.10	1.95	5.64	3.50	0.0626	0.11	0.01
Ferro	121	20.5	18	0.0561	1150	0.62	1.25	4.53	18.00	0.0228	0.32	0.06
La Verde	117	34.9	41	0.0560	1953	0.95	3.50	8.10	13.45	0.0117	0.19	0.08
Nicà	174	41.25	28	0.0279	1150	0.85	3.40	5.32	14.74	0.0063	0.32	0.05
Oliva	43	27.3	65	0.0480	1310	0.28	2.80	5.31	10.20	0.0217	0.16	0.08
Saraceno	86	19.5	89	0.0877	1710	0.40	4.10	5.42	18.80	0.0301	0.24	0.09
Savuto	405	72.4	55	0.0232	1680	0.35	8.15	3.31	27.30	0.0081	0.22	0.04
Scilotraco	18	13.9	73	0.0590	820	0.17	1.60	6.23	9.60	0.0090	0.11	0.05
Simeri	131	45.2	31	0.0365	1650	0.16	2.30	6.64	17.90	0.0098	0.12	0.07
Stilaro	95	28.1	33	0.0506	1422	0.35	1.95	5.93	16.55	0.0148	0.19	0.07
Triolo	18	10.2	7	0.0980	1000	0.05	0.60	5.78	2.15	0.0626	0.28	0.13
Trionto	279	40.5	18		1600	1.40	3.80	5.84	23.80	0.0163	0.30	0.05
Uria	60	27.8	53		1250	0.35	2.35	6.98	13.60	0.0103	0.16	0.06
Mean	110	30	42		1411	0.46	2.75	6.04	14.08	0.0210	0.20	0.07
CV	0.91	0.54	0.6		0.26	0.79	0.61	0.19	0.46	0.7962	0.36	0.41
Max	405	72	89		1980	1.40	8.15	8.10	27.30	0.0626	0.32	0.13
Min	18	10	7		800	0.05	0.60	3.31	2.15	0.0063	0.10	0.01

Table 1. Dataset 2

River	A, km_2	L, km	S, %	J, m/m	H_{max}, m asl
Acrifa	17.32	10.77	25	0.0604	651
Allaro	130.18	36.91	31	0.0385	1422
Amusa	39.40	20.17	37	0.0615	1240
Annunziata	22.52	20.69	35	0.0673	1393
Armo	15.05	11.16	37	0.0869	970
Bonamico	136.42	30.16	39	0.0648	1954
Bruzzano	52.62	17.85	31	0.0662	1181
Calopinace	53.46	23.89	33	0.0656	1566
Careri	92.08	22.60	28	0.0691	1561
Catona	68.48	27.13	34	0.0676	1834
Condoianni	66.53	19.81	30	0.0533	1055
Fiumetorbido	7.76	8.80	42	0.0869	765
Gallico	59.63	25.22	39	0.0706	1780
Gerace	38.98	18.03	32	0.0549	989
Lume	8.16	8.15	31	0.0881	718
Macellari	8.30	8.20	29	0.1009	827
Melito	80.01	29.96	37	0.0560	1679
Menga	7.36	7.98	18	0.0727	580
Molaro II	7.14	8.74	32	0.0965	843
Molaro II	7.29	6.39	34	0.1185	757
Novito	55.86	19.55	31	0.0496	970
Oliveto	13.64	12.38	26	0.0728	901
Palizzi	36.46	18.81	46	0.0673	1265
Portigliola	35.02	19.05	34	0.0544	1036
Precarito	55.71	24.11	32	0.0573	1381
S. Agata	52.33	28.76	37	0.0586	1685
S. Elia	29.95	16.00	36	0.0635	1016
S. Giovanni	5.96	7.34	28	0.1095	804
S. Pasquale	25.88	16.26	39	0.0801	1303
S. Vincenzo	8.04	9.81	35	0.0904	887
Scaccioti	7.31	7.78	38	0.0972	756
Sfalasà	24.03	13.18	27	0.0893	1177
Sideroni	10.77	9.27	31	0.0836	775
Spartivento	16.39	12.89	39	0.0702	905
Torbido	160.52	26.20	35	0.0471	1233
Valanidi	29.07	20.61	33	0.0577	1190
Vena		9.44	32	0.1071	1011
Mean		17.14	36	0.0675	1137
CV		0.46	0.4	0.32	0.32
Max		36.91	89	0.1185	1954
Min		6.39	7	0.0232	580

RESULTS

Geomorphology

The ephemeral streams of Calabria have peculiar hydrological and geomorphological characteristics. These rivers, in fact, are dry for most of the time, and water flow is resumed only in response to very intense rainfalls, whose extreme peaks may reach and occasionally exceed 500 mm in one day and 150 mm in one hour. In their terminal reaches, the fiumaras have a braided morphology (Fig. 4) and are very wide and choked with coarse-grained (boulder to cobbles) sediment. The study rivers have a small catchment area and are rather short. The catchment area and channel length of most of the study rivers vary between 10 and 100 km^2 (range 6 and 405 km^2, mean 63 km^2) and between 10 and 30 km (range 6.4-72 km, mean 21 km) respectively (Fig. 5).

The recent uplifting of the Calabria region resulted in many short rivers with a narrow and elongated catchment with rather steep slopes (Versace et al., 2017) (see Fig. 1) (see also the example of the Simeri River reported in Fig. 6 - Billi and Biamonte, 1995). The mean shape factor is 0.12 (range 0.06-0.23), which confirms the study that river catchments tend to a marked elongated and rectangular shape. The average relief ratio of the study fiumaras is high (0.07, range 0.01-0.13) (Table 1) and implies relatively high relief and steep slopes underlain by resistant rocks (Thomas et al., 2010). More than 57% of the study catchments have an average slope gradient in the 30-40% range (Fig. 7). It follows that the main channels also have high gradients (mean 0.0677, range 0.0232-0.1185) that are reflected by the steep gradient of the terminal reaches. The latter is obviously gentler, accounting for an average of one-third of the entire river gradient. Nevertheless, it is still quite steep, particularly for river reaches located just a few kilometers upstream of their outlet into the sea. The mean gradient of the terminal reaches is 0.021 and varies within the 0.0063-0.0626 range. For similar catchment areas, the terminal reaches of the Calabrian fiumaras are steeper than forested mountain rivers in the humid environment of northwestern USA mentioned by Hassan et al. (2005) (Fig. 8).

The steep gradient of the terminal reaches also accounts for their braided morphology (Fig. 4) and for the devastating energy of the flow during high floods. The high gradient of the terminal reaches results from the combination of recent uplifting and the high sediment supply propelled by the semiarid Mediterranean climate and the sparse vegetation on the catchment slopes. Dense forests cover only the highest parts of the mountain ranges. The terminal reaches are also rather short, 3.5-27.3 km, and high flood waves can quickly propagate through their lengths posing a serious threat to the coastal settlements.

The drainage density of Dataset 1 ranges between 3.3 and 8.1, mean value of 6.04 km/km^2. Drainage density is influenced by precipitation, rock permeability, slope gradient, and the scale of the topographic map used to measure it (1:10,000 in this study). Due to the interactions of these factors, drainage density is a highly variable parameter, and any comparison between data sets from different studies is also complicated by the use of maps at different scales. Nevertheless, according to the

Fig. 4. The Bonamico River is a typical example of a fiumara. It has a wide streambed and a distinctive braided channel morphology

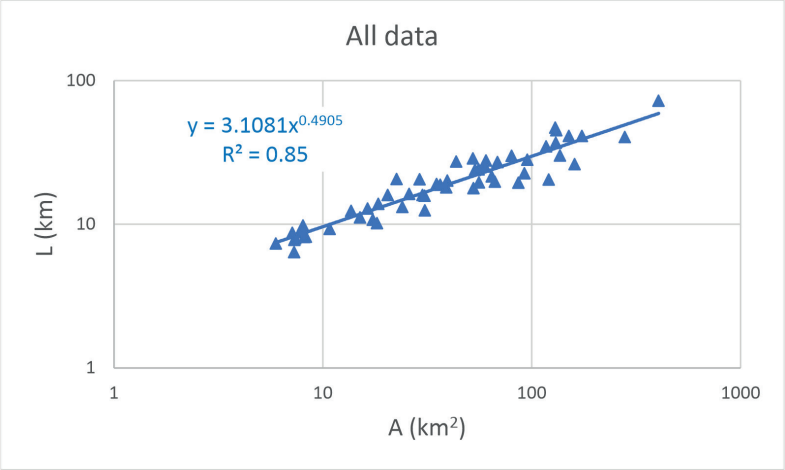

Fig. 5. Correlation between catchment area and river length

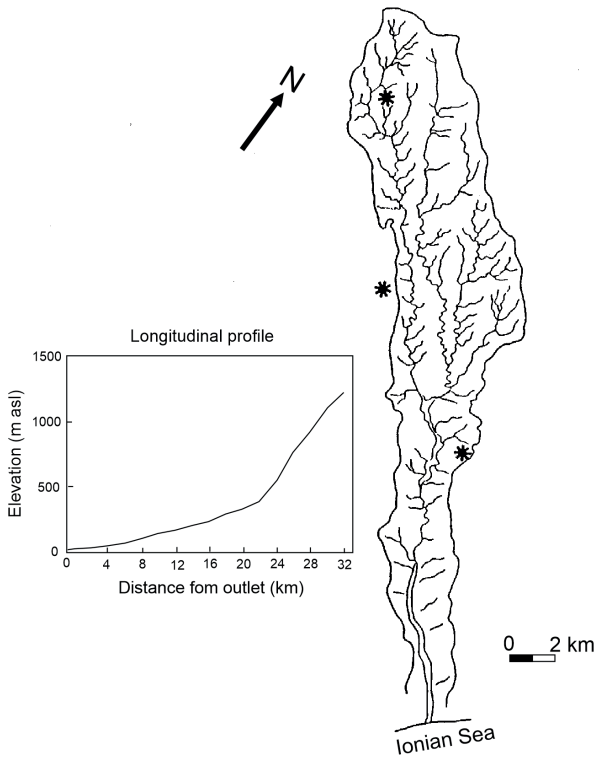

Fig. 6. Most of the Calabria rivers have a narrow and elongated catchment. An example is provided by the Simeri River. Rain gauges are indicated by the star symbols

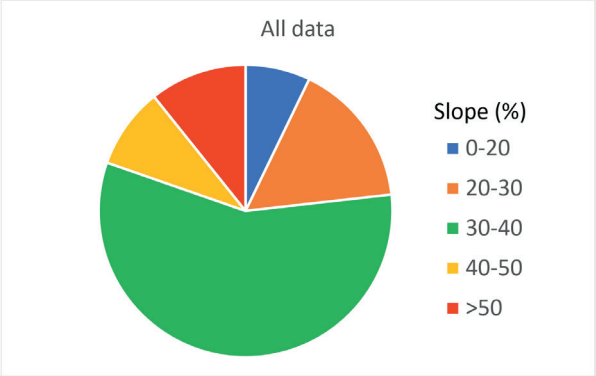

Fig. 7. Pie diagram of the average catchment slope variability. More than half of the catchment's average slope is in the 30-40% range

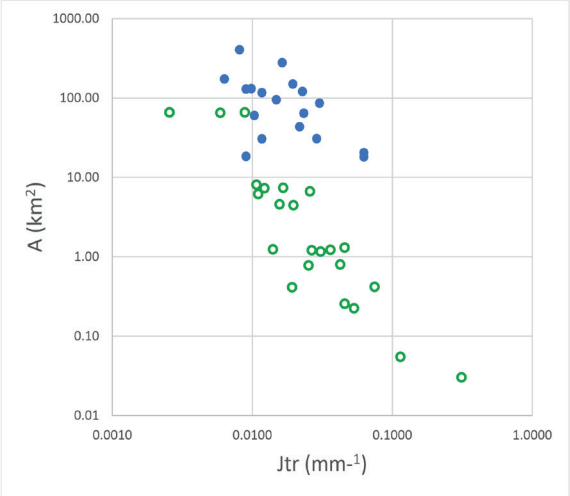

Fig. 8. Comparison of the fiumara data (solid dots) with the data of mountain rivers of the northwestern USA forested environment (open circles) (Hassan et al. 2005). For comparable catchment areas, the gradient of the fiumaras terminal reaches (Jtr) is substantially higher

classification of Ravi Shankar and Mohan (2006), a drainage density of 3.5 is considered a high value. For all but one of the Calabria rivers, drainage density is higher than 3.5 and for 16 out of 18 is higher than 5. This data indicates that the study rivers have a rather high drainage density, which, in general, implies a fast transfer of runoff from slopes to the main river stem, high river flow velocity, less infiltration, a short base flow period, and high unit peak discharges (Carlston, 1963). Such hazardous conditions result in higher floods, whose effects are exacerbated by the large proportion of the valley bottom taken up by the fiumaras. The ratio of the maximum streambed width to the average valley bottom width ranges between 0.01 and 0.50 (average 0.20). Infrastructures and urban areas are concentrated in the coastal belt, crossed by fiumaras spaced only a few kilometers apart, and, in the past decades, have been subjected to several destructive floods (Versace et al, 2017).

Sedimentology

Field investigations on the sedimentology of fiumaras were carried out in the terminal reaches of four rivers: Simeri, Scilotraco, La Verde, and Bonamico. The streambed of Scilotraco and Simeri was also sampled to obtain the grain-size distribution of surface and subsurface material (Fig. 9). In Fig. 9, we used the phi unit (phi = - $\log_2$D, in which D is the particle diameter) since this is the classical unit used by sedimentologists and geomorphologists for investigating streambed armoring. The ratio between surface and subsurface median diameter (D_{50}) is also known as the armoring index and expresses the degree of surface texture coarsening. According to Parker and Kingeman (1982), a riverbed is considered armored when the surface-to-subsurface ratio is 2. The Scilotraco and the Simer show no or poorly developed bed armoring since their average armoring index is 1.7 and 0.9, respectively. Contrary to expectations, the proportion of sand does not influence the formation of an armored bed. In the Simer, the average proportion of surface and subsurface sand is almost equivalent (33.6 and 29.7%, respectively), whereas in the Scilotraco, the average proportion of sand in the subsurface is double that of the surface material (49.8 and 24.4%, respectively).

The stratigraphy of the study fiumaras was investigated by field observations of exposed cutbanks and dissected bars. The deposits of these ephemeral streams are characterized by tabular units consisting of horizontal, crudely bedded, imbricated coarse-grained gravel (Fig. 10) with occasional thin (10-50 cm), massive or horizontal laminated sand lenses (Fig. 11). The gravel layers are commonly reversely graded with the largest boulders resting, especially on

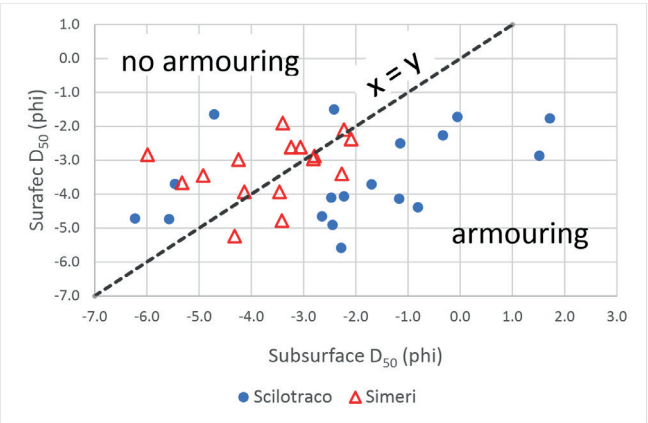

Fig. 9. Distribution of the surface to subsurface D_{50} ratio in the Simeri and Scilotraco rivers

top of the highest bars (Fig. 10). The study rivers' gravels are poorly organized, poorly sorted, clast-supported, and, subordinately, open-work or infilled with fine grains and locally matrix-supported (Fig. 12). Imbrication is not ubiquitous. In places, the gravel particles within the tabular beds are chaotically arranged, and imbrication is absent (Fig. 11). The tabular beds are 20 to 80 cm thick, and their erosive base is indistinct. The structureless, chaotic gravels reflect deposition under high flow energy and high sediment supply conditions, whereas the open-work gravels are deposited by quickly slowing flow and winnowing of fines (Maizels, 1993; Carling, 2017), leading to an armor layer.

The bar top is typically coarser than surface material of the channel bed (Fig. 13). In the Scilotraco, the average D_{50} is 11.3 and 1.1 mm, respectively, whereas in the Simeri it is 9.4 and 4.2 mm, respectively. The bar top is on average 17 and three times coarser than the channel bed in the Scilotraco and Simeri, respectively. The concentration of the coarser boulders on the bar top (Fig. 13) confirms

Fig. 10. Horizontal, tabular stratification. The beds are reversely graded, and the erosive bottom of the top layer (yellow dotted line) is barely visible. The upper layer is polymodal, clast-supported, and poorly imbricated. The upper part of the sediment below the dotted yellow line includes an open framework and clast-supported gravel, which is part of a preserved armor layer

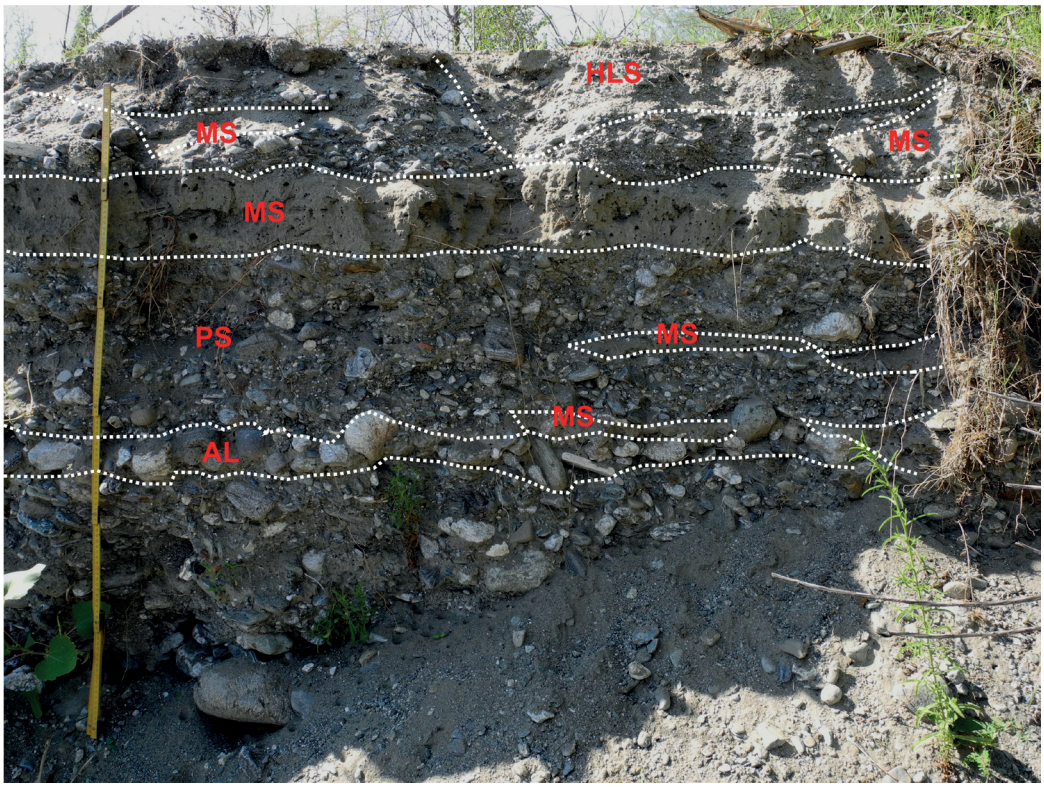

Fig. 11. Occasional occurrence of thin, spatially limited sand interbeds. MS = massive sand; HLS = horizontally laminated sand; AL = armored layer; PS = poorly sorted bed, no imbrication. In the PS, particle imbrication is not evident, indicating en masse bedload transport by hyperconcentrated flow

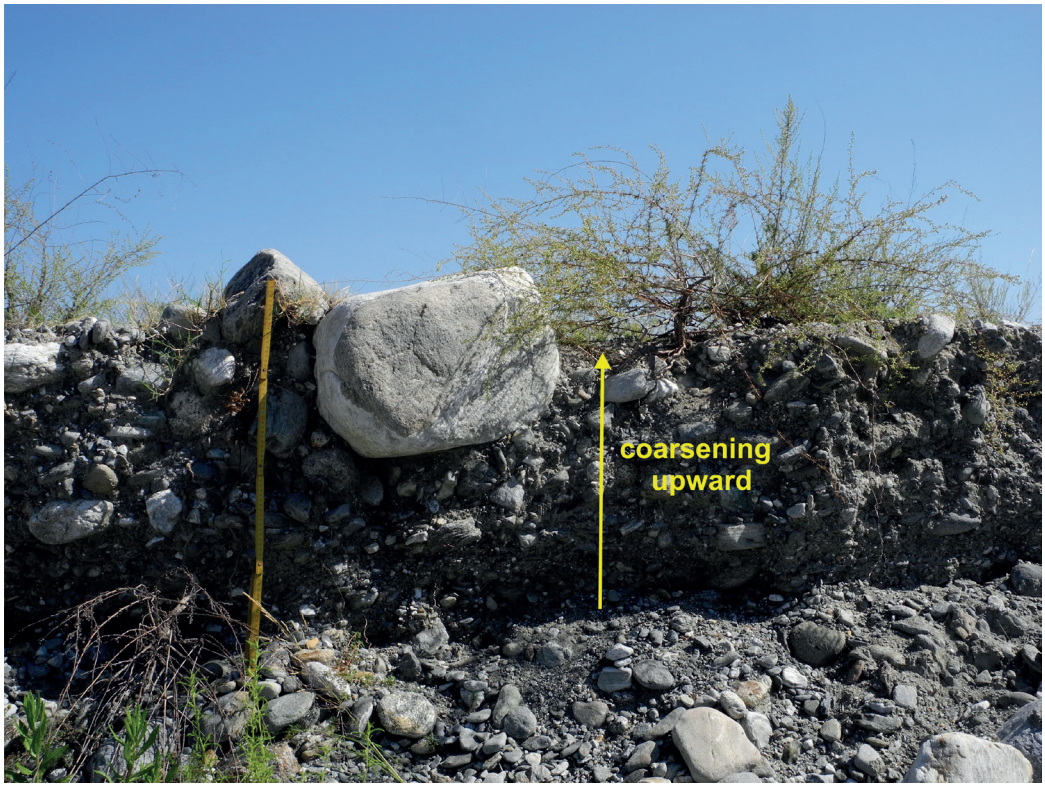

Fig. 12. Bar top layer. Coarsening upward is evident. The size of the boulder on top is close to D_{100}

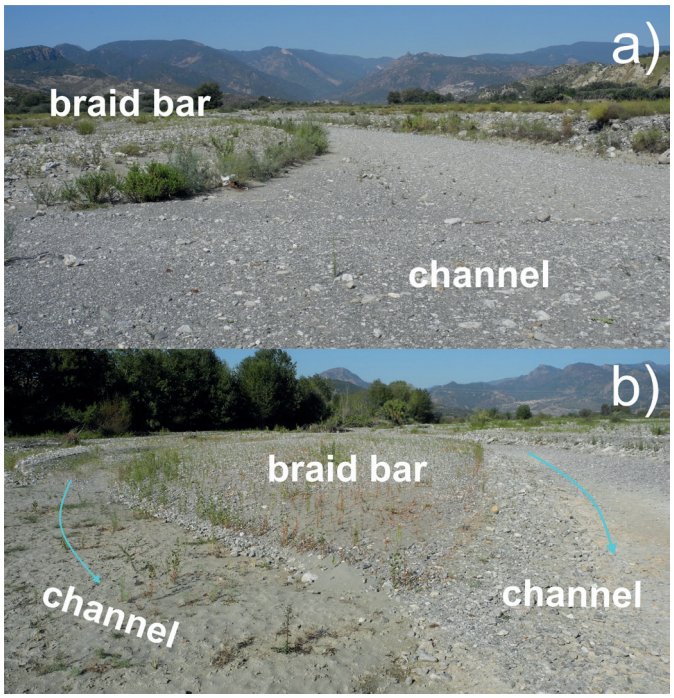

Fig. 13. Difference in surface grain size between channel and bar top: a) in the Bonamico River, the channel surface is filled with fine grains, whereas the bar top is covered with coarse boulders. Notice the vicinity of the basin headwaters to this channel section that is only a couple of kilometers from the sea; b) In the La Verde, bed material is finer. The secondary channels are locally covered with sand, whereas the main, larger channels are filled with fine grains and sand. Yet, notice the closeness of the headwaters

the large flow energy and shear stress experienced by the study rivers during floods. During low or receding flood flows, finer sediment is deposited in the channels, and, in some places, fine grains and/or sand drape the channel bottom (Fig. 13). The bars, by contrast, are not reworked. Their top surface material record the grain size of the bedload transported during high flows and winnowing of the finer particles as flow depth and velocity decrease. All these characteristics and the occurrence of the largest boulders (as much as 400 mm in mean diameter, equivalent to half of the active bedload layer) on top of the braid bars suggest en masse bedload transport and sedimentation from hyperconcentrated flows.

Riffle and pool sequences are not easily discernible for the common occurrence of channel filling with fine grains and coarse sand induced by backwater sedimentation at braided channel confluences (Fig. 13b, 14) and the crisscross overlapping of lobate gravel sheets, 20-40 cm thick. Very seldom, bars show a sand tail and downstream dipping foresets (Bluck, 1982), reflecting the lack of downstream accretionary fronts and the downstream migration of the longitudinal bars. Moreover, the gravel beds do not show

any downstream fining in grain size. This evidence suggests that, in the Calabria ephemeral streams, bars result from the dissection of thick bedload sheets/layers (Whiting et al., 1988) rather than from the downstream migration of the longitudinal bars (Billi, 2016).

Sandy bedforms predominantly consist of plane bed, and only massive and horizontally laminated sand is present in the natural cutbanks (Fig. 11). In places, sandy foresets are found at the confluence of a minor braid channel into a major, deeper channel (Fig. 14). This sand is deposited by the backwater effect when the larger channel is still conveying a substantial discharge while the minor channel is flushing out during the receding flood flows. No ripples and dunes were observed in the study fiumaras, whereas streaming lineation and cuspate ripples were occasionally found only in the Scilotraco river mouth.

Gravel bedforms include pebble clusters (Brayshaw, 1984; Billi, 1987; Billi, 1988) (Fig. 15a), crescent scours (Picard and High, 1973) (Fig. 15b), transverse ribs (Fig. 15c) and keystone interlockings (Fig. 15d). Transverse ribs occur as individual lines of larger particles across the braid channel, unlike the sequences seen in gravel-bed rivers of more humid climate (Billi et al., 2014). In the study of fiumaras, the keystone interlocking is a very common coarse-grained bedform and consists of a larger key boulder with smaller contact particles around it. It is not clear how this combination of coarse and finer particles forms (Zimmerman et al., 2010) but, as pebble clusters and transverse ribs, they play an important role in increasing the streambed roughness and flow resistance.

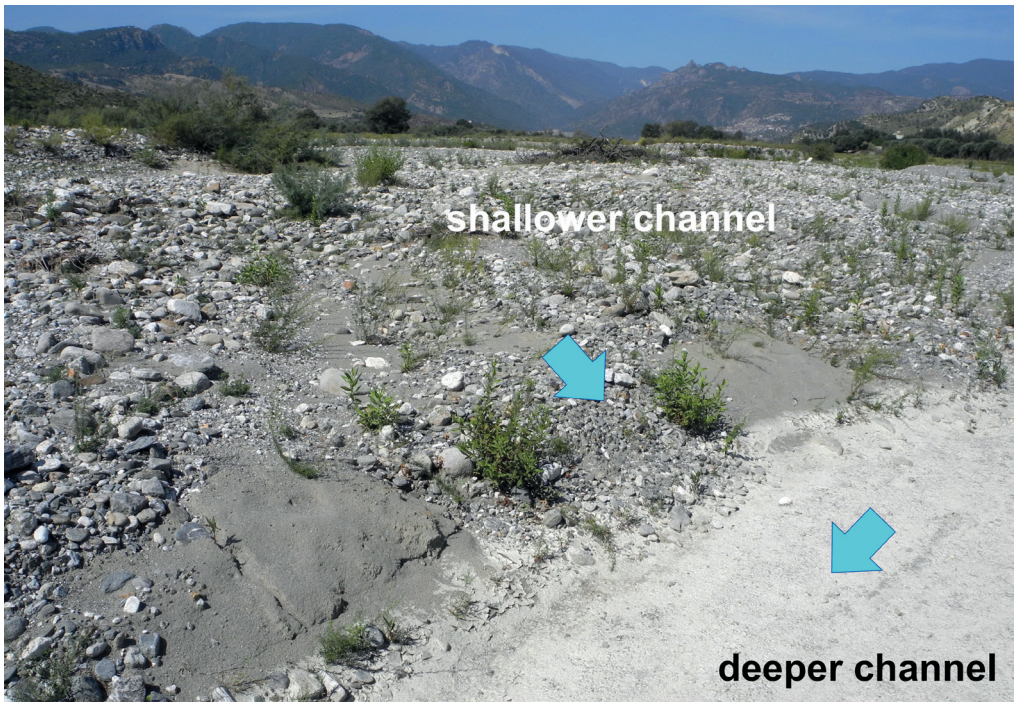

Fig. 14. Confluence of a shallow secondary channel into a deeper main braid channel downstream of a longitudinal bar. The backwater in the secondary channel favors the deposition of massive (or seldom, cross-laminated) sand

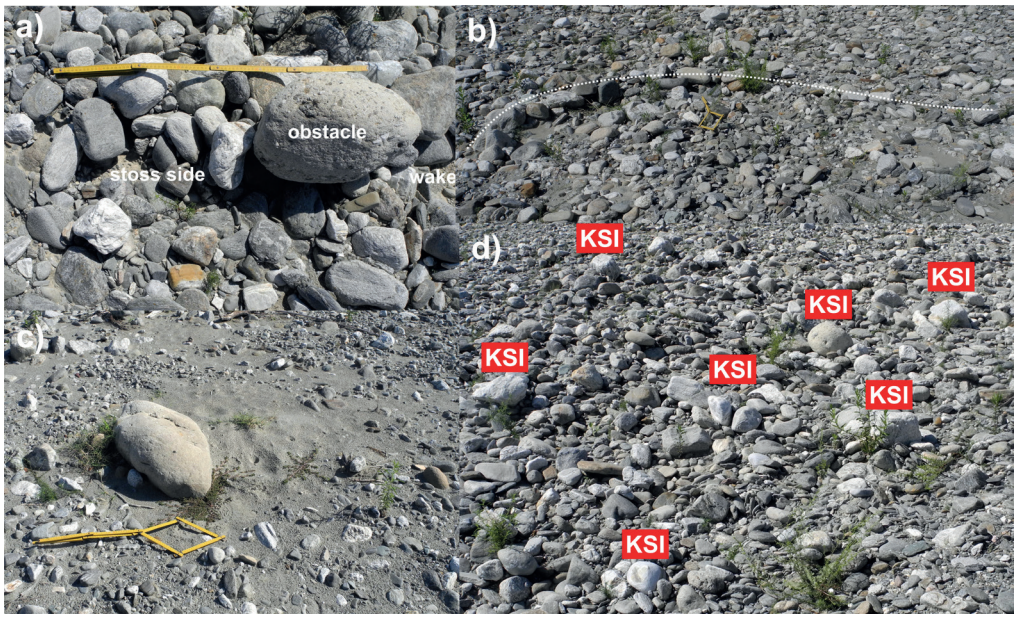

Fig. 15. Coarse-grained bedforms observed in the Bonamico and La Verde fiumaras: a) pebble cluster with the obstacle clast, the upstream stoss, and the downstream wake (Brayshaw, 1984). The stick ruler for the scale is 0.8 m. Flow from left to right; b) transverse rib highlighted by the dotted line across the channel. Flow is toward the reader; c) crescent scour. Notice the crescentic scour upstream of the boulder and the sand wake downstream. They are typically formed by shallow, receding flood flows. Flow to the right. The stake is about 0.8 m long; d) keystone interlocking. Several of these bedforms, consisting of a larger boulder surrounded by smaller particles are indicated by the notation KSI

DISCUSSION

In their study on the global distribution of rivers to terrestrial sinks, Nyberg et al. (2018) report the following relation between catchment area *(A)* and river length *(L)*: $L = 60.518A^{0.574}$

The study fiumaras also show a similar relation, though the coefficient (3.108) and the exponent (0.491) are somewhat different (Fig. 5). The difference in the coefficient can be explained by the larger data set of Nyberg et al. (2018) in which catchments with an area larger than 250 km^2 are by far the majority, whereas most of those considered in this study are less than 100 km^2 (only one is larger than 250 km^2 - Table 1). The exponent of the fiumaras is smaller, which indicates that, for comparable catchment areas, these rivers tend to be 30-40% shorter. The latter, in fact, exit the headwaters and cross the coastal plain with a short terminal reach, whose length is, on average, half of the total river length. Given the relief (high mountains close to the sea), the high drainage density, and the steepness of the terminal reaches, the transfer of water and large sediment loads (Sabato, 1989; Sabato and Tropeano, 2005) from the headwater to the coastal area during high flows is rather fast and capable of breaching the incoherent banks. Despite the small area of their headwaters, the geomorphic characteristics of the catchments and the lower channels lead the fiumaras to experience large, devastating floods.

The streambed gradient of the terminal reaches reported in Dataset 1 (Table 1) is typical of braided rivers (Rinaldi et al., 2016). However, some of them have steeper gradients, higher than 0.06, which in the literature are indicated as typical of single channels with step-pool or riffle pool morphology (Grant et al, 1990; Rosgen, 1996; Montgomery and Buffington, 1997). The ubiquitous occurrence of the braided morphology with river gradients typical of mountain streams can be accounted for by the lower, infrequent flow capability to entrain only a small portion of the incoming coarse-grained sediment load, resulting in high sedimentation rates. The downstream reaches of the fiumaras are, therefore, choked with sediment (Fig. 4) and reworked by lower-to-medium floods, mainly through channel incision (Fig. 14), providing them with the typical braided morphology.

The average drainage density of the study fiumaras is of the same order of magnitude as the rivers studied by Carlston (1963) in the northeastern United States. The latter, however, experiences a more humid climate with more uniform monthly precipitation compared to the Mediterranean climate of the Calabria region. Information about the drainage density of ephemeral and intermittent rivers is rather poor. Makhamreh et al. (2020) report rather low values of drainage density (1.49-1.85 km/km^2) for the Wadi Al-Shumar in northern Jordan. This river has a catchment with an elongated shape, similar to that of the fiumaras, but a lower maximum elevation of 1018 m asl. The annual precipitation of this Jordan River, 350-400 mm, is substantially lower than that of the Calabria rivers (especially in the headwaters). This can be considered as the main reason for the lower drainage density of Wadi Al-Shumar compared to the Calabrian fiumaras. Another factor leading to such a wide difference can be found in the smaller scale (1:25,000) of the topographic maps used by Makhamreh et al. (2020) whose detail about small streams is commonly inferior to a 1:10,000 map. Bedrock and soil characteristics are recognized by many scientists as key factors in determining drainage density, but, unfortunately, Makhamreh et al. (2020) do not report any information about them.

The streambed gradient of the terminal reaches of the study fiumaras is steeper than that of ephemeral streams of the same size investigated by Demissie et al. (2017) in the semiarid Raya graben in northeastern Ethiopia. The average gradient of the latter rivers is 0.013, whereas that of the study fiumara is almost twice (0.021). Both the study areas have been subjected to recent uplifting, but the Ethiopian ephemeral streams receive a lower average annual rainfall of 750 mm. The main reason for this marked difference in streambed gradient probably lies in the finer sandy gravel alluvium of the Raya graben rivers (average proportion of sand 59%) compared to the coarse gravel with very little sand of the Calabria fiumaras. The higher proportion of sand in the Raya ephemeral streams results from the hotter climate, the weathering-prone bedrock consisting of Eocene to recent volcanics, and the predominance of sparse bushy vegetation on slopes. For two large, predominantly sand and sandy gravel ephemeral streams draining the Daban basin in northern Somalia (Biyoguure and Kalajab), Billi (2022) measured a streambed gradient of 0.015. These rivers are very close to each other and share a similar bedrock mainly composed of Proterozoic granites and Eocene-Oligocene and Neogene sandstones and conglomerates. Very high temperatures year-round, modest rainfall only in the headwaters, occasional floods, and slopes without vegetation result in high sediment supply and aggradation rates. The predominance of fine sediment reflects the relatively lower streambed gradient, notwithstanding the Eocene to recent uplifting of the rift escarpment hosting the headwaters of both rivers.

The study fiumaras shares several sedimentological characteristics with other ephemeral streams in the world but also shows some differences. The structureless sedimentology of the alluvium, consisting of crude coarse gravel beds, typically 40-80 cm thick, poorly sorted, and organized is also reported by Hassan (2005) for his study of ephemeral streams in the Negev desert (Israel). Other similarities include the occurrence of the largest boulders on top of bars as observed by Billi (2016) in the boulder bed, seasonal Golina river crossing the Raya graben, or in the gravelly sand Biyoguure and Kalajab ephemeral streams (Billi 2022) in northern Somalia. According to Maizels (1993), the larger boulders are pushed upward by internal dispersive stresses. Manville and White (2003) consider the occurrence of large boulders on top of the active bedload layer as typical of hyperconcentrated flows. In the basal layer, these authors postulate debris flow conditions driven by internal inertial forces and the tangential boundary shear stress imposed by the overlaying turbulent flow. The particles larger than the basal flow are therefore pushed into the upper turbulent flow and move as contact bedload. In the fiumaras, the large boulders are rooted in the coarse core division of the tabular bed (Fig. 12) and the arrangement proposed by Manville and White (1993) is not evident. The presence of large boulders on the bar top of reversely graded beds seems to be better explained by the bipartite model of Sohn (1997) modified by Billi (2008) consisting of a frictional region at the base, above which, in the collisional region, the particle shear stress reaches its maximum. In this upper region of high shear stress, the largest particles are concentrated, with the outsized one protruding to the top of the active moving bedload layer. The winnowing of the receding flood flow contributes to removing the fines, leaving in place the coarse boulders, thus freezing a condition of high flow energy.

The alluvium of the Bonamico, La Verde, Simeri e Scilotraco fiumaras is typically structureless except for crudely bedded coarse-grained and poorly sorted gravels 05-1.0 m thick. These poorly organized deposits are also present in the Golina River and other ephemeral streams in the Raya graben, but in these rivers, the beds show a

typical internal organization consisting of divisions with different grain size characteristics associated with the vertical distribution of shear stress in hyperconcentrared flows (Billi, 2008). This feature is not so well developed in both the Calabria rivers and the Daban ephemeral streams (Billi, 2022). The currently available data is insufficient to explain why the Raya graben riverbed load sheets exhibit such an internal organization. The floods of these rivers probably have a higher intensity and a longer duration, as they are generated by monsoon-type rainfalls, which allow for hyperconcentrated flows capable of some internal organization that is not possible in the shorter floods on the Calabria and Daban basin rivers.

The lack of evidence of downstream migration of braid bars is also observed in the Raya and Daban rivers, and Hassan (2005) also found bar dissection processes that, in the fiumaras and in the Raya and Daban ephemeral streams, are considered to form longitudinal bars through the incision of diverging and rejoining channels. The occurrence of large boulders on the bar top and the coarser grain size of the bar top with respect to the finer channel filling observed in the fiumaras has been reported for the Raya graben (Billi, 2016) and the Daban ephemeral streams (Billi, 2022) as well. In these latter rivers, the grain size difference between bar top and channel fill is not as marked as in the fiumaras and the Raya rivers. In the Daban, the predominance of sandy sediment over gravel and boulders, the very large width-to-depth ratio (close to 300) and the shallowness of the braid channel, especially in the widest reaches, may reduce the difference in shear stress between the high flow on the bar top and the low flow of the receding flood phase in the channels.

Crescent scours are typical bedforms of ephemeral streams. They are very common on the streambeds of the Daban and the Raya graben rivers, whereas they are rare in the fiumaras. Such a difference may be accounted for by the small percentage of sand in the Calabria rivers since the occurrence of a thick sandy top layer is fundamental for the development of this bedform, which is one of the most typical and indicative of dryland ephemeral rivers.

Ripples and dune bedforms are uncommon in the study fiumaras as in the Ethiopia and Somalia counterparts. The short duration of floods and, likely, flows with Froude numbers close to one are conditions unfavorable for the formation of bedforms, except for the plane bed (Billi, 2008). In places, mud film deposited in the pools shows shrinkage cracks. This bedform witnesses the flashy character of floods and the quick change from humid to dry weather conditions. The ubiquitous occurrence of crescent scours and horizontal lamination and the lack of cross-stratified sands and ripple and dune bedforms can be considered diagnostic elements to identify old deposits as originated by ephemeral streams. Typical sedimentological features of the fiumaras, though not exclusive to them, include the lack of a clear stratification, the occurrence of an armored layer including the largest boulders, especially on the bar top, the bed reverse grading, the lack of internal organization and downstream fining, the occurrence of pebble clusters, and keystone interlockings. From this study, it is evident that the study fiumaras share some distinctive characteristics with dryland ephemeral streams, but the former show a poorer diversity of internal arrangements and bedforms.

Field observations indicate that the streambed of fiumaras is not armored. In the Simeri and Scilotraco, bed material sampling and grain size analysis returned low average values of armoring degree (0.9 and 1.7, respectively) that are comparable to that of 1.7 reported by Hassan (2005) for a hyper-arid ephemeral stream in the Negev desert of Israel. According to this author, armoring may not be apparent in dryland rivers. In the Scilotraco, the armoring is more pronounced (1.7) than in the Simeri (0.9), but in the former river, the sand content in the subsurface material is twice that on the surface, and, in the latter, it is almost equivalent (around 30%). These data suggest that, in the study fiumaras, the proportion of sand trapped in the subsurface material is not sufficient to produce the formation of an armored bed. In more humid environments, the development of a coarser streambed surface is associated with selective transport and winnowing processes (Parker and Klingeman, 1982) or sediment supply-limited conditions (Dietrich et al., 1989). These conditions are rarely found in the ephemeral streams of arid and semi-arid environments. In the fiumaras, sediment supply is high, the infrequent flash floods are short, and flow vanes quickly constrain the occurrence of winnowing processes. All these conditions and the bedload en masse transport are supposed to contrast the development of streambed armoring.

The lack of an armored layer also has been found in other ephemeral and intermittent rivers and seems to be a recurrent characteristic of arid and semiarid region rivers (Billi, 2008, 2016, 2022). In these environments, sediment supply-limited conditions are rarely met because the sparse vegetation, long intervals without rain, and high rates of rock weathering result in high rates of sediment supply, especially if compared with the very low frequency of floods. Moreover, in arid and semiarid regions, lower than bankfull flows do not necessarily result in washing out the fines. A few field studies on dryland rivers (e.g., Billi, 2011; Demissie et al., 2017) indicate that, during shallow flows, the deposition processes tend to prevail on winnowing.

Another issue about streambed armoring is the occurrence of several check dams in the study rivers. The Calabria region is affected by intense erosion processes and high sediment delivery rates, so one could expect that after a few years/decades, when the check dams are filled, their influence on the sediment supply quantity and quality should tend to be neglectable. In 1973, a landslide blocked the upstream third of the Bonamico River and formed a small lake. Though this event initially may have substantially affected the sediment supply, time sequences of satellite images show that around 2010, the river started to retrieve its original channel morphology, and in the reach downstream of the landslide, there is evidence of a progressive change from very coarse bed material to finer sediment and of the restoration of a sediment supply, likely comparable to that typical of the river reach before the landslide. Besides, it is worth mentioning that a substantial sediment supply to the lower reaches of the Bonamico was and comes from its largest tributary, which is located downstream of the 1973 landslide and was not affected by it.

Further field studies, especially hydraulic field measurements and data, are strongly recommended to strengthen our knowledge of the geomorphological processes and the sedimentological characteristics of peculiar rivers such as the fiumaras.

CONCLUSIONS

Southern Italy's ephemeral rivers are known by the local name of fiumaras. This name is associated with short and steep channels that are dry for most of the time but capable of turning quickly into high floods with devastating energy. In addition to heavy rains and notwithstanding the small size of their catchment, geomorphic factors such as the high relief ratio, the steep slopes, the high drainage

density, and the short and steep channel contribute to a fast transfer of water and sediment from the headwaters to the coastal plain reaches, resulting in channels chocked with sediment and high flood waves.

The alluvium of the fiumaras is coarse-grained, and its stratigraphy is very simple, as it consists mainly of horizontal, poorly sorted, commonly reversely graded, structureless beds with rare thin and spatially limited intercalations/lenses of massive or horizontally laminated sand. Crossbedding is very uncommon. The most common gravel bedforms are pebble clusters, keystone interlocking, and, subordinately, transverse ribs. Crescent scours, which are typical of dryland ephemeral streams, are seldom observed in the study fiumaras, probably because of the small proportion of sand. The largest boulders are typically found on the longitudinal bar top, whereas the main braid channels are filled with fine gravel and, subordinately, with sand.

The longitudinal bars do not show any evidence of downstream migration. They appear to result from the streambed dissection of thick bedload layers during the receding flood flow phase. The fiumaras' alluvium sedimentological characteristics indicate high rates of deposition from hyperconentrated flows. The fiumaras share some sedimentological features with coarse-grained ephemeral streams of other arid and semi-arid areas in the world, but further field studies are necessary to point out specific diagnostic elements for the interpretation of ancient deposits laid down by these peculiar Mediterranean rivers.

REFERENCES

Abdullatif O.M. (1989). Channel-filland sheet-flood facies sequences in the ephemeral River Gash, Kassala, Sudan. Sedimentary Geology, 63:171–184.

Biamonte A. (1993). Sedimentologia delle fiumare calabre. Unpublished thesis, Department of Earth Sciences, University of Florence, Italy.

Bill P. (1987). Sediment storage, bed fabric and particle features of two mountain streams at Plynlimon (mid- Wales). Institute of Hydrology Report No.97, 39 pp.

Billi P. (1988). A note on cluster bedform behaviour in a gravel-bed river. Catena, 15: 1-9.

Billi P. (2008). Flash floods, sediment transport and bedforms in the ephemeral streams of Kobo basin, northern Ethiopia, CATENA, 75 (1): 5-17. doi:10.1016/j.catena.2008.04.002

Billi P. (2011). Flash flood sediment transport in a steep sand-bed ephemeral stream. International Journal of Sediment Research, 26(2), 193-209.

Billi P. (2016). Channel processes and sedimentology of a boulder-bed ephemeral stream in the Western Afar margin, Zeitschrift für Geomorphologie, 60 (1): 35-52.

Billi P. (2022) Fluvial landscape of the Daban Basin, Northern Somalia. In: Billi, P. (ed.) Landscape and landforms of the Horn of Africa: Eritrea, Djibouti, Somalia. Springer, Cham, Switzerland, 265-280.

Billi P. and Biamonte, A. (1995). Trasporto solido e dinamica morfologica d'alveo. Studi ed esperienze su due fiumare calabre: il T. Scilotraco ed il F. Simeri (Prov. di Catanzaro). In: Bonardi, G., De Vivo, B., Gasparini, P., Vallario, A., "Cinquanta anni di attività didattica e scientifica del Prof. Felice Ippolito", Liguori Editore, Napoli, 27-47.

Billi P., Preciso E. and Salemi, E. (2014). Rhythmic roughness elements and channel morphology of gravel bed rivers. Zeitschrift für Geomorphologie, 58(3): 337-366. DOI: http://dx.doi.org/10.1127/0372-8854/2013/0127

Billi P., Demissie B., Nyssen J., Moges G., and Fazzini M. (2018). Meander hydromorphology of ephemeral streams: similarities and differences with perennial rivers. Geomorphology, 319: 35-46.

Bluck B.J. (1982). Texture of gravel bars in braided streams. In: Hey R.D., Bathurst J.C. and Thorne, C.R (Eds.), Gravel-Bed Rivers, Wiley, Chichester, 339-355.

Bryashaw A.C. (1984). Characteristics and origin of cluster bedforms in coarse-grained alluvial channels. In: Koster, E.H. and Steel, R.J. (Eds.), Sedimentology of Gravels and Conglomerates. Canadian Soc. Petrol. Geol., Memoir 10: 77-65.

Carling P., (2017). Catastrophic deposition of gravel from outbreak floods. In: Tsutsumi D. and Laronne J.B. (Eds.) Gravel-Bed Rivers: Processes and Disasters. Wiley, 299-327.

Carlston C.W. (1963). Drainage density and streamflow. US Geological Survey Professional Paper 422-C

Church M.A., McLean,D.G. and Wolcott, J.F. (1978). River bed gravels. Sampling and analysis. In: Thorne C.R., Bathurst J.C. and Hey, R.D. (Eds.) Sediment transport in gravel-bed rivers. Wiley, Chichester, 43-88.

Cirrincione R., Fazio E., Fiannacca P., Ortolano G., Pezzino A. and Punturo, R. (2015). 2015PM0446The Calabria-Peloritani Orogen, a composite terrane in Central Mediterranean; its overall architecture and geodynamic significance for a pre-Alpine scenario around the Tethyan basin. Periodico di Mineralogia, 84 (3B): 701-749. DOI: 10.2451/2015PM0446

Demissie B., Billi P., Frankl A., Haile M. and Nyssen, J. (2017). Excess river sedimentation at bridges in the Raya Graben (Northern Ethiopia). Land Degradation and Development, 28: 946–958. DOI: 10.1002/ldr.2572

Dietrich W.E., Kirchener J.V., Ikeda H. and Iseya, F. (1989). Sediment supply and the development of a coarse surface layer in gravel bedded rivers. Letters to Nature, 340:215–217.

Dunkerley D.L. (1992). Channel geometry, bed material and inferred flow conditions in ephemeral stream systems, Barrier Range, western N.S.W, Australia. Hydrological Processes, 6: 417–433.

ECMWF (European Centre for Medium-Range Weather Forecasts) - www.ecmwf.int/en/forecasts/datasets.

Ferrari E., Gabriele S. and Versace, P. (1988). L'analisi dei massimi idrologici in Calabria. Previsione e prevenzione degli eventi idrologici estremi e loro controllo. Report 88, GNDCI, CNR, Roma.

Ferro V., Porto P. (2011). Predicting the equilibrium bed slope in natural streams using a stochastic model for incipient sediment motion, Earth surface processes and landforms 36, 1007-1022, ISSN: 0197-9337.

Ferro V., Porto P. (2012). Identifying a dominant discharge for natural rivers in southern Italy. Geomorphology, 139-140, 313-321.

Foti G., Barbaro G., Bombino G., Barillà G.C., Mancuso P., Puntorieri P. (2022). River transport in Calabrian rivers. In: Calabrò F., Della Spina L., Piñeira Mantiñán M.J. (eds) New Metropolitan Perspectives. Lecture Notes in Networks and Systems, vol 482. Springer, Cham. https://doi.org/10.1007/978-3-031-06825-6_7.

Gavrilovic, S. (1972). Inzenjering o bujicnim tokovima i eroziji. Izgradnja. Beograd. (in Serbian).

Grant G.E., Swanson F.J. and Wolman, MG. (1990). Pattern and origin of stepped - bed morphology in high - gradient streams, Western Cascades, Oregon. Geological Society of America Bulletin, 102(3): 340-352,

Hassan M.A. (2005). Characteristics of gravel bars in ephemeral streams. Journal of Sedimentary Research, 75: 29–42.

Hassan M.A., Church M., Lisle T.E., Brandinoni F., Benda L. and Grant, G.E. (2005). Sediment transport and channel morphology of small, forested streams. Journal of the American Water Resources Association, 41(4): 853-876.

Horton R.E. (1932). Drainage basin characteristics. American Geophysical Union Trans 13:350–361.

Laronne J.B. and Shlomi, Y. (2007). Depositional character and preservation potential of coarse-grained sediments deposited by flood events in hyper-arid braided channels in the Rift Valley, Arava, Israel. Sedimentary Geology, 195: 21–37.

Leopold L.B. (1970). An improved method for size distribution of stream bed gravels. Water Resources Research, 6(5): 1357-1366.

Leopold L.B., Wolman M.G. and Miller, J.P. (1964). Fluvial processes in geomorphology. Freeman, San Francisco.

Maizels J. (1993). Lithofacies variations within sandur deposits: the role of runoff regime, flow dynamics and sediment supply characteristics. Sedimentary Geology, 85: 299-325.

Manville,V. and White J.D.L. (2003). Incipient granular mass flows at the base of sedimentladen floods, and the roles of flow competence and flow capacity in the deposition of stratified bouldery sands. Sedimentary Geology, 155: 157–173.

Montgomery D.R. and Buffington, J.M. (1997). Channel-reach morphology in mountain drainage basins. Geological Society of America Bulletin, 109(5): 596-611.

Nyberg B., Gawthorpe R.I., and Helland-Hansen, W. (2018). The distribution of rivers to terrestrial sinks: Implications for sediment routing systems. Geomorphology, 316: 1–23.

Parker G., and Klingeman P.C. (1982) On why gravel bed streams are paved: Water Resources Research, 18: 1409–1423.

Picard M.D. and High, Jr. L.R. (1973). Sedimentary structures of ephemeral streams. Developments in Sedimentology,17. Elsevier, Amsterdam.

Ravi Shankar M.N. and Mohan, G. (2006). Assessment of the groundwater potential and quality in Bhatsa and Kalu river basins of Thane district, western Deccan Volcanic Province of India. Environmental Geology, 49: 990–998. DOI 10.1007/s00254-005-0137-5

Rinaldi M., Gurnell A. M., Gonzalez del Tanago M., Bussettini M. and Hendrik, D. (2016). Classification of river morphology and hydrology to support management and restoration. Aquatic Sciences, 78: 17–33. DOI 10.1007/s00027-015-0438-z

Rosgen D.L. (1996). Applied river morphology. Wildland Hydrology, Pagosa Springs, Colorado.

Sabato L. (1989). Sedimentazione attuale in alcuni fiumi a breve corso fra le piane di Metaponto e Sibari (confine calabro-lucano). Memorie della Società Geologica Italiana, 42: 269–285.

Sabato L., and Tropeano M. (2004). Fiumara: a kind of high hazard river. Physics and Chemistry of the Earth 29: 707–715.

Schumm S.A. (1956) The evolution of drainage system and slopes in Badlands at Perth Amboy, New Jersey. Bulletin of the Geological Society of America, 67: 214–236.

Servizio Idrografico, 1916-1998. Annali Idrologici. Parte II. Ministero dei Lavori Pubblici, Roma.

Shepherd R.G. (1987). Lateral accretion surfaces in ephemeral-stream point bars, Rio Puerco, New Mexico. In: Ethridge F.G., Flores R.M. and Harvey M. (Eds.), Recent Developments in fluvial sedimentology. Society of Economic Paleontologists and Mineralogists, Special Publication No.39, Tulsa, OK, pp. 93–98.

Sohn Y.K. (1997). On traction-carpet sedimentation. Journal of Sedimentary Research, 67 (3): 502–509.

Thomas J., Joseph S., J. and Thrivikramaji, K.P. (2010). Morphometric aspects of a small tropical mountain river system, the southern Western Ghats, India. International Journal of Digital Earth, 3(2): 135-156.

Versace P., Ferrari E., Gabriele S. and Rossi F. (1989). Valutazione delle piene in Calabria. CNR-IRPI, Geodata, Cosenza.

Versace P., Ferrar, E. and Cruscomagno F. (2017). Le fiumare della provincia di Reggio Calabria. University of Calabria, Civil Protection of the Calabria Region.

Whiting P.J., Dietrich W.E., Leopold L.B., Drake T.G. and Shreve, R.L. (1988). Bedload sheets in heterogeneous sediment. Geology, 16: 105–108.

Williams G.E. (1971). Flood deposits of the sand-bed ephemeral streams of central Australia. Sedimentology, 17:1–40.

Zimmermann A., Church M. and Hassan, M.A. (2010). Step-pool stability: Testing the jammed state hypothesis. Journal of Geophysical Research, 115: F02008. doi:10.1029/2009JF001365.

RESEARCH PAPER

WINTER SPATIAL PATTERNS IN $PM_{2.5}$ CONCENTRATION AND AIR QUALITY INDEX IN THE ARCTIC TOWN

Iuliia V. Mukhartova[1,5], Alen A. Kospanov[1], Mariya E. Zubova[1], Anastasia A. Semenova[1], Uliana I. Antipina[4], Igor V. Malyutin[1], Daria Yu. Gushchina[1], Marina V. Slukovskaya[3], Varvara S. Maratkanova[1], Pavel I. Konstantinov[1,2]

[1]Lomonosov Moscow State University, Faculty of Geography, Leninskie Gory 1, Moscow, 119991, Russia
[2]Shenzhen MSU-BIT University, Longgang District, Shenzhen, 518172, PR China
[3]Kola Science Center of the Russian Academy of Sciences, Fersman str. 14, Apatity, 184209, Russia
[4]Institute of Global Climate and Ecology named after Academician Yu.A. Israel, Glebovskaya str. 20B, Moscow, 107258, Russia
[5]Lomonosov Moscow State University, Faculty of Physics, Leninskie Gory 1, Moscow, 119991, Russia
***Corresponding author:** kostadini@mail.ru
Received: December 3rd 2024 / Accepted: February 25th 2025 / Published: June 30th 2025
https://doi.org/10.24057/2071-9388-2025-3756

ABSTRACT. The current study presents the results of air quality research in the small mining and touristic city of Apatity (Kola Peninsula, Russian Federation, 67°34'03"N, 33°23'36"E) during the two winter expeditions in 2022 and 2024. A PurpleAir PA-II portable device was used for ground-based aerosol observations. Two measurement campaigns allowed to conduct route measurements in various synoptic conditions, including both frosty windless weather, characterized by temperature inversion (2022), and contrasting conditions of "warm" winter unusual in the Arctic and Kola Peninsula (January 2024). The obtained results demonstrate that, depending on the synoptic situation in the city, there can be both traditional accumulation of concentrations of $PM_{2.5}$ particles (up to 300 μg/m^3) dangerous for the health of inhabitants (in some areas exceeding the 20 min maximum allowable concentration of 160 μg/m^3 almost twice), and significant improvement of air quality due to precipitation and air mixing under warm winter conditions (on average, about 17 μg/m^3). The latter circumstance can noticeably improve the region's tourism potential in a warmer climate.

KEYWORDS: aerosol pollution, Arctic city, urban air quality, $PM_{2.5}$ particles, urban microclimate

CITATION: Mukhartova I. V., Kospanov A. A., Zubova M. E., Semenova A. A., Antipina U. I., Malyutin I. V., Gushchina D. Yu., Slukovskaya M. V., Maratkanova V. S., Konstantinov P. I. (2025). Winter Spatial Patterns In $PM_{2.5}$ Concentration And Air Quality Index In The Arctic Town. Geography, Environment, Sustainability, 2 (18), 164-174
https://doi.org/10.24057/2071-9388-2025-3756

ACKNOWLEDGEMENTS: The study was carried out with the support of the Russian Science Foundation under project No. 23-27-00254.

Conflict of interests: The authors reported no potential conflict of interests.

INTRODUCTION

During the last decades, air pollution has become one of the major natural and man-made hazards attracting more attention of researchers. The global community is increasingly emphasizing the causes and consequences of air pollution in terms of sustainable development and urban planning. Key challenges in such research have been the identification of factors contributing to air pollution and the development of adaptation and mitigation measures to improve the quality of life in cities.

$PM_{2.5}$ and PM_{10} are airborne mass concentrations with sizes ranging from 10 nm to 2.5 μm and up to 10 μm in diameter, respectively, either solid or as microscopic liquid droplets (Seinfeld and Pandis 2006). PM particles are divided into primary and secondary particles. Primary PM is directly emitted into the ambient air, while secondary PM can be formed by chemical reactions of substances such as sulfur dioxide, nitrogen oxides, and ammonia (various nitrates and sulfates). Primary PM can be of natural and anthropogenic origin. The source of natural PM can be, for example, soil erosion. Biological pollutants can also be considered as primary natural PM. Anthropogenic PM_{10} and $PM_{2.5}$ particles are fragments of soot, automobile tires and asphalt (due to wear and tear of road surfaces), as well as mineral salts and heavy metal oxides (Seinfeld and Pandis 2006; Arnold et al. 2016). Many papers have been devoted to the study of episodes with significant exceedances of $PM_{2.5}$ and PM_{10} standards (Chen et al. 2023; Groot Zwaaftink et al. 2022; Yasunari et al 2024; Sartz et al 2023). The main sources of anthropogenic $PM_{2.5}$ and PM_{10} are motor vehicles with internal combustion engines, combustion of solid fuels both in households and industry, as well as construction, mining, cement production, etc. Studies show that in mechanical engineering, the share of $PM_{2.5}$ and PM_{10} emissions can account for up to 13% and 40% of

total suspended particles (TSP - total suspended particles) emitted, respectively; in ferrous metallurgy up to 75% and 84%, in non-ferrous metallurgy up to 43% and 88%, and in mining up to 21% and 49%, respectively (Zagorodnov et al. 2019). Construction materials production also contributes significantly to PM_{10} and $PM_{2.5}$ emissions (Prosviryakova and Shevchuk 2018). One of the problems associated with the formation of PM_{10} and $PM_{2.5}$ in industry is that particles with aerodynamic sizes smaller than 10 μm are practically not captured by the most common dust cleaning plants, in contrast to larger particles captured in amounts up to 90-95% (Strelyaeva et al. 2014; Strelyaeva et al. 2017).

Special attention to the study of urban air quality, including the concentration of $PM_{2.5}$ particles, is due to the fact that these particles are able to overcome biological barriers and penetrate into the lungs and even blood, causing significant harm to human health (Kholodov et al. 2019; Bai et al. 2007; Polichetti et al. 2009; Kowalska and Kocot 2016; Dominici et al. 2006). The concentrations of PM_{10} and $PM_{2.5}$ in ambient air affect mortality rates, respiratory and cardiovascular disease occurrence statistics, and other health indicators (Zagorodnov 2018; Di et al. 2017). Table 1 shows the maximum allowable concentrations of PM particles according to WHO recommendations[1], as well as those adopted in Russia[2], Belarus[3] and EU countries[4].

In the present work, the concentrations of $PM_{2.5}$ particles were compared under the Arctic city conditions both in clear frosty weather after prolonged intense snowfalls and in "warm" winter conditions in the presence and absence of precipitation. The effect of precipitation washout on the optical properties of smoke, and thus in the amount of aerosol, is noted in many works (Burtsev and Burtseva 1971; Pkhalagov and Uzhegov 1980). Wet aerosol deposition from the atmosphere is one of the most effective processes for its purification from pollutants (Aloyan 2002; Wallace and Hobbs 2006). The analysis of atmospheric purification by precipitation under urban conditions presents a complicated problem. Decrease in the concentration of impurities due to precipitation has been proved, but the washout effect is observed only outside of the zone of direct impact of anthropogenic aerosol sources. In (Gorbarenko and Eremina 1998), a significant dependence of aerosol optical thickness on the duration, amount, and intensity of precipitation was observed only in the warm period of the year. In (Chubarova et al. 2020) the experiments conducted in April and May 2018 and 2019 showed an exponential dependence of the decrease in aerosol content with an increase in precipitation. It was also shown that the content of suspended and dissolved aerosol fractions in precipitation samples was consistent with the high aerosol content in the atmosphere before precipitation. Experiments have demonstrated that under all precipitation regimes, the contribution of the suspended fraction to the total aerosol washout was predominant (up to 67%) compared to the dissolved one.

In (Plaude et al. 2012), based on 15-year measurements of atmospheric aerosol characteristics in Dolgoprudny, it was shown that a statistically significant negative correlation of aerosol particle concentration with precipitation is observed only for monthly averages and is absent for semiannual and seasonal averages. Analysis of individual precipitation events revealed their small influence on aerosol concentration in the surface layer. In the winter period, the authors observed a decrease in aerosol concentration in a narrow range of particle sizes 0.03-0.1 μm, and it amounted to no more than 30% within a few hours. In our work, however, a significant difference in $PM_{2.5}$ particle concentrations was found in the presence and absence of precipitation (snow) in urban conditions, which can be explained by a number of meteorological reasons, including inversions and wind direction.

In the cold climate cities with temperatures below freezing and persistent snow cover over a significant part of year (Järvi et al. 2017; Qian et al. 2022) the persistent surface energy deficit in wintertime creates stronger surface layer stability and temperature inversions in the lower atmosphere (Wetzel and Brümmer 2011) and a thin stable ABL (Davy 2018). Research publications about cold climate urban meteorology are scarce (Varentsov et al. 2023; Brozovsky et al. 2020; Lappalainen et al. 2022; Varentsov et al. 2022; Konstantinov et al. 2022).

An important aspect of wintertime pollution in cold cities is the prevalence of temperature inversions, which reduce the vertical dispersion. Due to extremely stable atmospheric conditions in case of low winds pollution is trapped in the shallow atmospheric layer, which significantly worsens the air quality in Arctic cities (Simpson et. al. 2024). A number of studies have investigated the main sources of pollution in Arctic cities, in particular, in Fairbanks. Fairbanks wintertime sources of PM have been studied by chemical mass balance methods (Ward et al. 2012), which indicated that wood smoke sources caused

Table 1. Maximum allowable concentrations of PM_{10} and $PM_{2.5}$

Particles	Period	MAC, μg/m³			
		WHO	Russia	Belarus	EU
PM_{10}	20 min	-	300	150	-
	1 day	50	60	50	50
	1 year	20	40	40	40
$PM_{2.5}$	20 min	-	160	65	-
	1 day	25	35	25	-
	1 year	10	25	15	20

[1]WHO air quality guidelines for particulate matter, ozone, nitrogen dioxide and sulfur dioxide, 2006
[2]GN 2.1.6.3492-17 "Maximum permissible concentrations (MPC) of pollutants in the atmospheric air of urban and rural settlements" for Russian Federation
[3]Standards of maximum permissible concentrations of pollutants in atmospheric air: hygienic standard / approved by the decree of the Ministry of Health of the Republic of Belarus № 113 08.11.2016
[4]Air quality standards – European Commission, National ambient air quality standards for particulate matter, 2006

60–80% of ground-level PM from 2008–2011. The studies using positive matrix factorization (PMF) generally agreed that wood smoke was the largest single factor, but found lower percentages (40–52%) of influence in Fairbanks (Wang and Hopke 2014; Kotchenruther 2016).

The aim of this work was to study how different meteorological conditions influence the spatial distribution of pollution by $PM_{2.5}$ in Apatity during winter, as the formation of a temperature inversion and a weak mixing layer (or their absence) are bound to influence the pollutant accumulation patterns. To achieve the goal, the following tasks were performed: selection of points for measurements, direct measurements of $PM_{2.5}$ concentration in winter 2022 and 2024 on days with different meteorological conditions, and processing and analysis of measurement results.

MATERIALS AND METHODS

We conducted our research in the city of Apatity (67°34′03″N, 33°23′36″E), situated in the Murmansk region above the Arctic Circle. As noted above, for Arctic cities, air quality is a particularly critical indicator, which is associated with meteorological features of the region. Therefore, of particular interest in this work was the comparison of the spatial distribution of atmospheric pollution in different meteorological conditions: in the presence and absence of inversion, in the conditions of classical cold winter, as well as warm winter.

In addition to its geographical location, Apatity is also interesting because of its location in close proximity to the ANOF-2 and ANOF-3 apatite-nepheline enrichment plants, which are subdivisions of Apatit's Kirovsk branch. Both the ANOF factories themselves and their "tailings ponds" are sources of significant dust pollution in the cities of Kirovsk and Apatity. In this regard, it was also of interest to study the spatial distribution of pollution in Apatity under different meteorological conditions.

The studies were conducted in the winter of 2022 and 2024 as a part of the winter expedition of the Department of Meteorology and Climatology, Faculty of Geography, MSU (January 16 - 23, 2022 and January 25 - February 1, 2024). The measurements were carried out by automobile sounding for several hours. The points selected for measurements are presented in Fig. 1.

The map in Fig. 1, as well as the maps of the $PM_{2.5}$ concentration distributions presented in the Results section, were made using QGIS 3.34 software[5]. The distribution of concentration in the study area was obtained from point measurements using inverse distance weighted (IDW) interpolation method.

For both research cases, judgmental sampling was the primary sampling technique, as it allowed us to address the specifics of the $PM_{2.5}$ measurement campaigns during the two different expeditions. In 2022, the points were predominantly concentrated along the road from ANOF-2 to Apatity and in the northern part of the city (Fig. 1a) in order to detect the correlation between air quality and distance from the enterprise. Point 1 was located in the vicinity of the nepheline "tailings dump" and the ANOF-3 site (the tailings dump is located approximately 6.5 km east of point 1, ANOF-3 is located 10 km east of point 1). Point 8 is located directly at the entrance to ANOF-2, points 18 and 2 play the role of background points. Point 3, located in the village of Tik-Guba on the shore of Lake Imandra, was also considered a background point. In 2024, it was decided to distribute the points more evenly within the city (Fig. 1b), keeping point 8 near ANOF-2, point 3 on the shore of the lake (moving it closer to the weather station), as well as a number of points in the northern part of Apatity.

Ground-based aerosol observations were carried out using a PurpleAir PA-II portable device (PurpleAir LLC, Draper, UT, USA) incorporating a pair of PMS5003 laser optical particle counter sensors (Plantower Ltd., Beijing, China). The principle of particle concentration measurement in the PurpleAir PA-II device is based on optical light scattering technique. The use of light scattering technique makes the sensors cheaper to manufacture, reduces their power consumption and response time (Tanzer et al. 2019). When a particle passes through the sensor, it scatters light. The intensity of the scattered light is measured by a phototransistor and correlated with the dimension of the particle. This method is sensitive to air temperature and humidity, so the PurpleAir PA-II also contains temperature, relative humidity and barometric pressure sensors (BME 280, Bosch Sensortec GmbH, Reutlingen, Germany). In our study all measurements were provided in recommended temperature range -40°F to 185°F (-40°C to 85°C).

All sensors in PurpleAir PA-II are connected to a microcontroller with a wireless communication module. The device allows data to be recorded and transmitted via Wi-Fi to a cloud platform, from where it can be downloaded at 2-minute intervals. The PMS5003 sensor provides digital outputs for 12 data fields. The first three ones correspond

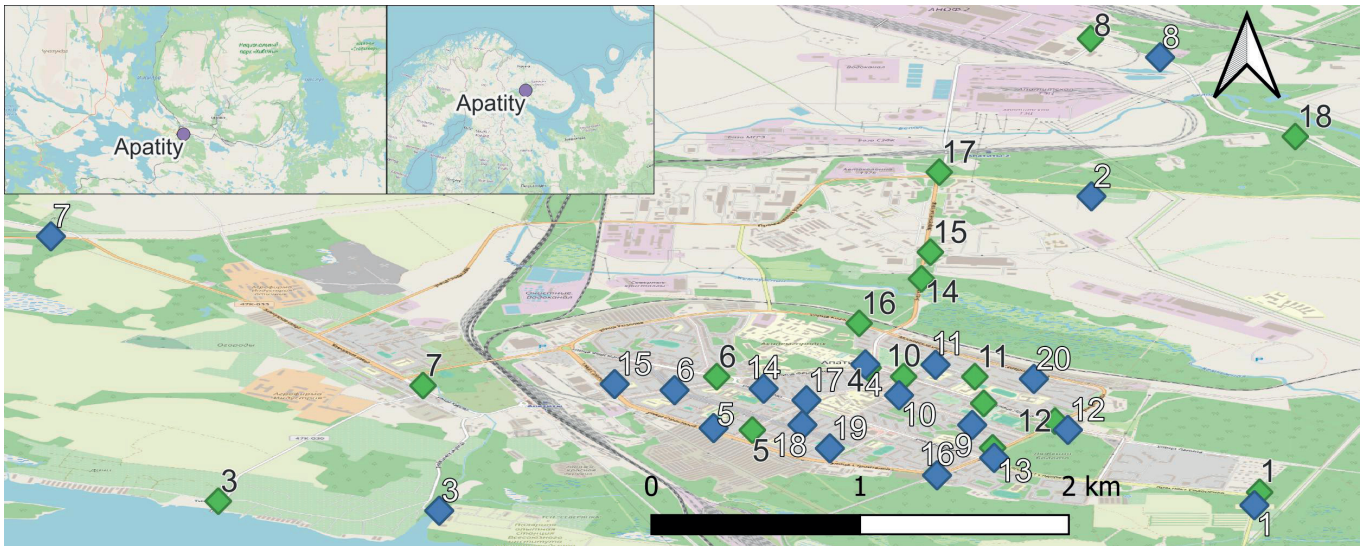

Fig. 1. The location of measurement points in and around Apatity for 2022 (green points) and for 2024 (blue points)

[5]QGIS.org, 2024. QGIS Geographic Information System. QGIS Association. http://www.qgis.org

to the mass concentrations of PM_1, $PM_{2.5}$ and PM_{10} fractions without applying any correction. The next three ones correspond to the corrected mass concentrations obtained after applying the proprietary algorithm developed by Plantower Ltd. The next six data fields contain the cumulative particle size distribution in six size ranges (>0.3 μm, >0.5 μm, >1 μm, >2.5 μm, >5 μm and >10 μm). In addition to these parameters, the PA-II instrument also reports temperature, relative humidity, and barometric pressure from each of the two PM5003 sensors (Stavroulas et al. 2020).

The study of accuracy of low-cost PurpleAir monitors for measuring ambient fine particulate matter ($PM_{2.5}$) and the exploration of methods for improving their precision were made in (Tryner et al. 2020). Initially, the researchers tested the linear response of PurpleAir monitors to a known $PM_{2.5}$ standard and derived a laboratory-based correction factor. Then they deployed the monitors alongside portable filter samplers at 15 outdoor sites to assess the effectiveness of ambient relative humidity (RH) data in improving measurement accuracy. Authors found out that 72-h $PM_{2.5}$ (μg m^{-3}) measured by portable and conventional filter samplers agreed.

The PurpleAir PA-II device was used to measure $PM_{2.5}$ concentration at each of the measurement points for 1-2 min. The data was updated every 10 seconds. For further work and analysis, averaging of measurement results was performed. Although we measured essentially instantaneous concentrations, the corresponding values of the sub-index AQI were calculated based on concentrations of $PM_{2.5}$ in μg/m^3 to illustrate the assessment of air quality. In the following, pollution distribution maps show data in AQI units. The relation of AQI index values and $PM_{2.5}$ concentrations in μg/m^3, as well as the classification of AQI levels and the corresponding recommendations for 24-hour human exposure to the corresponding pollution level are given in Table 2[6]. Recommendations on the relation between AQI levels and the degree of danger to human health have been developed for an average 24-hour exposure. In our study, measurements at each point were carried out for several minutes. Hence, to assess the level of pollution, we used concentrations in μg/m^3 and compared them with the 20-minute MAC according to accepted Russian standards.

The period of the 2022 expedition was characterized by strong snowfalls, which made it impossible to carry out measurements for several days. The measurements were carried out after the snowfall was over, on 22.01.2022, when typical anticyclonic conditions were established, characterized by almost complete absence of wind, significant temperature inversion, and air temperature of about -20°C. The concentration of $PM_{2.5}$ particles was measured in the morning and afternoon hours.

During the winter expedition of 2024, the synoptic situation was atypical for the Kola Peninsula and the time of the year. Constant active cyclonic activity accompanied by the passage of atmospheric fronts with sharp temperature variations at different altitudes, as well as gusty winds that provoked intensive vertical air mixing in the lower layers

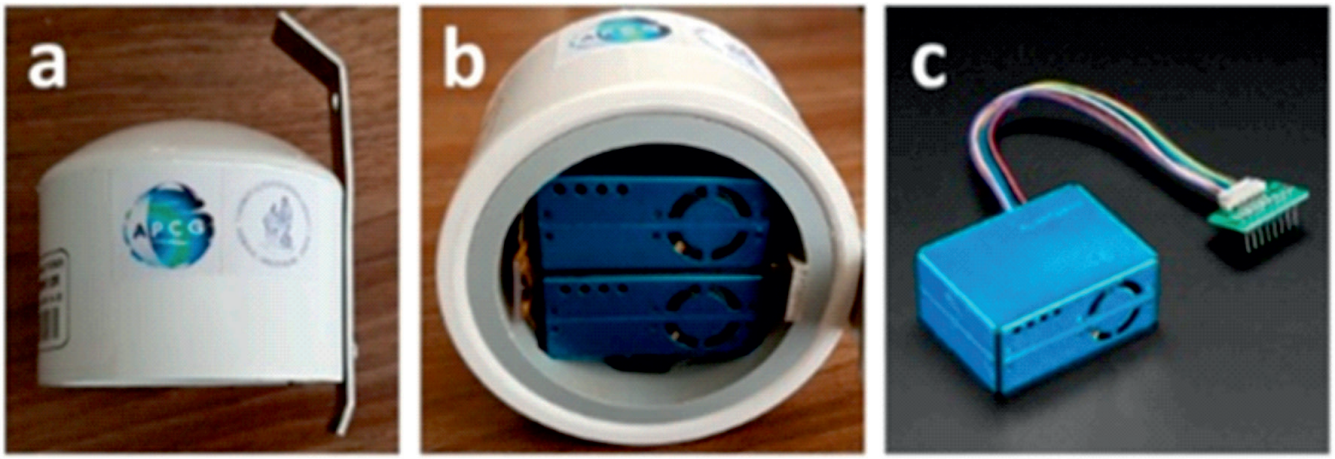

Fig. 2. The configuration of a Purple Air PA-II portable device (a); PMS5003 sensor from above (b); PMS5003 sensor with a microcontroller (c)

Table 2. The relation of AQI air quality index and $PM_{2.5}$ concentration in μg/m^3

AQI Levels (US)	$PM_{2.5}$, μg/m^3	Recommendations (at 24 hours exposure)
0-50 (good)	0-9.0	Good air quality, no or low health risk.
51-100 (satisfactory)	9.1-35.4	Sensitive groups of people are better off avoiding outdoor activity as they may experience respiratory symptoms.
101-150 (bad for sensitive groups of people)	35.5-55.4	People in the middle and particularly sensitive groups are at some risk of eye, skin and throat irritation, as well as respiratory problems.
151-200 (bad)	55.5-125.4	There is an increased likelihood of exacerbation of heart and lung disease in the general population.
201-300 (very bad)	125.5-225.4	Impact on the general population. Sensitive groups should limit outdoor activity.
301+ (dangerous)	225.5+	The general public is at risk of experiencing severe eye, skin and throat irritation, as well as having adverse health effects that can trigger cardiovascular and respiratory diseases. Outdoor activity should be avoided.

[6]Mintz D. (2016).Technical Assistance Document for the Reporting of Daily Air Quality – the Air Quality Index (AQI) U.S. Environmental Protection Agency, Office of Air Quality Planning and Standards (ERA-454/B-16-002), https://www.airnow.gov/sites/default/files/2018-05/aqi-technical-assistance-document-may2016.pdf

of the atmosphere, created difficult conditions for the fulfillment of the planned studies. However, this atypical situation also provided a unique opportunity to investigate the air quality of the city of Apatity during an unusually warm winter. Wind weakening by the beginning of the night on January 26 allowed the first air quality measurements to be made. During the measurements, precipitation in the form of heavy snow was observed; temperature ranged from -3 to -2.4°C. The second series of measurements was conducted in the afternoon of 26.01.2024, at a temperature of -5°C, with a westerly wind of about 1 m/s and showers of slight snow. The final series of air quality measurements was carried out in the morning and afternoon hours of 31.01.2024 under conditions of elevated inversion, a north wind of 0-1 m/s, and a temperature of -3°C.

RESULTS

Tables 4, 6, 8, and 10 show the results of $PM_{2.5}$ concentration measurements during the day on 22.01.2022, the night of 25.01.2024 to 26.01.2024, the day of 26.01.2024, and 31.01.2024, respectively. The graphs in Figs. 3-6 show the spatial distribution of the AQI index for $PM_{2.5}$ particles in Apatity on the indicated dates.

Measurements on 22.01.2022 were carried out in the morning and afternoon hours between 11:00 and 15:00. The meteorological conditions for the measurement period are presented in Table 3 (according to the Apatitovaya weather station, Russia, WMO_ID=22213).

The cloud cover is represented by low-level clouds (St neb. or St fr.) and middle-level clouds (As at 12:00 and Ac or Ac with As or Ns near 15:00).

Here in Table 3 and further, the following notations are used: *T* is the air temperature; P_0 is the atmospheric pressure at the station level; *P* is the atmospheric pressure reduced to the mean sea level; P_a is the baric tendency (change in atmospheric pressure over the last 3 hours); *DD* is the wind direction (at an altitude of 10-12 m above the surface); *Ff* is the wind speed; *U* is relative humidity of the air; *N* is total cloud cover (in %); Nh is the total number of low-level clouds and clouds of vertical development (in %).

The measurement period corresponded to a weak wind of east-southeast direction and no more than 1 m/s speed, or calm. There was no precipitation. Fog, or icy fog, was observed, and the diameter of the frost deposit was 25 mm. There was a strong inversion of about 10°C from the surface to the level of 920 hPa (approximately 660 m).

The results of measurements on 22.01.2022 showed that good air quality with a concentration of $PM_{2.5}$ less than 10 μg/m³ (AQI<50) was observed only at background points 2 and 14, located outside the city. The northeastern part of Apatity has better air quality than the southwestern part. At points 1, 3 (Tik-Guba village), 8 (near ANOF-2), 9, 13 and 18 (located on the side of a highway outside the city limits), air quality is satisfactory, on average, at about 20 μg/m³, that is 8 times lower than 20 min MAC of 160 μg/m³. The corresponding AQI index for $PM_{2.5}$ in these points is less than 100. At points 5 and 7 (southwestern part of the city), a hazardous level of $PM_{2.5}$ was recorded (300.94 μg/m³ and 269.91 μg/m³, respectively, that is approximately 1.9 and 1.7 times higher than 20 min MAC).

The measurements on the night of 25.01.2024 to 26.01.2024 were carried out between approximately 23:30 and 03:00. The northwesterly wind was of about 5 m/s with gusts up to 8 m/s. The first half of the measurement period was accompanied by showers of slight snow, which turned into light or moderate drifting snow closer to 03:00. The main meteorological parameters are presented in Table 5, and the results of measurements are presented in Table 6 and in Fig. 4.

The low-level clouds and clouds of vertical development were presented by Cb, Cu, St, and Frnb at 00:00 and by Sc at 3:00. The middle-level clouds were presented by Ac or Ac with As or Ns.

Very low $PM_{2.5}$ concentrations were obtained during this route. The single instantaneous outliers of values during the measurements led to average concentration values less than measurement error levels. Formally, the estimated measurement error was added to the data in Table 6 with a sign plus/minus for uniformity, but, of course, there can be no negative concentrations.

On the night from 25.01.2024 to 26.01.2024, the measurements detected very good air quality. This may be related to meteorological conditions: the day before

Table 3. Meteorological parameters for the period of 12:00-15:00, 22.01.2022

Time	T, °C	P_0, mmHg	P, mmHg	P_a, mmHg	DD	Ff, m/s	U, %	N, %	Nh, %
12:00	-18.2	751.3	764.9	0.1	-	-	94	100	60
15:00	-18.6	751.4	765.1	0.1	East – South-East	1	93	100	40

Table 4. Results of $PM_{2.5}$ concentration measurements during the period 11:00 – 15:00, 22.01.2022

№ of point	AQI value	$PM_{2.5}$, μg/m³	№ of point	AQI value	$PM_{2.5}$, μg/m³
1	69.47 ±7.77	19.01 ±1.40	10	136.03 ±12.76	49.73 ±2.30
2	36.69 ±8.31	6.61 ±1.50	11	132.17 ±8.29	48.16 ±1.49
3	73.03 ±10.39	20.92 ±1.87	12	103.06 ±12.65	36.33 ±2.28
4	164.81 ±2.81	75.19 ±0.51	13	75.33 ±11.95	22.16 ±2.15
5	374.86 ±63.86	300.94 ±16.00	14	38.06 ±10.92	6.85 ±1.97
6	150.19 ±11.95	54.35 ±2.15	15	90.03 ±9.06	30.05 ±1.63
7	335.19 ±20.08	260.91 ±3.61	16	165.00 ±8.47	75.47 ±1.52
8	69.36 ±6.25	18.96 ±1.12	17	126.06 ±8.62	45.68 ±1.55
9	73.00 ±8.73	20.91 ±1.57	18	72.06 ±6.40	20.40 ±1.15

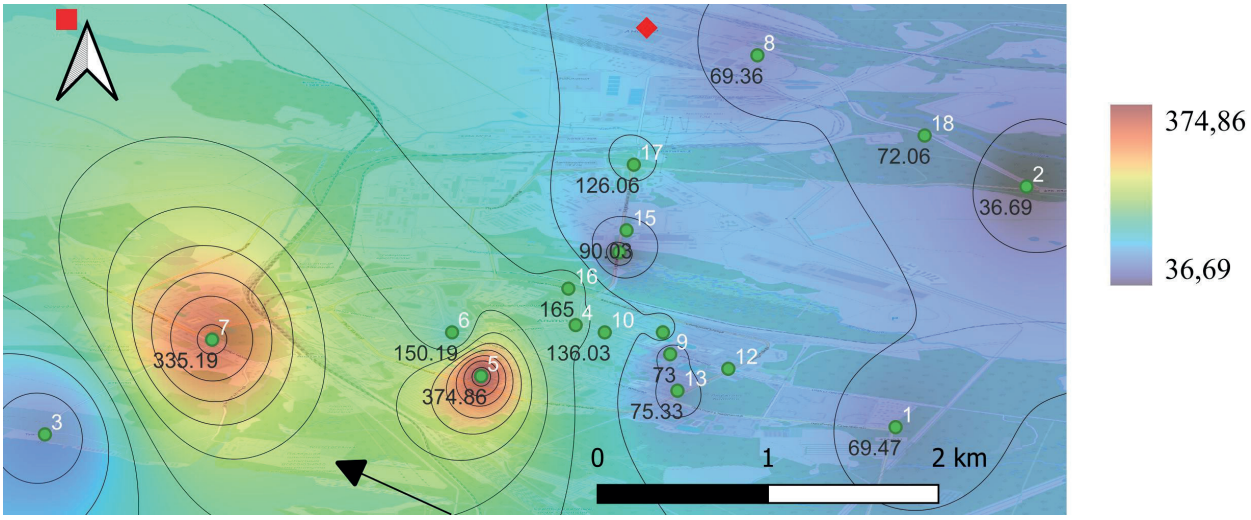

Fig. 3. Spatial distribution of AQI values in Apatity according to measurement data, 11:00-15:00, 22.01.2022. The points denote measurement sites, the numbers of key points are denoted in white color, the red diamond indicates the position of ANOF-2, the red square indicates the part of the ANOF-2 "tailings dump", the black arrow shows the mean wind direction

Table 5. Meteorological parameters for the period of 00:00-03:00, 26.01.2022

Time	T, °C	P_0, mmHg	P, mmHg	P_a, mmHg	DD	Ff, m/s	U, %	N, %	Nh, %
00:00	-2.4	746.6	759.3	1.1	North-West	5	79	90	60
03:00	-3.0	747.2	760.0	0.6	North-West	5	81	70-80	50

Table 6. Results of measurements during the period 23:30-03:00, the night from 25.01.2024 to 26.01.2024

№ of point	AQI value	$PM_{2.5}$, μg/m³	№ of point	AQI value	$PM_{2.5}$, μg/m³
1	2.86 ±3.02	0.51 ±0.54	11	1.71 ±2.14	0.31 ±0.38
2	2.29 ±3.15	0.41 ±0.57	12	0.57 ±1.51	0.10 ±0.27
3	1.71 ±2.14	0.31 ±0.38	13	0.57 ±1.51	0.10 ±0.27
4	3.57 ±7.83	0.64 ±1.41	14	1.71 ±2.14	0.31 ±0.38
5	0.57 ±1.51	0.10 ±0.27	15	2.29 ±3.15	0.41 ±0.57
6	1.14 ±1.95	0.21 ±0.35	16	0.57 ±1.51	0.10 ±0.27
7	0.00 ±0.00	0.00 ±0.00	17	0.00 ±0.00	0.00 ±0.00
8	0.00 ±0.00	0.00 ±0.00	18	2.86 ±1.95	0.51 ±0.35
9	0.57 ±1.51	0.10 ±0.27	19	0.00 ±0.00	0.00 ±0.00
10	2.86 ±3.02	0.51 ±0.54	20	1.71 ±2.14	0.31 ±0.38

measurements had a moderate westerly to northwesterly wind (5-6 m/s). There was no pronounced diurnal temperature variation, and during the measurements, precipitation in the form of snow was observed. Thus, the conditions were favorable for good mixing. During the nighttime measurements, there were practically no pollution sources. Precipitation also contributed to air purification.

In the afternoon of 26.01.2024 measurements were carried out approximately from 14:00 to 17:30 in conditions of weak (about 1 m/s) westerly wind and showers of slight snow. A very slight elevated inversion of about 2°C was observed at an altitude of 800 hPa. The corresponding meteorological parameters are presented in Table 7, and the results of measurements are presented in Table 8 and in Fig. 5.

The low-level clouds and clouds of vertical development were presented by Cb with St, Frnb (or without them). The middle-level clouds were presented by Ac or Ac with As or Ns in the first half of the day. Near 18:00, there were no mid-level clouds.

The measurement results in the afternoon of 26.01.2024 again demonstrated the difference between the air quality in different parts of Apatity. At point 7, the $PM_{2.5}$ concentration was actually 0, and at point 3 (Tik-Guba), the mean concentration was less than the measurement error level. The southwestern part of the city is more polluted than its northeastern part. The concentration of $PM_{2.5}$ did not reach health hazardous levels. At points 15 and 16 in the southwest and south of the city, the maximum values of $PM_{2.5}$ were obtained, which are 2.8 and 3.8 times lower than the instant (20min) MAC, respectively.

The last series of measurements was carried out on the afternoon of 31.01.2024 in the period from 12:00 to 15:00 in light wind conditions (calm around 12:00, turning into a light north wind up to 1m/s closer to 15:00) and an elevated

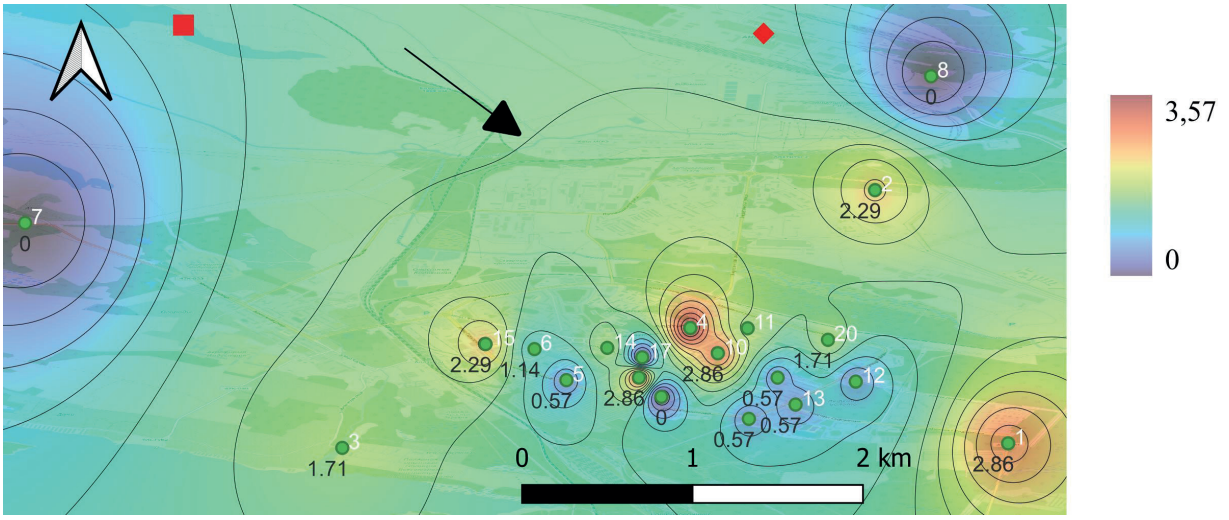

Fig. 4. Spatial distribution of AQI values in Apatity according to measurement data, 23:30-03:00, the night from 25.01.2024 to 26.01.2024. The points denote measurement sites, the numbers of key points are denoted in white color, the red diamond indicates the position of ANOF-2, the red square indicates the part of the ANOF-2 "tailings dump", the black arrow shows the mean wind direction

Table 7. Meteorological parameters for the period of 12:00-18:00, 26.01.2022

Time	T, °C	P_0, mmHg	P, mmHg	P_a, mmHg	DD	Ff, m/s	U,%	N, %	Nh, %
12:00	-5.0	748.1	760.9	-0.3	West	1	93	90	40
15:00	-4.7	747.5	760.3	-0.6	West	1	93	100	70-80
18:00	-5.2	746.9	759.7	-0.6	-	-	95	100	100

Table 8. Results of measurements in the daytime during the period 14:00-17:30 on 26.01.2024

№ of point	AQI value	$PM_{2.5}$, μg/m³	№ of point	AQI value	$PM_{2.5}$, μg/m³
1	54.43 ±8.41	10.94 ±1.51	11	22.86 ±3.61	4.11 ±0.65
2	16.71 ±1.90	3.01 ± 0.34	12	16.21 ±6.14	2.92 ±1.11
3	1.71 ±2.58	0.31 ±0.47	13	52.86 ±10.29	10.10 ±1.85
4	22.50 ±6.24	4.05 ±1.12	14	17.57 ±4.93	3.16 ±0.89
5	71.93 ±12.50	20.33 ±2.25	15	152.14 ±3.37	57.13 ±0.61
6	32.36 ±6.06	5.82 ±1.09	16	115.86 ±7.39	41.53 ±1.33
7	0.00 ±0.00	0.00 ±0.00	17	9.00 ±3.04	1.62 ±0.55
8	33.86 ±7.41	6.09 ±1.33	18	20.07 ±5.90	3.61 ±1.06
9	27.79 ±3.64	5.00 ±0.66	19	84.50 ±8.83	27.08 ±1.59
10	22.93 ±3.87	4.13 ±0.70	20	27.43 ±6.70	4.94 ±1.21

inversion of about 6°C from the level of 875 hPa to 800hPa. Precipitation was not observed during the measurement period. The meteorological parameters are presented in Table 9, and the results of measurements are presented in Table 10 and in Fig. 6.

The low-level clouds were presented by Sc, and the middle-level clouds were presented by Ac or Ac with As or Ns. Near 12:00 high-level clouds (Ci fib, sometimes Ci unc.) were also observed.

The measurements on 31.01.2024 showed no clear division into southwest and northeast parts of the city based on the air quality. No health hazardous $PM_{2.5}$ concentration values were observed. AQI values exceeded 70 at points 4, 15, and 18 within the urban area, as well as at point 3 at Tik-Guba on the lakeshore.

DISCUSSION

The study demonstrated the pronounced difference in air quality under varying winter conditions. In the "classic" cold winter of the Kola Peninsula with strong temperature inversions, $PM_{2.5}$ concentrations, which are unfavorable (and sometimes dangerous for human health) may be found in the city. In the afternoon of 22.01.2022, concentrations in its southwestern part were recorded to exceed the 20-min MAC of $PM_{2.5}$ by approximately 1.9 times. The maxima generally were located near the automobile road (Sovetskaya street) with an extensive territory occupied by garages and by low-rise residential buildings to the south. High concentrations of $PM_{2.5}$ were largely related to fuel combustion in the aforementioned buildings for heating purposes. The measurements were

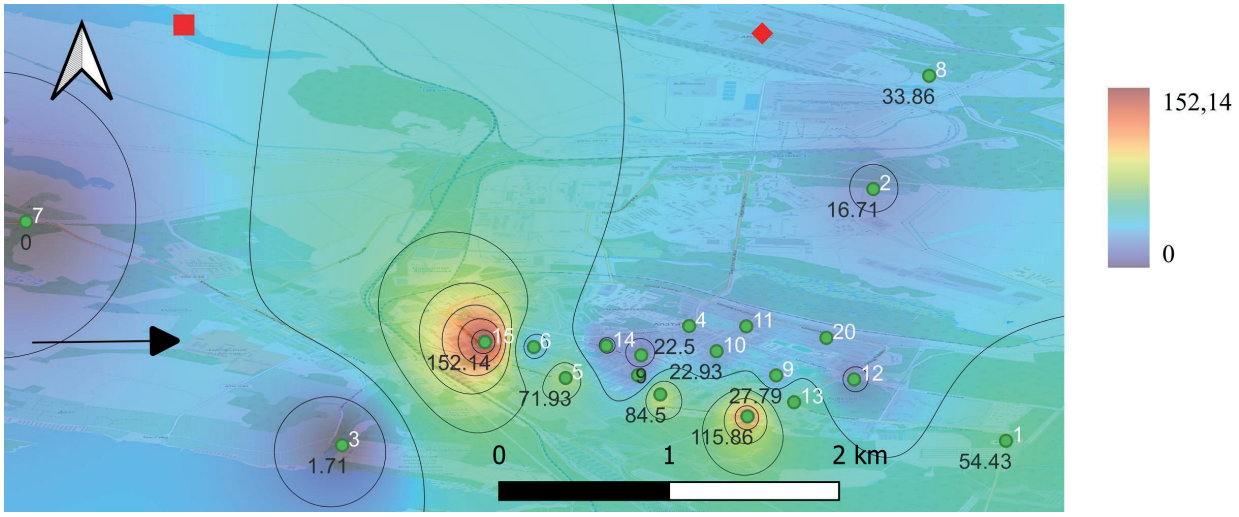

Fig. 5. Spatial distribution of AQI values in Apatity according to measurement data, 14:00-17:30, 26.01.2024. The points denote measurement sites, the numbers of key points are denoted in white color, the red diamond indicates the position of ANOF-2, the red square indicates the part of the ANOF-2 "tailings dump", the black arrow shows the mean wind direction

Table 9. Meteorological parameters for the period of 12:00-15:00, 31.01.2022

Time	T, °C	P_0, mmHg	P, mmHg	P_a, mmHg	DD	Ff, м/с	U, %	N, %	Nh, %
12:00	-3.5	735.7	748.2	-0.7	-	-	69	90	60
15:00	-2.3	735.0	747.4	-0.7	North	1	81	100	70-80

Table 10. Measurement results during the period 12:00-15:00, 31.01.2024

№ of point	AQI value	$PM_{2.5}$, μg/m³	№ of point	AQI value	$PM_{2.5}$, μg/m³
1	7.58 ±2.34	1.37 ±0.42	11	46.46 ±7.69	8.36 ±1.38
2	50.17 ±3.95	8.65 ±0.71	12	8.17 ±2.66	1.47 ±0.48
3	82.50 ±40.05	26.01 ±7.21	13	16.67 ±3.05	3.00 ±0.55
4	85.46 ±54.62	27.59 ±11.04	14	26.25 ±7.26	4.73 ±1.31
5	21.00 ±9.79	3.78 ±1.76	15	80.50 ±17.16	24.93 ±3.09
6	19.46 ±5.84	3.50 ±1.05	16	14.54 ±3.55	2.62 ±0.64
7	5.33 ±1.93	0.96 ±0.35	17	19.29 ±6.84	3.47 ±1.23
8	15.42 ±4.52	2.78 ±0.81	18	71.50 ±6.67	20.10 ±1.20
9	27.54 ±9.78	4.96 ±1.76	19	54.63 ±1.64	11.05 ±0.29
10	23.42 ±3.39	4.22 ±0.61	20	48.46 ±5.87	8.72 ±1.06

carried out in calm conditions or very weak wind of the East–South-East direction. There was also a calm in the previous hours (from 06:00 to 12:00) or a wind of the east or southeast direction up to 1 m/s (at night). Therefore, since ANOF-2 and its tailings dump are located to the north and northwest of the city, respectively, the observed high concentrations of $PM_{2.5}$ in the southern and southwestern parts of the city cannot be associated with advection from the enterprise. Thus, when winter inversions are observed, stove heating can contribute to the accumulation of hazardous concentrations of $PM_{2.5}$.

Routine air quality measurements in the afternoon of 26.01.2024 from 14:00-17:30 also showed the negative difference in the air quality between the southwestern part of the city and its northeastern part. A western wind of less than 1 m/s was observed during this period, which ceased in the evening, and windless weather was established. Air temperatures ranged from -5 to -6°C. The $PM_{2.5}$ concentration values significantly increased compared to the night measurements conducted from 25.01.2024 to 26.01.2024, specifically from 23:30 to 3:00. $PM_{2.5}$ concentrations did not reach health-hazardous levels, but the maximum concentration values at the points 15 and 16 reached 0.4 and 0.3 of instant (20 min) MAC, respectively. Point 13 (the Pushkin City Park) was characterized by high values of $PM_{2.5}$ particle concentration in two cases out of three route measurements. This finding may be explained by the accumulation of pollution from nearby sources due to weaker ventilation under the plant canopy.

High values of $PM_{2.5}$ concentration at the southern and southwestern borders of the city correlate with wind direction and the assumption about the presence of pollution sources (automobile road, garages, stove heating) at the southern and southwestern outskirts of Apatity and in the nearest suburb. At the same time, in these meteorological conditions, urban development

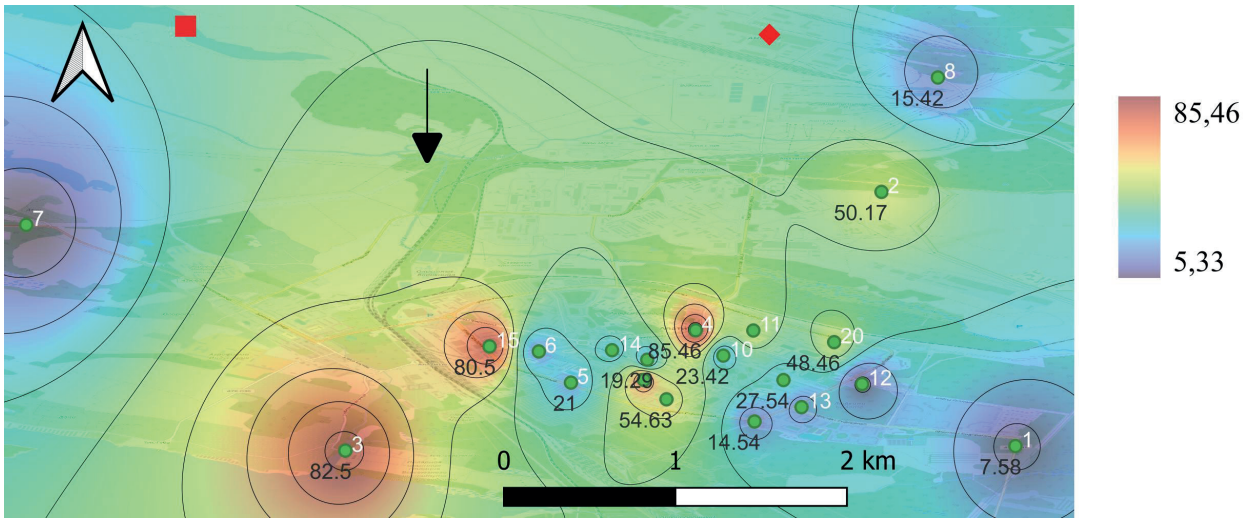

Fig. 6. Spatial distribution of AQI values in Apatity according to measurement data, 12:00-15:00, 31.01.2024. The points denote measurement sites, the numbers of key points are denoted in white color, the red diamond indicates the position of ANOF-2, the red square indicates the part of the ANOF-2 "tailings dump", the black arrow shows the mean wind direction

turns out to be a good barrier for pollution spreading, as there is an accumulation of $PM_{2.5}$ particles on the southern and southwestern border of the city, and it is enveloped by polluted air.

Final measurements of the air quality in Apatity were made in the afternoon of 31.01.2024 when weather conditions stabilized. The measurement period was characterized by light wind weather (the day before, 30.01.2024 there was a wind of western, northwestern direction with the speed of 2-4 m/s) and air temperatures between -2 and -3°C. An elevated temperature inversion of about 6°C was observed from the level of 875 hPa to 800 hPa. Maximum concentration values of $PM_{2.5}$ were observed at points 3, 4, 15 (>24.9 μg/m^3) and 18 (>20 μg/m^3). On the night of 31.01.2024, the wind was western or southwestern up to 3 m/s, which changed direction to eastern by 6:00. By 9:00, a calm was established, which lasted until 12:00. Closer to 15:00, a weak (up to 1m/s) northern wind was observed; therefore, closer to 15:00, an increase in the concentration of $PM_{2.5}$ in the northern part of the city may be explained by advection from ANOF-2. However, the high concentrations of $PM_{2.5}$ on the southern borders of the city and especially at point 3, located in the Tick-Guba village, are most likely related to the influence of stove heating because an accumulation of pollution happens in the conditions of windless weather and weak mixing.

At the time of measurements at point 15, snow plowing equipment was operating nearby. Therefore, a series of measurements was carried out directly at point 15 and at a distance of about 100 m from it in the visibility zone of snowplowing equipment. The mean $PM_{2.5}$ concentration values were almost identical (about 25 μg/m^3). However, the values in the nearest point 6 (two front yards separated from point 15 by residential buildings) were significantly lower (about 3.5 μg/m^3). It suggests that, under the conditions of weak mixing, urban development (mainly 5-storey buildings) in Apatity contributes to the accumulation of pollution near medium-height residential houses in the presence of sources. However, the same apartment buildings prevent a significant spatial spread of pollution.

CONCLUSIONS

During the winter expeditions of 2022 and 2024, we observed wide range variability of synoptic situations and study the microclimate of Apatity under conditions of a "classic" cold winter, with the temperature inversions that prevent air mixing present, as well as "warm" conditions for Russian Arctic. The conducted measurements allow us to better understand the effect of climatic changes on the region and its microclimatic features. Measurement results have demonstrated that, under the conditions of temperature inversion in the city, dangerous levels of $PM_{2.5}$ particle pollutant concentrations (up to 300 μg/m^3, that is approximately 1.9 times higher than 20 min MAC = 160 μg/m^3) are observed. A number of observations indicate that such pollution is largely caused by motor vehicles and fuel combustion for heating purposes in low-rise residential areas. In addition, the study has established that warm winters, characterized by higher wind speeds due to cyclonic activity and heavy precipitation, significantly improve air quality in the city of Apatity.

REFERENCES

Aloyan A.E. (2002). Dynamics and kinetics of gas impurities and aerosols in the atmosphere. Lections. M. IPM-RAS – 201p, ISBN 5-901854-05-5 (in Russian)

Arnold S. R., Law K. S. Brock C. A., et al. (2016). Arctic Air Pollution: Challenges and Opportunities for the next Decade. Elem. Sci. Anthr., 4, 000104, DOI: 10.12952/journal.elementa.000104

Bai N., Khazaei M., van Eeden S.F., Laher I. (2007). The pharmacology of particulate matter air pollution-induced cardiovascular dysfunction. Pharmacology & Therapeutics, 113(1), 16-29

Brozovsky J., Gaitani N., Gustavsen A. (2020). A systematic review of urban climate research in cold and polar climate regions. Renew. Sust. Energ. Rev., 110551, https://doi.org/10.1016/j.rser.2020.110551.

Burtsev I.I., Burtseva L.V. (1971). Comparison of characteristics of washout of hygroscopic and non-hygroscopic aerosol by cloud droplets. Proc. Institute of Experimental Meteorology, 21. (in Russian)

Chen D., Billmire M., Loughner C.P., Bredder A., French N.H.F., Kim H.C., Loboda T.V. (2023). Simulating spatio-temporal dynamics of surface PM2.5 emitted from Alaskan wildfires Science of the Total Environment, 898, art. no. 165594 DOI: 10.1016/j.scitotenv.2023.165594

Chubarova N.Ye., Zhdanova Ye.Yu., Androsova Ye.Ye., et al. (2020). The aerosol urban pollution and its effects on weather, regional climate and geochemical processes. Monograph, Max-Press, Moscow, ISBN 978-5-317-06464-8 (in Russian)

Di Q., Wang Y., Zanobetti A., Wang Y., Koutrakis P., Choirat C., Dominici F., Schwartz J.D. (2017). Air Pollution and Mortality in the Medicare Population. N Engl J Med., 376(26), 2513-2522, DOI: 10.1056/NEJMoa1702747.

Davy R. (2018). The climatology of the atmospheric boundary layer in contemporary global climate models. J. Clim., 31, 9151–9173, https://doi.org/10.1175/JCLI-D-17-0498.1

Dominici F., Peng R.D., Bell M.L., Pham L., McDermott A., Zeger S.L., Samet J.M. (2006). Fine particulate air pollution and hospital admissions for cardiovascular and respiratory diseases. JAMA, 295(10), 1127-1134, DOI: 10.1001/jama.295.10.1127

Gorbarenko E.V., Eremina I.D. (1998). The role of precipitation in the process of atmospheric aerosol purification. Optics of atmosphere and ocean, 11(5), 495-499 (in Russian)

Groot Zwaaftink C.D., Aas W., Eckhardt S., Evangeliou N., Hamer P., Johnsrud M., Kylling A., Platt S.M., Stebel K., Uggerud H., Yttri K.E. (2022). What caused a record high PM10 episode in northern Europe in October 2020? Atmospheric Chemistry and Physics, 22 (6), 3789 – 3810 DOI: 10.5194/acp-22-3789-2022

Järvi L., Grimmond C.S.B., McFadden J.P., Christen A., Strachan I.B., Taka M., et al. (2017). Warming effects on the urban hydrology in cold climate regions. Sci. Rep., 7, 1–8, https://doi.org/10.1038/s41598-017-05733-y.

Kholodov A.S., Kirichenko K.Yu., Zadornov K.S., Golokhvast K.S. (2019). The effect of atmospheric air suspended solids in populated areas on human health. Bulletin of the Kamchatka State Technical University, 49, 81-88, DOI: 10.17217/2079-0333-2019-49-81-88 (in Russian)

Konstantinov P.I., Varentsov M.I., Shartova N.V. (2022). North Eurasian thermal comfort indices dataset (NETCID): new gridded database for the biometeorological studies. Environmental Research Letters, 17(8), 085006. DOI: 10.1088/1748-9326/ac7fa9

Kotchenruther R. A. (2016). Source Apportionment of PM 2.5 at Multiple Northwest U.S. Sites: Assessing Regional Winter Wood Smoke Impacts from Residential Wood Combustion. Atmos. Environ., 142, 210– 219, DOI: 10.1016/j.atmosenv.2016.07.048

Kowalska M., Kocot K. (2016). Short-term exposure to ambient fine particulate matter (PM2.5 and PM10) and the risk of heart rhythm abnormalities and stroke. Postepy. Hig. Med. Dosw., [online], 70, 1017-1025, DOI: 10.5604/17322693.1220389 (in Polish)

Lappalainen H., Petäjä T., Vihma T., et al. (2022) Overview: Recent advances in the understanding of the northern Eurasian environments and of the urban air quality in China – a Pan-Eurasian Experiment (PEEX) program perspective. Atmos. Chem. Phys., 22, 4413–4469, https://doi.org/10.5194/acp-22-4413-2022.

Pkhalagov O.A., Uzhegov V.N. (1980). Influence of heavy rainfall on optical properties of sea coastal haze. Izv. of the Academy of Sciences. USSR. Ser. FAO, 16(4), 345-351 (in Russian)

Plaude N.O., Stulov E.A., Parshutkina I.P., Pavlyukov Yu.B., Monakhova N.A. (2012). Influence of precipitation on aerosol concentration in the surface layer of the atmosphere. Meteorology and Hydrology, 5, 53-63 (in Russian)

Polichetti G., Cocco S., Spinali A., Trimarco V., Nunziata A. (2009). Effects of particulate matter (PM10, PM2.5 and PM1) on the cardiovascular system. Toxicology, 261(1-2), 108, DOI: 10.1016/j.tox.2009.04.035

Prosviryakova I.A., Shevchuk L.M. (2018). Hygienic assessment of PM10 and PM2.5 particulate matter content in atmospheric air and health risk for residents in the zone of influence of emissions from stationary sources of industrial enterprises. Health risk analysis, №2, 14-22, DOI: 10.21668/health.risk/2018.2.02 (in Russian)

Sartz P.P., Hasan M.I., Aggarwal S. (2023). Air quality impacts in the vicinity of a chemical herder mediated in-situ burn for Arctic oil spill response. Science of the Total Environment, 892, art. no. 163860 DOI: 10.1016/j.scitotenv.2023.163860

Seinfeld J.H., Pandis S.N. (2006). Atmospheric Chemistry and Physics. From Air Pollution to Climate Change. Second edition. A Wiley-Interscience Publication, John Wiley & Sons, Inc., 1225 p.

Simpson W.R., Mao J.; Fochesatto G.J., et. al. (2024). Overview of the Alaskan Layered Pollution and Chemical Analysis (ALPACA) Field Experiment. ACS EST Air, 1(3), 200-222, https://doi.org/10.1021/acsestair.3c00076

Stavroulas I., Grivas G., Michalopoulos P., Liakakou E., Bougiatioti A., Kalkavouras P., Fameli K.M., Hatzianastassiou N., Mihalopoulos N., Gerasopoulos E. (2020). Field Evaluation of Low-Cost PM Sensors (Purple Air PA-II) Under Variable Urban Air Quality Conditions, in Greece. Atmosphere, 11(9), 926, https://doi.org/10.3390/atmos11090926

Strelyaeva A.B., Barakaeva N.S., Kalyuzhina E.A., Nikolenko D.A. (2014). Analysis of sources of atmospheric air pollution by fine dust. Internet-vestnik VolgGASU. Series: Polytechnic, 3(34), [online], URL: http://vestnik.vgasu.ru/?source=4&articleno=1715 (in Russian)

Strelyaeva A.B., Lavrentieva L.M., Lupinogin V.V., Gvozdikov I.A. (2017). Studies of dustiness in the residential area located near industrial enterprises by PM10 and PM2.5 particles. Engineering Bulletin of the Don, 45(2), 154-156 (in Russian)

Tanzer R., Malings C., Hauryliuk A., Subramanian R., Presto A.A. (2019). Demonstration of a Low-Cost Multi-Pollutant Network to Quantify Intra-Urban Spatial Variations in Air Pollutant Source Impacts and to Evaluate Environmental Justice. Int. J. Environ. Res. Public Health, 16, 2523, https://doi.org/10.3390/ijerph16142523

Tryner J., L'Orange C., Mehaffy J., Miller-Lionberg D., Hofstetter J. C., Wilson A., Volckens J. (2020). Laboratory evaluation of low-cost PurpleAir PM monitors and in-field correction using co-located portable filter samplers. Atmospheric Environment, 220, 117067.

Varentsov M., Konstantinov P., Repina I., Artamonov A., Pechkin A, Soromotin A., Esau I., Baklanov A. (2023). Observations of the urban boundary layer in a cold climate city. Urban Climate, 47, 101351, Doi: 10.1016/j.uclim.2022.101351

Varentsov M.I., Repina I.A., Glasunov A.V., Samsonov T.E., Konstantinov P.I., Stepanenko V.M., Lykosov V.N., Artamonov A.Yu., Debolskiy A.V., Pechkin A.S., Soromotin A.V. (2022). Features of the atmospheric boundary layer of the city of Nadym according to experimental measurements and vortex-resolving modeling. Bulletin of the Moscow University. Seria 5: Geography, 6, 64-78 (in Russian)

Wallace J.M., Hobbs P.V. (2006). Atmospheric science: an introductory survey. Elsevier, Vol.92.
Wang Y., Hopke P. K. (2014). Is Alaska Truly the Great Escape from Air Pollution? – Long Term Source Apportionment of Fine Particulate Matter in Fairbanks, Alaska. Aerosol Air Qual. Res., 14 (7), 1875– 1882, DOI: 10.4209/aaqr.2014.03.0047
Ward T., Trost B., Conner J., Flanagan J., Jayanty R. K. M. (2012). Source Apportionment of PM2.5 in a Subarctic Airshed - Fairbanks, Alaska. Aerosol Air Qual. Res., 12, 536- 543, DOI: 10.4209/aaqr.2011.11.0208
Wetzel C., Brümmer B. (2011). An Arctic inversion climatology based on the European Centre reanalysis ERA-40. Meteorol., Z. 20, 589–600, https://doi.org/10.1127/0941-2948/2011/0295.
Yasunari T.J., Kajikawa T., Matsumi Y., Kim K.-M. (2024). Increased atmospheric PM2.5 events due to open waste burning in Qaanaaq, Greenland, summer of 2022 Atmospheric Science Letters, 25 (7), art. no. e1231 DOI: 10.1002/asl.1231
Zagorodnov S.Yu. (2018). Dust pollution of urban atmospheric air as an underestimated risk factor for human health. Bulletin of Perm National Research Polytechnic University. Applied ecology. Urbanistics., 2(30), 124-133 (in Russian)
Zagorodnov S.Yu., Mai I.V., Kokoulina A.A. (2019). Fine particles (PM2.5 and PM10) in the atmospheric air of a large industrial region: problems of monitoring and rationing in the composition of industrial emissions. Hygiene & Sanitation, 98(2), 142-147, DOI: http://dx.doi.org/10.18821/0016-9900-2019-98-2-142-147 (in Russian)

RESEARCH PAPER

THE COVID-19 PANDEMIC AND ITS CONSEQUENCES FOR PUBLIC HEALTH: MEDICO-GEOGRAPHICAL ASPECT

Svetlana M. Malkhazova[1,2], Fedor I. Korennoy[3], Tamara V. Vatlina[4], Li Wang[5], Dmitry S. Orlov[2*]

[1]Faculty of Geography, Shenzhen MSU-BIT University, Shenzhen, 517182, China
[2]Faculty of Geography, Lomonosov Moscow State University, Moscow, 119991, Russian Federation
[3]Federal Center for Animal Health (FGBI ARRIAH), Vladimir, 600901, Russian Federation
[4]Faculty of Natural Sciences and Geography, Smolensk State University, Smolensk, 214000, Russian Federation
[5]Institute of Geographic Sciences and Natural Resources Research, CAS, Beijing, 100101, China
***Corresponding author:** orlovds@list.ru
Received: January 23th 2025 / Accepted: March 5th 2025 / Published: June 30th 2025
https://doi.org/10.24057/2071-9388-2025-3857

ABSTRACT. The paper consists of a review of the public health consequences of the COVID-19 pandemic. The study focuses on the assessment of the impact of the COVID-19 pandemic on the incidence of the leading disease categories, such as Diseases of the Circulatory System (DCS), Malignant Neoplasms (MN) and External Causes of Morbidity and Mortality (EC) in the Russian Federation. Time series of standardized incidence for each category were examined for the period 2007–2019 (pre-COVID-19), and 2020–2023 (COVID-19 and post-COVID-19). The post-COVID trends were compared to those hypothetically expected with no COVID impact. For the majority of the RF regions, upward trends of DCS and MN incidence were detected both in pre-COVID and post-COVID years. In the first year of the pandemic, a decline in morbidity was observed for all categories. The EC incidence trend was decreasing in pre-COVID years, but it increased in the post-COVID period. The median incidence rates of MN in the post-COVID period were lower than expected in most of the country, while those of DCS demonstrated heterogeneous distribution with no clear spatial patterns. A decline in the incidence of all nosoforms in 2020 may not have been related to the actual decrease of morbidity, but rather to the significant reduction of healthcare and diagnostics accessibility, which led to a reduction in the detection of diseases new cases.

KEYWORDS: COVID-19, Russian Federation, ICD disease categories, time series, incidence trends, trend change point, public health consequences

CITATION: Malkhazova S. M., Korennoy F. I., Vatlina T. V., Wang Li, Orlov D. S. (2025). The Covid-19 Pandemic And Its Consequences For Public Health: Medico-Geographical Aspect. Geography, Environment, Sustainability, 2 (18), 178-188
https://doi.org/10.24057/2071-9388-2025-3857

ACKNOWLEDGEMENTS: The study was carried out with the support of Lomonosov Moscow State University research project No. 121051100137-4 and supported by MSU Development Program of the Interdisciplinary Scientific and Educational School «Future Planet and Global Environmental Change» and MSU Program of Development (P. 1220).

Conflict of interests: The authors reported no potential conflict of interests.

INTRODUCTION

Coronavirus infection COVID-19 is a dangerous infectious disease caused by the RNA-containing virus SARS-CoV-2, which often has a multisystemic nature of infection and has a multifaceted impact on public health (Lu et al. 2020; Peng 2020; Richardson et al. 2020). Due to the very high contagiousness of the virus, the disease has spread rapidly throughout the world, affecting millions of people in different countries. Currently, more than 777 million people are infected, of whom more than 7 million people have died (as of December 8, 2024)[1]. Although WHO declared the end of the COVID-19 pandemic in May 2023, coordination of the global response to the pandemic continues[2]. Apart from the profound environmental, economic, and socio-cultural changes in the world (Bedford et al. 2020; Khalifa et al. 2021), such as lockdown measures and a sharp reduction in industrial production have resulted in a decrease in anthropogenic emissions into the atmosphere, resulting in a decrease in the concentration of air pollutants and greenhouse gas levels in many regions, especially in large urban agglomerations (Ginzburg et al. 2020; Baklanov et al. 2021). The COVID-19 pandemic has had many consequences for global health in addition to those caused by the disease itself.

Prolonged exposure to the virus can lead to post-COVID syndrome, which manifests itself in various chronic symptoms. This has been diagnosed and confirmed in most countries with very diverse symptoms, covering neurological complications, cardiovascular symptoms, chronic health outcomes, etc.

[1] WHO. (2020, February 28). Director-General's opening remarks at the media briefing on COVID-19. Retrieved from https://www.who.int/director-general/speeches/detail/who-director-general-s-opening-remarks-at-the-media-briefing-on-covid-19-28-february-2020.
[2]WHO. (n.d.). Coronavirus (COVID-19) Dashboard. Retrieved from https://data.who.int/dashboards/covid19/deaths

(Ong et al. 2023; Filev et al. 2024). The situation is especially complicated in the case of the development of combined pathology in patients under observation for chronic non-communicable diseases.

The high contagiousness of COVID-19 and the variability of clinical manifestations have led to an increase in the number of hospitalizations, which required significant resources from healthcare institutions. There has been a decrease in the number of hospital visits during the pandemic, which has led to an increase in mortality from other causes. In addition, the pandemic has caused significant changes in the lifestyle of the population due to the transition to remote working, the introduction of restrictions on movement and social interaction, and the deterioration of the financial situation, and all these factors have adversely affected the mental health of the population.

The purpose of this article is to analyze the consequences of the COVID-19 pandemic on public health and its impact on the dynamics of morbidity among the leading classes of diseases in the Russian Federation in the COVID and post-COVID periods.

To achieve this goal, the following objectives were formulated:

1) review of the literature on the main consequences of the COVID-19 pandemic for public health;

2) collecting epidemiological information and creating a database on the incidence of the population with leading categories of diseases in the Russian Federation;

3) modeling morbidity trends;

4) creating a series of medico-geographical maps to identify geographic differentiation in the dynamics of morbidity in the pre-COVID, COVID, and post-COVID periods.

MATERIALS AND METHODS

Materials

The review of the literature on the main consequences of the COVID-19 pandemic for public health, as well as the healthcare sector, was prepared on the basis of a significant number of publications according to the eLibrary, Google Scholar, PubMed, Scopus, and Web of Science databases.

Three categories of diseases according to the international classification ICD-10 were considered for analysis in the Russian Federation: II Neoplasms, IX Diseases of the circulatory system, and XX External causes of morbidity and mortality. These categories are the leading causes of death for the period between 2007 and 2023, accounting for more than 70% of all causes of mortality in the population (Fig. 1). Data on relative morbidity (per 100 thousand people) annually for the period 2007-2023 were obtained from official information of the Federal Service for State Statistics (Rosstat)[3].

Methods

To assess changes in the dynamics of incidence in the population before and after the emergence of COVID-19, the median incidence values were considered for two periods: 2007–2019 (pre-COVID-19) and 2020–2023 (COVID-19 and post-COVID). For each of the periods, incidence trends were also determined by fitting a linear regression model using the Least Squares Method. The reliability of the trend was assessed using the determination coefficient R^2 (the proportion of variation explained by regression). A trend was considered reliable if $R^2 \geq 0.5$.

Additionally, the change in incidence in the first year of the pandemic (2020) was assessed compared to the previous year. Furthermore, expected incidence values for the period from 2020 to 2023 were modeled in the absence of COVID-19 and compared with the observed values for this period. The simulation was carried out using a linear trend for the period from 2007 to 2019. A difference between the expected and observed incidence values was mapped. A spatial pattern of their distribution was assessed by Moran's I global spatial autocorrelation test (Getis and Ord 1992). Statistically significant test results (*p-value* ≤ 0.05) indicate the presence of spatial autocorrelation (i.e., high values tend to group together forming clusters), while statistically insignificant *p-value* >0.05 suggests nearly random spatial distribution.

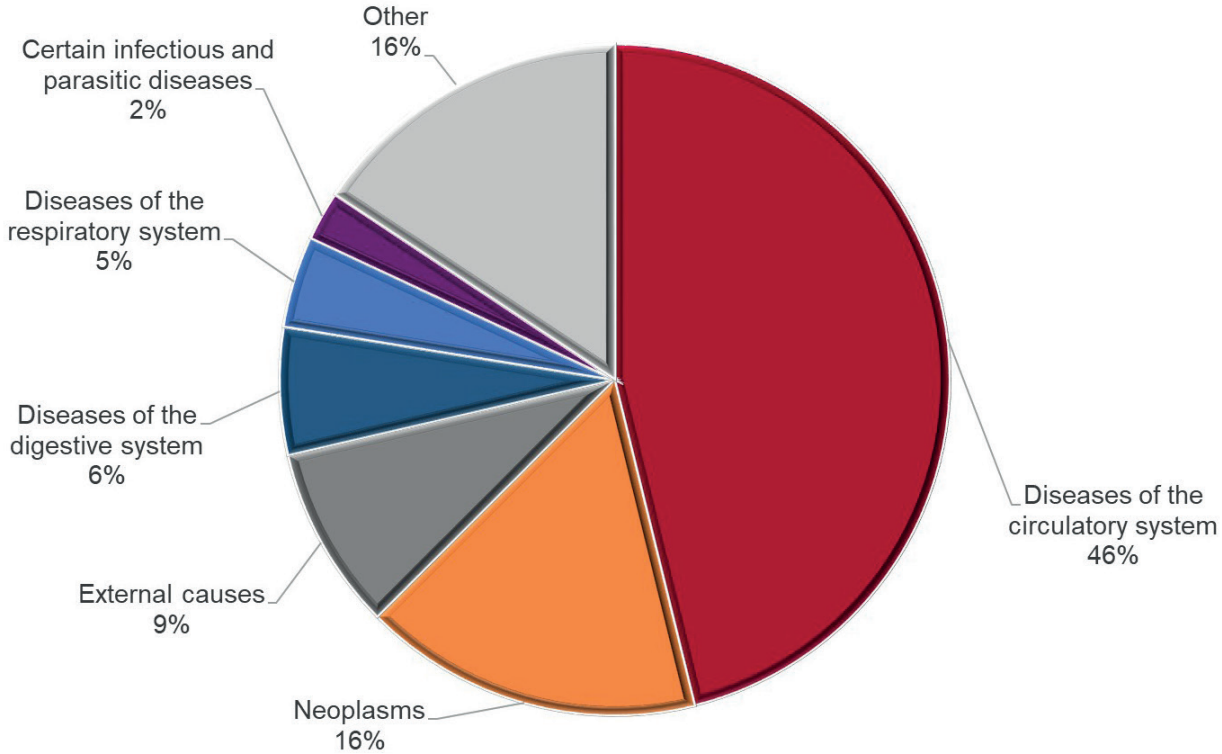

Fig. 1. Mortality structure of the population in the Russian Federation. 2023

[3]Federal State Statistics Service. URL: https://eng.rosstat.gov.ru/. Accessed 09.12.24

Study area

The Russian Federation is a country located in both Europe and Asia, ranking first in the world in terms of area (more than 17 million km^2). The country's population is more than 146 million people with an average density of 8.53 people per km2. Administratively, the country is divided into 89 first-level units (subjects or regions), represented by oblasts, republics, autonomous okrugs, and three cities of federal significance. The research was conducted on the regional level of 85 subjects, for whom incidence data are available for the entire analyzed period.

COVID-19 in Russia

The first cases of COVID-19 were registered in Russia in the first ten days of March 2020. By April 16, COVID-19 had been recorded in all regions of the country, and by the end of the month, the number of cases in Russia exceeded 100,000. A sharp rise occurred in late April - early May when the number of infections increased from 6,000 to 11,000 reaching a maximum on May 11, 2020 (11,656 cases). Then, in the summer months of 2020, the incidence rate began to decline (Malkhazova et al. 2021).

After the number of cases decreased to less than 5,000 per day by the end of August 2020, a new increase in cases ("second wave") emerged in the fall and was considered most intense in the second half of September 2020. In November, more than 20,000 infected people were detected each day. The second wave of the disease peaked in late December 2020 when the number of daily COVID-19 cases was almost 30,000, more than 2.5 times higher than the corresponding figure during the first wave. According to Rosstat, 144,691 people with coronavirus infection died in Russia in 2020, which accounted for 6.8% of the total number of deaths in 2020. Despite significantly higher incidence and mortality rates, the country did not introduce a general lockdown. Essentially, only the universal mask regime and a ban on mass events were maintained on the federal level. The decision to apply additional restrictive measures was made by regional authorities. In December 2020, vaccination against COVID-19 began in Russia amid an increase in the number of infections. From January to June 2021, the number of infections decreased. For example, 27,039 cases of COVID-19 were confirmed on January 1, while the number was only 9,500 on June 1.

A new surge in COVID-19 cases (the "third wave") was recorded in Russia in the last ten days of June 2021. The number of new cases exceeded 20,000 on June 24. Thus, the growth in registered cases of infection since the beginning of the month was 100%. During August, as well as the first and second ten days of September, the daily number of infected people was between 17,813 and 19,905.

Another surge in cases called the "fourth wave" was recorded on September 23, 2021. A new maximum since the beginning of the pandemic was recorded on November 6, 2021, when the daily number of cases reached 41,335.

Thus, despite the measures taken, Russia turned out to be one of the most affected countries.

In the following years, the COVID-19 situation gradually stabilized. The coronavirus has ceased to be a source of anxiety and a serious burden on the healthcare system as it was in the first year of the pandemic, but its strains are still circulating and continuing to mutate.

RESULTS

Consequences of the COVID-19 pandemic. Literature review

Many researchers, analyzing the impact of the SARS-CoV-2 virus on the human body, distinguish between "acute health effects" and long-term health effects (so-called "long COVID") (Yong and Liu 2021; O'Mahoney et al. 2022; Lee et al. 2023).

The main manifestation of COVID-19 is a respiratory disease, ranging from mild symptoms to severe pneumonia and acute respiratory distress syndrome. In addition to the respiratory system, the virus can affect multiple organs, leading to complications such as cardiovascular problems, neurological symptoms, loss of taste and smell, and headaches (McBane 2021; Poyiadji et al. 2021).

A significant proportion of people experience persistent symptoms after the acute phase, called post-COVID syndrome. These symptoms can include fatigue, cognitive impairment (Rodríguez-Rey et al. 2020; Ueda et al. 2021) and negative psychological effects such as depression and anxiety (Nguyen et al. 2020; Zhang and Ma 2020). Even mild cases of the disease can lead to long-term cognitive problems, especially in older adults (Bianchetti et al. 2020; Mendes et al. 2021; Poloni et al. 2021).

Acute symptoms and long-term complications are most common in adult patients, with an average age of 34 to 59 years (Bai et al. 2020; Wang et al. 2020). The highest proportion of severe cases occurs in patients over 60 years old and in people with certain comorbidities, such as cardiovascular disease, cerebrovascular disease, and diabetes (Chen et al. 2020; Fei et al. 2020; Petrilli et al. 2020).

Preconditions such as cardiovascular disease and chronic lung disease, smoking and alcohol consumption are risk factors for long COVID symptoms.

In addition, a cohort study based on 541 pregnant women found that pregnant women who were infected by COVID-19 during pregnancy had a higher level of coagulation disorder, indicating that pregnant women were more likely to have postpartum hemorrhage than those without infection (Zhang and Zhang 2024). Women have a higher incidence of joint or muscle pain. Chest pain and tightness are more common at older ages (45 years old).

The impact of COVID-19 on mortality

Several publications characterizing the situation in Russia during the pandemic are devoted to the high level of excess mortality. This indicator is considered a representation of the impact of the pandemic, including direct (deaths from COVID-19) and indirect (impact on the healthcare system and socio-economic factors) effects. The presence of excess mortality in all regions of the Russian Federation is confirmed by all authors who have studied this topic (Danilova 2020; Kotov et al. 2022; Kvasha 2022, etc.), the differences are only in the quantitative parameters of these estimates. According to some authors, excess mortality in 2020 amounted to 288,000 people, and COVID-19 caused approximately 60% of those deaths (Goroshko et al. 2022). However, another study says that official data on mortality from COVID-19 in Russia are underestimated by more than two times (Livshits and Neklyudova 2020; Druzhinin and Molchanova 2021).

According to the Federal State Statistics Service, the natural population decline exceeded one million people in 2021 (Federal Service..., 2024).

COVID-19 has caused excess mortality in Russia. An assessment of excess mortality in the regions of Russia from April 2020 to February 2021 compared to the five-year average based on regression analysis showed (Kotov et al. 2022) that the most significant factors increasing excess mortality are the share of the elderly population and the employment structure represented by the share of workers in the manufacturing industry (economic activity C, European Skills, Competences and Occupations classification).

An assessment of excess mortality rates for the Russian Federation and its regions, as well as equivalent rates for 36 countries, showed that Russia had the highest excess mortality rate among all the countries considered. Most excess mortality cases were registered in the fourth quarter of 2020, and the level and trajectory of excess mortality in Russia and most Eastern European countries differed from those in Western countries. While the cumulative number of COVID-19 cases and deaths was positively correlated with excess mortality across countries, in Russia an inverse negative relationship was observed between excess mortality and cumulative incidence at the regional level, which may be due to common underreporting of COVID-19 cases (Timonin et al. 2021).

Rosstat published monthly statistics on deaths from coronavirus infection, distinguishing four groups of deaths of patients diagnosed with COVID-19: 1) cases in which coronavirus was the main cause of death; 2) cases requiring additional research, when it is assumed that death occurred due to coronavirus; 3) cases in which coronavirus as a concomitant disease affected the underlying disease that caused death; 4) cases in which coronavirus did not cause complications of the diseases that caused death.

As a result of a comparative analysis of COVID-19-related mortality data, significant territorial heterogeneity was revealed across regions of the Russian Federation (Goldstein 2020).

The impact of COVID-19 on chronic non-communicable diseases

Special attention was paid by the experts to the analysis of the influence of COVID-19 on the occurrence of new cases of chronic non-communicable diseases and the aggravation of their course (Shelgunov et al. 2023). The literature review conducted by the authors is based on the results of 64 papers published between April 1, 2020 and January 31, 2023, exploring the impact of COVID-19 on various organs and systems as well as the aggravation of chronic non-communicable diseases.

The analysis indicated that the infection not only affected various organs and systems and increased the risk of complications in the course of chronic non-communicable diseases but also contributed to the emergence of new cases.

It is understood that COVID-19 is the primary cause of new cases of chronic non-communicable diseases in healthy people and also contributes to the development of combined pathology in patients undergoing dispensary observation for another reason.

At the same time, patients with comorbidities are at higher risk of severe COVID-19 with an unfavorable outcome. Given the scale of the spread of COVID-19 and its consequences, it is important for healthcare workers to have a clearer understanding of the possible consequences for patients, including in terms of the development and exacerbation of chronic non-communicable diseases that this infection can cause. According to the authors of the review (Shelgunov et al. 2023), it is important not only to understand the extent of the impact of COVID-19 on the development of chronic pathology in patients but also to keep in mind the ever-increasing volume of medical care for such patients.

Impact on diseases of the circulatory system

The COVID-19 virus has an adverse effect on the cardiovascular system (Xu et al. 2021; Burn et al. 2022). Manifestations can be varied: myocardial damage, myocarditis, acute heart failure, acute myocardial infarction, cardiac arrhythmia, cardiac arrest, venous thromboembolism, and others (Desai et al. 2020; Driggin et al. 2020; Libby and Luscher 2020; Varga et al. 2020; Gushhina and Lozhkina 2021; McBane 2021; Sugraliev 2021; Romanov 2022; Vorobyeva and Romanova 2022; Huseynov et al. 2023; Pogosova et al. 2023; Yusov and Alpidovskaya 2023).

It has been established that patients with COVID-19 have a high prevalence of cardiovascular manifestations due to a systemic inflammatory response and immune system disorders as the disease progresses (Docherty et al. 2020; Kemerley 2024).

According to the conducted studies, the most common complication from the cardiovascular system is the progression of forms of ischemic disease (41.9%). COVID-19 can also cause both primary cardiac pathology and aggravate existing cardiovascular diseases (Hessami 2021; Kravtsiva et al. 2021; Xie et al. 2022).

Although some studies have suggested a link between cardiovascular diseases and severe COVID-19, the efforts to accurately assess the prevalence of cardiovascular diseases in patients with COVID-19 are complicated by the lack of widespread testing, national surveillance, or standardized data collection in the Russian Federation.

There are concerns that people with cardiovascular diseases do not seek timely treatment during the pandemic and die at home. The shortage of essential medications is also important.

For circulatory system-related studies, a study covering 117 athletes (volleyball, handball, freestyle wrestling, judo, classical wrestling, synchronized swimming, swimming, and diving) who have fully recovered from covid and are back to normal training found that there is a slight increase (52.99% to 53.85%) in resting heart rate, minimum heart rate during sleep, and average heart rate during sleep, but no electrocardiogram (EKG) abnormality is observed among the participants. A study with 59 adult patients (14~60 years old) with post-COVID infection (observation group) and 60 people as a control group found that, when excluding the acute COVID infection (acute and long last impact and 28 days after covid infection), patients after COVID infection often experience a decrease in left ventricular diastolic function and global longitudinal strain, and the above indicators show a gradual improvement trend with recovery time. Apart from these, one study reported a diagnosed case of myocarditis associated with suspected covid infection (Liu et al. 2024).

The impact of COVID-19 on oncologic incidence

Cancer patients are at increased risk of severe COVID-19 outcomes due to immune suppression (Moujaess et al. 2020). The pandemic has also disrupted cancer care, leading to delays in diagnosis and treatment and more advanced disease (Harris 2020; Brest et al. 2021). The overall impact of COVID-19 on cancer patients has been detrimental, with increased mortality and challenges in providing cancer care during the pandemic.

Cancer patients are at higher risk of contracting infectious diseases or developing serious complications caused by the virus due to the immunodeficiency caused by the underlying disease. Many anticancer drugs are known to have an immunosuppressive effect. Surgery is another risk factor for developing infections. Cancer patients are a special group since their treatment cannot be stopped.

The need to find a balance between the risk of cancer patients and healthcare workers becoming infected with coronavirus and the need to continue treatment changes the work of oncology institutions. The high incidence of COVID-19 among healthcare workers significantly reduces the number of personnel to provide specialized care. The global healthcare system is faced with an atypical situation that requires, on the one hand, an urgent revision of the standards of treatment for cancer patients and, on the other hand, maintaining the quality of care provided. The available experience is extremely limited, heterogeneous, and, in most cases, based on isolated observations. Therefore, it is important to organize the provision of care to patients during a pandemic as well as to search for an answer to the question of how coronavirus infection affects the prognosis and methods of treatment of malignant neoplasms.

The leading oncology institute in the Russian Federation, the Hertsen Moscow Oncology Research Institute, conducted a detailed, systematic review of world literature data, including all aspects that reflect the impact of the COVID-19 pandemic on oncological practice (Kaprin et al. 2020). The review reflects the experience of Russian and foreign researchers, presents data on the impact of COVID-19 on cancer patients, the mortality of cancer patients infected with COVID-19, the possibilities of treating COVID-19, etc. It is noted that, despite the pandemic, treatment of cancer patients must be continued since the presence of a tumor process does not allow a delay in therapy. The global oncology community continues to actively develop recommendations for the optimal management of cancer patients during the pandemic. High-risk groups for infection with the new coronavirus have been identified, including patients with cancer.

The impact of COVID-19 on the central nervous system and mental status

COVID-19 is associated with both acute and chronic neurological and psychological symptoms (Ferrando et al. 2021; Rogers et al. 2021). Neurological manifestations may result from direct viral infection, immune responses, or vascular injury (Alnefeesi et al. 2020; Manchia et al. 2022).

Reported nervous system manifestations range from relatively simple symptoms to cerebral hemorrhage and infarction. Postmortem studies of human brains indicate that human coronavirus variants and SARS-CoV-2 can infect neurons and neuroglia. Furthermore, studies have demonstrated increased serum cytokine levels following SARS-CoV-2 infection, consistent with the notion that cytokine overproduction and toxicity may be an important potential mechanism of neurological injury parallel to the known lung injury pathway. Evidence that SARS-CoV-2 may be a vasculotropic and neurotropic virus is discussed. Early reports suggest that COVID-19 may be associated with severe neurological complications, and there are several plausible mechanisms to explain these observations. Detailed information on the potential neurological injury and further exploration of relevant pathophysiological interventions are needed to understand and ultimately mitigate SARS-CoV-2-associated neurological injury.

Psychological consequences include increased rates of depression, anxiety, and posttraumatic stress disorder among patients and the general population (Rodríguez-Rey et al. 2020; Sher 2020; Brown and Schuman 2021; Ueda et al. 2021).

In terms of psychological health, a study based on 161 adults in Hebei province find that, 32.3% have a psychological condition (based on GHQ-12 questionnaire) and 53.4% have poor sleep quality (based on PSQI questionnaire). Among these, female, low education, and being single have a higher risk for psychological conditions, and higher education is a proactive factor for sleeping quality, while worrying about long COVID symptoms is a risk factor for poor sleeping quality (Cai et al. 2022). For very early cognitive impairment, a study covering 311 people who suffered covid during the Wuhan outbreak found that 170 (54.7%) people had very early cognitive impairment and 230 (23.9%) had residual symptoms after discharge from the hospital. Among these, females, elderly, and people with generalized anxiety disorder have a higher risk of very early cognitive impairment after being infected with COVID. People with very early cognitive impairment after covid have much higher chances for other long COVID symptoms, including insomnia, fatigue, chest tightness, shortness of breath, and loss of appetite (Hua et al. 2023).

A recent study covering 68,200 Chinese populations found that fatigue (30.53%), memory decline (27.93%), decreased exercise ability (18.29%), and brain fog (16.87%) are the main long COVID symptoms for the Chinese population. These symptoms were less prevalent among those infected only once: fatigue (24.85%), memory decline (18.11%), and decreased exercise ability (12.52%), etc. (Qin et al. 2024).

As COVID-19 continues to be reported, recent literature on the effects of this new virus on the central nervous system may help guide clinical practice and identify potentially important research directions. In addition, understanding the potential mechanisms of neurological injury may focus efforts on more accurate detection and prevention of these complications (Belopasov et al. 2020; Simonenko et al. 2021; Ekusheva et al. 2022; Parfenov and Kulesh 2022).

The impact of COVID-19 on infectious diseases

Several countries have seen a notable decline in the spread of sexually transmitted infections, including HIV/AIDS, attributed to COVID-19 quarantines, social distancing measures, and advice against casual sex. Similarly, in some places, transmission rates of influenza and other respiratory viruses have dropped significantly during the pandemic. In addition, the influenza B/Yamagata lineage may have disappeared in 2020 or 2021 due to measures to control the COVID-19 pandemic, and no natural cases have been confirmed since March 2020. In 2023, the World Health Organization concluded that protection against the Yamagata lineage is no longer required in the seasonal influenza vaccine, reducing the number of lineages targeted by the vaccine from four to three.

An assessment of the course of the COVID-19 pandemic and its impact on the epidemics of HIV infection, viral hepatitis C (HCV), tuberculosis, influenza, and acute respiratory infections was carried out in the Northwestern Federal District of the Russian Federation over two years of the spread of COVID-19 from the standpoint of the possible formation of a syndemic, or interference between the diseases (Belyakov et al. 2022). The pandemic did not significantly affect the patterns of the epidemic course of HIV, HCV, and tuberculosis, indicating there was no syndemic between these pathogens. Interference with respiratory infections was noted, with a clear predominance of SARS-CoV-2.

The impact of COVID-19 on the category external causes of morbidity and mortality

Experts paid special attention to the analysis of the influence of COVID-19 in terms of stress and anxiety that accompanied the pandemic's course, which can be associated with an increase in mortality rates from injuries, poisoning, and conditions associated with alcohol and drug use (Briko et al. 2020; Nikiforov et al. 2020; Nikitina et al. 2021; Yakovleva et al. 2023).

According to experts, concerns about a possible sharp increase in suicide mortality were not confirmed; on the contrary, at the first stages, during the period with the strictest quarantine measures, the suicide rate decreased (Boyko et al. 2020; Rozanov 2020; Rozanov and Semenova 2022).

Below, a more detailed analysis of the impact of the COVID-19 pandemic on the dynamics of leading classes of diseases in the Russian Federation is carried out.

Impact of the COVID-19 Pandemic on the Incidence Dynamics of Leading Disease Categories in the Russian Federation

Diseases of the circulatory system (DCS)

The annual dynamics of the incidence of DCS on average in the subjects of the Russian Federation are presented in Fig. 2. The point of change in the trend in 2020 is obvious, followed by a continuation of the upward trend. On average, the country's incidence declined by 6.2% ± 7.5% in 2020 compared to 2019. At the same time, an increase in incidence was observed only in some regions in the southern part of the Russian Federation, such as Astrakhan and Kurgan oblasts, and the Republics of Chechnya, Kabardino-Balkaria, Adygea, Altai, and Buryatia.

The average incidence of DCS in the pre-COVID period in all regions of the Russian Federation was 22,177±5,748 cases per 100,000 population. In most (66 out of 85) regions, an increasing trend was observed, and in 44 out of 66 subjects, the trend significance exceeded 0.5. In eight regions, a significant negative trend in the incidence of DCS was observed. These regions included the federal cities of Moscow, St. Petersburg, and Sevastopol, the Republic of Crimea, Astrakhan Oblast, Altai Krai, Vladimir Oblast, and Nenets Autonomous Okrug (Fig. 3). During the COVID-19 period, the average incidence rate in all regions increased and amounted to 24,954±6,382 cases per 100,000 population. At the same time, in 70 out of 85 regions, a stable trend towards increasing incidence continues to form. Only four regions show a significant downward trend in the incidence of DCS during this period; these are the Tomsk and Novgorod oblasts as well as the Republics of Tyva and Khakassia.

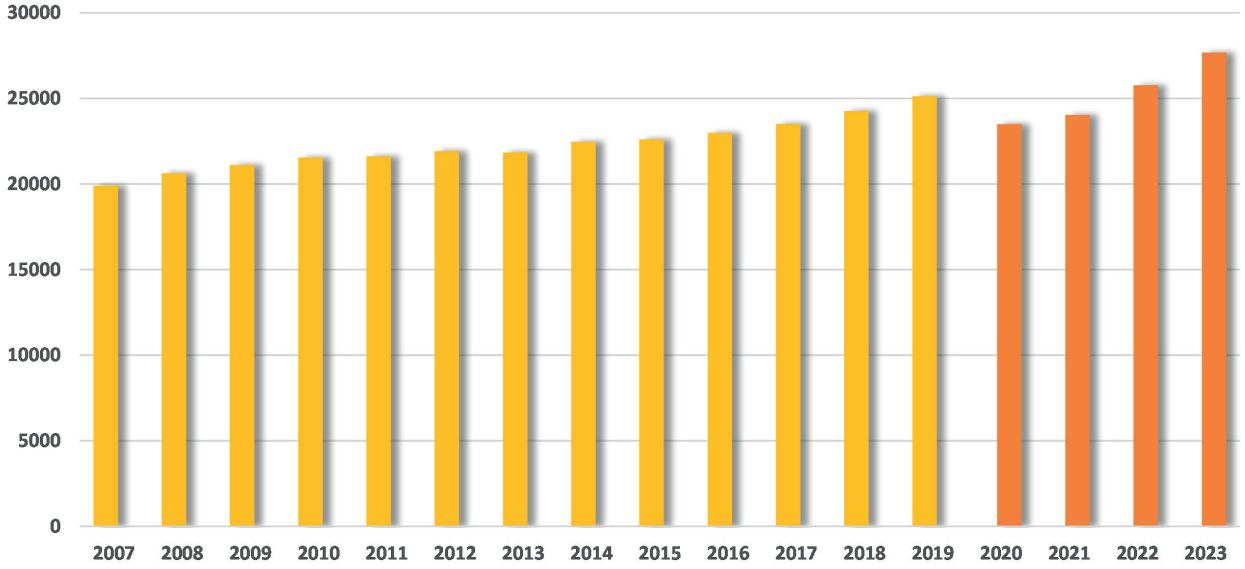

Fig. 2. Annual dynamics of the average incidence of diseases of the circulatory system in the Russian Federation for the period from 2007 to 2023

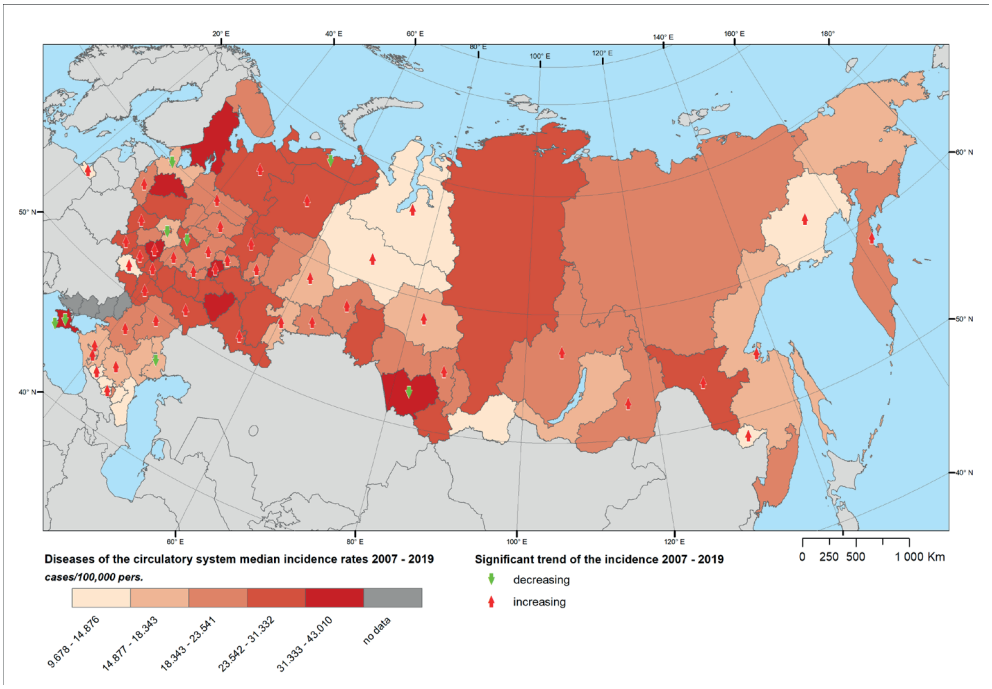

Fig. 3. Distribution of median incidence of diseases of the circulatory system in the Russian Federation in the period 2007–2019 and significant trends in its change

Compared with the hypothetical incidence for 2020–2023 (assuming the continuation of the pre-COVID trend), in 40 of the 85 regions studied, the actual median incidence was higher by up to 35%. In the remaining regions, a lower median incidence of up to 28% is observed. The spatial distribution of regions with an increase and decrease in the incidence of DCS is very heterogeneous and does not reveal any clear patterns ($p = 0.69 > 0.05$) (Fig. 4).

Malignant neoplasms (MN)

The annual dynamics of the incidence of MN on average in the regions of the Russian Federation are presented in Fig. 5. The point of change in the trend in 2020 with the subsequent continuation of the upward trend can be seen. On average, the country's incidence declined by 11.8% ± 7.4% in 2020 compared to 2019. At the same time, an increase in incidence was observed only in two regions, these being the Republic of Ingushetia and the Chukotka Autonomous Okrug.

The average incidence rate of malignant neoplasms in the pre-COVID period in all regions of Russia was 373.5±81.3 cases per 100,000 population. In the overwhelming majority (84 out of 85) of regions, an upward trend was observed, and in 77 out of 84 regions, the trend significance exceeded 0.5. A significant negative incidence trend was observed only in the Chechen Republic (Fig. 6). During the COVID-19 period, the average incidence rate in all regions increased and amounted to 417.8±97.7 cases per 100,000 population. The upward trend in incidence continued in 83 out of 85 regions studied (significant trend in 73 out of 83 regions). An insignificant downward trend is observed in the Leningrad Oblast and the Republic of Ingushetia.

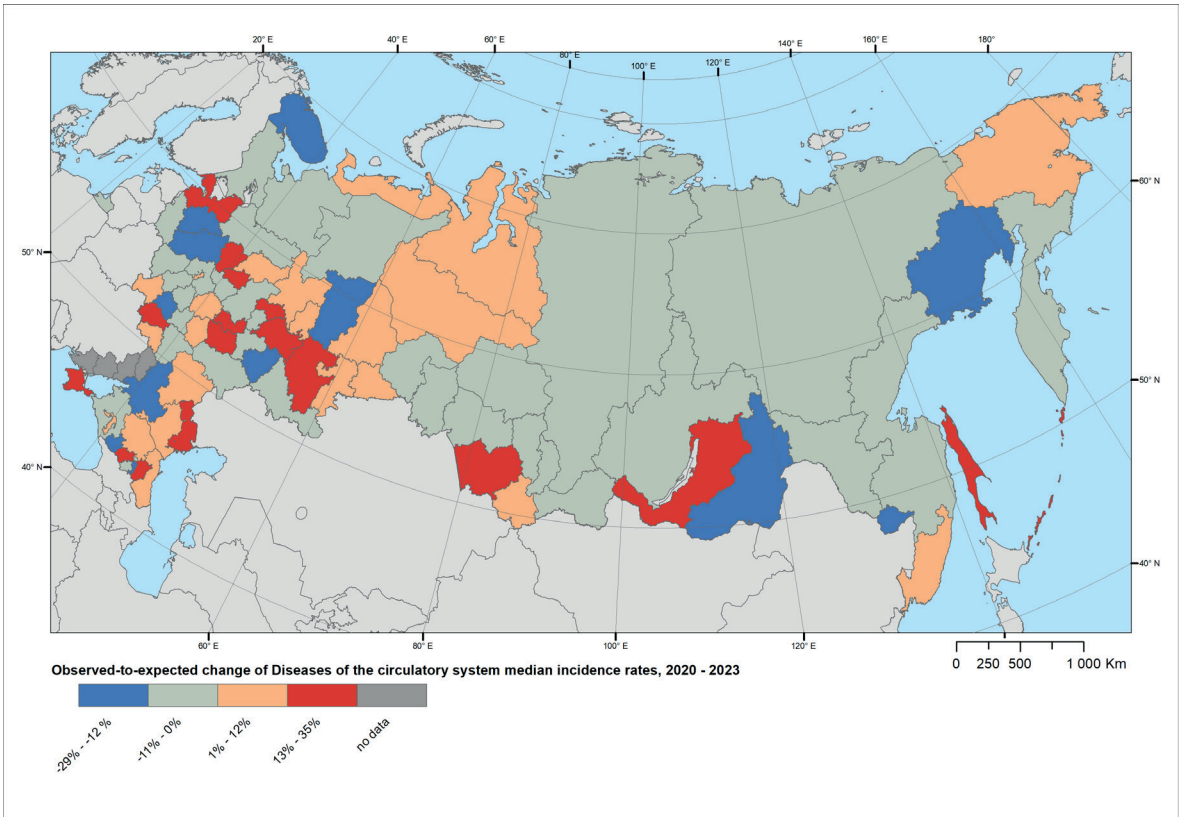

Fig. 4. Change in the actual median incidence of DCS in 2020–2023 compared to the expected hypothetical value without the influence of COVID

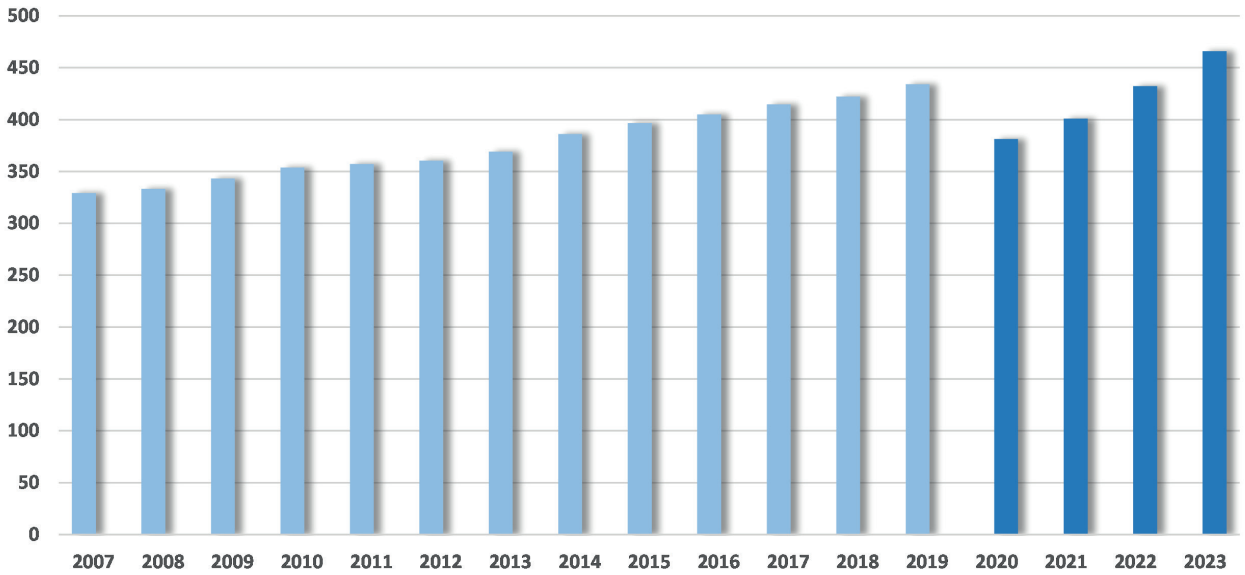

Fig. 5. Annual dynamics of the average incidence of malignant neoplasms in the Russian Federation for the period 2007–2023

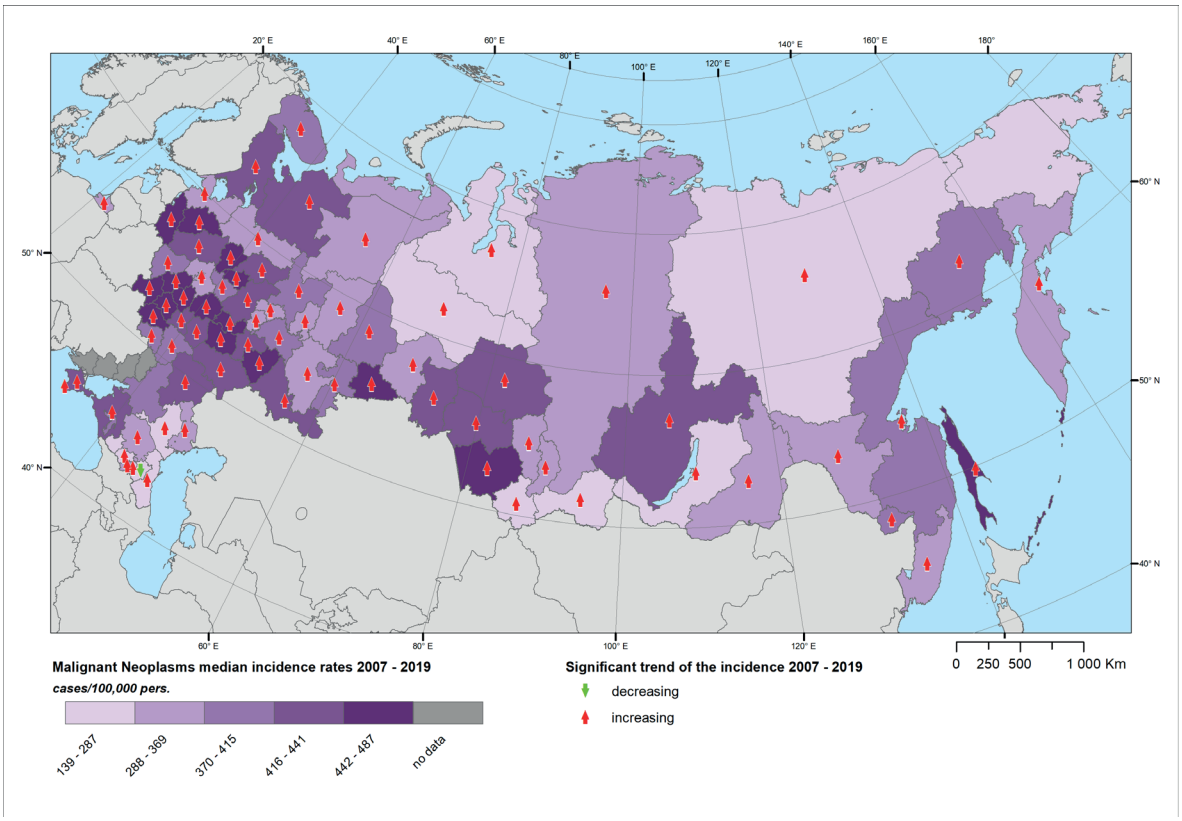

Fig. 6. Distribution of median incidence of malignant neoplasms in the Russian Federation in the period 2007–2019 and significant trends in its change

Compared with the hypothetical incidence rate for 2020–2023 (assuming the pre-COVID trend continues), the actual median incidence rate was higher in only 9 out of 85 regions. Moreover, 8 out of 9 regions demonstrate only a slight excess (up to 8%), while the Chechen Republic shows a 97% excess. Most regions have a lower median incidence rate of up to 30% (Fig. 7). The spatial distribution of regions with an increase and decrease in the incidence of MN is very heterogeneous and does not reveal any clear patterns ($p = 0.44 > 0.05$)

External Causes of Morbidity and Mortality

The annual dynamics of incidence from external causes on average in the subjects of the Russian Federation are presented in Fig. 8. In the period from 2007 to 2019, a

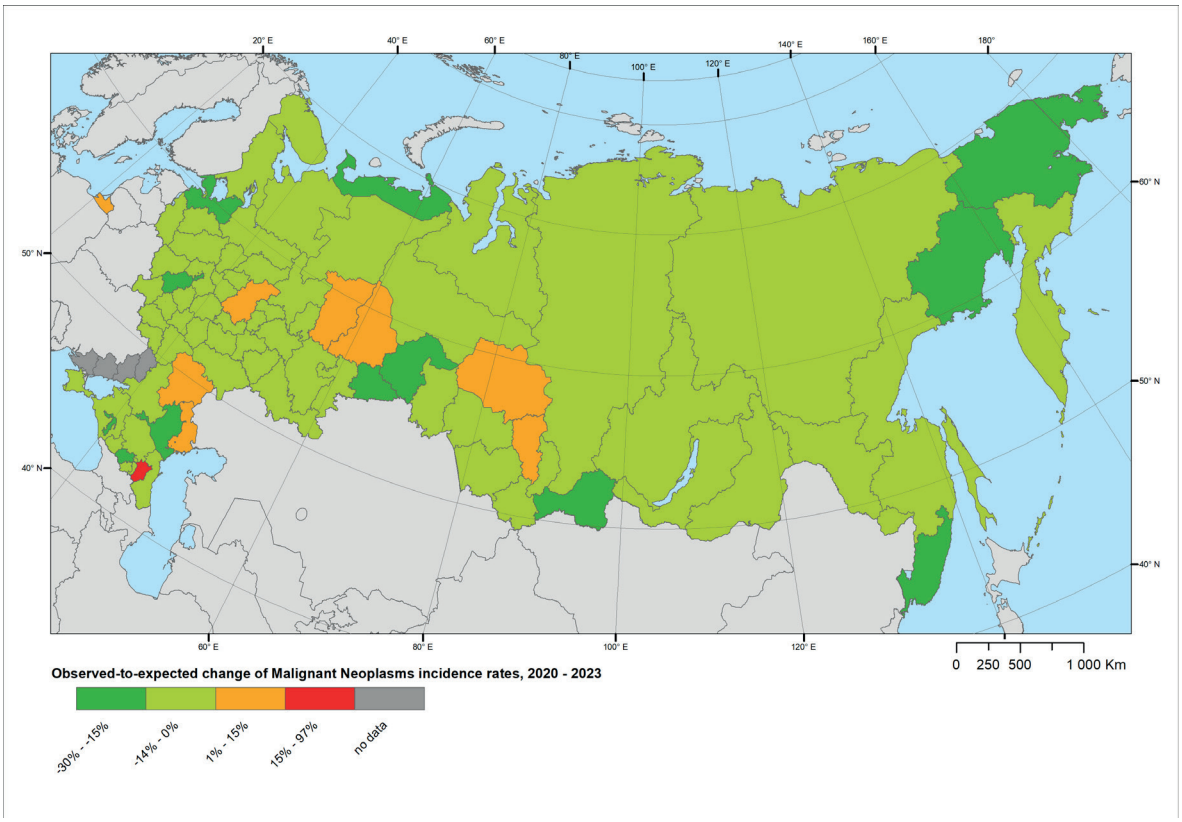

Fig. 7. Change in the actual median incidence of malignant neoplasms in 2020–2023 compared to the expected hypothetical value without the influence of COVID

decreasing trend in morbidity was observed. The point of change in the trend in 2020 with a transition to an increase is visualized. On average in the country, the decline in morbidity in 2020 compared to 2019 was 9.6% ± 6.8%. At the same time, an increase in morbidity was observed only in four subjects: the Leningrad Oblast, the Republics of Altai, Ingushetia, and Kabardino-Balkaria.

The average incidence from external causes for the pre-COVID period in all subjects of the Russian Federation was 8864±2238 cases per 100 thousand population. Only 23 out of 85 subjects showed a significant trend in incidence, with the trend decreasing in 7 out of 23 subjects and increasing in the remaining 16 subjects (Fig. 9). During the COVID-19 period, the average incidence in all subjects slightly decreased and was 8094±2354 cases per 100,000 population. The downward trend in incidence continued in 24 out of 85 subjects (significant for 9 out of 24). The remaining subjects demonstrated a trend towards an increase in incidence due to external causes.

Compared with the hypothetical incidence rate for 2020–2023 (assuming the pre-COVID trend continues), in 53 out of 85 regions, the actual median incidence rate was lower by up to 44%. In the remaining regions, the median incidence rate was exceeded by up to 28% (Fig. 10). The spatial distribution of regions with increases and decreases in incidence from external causes is highly heterogeneous and does not reveal any clear patterns ($p = 0.23 > 0.05$).

Thus, in 2020 (the year the COVID-19 pandemic began), there was a decline in the incidence rate, followed by a resumption of the upward trend in all three classes of diseases (cardiovascular, oncological and external causes of morbidity and mortality). Such a decline in the

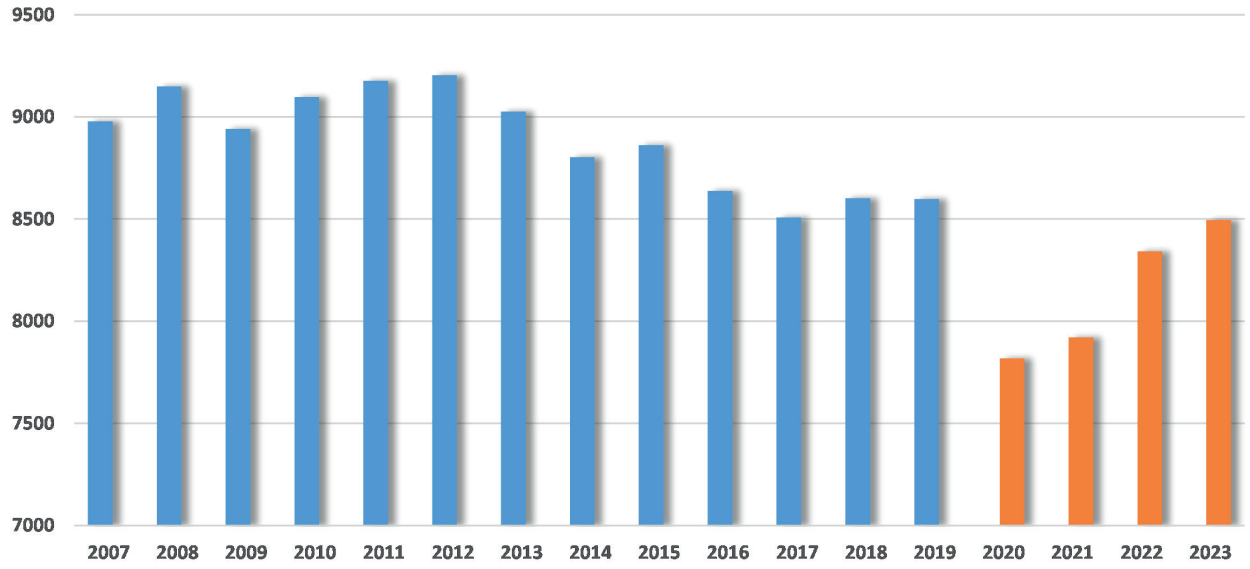

Fig. 8. Annual dynamics of average incidence from external causes in the Russian Federation for the period between 2007 and 2023

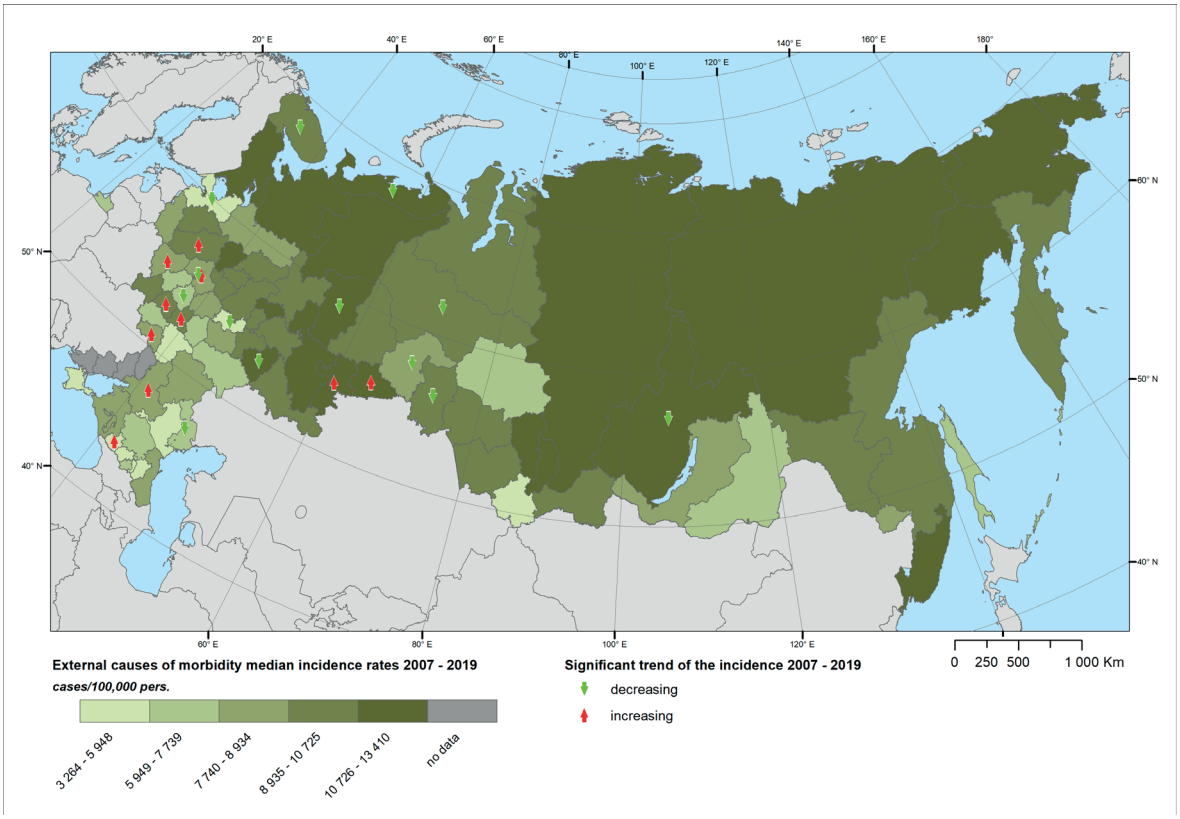

Fig. 9. Distribution of median morbidity caused by external factors in the Russian Federation in the period 2007–2019 and significant trends in its change

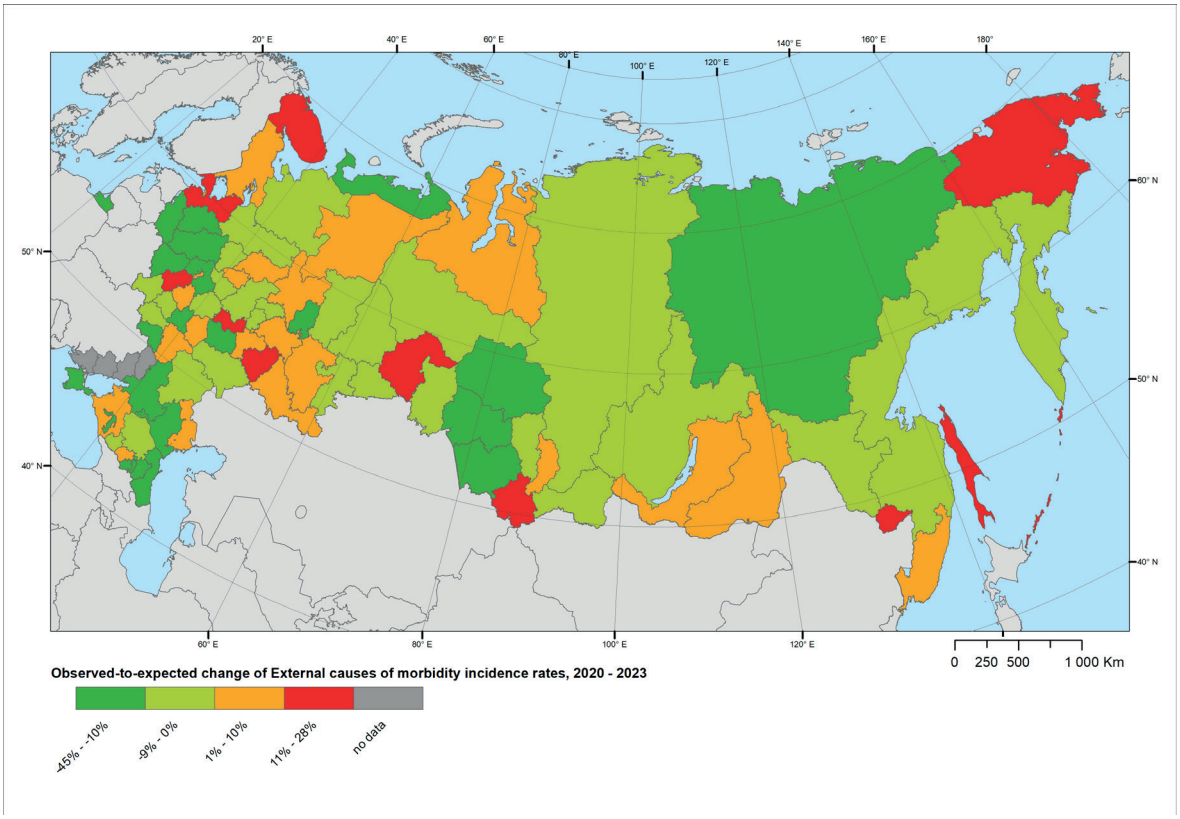

Fig. 10. Change in actual median incidence due to external causes in 2020–2023 compared to the expected hypothetical value without the influence of COVID-19

incidence rate can be explained, obviously, not so much by a decrease in the number of cases but by the peculiarities of the situation in healthcare during the quarantine period.

The quarantine period certainly affected the statistics of COVID-19 cases. The introduction of restrictions on movement and social interaction, during which access to medical institutions was more difficult, led to a reduction in the number of visits to hospitals. Additionally, the behavior of patients with chronic pathologies changed since they often preferred not to have unnecessary contact with anyone outside the home. Of course, the redistribution of medical resources in favor of treating patients with COVID-19 also had an impact. The reduction in government spending on health care before the pandemic and the reduction in the number of infectious disease beds served as prerequisites for the emergence of difficulties during the pandemic. Many medical institutions were forced to adapt to the changed working conditions and redistribute resources. In general, in the context of a massive increase in COVID-19 cases, medical institutions were overloaded, and there was a shortage of personnel, equipment, and medication, which affected the recording of chronic diseases. At the same time, as subsequent analysis showed, with a decrease in the registration of cases during the COVID-19 pandemic, there was no decrease in mortality, particularly from cancer (Medico-geographical Atlas of Russia «Risk Factors for Oncological Diseases» 2024).

DISCUSSION AND CONCLUSIONS

It should be noted that many consequences of the pandemic are not yet fully understood, for example, the level of immunity and immune response, the full spectrum of diseases and long-term effects (Al-Aly et al. 2021, etc.), the consequences of past infection, especially for the child's body (Ranasinghe et al. 2022; Nygaard et al. 2024, etc.).

The COVID-19 pandemic has dealt significant damage to healthcare systems around the world, affecting thousands of people in different countries, and is considered a serious threat to global health. Patients with underlying chronic diseases are at higher risk of a severe COVID-19 case with an unfavorable outcome. Moreover, as research results show, COVID-19 can lead to new cases of chronic non-communicable diseases in healthy people and the development of combined pathology in patients who are getting treatment for another reason.

An analysis of data on the incidence of diseases of the circulatory system, malignant neoplasms, and diseases caused by external causes in the population for the period from 2007 to 2023 showed that for the first two nosological entities in the Russian Federation, before COVID-19, there was a steady increase in incidence, while the incidence from external causes showed a decrease. In the year of the onset of the COVID-19 pandemic (the COVID period), there was a decline in incidence followed by a resumption of the upward trend for all three nosological entities. At the same time, regarding malignant neoplasms, the decline in incidence was more pronounced: most regions of the country demonstrated lower average incidence rates of malignant neoplasms after 2020 than would have been hypothetically expected without the influence of COVID-19.

The decline in the incidence of all nosoforms in 2020 may have been not related to the actual decrease of morbidity, but rather to the significant reduction of healthcare and diagnostics accessibility, which led to a reduction in the detection of new cases. There was a reduction in the number of hospital visits, which led to an increase in mortality from other causes. Patients with other nosological forms did not seek timely treatment during the pandemic and died at home. The overload of medical institutions and the shortage of personnel, equipment, and necessary medications were significant. A similar situation has been noted in other countries.

All this initiatives required significant resources from medical institutions. Many studies note the vulnerability of the healthcare system in the context of a massive increase in COVID-19 cases due to an overload of medical institutions and a shortage of personnel, equipment, and medications (Krivenko 2021; Ulumbekova and Ginoyan 2022).

Journals have been devoting special editions to assessments of the scale of the coronavirus pandemic, analysis of the main mechanisms of its impact on the economy and socio-economic consequences in different geographical conditions, medical and social problems, as well as the impact of the pandemic on the environment and air quality (Geography, Environment, Sustainability 2021).

The assessment of the impact of the pandemic on the health of the population, as well as the healthcare sector, continues, as evidenced by a significant number of publications according to the different databases.

The study of the impact of COVID-19 on public health and the healthcare system in the Russian Federation (Malkhazova et al. 2021) is still highly relevant at present due to the scale of the pandemic, which has had a significant impact on Russian society. These developments led to the need for an in-depth analysis of the consequences of the pandemic for the health of individual population groups, as well as for the healthcare system as a whole (Ulumbekova and Ginoyan 2022; Alov and Pilyasov 2023; Rugol 2023; Tsvetkova et al. 2024).

According to some authors, the so-called optimization of the healthcare system implemented in Russia in recent years has provoked the emergence of several problems that have manifested themselves during the COVID-19 pandemic (Starodubov et al. 2020; Chernyshev et al. 2021). The reduction of infectious disease beds before the pandemic, the mergers of medical institutions, and the reduction of government funds for healthcare served as prerequisites for the emergence of difficulties during the pandemic (Perkhov and Gridnev 2020; Goroshko et al. 2022).

Many medical institutions were forced to adapt to changed working conditions, redistribute resources, and introduce new treatment protocols (Starodubov et al. 2020). There is a need to develop new strategies for resource management and optimization of healthcare delivery processes (Minakir 2020; Pesennikova and Perkhov 2020; Ulumbekova 2020).

The study of the impact of COVID-19 on health and the healthcare system at the local, regional, and global levels, identifying spatiotemporal patterns of infection spread, is highly important since the development of effective solutions to improve public health and increase the resilience of healthcare systems to global challenges is only possible through multi-scale experience (Coronavirus…, 2021).

Given the research data, it is important to have a good understanding of the extent of the impact of COVID-19 on the development of chronic pathology and, accordingly, on the likely increasing volume of medical care for such patients in order to plan medical care rationally within the framework of the free state medical care.

REFERENCES

Al-Aly Z., Xie Y. and Bowe B. (2021). High-dimensional characterization of post-acute sequelae of COVID-19. Nature, 594(7862), 259–264, DOI: 10.1038/s41586-021-03553-9.

Alnefeesi Y., Siegel A., Lui L.M.W, Teopiz K.M., Ho R.C.M., Lee Y., Nasri F., Gill H., Lin K., Cao B., Rosenblat J.D. and McIntyre R.S. (2020). Impact of SARS-CoV-2 Infection on Cognitive Functions: A Systematic Review. Frontiers in Psychiatry, 11, 1629, DOI: 10.13140/RG.2.2.14530.40649.

Alov I.N. and Pilyasov A.N. (2023). The spread of the COVID-19 infection in Russia. Baltic macroregion: internal differences, Balt. Reg., Vol. 15, No. 1, 96–119, (in Russian), DOI: 10.5922/2079-8555-2023-1-6.

Bai Y., Yao L., Wei T., Tian F., Jin D.Y. and Chen L. (2020). Presumed asymptomatic carrier transmission of COVID-19. JAMA, DOI: 10.1001/jama.2020.2565.

Baklanov A.A., Chubarova N.E., Kolosov V.A., Malkhazova S.M. and Porfiriev B.N. (2021). Introduction to Geography of Covid-19 Pandemic: Environmental Issues, Public Health and Socio-Economic Consequences. Geography, Environment, Sustainability, 14(4), 105–108, DOI: 10.24057/2071-9388-2021-044.

Bedford J., Enria D., Giesecke J., Heymann D.L., Ihekweazu C., Kobinger G., Ungchusak K. and Wieler L.H. (2020). Living with the COVID-19 pandemic: act now with the tools we have. The Lancet, 396(10259), 1314–1316, DOI: 10.1016/S0140-6736(20)32117-6.

Belopasov V.V., Yashu Ya., Samoilova E.M. and Baklaushev V.P. (2020). Damage to the nervous system in COVID-19. Klinicheskayapraktika, 11 (2), 60–80. (in Russian)

Belyakov N.A., Boeva E.V., Simakina O.E., SvetlichnayaYu.S., Ogurtsova S.V., Serebryakova S.L., Esaulenko E.V., Zagdyn Z.M., Yazenok A.V., Lioznov D.A. and Stoma I.O. (2022). COVID-19 pandemic and its impact on other infections in Northwest Russia. HIV Infection and Immunosuppressive Disorders, 14(1), 7–24, (in Russian), DOI: 10.22328/2077-9828-2022-14-1-7-24.

Bianchetti A., Rozzini R., Guerini F., Boffelli S., Ranieri P., Minelli G., Bianchetti L. and Trabucchi M. (2020). Clinical presentation of COVID-19 in dementia patients. J Nutr Health Aging, 24(6), 560–562, DOI: 10.1007/s12603-020-1389-1.

Boyko O.M., Medvedeva T.I., Enikolopov S.N., Vorontsova O.Yu. and Kazmina O.Yu. (2020). Psychological state of people during the COVID-19 pandemic and targets of psychological work. Psikhologicheskieissledovanija, 13(70), 1–12, (in Russian), DOI: 10.54359/ps.v13i70.196.

Brest P., Mograbi B., Hofman P. and Milano G. (2021). More light on cancer and COVID-19 reciprocal interaction. British Journal of Cancer, 124, 1344–1345, DOI: 10.1038/s41416-020-01246-0.

Briko N.I., Kagramanjan I.N., Nikiforov V.V. Suranova T.G., Chernyavskaya O.P. and Polezhaeva N.A. (2020). Pandemic COVID-19. Prevention Measures in the Russian Federation. Epidemiologija i Vakcinoprofilaktika, 19(2), 4–12, (in Russian), DOI: 10.31631/2073-3046-2020-19-2-4-12.

Brown S. and Schuman D.L. (2021). Suicide in the time of COVID-19: A perfect storm. Journal of Rural Health, 37(1), 211–214, DOI: 10.1111/jrh.12458.

Burn E., Duarte-Salles T., Fernandez-Bertolin S., et al. (2022). Venous or arterial thrombosis and deaths among COVID-19 cases: a European network cohort study. The Lancet Infectious Diseases, 22(8), 1142–1152, DOI: 10.1016/S1473-3099(22)00223-7.

Cai S., Shi W., Xu T., Zhang S., Sun J., Liu Y., Zhang Y. and Li K. (2022). Mental health and sleep quality in patients recovered from COVID-19. Chinese Mental Health Journal, Vol 36, No. 6.

Chen N., Zhou M., Dong X., Qu J., Gong F., Han Y. (2020). Epidemiological and clinical characteristics of 99 cases of 2019 novel coronavirus pneumonia in Wuhan, China: a descriptive study. The Lancet, DOI: 10.1016/S0140-6736(20)30211-7.

Chernyshev V.M., Voevoda M.I., Strelchenko O.V., Shalygina L.S. and Mingazov I.F. (2021). On the state of health of the population and healthcare in the Siberian Federal Okrug during the pandemic (some results of 2020). Sibirskijj nauchnyjj medicinskijj zhurnal, 41(6), 101–109, (in Russian), DOI: 10.18699/SSMJ20210612.

Coronavirus (COVID-19) Outbreaks, Environment and Human Behaviour. Editor Rais Akhtar. Springer Nature (2021). 480 p. DOI: 10.1007/978-3-030-68120-3.

Danilova I.A. (2020). Morbidity and Mortality from COVID-19. The Problem of Data Comparability. Demograficheskoeobozrenie, 7(1), 6–26. (in Russian)

Desai R., Gandhi Z., Singh S., et al. (2020). Prevalence of Pulmonary Embolism in COVID-19: a Pooled Analysis. SN Comprehensive Clinical Medicine, 2(12), 2722–2725, DOI: 10.1007/s42399-020-00605-5.

Docherty A.B., Harrison E.M., Green C.A., et al. (2020). Features of 20133 UK patients in hospital with COVID-19 using the ISARIC WHO Clinical Characterisation Protocol: prospective observational cohort study. BMJ, 369, m1985, DOI: 10.1136/bmj.m1985.

Driggin E., Madhavan M.V., Bikdeli B., Chuich T., Laracy J., Biondi-Zoccai G., Brown T.S., Der Nigoghossian C., Zidar D.A., Haythe J., Brodie D., Beckman J.A., Kirtane A.J., Stone G.W., Krumholz H.M. and Parikh S.A. (2020). Cardiovascular considerations for patients, health care workers, and health systems during the COVID-19 pandemic. J Am CollCardiol, 75(18), 2352–2371, DOI: 10.1016/j.jacc.2020.03.031.

Druzhinin P.V. and Molchanova E.V. (2021). Mortality of the Population of Russian Regions in the Context of the COVID-19 Pandemic. Regionologija, 29(3), 666–685, (in Russian), DOI: 10.15507/2413-1407.116.029.202103.666-685.

Ekusheva E.V., Kovalchuk V.V. and Shchukin I.A. Neurological Complications of COVID-19 and Post-Covid Syndrome. 2022. 104 pp. (in Russian)

Fei Z., et al. (2020). Clinical course and risk factors for mortality of adult inpatients with COVID-19 in Wuhan, China: a retrospective cohort study. The Lancet, 395(10229), 1054–1062, DOI: 10.1016/S0140-6736(20)30566-3.

Ferrando S. J., Klepacz L., Lynch S., et al. (2020). COVID-19 psychosis: A potential new neuropsychiatric condition triggered by novel coronavirus infection and the inflammatory response? Psychosomatics, 61, 551–555, DOI: 10.1016/j.psym.2020.05.012.

Filev R., Lyubomirova M., Bogov Boris., Kalinov K., Hristova J., Svinarov D., Garev A. and Rostaing L. (2024). Post-Acute Sequelae of SARS-CoV-2 Infection (PASC) for Patients-3-Year Follow-Up of Patients with Chronic Kidney Disease. Biomedicines, 12, 1259.

Geography, Environment, Sustainability. Special Issue «Geography of the COVID-19 pandemic: public health, economic and environmental consequences». 2021. Vol 14, No 4.

Getis, A. and Ord, J.K. (1992), The Analysis of Spatial Association by Use of Distance Statistics. Geographical Analysis, 24: 189-206. https://doi.org/10.1111/j.1538-4632.1992.tb00261.x

Ginzburg A.S., Semenov V.A., Semutnikova E.G., Aleshina M.A., Zakharova P.V. and Lezina E.A. (2020). The Impact of COVID-19 Restrictions on Air Quality in Moscow. Reports of the Russian Academy of Sciences. Nauki o Zemle, №1, 74–79. (in Russian)

Goldshteyn E.M. (2020). Factors Affecting Mortality from a New Coronavirus Infection in Different Subjects of the Russian Federation. Zhurnal mikrobiologii, ehpidemiologii i immunobiologii, 97(6), 604-607, (in Russian), DOI: 10.36233/0372-9311-2020-97-6-11.

Goroshko N.V., Patsala S.V. and Emelyanova E.K. (2022). Barriers to the fight against the COVID-19 pandemic in the healthcare system of Russia and its regions. Ekonomika. Informatika, 49(2), 217–233, (in Russian), DOI: 10.52575/2687-0932-2022-49-2-217-233.

Gushhina O.I. and Lozhkina N.G. (2021). Cardiovascular diseases combined with SARS-CoV-2 viral infection: course and prognosis. Ateroskleroz, 17(3), 97–105, (in Russian), DOI: 10.52727/2078-256X-2021-3-97-1055.

Harris A.L. (2020). COVID-19 and cancer research. British Journal of Cancer, 123, 689–690, DOI: 10.1038/s41416-020-0960-1.

Hessami A., Shamshirian A., Heydari K., Pourali F., Alizadeh-Navaei R., Moosazadeh M., Abrotan S., Shojaie L., Sedighi S., Shamshirian D. and Rezaei, N. (2021). Cardiovascular diseases burden in COVID-19: Systematic review and meta-analysis. American Journal of Emergency Medicine, 46, 382–391, DOI: 10.1016/j.ajem.2020.10.022.

Hua Q., Liu H.g, Xu X., Zheng D., Wang Q., Liu Y., Zhoy X., Yang R., Ding B., Guo J. and Zhang Z. (2023). Prevalence and associated factors of very early cognitive impairment in COVID-19 convalescents: a study using data from a questionnaire survey. Chinese General Practice, 26 (10), 1234-1240.

Huseynov A., Akin I., Duerschmied D. and Scharf R.E. (2023). Cardiac Arrhythmias in Post-COVID Syndrome: Prevalence, Pathology, Diagnosis, and Treatment. Viruses, 15(2), 389, DOI: 10.3390/v15020389.

Kaprin A.D., Gameeva E.V., Polyakov A.A., Korniyetskaya A.L., Rubtsova N.A. and Fedenko A.A. (2020). The Impact of the COVID-19 Pandemic on Oncology Practice. Sibirskijj onkologicheskijj zhurnal, 19(3), 5–22, (in Russian), DOI: 10.21294/1814-4861-2020-19-3-5-22.

Kemerley A., Gupta A., Thirunavukkarasu M., Maloney M., Burgwardt S. and Maulik N. (2024). COVID-19 Associated Cardiovascular Disease – Risks, Prevention and Management: Heart at Risk Due to COVID-19. Current Issues in Molecular Biology, 46(3), 1904–1920, DOI: 10.3390/cimb46030124.

Khalifa S., et al. (2021). Beyond the Pandemic: COVID-19 Pandemic Changed the Face of Life. International Journal of Environmental Research and Public Health, 18(11), 5645, DOI: 10.3390/ijerph18115645.

Kotov E.A., Goncharov R.V., Kulchitsky Y.V., Molodsova V.A. and Nikitin B.V. (2022). Spatial Modelling of Key Regional Level Factors of Covid-19 Mortality in Russia. Geography, Environment, Sustainability, 2(15), 71–83, DOI: 10.24057/2071-9388-2021-076.

Kravtsiva A.V., Gulyaeva A.A., Golovanova E.D. and Airapetov K.V. (2021). Cardiovascular damage in COVID-19. Vestnik Smolenskojj gosudarstvennojj medicinskojj akademii, 20 (4), 59–65. (in Russian)

Krivenko N.V. (2021). Trends in Economic Development and Aspects of Healthcare Reform in Russia in the Context of the COVID-2019 Pandemic. Uroven' zhizni naselenija regionov Rossii, 17(4), 503–513, (in Russian), DOI: 10.19181/lsprr.2021.17.4.7.

Kvasha E.A. and Kharkova T.L. (2022). The COVID-19 Pandemic and Mortality from the Main Causes of Death in the Regions of the Russian Federation in 2020. Regional'nyeissledovanija, 4(78), 61–75, (in Russian), DOI: 10.5922/1994-5280-2022-4-6.

Lee J., Kothari A., Bhatt G., Gupta N., Ali A.E., Najam N., Mazroua M., Mansoor T., Amal T., Elsaban M., Deo R., Bansal V. and Kashyap, R. (2023). Cardiac Complications Among Long Covid Patients: A Systematic Review and Meta-Analysis. Journal of the American College of Cardiology, 81(8 suppl), 2115, DOI: 10.1016/S0735-1097(23)02559-7.

Libby P. and Luscher T. (2020). COVID-19 is, in the end, an endothelial disease. European Heart Journal, 41(32), 3038–3044, DOI: 10.1093/eurheartj/ehaa623.

Liu X., Cheng H. and Jiang F. (2024). Diagnosis and treatment of a case of myocarditis associated with suspected neocoronary infection. Medical Theory and Practice, vol 37, no. 20.

Livshits M.L. and Neklyudova N.P. (2020). COVID-19 mortality rate in Russian regions: forecasts and reality. R-Economy, 6(3), 171–182, DOI: 10.15826/recon.2020.6.3.015.

Lu H., Stratton C.W. and Tang Y.W. (2020). Outbreak of pneumonia of unknown etiology in Wuhan China: the mystery and the miracle. Journal of Medical Virology, DOI: 10.1002/jmv.25678.

Malkhazova S.M., Korennoy F.I., Shartova N.V. and Vatlina T.V. (2021). Covid-19 in the Russian Federation: Regional differences and public health response. Coronavirus (COVID-19) Outbreaks, Environment and Human Behaviour.Cham, Switzerland. Springer International Publishing AG, 283–307.

Manchia M., Gathier A.W., Yapici-Eser H., Schmidt M.V., de Quervain D., van Amelsvoort T., Bisson J.I., Cryan J.F., Howes O.D., Pinto L., van der Wee N.J., Domschke K., Branchi I. and Vinkers C.H. (2022). The impact of the prolonged COVID-19 pandemic on stress resilience and mental health: A critical review across waves. European Neuropsychopharmacology, 55, 22–83, DOI: 10.1016/j.euroneuro.2021.10.864.

McBane R.D. (2021). Arterial thrombosis and coronavirus disease 2019. Mayo Clinic Proceedings, 96(2), 274–276, DOI: 10.1016/j.mayocp.2020.12.009.

Medico-geographical Atlas of Russia «Risk Factors for Oncological Diseases» / ed. S.M. Malkhazova. Faculty of Geography, Lomonosov Moscow State University, 2024. 254 p.

Mendes A., Herrmann F.R., Perivier S., et al. (2021). Delirium in older patients with COVID-19: prevalence, risk factors and clinical relevance. The Journals of Gerontology: Series A, 76(8), 142-146, DOI: 10.1093/gerona/glab039.

Minakir P.A. (2020). Pandemic Economy: The Russian Path. Prostranstvennajaehkonomika, 16(2), 7–18, (in Russian), DOI: 10.14530/se.2020.2.007-018.

Moujaess E., Kourie H.R. and Ghosn M. (2020). Cancer patients and research during COVID-19 pandemic: A systematic review of current evidence. Critical Reviews in Oncology/Hematology, 150, 102972, DOI: 10.1016/j.critrevonc.2020.102972.

Nguyen H.C., Nguyen M.H., Do B.N., Tran C.Q., Nguyen T.T., Khue P.M., Van L.P., Tran K.V., Duong T.T., Tran T.V., et al. (2020). People with suspected COVID-19 symptoms were more likely depressed and had lower health-related quality of Life: The potential benefit of health literacy. Journal of Clinical Medicine, 9, 965, DOI: 10.3390/jcm9040965.

Nikiforov V.V., Suranova T.G. and ChernobrovkinaT.Ya. (2020). Novel coronavirus infection (COVID-19): clinical and epidemiological aspects. Arkhiv vnutrennejj mediciny, 10(2), 87–93, (in Russian), DOI: 10.20514/2226-6704-2020-10-2-87-93.

Nikitina A.Yu., Chimagomedova A.Sh. and Levin O.S. (2021). Neurological manifestations of COVID-19 in the elderly. Zhurnalnevrologiiipsikhiatrii, 121:10:2, 5–15, (in Russian), DOI: 10.17116/jnevro20211211025.

Nygaard U., Holm M., Rabie H. et al. (2024). The pattern of childhood infections during and after the COVID-19 pandemic. The Lancet Child & Adolescent Health, Volume 8, Issue 12, 910-920, DOI: 10.1016/S2352-4642(24)00236-0.

Ong I., Kolson D. and Schindler M. (2023). Mechanisms, Effects, and Management of Neurological Complications of Post-Acute Sequelae of COVID-19 (NC-PASC). Biomedicines, 11, 377.

O'Mahoney L.L., Routen A., Gillies C., Ekezie W., Welford A., Zhang A., Karamchandani U., Simms-Williams N., Cassambai S., Ardavani A., Wilkinson T.J., Hawthorne G., Curtis F., Kingsnorth A.P., Almaqhawi A., Ward T., Ayoubkhani D., Banerjee A., Calvert M., Shafran R., Stephenson T., Sterne J., Ward H., Evans R.A., Zaccardi F., Wright S. and Khunti K. (2022). The prevalence and long-term health effects of Long Covid among hospitalised and non-hospitalised populations: A systematic review and meta-analysis. eClinicalMedicine, 55, 101762, DOI: 10.1016/j.eclinm.2022.101762.

Parfenov V.A. and Kulesh A.A. (2022). Acute and late neurological disorders in patients who have had coronavirus infection. Nevrologija, nejjropsikhiatrija, psikhosomatika, 14(3), 4–11. (in Russian)

Peng M. (2020). Outbreak of COVID-19: An emerging global pandemic threat. Biomedicine & Pharmacotherapy, 129, 110499, DOI: 10.1016/j.biopha.2020.

Perkhov V.I. and Gridnev O.V. (2020). Lessons of the COVID-19 pandemic for public health policy. Sovremennye problem zdravookhranenijaimedicinskojjstatistiki, 2, 206–222, (in Russian), DOI: 10.24411/2312-2935-2020-10043.

Pesennikova E.V. and Perkhov V.I. (2020). Directions for the Development of Medicine and Healthcare in the Post-Pandemic World. Sovremennye problem zdravookhranenijaimedicinskojjstatistiki, 4, 535–551, (in Russian), DOI: 10.24411/2312-2935-2020-00130.

Petrilli C.M., Jones S.A., Yang J., Rajagopalan H., O'Donnell L., Chernyak Y., Tobin K.A., Cerfolio R.J., Francois F. and Horwitz L.I. (2020). Factors associated with hospital admission and critical illness among 5279 people with coronavirus disease 2019 in New York City: prospective cohort study. BMJ, 369, m1966, DOI: 10.1136/bmj.m1966.

Pogosova N.V., Kuchiev D.T. and Popova A.B. (2023). Consequences of COVID-19 at a Remote Stage after Hospitalization According to Clinical, Instrumental and Laboratory Research Methods. Kardiologicheskijjvestnik, 18(4), 56–66, (in Russian), DOI: 10.17116/Cardiobulletin20231804156.

Poloni T.E., Carlos A.F., Cairati, M., et al. (2020). Prevalence and prognostic value of Delirium as the initial presentation of COVID-19 in the elderly with dementia: an Italian retrospective study. Clinical Medicine, 26, 100490, DOI: 10.1016/j.eclinm.2020.100490.

Poyiadji N., Shahin G., Noujaim D., et al. (2020). COVID19 associated acute hemorrhagic necrotizing encephalopathy: imaging features. Radiology, 296(2), 119–120, DOI: 10.1148/radiol.2020201187.

Qin S., Yanan Z., Yanhua L., Ling H., Ting Y., Jiahui S., Likui W., Xin Z., Xiaopeng M. and George F.G. (2024). Long COVID facts and findings: a large-scale online survey in 74,075 Chinese participants. The Lancet Regional Health – Western Pacific, Volume 52, 101218.

Ranasinghe L., Achar J., Gröschel M.I. et al. (2022). Global impact of COVID-19 on childhood tuberculosis: an analysis of notification data. Lancet Glob Health, Dec 10(12), e1774-e1781, DOI: 10.1016/S2214-109X(22)00414-4.

Richardson, S., Hirsch, J. S., Narasimhan, M., et al. (2020). Presenting characteristics, comorbidities, and outcomes among 5700 patients hospitalized with COVID-19 in the New York City Area. JAMA, 323(20), 2052–2059, DOI: 10.1001/jama.2020.6775.

Rodríguez-Rey R., Garrido-Hernansaiz H. and Collado S. (2020). Psychological impact and associated factors during the initial stage of the coronavirus (COVID-19) pandemic among the general population in Spain. Frontiers in Psychology, 11, 1540, DOI: 10.3389/fpsyg.2020.01540.

Rogers J., Chesney E., Oliver D., et al. (2020). Psychiatric and neuropsychiatric presentations associated with severe coronavirus infections: a systematic review and meta-analysis with comparison to the COVID-19 pandemic. The Lancet Psychiatry, 7(7), 611–627, DOI: 10.1016/S2215-0366(20)30203-0.

Romanov Yu.A. (2022). SARS-CoV-2, COVID-19 and cardiovascular complications: a view from the perspective of vascular endothelium. Kardiologicheskijj vestnik, 17(1), 21–28, (in Russian), DOI: 10.17116/Cardiobulletin20221701121.

Rozanov V.A. (2020). Urgent Tasks in the Sphere of Suicide Prevention in Connection with the COVID-19 Pandemic. Suicidologija, 11(1), 39–52, (in Russian), DOI: 10.32878/suiciderus.20-11-01(38)-39-52.

Rozanov V.A. and Semenova N.V. (2022). Suicidal behavior in the context of the COVID-19 pandemic. Psikhiatrija, 20(3), 74–84, (in Russian), DOI: 10.30629/2618-6667-2022-20-3-74-84.

Rugol L.V. (2023). Assessing hospital emergency preparedness. Social'nye aspekty zdorov'a naselenia; 69(5):6, (in Russian), DOI: 10.21045/2071-5021-2023-69-5-6.

Shelgunov V.A., Zubko A.V., Kungurcev O.V. and Zaporozhchenko V.G. (2023). The impact of a new coronavirus infection on the development of chronicnon-communicable diseases. Social'nyeaspektyzdorov'janaselenija, 69(3), 5, (in Russian), DOI: 10.21045/2071-5021-2023-69-3-5.

Sher L. (2020). The impact of the COVID-19 pandemic on suicide rates. QJM: An International Journal of Medicine, 113(10), 707–712, DOI: 10.1093/qjmed/hcaa202.

Simonenko V.V., Vakal T.N., Mikhalik D.S., Zhukov G.V. and Nikolaenkova L.I. (2021). Neurological complications after coronavirus infection. Vestnik Smolenskojj gosudarstvennojj medicinskojj akademii, 20 (2), 59–64. (in Russian)

Starodubov V.I., Kadyrov F.N., Obukhova O.V., Bazarova I.N., EndovitskayaYu.V. and NesvetailoN.Ya. (2020). The impact of coronavirus COVID-19 on the situation in Russian healthcare. Menedzher zdravookhranenija, 4, 58–71. (in Russian)

Sugraliev A.B. (2021). Heart damage in patients with COVID-19. Kardiologija, 61(4), 15–23, (in Russian), DOI: 10.18087/cardio.2021.4.n1408.

Timonin S.A., Klimkin I., Shkolnikov V.M., Andreev E.M., Mckee M. and Leon D.A. (2021). Excess mortality in Russia and its regions compared to high income countries: An analysis of monthly series of 2020. Population Health, 17.

Tsvetkova L.A., Kurakov F.A. and Karmina R.L. (2024). Key trends in the development of global public health: 2021–2023. Public Health, 4(2):4–17, (in Russian), DOI 10.32687/0869-866X-2024-32-2-127-133.

Ueda M., Nordström R. and Matsubayashi T. (2021). Suicide and mental health during the COVID-19 pandemic in Japan. Journal of Public Health (Oxf), DOI: 10.1093/pubmed/fdab113.

Ulumbekova G.E. (2020). Proposals for the reform of healthcare in the Russian Federation after the peak of the COVID-19 pandemic. Vestnik VSHOUZ, 6(2), 9–26, (in Russian), DOI: 10.24411/2411-8621-2020-12001.

Ulumbekova G.E. and Ginoyan A.B. (2022). Lessons of the COVID-19 pandemic for healthcare in Russia. Nauchnye Trudy Vol'nogo ekonomicheskogo obshhestva Rossii, 234(2), 54–86, (in Russian), DOI: 10.38197/2072-2060-2022-234-2-54-86.

Varga Z., Flammer A.J., Steiger P., et al. (2020). Endothelial cell infection and endotheliitis in COVID-19. The Lancet, 395, 1417–1418, DOI: 10.1016/S0140-6736(20)30937-5.

Vorobyeva O.V. and Romanova L.P. (2022). Clinical case of SARS-CoV-2 infection with the development of acute myocardial infarction, myomalacia and hemopericardium. Profilakticheskaja medicina, 25(6), 75–79, (in Russian), DOI: 10.17116/profmed20222506175.

Wang D., Hu B., Hu C., Zhu F., Liu X. and Zhang J. (2020). Clinical characteristics of 138 hospitalized patients with 2019 novel coronavirus-infected pneumonia in Wuhan, China. JAMA, DOI: 10.1001/jama.2020.1585.

Xie Y., Xu E., Bowe B., et al. (2022). Long-term cardiovascular outcomes of COVID-19. Nature Medicine, 28(3), 583–590, DOI: 10.1038/s41591-022-01689-3.

Xu J., Xiao W., Liang X., et al. (2021). A meta-analysis on the risk factors adjusted association between cardiovascular disease and COVID-19 severity. BMC Public Health, 21(1), 1533, DOI: 10.1186/s12889-021-11051-w.

Yakovleva O.B., Safarova T.P. and Tsvetaeva D.A. (2023). The Impact of the COVID-19 Pandemic on the Occurrence and Course of Mental Illnesses in the Elderly. Zhurnal nevrologii i psikhiatrii, 123(5), 131–138, (in Russian), DOI: 10.17116/jnevro2023123051131.

Yong S. and Liu S. (2021). Proposed subtypes of post-COVID-19 syndrome (or long COVID) and their respective potential therapies. Reviews in Medical Virology, DOI: 10.1002/rmv.2315.

Yusov A.A. and Alpidovskaya O.V. (2023). Left ventricular thrombosis and a cute cardiovascular failure in patients after SARS-CoV-2 infection. Profilakticheskaja medicina, 26(11), 78–81, (in Russian), DOI: 10.17116/profmed20232611178.

Zhang L. and Zhang M. (2024). Changes in coagulation indices and obstetric complications in third trimester pregnant women with COVID-19. Chin J School Doctor, Vol.38, No.6, 455–458.

Zhang Y. and Ma Z.F. (2020). Impact of the COVID-19 pandemic on mental health and quality of life among local residents in Liaoning Province, China: A cross-sectional study. International Journal of Environmental Research and Public Health, 17, 2381, DOI: 10.3390/ijerph17072381.

Zhao Y., Shi L., Jiang Z., Zeng N., Mei H., Lu Y., Yang J., Jin F., Ni S., Wu S., Su S., Zheng Y., Yuan K., Yan W., Sun S., Meng S., Sun J., Khan Z., Aarsland D., Shi J., Li X., Bao Y. and Lu L. (2023). The phenotype and prediction of long-term physical, mental and cognitive COVID-19 sequelae 20 months after recovery, a community-based cohort study in China. Mol Psychiatry. Apr; 28(4):1793-1801. DOI: 10.1038/s41380-023-01951-1.

RESEARCH PAPER

MULTI-OBJECTIVE VALIDATION OF THE RUNOFF FORMATION MODEL IN THE HIGH-MOUNTAIN RIVER BASIN OF THE CENTRAL CAUCASUS

Ekaterina D. Pavlyukevich[1,2], Nelly E. Elagina[3]*, Inna N. Krylenko[1,2], Ekaterina P. Rets[2], Abror A. Gafurov[4], Yuri G. Motovilov[2]

[1]Lomonosov Moscow State University, 119991, Moscow, Russia
[2]Water Problems Institute of the Russian Academy of Sciences, 119333, Moscow, Russia
[3]Institute of Geography of the Russian Academy of Sciences, 119017, Moscow, Russia
[4]German Research Centre for Geoscience, Telegrafenberg, 14473, Potsdam, Germany
***Corresponding author:** nelly_elagina@igras.ru
Received: February 12th 2025 / Accepted: April 30th 2025 / Published: June 30th 2025
https://doi.org/10.24057/2071-9388-2025-3887

ABSTRACT. This study demonstrates the effectiveness of a multi-objective validation approach for a distributed hydrological model in a high mountain river basin. Focusing on the Baksan River Basin in the Central Caucasus, where snow and glacier melt play a crucial role in runoff formation, we applied the ECOMAG model, which has proven its reliability in high-altitude hydrology. To enhance the validation accuracy, we integrated diverse data sources, including observed river discharge, MODIS-derived snow cover, stable isotope hydrograph separation, glacier mass balance observations, and glacial runoff simulations from the A-Melt model. The results confirm the high performance of the model across multiple hydrological components. The simulated and observed discharge values showed strong agreement, with the Nash-Sutcliffe efficiency exceeding 0.8 for both the calibration and validation periods. The model successfully captured seasonal snow cover variations, achieving an R^2 of 0.85 when compared with the MODIS data. Isotopic hydrograph separation further validated the accuracy of the simulated meltwater and rainfall contributions to runoff. Although glacier ablation simulations showed some deviations, particularly for the Djankuat Glacier, these findings highlight opportunities for refining glacial process representation. Overall, this study confirms the robustness and applicability of multi-objective validation for hydrological modeling in complex mountainous regions. The integration of multiple observational datasets significantly enhances the reliability of modeling results, providing valuable insights into water resource management, climate impact assessments, and sustainable development in glacier-fed river basins.

KEYWORDS: mountain hydrology, runoff formation modeling, mountainous regions, glacier modeling, Central Caucasus, A-melt, ECOMAG

CITATION: Pavlyukevich E. D., Elagina N. E., Krylenko I. N., Rets E. P., Gafurov A. A., Motovilov Y. G. (2025). Multi-objective validation of the runoff formation model in the high-mountain river basin of the Central Caucasus. Geography, Environment, Sustainability, 2 (18), 189-200
https://doi.org/10.24057/2071-9388-2025-3887

ACKNOWLEDGEMENTS: The study was carried out under the Governmental Order to Water Problems Institute, Russian Academy of Sciences, subject no. FMWZ-2025-0003 (ECOMAG model adaptation and calibration), under the state assignment of the Research Laboratory of Soil Erosion and Fluvial Processes, Faculty of Geography, Lomonosov Moscow State University (CITIS 121051100166-4 (results analysis), 121051400038-1 (snow cover data analysis)), and under the Russian Science Foundation Grant No. 23-17-00247 «Development of parameterization of mountain glaciers for Earth system models» (A-Melt modeling).

Conflict of interests: The authors reported no potential conflict of interests.

INTRODUCTION

Assessing the spatial and temporal variability of water balance components using distributed hydrological models at a regional scale is crucial for addressing practical challenges in managing water resource, including evaluating the impact of climate variability on water resources. Such studies require accurate model calibration and validation, which are typically performed using a traditional method based on observed discharge data. Previous research has highlighted that process-based multi-objective calibration and validation effectively reduce uncertainty and improve forecasting accuracy in hydrological modeling (Efstratiadis and Koutsoyiannis 2010). Many studies have incorporated additional data sources to enhance model validation. Remotely sensed hydrological variables, such as actual evapotranspiration (Immerzeel and Droogers 2008; Zhang et al. 2009), soil moisture (Li et al. 2018; Parajka et al. 2009; Poméon et al. 2018; Wanders et al. 2014), snow cover (Duethmann et al. 2014; Han et al. 2019; Tong et al. 2021; Udnæs et al. 2007), and total water storage (Bai et

al. 2018; Trautmann et al. 2018) have been frequently used to assess model performance. Stable isotope tracer data also offer valuable insights for evaluating hydrological models by providing information on water flow pathways and sources (Ala-Aho et al. 2017; Holmes et al. 2020; Holmes et al. 2023).

However, multi-objective validation is commonly used in lowland areas because of the availability of extensive data from monitoring stations, simpler terrain, and more predictable hydrological processes. Mountainous areas present challenges for multi-objective validation. The complex terrain, steep slopes, and varying land cover create heterogeneous hydrological processes that are more complicated for modeling. Additionally, data availability is often limited with fewer monitoring stations. This makes validation more challenging than in the lowland regions. Assessment of snow cover is crucial for more complex hydrological modeling and is perhaps one of the most important unresolved problems for modeling in mountainous areas (Dozier et al. 2016; Lettenmaier et al. 2015; Treichler and Kääb 2017). This problem becomes more pronounced in the case of complex distribution mechanisms for solid precipitation due to differences in moisture and wind conditions in complex high-mountainous topographies (Mikhalenko et al. 2020). Typically, spatially distributed snow information over large areas is the result of a combination of modeling or interpolation based on sparse in situ measurements, remote sensing data, or climate reanalysis (Treichler and Kääb 2017). The approach of determining snowpack thickness was presented in a recent study (N. E. Elagina et al. 2024), where the glacial runoff model A-Melt (Rets et al. 2021) in combination with geodetic estimates for Mount Elbrus (North Caucasus) was used (Kutuzov et al. 2019) (Kutuzov et al., 2019).

This study focuses on the significantly glaciated Baksan River basin in the North Caucasus. Snow and glaciers provide a stable water supply throughout the year, which supports drinking water, irrigation, and hydropower generation. Modeling of runoff processes provides detailed knowledge of the glacier and snow-fed components of runoff, which is essential for assessing water availability and planning for future climate impacts. Validating hydrological models ensures reliable forecasts of water availability, helps to manage water resources, reduces flood risks, and sustains essential sectors in this mountainous region.

One of the models that has proven to be effective in high-altitude river runoff modeling is the ECOMAG model (ECOlogical Model for Applied Geophysics) (Motovilov 1999), which has been applied to understand the behavior of hydrological systems and explain the impacts of different climate and land-use scenarios across a wide range of geographic regions (Moreido and Kalugin 2017; Kalugin and Motovilov 2018), including mountainous areas with present-day glaciers and permafrost (Gelfan et al. 2017; Kornilova et al. 2024; Kornilova et al. 2021; Lisina et al. 2023; Motovilov et al. 2017). Various datasets were used to test and validate the ECOMAG model in lowland basins to ensure its performance across multiple hydrological components. Simulation results based on data from the NOPEX experiment in Sweden (Motovilov 1999) showed that the model effectively captured spatial and temporal variations in water balance components, including soil moisture and groundwater levels. In the process of step-by-step calibration of parameters and modeling of snow cover and soil moisture fields in the Volga Basin, the actual fields of these characteristics were constructed based on the data of en-route snow measurement observations and productive moisture measurements at agrometeorological stations (Motovilov and Gelfan 2018). Using a modification of the ECOMAG-HM model for the Kama River basin, modeled copper concentrations were compared on a daily basis with episodic measurements at two hydrochemical monitoring stations (Motovilov and Fashchevskaya 2019). However, the model has been specifically adapted for the first time (Kornilova et al. 2023; Kornilova et al. 2024) to provide a detailed multi-objective validation in an upland basin.

The aim of this study is to consider the possibilities and limitations of multi-objective validation of a distributed hydrological model in a high-mountain river basin. For the multi-objective validation of the ECOMAG hydrological model, we used available data on different components of the water balance for the Baksan River Basin, including MODIS snow cover data, ablation of representative glaciers, and isotope analysis data in the high-mountain Baksan River Basin of the Central Caucasus. Additionally, the results of the glacial runoff calculations using the A-Melt model were used to cross-validate both the ECOMAG and A-Melt models.

Data and methodology

Study area

The Baksan River Basin is located within the Central Caucasus region, which is part of the larger Caucasus Mountain range known for its high and inaccessible topography. This area represents one of the most important centers of glacial activity in the Caucasus. Approximately 232 km^2 of the region is covered by glaciers, and approximately 30% of this total area belongs to the Elbrus volcanic massif. Mount Elbrus, the highest peak in the Caucasus at 5,642 m a.s.l., has a glacier covering approximately 109 km2 (in 2017), which is approximately 10% of the total area glaciated in the whole of the Caucasus.

The overall glacier coverage within the Baksan Basin ranges from 7.4% at the Zayukovo outlet to 16.5% at the Tyrnyauz outlet (Fig. 1). The river's hydrological regime is characterized by relatively low flows during the autumn and winter months, and significantly higher flows during the spring and summer months, complicated by sporadic peaks of rainfall floods. In this study, the gauging station "Zayukovo" was selected as the outlet point, which collected the majority of glacial runoff from the Baksan River (Fig.1). The average elevation of the river basin is 2,350 m with a total area of 2,100 km^2. Of this area, 64% is located in the high-altitude region of the basin above 2,000 m. According to data from hydrological gauges Tyrnyauz and Zayukovo between 1970 and 2022, mean long-term discharge values were 24.6 m^3/s and 35.4 m^3/s for these stations, respectively.

Runoff formation model

ECOMAG is a hydrological model designed to simulate key processes within the water cycle. It accounts for infiltration, evaporation, soil heat and water dynamics, snow accumulation and melt, freezing within the snowpack, as well as surface, subsurface, and groundwater flow - ultimately modeling river discharge. A comprehensive list of model parameters and equations is available in the study by Motovilov et al. (1999).

A simplified glacier block was used in the ECOMAG model for the study basin, based on the simple temperature index approach, assuming that ice and snow melting occurs during periods of positive temperatures (Hock 2003). The glacier block of the ECOMAG runoff formation model operates as follows: elementary watersheds containing glaciation are defined along with the percentage of glaciation within each watershed. The ice melt calculation subroutine is always activated in computational watersheds where glaciers are present. At the beginning of summer, when the watershed is covered with snow, only snow melts, using the snowmelt coefficient. As snow melts and recedes, the snow-covered area of the computational unit decreases. When the snow-covered

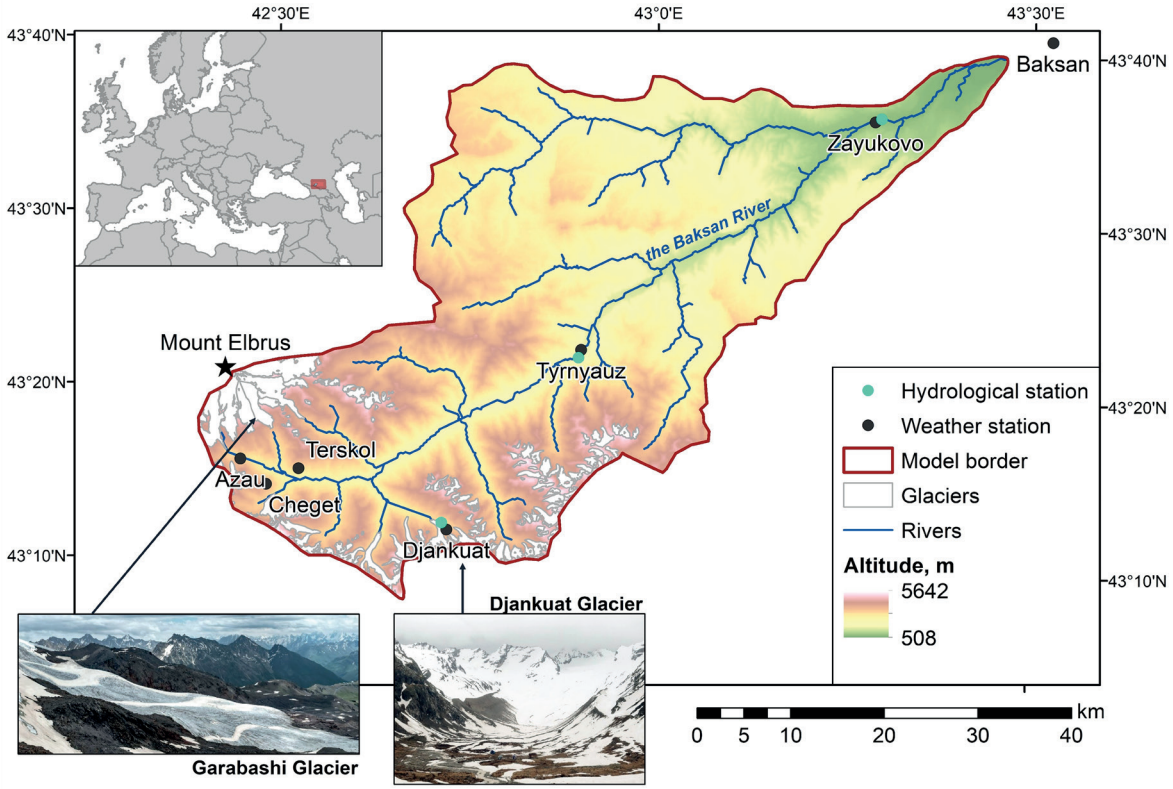

Fig. 1. The Baksan River basin

area becomes smaller than the glaciated area, ice melting begins on the exposed surface using the ice melt coefficient. The melt coefficients may differ from basin to basin since they must implicitly take into consideration every element affecting the heat balance. Therefore, in the core version of the ECOMAG model, the possibility of calibrating the melt coefficients was retained while ensuring that the values remained within the natural range.

For this study, the basin was divided into 662 elementary watersheds, 102 of which were glaciated, 30 of which were more than 50% glaciated. For meteorological input, we used data from seven stations in the region's meteorological network for the period 1977-2022 (Fig. 1). Information about the underlying surface, including topographic, soil, and landscape maps as well as glaciation data, was determined for every elementary watershed (Table 1).

Water discharge is a common hydrological modeling method, so it was used to calibrate and validate the model. We compared the observed and simulated values to assess the ability of the model to accurately reproduce river flow dynamics. Using this approach, we calibrated the model and evaluated its accuracy during validation to ensure realistic simulation of river behavior. We utilized criteria generally accepted in hydrology (Motovilov and Gelfan 2018), such as BIAS and Nash-Sutcliffe efficiency, to assess the quality of our modeling. The results are presented in section 3.1.

Data and methods of runoff formation model validation

We used remotely sensed snow cover data, isotope analysis data, observed ablation data from representative glaciers, and glacier melt modeling results to validate

Table 1. Inputs to ECOMAG model in the Baksan River basin

Data type	Period / Date of publication of the data	Spatial/temporal resolution	Source
Physical characteristics of the basin			
Digital Elevation Model (SRTM)	2000	90m×90m	Consultative Group for International Agriculture Research Consortium for Spatial Information (CGIAR-CSI)
Landuse	1990 (Republic of North Ossetia), 1997 (Kabardino-Balkarian Republic)	1:750,000	Atlas of the Kabardino-Balkarian Republic and Republic of North Ossetia
Soil	1990 (Republic of North Ossetia), 1997 (Kabardino-Balkarian Republic)	1:750,000	Atlas of the Kabardino-Balkarian Republic and Republic of North Ossetia
Meteorological and glaciological data			
Precipitation, temperature	1977–2022	Daily	Meteorological annual: Terskol (2141 m), Cheget (3040 m), Tyrnyauz (1275 m), Zayukovo (673 m), Baksan (457 m), Azau (2350 m), Dzhankuat (2600 m)
Glaciation area	2001–2003	10m×10m	RGI 6.0 (Randolph Glacier Inventory-A Dataset of Global Glacier Outlines: Version 6.0, 2017)

Table 2. Data for validation of ECOMAG model in the Baksan River basin

Data	Compared values	Period	Temporal resolution	Source of model validation
River discharge	Average daily discharge (m^3/s)	1977-2022	Daily	Hydrology annual
Snow cover	Spatial and temporal variability of snow cover (%)	2000-2019	Daily	Terra-Aqua MODIS (Justice et al. 2002)
Isotopic hydrograph separation	Meltwater and rainfall runoff components (m^3/s)	2020-2021	Daily	Stable isotopes sampling (Rets et al. 2024)
Mass balance glacier observations	Ablation measured on representative glaciers (mm)	2000-2010	Yearly	World Glacier Monitoring Service (Zemp et al. 2015)
Glacier melting modeling	Snow and glacial melt runoff (m^3/s)	1997-2022	Yearly	A-Melt (Rets et al. 2021)

the ECOMAG model (Table 2). This section provides an overview of the data used in the multi-objective validation.

Snow cover

We used data on snow cover derived from Moderate Resolution Imaging Spectroradiometer (MODIS) images, which are instruments used by the Earth Observing System (EOS) satellites Terra and Aqua (Justice et al. 2002), to help check our model's accuracy. The spatial resolution for interpreting snow cover information was 500 m, with a revisit time of one day per area. Snow cover masks derived from MODIS satellite data with daily temporal resolution were obtained using the MODISNOW tool developed by Gafurov et al. (2016). The method was developed to estimate the actual pixel coverage for cloud-covered areas by using spatial and temporal information about cloud-covered pixels and processing the portion of input data by removing a fraction of cloud-covered pixels. The ECOMAG model consists of a module that generates the outputs of individual characteristics that determine the runoff formation for each small catchment. This information was used to create maps showing the spatial distribution of snow cover on any selected day within the study area. In this study, we explored the potential of using additional data from MODIS Aqua and Terra images to validate the temporal and spatial distributions of snow cover. Daily data from 2000 to 2019 were used to validate the simulation of basin snow cover (%) using the ECOMAG model. Additionally, the spatial distribution of snow cover was validated using the example of the outstanding water year 2017.

Isotopic hydrograph separation

The results of isotopic analysis of natural waters can serve as an additional source for validating the runoff formation model. The distinct differences in the isotopic composition of glacial meltwater, snow water, and liquid precipitation allow for the estimation of the proportion of these components in total river runoff.

Dissecting a hydrograph into its genetic components using natural tracers is a widely used method for glacier-fed basins (Hoeg et al. 2000; Vasil'chuk et al. 2016). Tracers can be either total mineralization or specific ions, atoms, or molecules.

The results of the isotopic hydrograph separation performed for the Baksan River by Rets et al. (2024) were used in this study. Event-based isotope sampling was conducted along the Baksan River during the 2020-2021 period, approximately 5-6 times per season (Table 3, Fig. 2). A heavy oxygen isotope with an atomic mass of 18 (δ18O) was used as the tracer. After the sample analysis, the hydrograph of the Baksan River was divided into two components: meltwater runoff (seasonal snow and glacier meltwater) and rainfall runoff (Rets et al. 2024). The study does not outline subsurface/groundwater flow as a runoff source; instead, it considers it as a mixture of liquid precipitation, seasonal snow, and glacier ice melt navigating through the subsurface portion of the watershed. Since water stable isotopes are conservative tracers, their concentration remains unaffected by the flow pathway unless it is associated with substantial kinetic fractionation, such as evaporation from water reservoirs or watershed surfaces, or snow sublimation (Oshun et al. 2016). Genetic partitioning of a hydrograph using natural tracers is based on the water balance equation (Rets et al. 2024).

The ECOMAG model of runoff formation, based on the available set of model outputs, allows for the estimation of runoff components only for a month. To estimate the genetic components, the monthly average outputs of the water yield from snow and ice, precipitation on soil, and evaporation from soil for each elementary catchment were used. These data were compared with the meltwater and rainfall runoff components (m3/s, %) based on the results of the isotope analysis. The contribution of the glacial component was considered by increasing runoff when the model's glacier block was activated. From all sampling dates, the mid-month dates were chosen for comparison with the model results.

Mass balance glacier observations

The mass balance time series from the World Glacier Monitoring Service (WGMS) dataset can serve as a valuable reference for validating ice-melt simulations. By comparing modeled glacier ablation with observed data, researchers can assess the accuracy of simulated ice-melt processes (Eis et al. 2021; Schaefli et al. 2005). The outcomes of the mass balance studies of the reference glaciers of the North Caucasus were employed to validate the runoff formation model. The continuous series of observations on the small valley glacier Djankuat (2750-3670 m a.s.l, 2.5 km^2) started in 1967 and continues to date (Popovnin et al. 2024). The Garabashi glacier is a part of the Mt. Elbrus glacier volcanic massif and is located on the southern slope of the glacier system (3400-4900 m a.s.l., 3.9 km^2). Monitoring began in 1982 and has continued to date (Rototaeva et al. 2019). Both glaciers are included in the observation system of the World Glacier Monitoring Service (WGMS) and are now considered representative of the Caucasus region. The mass balance observations included annual, winter, and summer measurements of mass balance according to ablation stakes, radar and manual snow measurements, and snow pits.

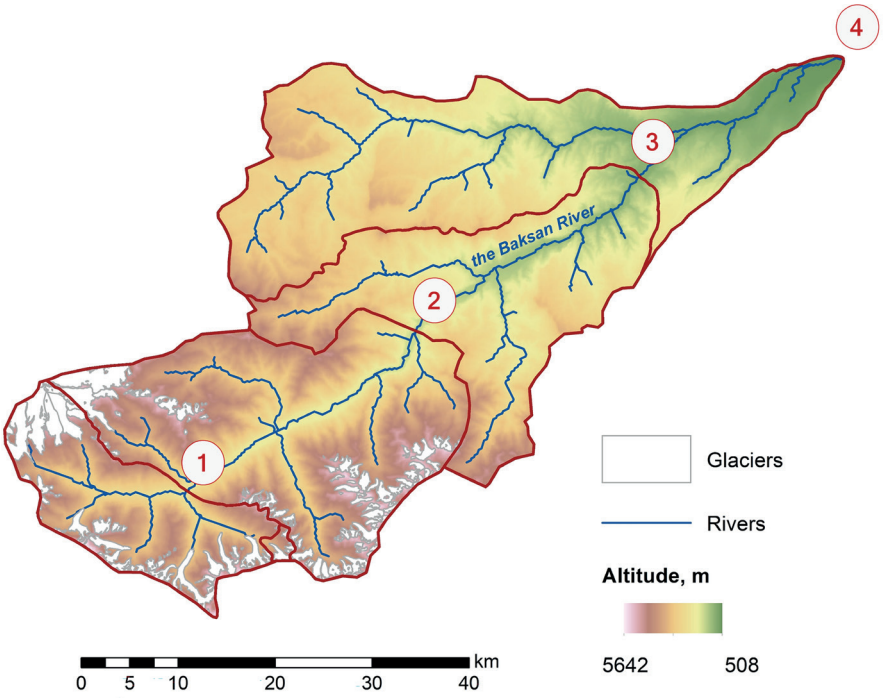

Fig. 2. Sampling points for isotope analysis from the Baksan River at different sites

Table 3. Characteristics of isotope sampling sites in 2020-2021

№	Cross-section	Basin area, km^2	Sampling point elevation, m	Glaciation, %
1	Elbrus	296	1783	27
2	Tyrnyauz	964	1247	16
3	Zhanhoteko	1500	790	11
4	Islamay	2259	510	7

Glacier melting modeling

The additional method used for validation was glacial runoff calculated using the A-melt energy-balance model. One of the most important hydrological variables is glacial runoff, which is a component of the water–ice balance. More complex methods of calculating the glacier melting amount based on energy-balance methods are commonly developed for glaciological purposes (Gabbi et al. 2014; Reveillet et al. 2017; Sakai and Fujita 2017; Shannon et al. 2019). These models require detailed meteorological data as inputs, such as long and shortwave radiation balance, wind speed, humidity, and pressure. At the same time, it is complicated to transfer energy-balance calculations to a regional scale because of the large amount of input data required for such models. Simpler temperature index approaches are commonly used for regional runoff modeling in large basins. In this study, we used the results of runoff modeling from the Elbrus glaciers in the Baksan River basin using an energy-balance A-Melt model of snow and ice melt in the high mountain zone and the ECOMAG runoff formation model results for the cross-validation of both models.

The A-Melt model is based on the heat balance equation and calculates the mass balance of the glacier and its components based on meteorological data. The model simulates the vertical distribution of density, temperature, and water content in the snowpack, considering water seepage, refreezing in the snow thickness, and the snow–ice and firn thickness boundary and runoff. The A-Melt model has been successfully adopted for glaciers of the North Caucasus (Rets et al. 2011), Central Tien-Shan (Rets et al. 2021), and Svalbard Archipelago (Elagina et al. 2021). A more precise description of the A-Melt model has been provided in previous studies (Elagina et al. 2021; Rets et al. 2011; Rets et al. 2021). The A-Melt model experiment procedure and the results used in the current study for ECOMAG model validation are fully described step-by-step in (Elagina et al. 2024) and will be briefly described further.

Glacial runoff from the southern slope glaciers of Mt. Elbrus contributes to the formation of river runoff in the Baksan River Basin. After the model was applied for the entire Mt. Elbrus glacier system, the model output was extracted for the glaciers Bolshoy Azau, Maliy Azau, Garabashi, Terskol, Basin 25, Irik, and Irikchat, which supply the Baksan River basin with meltwater.

The model computes the heat balance equation for each point of the 250-m spatial grid. As meteorological input, we used data from the ERA5 reanalysis (Hersbach et al. 2020), which allows the reliable reconstruction of the meteorological conditions on Elbrus in accordance with the experiments given in the study (Mikhalenko et al. 2020). For the incoming radiation data, we used reanalysis data for a single level. Reanalysis data for air temperature, relative humidity, and wind speed were obtained for various pressure levels (500, 550, 600, 650, and 700 hPa), corresponding to an altitude range of 3000–5500 m above sea level. The values of the aforementioned meteorological parameters that fell between the input pressure levels were interpolated. The input data related to topographical features such as glacier area and outlines and surface elevation were obtained by analyzing available space data. The data sources include Spot 7, Landsat imagery, 2017 Pléiades DEM by the Pléiades Glacier Observatory initiative of the French Space Agency (CNES) and the 1997 0.5m-resolution DEM by the Faculty of Geography, Moscow State University (Zolotarev and Kharkovets 2000). To

identify the surface type (ice/firn/snow), we used the Google Earth Engine automated algorithm proposed by Li et al. (2022), which allows classification of bare ice and snow cover on glaciers using Landsat images. The model does not simulate ice flow, so the topography features, surface type, and glacier boundaries were updated in the input data in 1984, 1996, 2006, 2011, 2016.

Because the model does not include the orographic component of precipitation distribution, a spatial coefficient distributed over the 250-m spatial grid was applied to distribute the solid precipitation amount over the entire area of Mt. Elbrus. The procedure is as follows:

1. We calculated the average summer mass balance and obtained a map of its average distribution for Mt. Elbrus from 1997 to 2017

2. The average winter mass balance map for 1997-2017 was determined by subtracting the geodetic mass balance map of the Elbrus glacier system for 1997-2017, obtained from Kutuzov et al. (2019) and the modeled average summer balance map for the same period. This subtraction provides an understanding of solid precipitation patterns across the glacier system.

3. The average winter mass balance at every grid point was then normalized by the amount of precipitation according to the ERA5 reanalysis data for the future calculation of winter mass balance for each balance year.

The water that formed during the ablation process, excluding the water that refreezes in the snow and firn layer and at the boundary with ice, that is, gravitationally free water ready to flow off the glacier, is considered glacial runoff in these calculations. The contribution of seasonal snow covering the surrounding slopes was excluded from the calculation of glacial runoff by Elbrus. Meltwater infiltration into the soil was not considered in the calculations. The values of glacial runoff from Elbrus were converted to units of volume per unit time. These data were then compared to the glacier runoff calculations obtained using the ECOMAG model. The glacier runoff in the ECOMAG model was calculated as glacier and snow ablation, excluding water refreezing in the snowpack.

Results

River discharge

The study (Kornilova et al. 2023) provides a step-by-step description of the model calibration and validation process. Briefly, data from the Tyrnyauz and Zayukovo gauging stations on the Baksan River were used, with a calibration period of 2000–2008 and a validation period of 2009–2017. Key runoff-influencing parameters were adjusted, including evaporation coefficients, active layer thickness, melting coefficient, snow water-holding capacity, and temperature gradients. The model demonstrated high accuracy (NSE > 0.8, annual runoff deviation < 6%), as illustrated in Fig. 3 and Table 4.

Snow cover

MODIS daily snow cover data from 2000 to 2019 were used to validate the ECOMAG model. The model effectively captured snow cover dynamics (Fig. 4a). The coefficient of determination R^2 for the average monthly snow cover values was 0.85, with a relative error of 20% (Fig. 4b). However, the model tended to overestimate snow cover values, particularly during the spring and winter (Fig. 4c).

To validate the runoff formation model for the spatial distribution of snow cover, the calculation results for the first day of each month in 2017 were used and compared with the snow cover data from the MODIS Terra and Aqua satellites (Fig. 4d). Overall, the model accurately simulated the annual

Table 4. ECOMAG model calibration and validation periods performance criteria

Gauging station	Glaciation, %	Watershed area, km²	Calibration period 2000-2008		Validation period 2009-2017	
			NSE	pBIAS, %	NSE	pBIAS, %
Tyrnyauz	17.5	838	0.82	−1.71	0.90	+5.98
Zayukovo	7.4	2100	0.85	+3.24	0.90	+3.58

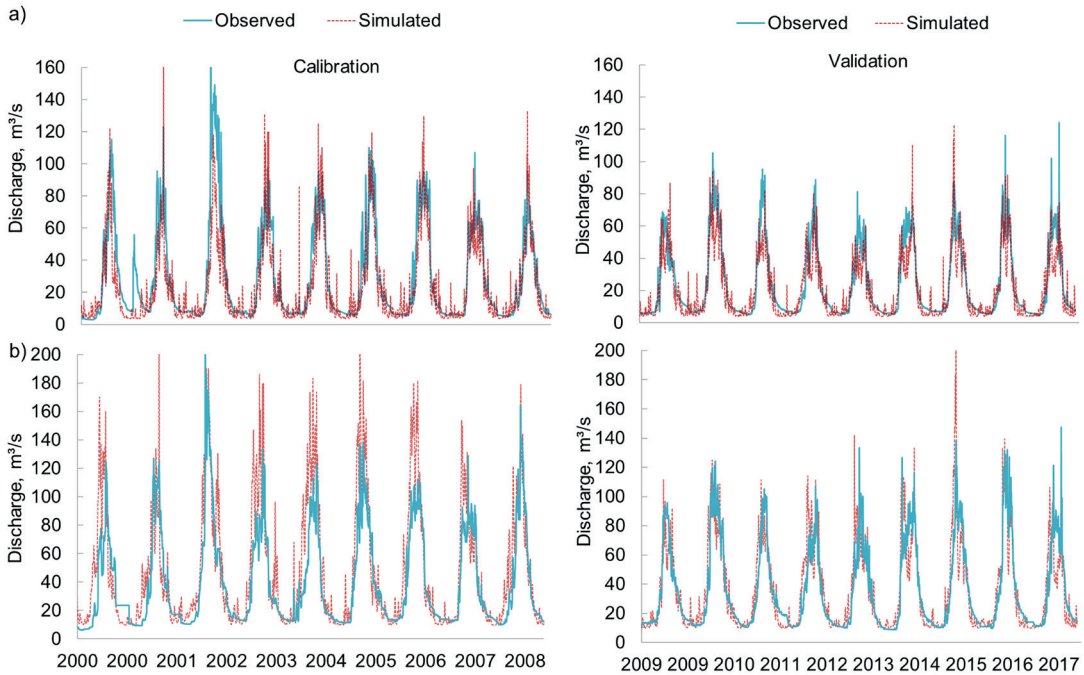

Fig. 3. Model performance at Tyrnyauz (a) and Zayukovo (b) gauges during the calibration (2000–2008) and validation (2009–2017) periods

course of snow cover changes. The peak was observed in February, followed by a gradual decrease until a minimum was reached in August and then an increase until December. However, during the spring months, the modeling results showed higher snow coverage than that observed in the MODIS data. Nevertheless, the modeling results for snow cover at the end of August agreed well with the MODIS data and generally corresponded to the mean annual position of the climatic snowline. It should be noted that the model data were presented for specific catchments with an average area of 9.9 km^2. Furthermore, within a specific catchment area, all model parameters were averaged. The pixel area of the satellite image was 0.25 km^2, which could be one reason for the ECOMAG snow cover model's overestimation of snow cover model.

Isotopic hydrograph separation

From all sampling dates, mid-month dates were chosen for comparison of the isotopic analysis and model results (Fig. 5a-d). Based on the comparison, it can be seen that the model follows the intra-annual variability in the runoff sources, specifically a decrease in meltwater runoff and an increase in rain runoff during the summer months.

The data suggest that the proportion of snowmelt runoff decreased during the summer months, whereas the proportion of rain runoff increased. According to the model data, snowmelt accounts for approximately 70% of the total runoff in June but only approximately 35% in August. Additionally, the amount of snowmelt naturally decreases from the source to the downstream areas, while rain runoff increases. At the Elbrus station, the proportion of snowmelt ranged from 40% in August to 90% in June. It varied between 20% and 45% at Islamey station.

The average relative error between the model and the actual values for all measurements (four sampling points) was 19 %. The coefficient of determination for the meltwater component is 0.81 and for the rainfall component it is 0.86. The model tends to overestimate snowmelt values in June and underestimate them in July and August, on average.

Mass balance glacier observations

The actual values of ablation for reference glaciers for the period 2000-2009, obtained from the data of the World Glacier Monitoring Service (Zemp et al. 2015) and (Popovnin et al. 2024), were compared with the model values of snow and ice melting for the period of field observations (May-September) in the elementary catchment where the glacier is located (Fig. 6).

For the Garabashi Glacier, there was a good agreement between the modeled and actual values, with a discrepancy of -12%. However, for the Djankuat Glacier, the relative error was much higher, averaging -55% over the study period. Coefficient of determination R^2 is 0.20 for the Garabashi Glacier and 0.18 for the Djankuat Glacier, respectively.

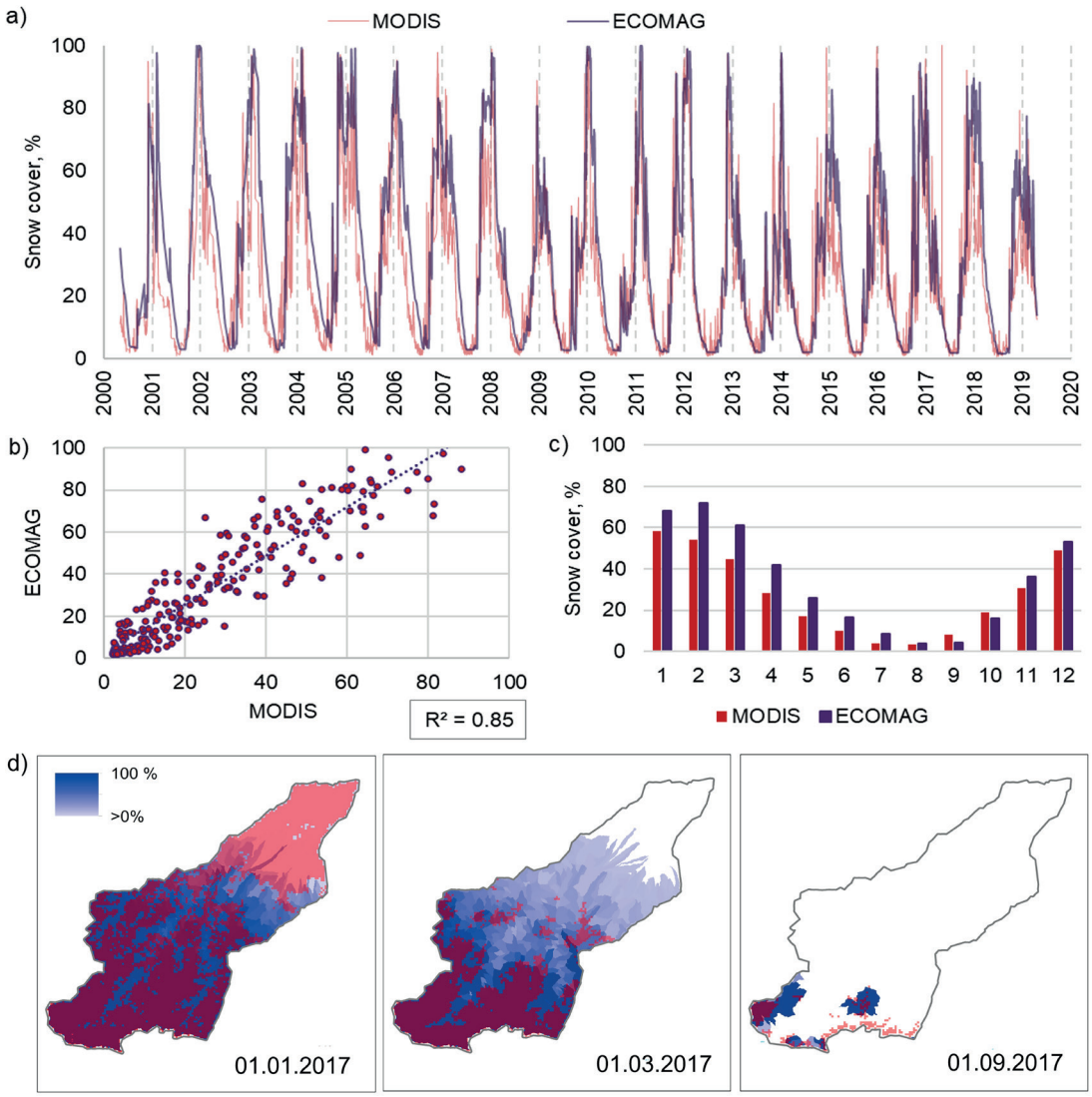

Fig. 4. Changes in snow cover (a), scatter plots (b) and mean monthly snow cover (c) from MODIS and ECOMAG data from 2000 to 2019; spatial distribution of snow cover (d) within the Baksan River basin in 2017: red - MODIS data, blue - modeling results (% of elementary catchment coverage)

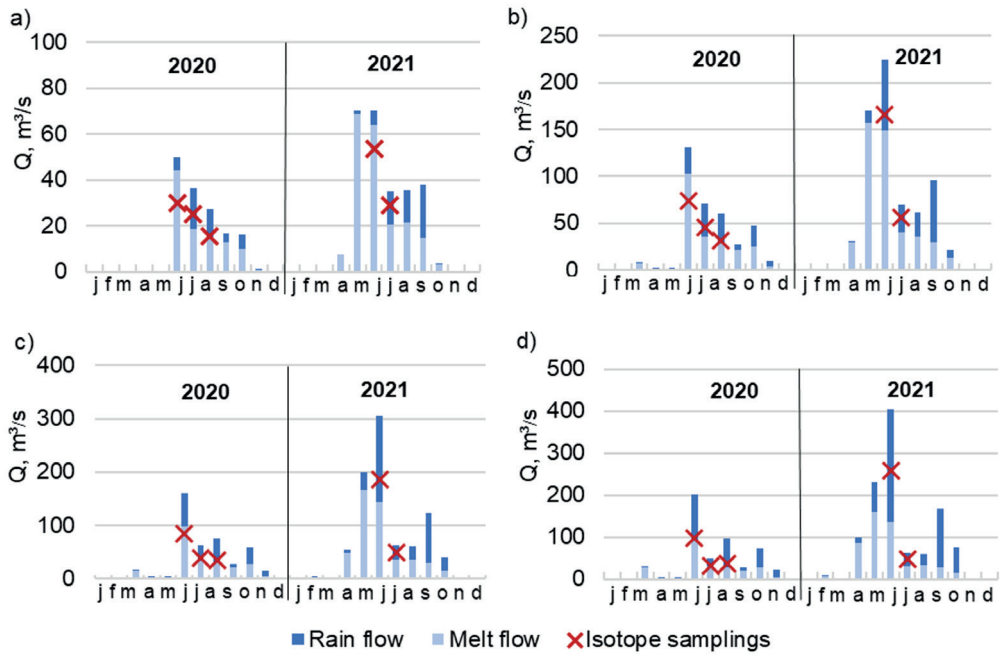

Fig. 5. Shares of melt and rainwater for different months according to model data and isotope analysis for different sites in 2020–2021: Elbrus (a), Tyrnyauz (b), Zhankhoteko (c), and Islamey (d)

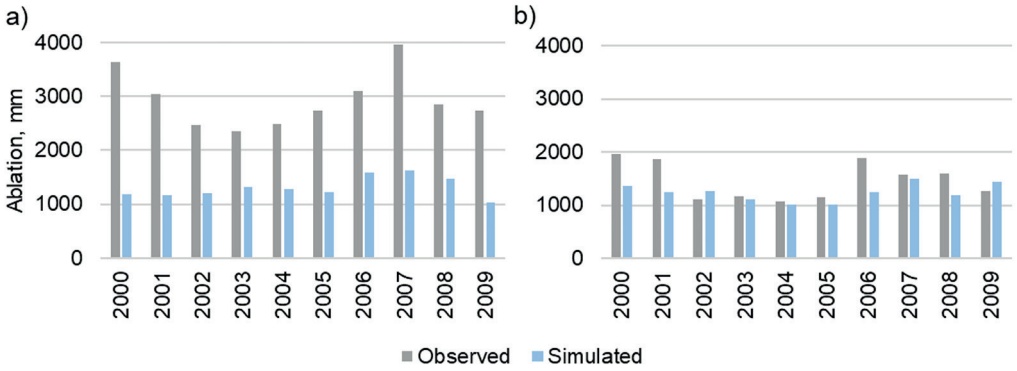

Fig. 6. Actual and calculated ablation values of (a) Djankuat and (b) Garabashi glaciers for the period 2000-2009.

Glacier melting modeling

The results of the runoff simulation for the Mt. Elbrus glaciers using the ECOMAG and A-Melt models are shown in Fig. 7. Fig. 7a presents the annual runoff values from the ECOMAG model extracted for the Elbrus Basin and the annual glacial runoff series according to the A-Melt model, which includes ice and snow meltwater. The series obtained using the A-Melt energy-balance model reflects the values of the average annual flow, considering meltwater, freezing in the snow and firn layers, and at the border of snow and ice. The model results were compared with the model output extracted for the glaciers Bolshoy Azau, Maliy Azau, Garabashi, Terskol, Basin 25, Irik, and Irikchat, which supply the Baksan River Basin with meltwater. Fig. 8b shows a comparison of the annual runoff values. The results of simulations indicate that the average runoff values are in good agreement (2.0 m^3/sec by ECOMAG and 2.4 m^3/sec by A-Melt, pBias = 18%). The average snow and ice glacial runoff components assessed by A-Melt model are 1.0 and 1.5 m^3/sec, and 1.4 and 0.6 m^3/sec assessed by ECOMAG model correspondingly. The higher values of the snow component of runoff and the lower values of the ice component of runoff according to the ECOMAG model compared to the results of modeling according to the A-Melt model are due to the difference in approaches to determine the type of surface for which the calculation is made (see Discussion).

DISCUSSIONS

In mountainous areas, access to observational hydrometeorological data can be limited because of the difficult terrain, harsh weather conditions, and high costs of monitoring stations. Considering these challenges, it seems unrealistic to expect an increase in observational network density in the study regions in the near future. Therefore, relying solely on traditional methods for validating discharge may not provide a complete assessment of hydrological model performance.

Multi-objective validation offers a way to evaluate the model's performance in multiple aspects of the water balance, enhancing the reliability of the assessment by incorporating various hydrological components and providing a more comprehensive understanding of the accuracy and ability to simulate complex mountain hydrology (Table 5)..

In general, the ECOMAG snow cover model showed good agreement with MODIS data in terms of inter- and intra-annual variability. However, the runoff formation model indicated that snow cover during the spring months was higher than that observed from the remote sensing data. This finding suggests that meteorological data from stations located in the Baksan River Valley may not be sufficient to accurately represent the snow cover in adjacent side valleys with complex topographic conditions.

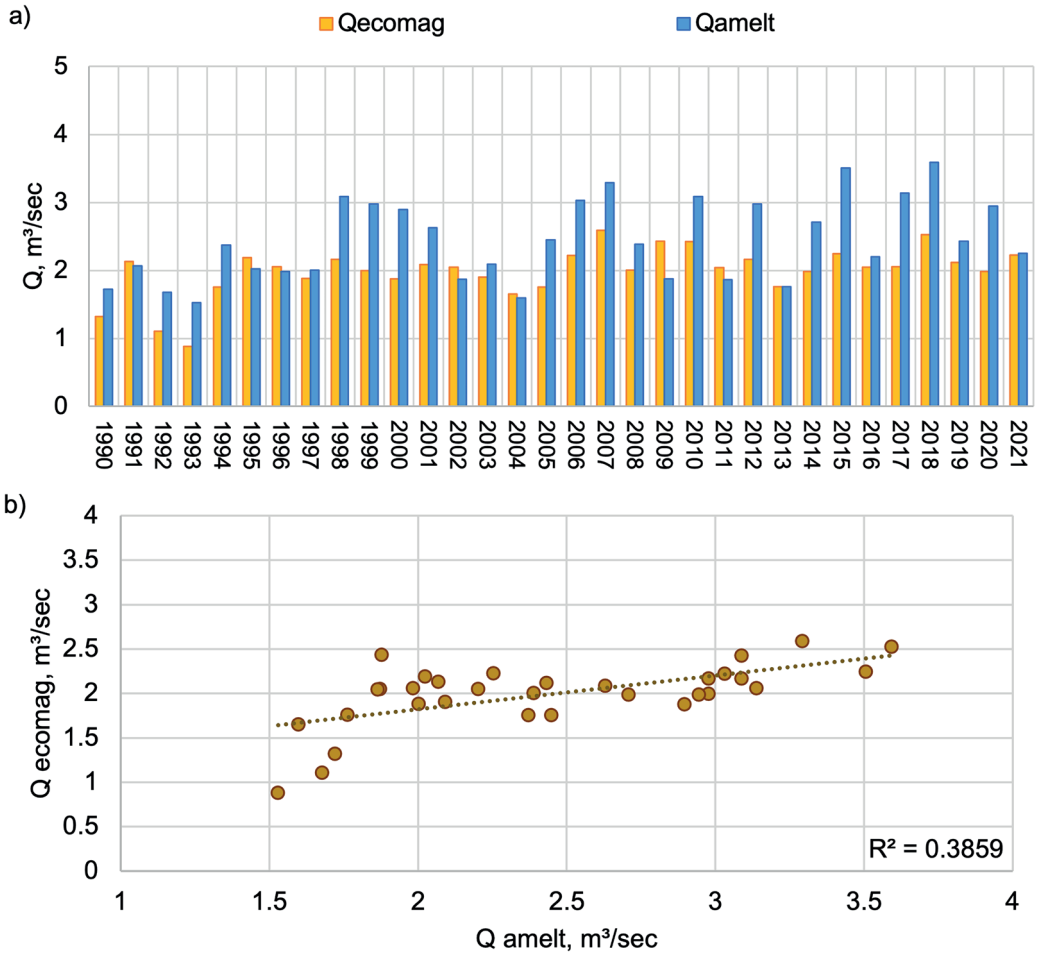

Fig. 7. The results of runoff modeling using the ECOMAG and A-Melt models are as follows: (a) annual runoff values; (b) comparison of model runoff values for Bolshoy Azau, Maliy Azau, Garabashi, Terskol, Basin 25, Irik, and Irikchat glaciers that supply the Baksan River basin with meltwater

Table 5. Results of multi-objective validation of ECOMAG model in the Baksan River basin

Data	Values	Distribution	NSE	R^2	pBIAS, %
Snow data (MODIS)	Snow cover (%)	Daily	0.55	0.72	+19%
		Monthly	0.64	0.85	+20%
Isotopic hydrograph separation	Meltwater runoff (m^3/s)	Monthly	0.74	0.81	–18%
	Rainfall runoff (m^3/s)	Monthly	0.37	0.86	+20%
Mass balance glacier observations (WGMS)	Garabashi ablation (mm)	Yearly	<0	0.20	–15%
	Djankuat ablation (mm)	Yearly	<0	0.18	–55%
Glacier melting modeling (A-Melt)	Glacial runoff (m^3/s)	Yearly	<0	0.39	–18%

To address this issue, the use of high-resolution meteorological data, reanalysis, mesoscale modeling, and orographic precipitation modeling (Toropov et al. 2023) could improve the model's ability to simulate snowmelt dynamics and overall hydrological processes in the Baksan River Basin.

MODIS data provide information only on the extent of snow cover but not on snow depth. In high-mountain regions, the accurate monitoring of snow depth is challenging because of the extremely limited number of snow measurement stations. Therefore, when validating the model based on snow cover, we primarily assessed the spatiotemporal dynamics of its distribution, whereas the contribution of snowmelt to total runoff can only be inferred indirectly through isotope analysis.

The similarity between the daily values of snowmelt and rainfall runoff, estimated through isotope partitioning, and the corresponding monthly average values derived from the model increases confidence in the accurate representation of runoff formation processes in the Baksan River Basin. Such evidence is essential for the physical justification of the long-term runoff change forecasts based on this model.

To accurately compare the absolute values of runoff components from the ECOMAG model simulation with isotope analysis results, continuous sampling at selected river cross-sections is necessary.

The comparison between simulated glacial runoff and ablation produced less than optimal results. The outcome suggests potential inaccuracies in the parameterization of the model or limitations in its ability to represent the complex glacial topography. The underestimation of the model's ablation can be explained by the fact that the

catchment where the glacier is located has a dissected relief with steep slopes, resulting in uneven distribution and melting of the snow cover. In the model, the entire catchment is given a single elevation corresponding to its geometric center, which does not accurately reflect the complex processes of snow and ice melting in such a terrain.

In reality, these processes are much more complex, leading to a systematic error in the model results, which are underestimated compared with the actual conditions. The large relative error in the ablation model for the Djankuat glacier may be due to the significant proportion of avalanche-fed ice, for which the runoff formation model did not account. In contrast, avalanche activity is absent on the Garabashi glacier, making it a more suitable location for testing these models. Detailed models of snow and ice melting in the nival-glacial zone for individual glaciers, such as those proposed by other authors (Fyffe et al. 2021; Kinnard et al. 2021; Rets et al. 2021; Van Pelt et al. 2019), provide the opportunity to take into account the topographic features and describe the melting process in greater detail.

According to the results of this study, the simulated glacial runoff of the Elbrus glaciers using the A-Melt model is in good agreement with the values obtained by the ECOMAG model. At the same time, the ECOMAG model showed higher values of the snow component of runoff and lower values of the ice component of runoff compared to the results of modeling according to the A-Melt model. This variation can be explained by the differences in approaches to glacial runoff calculations. The glacier block of the ECOMAG runoff formation model operates as follows: elementary catchments with glaciation are delineated, as well as the fractional extent of glaciation within each elementary catchment. At the onset of summer, when the catchment is snow-covered, only the snow melts. As snowmelt proceeded, the fractional snow cover of the computational element decreased. When the fractional snow cover became less than the fractional extent of glaciation, ice began to melt in the area exposed to snow. The ice melt calculation depended on the ice melt coefficient set in the model. The values for the ECOMAG model were obtained at the central point of the catchment. The snow and ice delineation in the A-Melt model is based on process modeling, and a surface type is determined for each point of the spatially distributed grid. The differences in the results are primarily due to the greater detail of the description of the processes in the A-melt model. In the ECOMAG model, the quantitative assessment of ice and snow melting and all related processes is described mainly by the snow and ice melting coefficients. Therefore, the resulting differences in the estimates of the ice and snow components of runoff are likely due to an underestimation of the ice melt coefficient in the ECOMAG model or an underestimation of the percentage of the elementary catchment area occupied by glaciers. This conclusion is supported by the fact that the ECOMAG model underestimates the melt rates of the Garabashi and Djankuat glaciers.

Refining glacier-related inputs, such as surface type, melt coefficients, and meteorological data, can enhance the performance of the model in simulating glacial runoff dynamics. Research has long focused on improving the glacial component of hydrological models (Addor et al. 2014; Etter et al. 2017; Finger et al. 2015; Horton et al. 2006). However, glaciers are not well represented in large-scale models. Most models use the temperature index method, which applies a melting coefficient to simplify complex glacial processes. To improve accuracy, it is essential to couple glacial and hydrological models that can help predict future discharge changes more reliably, especially in large glacier-fed rivers, where meltwater plays a crucial role. A better representation of glaciers is particularly important for assessing the impact of climate change, especially during summer and extreme years.

CONCLUSIONS

For the first time, the ECOMAG model was tested and validated using a range of resources, including MODIS snow cover data, isotope hydrograph separation, glacier mass balance observations, and glacial runoff simulations from the A-Melt model. This study is the first to compare the results from two independent models (ECOMAG and A-Melt) to assess glacial runoff and refine the distribution of snow and ice melt contributions. Additionally, a quantitative comparison of modeled runoff sources with isotope analysis data was performed for the first time to enhance the accuracy of seasonal runoff simulations in glacier-snow-fed basins.

The findings indicate that the ECOMAG simulations performed well in the sparsely gauged Baksan River basin. A good correlation was observed between the simulated and observed daily discharge values for both the calibration and validation periods at Tyrnyauz and Zayukovo stations. The percentage bias in annual runoff volumes was less than 6.5%, and the Nash-Sutcliffe efficiency (NSE) criterion for daily discharge exceeded 0.8 for both periods and locations.

To validate the model, data form the MODIS satellite spectroradiometer were used to measure snow cover in the catchment, confirming that the model accurately simulated seasonal variations in snow cover. The coefficient of determination for the monthly mean snow cover values was 0.85, with a relative error of approximately 20%.

The validation of the snowmelt runoff model based on isotope analysis showed that it accurately reflected the seasonal variation of the input sources. Furthermore, the proportion of meltwater runoff decreased naturally when moving downstream, whereas the proportion of rainfall runoff increased. The similarity between the daily meltwater and liquid precipitation runoff values obtained from isotope hydrograph separation and the monthly averages of the model adds confidence to the accuracy of the representation of snowmelt processes in the Baksan River Basin.

The validation of the model against mass balance measurements of reference glaciers in the central Caucasus (Djankuat and Garabashi) revealed that the processes of snow and ice melting and redistribution in such dissected terrain are more complex in reality, leading to systematic errors. The best agreement was achieved for the Garabashi glacier, with an average relative error of 12%.

Based on a comparison of the model outputs from ECOMAG and A-Melt, the simulated glacial runoff values were in good agreement. However, the results of the modeling indicated differences in the proportion of snow and ice components in the runoff, which can be attributed to differences in the snow and ice delineation methods and methods used to calculate the melting layer of ice and snow within the computational blocks of the models.

The successful calibration and validation processes further demonstrated the flexibility of the ECOMAG model in conducting comprehensive water resource assessments in complex mountainous regions.

REFERENCES

Addor N., Rössler O., Köplin N., Huss M., Weingartner R. and Seibert J. (2014). Robust changes and sources of uncertainty in the projected hydrological regimes of Swiss catchments. Water Resources Research, 50(10), 7541-7562, DOI: 10.1002/2014WR015549.

Ala-Aho P., Tetzlaff D., McNamara J.P., Laudon H. and Soulsby C. (2017). Using isotopes to constrain water flux and age estimates in snow-influenced catchments using the STARR (Spatially distributed Tracer-Aided Rainfall-Runoff) model. Hydrology and Earth System Sciences, 21(10), DOI: 10.5194/hess-21-5089-2017.

Bai P., Liu X. and Liu C. (2018). Improving hydrological simulations by incorporating GRACE data for model calibration. Journal of Hydrology, 557, DOI: 10.1016/j.jhydrol.2017.12.025.

Dozier J., Bair E.H. and Davis R.E. (2016). Estimating the spatial distribution of snow water equivalent in the world's mountains. WIREs Water, 3(3), 461-474, DOI: 10.1002/wat2.1140.

Duethmann D., Peters J., Blume T., Vorogushyn S. and Güntner A. (2014). The value of satellite-derived snow cover images for calibrating a hydrological model in snow-dominated catchments in Central Asia. Water Resources Research, 50(3), 2002-2021, DOI: 10.1002/2013WR014382.

Efstratiadis A. and Koutsoyiannis D. (2010). One decade of multi-objective calibration approaches in hydrological modelling: a review. Hydrological Sciences Journal, 55(1), DOI: 10.1080/02626660903526292.

Eis J., Van der Laan L., Maussion F. and Marzeion B. (2021). Reconstruction of Past Glacier Changes with an Ice-Flow Glacier Model: Proof of Concept and Validation. Frontiers in Earth Science, 9, DOI: 10.3389/feart.2021.595755.

Elagina N., Kutuzov S., Rets E., Smirnov A., Chernov R., Lavrentiev I. and Mavlyudov B. (2021). Mass Balance of Austre Grønfjordbreen, Svalbard, 2006–2020, Estimated by Glaciological, Geodetic and Modeling Aproaches. Geosciences, 11(2), 78, DOI: 10.3390/geosciences11020078.

Elagina N.E., Rets E.P., Korneva I.A. and Lavrentiev I.I. (2025). Simulation of mass balance and glacial runoff of Mount Elbrus from 1984 to 2022. Proceedings of the national open conference State of Mountain Glaciers in the Context of Modern Climate Change, 26-27 (in Russian).

Etter S., Addor N., Huss M. and Finger D. (2017). Climate change impacts on future snow, ice and rain runoff in a Swiss mountain catchment using multi-dataset calibration. Journal of Hydrology: Regional Studies, 13, 222-239, DOI: 10.1016/j.ejrh.2017.08.005.

Finger D., Vis M., Huss M. and Seibert J. (2015). The value of multiple data set calibration versus model complexity for improving the performance of hydrological models in mountain catchments. Water Resources Research, 51(4), 1939-1958, DOI: 10.1002/2014WR015712.

Fyffe C.L., Potter E., Fugger S., Orr A., Fatichi S., Loarte E., Medina K., Hellström R., Bernat M., Aubry-Wake C., Gurgiser W., Perry L.B., Suarez W., Quincey D.J. and Pellicciotti F. (2021). The Energy and Mass Balance of Peruvian Glaciers. Journal of Geophysical Research: Atmospheres, 126(23), 1-22, DOI: 10.1029/2021JD034911.

Gabbi J., Carenzo M., Pellicciotti F., Bauder A. and Funk M. (2014). A comparison of empirical and physically based glacier surface melt models for long-term simulations of glacier response. Journal of Glaciology, 60(224), 1140-1154, DOI: 10.3189/2014JoG14J011.

Gelfan A., Gustafsson D., Motovilov Y., Arheimer B., Kalugin A., Krylenko I. and Lavrenov A. (2017). Climate change impact on the water regime of two great Arctic rivers: modeling and uncertainty issues. Climatic Change, 141(3), 499-515, DOI: 10.1007/s10584-016-1710-5.

Han P., Long D., Han Z., Du M., Dai L. and Hao X. (2019). Improved understanding of snowmelt runoff from the headwaters of China's Yangtze River using remotely sensed snow products and hydrological modeling. Remote Sensing of Environment, 224, DOI: 10.1016/j.rse.2019.01.041.

Hersbach H., Bell B., Berrisford P., Hirahara S., Horányi A., Muñoz-Sabater J., Nicolas J., Peubey C., Radu R., Schepers D., Simmons A., Soci C., Abdalla S., Abellan X., Balsamo G., Bechtold P., Biavati G., Bidlot J., Bonavita M., Thépaut J. (2020). The ERA5 global reanalysis. Quarterly Journal of the Royal Meteorological Society, 146(730), 1999-2049, DOI: 10.1002/qj.3803.

Hock R. (2003). Temperature index melt modelling in mountain areas. Journal of Hydrology, 282, 104-115, DOI: 10.1016/S0022-1694(03)00257-9.

Hoeg S., Uhlenbrook S. and Leibundgut C. (2000). Hydrograph separation in a mountainous catchment - combining hydrochemical and isotopic tracers. Hydrological Processes, 14(7), DOI: 10.1002/(SICI)1099-1085(200005)14:7<1199::AID-HYP35>3.0.CO;2-K.

Holmes T., Stadnyk T.A., Kim S.J. and Asadzadeh M. (2020). Regional Calibration With Isotope Tracers Using a Spatially Distributed Model: A Comparison of Methods. Water Resources Research, 56(9), DOI: 10.1029/2020WR027447.

Holmes T.L., Stadnyk T.A., Asadzadeh M. and Gibson J.J. (2023). Guidance on large scale hydrologic model calibration with isotope tracers. Journal of Hydrology, 621(12), 129604, DOI: 10.1016/j.jhydrol.2023.129604.

Horton P., Schaefli B., Mezghani A., Hingray B. and Musy A. (2006). Assessment of climate-change impacts on alpine discharge regimes with climate model uncertainty. Hydrological Processes, 20(10), 2091-2109, DOI: 10.1002/hyp.6197.

Immerzeel W.W. and Droogers P. (2008). Calibration of a distributed hydrological model based on satellite evapotranspiration. Journal of Hydrology, 349(3-4), DOI: 10.1016/j.jhydrol.2007.11.017.

Justice C.O., Townshend J.R.G., Vermote E.F., Masuoka E., Wolfe R.E., Saleous N., Roy D.P. and Morisette J.T. (2002). An overview of MODIS Land data processing and product status. Remote Sensing of Environment, 83(1-2), DOI: 10.1016/S0034-4257(02)00084-6.

Kinnard C., Larouche O., Demuth M. and Menounos B. (2022). Mass balance modelling and climate sensitivity of Saskatchewan Glacier, western Canada. The Cryosphere Discussions, 16(8), 3071-3099, DOI: https://doi.org/10.5194/tc-16-3071-2022.

Kornilova E. D., Krylenko I.N., Rets E.P., Motovilov Y.G., Korneva I.A., Postnikova T.N. and Rybak O.O. (2024). Changes in water regime in the high-mountain region of the Terek River (North Caucasus) in connection with climate change and degradation of glaciation. Ice and Snow, 64(2), 173-188 (in Russian with English summary), DOI: 10.31857/S2076673424020014.

Kornilova E., Krylenko I., Rets E., Motovilov Y., Atabieva F. and Kuchmenova I. (2023). Simulating Runoff Regime in a Glaciated High-Mountainous Basin: A Case Study of the Baksan River (Caucasus, Russia). Water Resources, 50, 569-576, DOI: 10.1134/S0097807823040140.

Kornilova E.D., Krylenko I.N., Rets E.P., Motovilov Y.G., Bogachenko E.M., Krylenko I.V. and Petrakov D.A. (2021). Modeling of Extreme Hydrological Events in the Baksan River Basin, the Central Caucasus, Russia. Hydrology, 8(1), DOI: 10.3390/hydrology8010024.

Kutuzov S., Lavrentiev I., Smirnov A., Nosenko G. and Petrakov D. (2019). Volume Changes of Elbrus Glaciers From 1997 to 2017. Frontiers in Earth Science, 7, 153, DOI: 10.3389/feart.2019.00153.

Lettenmaier D.P., Alsdorf D., Dozier J., Huffman G.J., Pan M. and Wood E.F. (2015). Inroads of remote sensing into hydrologic science during the WRR era. Water Resources Research, 51(9), 7309-7342, DOI: 10.1002/2015WR017616.

Li X., Wang N. and Wu Y. (2022). Automated Glacier Snow Line Altitude Calculation Method Using Landsat Series Images in the Google Earth Engine Platform. Remote Sensing, 14(10), 2377, DOI: 10.3390/rs14102377.

Li Y., Grimaldi S., Pauwels V.R.N. and Walker J.P. (2018). Hydrologic model calibration using remotely sensed soil moisture and discharge measurements: The impact on predictions at gauged and ungauged locations. Journal of Hydrology, 557, DOI: 10.1016/j.jhydrol.2018.01.013.

Lisina A.A., Krylenko I.N., Kalugin A.S., Motovilov Y.G., Sazonov A.A. and Frolova N.L. (2023). Assessment of the Kolyma Runoff under Current Climate Changes. Water Resources, 50, 318-322, DOI: 10.1134/S0097807823700513.

Mikhalenko V.N., Kutuzov S.S., Lavrentiev I.I., Toropov P.A., Abramov A.A., Aleshina M.A., Gagarina L.V., Doroshina G.Y., Guinot P., Kozachek

A.V., Legrand M., Lim S., Nagornov O.V., Nosenko G.A., Polukhov A.A., Potemkin A.D., Preunkert S., Rototaeva O.V., Smirnov A.M., Yarinich Y.. (2020). Glaciers and climate of Elbrus. 1st ed. St. Petersburg, Russia: Nestor-Istoriya Publisher. (in Russian)

Motovilov Y.G. (1999). Validation of a distributed hydrological model against spatial observations. Agricultural and Forest Meteorology, 96, 257–277.

Motovilov Y.G. and Gelfan A.N. (2018). Models of flow formation in river basin hydrology. Moscow, Russia: Publisher of the Russian Academy of Sciences (in Russian), DOI: 10.31857/S9785907036222000001.

Motovilov Y. G., Kalugin A.S. and Gelfan A.N. (2017). An ECOMAG-based Regional Hydrological Model for the Mackenzie River basin. EGU General Assembly Conference Abstracts, 8064.

Motovilov Yury G. and Fashchevskaya T.B. (2019). Simulation of spatially-distributed copper pollution in a large river basin using the ECOMAG-HM model. Hydrological Sciences Journal, 64(6), 739-756, DOI: 10.1080/02626667.2019.1596273.

Oshun J., Dietrich W.E., Dawson T.E. and Fung I. (2016). Dynamic, structured heterogeneity of water isotopes inside hillslopes. Water Resources Research, 52(1), 164-189, DOI: 10.1002/2015WR017485.

Parajka J., Naeimi V., Blöschl G. and Komma J. (2009). Matching ERS scatterometer based soil moisture patterns with simulations of a conceptual dual layer hydrologic model over Austria. Hydrology and Earth System Sciences, 13(2), DOI: 10.5194/hess-13-259-2009.

Poméon T., Diekkrüger B., Springer A., Kusche J. and Eicker A. (2018). Multi-Objective Validation of SWAT for Sparsely-Gauged West African River Basins—A Remote Sensing Approach. Water, 10(4), 451, DOI: 10.3390/w10040451.

Popovnin V., Gubanov A., Lisak V. and Toropov P. (2024). Recent Mass Balance Anomalies on the Djankuat Glacier, Northern Caucasus. Atmosphere, 15, 107, DOI: 10.3390/atmos15010107.

Rets E., Khomiakova V., Kornilova E., Ekaykin A., Kozachek A. and Mikhalenko V. (2024). How and when glacial runoff is important: Tracing dynamics of meltwater and rainfall contribution to river runoff from headwaters to lowland in the Caucasus Mountains. Science of The Total Environment, 927, 172201, DOI: 10.1016/j.scitotenv.2024.172201.

Rets E.P., Frolova N.L. and Popovnin V. V. (2011). Simulation of melting of a mountain glacier surface. Ice and Snow, 4, 24–31. (in Russian)

Rets E.P., Petrakov D.A., Belozerov E. V. and Shpuntova A.M. (2021). Mass balance modelling for the sary-tor glacier (The Ak-Shyirak massif, Inner Tien Shan). Earth's Cryosphere, 25(5), DOI: 10.15372/KZ20210504.

Reveillet M., Six D., Vincent C., Rabatel A., Dumont M., Lafaysse M., Morin S., Vionnet V. and Litt M. (2018). Relative performance of empirical and physical models in assessing seasonal and annual glacier surface mass balance of Saint-Sorlin Glacier (French Alps). The Cryosphere, 12, 1367-1386, DOI: 10.5194/tc-12-1367-2018.

RGI Consortium. (2017). Randolph Glacier Inventory - A Dataset of Global Glacier Outlines. (NSIDC-0770, Version 6). National Snow and Ice Data Center. Available at: https://nsidc.org/data/nsidc-0770/versions/6 [Accessed 20 July 2024], DOI: 10.7265/4m1f-gd79.

Rototaeva O.V., Nosenko G.A., Kerimov A.M., Kutuzov S.S., Lavrentiev I.I., Kerimov A.A., Nikitin S.A. and Tarasova L.N. (2019). Changes in the mass balance of the Garabashi glacier (Mt. Elbrus) at the turn of the XX-XXI centuries. Ice and Snow, 59(1), 5-22 (in Russian with English summary), DOI: 10.15356/2076-6734-2019-1-5-22.

Sakai A. and Fujita K. (2017). Contrasting glacier responses to recent climate change in high-mountain Asia. Scientific Reports, 7(1), 1-8, DOI: 10.1038/s41598-017-14256-5.

Schaefli B., Hingray B., Niggli M. and Musy A. (2005). Hydrology and Earth System Sciences A conceptual glacio-hydrological model for high mountainous catchments. Hydrology and Earth System Sciences, 9, 95-109.

Shannon S., Smith R., Wiltshire A., Payne T., Huss M., Betts R., Caesar J., Koutroulis A., Jones D. and Harrison S. (2019). Global glacier volume projections under high-end climate change scenarios. Cryosphere, 13(1), 325-350, DOI: 10.5194/tc-13-325-2019.

Tong R., Parajka J., Salentinig A., Pfeil I., Komma J., Széles B., Kubáň M., Valent P., Vreugdenhil M., Wagner W. and Blöschl G. (2021). The value of ASCAT soil moisture and MODIS snow cover data for calibrating a conceptual hydrologic model. Hydrology and Earth System Sciences, 25(3), 1389-1410, DOI: 10.5194/hess-25-1389-2021.

Toropov P.A., Shestakova A.A., Yarinich Y.I. and Kutuzov S.S. (2023). Modeling Orographic Precipitation Using the Example of Elbrus. Izvestiya, Atmospheric and Oceanic Physics, 59(S1), S8-S22, DOI: 10.1134/S0001433823130108.

Trautmann T., Koirala S., Carvalhais N., Eicker A., Fink M., Niemann C. and Jung M. (2018). Understanding terrestrial water storage variations in northern latitudes across scales. Hydrology and Earth System Sciences, 22(7), DOI: 10.5194/hess-22-4061-2018.

Treichler D. and Kääb A. (2017). Snow depth from ICESat laser altimetry — A test study in southern Norway. Remote Sensing of Environment, 191, 389-401, DOI: 10.1016/j.rse.2017.01.022.

Udnæs H.-C., Alfnes E. and Andreassen L.M. (2007). Improving runoff modelling using satellite-derived snow covered area? Hydrology Research, 38(1), 21-32, DOI: 10.2166/nh.2007.032.

Van Pelt W., Pohjola V., Pettersson R., Marchenko S., Kohler J., Luks B., Hagen J.O., Schuler T. V., Dunse T., Noël B. and Reijmer C. (2019). A long-term dataset of climatic mass balance, snow conditions and runoff in Svalbard (1957-2018). The Cryosphere Discussions, 13(9), 2259-2280, DOI: 10.5194/tc-2019-53.

Vasil'chuk Y.K., Rets E.P., Chizhova J.N., Tokarev I. V., Frolova N.L., Budantseva N.A., Kireeva M.B. and Loshakova N.A. (2016). Hydrograph separation of the Dzhankuat River, North Caucasus, with the use of isotope methods. Water Resources, 43(6), 847-861, DOI: 10.1134/S0097807816060087.

Wanders N., Bierkens M.F.P., de Jong S.M., de Roo A. and Karssenberg D. (2014). The benefits of using remotely sensed soil moisture in parameter identification of large-scale hydrological models. Water Resources Research, 50(8), 6874-6891, DOI: 10.1002/2013WR014639.

Zemp M., Frey H., Gärtner-Roer I., Nussbaumer S.U., Hoelzle M., Paul F., Haeberli W., Denzinger F., Ahlstrøm A.P., Anderson B., Bajracharya S., Baroni C., Braun L.N., Càceres B.E., Casassa G., Cobos G., Dàvila L.R., Delgado Granados H., Demuth M.N., Vincent C. (2015). Historically unprecedented global glacier decline in the early 21st century. Journal of Glaciology, 61(228), 745-762, DOI: 10.3189/2015JoG15J017.

Zhang Y., Chiew F.H.S., Zhang L. and Li H. (2009). Use of remotely sensed actual evapotranspiration to improve rainfall-runoff modeling in Southeast Australia. Journal of Hydrometeorology, 10(4), DOI: 10.1175/2009JHM1061.1.

Zolotarev E.A. and Kharkovets E.G. (2000). Glaciation of Elbrus in the end of XX century (digital orthophoto map of Elbrus for 1997). Materialy Glyatsiologicheskikh Issledovaniy. Data of Glaciological Studies, 89, 175-181.

ges.rgo.ru/jour/

ISSN 2542-1565 (Online)